Dalitz analysis of the three-body charmless decay B0 → K0Sπ+π− with the LHCb spectrometer

Marouen Baalouch

Numéro d'ordre : DU 2652 PCCF T 1511
EDSF : 853

UNIVERSITE BLAISE PASCAL
(U.F.R. Sciences et Technologies)

ECOLE DOCTORALE DES SCIENCES FONDAMENTALES

THESE

présentée pour obtenir le grade de

DOCTEUR D'UNIVERSITE
(SPECIALITE PHYSIQUE DES PARTICULES)

par

Marouen BAALOUCH

DALITZ ANALYSIS OF THE THREE-BODY CHARMLESS DECAY $B^0 \to K^0_S \pi^+ \pi^-$ WITH THE LHCb SPECTROMETER

Thèse soutenue le 14 December 2015 devant la commission d'examen :

Président :	M.	S.	Descotes-Genon
Rapporteurs :	Mme	M.H.	Schune
	M	T.	Latham
Examinateurs :	Mme	H.	Fonvieille
	M	O.	Deschamps
Directeur de thèse :	M	S.	Monteil

Abstract

Studies of charmless three-body decays of the neutral B mesons with a K^0_S in the final state are presented in this thesis. The analyses are performed with the full statistics recorded by the LHCb spectrometer during the Run I of the LHC. The amplitude analysis of the decay $B^0 \to K^0_S\pi^+\pi^-$ represents the main part of this thesis analysis. A time-integrated untagged Dalitz-Plot analysis of the decay is performed. The fit fractions of the quasi-two-body decays are obtained. Likewise, the direct *CP* asymmetries of the quasi-two-body decays $B^0 \to K^{*+}(892)\pi^-$, $B^0 \to K^{*+}_0(1430)\pi^-$, $B^0 \to K^{*+}_2(1430)\pi^-$ and $B^0 \to f_0(980)K^0_S$ are obtained. The largest sensitivity is obtained for $A_{CP}(B^0 \to K^{*+}(892)\pi^-)$. This measurement is the first observation of the *CP* asymmetry with a significance larger then five standard deviations. The measurement is in agreement with the world average, with an improved precision.

Keywords

LHC - CERN - LHCb detector - Standard Model - Particle Physics - Heavy Flavour Physics - CKM Triangle - *CP* Violation - *B* Physics - Direct *CP* Asymmetry - Branching Ratio - Fit Fraction - Charmless decay - Dalitz-Plot - $B^0_{d,s} \to K^0_S h^+h^-$ - $B^0 \to K^0_S\pi^+\pi^-$ - $B^0 \to K^{*+}(892)\pi^-$ - $B^0 \to f_0(980)K^0_S$.

Résumé

Le travail présenté dans cette thèse concerne l'étude des désintégrations en trois corps sans quark charmé des mésons beaux neutres, dont l'état final contient un K^0_S. Ce travail de recherche s'est réalisé dans le cadre de l'éxpérience LHCb au LHC, en analysant un échantillon d'événements de 3 fb^{-1} collecté dans le Run I du LHC. L'analyse d'amplitude de la désintégration $B^0 \to K^0_S\pi^+\pi^-$ représente la partie principale de ce travail de thèse. La mesure des amplitudes est effectuée au moyen d'une étude du plan de Dalitz de la désintégration intégrée dans le temps sans étiquetage de la saveur de la particule belle. Nous avons mesuré les rapports d'embranchements relatives des désintégrations quasi-deux-corps à partir de cette analyse de Dalitz. Également, nous avons mesuré l'asymétrie *CP* directe des désintégrations quasi-deux-corps $B^0 \to K^{*+}(892)\pi^-$, $B^0 \to K^{*+}_0(1430)\pi^-$, $B^0 \to K^{*+}_2(1430)\pi^-$ et $B^0 \to f_0(980)K^0_S$. Nous avons observé pour la première fois l'asymétrie *CP* directe dans la désintégration $B^0 \to K^{*+}(892)\pi^-$ avec une signifiance supérieure à cinq déviations standard. Cette mesure est en accord avec la moyenne mondiale, avec une précision améliorée.

Mots Clés

LHC - CERN - Detecteur LHCb - Physique des Particules - Modèle Standard - Physique des Saveurs Lourdes - Triangle CKM - Violation *CP*- Physique des mesons *B*- Asymétrie *CP* Directe - Rapport d'embranchement - Désintégration sans quark charm - Dalitz-Plot - $B^0_{d,s} \to K^0_S h^+h^-$**-** $B^0 \to K^0_S\pi^+\pi^-$**-** $B^0 \to K^{*+}(892)\pi^-$ **-** $B^0 \to f_0(980)K^0_S$**.**

Remerciements

Depuis des mois j'attends d'écrire cette partie de la thèse qui vient typiquement à la fin de la rédaction et ... nous y voilà !

Ce travail doctoral n'aurait pas pu être réalisé sans le soutien d'un grand nombre de personnes et surtout mon directeur de thèse, M. Stéphane Monteil, professeur à l'université Blaise Pascal. Je ne pourrais jamais le remercier assez pour tout ce qu'il m'a donné. Je suis très reconnaissant pour le temps conséquent qu'il m'a accordé et pour l'aide compétente qu'il m'a apportée, pour sa patience et son encouragement. J'ai beaucoup appris de ses qualités pédagogiques et scientifiques, sa franchise et sa sympathie ainsi de ses qualités humaine exceptionnels.

Je tiens à exprimer toute ma gratitude aux membres du jury. Je remercie M. Sébastien Descotes-Genon qui a bien voulu présider le jury. Merci à mes deux rapporteurs M. Thomas Latham et Mme Marie-Hélène Schune pour leurs suggestions et corrections, ainsi que pour leurs conseils et leur soutien. Je souhaite remercier aussi mes deux examinateurs Mme Hélène Fonvieille et M. Olivier Deschamps pour avoir participé à la soutenance et d'avoir apporté un regard extérieur critique à ce travail.

Je tiens évidemment à remercier tout le groupe LHCb de Clermont-Ferrand pour leur soutien et leurs conseils: M. Pascal PERRET responsable de l'équipe, M. Régis Lefèvre, M. Ziad Ajaltouni, M. Olivier Deschamps, M. Eric Cogneras et M. Valentin Niess. Je souhaite remercier aussi le directeur de laboratoire LPC, M. Alain Falvard pour m'avoir accueilli au sein de ce laboratoire. Mes remerciements vont également à mes collègues pour tous les moments inoubliables partagés dans le laboratoire: Mostafa Hoballah, Jan Maratas, Meriem Ben Ali, Ibrahim El Rifai, Diego Roa Romero, Mohamed Kozeiha, Maxime Vernet, Giulio Gazzouni, Arianna Batista Camejo, Luigi Ligioi et Christos Hadjivasiou. J'ai aussi une pensée pour toutes les personnes avec lesquelles j'ai partagé les pauses-café pleines d'humour et conversations scientifiques: encore Mostafa Hoballah (thanks khayi), Xavier Lopez mon parrain, Alouane Selmi, Arnaud Rozes, Romano Marino, Siavach et Alexandre Claude. Je remercie toutes les personnes formidables que j'ai rencontrées par le biais de LPC ou de CERN. Merci pour votre support et vos encouragements.

Je souhaite remercier spécialement M. Adel Trabelsi, professeur à l'université Tunis El-Manar, pour son encouragement, ses multiples conseils et son soutien, depuis mon master en Tunisie jusqu'à la fin de ma thèse. Enfin, quatre personnes ont fait preuve d'un énorme soutien à mon égard, mes parents, mon frère et mon épouse. Merci à mon père pour tout ce

que m'a apporté et tout ce que m'a donné, merci pour ses soutiens sans failles depuis toujours. Merci à ma mère, elle était toujours à coté de moi malgré la distance et les engagements. Tout ce que je suis ou aspire à devenir, c'est à ma mère que je le dois. Merci à ma très chère et "my beloved" Marwa, pour m'avoir supporté ces derniers temps, toujours avec douceur et bonté. Sa présence et ses encouragements sont pour moi les piliers fondateurs de ce que je suis et de ce que je fais.

Contents

Introduction

The *CP*-violating phase emerging from the Cabibbo-Kobayashi-Maskawa paradigm [1, 2] is enough to describe all *CP*-violating observables measured so far in particle systems [3]. This is the only source of *CP* violation in the Standard Model (SM) which yields measurable *CP*-violating phenomena to date. The existence of new sources of *CP* violation in addition to that predicted by the CKM matrix is made necessary to account for the baryonic asymmetry in the Universe [4] and hence the search for it constitutes an important goal of the current researches in high energy physics.

One appealing approach to search for new sources of *CP* violation consists in studying the decay-time distribution of neutral B meson decays to *CP*-eigenstates hadronic final states mediated by a $b \to s$ loop amplitude (so-called penguin amplitude). Many measurements have been performed by the BaBar and Belle experiments in that respect, such as B^0 decays to ϕK^0_S or $\eta' K^0_S$ to cite only the most sensitive. Gathering all of these studies, the latest results [5] provide a consistent picture with the SM predictions, demanding an improved precision to increase the sensitivity to new *CP*-violating phases.

The decays mentioned above into a final *CP* eigenstate quasi-two body are often contributing to a three-body decay ($B^0 \to f_0(980) K^0_S$ is one of the contributing amplitude to the $B^0 \to K^0_S \pi^+ \pi^-$ decay for instance) and experience from previous experiments has shown that full decay-time-dependent Dalitz plot analysis of a three-body decay is more sensitive than a "quasi-two-body" approach, in particular in the case where broad resonances are contributing to the decay amplitude [6–8]. On a similar note, the Dalitz plot analysis of these decays are necessary inputs in methods to determine CKM phase γ [9–13].

The inclusive decay $B^0 \to K^0_S \pi^+ \pi^-$ provides a rich structure of interfering amplitudes, involving both *CP* eigenstate amplitudes ($B^0 \to \rho^0 K^0_S$, $B^0 \to f_0(980) K^0_S$, *etc.*) and flavour specific amplitudes ($B^0 \to K^{*+}(892)\pi^-$, $B^0 \to K^{*+}_0(1430)\pi^-$ *etc.*). Full decay-time-dependent Dalitz plot analyses of $B^0 \to K^0_S \pi^+ \pi^-$ have been performed by BaBar and Belle experiments [14, 15]. These amplitude analyses rely on model-dependent parameterization of the decay amplitudes. Similar studies of the decay $B^0 \to K^0_S \pi^+ \pi^-$ reconstructed with the LHCb spectrometer are the ultimate goals of the analysis presented in this thesis. However, the statistics of reconstructed decays in the light of the modest flavour tagging w.r.t. the B-factories experiments make that attempt not competitive with the LHC Run I data set. On the contrary, the selection of the reconstructed $B^0 \to K^0_S \pi^+ \pi^-$ that we designed with the LHCb spectrometer results in a purer sample of signal decays than the one obtained in for-

mer experiments. A time-integrated untagged analysis will hence provide a novel view of the hadronic amplitudes model. On top of this, the study of flavour specific quasi two-body decays benefits as well from the cleanliness of the signal events selection, allowing in principle a competitive determination of direct *CP*-violating asymmetries.

Chapter 1

Charmless decays of B mesons in the Standard Model

In this chapter, we describe the scientific context of this thesis work. We start with a brief review of the Standard Model (SM) describing the interactions between elementary particles. Thereafter we discuss the symmetries in particle physics to introduce the formalism used to describe the violation of *CP* symmetry in the SM framework. Finally, we present the physics interest of the three-body charmless hadronic decays.

1.1 *CP* violation in the SM

The SM is a theory that describes all the known phenomena at the subatomic scale. It embodies electromagnetic, strong and weak interactions. The principle of local gauge invariance, which keeps the Lagrangian of the theory invariant under local transformation, plays a crucial role in the construction of the SM. There are two sources of *CP* violation in the SM and we will examine in this Chapter the one provided by the weak interaction.

1.1.1 Introduction to Standard Model

The SM is a renormalizable quantum field theory constructed under the principle of local gauge invariance under the $SU(3)_c \otimes SU(2)_L \otimes U(1)_Y$ symmetry group transformations. These local gauge invariances generate strong, weak and electromagnetic interactions between the elementary fermions, through the exchange of gauge bosons: eight gluons, massless and electrically neutral, for strong interaction, one massless photon for electromagnetic interaction and three massive bosons, charged $W^{\pm}$ and neutral Z for weak interactions. The strong interactions are governed by the group $SU(3)_C$ (the subscript C stands here for the colour, charge of the interaction), whereas the groups $SU(2)_L$ and $U(1)_Y$ give a unified description of electroweak interactions. $SU(2)_L$ is a non-abelian group with the weak isospin as the charge of the interaction and acts only on left-handed fermions. $U(1)_Y$ is the weak hypercharge group, defined by $\frac{Y}{2} = I_3 + Q$, where I_3 is the third weak isospin component and Q is the electric charge.

The masses of both the fermions and mediating bosons are vanishing to preserve the invariance under $SU(2)_L \otimes U(1)_Y$. However, the introduction of a doublet of complex scalar

fields of $SU(2)_L$ breaks spontaneously the symmetry. Three degrees of freedoms can be used to provide masses to the $W^{\pm}$ and Z bosons, while keeping the photon massless. The remaining degree of freedom is the Brout-Englert-Higgs fundamental scalar [16–18]. The discovery of a narrow bosonic state by the ATLAS and CMS experiments (CERN), so far experimentally consistent with both the BEH boson hypothesis and the electroweak precision observables [19], signs a tremendous success of the SM to adequately describe the Nature up to an energy scale $\mathcal{O}(100)$ GeV. The Yukawa couplings of the BEH boson with elementary fermions are proportional to a mass and can be used to describe the fermion masses accordingly. Nothing in the symmetries is fixing there values though. They are hence free parameters of the theory.

The quarks and leptons are divided into three generations, each of them being a doublet of $SU(2)_L$. The first generation of quarks consists of the up- and down-quarks, the second of the charm- and strange-quarks, and the third generation of the top- and beauty-quarks. The leptons and their associated lepton-neutrinos are divided into the electron, muon and tau generations. In addition, each particle has an associated anti-particle with opposite internal quantum numbers. An illustration of the SM matter contents is given in Table 1.1.

Table 1.1: *The three lepton and quark generations. The indices L and R note the particle chirality state, left and right, respectively.*

Generation	Leptons	Quarks
I	$\begin{pmatrix}\nu_e\\ e\end{pmatrix}_L$, e_R	$\begin{pmatrix}u\\ d\end{pmatrix}_L$, u_R, d_R
II	$\begin{pmatrix}\nu_\mu\\ \mu\end{pmatrix}_L$, μ_R	$\begin{pmatrix}c\\ s\end{pmatrix}_L$, c_R, s_R
III	$\begin{pmatrix}\mu_\tau\\ \tau\end{pmatrix}_L$, τ_R	$\begin{pmatrix}t\\ b\end{pmatrix}_L$, t_R, b_R

1.1.2 CKM mixing matrix

The local gauge invariance in the SM forbids fermions and bosons to be massive. The fermion masses are introduced after the spontaneous electroweak symmetry breaking, via Yukawa coupling of fermions, with left and right chirality, to Higgs field, which the Lagrangian density is given by

$$\mathcal{L}_Y = -\lambda^d_{ij}\bar{Q}^{\mathrm{I}_3}_{Li}\phi D^{\mathrm{I}_3}_{Rj} - \lambda^u_{ij}\bar{Q}^{\mathrm{I}_3}_{Li}\phi^* U^{\mathrm{I}_3}_{Rj} + h.c, \tag{1.1}$$

- i and j are for the generation indices,
- $Q^{\mathrm{I}_3}_L, D^{\mathrm{I}_3}_R, U^{\mathrm{I}_3}_R$ are the multiplets of $SU(2)_L \otimes SU(3)_c \otimes U(1)_Y$. $Q^{\mathrm{I}_3}_L = (U, D)^{\mathrm{I}_3}_L$ are the left chirality doublets and $U^{\mathrm{I}_3}_R, D^{\mathrm{I}_3}_R$ the couples of right chirality singlets in weak interaction eigenstates basis.
- ϕ is the Higgs field.

- $\lambda_{ij}^{d,u}$ are the complex matrices 3×3 of the quark-down and -up coupling, respectively.

When the Higgs field acquires a value in the vacuum (v.e.v.) $v = \langle 0|\phi|0\rangle$, the fermion mass terms appear

$$-\frac{\lambda_{ij}^{d}.v}{\sqrt{2}}.\bar{D}_{Li}^{\mathrm{I_3}}D_{Rj}^{\mathrm{I_3}} - \frac{\lambda_{ij}^{u}.v}{\sqrt{2}}.\bar{U}_{Li}^{\mathrm{I_3}}U_{Rj}^{\mathrm{I_3}} + h.c. \tag{1.2}$$

It is worthwhile to move from the basis of the weak interaction eigenstates to mass eigenstates, wherein the coupling matrices will be diagonal of real values. This transformation is made using unitary matrices $\mathcal{U}_L^{u(d)}$ and $\mathcal{U}_R^{u(d)}$

$$\mathcal{U}_L^{u(d)}\frac{\lambda_{ij}^{u}.v}{\sqrt{2}}\mathcal{U}_R^{u(d)} = \begin{pmatrix} m_{u(d)} & 0 & 0 \\ 0 & m_{c(s)} & 0 \\ 0 & 0 & m_{t(b)} \end{pmatrix}.$$

The diagonalization uses separate transformations for quarks of type up and down for the same weak doublet, therefore it is customary to redefine the transformations so that they only apply to type down quark

$$Q_L^{\mathrm{I_3}} = \begin{pmatrix} U_L^{I_3} \\ D_L^{I_3} \end{pmatrix} = (\mathcal{U}_L^{u\dagger})_j \begin{pmatrix} U_{Lj} \\ (\mathcal{U}_L^{u}\mathcal{U}_L^{d\dagger})_{jk}D_{Lk} \end{pmatrix},$$

where the so-called Cabbibo, Kobayashi and Maskawa (CKM) matrix appears

$$V_{CKM} = \mathcal{U}_L^{u}\mathcal{U}_L^{d\dagger} = \begin{pmatrix} V_{ud} & V_{us} & V_{ub} \\ V_{cd} & V_{cs} & V_{cb} \\ V_{td} & V_{ts} & V_{tb} \end{pmatrix}.$$

Thus, the currents responsible for weak interaction are transformed under the influence of the change of weak eigenstates basis to the mass eigenstates by making explicitly appear the CKM matrix elements. The corresponding Lagrangian density invariant under the SU(2) transformations is given by

$$\mathcal{L}_W = i\frac{g_1}{2}\bar{Q}_{Li}^{I_3}\gamma^{\mu}(\vec{\tau}.\vec{W})_{\mu}Q_{Li}^{I3}, \tag{1.3}$$

where g_1 is the weak coupling constant, $\vec{\tau}$ are the Pauli matrices, generators of the SU(2) group and $\vec{W}$ the three additional vectors field brought by the requirement of local gauge invariance. This density becomes in the mass eigenstates basis

$$\mathcal{L}_W = i\frac{g_1}{\sqrt{2}}(\bar{U}_{Li}\gamma^{\mu}\mathcal{U}_{ik}^{u}\mathcal{U}_{kj}^{d\dagger}D_{Lj}{W_{\mu}}^{+} + \bar{D}_{Li}\gamma^{\mu}\mathcal{U}_{ik}^{d}\mathcal{U}_{kj}^{u\dagger}U_{Lj}{W_{\mu}}^{-}) + \frac{ig_1}{2}\bar{Q}_{Li}\gamma^{\mu}\tau^3{W_{\mu}}^{3}Q_{Li}. \tag{1.4}$$

It should be noted that the interactions through neutral currents (the third term in Eq. (1.4)) are not modified. There is actually no tree-level process of flavor changing by neutral current in the Standard Model (FCNC).

1.1.3 CKM parameterisations and representations

The CKM matrix is a 3×3 complex unitary matrix and can as such be parameterised by only four parameters: three mixing angles (rotation angles) and one phase δ

$$V_{\rm CKM} = \mathcal{R}_{23}(\theta_{23}, 0) \otimes \mathcal{R}_{13}(\theta_{13}, \delta_{13}) \otimes \mathcal{R}_{12}(\theta_{12}, 0) \; . \tag{1.5}$$

Among the many possible conventions, a standard choice, adopted by the Particle Data Group [20] reads as

$$V_{\rm CKM} = \begin{pmatrix} c_{12}c_{13} & s_{12}c_{13} & s_{13}e^{-i\delta_{13}} \\ -s_{12}c_{23} - c_{12}s_{23}s_{13}e^{i\delta_{13}} & c_{12}c_{23} - s_{12}s_{13}s_{23}e^{i\delta_{13}} & s_{23}c_{13} \\ s_{12}s_{23} - c_{12}c_{23}s_{13}e^{i\delta_{13}} & -c_{12}s_{23} - s_{12}c_{23}s_{13}e^{i\delta_{13}} & c_{23}c_{13} \end{pmatrix}$$

where $c_{ij} = \cos\theta_{ij}$ and $s_{ij} = \sin\theta_{ij}$, with $i, j = 1, 2, 3$.

There is an alternative popular parameterisation which has been first introduced by Altomari and Wolfenstein [21, 22]. It is inspired by the experimentally observed hierarchy between the matrix element magnitudes $s_{13} \ll s_{23} \ll s_{12} \ll 1$. The four independent parameters are noted λ (which is the sine of Cabibbo angle, $\lambda = 0.22537 \pm 0.00061$ [20]), A, ρ and η and the parameterisation consists of developing the CKM matrix in order of λ power according to

$$s_{12} = \lambda, \; s_{23} = A\lambda^2, \; s_{13}e^{-i\delta} = A\lambda^3(\rho - i\eta) \; . \tag{1.6}$$

This definition ensures the matrix unitarity at all orders. For example, at order $\mathcal{O}(\lambda^4)$, the CKM matrix reads

$$V_{\rm CKM} = \begin{pmatrix} 1 - \lambda^2/2 - 1/8\lambda^4 & \lambda & A\lambda^3(\rho - i\eta) \\ -\lambda & 1 - \lambda^2/2 - 1/8\lambda^4(1 + 4A^2) & A\lambda^2 \\ A\lambda^3(1 - \rho - i\eta) & -A\lambda^2 + A\lambda^4(1 - 2(\rho + i\eta))/2 & 1 - A^2\lambda^4/2 \end{pmatrix} + \mathcal{O}(\lambda^5).$$

The unitarity of the CKM matrix implies various relations between its elements. In particular, the relations involving the b quark are

$$\frac{V_{ud}V_{ub}^*}{V_{cd}V_{cb}^*} + \frac{V_{cd}V_{cb}^*}{V_{cd}V_{cb}^*} + \frac{V_{td}V_{tb}^*}{V_{cd}V_{cb}^*} = 0 \; , \tag{1.7}$$

$$\frac{V_{td}V_{ud}^*}{V_{cd}V_{cb}^*} + \frac{V_{ts}V_{us}^*}{V_{cd}V_{cb}^*} + \frac{V_{tb}V_{ub}^*}{V_{cd}V_{cb}^*} = 0 \; . \tag{1.8}$$

A convenient way of representing the unitarity relations is to display them in the complex plane, hence as a triangle. Fig. 1.1 proposes such a representation of the unitarity triangle for b-quark transitions. The triangle is defined by the angles α, β and γ

$$\alpha = \arg\left(-\frac{V_{td}V_{tb}^*}{V_{ud}V_{ub}^*}\right), \beta = \pi - \arg\left(\frac{V_{td}V_{tb}^*}{V_{cd}V_{cb}^*}\right), \gamma = \arg\left(-\frac{V_{ud}V_{ub}^*}{V_{cd}V_{cb}^*}\right).$$

The apex of the triangle is defined by its coordinates $\bar{\rho} + i\bar{\eta} = -\left(\frac{V_{ud}V_{ub}^*}{V_{cd}V_{cb}^*}\right)$, where

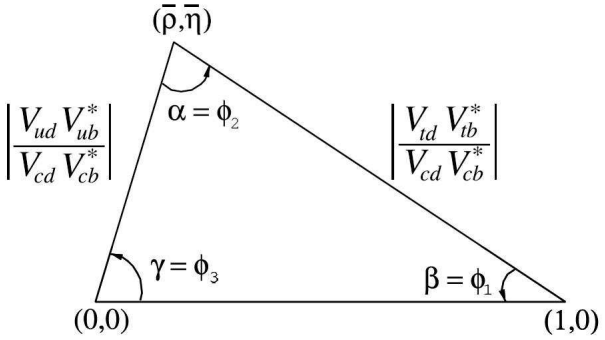

Figure 1.1: *The unitarity triangle with sides of the same λ order with α, β and γ angles associated. The real axis of the complex plane is defined by $\Im(V_{cd}V_{cb}^*) = 0$ and the side lengths are normalized w.r.t. $|V_{cd}V_{cb}^*|$.*

$$\bar{\rho} + i\bar{\eta} = \frac{\sqrt{1-\lambda^2}(\rho + i\lambda)}{\sqrt{1 - A^2\lambda^2} + A^2\lambda^4\sqrt{1-\lambda^2}(\rho + i\lambda)}\,. \tag{1.9}$$

Any non-vanishing value of $\bar{\eta}$ is synonymous of *CP* violation.

1.1.4 *CP* Symmetry

In quantum mechanics, the *CP* transformation combines charge conjugation C with parity P transformations. The parity operator, P, inverts the algebraic sign of all space coordinates used in the description of a physical process. As example, if the parity operator is performed on a scalar wavefunction $\psi(x, y, z, t)$, the latter will transform it to $\psi(-x, -y, -z, t)$. The parity conservation or P-symmetry implies that any physical process will proceed identically when is transformed under parity operator. Before 1956, the general feeling was that all physical process would conserve parity. However, a number of experiments were performed (*e.g.* Wu experiment [23]) and showed that, for processes involving weak interaction, the P-symmetry violated.

Regarding the charge conjugation operator, this transformation changes the sign of all intrinsic additive quantum numbers, as the electric charge, the baryon quantum number, the lepton quantum number, the strangeness, *etc.* The C-symmetry, as the P-symmetry, means the symmetry of physical laws under the charge conjugation transformation. This symmetry is conserved by electromagnetism, gravity and strong interaction, but violated in the weak interactions [24].

Thus, combining the two operators P and C, the *CP* operator will transform, for instance, a left-handed electron e_L^- into a right-handed positron e_R^+ [1]. Therefore, if *CP* were an exact symmetry, the laws of Nature would be the same for matter and antimatter. The violation of this symmetry is subtle and has been difficult to explore. However, Cronin and Fitch [25] performed a beam experiment in 1964 in which they measured the decay of neutral kaons in

[1] In the same space coordinates, P operator inverts the helicity.

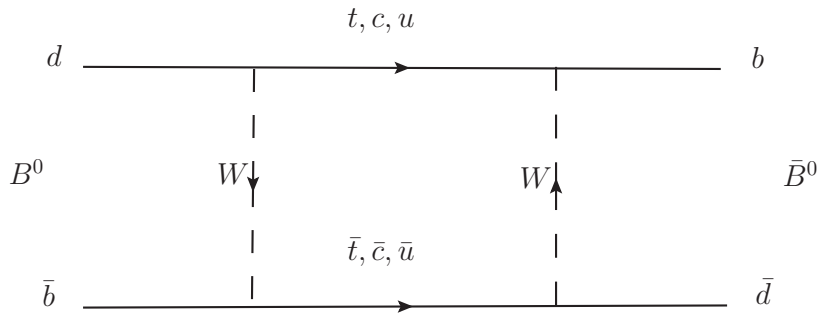

Figure 1.2: *One of the two box diagrams describing the B^0-$\overline{B}^0$ mixing in the SM.*

two pions at the end of long beamline. This experiment showed that there was a small *CP* violation, within weak interaction, in the neutral kaon mixing.

To illustrate the manifestation of *CP* violation with weak interaction in the SM, let's apply the operator *CP* to the first term of the Lagrangian density shown in Eq. (1.4) ($\mathcal{L}_W^{(1)} \xrightarrow{CP} \mathcal{L}_W^{(1)\prime}$)

$$\mathcal{L}_W^{(1)} = i\frac{g_1}{\sqrt{2}}(\bar{U}_{Li}\gamma^\mu \mathcal{U}_{ik}^u \mathcal{U}_{kj}^{d\dagger} D_{Lj} {W_\mu}^+) \,, \tag{1.10}$$

$$\mathcal{L}_W^{(1)\prime} = i\frac{g_1}{\sqrt{2}}(\bar{D}_{Li}\gamma^\mu \mathcal{U}_{ik}^d \mathcal{U}_{kj}^{u\dagger} U_{Lj} {W_\mu}^-) \,. \tag{1.11}$$

Therefore if the matrix element $\mathcal{U}_{ik}^d \mathcal{U}_{kj}^{u\dagger}$ is complex we will have $\mathcal{L}_W^{(1)} \neq \mathcal{L}_W^{(1)\prime}$, which implies a *CP* violation. Then the δ phase introduced in the CKM matrix is a source of *CP* violation in the weak interaction.

1.1.5 *CP* violation in neutral B sector

Despite a large number of attempts to observe *CP* violation phenomena, it took almost forty years to reach a second observation of it. Before addressing the *CP* violation in neutral B mesons, a brief overview is given in the following subsection discussing the quantum mechanics of neutral B mesons.

1.1.5.1 The quantum mechanics of neutral B meson mixing

The neutral B mesons are pseudo-scalar mesons which can have two flavor states, B^0 made of d-quark and $\bar{b}$-quark, and B_s^0 made of s-quark and $\bar{b}$-quark. They can each mix with their respective antiparticle, as illustrated by the Feynman diagram (for B^0-$\overline{B}^0$ mixing) given in Fig. 1.2 (in the following only B^0 meson is considered).

The B^0 and $\overline{B}^0$ mesons are dubbed the flavour eigenstates, whilst the eigenstates of the propagation Hamiltonian are dubbed the mass eigenstates, denoted by B_H and B_L. Thus, the neutral B mesons can be described in term of two physical states combination of the flavor eigenstates

$$\begin{aligned} |B_L\rangle &= p|B^0\rangle + q|\bar{B}^0\rangle \,, \\ |B_H\rangle &= p|B^0\rangle - q|\bar{B}^0\rangle \,, \end{aligned} \tag{1.12}$$

where p and q are the linear complex coefficients satisfying the relation $|p|^2 + |q|^2 = 1$. The states $|B_L\rangle$ and $|B_H\rangle$ are the lighter and heavier mass eigenstates, respectively. The time-dependent Schroedinger equation for these states reads

$$i\frac{\partial}{\partial t}\begin{pmatrix} p \\ q \end{pmatrix} = \mathcal{H}_{\text{eff}}\begin{pmatrix} p \\ q \end{pmatrix} \,, \tag{1.13}$$

where $\mathcal{H}_{\text{eff}}$ is the effective Hamiltonian describing the neutral mesons mixing as follows

$$\begin{aligned} \mathcal{H}_{\text{eff}} = \mathbf{M} - i\frac{\mathbf{\Gamma}}{2} &= \left[\begin{pmatrix} M_{11} & M_{12} \\ M_{21} & M_{22} \end{pmatrix} - \frac{i}{2}\begin{pmatrix} \Gamma_{11} & \Gamma_{12} \\ \Gamma_{21} & \Gamma_{22} \end{pmatrix}\right] \,, \\ &= \begin{pmatrix} \omega_L & 0 \\ 0 & \omega_H \end{pmatrix} \,. \end{aligned} \tag{1.14}$$

$\mathbf{M}$ and $\mathbf{\Gamma}$ are 2×2 Hermitian matrices describing the mass and decay rate component of $\mathcal{H}_{\text{eff}}$, respectively. We take note that the $\mathcal{H}_{\text{eff}}$ matrix is on the contrary not hermitian. In the mass eigenstates $\{|B_L\rangle, |B_H\rangle\}$ basis, $\mathcal{H}_{\text{eff}}$ is diagonal with complex eigenvalues, ω_L and ω_H, expressed as

$$\omega_L = m_L - i\frac{\Gamma_L}{2} \,, \quad \omega_H = m_H - i\frac{\Gamma_H}{2} \,, \tag{1.15}$$

where m_L and m_H are the masses of the eigenstates $|B_L\rangle$ and $|B_H\rangle$, respectively, and Γ_L and Γ_H their decay rate counterpart. The 2-particle system $\{B^0, \bar{B}^0\}$ is characterized by 5 physical observables (named also mixing observables): the mass and decay rate averages, the differences in mass and decay rate, and its "composition fraction" $|q/p|$. The mass and decay rate averages are

$$m = \frac{m_H + m_L}{2} \,, \quad \Gamma = \frac{\Gamma_H + \Gamma_L}{2} \,. \tag{1.16}$$

The differences in mass and decay rate are given by

$$\Delta m = m_H - m_L \,, \quad \Delta\Gamma = \Gamma_H - \Gamma_L \,. \tag{1.17}$$

Δm is always positive in this definition, the sign of $\Delta\Gamma$ depends on which mass eigenstate has the longer lifetime. The sign of $\Delta\Gamma$ is predicted, by the SM, to be negative, but has not yet been established, while is well established in B_s^0-$\overline{B}_s^0$ mixing ($\Delta\Gamma_s = (0.091 \pm 0.008) \times 10^{12}\,\text{s}$ [20]). The values found for the world average of the mass difference measurements [20], are $\Delta m_{B^0} = (3.337 \pm 0.033) \times 10^{-10}\,\text{MeV}$ and $\Delta m_{B_s^0} = (1.1691 \pm 0.00014) \times 10^{-8}\,\text{MeV}$. As mentioned above, the decay rate difference has on the contrary not yet been observed and we consider it negligible in the following study.

The parameters p and q are related to the off-diagonal elements of $\mathcal{H}_{\text{eff}}$ along

$$\left(\frac{q}{p}\right)^2 = \frac{M_{12}^* - \frac{i}{2}\Gamma_{12}^*}{M_{12} - \frac{i}{2}\Gamma_{12}} \,, \tag{1.18}$$

If *CP* were a symmetry of $\mathcal{H}_{\rm eff}$, then Γ_{12}/M_{12} would be real, leading to

$$\left(\frac{q}{p}\right)^2 = e^{2i\theta(B^0)} \quad \Rightarrow \quad \left|\frac{q}{p}\right| = 1 \,, \tag{1.19}$$

where $\theta(B^0)$ is an arbitrary phase occurring in the action of *CP* operator on the state $|B^0\rangle$ ($|\overline{B}^0\rangle$) which transforms it to $|\overline{B}^0\rangle$ ($|B^0\rangle$)

$$CP|B^0\rangle = e^{2i\theta(B^0)}|\overline{B}^0\rangle \,, \quad CP|\overline{B}^0\rangle = e^{-2i\theta(B^0)}|B^0\rangle \,. \tag{1.20}$$

1.1.5.2 Time evolution of B^0 ($\overline{B}^0$) meson

The time evolution of the states $|B^0(t)\rangle$ and $|\overline{B}^0(t)\rangle$ can be expressed in terms of initially pure flavor states $|B^0(t=0)\rangle \equiv |B^0\rangle$ and $|\overline{B}^0(t=0)\rangle \equiv |\overline{B}^0\rangle$

$$\begin{aligned} |B^0(t)\rangle &= g_+(t)|B^0\rangle - \frac{q}{p}g_-(t)|\overline{B}^0\rangle \,, \\ |\overline{B}^0(t)\rangle &= g_+(t)|\overline{B}^0\rangle - \frac{q}{p}g_-(t)|B^0\rangle \,, \end{aligned} \tag{1.21}$$

with

$$g_\pm(t) = \frac{1}{2}\left(e^{-im_Ht-\frac{1}{2}\Gamma_Ht} \pm e^{-im_Lt-\frac{1}{2}\Gamma_Lt}\right) \,. \tag{1.22}$$

We then find

$$\begin{aligned} |g_\pm(t)|^2 &= \frac{1}{4}\left[e^{-\Gamma_Ht} - e^{-\Gamma_Lt} \pm 2\,{\rm Re}\left(e^{-\frac{1}{2}(\Gamma_H+\Gamma_L)-i(m_H-m_L)t}\right)\right] \,, \\ &= \frac{1}{2}e^{-\Gamma t}\left[\cosh\left(\frac{\Delta\Gamma t}{2}\right) \pm \cos(\Delta m t)\right] \,. \end{aligned} \tag{1.23}$$

and

$$\begin{aligned} g_+^*(t)g_-^*(t) &= \frac{1}{4}\left[e^{-\Gamma_Ht} - e^{-\Gamma_Lt} - 2i\,{\rm Im}\left(e^{-\frac{1}{2}(\Gamma_H+\Gamma_L)-i(m_H-m_L)t}\right)\right] \,, \\ &= -\frac{1}{2}e^{-\Gamma t}\left[\sinh\left(\frac{\Delta\Gamma t}{2}\right) + i\sin(\Delta m t)\right] \,. \end{aligned} \tag{1.24}$$

The decay rate of a $|B^0\rangle$ meson produced at time $t = 0$ to a final state f at time t is given by

$$\begin{aligned}\frac{\mathrm{d}\Gamma_{B^0\to f(\bar{f})}(t)}{\mathrm{d}t} &= |\langle f(\bar{f})|\mathcal{T}|B^0(t)\rangle|^2 \,, \\ \frac{\mathrm{d}\Gamma_{\overline{B}^0\to \bar{f}(f)}(t)}{\mathrm{d}t} &= |\langle \bar{f}(f)|\mathcal{T}|\overline{B}^0(t)\rangle|^2 \,, \end{aligned} \tag{1.25}$$

where $\mathcal{T}$ is the transition matrix.

The time-dependent decay rates of the initially produced flavor eigenstates $|B^0\rangle$ and $|\overline{B}^0\rangle$, assuming $\Delta\Gamma = 0$ ($\cosh\left(\frac{\Delta\Gamma t}{2}\right) = 1$, $\sinh\left(\frac{\Delta\Gamma t}{2}\right) = 0$), are given by the four possible decay equations

$$\frac{\mathrm{d}\Gamma_{B^0\to f}(t)}{\mathrm{d}t} = \frac{e^{-\Gamma t}}{2}|A_f|^2(1+|\lambda_f|^2)[1 + C_f\cos(\Delta m t) - S_f\sin(\Delta m t)] \,, \tag{1.26}$$

$$\frac{\mathrm{d}\Gamma_{\overline{B}^0\to f}(t)}{\mathrm{d}t} = \frac{e^{-\Gamma t}}{2}\left|\frac{q}{p}\right|^2|A_f|^2(1+|\lambda_f|^2)[1 - C_f\cos(\Delta m t) + S_f\sin(\Delta m t)] \,, \tag{1.27}$$

$$\frac{\mathrm{d}\Gamma_{\overline{B}^0\to \bar{f}}(t)}{\mathrm{d}t} = \frac{e^{-\Gamma t}}{2}|\bar{A}_{\bar{f}}|^2(1+|\bar{\lambda}_{\bar{f}}|^2)[1 + C_{\bar{f}}\cos(\Delta m t) - S_{\bar{f}}\sin(\Delta m t)] \,, \tag{1.28}$$

$$\frac{\mathrm{d}\Gamma_{B^0\to \bar{f}}(t)}{\mathrm{d}t} = \frac{e^{-\Gamma t}}{2}\left|\frac{q}{p}\right|^2|\bar{A}_{\bar{f}}|^2(1+|\bar{\lambda}_{\bar{f}}|^2)[1 - C_{\bar{f}}\cos(\Delta m t) + S_{\bar{f}}\sin(\Delta m t)] \,, \tag{1.29}$$

where $A_f = \langle f|\mathcal{T}|B^0\rangle$ and $\bar{A}_{\bar{f}} = \langle \bar{f}|\mathcal{T}|\overline{B}^0\rangle$ are the decay amplitudes for $|B^0\rangle$ and $|\overline{B}^0\rangle$ decaying to the final state $|f\rangle$ and $|\bar{f}\rangle$, respectively, and λ_f and $\bar{\lambda}_{\bar{f}}$ are defined as

$$\lambda_f = \frac{1}{\bar{\lambda}_f} = \frac{q}{p}\frac{\bar{A}_f}{A_f} \,, \qquad \bar{\lambda}_{\bar{f}} = \frac{1}{\lambda_{\bar{f}}} = \frac{q}{p}\frac{A_{\bar{f}}}{\bar{A}_{\bar{f}}} \,. \tag{1.30}$$

Similarly, $\bar{A}_f = \langle f|\mathcal{T}|\overline{B}^0\rangle$ and $A_{\bar{f}} = \langle \bar{f}|\mathcal{T}|B^0\rangle$. Here, C_f, S_f, $C_{\bar{f}}$ and $S_{\bar{f}}$ are the *CP violation observables*, discussed in details in the following section. they can be defined as

$$\begin{aligned} C_f &= \frac{1-|\lambda_f|^2}{1+|\lambda_f|^2} \,, \quad S_f = \frac{2\mathrm{Im}(\lambda_f)}{1+|\lambda_f|^2} \,, \\ C_{\bar{f}} &= \frac{1-|\lambda_{\bar{f}}|^2}{1+|\lambda_{\bar{f}}|^2} \,, \quad S_{\bar{f}} = \frac{2\mathrm{Im}(\lambda_{\bar{f}})}{1+|\lambda_{\bar{f}}|^2} \,. \end{aligned} \tag{1.31}$$

The evaluation of the *CP* violation parameters is performed by the comparison between the decay rates $\Gamma(B^0 \to f)$ and $\Gamma(CP(B^0 \to f))$, where $CP(B^0 \to f)$ is the process $B^0 \to f$ transformed under *CP* operator. The definition of the *CP* asymmetry is given by

$$\mathcal{A}_{CP} = \frac{\Gamma_{CP(B^0\to f)} - \Gamma_{B^0\to f}}{\Gamma_{CP(B^0\to f)} + \Gamma_{B^0\to f}} \,. \tag{1.32}$$

$\mathcal{A}_{CP} \neq 0$ is a sign of *CP* violation. In general, the observation of *CP* violation relies on noticeable differences among processes and their corresponding *CP*-conjugates. The observation of *CP* is related to the interference between different amplitudes that contribute to these processes, manifested by the complex phase in the coupling that breaks *CP* invariance, more

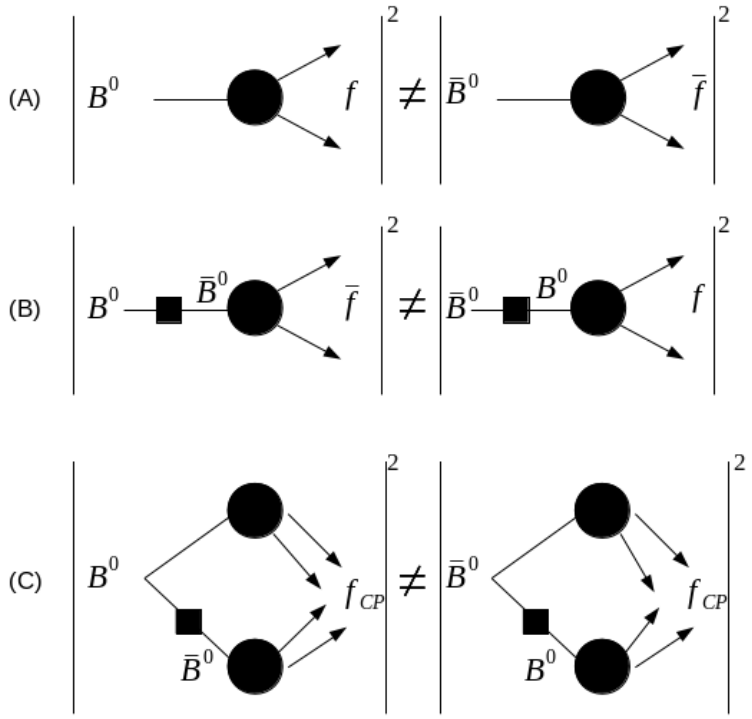

Figure 1.3: *Diagrams showing the three type of CP violation: (A) CP violation in decay, (B) CP violation in mixing and (C) CP violation between decays with and without mixing.*

details are given in Section 1.1.5.3. The possible manifestation of *CP* violation can be classified in three categories: (A) *CP* violation in decay, (B) *CP* violation in mixing and (C) *CP* violation between decays with and without mixing (Mixing-induced *CP* violation). Fig. 1.3 illustrates each manifestation type of *CP* violation. In each case there is a corresponding observable of *CP* violation. All *CP* violation observables in the processes of $B^0/\overline{B}^0$ decaying to the final state $f(\bar{f})/\bar{f}(f)$ can be expressed in terms of phase-convention-independent combination of A_f, $\bar{A}_f$, $A_{\bar{f}}$ and $\bar{A}_{\bar{f}}$ with q/p.

1.1.5.3 *CP* violation in decay

This type of *CP* violation is a direct *CP* violation, which requires a flavour-tagging information on the initial state in the neutral B decays, *i.e.* a distinction between the decays of B^0 and $\overline{B}^0$ to a final state f and $\bar{f}$, respectively, where

$$CP|f\rangle = e^{2i\theta(f)}|\bar{f}\rangle \ .$$

$\theta(f)$ here is is an arbitrary phase. The manifestation of *CP* violation in this case occurs if $\Gamma(B^0 \to f)$ is different from $\Gamma(\overline{B}^0 \to \bar{f})$. The terms λ_f and $\bar{\lambda}_{\bar{f}}$ in equations (1.26) and (1.28) are zero. Thus the process rate will be proportional to the total amplitude square. The *CP* asymmetry can be written as

$$\mathcal{A}_{CP} = \frac{|\bar{A}_{\bar{f}}|^2 - |A_f|^2}{|\bar{A}_{\bar{f}}|^2 + |A_f|^2} \ , \tag{1.33}$$

hence, the *CP* violation in decay occurs when

$$\frac{|\bar{A}_{\bar{f}}|}{|A_f|} \neq 1 \quad \Longrightarrow \quad CP \text{ violation.} \tag{1.34}$$

If several amplitudes j contribute to the decay $B^0(\overline{B}^0) \to f(\bar{f})$, the total amplitude A_f and its *CP* conjugate amplitude $\bar{A}_{\bar{f}}$ can be defined in term of a real magnitude a_j, weak phase ϕ_j and strong phase δ_j:

$$\begin{aligned} A_f &= \sum_j a_j e^{i(\delta_j+\phi_j)} , \\ \bar{A}_{\bar{f}} &= \sum_j a_j e^{i(\delta_j-\phi_j)} . \end{aligned} \tag{1.35}$$

The *CP* asymmetry becomes

$$\mathcal{A}_{CP} = \frac{2\sum_{jk} a_j a_k \sin(\delta_j - \delta_k)\sin(\phi_j - \phi_k)}{\sum_{jk} a_j^2 + a_k^2 + 2a_j a_k \cos(\delta_j - \delta_k)\cos(\phi_j - \phi_k)} , \tag{1.36}$$

From equation (1.36) it can been seen that $\mathcal{A}_{CP}$ will have a non-zero value if the weak phases, as well as the strong phases, from the processes that contributes to the final state are different. The interference is a key requirement for the manifestation of *CP* violation, which the amplitude A_f should have at least two contributing complex amplitudes with different weak and strong phase, the reason for that comes from the fact that *CP*-conjugate amplitude differ from the original amplitudes at most by a phase factor. The *CP* violation in decay is most thoroughly studied in b-hadron decays to charmless two body final states. An appropriate example is $B^0 \to K^+\pi^-$ [26].

1.1.5.4 *CP* violation in mixing

The *CP* violation in mixing is an indirect *CP* violation, which implies that the oscillation from B^0 to $\overline{B}^0$ is different from the oscillation $\overline{B}^0$ to B^0

$$\Gamma(B^0 \to \overline{B}^0) \neq \Gamma(\overline{B}^0 \to B^0) \quad \Longrightarrow \quad CP \text{ violation in mixing.} \tag{1.37}$$

The *CP* asymmetry can be written as

$$\begin{aligned} \mathcal{A}_{cp} &= \frac{\Gamma_{\overline{B}^0\to B^0} - \Gamma_{B^0\to\overline{B}^0}}{\Gamma_{\overline{B}^0\to B^0} + \Gamma_{B^0\to\overline{B}^0}} , \\ &= \frac{\left|\langle B^0|\mathcal{H}_{\text{eff}}|\overline{B}^0\rangle\right| - \left|\langle\overline{B}^0|\mathcal{H}_{\text{eff}}|B^0\rangle\right|}{\left|\langle B^0|\mathcal{H}_{\text{eff}}|\overline{B}^0\rangle\right| + \left|\langle\overline{B}^0|\mathcal{H}_{\text{eff}}|B^0\rangle\right|} . \end{aligned} \tag{1.38}$$

To check that the difference between $\left|\langle B^0|\mathcal{H}_{\text{eff}}|\overline{B}^0\rangle\right|$ and $\left|\langle\overline{B}^0|\mathcal{H}_{\text{eff}}|B^0\rangle\right|$ is a sign of mixing *CP* violation, we apply the *CP* operator on the two terms

$$\begin{aligned}
\langle B^0|\mathcal{H}_{\rm eff}|\overline{B}^0\rangle &\xrightarrow{CP} \langle B^0|(CP)^\dagger(CP)\mathcal{H}_{\rm eff}(CP)^\dagger(CP)|\overline{B}^0\rangle \\
&= \langle B^0|(CP)^\dagger\mathcal{H}_{\rm eff}^{CP}(CP)|\overline{B}^0\rangle \\
&= e^{-4i\theta(B^0)}\langle\overline{B}^0|\mathcal{H}_{\rm eff}^{CP}|B^0\rangle\ , \qquad (1.39)\\
\langle\overline{B}^0|\mathcal{H}_{\rm eff}|B^0\rangle &= e^{4i\theta(B^0)}\langle B^0|\mathcal{H}_{\rm eff}^{CP}|\overline{B}^0\rangle\ , \qquad (1.40)
\end{aligned}$$

where $\mathcal{H}_{\rm eff}^{CP} = (CP)\mathcal{H}_{\rm eff}(CP)^\dagger$ and $\theta(B^0)$ is the arbitrary unphysical phase introduced in Eq. (1.20). So, if CP is a symmetry of $\mathcal{H}_{\rm eff}$ then $[\mathcal{H}_{\rm eff}, CP] = 0$, which implies

$$\mathcal{H}_{\rm eff} = \mathcal{H}_{\rm eff}^{CP} \quad \Longrightarrow \quad \left|\langle B^0|\mathcal{H}_{\rm eff}|\overline{B}^0\rangle\right| = \left|\langle\overline{B}^0|\mathcal{H}_{\rm eff}|B^0\rangle\right|\ . \qquad (1.41)$$

If the terms of Eq. (1.38) are described in the mass eigenstates basis $\{|B_L\rangle, |B_H\rangle\}$, the CP asymmetry becomes

$$\mathcal{A}_{CP} = \frac{\left|\frac{p}{q}\right| - \left|\frac{q}{p}\right|}{\left|\frac{p}{q}\right| + \left|\frac{q}{p}\right|}\ . \qquad (1.42)$$

Therefore, CP violation in mixing occurs if

$$\left|\frac{p}{q}\right| \neq 1 \quad \Longrightarrow \quad CP \text{ violation in mixing.} \qquad (1.43)$$

as was introduced earlier in this Chapter.

The CP violation in mixing was observed experimentally in the neutral kaon system in 1964 [25]. CP violation in the B^0-$\overline{B}^0$ or B_s^0-$\overline{B}_s^0$ mixings is expected to be negligible in the SM [27–29]. It has not been observed so far. In the following, we will assume that $|q/p| = 1$, unless otherwise stated.

1.1.5.5 Mixing-induced CP violation

CP violation in the interference between decays with and without mixing occurs for the decays of B^0 and $\overline{B}^0$ to a final state f which is a CP-eigenstate

$$B^0(\rightarrow\overline{B}^0) \rightarrow f \leftarrow (B^0\leftarrow)\overline{B}^0\ , \quad CP|f\rangle = \eta_{CP}|f\rangle\ ,$$

where η_{CP} is a CP-eigenvalue equal to 1 or -1. In the following, the final state CP-eigenstate will be noted as f_{CP}.

This type of CP violation comes from the interference of mixing and decay amplitudes $A(B^0 \rightarrow \overline{B}^0 \rightarrow f_{CP})$ and $A(B^0 \rightarrow f_{CP})$, respectively.

The time-dependent mixing-induced CP asymmetry reads

$$\mathcal{A}_{CP}(t) = \frac{\frac{{\rm d}\Gamma_{\overline{B}^0\rightarrow f}(t)}{{\rm d}t} - \frac{{\rm d}\Gamma_{B^0\rightarrow f}(t)}{{\rm d}t}}{\frac{{\rm d}\Gamma_{\overline{B}^0\rightarrow f}(t)}{{\rm d}t} + \frac{{\rm d}\Gamma_{B^0\rightarrow f}(t)}{{\rm d}t}}\ . \qquad (1.44)$$

using Eq.(1.26) and (1.27) (or Eq.(1.28) and (1.29)), the CP asymmetry reads

$$\mathcal{A}_{CP}(t) = S\sin(\Delta m t) - C\cos(\Delta m t)\ , \qquad (1.45)$$

where

$$S \equiv S_{f_{CP}} = \eta_{f_{CP}} \frac{2\mathrm{Im}(\lambda_{f_{CP}})}{1+|\lambda_{f_{CP}}|^2}\,, \quad C \equiv C_{f_{CP}} = \eta_{CP} \frac{1-|\lambda_{f_{CP}}|^2}{1+|\lambda_{f_{CP}}|^2}. \tag{1.46}$$

Therefore, mixing-induced *CP* violation occurs if $S \neq 0$.

1.2 Constraints on CKM matrix elements

1.2.1 Magnitudes of the matrix elements

The nine CKM matrix elements V_{jk} are, in principle, accessible experimentally thanks to the coupling $W^{\pm}q^j\bar{q}^k$. The aim of this section is to recapitulate the numerical values of the CKM matrix elements currently measured:

- $|V_{ud}|$: this matrix element can be measured by means of three different methods: the nuclear β decay, the neutron lifetime and the pion β decay $\pi^+ \to \pi^0 e^+ \nu$. Currently, the world best average [30] reads: $|V_{ud}| = 0.97425 \pm 0.00022$.

- $|V_{us}|$: this matrix element is mainly determined from the measurement of the semileptonic kaon decays. The current average value from the PDG [20] is $|V_{us}| = 0.2253 \pm 0.0008$.

- $|V_{cd}|$: the magnitude of this matrix element can be evaluated from semileptonic charm decays, *e.g.* $D \to \pi l \nu$. The other possibility to measure this parameter is via neutrino and antineutrino interactions [31]. The average value given by the PDG [20] is $|V_{cd}| = 0.225 \pm 0.008$.

- $|V_{cs}|$: the magnitude of this matrix element can be determined directly by means of the semileptonic decays of D or leptonic decays of D_s. It is also possible to use flavour tagged W decays [32]. The world average value [20] reads: $|V_{cd}| = 0.986 \pm 0.016$.

- $|V_{cb}|$: this parameter can be determined from exclusive and inclusive semileptonic decays of B mesons into charm, its average value given by the PDG [20] reads: $|V_{cb}| = (41.1 \pm 1.3) \times 10^{-3}$.

- $|V_{ub}|$: the determination of this parameter can be performed from the inclusive decay $B \to X_u l \bar{\nu}$, where X_u is charmless hadronic final state. In addition, exclusive determination of $|V_{ub}|$ come from the study of $B \to \pi l \bar{\nu}_l$. The average value given by the PDG [20] is $|V_{ub}| = (4.13 \pm 0.49) \times 10^{-3}$.

- $|V_{td}|$ and $|V_{ts}|$: These two parameters can be measured in the oscillation of B^0-$\overline{B}^0$ and B_s^0-$\overline{B}_s^0$, where top quark appears in box diagrams, or in rare decays where top quark can be found in loop diagrams in the SM. The average value given by the PDG [20] for the ratio of the magnitudes of these matrix elements is: $|V_{td}/V_{ts}| = 0.21 \pm 0.04$.

- $|V_{tb}|$: the determination of this element matrix is made using the ratio of branching fractions [33] $R = \mathcal{B}(t \to Wb)/(t \to Wq) = |V_{tb}|^2/(\sum_q |V_{tq}|^2) = |V_{tb}|^2$, where $q = b, s, d$. Another possible determination of $|V_{tb}|$ makes used the single top-quark-production cross section. The average given by the PDG [20] for the magnitude of this matrix element is: $|V_{tb}| = 1.021 \pm 0.032$.

1.2.2 CKM angles

The measurements of the angles of the unitarity CKM triangle Fig. 1.1 are important for determining the degree of *CP* violation in the standard model. To constraint these three angles α, β and γ, several *CP*-violating observables can be used:

- α angle: the time-dependent *CP* asymmetry in $b \to u\bar{u}d$ decay dominated modes, allows to measure $\sin 2\alpha$. Practically, the measurements are taken on the decays $B \to \pi\pi$, $B \to \rho\pi$ and $B \to \rho\rho$.

- β angle: it represents the mixing angle of the B^0 mesons in the SM and is measured through time-dependent *CP* asymmetry to a final state *CP*-eigenstate (cf: Section 1.3.1).

- γ angle: it can be measured in tree-level B decays. For example, the interference of $B^- \to D^0 K^-$ and $B^- \to \bar{D}^0 K^-$ gives access to the γ angle.

Fig. 1.4 superimpose all recent CKM constraints determined under the SM hypothesis in the plane $(\bar{\rho}, \bar{\eta})$ (see Ref. [3]).

1.3 Charmless three-body neutral B decays

The B^0 and B_s^0 mesons offer a relevant environment for studying *CP* violation as the non-squashed unitarity triangles involve quark transitions with the b-quark. Several parameters of the unitarity CKM triangle can be accessible by B mesons physics, such as the magnitude of the matrix elements $|V_{cb}|$, $|V_{ub}|$, $|V_{td}|$ and $|V_{ts}|$ as well as the three angles given in the previous section α, β and γ.

Among the different types of neutral B decays, the three-body charmless neutral B decays is the process studied in this thesis work. This type of decays provides a rich laboratory for studying different aspects as *CP* violation, strong interaction, constraints in the CKM triangle *etc.*. In addition, the specific charmless hadronic final state, including a K_S^0 meson, namely $B_{d,s}^0 \to K_S^0\pi^+\pi^-$, $B_{d,s}^0 \to K_S^0 K^\pm\pi^\mp$ and $B_{d,s}^0 \to K_S^0 K^+ K^-$, has a variety of physics interpretations. The final states $B^0 \to K_S^0\pi^+\pi^-$ and $B^0 \to K_S^0 K^+ K^-$ allow for the measurement of the weak phase of B^0-$\overline{B}^0$ mixing in $b \to q\bar{q}s$ transitions, which can be obtained, for example, by a time-dependent tagged analysis of the three-body Dalitz plot. The comparison of the weak phase determination in $b \to q\bar{q}s$ and $b \to c\bar{c}s$ transitions can be a measure of New Physics (NP) contributions (see Section 1.3.1), under the assumption that the $b \to c\bar{c}s$ transition is dominated by SM processes. Studying the decay $B_s^0 \to K_S^0\pi^+\pi^-$ is a necessary ingredient for a clean extraction of γ in charmless decays (Ref. [35]) by means of an analysis of the ratio of the amplitude of the isospin-related mode $B_s^0 \to K^-\pi^+\pi^0$ and its charge conjugate, where a direct dependence on the weak phase $(\beta_s + \gamma)$ is exhibited. In that case, an analysis of the $B_s^0 \to K_S^0\pi^+\pi^-$ Dalitz plot will be required [36]. Eventually the decay $B_s^0 \to K_S^0 K^\pm\pi^\mp$ can allow to measure the weak phase of B_s^0-$\overline{B}_s^0$ mixing, analogously to $B^0 \to K_S^0\pi^+\pi^-$. However, the significant lifetime difference between the light and heavy B_s^0

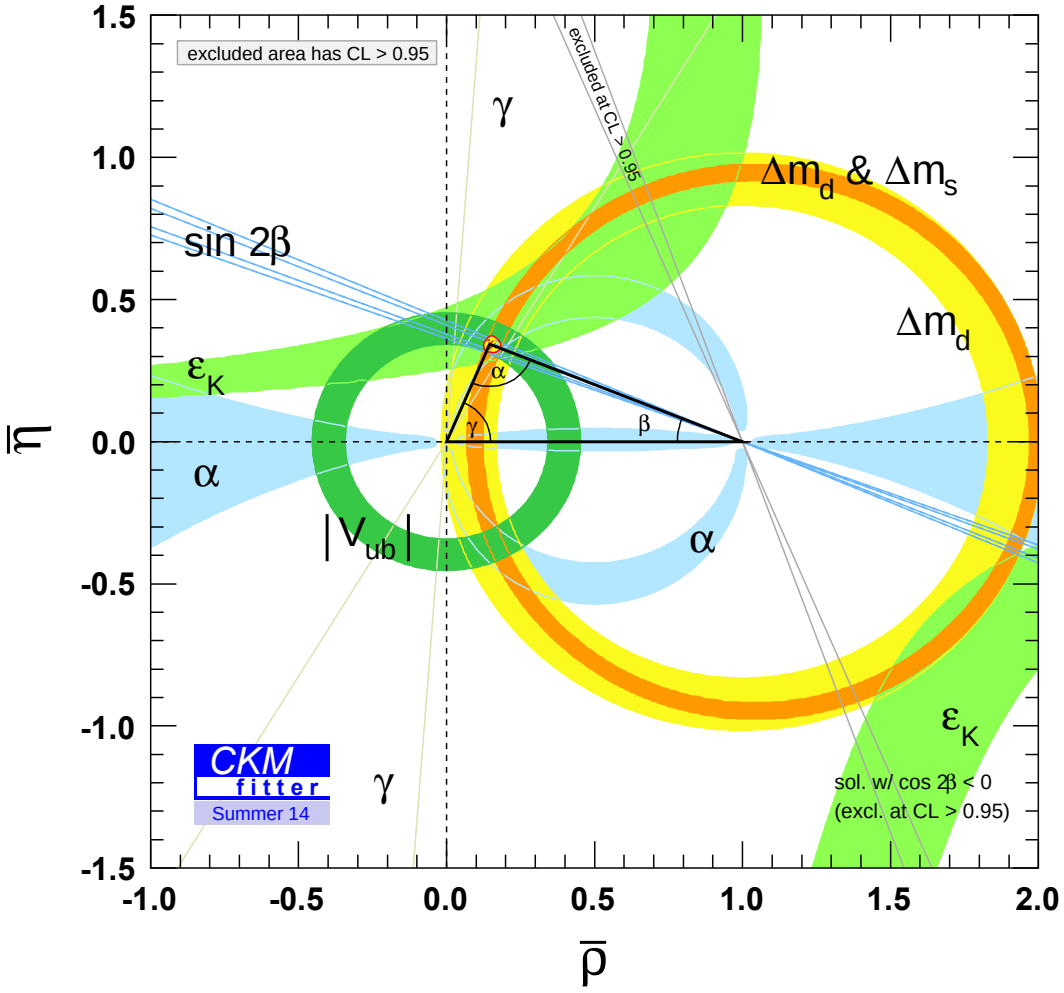

Figure 1.4: *Constraint on the unitarity triangle parameters at $CL > 95\%$ [34].*

eigenstates provide a sensitivity to the B_s^0-$\overline{B}_s^0$ mixing weak phase without a time-dependent study. The tagging of the initial flavour of the B_s^0 meson is nonetheless required.

1.3.1 β angle and New Physics

The decays $B^0 \to K_S^0\pi^+\pi^-$ and $B^0 \to K_S^0K^+K^-$ are dominated by $b \to q\bar{q}s$ ($q = u, d, s$) quark transitions. Since FCNC are forbidden at tree-level in the SM, the $b \to s$ transition proceeds via loop diagrams, also called penguin diagrams. The Feynman diagrams, tree and penguin, for $b \to q\bar{q}s$ transition are given in Fig. 1.5.

A study of the neutral B decay modes governed by $b \to q\bar{q}s$ transition gives access to the CKM angle β. Also, the decays governed by $b \to c\bar{c}s$ transition are the cleanest, from the theoretical point of view, to extract β. To clarify the way to access the β angle, the golden

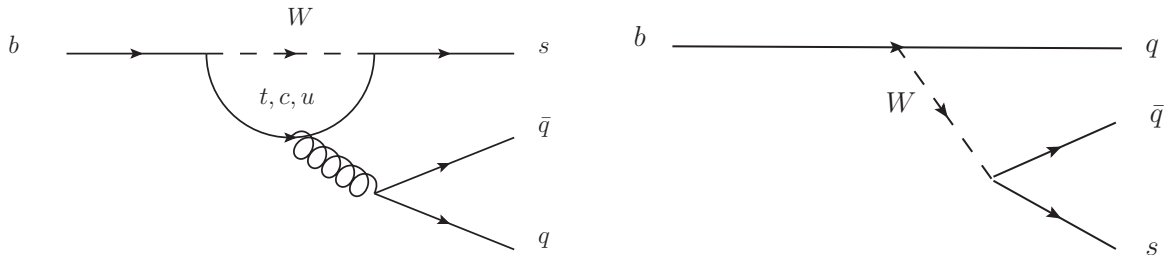

Figure 1.5: *The penguin (left) and tree (right) $b \to q\bar{q}s$ transition.*

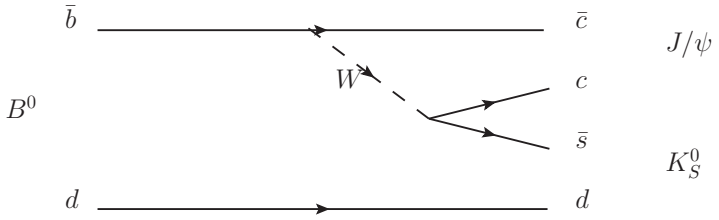

Figure 1.6: *Feynmann diagram of the Golden mode $B^0 \to J/\psi K^0_S$.*

mode $B^0 \to J/\psi K^0_S$ (Fig. 1.6), is taken as example. This decay $B^0 \to (c\bar{c})K^0$ involves a $\bar{b} \to \bar{c}cs$ transition with an amplitude proportional to $[V^*_{cb}V_{cs}]$, while $\bar{B}^0 \to (c\bar{c})K^0$ provides a factor $\eta_{f_{CP}}[V_{cb}V^*_{cs}]$. Because B^0-$\overline{B}^0$ oscillation is dominated by a loop diagram with a t-quark, it introduces a factor $[V^*_{td}V_{tb}/V_{td}V^*_{tb}]$. While K^0-$\overline{K}^0$ mixing, dominated by the c-quark loop, adds a factor $[V^*_{cd}V_{cs}/V_{cd}V^*_{cs}]$. $\lambda_{f_{CP}}$ for this transition reads

$$\begin{aligned} \lambda_{f_{CP}} &= \eta_{f_{CP}} \left(\frac{V_{td}V^*_{tb}}{V^*_{td}V_{tb}}\right)\left(\frac{V_{cb}V^*_{cs}}{V^*_{cb}V_{cs}}\right)\left(\frac{V^*_{cd}V_{cs}}{V_{cd}V^*_{cs}}\right) , \\ &= \eta_{f_{CP}} \left(\frac{V_{td}V^*_{tb}}{V^*_{cb}V_{cd}}\right)\left(\frac{V_{tb}V^*_{td}}{V^*_{cd}V_{cb}}\right)^{-1} . \end{aligned} \tag{1.47}$$

Since $\arg\left(\frac{V_{td}V^*_{tb}}{V^*_{cb}V_{cd}}\right) = \pi - \beta$ and $\left|\frac{V^*_{td}V_{tb}}{V_{td}V^*_{tb}}\right| = 1$, then,

$$\lambda_{f_{CP}} = \eta_{f_{CP}} e^{-2i\beta} . \tag{1.48}$$

For this mode $|\lambda_{f_{CP}}|^2 = 1$, thus according to Eq.(1.46) we get

$$\begin{aligned} S &= \eta_{f_{CP}}\mathrm{Im}(\lambda_{f_{CP}}) = (\eta_{f_{CP}})^2\mathrm{Im}(e^{-2i\beta}) , \\ &= \sin 2\beta . \end{aligned} \tag{1.49}$$

The current average of $\sin(2\beta)$ for all the charmonia modes given by the Heavy Flavor Averaging Group (HFAG [5]) is

$$\sin(2\beta) = 0.69 \pm 0.02 . \tag{1.50}$$

Mixing-induced *CP*-violating phase can similarly be determined from quasi-2-body B^0 decays resulting from a $b \to s$ transition, *e.g* $B^0 \to \phi K_S^0$ or $B^0 \to f^0(980)K_S^0$ to cite two of them. However, it has been shown [14, 37] that the comprehensive handling of the inclusive $B^0 \to K_S^0\pi^+\pi^-$ or $B^0 \to K_S^0 K^+ K^-$ decays by means of a time-dependent flavour-tagged analysis of their three-body Dalitz plot improves the sensitivity on the weak phase determination. These measurements of the *CP*-violating phase are predicted to be approximately equal to those in $b \to c\bar{c}s$, discussed previously, by the CKM mechanism. Under the assumption that the $b \to c\bar{c}s$ transition is dominated by the SM process, the comparison of the weak phase extraction in $b \to q\bar{q}s$ and $b \to c\bar{c}s$ transition can be a measure of New Physics (NP) if there is a difference, since the loop diagrams that dominate the charmless decays can have contribution from new particles in several extensions of the SM, which could introduce additional weak phases.

Chapter 2

$B^0 \to K^0_S\pi^+\pi^-$ and Dalitz Plot formalism

In the amplitude analysis of the decay $B^0 \to K^0_S\pi^+\pi^-$, the main challenge is the determination of the signal probability density function (p.d.f.), from the partial decay rate, which describes both the kinematics and the dynamics properties of the decay process. Therefore, I discuss in the first part of this chapter the kinematics features of the decay process $B^0 \to K^0_S\pi^+\pi^-$ and the Dalitz Plot (DP) technique [38, 39] used in this thesis. The decays of heavy mesons to three-body final states have a large phase space and are generally dominated by intermediate resonances, which can be described as quasi-two-body (Q2B). In case of $B^0 \to K^0_S\pi^+\pi^-$ for example, the decay can proceed via $B^0 \to (K^*(892)^+ \to K^0_S\pi^-)\pi^+$, $B^0 \to (f_0(980) \to \pi^+\pi^-)K^0_S$, *etc.* After having described the DP technique, the second part of this chapter will focus on the decay dynamics models. All the figures provided in this chapter are made in the framework of the CRAFT software described in Appendix E.

2.1 Three-body kinematics: The Dalitz-plot

The decay $B^0 \to K^0_S\pi^+\pi^-$ has three particles in the final state, hence the variables describing the kinematics of this system are the four 4-vectors energy-momenta, $p_{B^0}(m_{B^0}, \vec{0})$, $p_{K^0_S} \equiv p_0(E_0, \vec{p}_0)$, $p_{\pi^+} \equiv p_+(E_+, \vec{p}_+)$ and $p_{\pi^-} \equiv p_-(E_-, \vec{p}_-)$. The original number of unknowns in this system is twelve. The partial decay rate of $B^0 \to K^0_S\pi^+\pi^-$ can be written as

$$\mathrm{d}\Gamma = \frac{(2\pi)^4}{2m_{B^0}}|\mathcal{A}|^2 \mathrm{d}\Phi_3(p_{B^0}, p_0, p_+, p_-) \ , \tag{2.1}$$

where $\mathcal{A}$ is the decay amplitude described in Section 1.1.5.2 and $\mathrm{d}\Phi_3$ is the phase space element of the process $B^0 \to K^0_S\pi^+\pi^-$ given by

$$\mathrm{d}\Phi_3(p_{B^0}, p_0, p_+, p_-) = \delta(m_{B^0} - (E_0 + E_+ + E_-))\frac{\mathrm{d}p_0}{E_0}\frac{\mathrm{d}p_+}{E_+}\frac{\mathrm{d}p_-}{E_-} \tag{2.2}$$

According to several features of the three-body decays this number of unknowns can be reduced:

- The masses of the three particle daughters are known: 3 constraints.
- Energy and momentum conservation: 4 constraints.
- The two spatial angles are irrelevant (B^0 is spin 0): 3 constraints.

In total there are 10 constraints that reduce the unknowns to two for a spin 0 particle (for more details see Appendix A). The two-body invariant masses squared, named also DP variables, are used to describe the kinematics of the system

$$m^2_{K^0_S\pi^+} \equiv s_+ = (p_+ + p_0)^2 \ , \quad m^2_{K^0_S\pi^-} \equiv s_- = (p_- + p_0)^2 \ . \tag{2.3}$$

The third DP variable is the invariant mass square of the two pions

$$m^2_{\pi^+\pi^-} \equiv s_0 = (p_+ + p_-)^2 \ , \tag{2.4}$$

which can be related with the other two variables by the DP boundary equation

$$s_0 = m^2_{B^0} + m^2_{K^0_S} + m^2_{\pi^+} + m^2_{\pi^-} - (s_+ + s_-) \ . \tag{2.5}$$

Using the DP variables to describe the $B^0 \to K^0_S\pi^+\pi^-$ decay, the partial decay rate reads

$$\mathrm{d}\Gamma = \frac{1}{(2\pi)^3}\frac{|\mathcal{A}|^2}{32 m_{B^0}}\mathrm{d}s_+\mathrm{d}s_- \ . \tag{2.6}$$

In the following $\mathcal{A}$ and $\bar{\mathcal{A}}$ will describe the decay amplitude of $B^0 \to K^0_S\pi^+\pi^-$ and $\overline{B}^0 \to K^0_S\pi^+\pi^-$, respectively.

The extreme edges of the boundary for each axis describe situations where the momenta of two particles are parallel (same direction) or anti-parallel (reversed direction). Fig. 2.1 illustrates the status of daughter particles in the Dalitz plane of $B^0 \to K^0_S\pi^+\pi^-$.

2.2 Helicity angle

We note i, j and k the indices of the three daughters in the decay $B^0 \to K^0_S\pi^+\pi^-$. The helicity angle, $(\theta_H)_{ij}$, is defined by the angle between the hadrons j and k in the ij rest frame, expressed as

$$\cos(\theta_H)_{ij} = \frac{(m^2_{jk})_{\max} + (m^2_{jk})_{\min} - 2m^2_{jk}}{(m^2_{jk})_{\max} - (m^2_{jk})_{\min}} \ . \tag{2.7}$$

The helicity frame is useful since the spin of a resonance can be identified by the distribution in $\cos\theta_H$. A scalar resonance (spin 0) for instance has a uniform distribution in $\cos\theta_H$, hence uniform as well in the DP, whereas the distribution for a vector resonance (spin 1) in DP populates two regions separated by a depleted node. A tensor resonance (spin 2) is distributed in the DP along three consecutive regions separated by two depleted nodes. Eq. (2.7) illustrates these features in DP for $B^0 \to K^0_S\pi^+\pi^-$, for each spin value.

Figure 2.1: *Graphical representation of the final state daughters kinematics in the Dalitz Plot of the decay* $B^0 \to K^0_S\pi^+\pi^-$. *The dashed lines represent the kinematics limits of the Dalitz plane.*

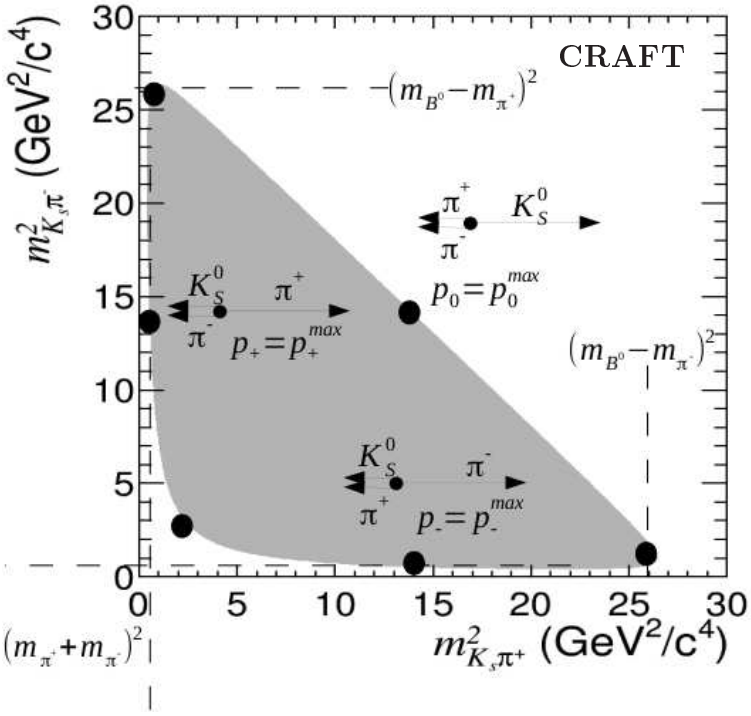

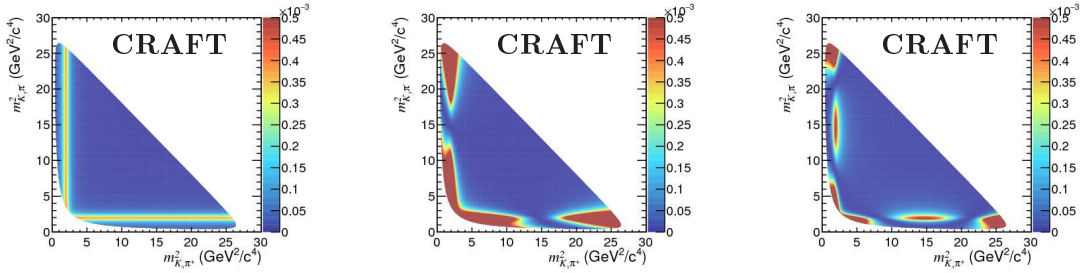

Figure 2.2: *The distribution of the resonance* $K^*(1430)$ *(*$m_0 = 1425$ *MeV,* $\Gamma_0 = 270$ *MeV) in the DP of* $B^0 \to K^0_S\pi^+\pi^-$, *with different spin, spin 0 (left), spin 1 (middle) and spin 2 (right).*

2.3 Three-body dynamics: Isobar Model

Following the decay rate expression (2.6), a constant DP-dependent amplitude $\mathcal{A}$ will uniformly populate the DP (phase space). The non-uniformity in the DP, in the form of excess of events in specific regions, gives information on the amplitude $\mathcal{A}$, which actually contains all the underlying dynamics of the decay.

Usually, the decay amplitudes are parametrised using the *Isobar Model* [40]. The Isobar Model approximates the total amplitude as a coherent sum of terms with individual complex

probability amplitude and dynamical function, each representing an intermediate resonance in one pair of particles, a non-resonant but strongly interacting pair of particles and/or a non-resonant phase space decay. This reads mathematically

$$\begin{aligned} |\mathcal{A}(s_+, s_-)|^2 &= \left|\sum_j c_j F_j(s_+, s_-)\right|^2 = \left|\sum_j a_j e^{i\phi_j} F_j(s_+, s_-)\right|^2 , \\ \left|\bar{\mathcal{A}}(s_+, s_-)\right|^2 &= \left|\sum_j \bar{c}_j \bar{F}_j(s_+, s_-)\right|^2 = \left|\sum_j \bar{a}_j e^{i\bar{\phi}_j} \bar{F}_j(s_+, s_-)\right|^2 , \end{aligned} \tag{2.8}$$

where a_j and ϕ_j are the relative magnitude and phase, denoted isobar parameters, of the component j. F_j is the spin-dependent dynamical function, described in more details in the following. The isobar parameters contain the weak and the strong phases dependence, whereas F_j contains the strong dynamics only. Therefore

$$F_j(s_+, s_-) = \bar{F}_j(s_-, s_+) \, . \tag{2.9}$$

The spin-dependent dynamical function F_j can be expanded in terms of resonance mass function, angular distribution probabilities and corrective factors to conserve the angular momentum due to the spin of the intermediate resonance

$$F_j(s_+, s_-, L) = \mathcal{R}_j(s) \times X^L(|\vec{p}|r) \times X^L(|\vec{q}|r) \times T_j(L, \vec{p}, \vec{q}) \, , \tag{2.10}$$

where:

- s is the invariant mass square (in this analysis, it can be s_+, s_- or s_0) of the decay products of the resonance,
- $\vec{p}$ and $\vec{q}$ are the momenta of the bachelor particle and one of the resonance daughters respectively, both evaluated in the rest frame of the resonance.
- L is the orbital angular momentum between the resonance and the bachelor particle,
- $R_j(s)$ is the resonance mass term or line-shape describing the resonance j,
- $T_j(L, \vec{p}, \vec{q})$ corresponds to the angular distribution of the resonance daughters,
- $X^L(|\vec{p}|r)$ and $X^L(|\vec{q}|r)$ are the barrier factors for the production of the resonance and the bachelor particle, and the production of daughters resonance, respectively.

The two latter quantities are made explicit in the next subsection.

2.3.1 Angular distributions

In the Zemach tensor formalism [41], the angular probability distribution terms, $T_j(L, \vec{p}, \vec{q})$, are given by

$$T_j(0,\vec{p},\vec{q}) = 1\,, \tag{2.11}$$
$$T_j(1,\vec{p},\vec{q}) = -2\vec{p}\cdot\vec{q}\,, \tag{2.12}$$
$$T_j(2,\vec{p},\vec{q}) = \frac{4}{3}[3(\vec{p}\cdot\vec{q}) - (|\vec{p}||\vec{q})|] \tag{2.13}$$

The function $X^L(z)$ in Eq. (2.10) , where $z = |\vec{p}|r$ or $|\vec{q}|r$, represents the Blatt-Weisskopf barrier factor [42], which depends on a single parameter, the resonance radius r. Since the Zemach tensor formalism is used to describe the angular distribution term, the so-called "primed" form of the Blatt-Weisskopf barrier factors, given in Ref. [20], is used instead of the standard expression. This expression for a given angular momentum L can be expressed as

$$X^{L=0}(z) = 1\,, \tag{2.14}$$
$$X^{L=1}(z) = \sqrt{\frac{1+z_0^2}{1+z^2}}\,, \tag{2.15}$$
$$X^{L=2}(z) = \sqrt{\frac{z_0^4+3z_0^2+9}{z^4+3z^2+9}}\,. \tag{2.16}$$

where z_0 represents the value of z when the invariant mass is equal to the mass pole of the resonance.

2.4 Mass term description

In the DP analysis of $B^0 \to K^0_S\pi^+\pi^-$, most of the resonances are modelled by a *Relativistic Breit-Wigner* (RBW). Some decay resonances of interest deserve a dedicated modelling. The different form of lineshapes used in the $B^0 \to K^0_S\pi^+\pi^-$ amplitude analysis are described in the following.

2.4.1 Relativistic Breit Wigner lineshape

The relativistic Breit Wigner (RBW) commonly models the invariant mass distribution ($m = \sqrt{s}$) of an unstable particle travelling at relativistic speeds. The RBW mass lineshape is expressed as

$$\mathcal{R}(m) = \frac{m_0\Gamma_0}{m^2 - m_0^2 - im_0\Gamma(m)}\,, \tag{2.17}$$

where m_0 is the pole mass of the resonance and Γ_0 is its natural width. $\Gamma(m)$ is the mass-dependent width given by

$$\Gamma(m) = \Gamma_0\frac{m_0}{m}\left(\frac{p(m)}{p(m_0)}\right)^{2J+1}\frac{X_J(z(m))}{X_J(z(m_0))}\,. \tag{2.18}$$

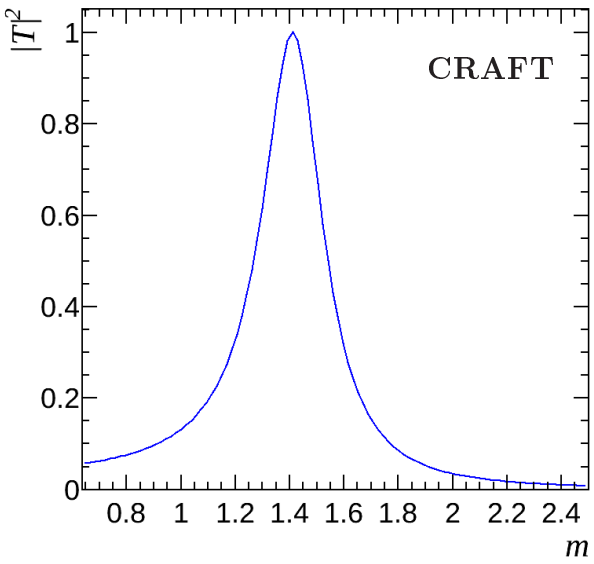

Figure 2.3: *The relativistic Breit-Wigner probability density function of the scalar resonance* $K_0^*(1430)$.

We noted J the spin of the resonance and p the momentum of one of the resonance daughters. The latter can be expressed as a function of m

$$p(m) = \frac{m}{2}\left(1 - \frac{(m_a + m_b)^2}{m^2}\right)^{1/2}\left(1 - \frac{(m_a - m_b)^2}{m^2}\right)^{1/2}, \tag{2.19}$$

where m_a and m_b are the masses of the resonance daughters.

A Breit-Wigner parametrisation describes adequately isolated, non overlapping resonances far from the threshold of additional decay channels, in order to ensure the unitarity. The scalar intermediate resonance $K_0^{*+}(1430)$ (involved in the amplitude of the decay $B^0 \to (K_0^{*+}(1430) \to K_S^0\pi^+)\pi^-$) is used here to illustrate the Breit-Wigner model characteristics. Fig. 2.3 shows the amplitude square of the Breit-Wigner distribution. The Argand diagram of this distribution should be a unit circle, as shown in Fig. 2.4. The Breit-Wigner function, for a scalar resonance, can be expressed in term of the phase shift $\delta(m)$ as

$$\mathcal{R}(m) = \frac{1}{i + \cot\delta(m)}\,. \tag{2.20}$$

When the invariant mass reaches the mass pole ($m = m_0$), the phase-shift is equal to $\delta = \frac{\pi}{2}$. This feature is displayed in Fig. 2.5. Another important characteristic of the RBW parametrisation is that the derivative of $\delta(m)$ over m should have a pole in the mass resonance as shown in Fig. 2.5.

We will review in the following the additional parametrisations used in the $B^0 \to K_S^0\pi^+\pi^-$ DP analysis, emphasizing each time why the RBW fails at providing a relevant mass lineshape.

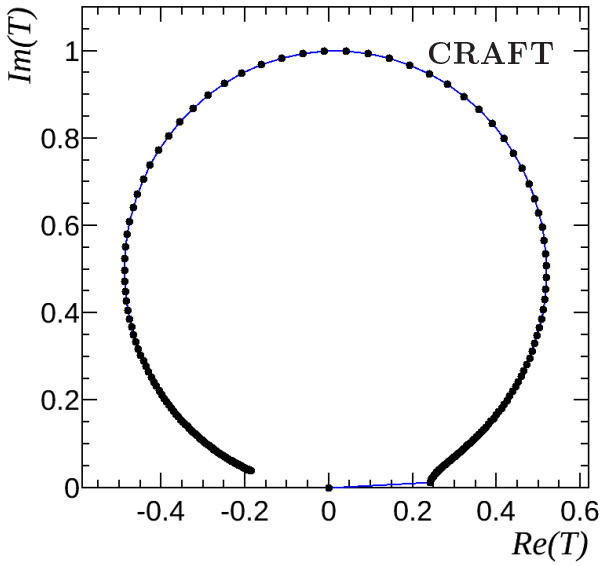

Figure 2.4: *Argand diagram of the scalar resonance* $K_0^*(1430)$. *The black points represent the lineshape amplitude evaluated at various equally spaced point in the invariant mass.*

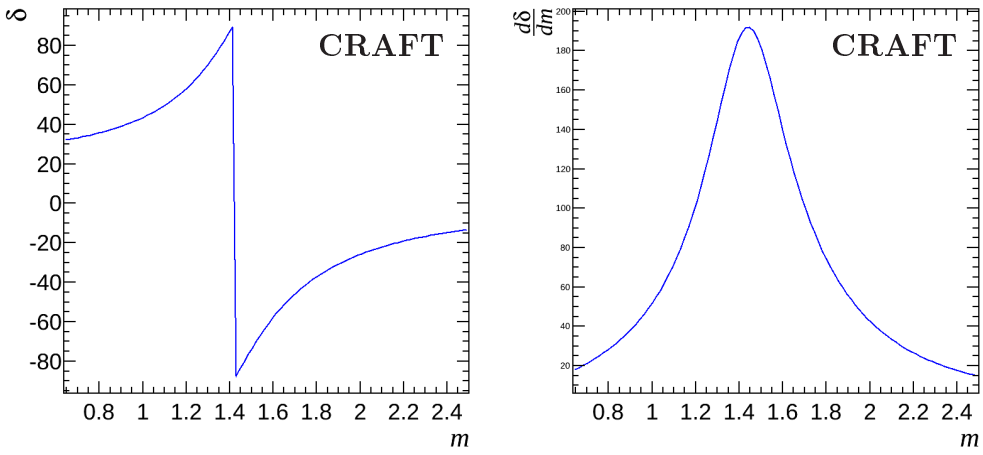

Figure 2.5: *The phase-shift distribution (left) and its derivative (right), of the scalar resonance* $K_0^*(1430)$.

2.4.2 Gounaris-Sakurai (GS) lineshape

This mass lineshape, displayed in Fig. 2.6, is a modified relativistic Breit-Wigner. GS distribution [43] describes adequately the P-wave $\pi\pi$ scattering amplitude for a broad resonance (*e.g.* $\rho(770)$). The GS lineshape is defined as

$$\mathcal{R}(m) = \frac{1 + d \cdot \Gamma_0/m_0}{(m_0^2 - m^2) + f(m) - im_0\Gamma(m)} \,, \tag{2.21}$$

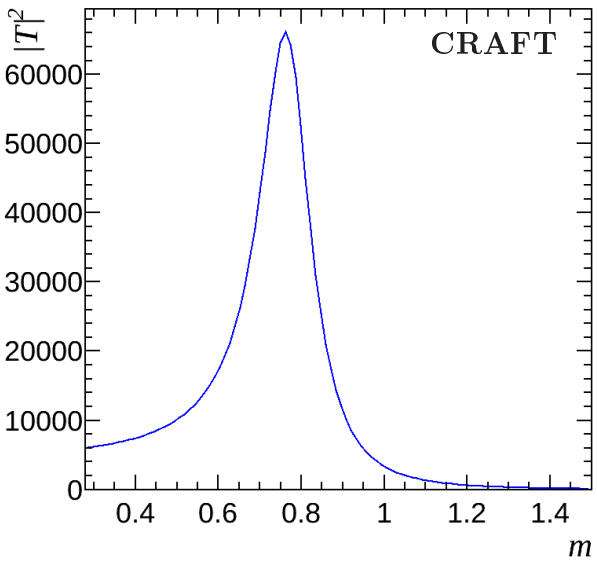

Figure 2.6: *Gounaris-Sakurai p.d.f. shape of the vector resonance* $\rho^0(770)$.

where

$$f(m) = \Gamma_0 \frac{m_0^2}{p^3(m_0)} \left[p^2(m)(h(m) - h(m_0)) + (m_0^2 - m^2)p^2(m_0) \left. \frac{\mathrm{d}h}{\mathrm{d}m^2} \right|_{m=m_0} \right] , \tag{2.22}$$

$$h(m) = \frac{2}{\pi} \frac{p(m)}{m} \ln \left(\frac{m + 2p(m)}{2m_\pi} \right) , \tag{2.23}$$

with

$$\left. \frac{\mathrm{d}h}{\mathrm{d}m^2} \right|_{m=m_0} = h(m_0) \left(\frac{1}{8p^2(m_0)} - \frac{1}{2\pi m_0^2} \right) . \tag{2.24}$$

m_0, Γ_0 are the mass and the width of resonance, p is the momentum of one of resonance daughters described in Eq. (2.19). The normalization condition at $\mathcal{R}(0)$ fixes the parameter $d = f(0)/(\Gamma_0 m_0)$. It is found to be

$$d = \frac{3}{\pi} \frac{m_\pi^2}{p(m_0)^2} \ln \left(\frac{m_0 + 2p(m_0)}{2m_\pi} \right) + \frac{m_0}{2\pi p(m_0)} - \frac{m_\pi^2 m_0}{\pi p(m_0)^3} . \tag{2.25}$$

2.4.3 Flatté mass lineshape

The vicinity of a threshold in the resonance shape distorts the mass lineshape from a simple Breit-Wigner. This type of resonance is best modelled by the Flatté parametrisation [44]. In the context of this analysis, the most striking example is the resonance $f_0(980)$ which can

decay in both $\pi^+\pi^-$ and K^+K^- final states. The K^+K^- kinematic threshold opens close to the pole mass of the $f_0(980)$.

The Flatté lineshape, displayed in Fig. 2.7, is similar to the RBW lineshape where the mass-dependent width is given by the sum of the widths in the two different decay channels 1 and 2

$$\Gamma(m) = \Gamma_1(m) + \Gamma_2(m) \ , \tag{2.26}$$

In the example of the $f_0(980)$ resonance reconstructed as $\pi\pi$, the total width of this resonance is given by

$$\Gamma(m_{\pi\pi}) = \Gamma_{\pi\pi}(m_{\pi\pi}) + \Gamma_{KK}(m_{\pi\pi}) \ , \tag{2.27}$$

where

$$\Gamma_{\pi\pi}(m_{\pi\pi}) = g_\pi \rho_{\pi\pi}(m_{\pi\pi}) \ , \tag{2.28}$$
$$\Gamma_{KK}(m_{\pi\pi}) = g_K \rho_{KK}(m_{\pi\pi}) \ . \tag{2.29}$$

g_π and g_K are the coupling constants, $\rho_i(m_{\pi\pi})$ represents the phase space and is given by

$$\rho_{\pi\pi} = \frac{p_\pi(m_{\pi\pi})}{m_{\pi\pi}} \ , \tag{2.30}$$
$$\rho_{KK} = \frac{p_K(m_{\pi\pi})}{m_{\pi\pi}} \ , \tag{2.31}$$

where $p_\pi(m_{\pi\pi})$ is described by Eq. (2.19) and $p_K(m_{\pi\pi})$ is described as

$$p_K = \left(\frac{m^2_{\pi\pi}}{4} - m^2_K\right)^{1/2} , \quad m_{\pi\pi} \geq 2m_K \tag{2.32}$$
$$p_K = i\left(\frac{m^2_{\pi\pi}}{4} - m^2_K\right)^{1/2} , \quad m_{\pi\pi} < 2m_K \ . \tag{2.33}$$

2.4.4 LASS mass lineshape

The LASS parametrisation [45] is defined to model the S-wave component $(K\pi)^{*\pm}_0$, which consists of the $K^*(1430)$ resonance together with an effective range non-resonant component

$$\mathcal{R}(m_{K\pi}) = \frac{m_{K\pi}}{p(m_{K\pi})\cot\delta_B - ip(m_{K\pi})} + e^{2i\delta_B}\frac{m_0^2\Gamma_0/p(m_0)}{(m_0^2 - m^2_{K\pi} - im_0\frac{p(m)}{m_{K\pi}}\frac{m_0}{p(m_0)})} \ , \tag{2.34}$$

where $\cot\delta_B = \dfrac{1}{ap(m) + \frac{1}{2}rp(m)}$. Here, δ_B represents the non-resonant phase shift, a is the scattering length and r is the effective range. In the literature, most of the analyses making

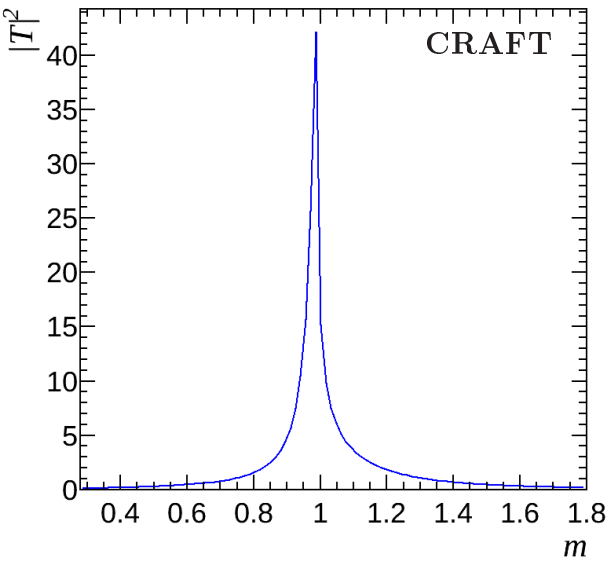

Figure 2.7: *An example of the Flatté p.d.f. shape describing the scalar resonance* $f_0(980)$.

use of this parametrisation cut off the effective range term at an invariant mass value typically in the range [1600; 1800] MeV/c^2. Actually, the parameters of the LASS function are derived from the inelastic scattering experiments which were either limited in the mass range or provided an ambiguous interpretation of their data above a certain energy. For the analysis of this thesis, the values of the scattering length and the effective range are taken from BaBar analysis [14] ($a = 2.07 \pm 0.10$ (GeV/c)$^{-1}$, $r = 3.32 \pm 0.34$ (GeV/c)$^{-1}$). Fig. 2.8 shows the LASS lineshape describing the $K\pi$ S-wave.

2.4.5 Reduced K-matrix

The reduced K-matrix is used in this thesis analysis to describe the $\pi\pi$ S-wave at low invariant mass ($m_{\pi\pi} < 0.9\,\text{GeV}$), represented by a combination of $f_0(500)$ resonance and a non-resonant $\pi^+\pi^-$ S-wave. The mass-dependent amplitude of this parametrisation used for low mass $\pi\pi$ S-wave reads

$$\mathcal{R}(m_{\pi\pi}) \propto \frac{K(m_{\pi\pi})}{1 - i\rho(m_{\pi\pi})K(m_{\pi\pi})} \,, \tag{2.35}$$

with

$$K(m_{\pi\pi}) = K_{\text{res}}(m_{\pi\pi}) + K_{\text{non-res}} = \frac{m_0\Gamma(m_{\pi\pi})}{(m_0^2 - m_{\pi\pi}^2)\rho(m_{\pi\pi})} + \kappa \,, \tag{2.36}$$

where $\rho(m_{\pi\pi})$ is the phase-space factor as given in Eq. (2.27). κ is a real constant meant to describe the non-resonant component, m_0 and $\Gamma(m_{\pi\pi})$ are the pole mass and mass-dependent width of $f_0(500)$ resonance, respectively.

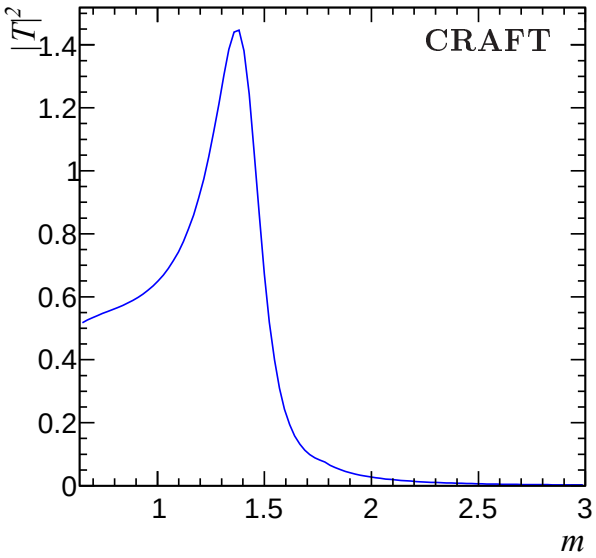

Figure 2.8: *LASS p.d.f. shape describing the $K\pi$ S-wave ($K_0^*(1430)+$ non-resonant).*

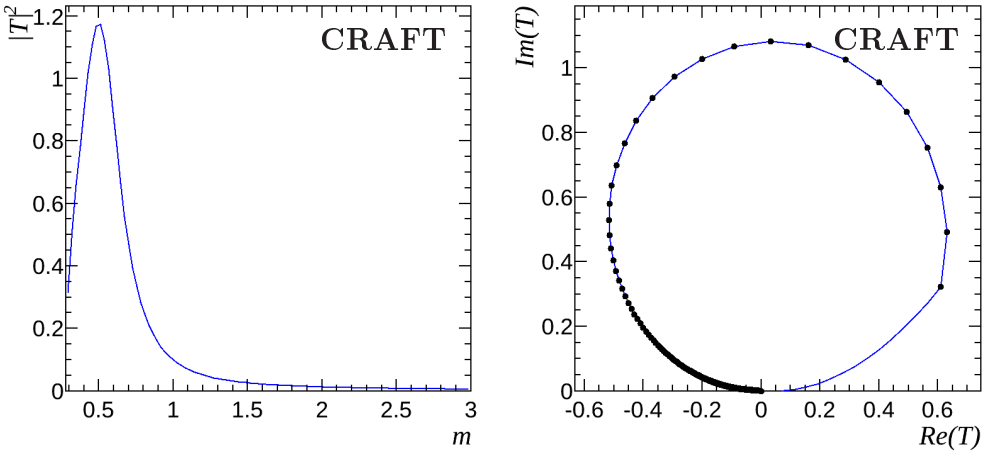

Figure 2.9: *An example of the reduced K-matrix formalism describes the combination of the scalar resonance $f_0(500)$ and small amplitude of non-resonant: the amplitude shape (left), the Argand diagram (right). The unit circle is not complete due to the threshold of $m_{\pi\pi}$.*

In the K-matrix formalism, the unitary of the scattering matrix is automatically respected, which implies that the Argand diagram of this model is described by a unit circle, sketched in Eq. (2.36). The same figure shows the reduced K-matrix line-shape describing a combination of the scalar resonance $f_0(500)$, with a nominal mass $m_0 = 513$ MeV and nominal width $\Gamma_0 = 335$ MeV, and a non-resonant part with $\kappa = -0.07$.

One interesting feature of this lineshape is that a cusp point occurs when the phase-shift of the amplitude is equal to zero

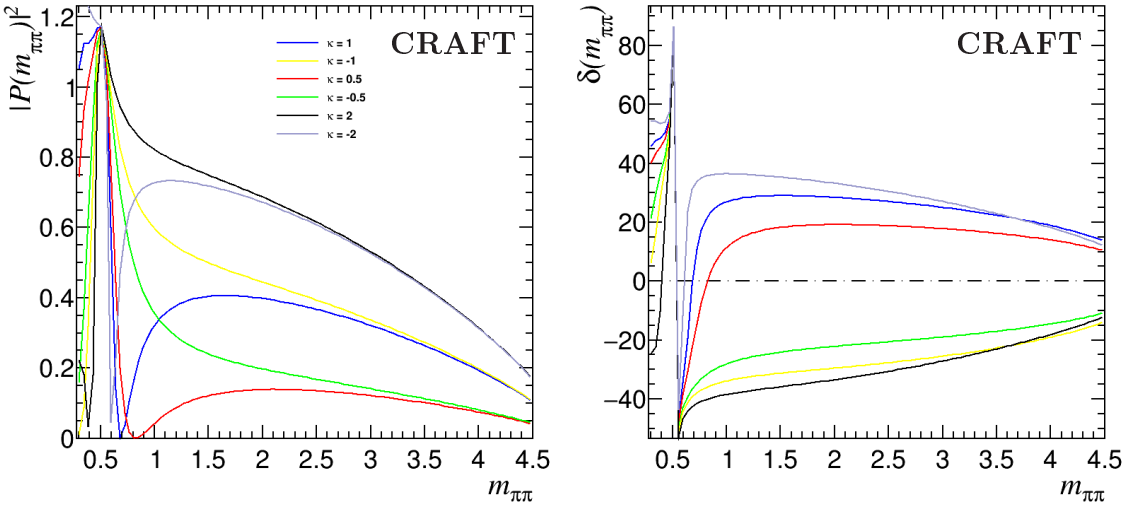

Figure 2.10: *The amplitude and phase-shift of the combination* $f_0(500) + \kappa$ *as a function of the invariant mass* $m_{\pi\pi}$ *with different values of* κ*: 0.5(red), -0.5(green), 1(red), -1(yellow), 2(black), -2(grey).*

$$\delta(m_{\pi\pi}) = \frac{1}{2}\arctan\left(\frac{(K(m_{\pi\pi})+\kappa)^2 - 1}{2(K(m_{\pi\pi})+\kappa)}\right) + \frac{\pi}{4} = 0\,, \tag{2.37}$$

$$\Longrightarrow\ K(m_{\pi\pi}) = -\kappa\,. \tag{2.38}$$

The coordinate of the cusp in the $m_{\pi\pi}$ axis is expressed by

$$m_{\text{cusp}}(\kappa) = m_0\sqrt{1 + \frac{\Gamma_0}{\kappa\sqrt{m_0^2 - 4m_\pi^2}}}\,. \tag{2.39}$$

It is clear from the previous equation that the cusp point coordinate relates directly to the value of κ. To illustrate the effect of the non-resonant, six models of the reduced K-matrix describing the combination $f_0(500)$ and non-resonant with different κ value are proposed in Eq. (2.39).

2.5 DP probability density function and *CP* Observables attached to the $B^0 \to K^0_S\pi^+\pi^-$ decay

The Dalitz Plot technique allows to construct a realistic signal p.d.f., where both the kinematical and dynamical properties of the decay can be accurately modelled. In the following, the general formalism of the time-dependent p.d.f. is spelled out and the untagged time-integrated form is eventually derived.

2.5.1 Probability density function

The DP time-dependent p.d.f. of the decay $(B^0,\overline{B}^0)\to K^0_S\pi^+\pi^-$ is given by

$$\begin{aligned}\mathcal{P}(s_+,s_-,t,r_{\rm tag}) &= \frac{{\rm d}\Gamma_{B^0,\bar{B}^0}(t)}{{\rm d}t}\,, \\ &= \frac{\Gamma}{2}e^{-\Gamma t}(|\mathcal{A}(s_+,s_-)|^2+|\bar{\mathcal{A}}(s_+,s_-)|^2)[1+r_{\rm tag}(C\cos(\Delta m t)-S\sin(\Delta m t))]\,,\end{aligned} \tag{2.40}$$

where $r_{\rm tag}$ is the tagging parameter, determining whether the signal candidate is a B^0 or $\overline{B}^0$ meson at the time of production. Each tagged B candidate is thus assigned a value $r_{\rm tag}=1,-1$ or 0. The value 1 means the B candidate at time of production was a B^0 whereas a value of -1 is assigned to candidates which were a $\overline{B}^0$ at time of production. The tagging parameter equal to 0 states that no tagging information (untagged) is available for this candidate.

Defining the following three integration terms

$$\int_0^\infty e^{-\Gamma t}\cos(\Delta m t){\rm d}t = \frac{\Gamma}{\Delta m^2+\Gamma^2}\,, \tag{2.41}$$

$$\int_0^\infty e^{-\Gamma t}\sin(\Delta m t){\rm d}t = \frac{\Delta m}{\Delta m^2+\Gamma^2}\,, \tag{2.42}$$

$$\int_0^\infty \Gamma e^{-\Gamma t}{\rm d}t = 1, \tag{2.43}$$

the DP-dependent p.d.f. reads

$$\mathcal{P}(s_+,s_-,r_{\rm tag}) = (|\mathcal{A}(s_+,s_-)|^2+|\bar{\mathcal{A}}(s_+,s_-)|^2)\left[1+r_{\rm tag}\left(\frac{C-x_dS}{x_d^2+1}\right)\right]\,, \tag{2.44}$$

where x_d is the B^0-$\overline{B}^0$ mixing parameter, $x_d=\Delta m/\Gamma$. The world average of its measurements given in [20] is $x_d=0.774\pm0.006$.

It is important to notice that the tagging information and the value of the x_d parameter are required to have access to *CP* observables C and S, and the mixing parameter x_d. In case where no information of tagging is present, which occurs for the DP analysis of the decay $B^0\to K^0_S\pi^+\pi^-$ presented in this document, the DP p.d.f. simplifies as an incoherent sum of amplitudes

$$\mathcal{P}(s_+,s_-) = |\mathcal{A}(s_+,s_-)|^2+|\bar{\mathcal{A}}(s_+,s_-)|^2\,. \tag{2.45}$$

2.5.2 The Square Dalitz Plot

The boundaries of the $B^0\to K^0_S\pi^+\pi^-$ DP are particularly important since most of the interferences between amplitudes implying intermediate resonances are located there. As a consequence, the interesting physics of the decay of interest lies in small areas of the DP. In order to better describe and display these interference regions, one can advantageously apply a transformation to the standard DP kinematics variables for the decay $B^0\to K^0_S\pi^+\pi^-$

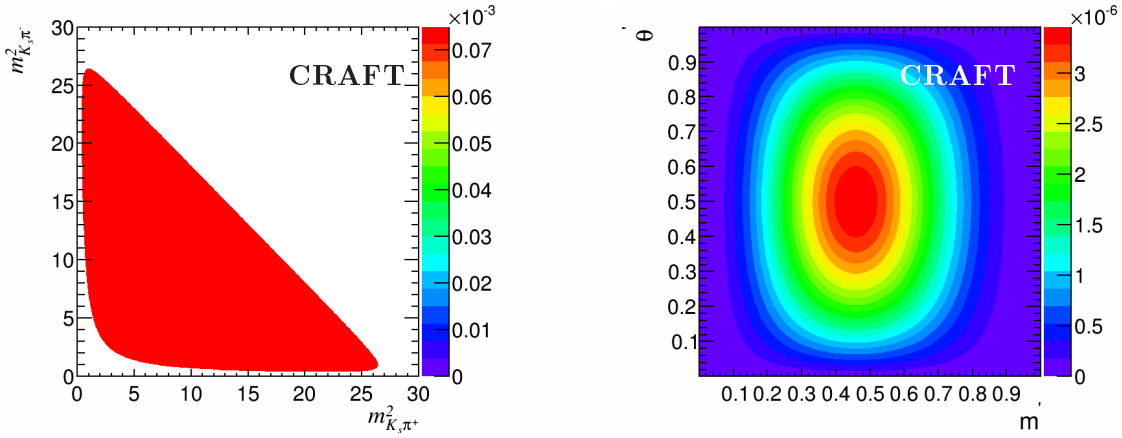

Figure 2.11: *The plot on the left shows a flat distribution over the nominal DP for* $B^0 \to K^0_S\pi^+\pi^-$ *decays and the plot on the right displays its transformation to SDP coordinates where the distribution is nothing else than the determinant of the Jacobian of the transformation, provided Eq.* (2.48).

$$m' = \frac{1}{\pi}\arccos\left(2\frac{m_{\pi^+\pi^-} - m^{\min}_{\pi^+\pi^-}}{m^{\max}_{\pi^+\pi^-} - m^{\min}_{\pi^+\pi^-}} - 1\right) , \tag{2.46}$$

$$\theta' = \frac{1}{\pi}\theta_{\pi^+\pi^-} , \tag{2.47}$$

where $m^{\min}_{\pi^+\pi^-}$ and $m^{\max}_{\pi^+\pi^-}$ are the kinematics limits of $m_{\pi\pi}$ and $\theta_{\pi^+\pi^-}$ is the helicity angle of the *CP*-eigenstate resonances.

That transformation maps the DP into a rectangle denoted *square Dalitz plot* (SDP).

For $B^0 \to K^0_S\pi^+\pi^-$, the SDP differential element is obtained by the transformation

$$\mathrm{d}m^2_{K_S\pi^+}\mathrm{d}m^2_{K_S\pi^-} \to |\mathrm{det}J|\mathrm{d}m'\mathrm{d}\theta' , \tag{2.48}$$

where J is the Jacobian of the transformation. Fig. 2.11 illustrates its effect for a flat distribution in the DP. This technique was used for the first time in the analysis of $B^+ \to \pi^+\pi^+\pi^-$ [46].

Chapter 3

Large Hadron Collider and the LHCb experiment

The data analysed in this thesis were recorded during the years 2011 and 2012 by the LHCb detector, one of the four main experiments at the *Large Hadron Collider* (LHC). The following chapter describes shortly the designs of the LHC machine and LHCb experiment. Basic information on the accelerator is provided. The LHCb description is rapid as well and the interested reader can go to the comprehensive discussion of the LHCb detector given in [47]. However, a focus is given in this document to the sub-detector components that are important for our analysis.

3.1 The Large Hadron Collider at CERN

The LHC is a two rings accelerator, circulating proton or ion beams in opposite directions. It is located at the European Organisation for Nuclear Research (CERN). The LHC has a $\sim$ 27 km circumference, housed in a tunnel 100 m underground, previously used by the Large Electron Positron Collider (LEP). Fig. 3.1 displays the tunnel location. The LHC can accelerate proton beams up to an energy of 6.5 TeV. The first collisions at 900 GeV were delivered on September 10th, 2008. A technical accident in one of superconducting magnetic dipoles damaged a part of the infrastructure, which forced an unscheduled stop of one year and a revision of the maximal beam energy during the Run I. Stable beams were again present in the LHC on November 20th, 2009. After the winter shut-down, in March 2010, the first collisions at 7 TeV in the center-of-mass were recorded. After two years of data taking, the center-of-mass energy was increased to 8 TeV.

3.1.1 The LHC accelerator system

The proton are accelerated via a series of different systems before being injected into the LHC. First hydrogen molecules are ionized to get protons and accelerated by the LINAC2 accelerator at an energy of 50 MeV. The accelerated protons are then injected into the Proton Synchrotron Booster, which accelerates them further up to 1.4 GeV. Afterwards, the protons are transferred to the Proton Synchrotron (PS) where they reach the energy of 25 GeV. The final step before the injection to the LHC is the Super Proton Synchrotron,

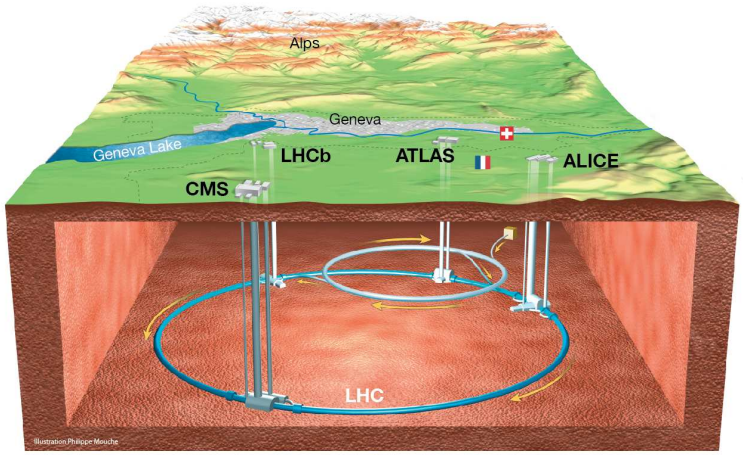

Figure 3.1: *Schematic overview of LHC and the position of the four major LHC experiments.*

which accelerates the protons to 450 GeV. The Fig. 3.2 provides a schematics of the CERN accelerators complex.

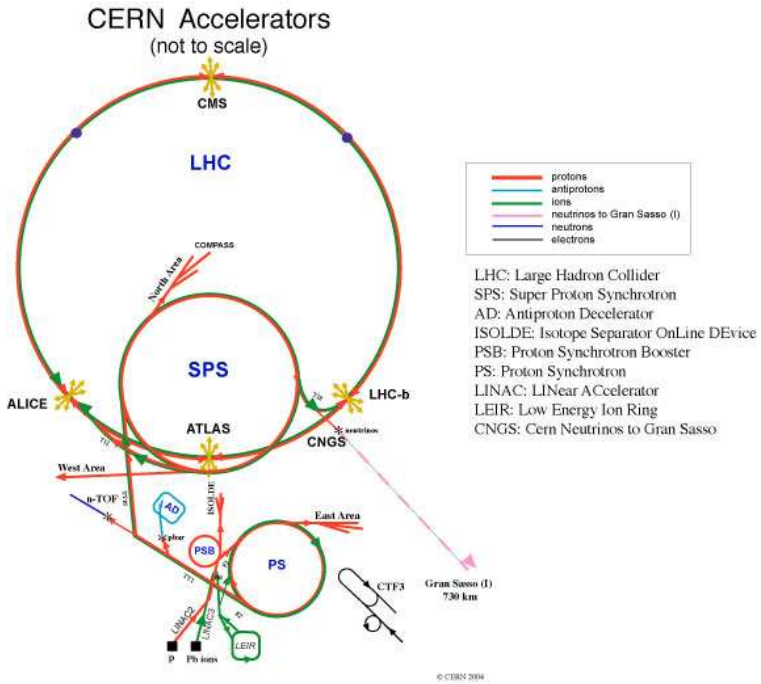

Figure 3.2: *CERN accelerator complex. The four interaction points along the LHC are indicated.*

3.1.2 Experiments at the LHC

The LHC hosts four major particle physics experiments. The two experiments ATLAS [48] and CMS [49] are multi-purpose detectors. The Higgs boson study and the search for New Physics constitute their main physics goals. Both experiments successfully discovered the Higgs boson in July 2012 [50,51]. The ALICE experiment [52] is heavy-ion detector, aiming at studying the physics of the quark-gluon plasma medium. The Large Hadron Collider beauty experiment, LHCb [47], is designed to study *CP* violation in the charmed and beautiful hadrons decays and the mixing of neutral c- and b-mesons as well as rare decays of heavy flavoured particles. The LHCb detector will be described in the following sections.

3.1.3 Luminosity and $b\bar{b}$ quark pair production

The luminosity of the machine at an interaction point is given by (Ref [53]):

$$\mathcal{L} = \frac{N_1 \, N_2 \, k_b \, f \gamma \, F}{4\pi\beta^* \epsilon}, \tag{3.1}$$

where N_i $(i = 1, 2)$ is the number of protons in each bunches, k_b is the number of bunches, f is the revolution frequency, $\gamma = E_p/m_p$ is the Lorentz factor, β^* is the value of the betatron function at the interaction point, ϵ is the emittance and F is the reduction factor. The corresponding values for these parameters at the peak performance of the LHC in 2012 are shown in Table 3.1

Table 3.1: *Performance related parameter overview [54].*

Parameter	Value in 2012	Design value
Beam energy [TeV]	4	7
β^* in IP 1,2,5,8 [m]	$0.6, 3.0, 0.6, 3.0$	0.55
Bunch spacing [ns]	50	25
Number of bunches	1374	2808
Average bunch intensity [protons per bunch]	1.6 - 1.7 $\times 10^{11}$	1.15×10^{11}
Normalized emittance at start of fill [mm.mrad]	2.5	3.75
Peak luminosity [$\mathrm{cm^{-2}s^{-1}}$]	7.7×10^{33}	1×10^{34}
Max. mean number of events per bunch crossing	≈ 40	19
Stored beam energy [MJ]	≈ 140	362

The LHCb experiment does not operate at the nominal luminosity of the machine. Fig. 3.3 shows the evolution of the number of primary vertices as a function of the luminosity. Since the association of the weakly decaying b- or c-hadron decay vertex with its production vertex is a crucial physics requirement for most of the LHCb analyses, it is mandatory to limit the luminosity to values below 10^{33}. This has been realized by adjusting the beam positions along the fill to maintain a constant and adequate luminosity. This technique is known as

the luminosity levelling [47, 55]. The integrated luminosity recorded during 2010 and 2011 is about 1.1 fb^{-1} at center-of-mass energy $\sqrt{s} = 7$ TeV and that recorded in 2012 at $\sqrt{s} = 8$ TeV is about 2 fb^{-1}. The integrated luminosity as a function of time is shown in Fig. 3.7.

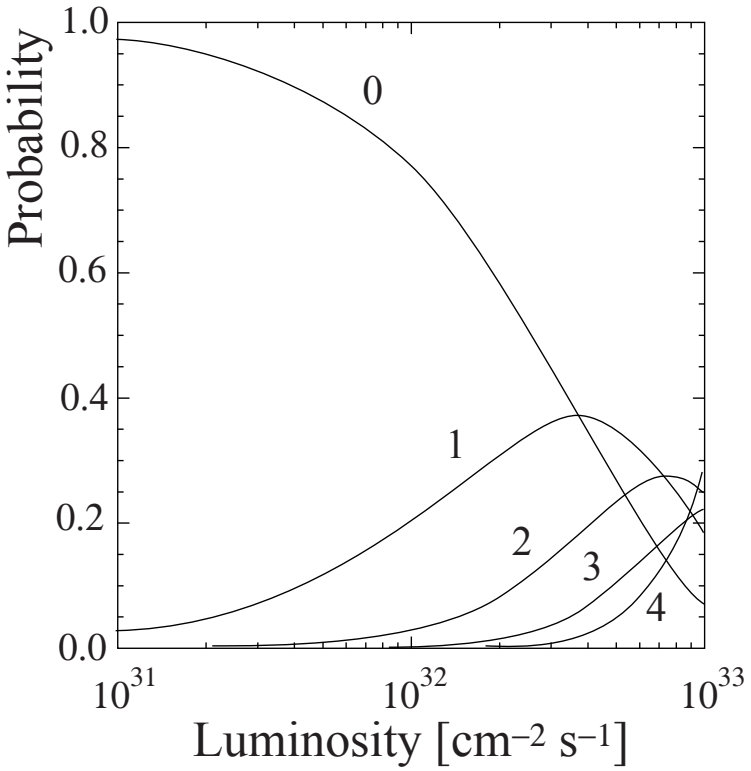

Figure 3.3: *Probability for 0, 1, 2, 3 or 4 inelastic collisions per bunch crossing as function of the luminosity.*

The dominant mechanism of the $b\bar{b}$ quark pair production in the proton-proton collision is the gluon fusion. Fig. 3.4 shows some diagrams of the most significant contributions. The gluon interactions lead to a production of $b\bar{b}$ quark pair predominantly in the same forward or backward cone as shown in Fig. 3.5.

In LHCb, the decays of b hadron into final states containing a D^0 meson and a muon are used to measure the $b\bar{b}$ production cross-section. In pp collisions at a center-of-mass energy of 7 TeV, as well in the pseudorapidity interval $2 < \eta < 6$ and integrated over all transverse momenta, the measurement of the average cross-section to produce b-flavoured or $\bar{b}$-flavoured hadrons is found to be $\approx 75.3 \pm 14\,\mu\text{b}$ ($\approx 280\,\mu\text{b}$ in the full phase space).

3.2 The LHCb detector

3.2.1 General overview

The design of the LHCb detector is driven by the properties of heavy quarks production. As discussed previously in Section 3.1.2, the heavy quark pair $b\bar{b}$, is produced in the forward

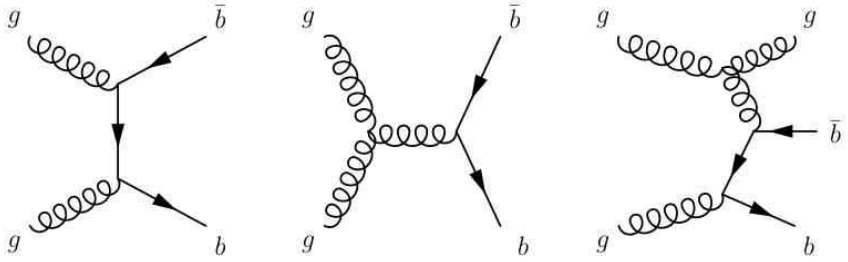

Figure 3.4: *Examples of gluon-gluon interaction producing a $b\overline{b}$ quark pair.*

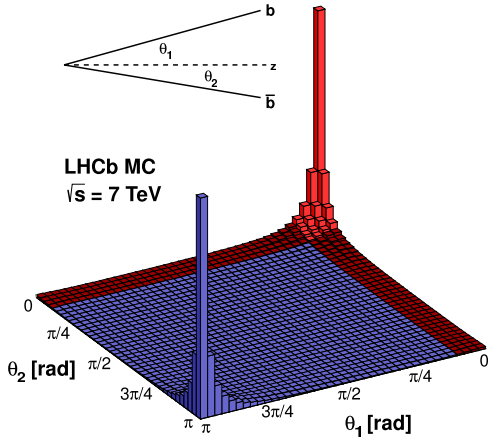

Figure 3.5: *Angular distribution of the $b\overline{b}$ quarks pair in the LHCb, computed with* Pythia *[56]. The red histogram shows the quarks pair angular distribution within LHCb acceptance.*

or backward direction with very small angle w.r.t. the direction of the beam. Due to the very asymmetric parton collisions, the $b\overline{b}$ pairs are produced with a large boost along the direction of the higher momentum parton. Therefore, the LHCb detector is designed as a single-arm magnetic dipole spectrometer, which sits forward of the interaction point, covering an acceptance of 10 mrad, to 250 mrad in the horizontal plane w.r.t. the beam line and 10 mrad, to 300 mrad in the vertical plane, which correspond to a $2 < \eta < 5$ pseudorapidity range. The highlighted distribution in red in Fig. 3.5 shows the distribution of $b\overline{b}$ quark pairs within LHCb acceptance which illustrates the motivation behind the choice of the detector geometry. The layout of the detector is given in Fig. 3.6.

The right-handed Cartesian coordinate system is used to describe the LHCb dimension. The origin of the coordinate system is chosen to be at the pp interaction point, which is the region surrounded by the VErtex LOcator (VELO).

As mentioned in Section 3.1.3, the lower luminosity than the nominal one eases the reconstruction of tracks in the high multiplicity forward region. Accordingly, a very good

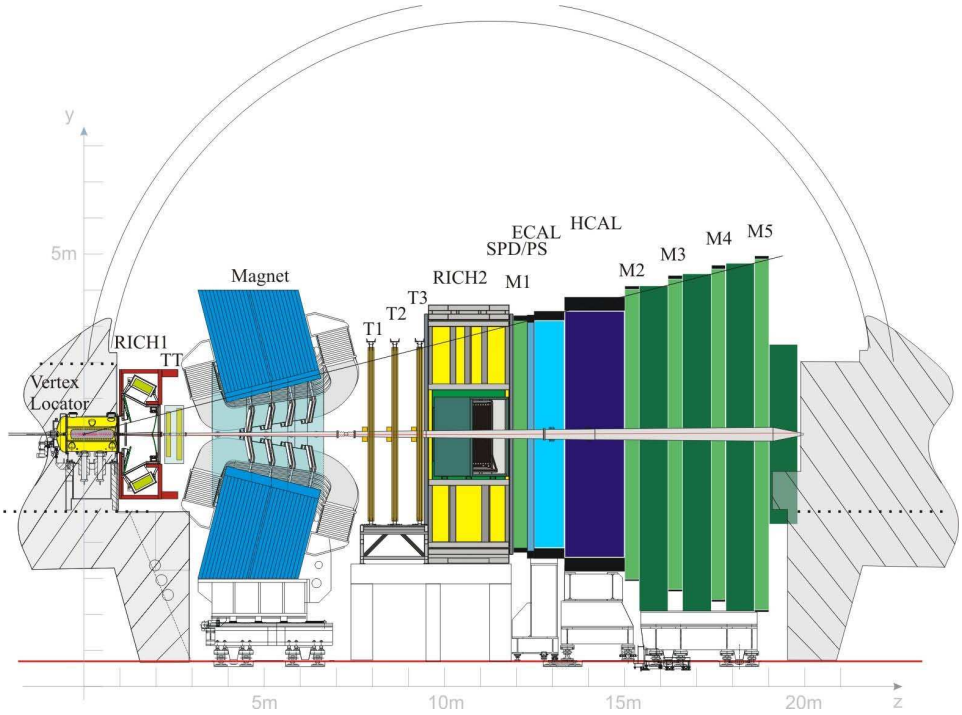

Figure 3.6: *LHCb schematic overview.*

separation of the Primary Vertices (PV: p-p interaction point) and Secondary Vertices (SV: decay point) is obtained. This is of major importance since the displaced decay vertex is a distinctive feature of b and c hadrons.

The detector components can be divided into two main categories, the tracking system which consists of the VELO, the Tracker Turicensis (TT) and the T stations. The second category consists of sub-detectors dedicated to particle identification (and trigger purposes) composed by the two Ring-Imaging CHerenkov detectors (RICH), the calorimetry system and muon chambers. In the following sections, each of the LHCb subsystems will be described.

3.2.2 Tracking system

Most of the physics studies in LHCb experiment require an accurate vertex reconstruction and excellent momentum resolution. These challenging requirements are met thanks to the tracking system. The VELO and the TT stations are located upstream the dipole magnet, whereas the T stations are placed downstream the magnet.

3.2.2.1 Vertex Locator

The vertex locator is a silicon strip detector enclosing the interaction point. It consists of 21 stations arranged along the beam direction, illustrated in Fig. 3.8. Each station consists of two layers of silicon microstrips. The VELO measures the track coordinates r, read by the R-Sensor, and ϕ, read by the Phi-Sensor. The z coordinate is given by the location of the station. These cylindrical coordinate measurements are used to reconstruct the displaced

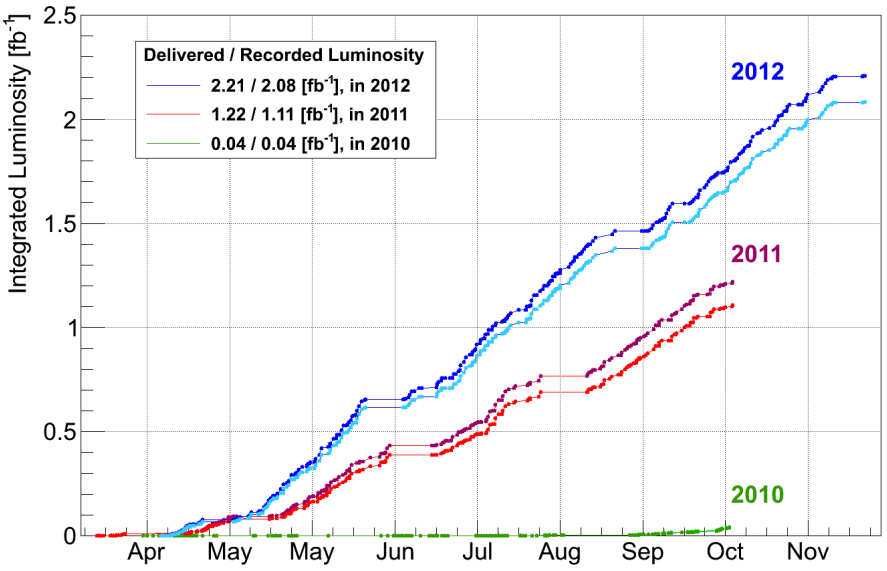

Figure 3.7: *LHCb delivered and recorded luminosity in Run 1.*

secondary vertices, generated by the lifetime of the heavy flavoured weakly-interacting hadron decays. The use of the cylindrical coordinates rather than the Cartesian is required by the High Level Trigger (HLT) performance, for which 2D (rz) tracking has been demonstrated to yield a faster reconstruction with enough impact parameters resolution. The layout of the two different types of sensors is displayed in Fig. 3.10. The sensitive area of the modules starts at 8 mm, while this radius is much smaller than the aperture required by the LHC during the injection. Accordingly, the sensors are retracted to a distance of 3 cm during injection and ramping phases of the LHC (*cf.* Fig. 3.9).

The VELO permitting precision measurements of the production and decay vertices of beauty and charm particles which allow to make accurate measurements of the decay lifetimes. The accurate measurement of decay lifetimes is required for the *CP* violation studies, therefore precise vertex reconstruction is important for this thesis analysis. The PV resolution is strongly correlated to the number of tracks N used to reconstruct the vertex, Fig. 3.11 shows the PV resolution of events with exactly one PV in 2011 and 2012 data as a function of track multiplicity N in the transverse plane.

The B mesons are long lived particles and hence their decay vertex is generally displaced from the PV. The tracks made by particles coming from the decay of long lived particles therefore tend to have larger impact parameters than those made by particles produced at the PV. Consequently, cuts on the IP are very effective at excluding prompt backgrounds, and maximising the signal content of a data set. It is thus of great importance to be able to measure IP to a high precision. The IP resolution is correlated to the particle momentum, Fig. 3.12

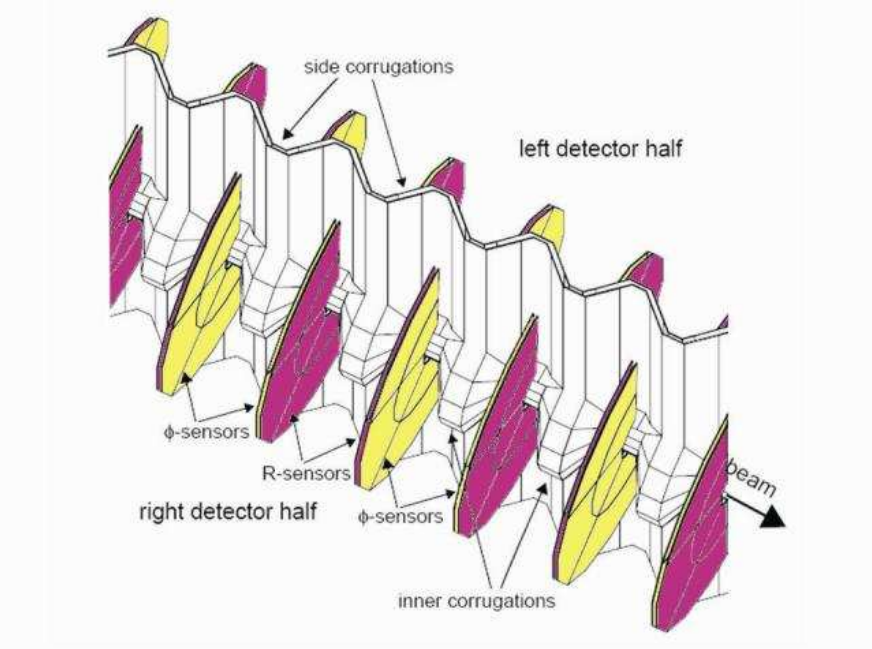

Figure 3.8: *Zoom on the inside of an RF-foil, as modelled in GEANT, with the detector halves in the fully closed position. The r- and ϕ-sensors are illustrated with alternate shading. The figure is published in Ref. [47].*

3.2.2.2 Magnet

The LHCb detector uses a warm dipole magnet with integrated magnetic field of $\int B\mathrm{d}l = 4$ T.m [47], located about 5 m downstream of the interaction region. The total weight of the yoke is 1500 tons and the two coils are together 54 tons. The generated magnetic field lines, oriented vertically along y-axis, bend the trajectory of the charged particles in the horizontal x-z plane, which enables the momentum of charged tracks to be determined by measuring the curvature of their trajectory. Thanks to the bending power of the magnet, the momentum of the particle traversing the entire tracking system can be measured with a resolution ($\Delta p/p$) of 0.4% at 2 GeV and 0.6% at 100 GeV. A schematic representation of the LHCb magnet is displayed in Fig. 3.13.

The magnetic field is swapped periodically (typically each two weeks in routine operation) to collect the same amount of data for each polarity, `MagUp` and `MagDown`. This swapping is useful in studying any charge detection asymmetry due to imperfections in the detector which could mimic a *CP*-violating asymmetry.

3.2.2.3 Silicon Trackers

The tracks close to the beam pipe, where the occupancy is the largest, are reconstructed by means of the Silicon Trackers (ST). The ST system consists of two detectors, the Tracker Turicensis (TT) (also known as the Trigger Tracker) and the Inner Trackers (IT). Both detectors use silicon micro-strip sensors with a strip pitch of about 200 μm providing single hit spatial resolution of 50 μm. The TT is located in the front of the magnet and the IT,

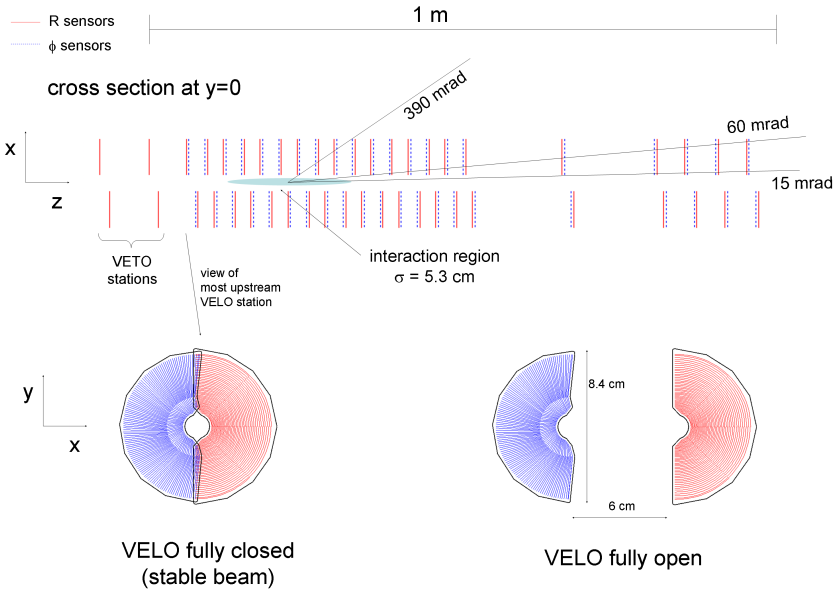

Figure 3.9: *(a) An overview of the velo detector showing the projection of the sensors on the x-z plane (top) and illustration of a one sensor in the closed and open configuration (bottom). The figure is published in Ref. [47].*

mounted in the center of the three tracking stations (T1-T3), located behind the magnet.

Tracker Turicensis: The TT detector is installed between the RICH1 and the dipole magnet and covers the full LHCb acceptance. Its four layers are 150 cm wide and 130 cm high. The four detection layers are in an (x-u-v-x) arrangement with vertical strips in the first and the last layer, and strips rotated by a stereo angle of $-5°$ and $+5°$ in the second and the third layer (*cf.* Fig. 3.14). The two layers (x, u) are placed at a distance of about 27 cm from the second two layers (v, z), in order to favour the tracking reconstruction algorithm. The configuration (x-u-v-x) allows to reconstruct track parameters with a high resolution in the bending plane (x-z) but also gives additional information in y-axis to reduce the combinatorics background. The layout of the TT detector is sketched on Fig. 3.14.

Inner tracker: The IT covers a 120 cm wide and 40 cm high, shaped like a cross and it is located in the center of three tracking stations downstream of the magnet, where the track density is higher. The active area of the IT is 4.0 m^2 and is composed of four independent detector boxes placed around the beam pipe, as sketched on Fig. 3.15. The four boxes share a similar structure, each of them containing four layers made of seven detectors modules. The modules of the boxes above and below the beam pipe consists in single 320 μm thick sensor and a readout hybrid, while the modules of the left and the right boxes are made of two 410 μm thick sensors plus the hybrid readout.

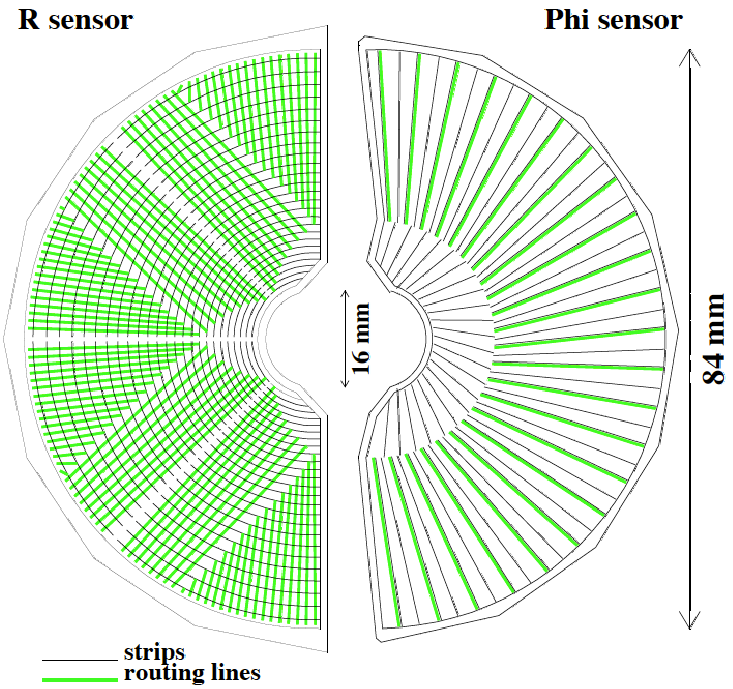

Figure 3.10: *LHCb Schematic representation of an R-type and a phi-type sensor, with the routing lines orientated perpendicular and parallel to the silicon strips, respectively. The figure is taken from Ref. [57].*

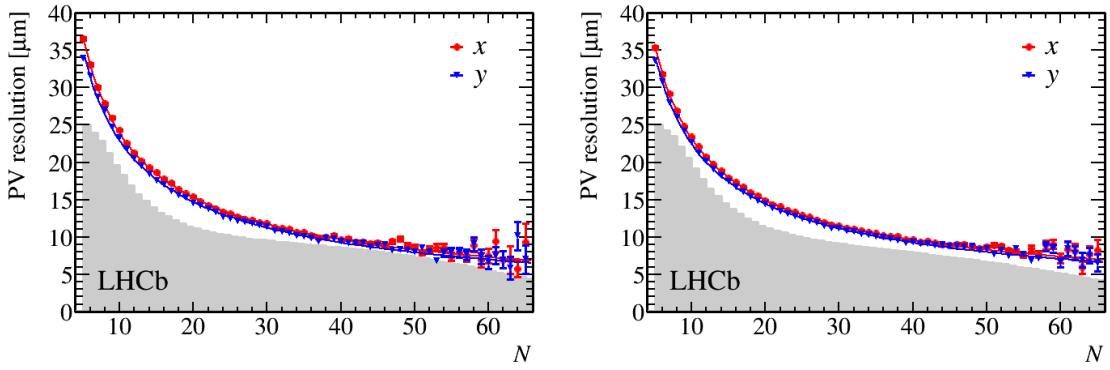

Figure 3.11: *PV resolution of events with exactly one PV in 2011 (left) and 2012 (right) data as a function of track multiplicity. The red (blue) points corresponds to the x (y) resolution. Grey histogram contains number of tracks per vertex in data (before applying the vertex resolution procedure). The figures are taken from [58].*

3.2.2.4 Outer tracker

The Outer tracker (OT), illustrated in Fig. 3.15, is a drift-time detector. It is mounted in the (T1-T3) stations around the IT and used to reconstruct tracks in the region of the

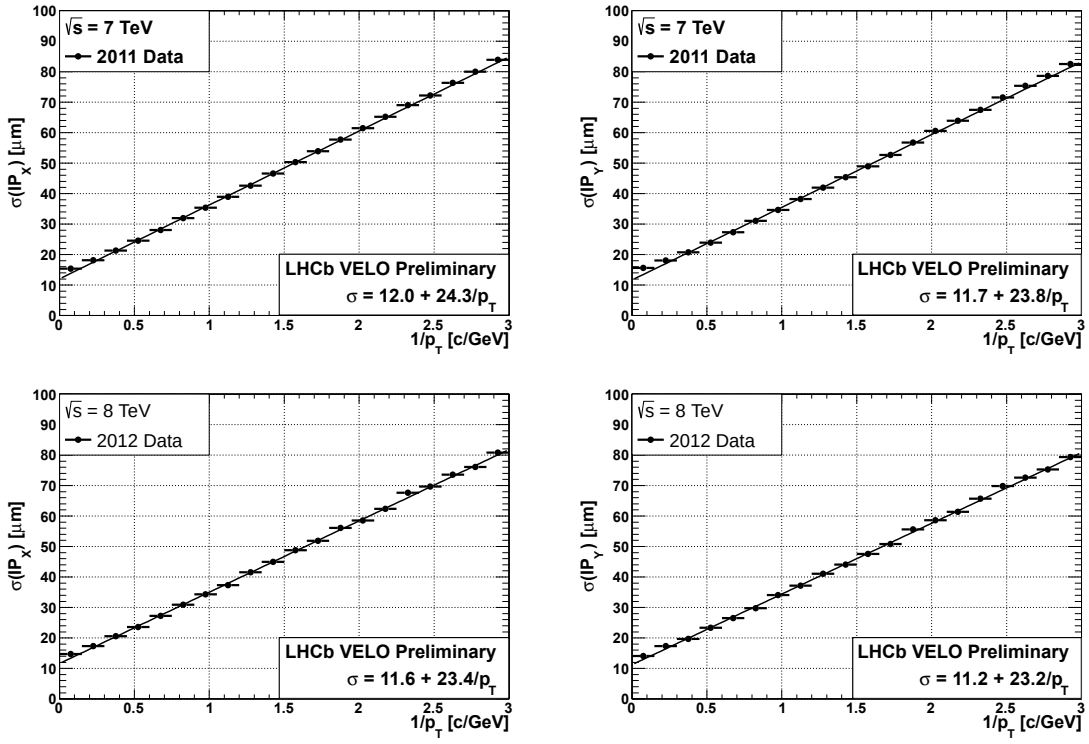

Figure 3.12: *IP_x (left) and IP_y (right) resolution as a function of the inverse of transverse momentum, determined with 2011 (top) and 2012 (bottom) data. The figures are taken from [58].*

LHCb acceptance not covered by the IT. In each tracking stations there are four layers of detectors, the third and fourth layer are arranged with a skew of $\pm 5°$. Unlike the other tracker detectors, the OT is the only non-silicon tracking detector. It is designed as an array of individual straw-tube modules, each containing two staggered layers of drift tubes with inner diameters of 4.9 mm (*cf.* Fig. 3.16).

3.2.2.5 Track reconstruction categories

The hits in the LHCb detector are defined by a point or a line in the space, which corresponds to a detector signal that has been induced by the passage of charged particle through a part of the tracking system. The track reconstruction consists in combining the hits in the VELO, the TT, the OT and the IT detectors to form particle trajectories. The reconstructed tracks are sorted in five categories:

- **VELO tracks:** these track candidates are reconstructed from the hits in the VELO, so-called VELO-seeds. They are useful for the reconstruction of the primary vertices.
- **Upstream tracks:** These tracks usually have a low momentum so that the magnet bends them out of the acceptance of the T stations. Therefore, they contain information only from the VELO and the TT.

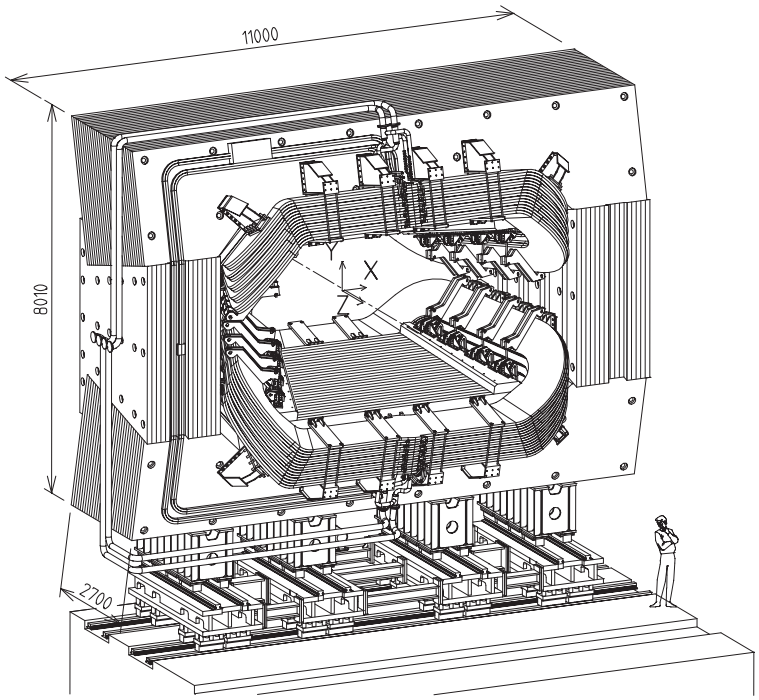

Figure 3.13: *A schematic representation of the LHCb dipole magnet (units in* mm*). The figures taken from [58].*

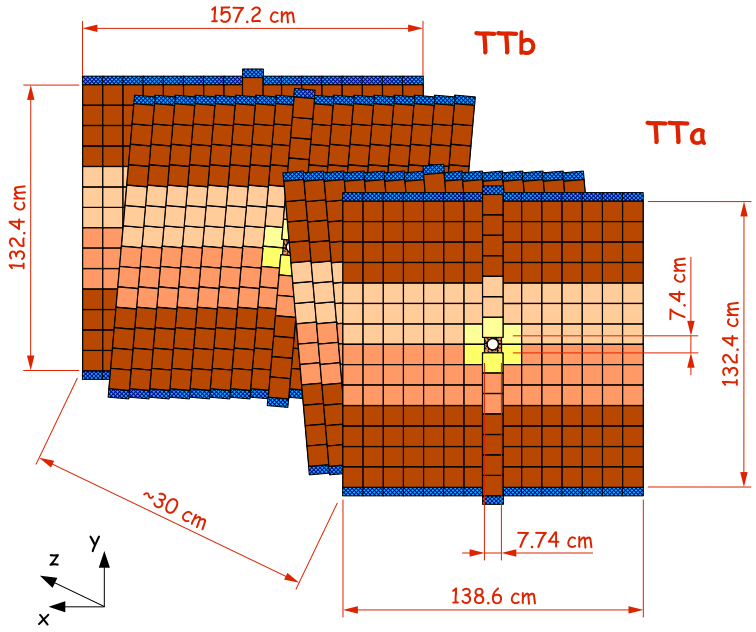

Figure 3.14: *Illustration of the four TT detector layers. The figure is published in Ref. [47].*

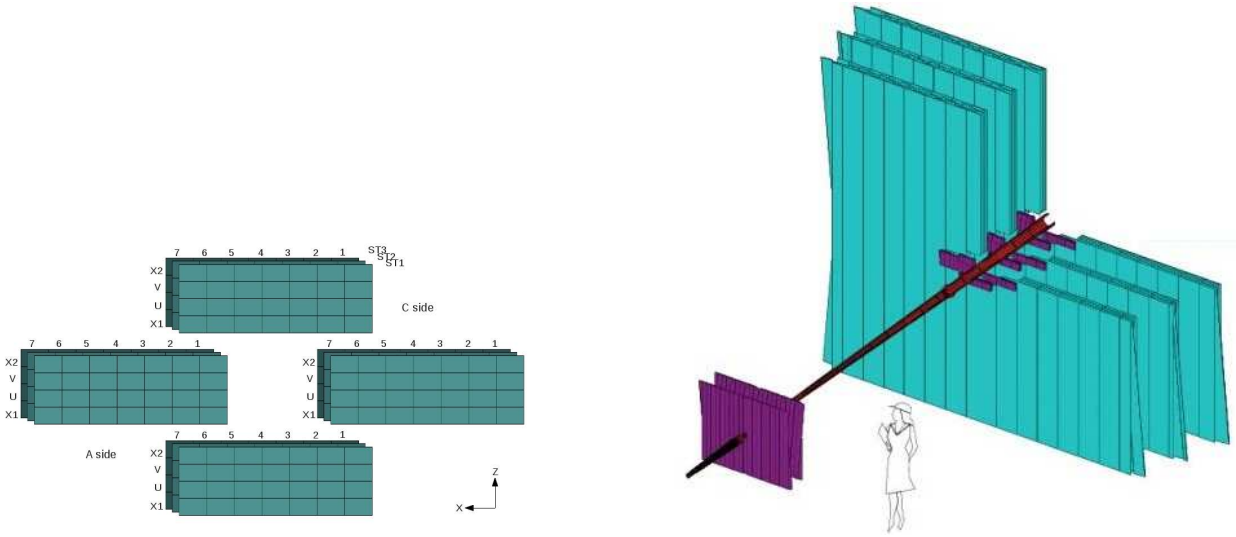

Figure 3.15: *Left plot: illustration of the IT layer sub-detectors. Right plot: scheme of the TT, T1, T2 and T3 stations. The Cyan colour corresponds to the OT and the violet colour corresponds to the all ST system. Figures are taken from Ref. [47].*

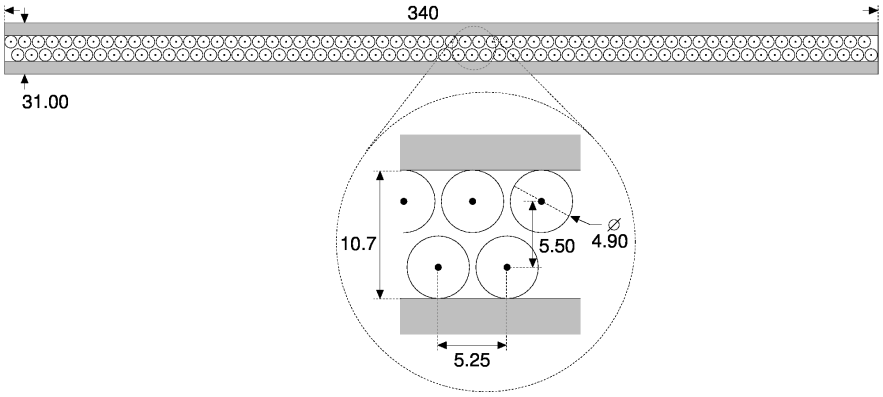

Figure 3.16: *Illustration of the OT layer and zoom on the arrangement of straw tubes (Measurements in* cm*). The figure is published in Ref. [47].*

- **Long tracks:** This type of tracks combine information from the VELO, TT and T stations, hence having crossed the entire tracking system. As such, they have the best momentum resolution among the track categories.
- **Downstream tracks:** Some long-lived particles, as K_S^0 or Λ, decay outside of the VELO, implying that their tracks will be reconstructed only by the TT and the T stations. They have a lower resolution compared to that of long tracks due to the missing information from the VELO and the resulting longer lever arm.
- **T tracks:** These tracks are exclusively reconstructed in the T stations, and are usually the product of secondary interactions.

A summary of the different types of track is sketched on Fig. 3.17. The analysis presented in this document will make an intensive use of Longstream and Downstream track categories.

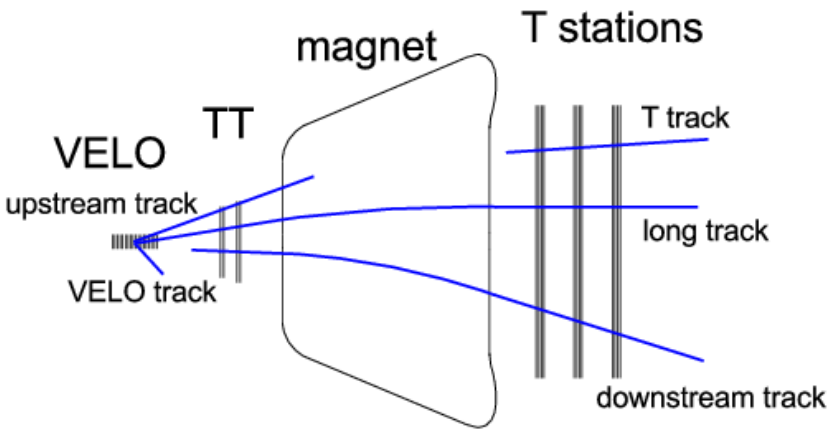

Figure 3.17: *Illustration of the five different track types in LHCb. Figure taken from Ref. [59].*

3.2.3 Particle identification detectors

For many flavour physics analyses, including the work presented in this thesis, it is crucial to identify the long-lived particle species (π, K, p, e, γ and μ) in the decay final state. Particle Identification (PID) is provided by the LHCb experiment with excellent resolution, by combining information from different sub-detectors, namely the Cherenkov detectors, the calorimeter system and the muon system. Fig. 3.18 illustrates how the reconstruction of the decay mode $B^0 \to \pi^+\pi^-$ is eased with a dedicated particle identification. In the following, the sub-detectors dedicated for particle identification will be explained briefly.

3.2.3.1 RICH detectors

LHCb has two RICH (Ring Imager Cherenkov) detectors, covering different momentum ranges to get an efficient PID over the full momentum range. The upstream detector, RICH1, covers the low momentum charged particle range from ~ 1 GeV/c to 60 GeV/c, and uses aerogel and C_4F_{10} as radiators. The downstream detector, RICH2, covers larger momenta range, from ~ 15 GeV/c to 100 GeV/c and uses as radiator the CF_4. Fig. 3.19 illustrates the separation power of the different radiators as a function of the particle momentum. RICH1 covers the full LHCb acceptance from ± 25 mrad to ± 300 mrad in the bending plane, and to ± 250 mrad in the vertical plane. Regarding the second RICH detector, since particles with high momenta are produced at small angles w.r.t. the beam line, then the RICH2 is chosen to cover a limited angular region, from ± 15 mrad to ± 120 mrad in the bending plane, and to ± 100 mrad in the vertical plane. In both RICH detectors, the Cherenkov light is deflected out of the spectrometer acceptance by spherical and flat mirrors. The Cherenkov light is detected by Hybrid Photon Detectors (HPDs) placed outside the spectrometer acceptance

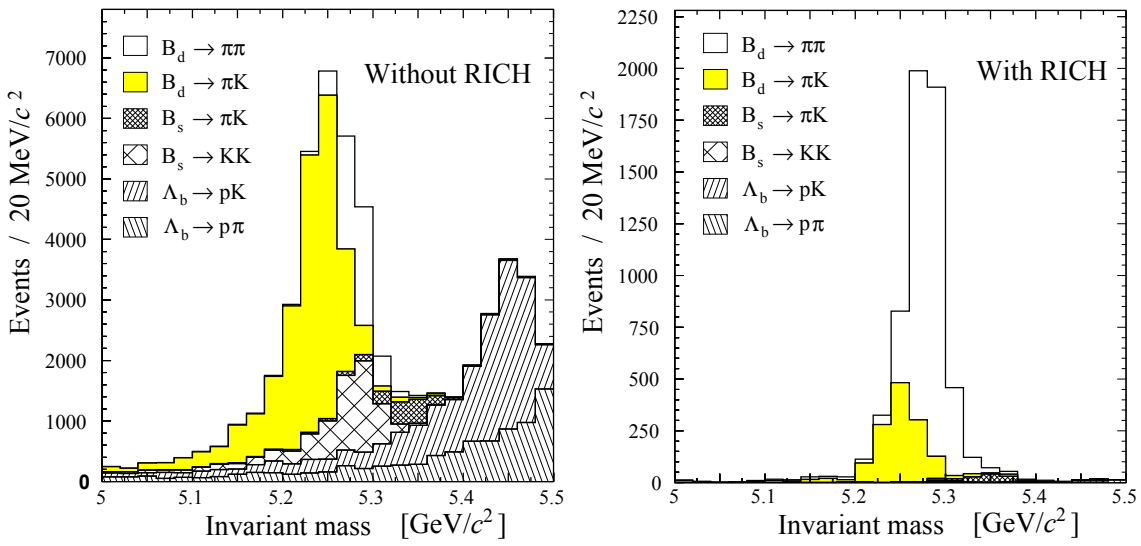

Figure 3.18: *Reconstructed invariant mass for several two-body decays without (left) and with (right) particle identification requirement optimized for* $B^0 \to \pi^+\pi^-$ *[60].*

and shielded from the magnetic field with iron screens. The layout of the two RICH detectors is illustrated in Fig. 3.20.

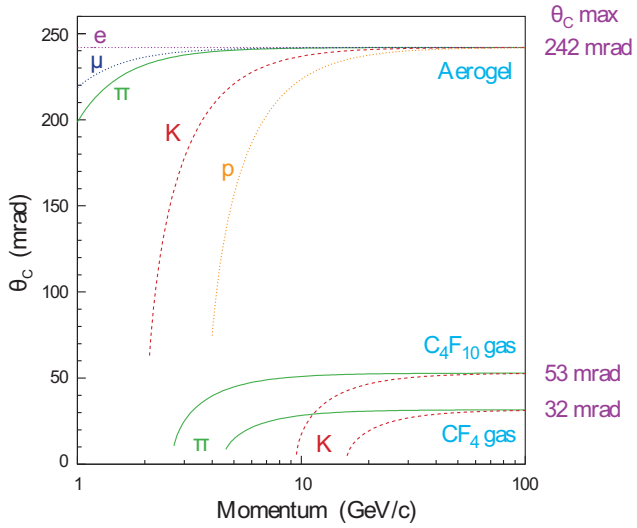

Figure 3.19: *Cherenkov angle of different radiators as a function of the particle momentum. The figure is published in Ref. [47].*

3.2.3.2 Calorimeter systems

The LHCb calorimeter system is designed to have three main functionalities:

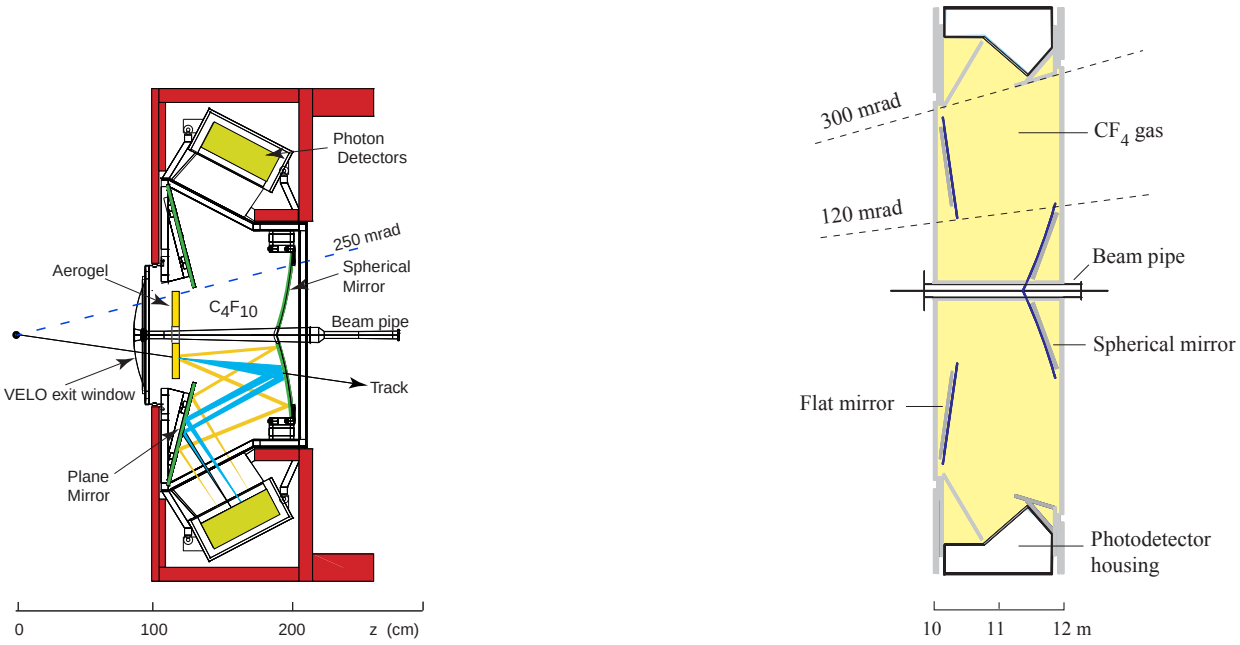

Figure 3.20: *The layout of the RICH1 (left) and RICH2 (right) detector. The figures are published in Ref. [47].*

- providing the transverse energy measurement for charged hadron, electron and photon candidates for the first level of trigger (L0).
- providing particle identification to distinguish between electron, photon and hadrons.
- separating the single photon from the double photons generated by the decay of π^0 mesons.

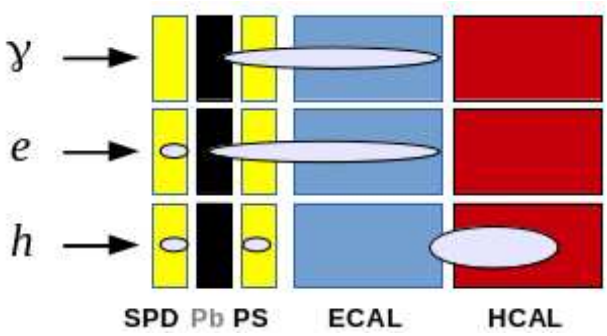

Figure 3.21: *Schematics indicating the separation between electrons, photons and hadrons showers within the LHCb calorimeter sub-detectors. The figure is published in Ref. [47].*

The LHCb calorimeter system consists of a Scintillator Pad Detector (SPD) and Preshower detector (PS), separated by a lead converter, followed by an Electromagnetic

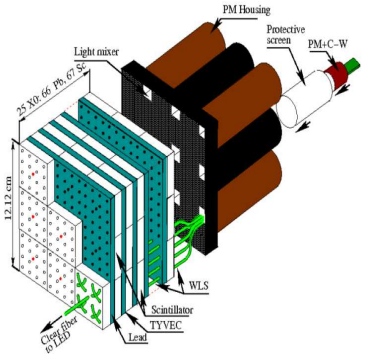

Figure 3.22: *Illustration of ECAL cell structure. The figure is published in Ref. [47].*

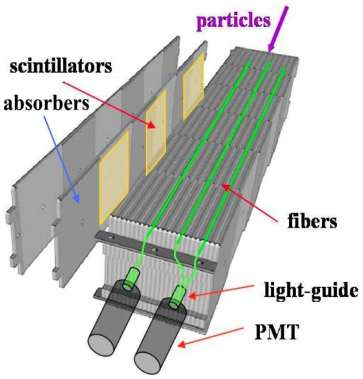

Figure 3.23: *Illustration of HCAL cell structure. The figure is published in Ref. [47].*

(ECAL) and Hadronic (HCAL) Calorimeters. The four sub-detectors of the calorimeter system have scintillators as active materials. The ECAL is made of a *shashlik* calorimeter technology, *i.e.* a sampling scintillator / lead structure readout by plastic wave length shifting (WLS) fibers to PhotoMultiplier Tubes (PMT). The HCAL uses iron as an absorber. Fig. 3.21 visualizes the components of the calorimeter system with a schematic indicating the separation between photons, electrons and hadrons.

SPD/PS represents the first part of the calorimeter system, located behind the first muon station. The two sub-detectors consists of two high-granularity scintillating planes separated by a lead plane with a thickness of 2.5 X_0. The SPD is a 15 mm thick layer of scintillator which aims at registering the passage of charged particles. The PS has the same construction as the SPD but evaluates the energy deposited in the upstream lead converter, hence requiring a large dynamical range electronics readout.

The ECAL is located after the PS and is designed to measure particles showers of photons and electrons. As mentioned above, the ECAL is a sampling calorimeter. The scintillators are 2 mm thick, and the lead material between two scintillator cells is 4 mm thick. The ECAL layout is presented in Fig. 3.21.

The HCAL is placed between the ECAL and the muon system (M2-M5). It aims at measuring showers induced by hadrons. As the ECAL, the HCAL is a sampling calorimeter, made of 4 mm scintillators and 16 mm thick sheets of iron, arranged differently than the ECAL. The HCAL layout is presented in Fig. 3.22.

Since the hit density varies by two orders of magnitude over the calorimeter surface, the PS/SPD, ECAL and HCAL adopt a variable lateral segmentation (*cf.* Fig. 3.24). As hadronic showers are broader compared to electromagnetic showers, the HCAL is segmented into two zones with larger cell sizes.

3.2.3.3 Muon system

Given the large number of rare and *CP*-sensitive B decays with at least one muon in the final state, the muon triggering and off-line muon identification are basic requirements of the LHCb experiment. As an example, three processes made the core of the LHCb physics case in the recent years: $B_s^0 \to \mu^+\mu^-$ [61] a very rare decay potentially sensitive to generic NP

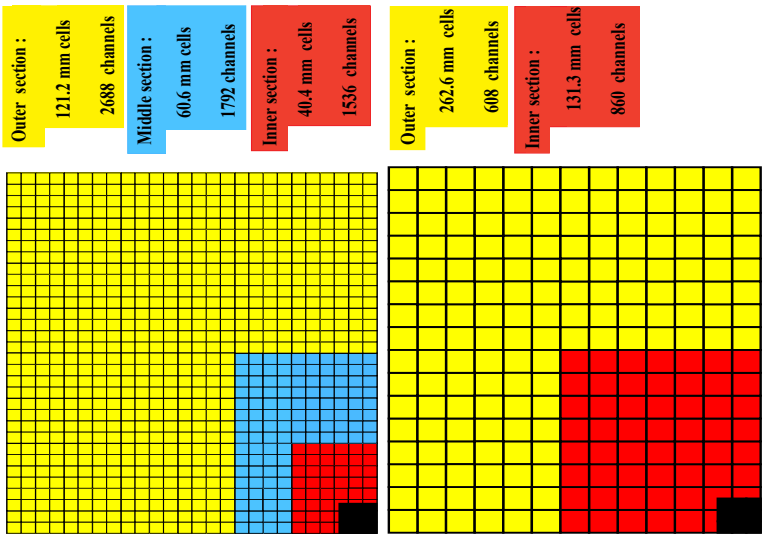

Figure 3.24: *Lateral segmentation of the SPD/PS and ECAL (left) and the HCAL (right). Only one quarter of the detector front face is presented. The figures are published in Ref. [47].*

contribution, $B_s^0 \to J/\psi(\to \mu^+\mu^-)\phi$ [62] yielding the β_s weak phase of the B_s^0-$\overline{B}_s^0$ mixing and the decay $B^0 \to K^*\mu^+\mu^-$ [63].

The muon system provides information to the L0 trigger by selecting high-p_T muons. It is also used in the high-level trigger and the off-line analysis for the muon reconstruction and identification. The muon system consists of five stations (M1-M5), M1 is located upstream of the SPD and M2-M5 are downstream of the HCAL (*cf.* Fig. 3.25). The sub-detectors (M2-M5) are composed of 1380 Multi Wire Proportional Chambers (MWPC), while M1 active detector is a triple-GEM detector (Gas Electron Multiplier) for its innermost part and MWPC for the rest. The full muon system covers an area of 435 m^2.

The purpose of M1 is to improve the transverse momentum resolution of muons in the trigger, as there is less multiple scattering before entering the calorimeter system. The stations M2-M5 are interleaved with 80 cm thick iron plates acting as an absorber for all remaining detectable particle except muons. The total absorber thickness (including the calorimeter system) is approximately 20 interaction lengths which translates in selecting muons with a minimum momentum of 6 GeV/c to cross the five stations. Stations M1-M3 have a high spatial resolution along the bending plane and they are hence used to define the track direction and to calculate the transverse momentum of muon candidates with a resolution of 20%. Stations M4 and M5 have a limited spatial resolution and are helping the identification of penetrating particles. In the off-line reconstruction, trajectories from the tracking stations are extrapolated to the muon system and if there are hits found in the muon stations, such long track are considered to be muon candidates.

3.2.4 Particle identification techniques

The Particle Identification (PID) in LHCb experiment is achieved by combining the information from the particle identification sub-detectors when available : RICH detectors,

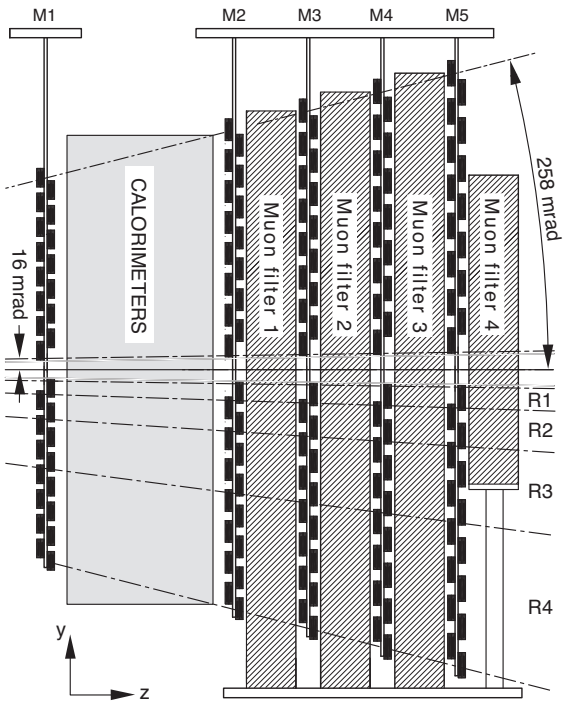

Figure 3.25: *Overview of the LHCb muon stations. The figure is published in Ref. [47].*

calorimeters, muon stations for charged tracks, the calorimeters for photons and neutral pions.

For each track the available PID information is elaborated into two variables of different nature, but with same functionality: the log-likelihood difference (DLL) and `ProbNN`, which has been recently introduced in the collaboration. The DLL is the difference between a given PID hypothesis (h) and the pion hypothesis:

$$\mathrm{DLL}_h = \ln \mathcal{L}_h - \ln \mathcal{L}_\pi = \ln \left(\frac{\mathcal{L}_h}{\mathcal{L}_\pi} \right) \ , \tag{3.2}$$

where $\mathcal{L}_i$ is the combination of the information of the various sub-detectors used for the identification.

The `ProbNN`, which is the variable used for the analysis presented in this thesis, uses a recursive Neural Network (NN) called Hopkins network [64].

3.2.5 Trigger system

The bunch crossing frequency at the LHC is 40 MHz. Not all bunch crossings provide proton collisions and the event rate of visible interaction is typically 10 MHz. The purpose of the whole trigger system is to reduce the event rate from 10 MHz to 4-5 kHz before recording the events for off-line analysis, because of the current limitation for writing events to storage. The trigger system is separated in two main levels: a custom-electronics hardware Level 0 trigger (L0) operating synchronously with the collisions and a software High Level Trigger

(HLT) run on processor farm, so-called the Event Filter Farm (EFF). A scheme of the LHCb trigger system is illustrated in Fig. 3.26.

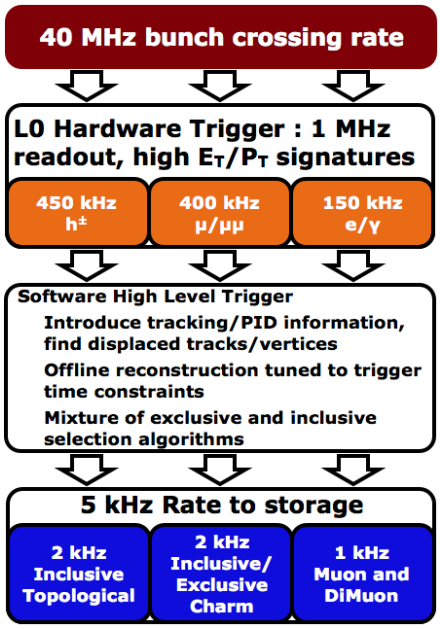

Figure 3.26: *Scheme of the LHCb trigger system during* 2011-2012 *data-taking period.*

3.2.5.1 Level 0 trigger

The L0 trigger is an extremely fast trigger implemented on custom-electronics hardware aimed at fast rejection of uninteresting events. It reduces the rate of the events from the collision rate to less than 1.1 MHz. The L0 trigger consists of three detector-based subsystems: the pile-up system, the L0 calorimeter trigger and the L0 muon trigger, as illustrated in Fig. 3.27. The calorimeter and muon triggers select events with large transverse momentum and energy hadron, electron, photon or muon, which are common characteristics in many heavy flavour decays topologies. The pile-up system estimates the overall number of primary vertices in event. The Level 0 Decision Unit (L0DU), which is a single electronics board, collects all the information from the three detector-based subsystems, to take the final decision on the event. This decision is passed to the Readout Supervisor (RS) which in turn transmits it to each detector front-end electronics to read-out the event in view of a further processing by the Data Acquisition (DAQ) system. The time between the collision and a L0 decision being accepted in the front-end electronics is 4 μs including the cable delay and delays in the front-end electronics.

3.2.5.2 High level trigger HLT

Events passing the L0 are processed by the HLT. This trigger part is a C++ built application running on every node of the EFF. The HLT trigger is subdivided in two stages: the HLT1 trigger consists in a set of inclusive trigger requirements or *lines* grouped in various classes,

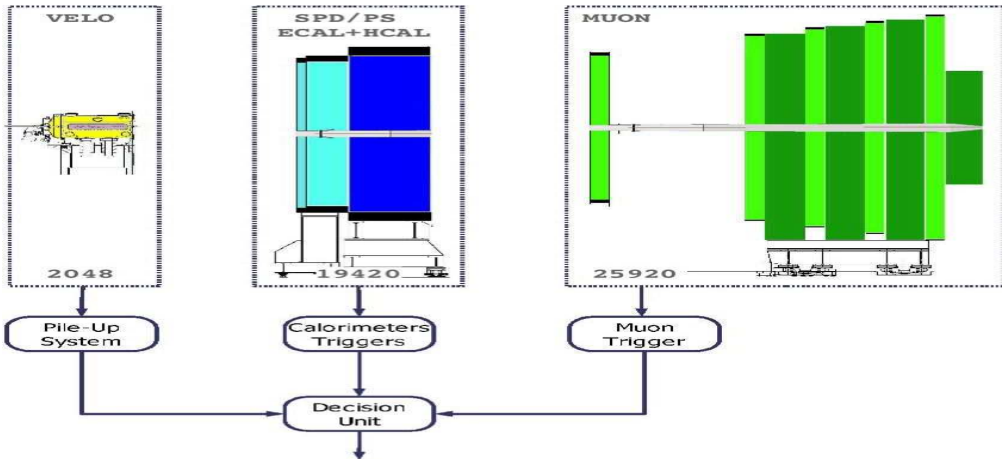

Figure 3.27: *Overview of the L0 trigger. The figure is published in Ref. [47]*

such as physical, technical and muon dedicated trigger lines. The HLT2 is composed of many lines, inclusive and exclusive, each of them optimised for a specific analysis.

HLT1 performs a partial event reconstruction and selection based on information from the VELO and tracking stations, and aims at reducing the rate by a factor ~ 20. It is based on the concept of selecting one very good quality track with high transverse momentum and a large impact parameter (IP, shortest distance between a track and the PV) w.r.t all PV in the event. The selection in HLT1 contains several different lines running in parallel, which allow to tune (by changing transverse momentum threshold) the efficiency of selecting inclusively different decay types by daughters type (e, γ, μ).

HLT2 algorithms are performed on all the events passing the HLT1, no matter of the candidate type. In HLT2, the different tracks are combined to reconstruct a composite particle (as $K^0_S \to \pi^+\pi^-$ in the analysis presented in this thesis or $J/\psi \to \mu^+\mu^-$, *etc.*) used as input to the different inclusive and exclusive selections. The inclusive selection requires at least two charged tracks in the final state and a displaced secondary vertex. Exclusive selection requires all the decay products in a specific decay chain to be reconstructed.

3.2.5.3 Trigger decision categories

A unique key, called trigger Configuration Key (TCK), is assigned to the combination of trigger algorithm with their selection parameters. In the stored data, the TCK is identified as a 32-bit encoded for every event. Each event can be classified, at any level of the trigger, in three non-exclusive categories:

- Event classified as TOS (Trigger On Signal) if the trigger objects that are associated with the signal are sufficient to trigger the event.
- Event classified as TIS (Trigger Independent of Signal) if it could have been triggered by those trigger objects that are not associated to the signal.
- Event classified as TIS and TOS simultaneously.

L0 and HLT trigger requirements used for the analysis of this thesis are discussed in Section 4.1.1 and gathered in 4.2.

3.2.6 LHCb reconstruction and data stripping

Data that passed HLT2 are written on disk storage. Thereafter, these raw data are processed along the reconstruction procedure using BRUNEL package [65], which is designed to determine or fit physical quantities such as vertices, momenta, energies, PID probabilities *etc...* After the reconstruction procedure, the output will be a Data Summary Table (DST) containing all information about the events. Afterwards, a further selection, so-called *Stripping*, is applied using the DAVINCI software package. The stripping consists of several algorithms named Stripping line, building candidates and applying selection typically by combining tracks of a given particle hypothesis into composite particles candidates. Almost every analysis has its own dedicated stripping line, but there are some stripping lines shared by several analyses, as the one used in the analysis presented in this thesis. The stripping selection requirement made on candidates used in the analysis of this thesis are listed in Section 4.1.2.

3.2.7 LHCb software

The LHCb software comprises several packages used for simulation, events reconstruction and physics analysis. These packages are all built within the GAUDI framework [66], which is an object-oriented framework. It is designed to provide a common infrastructure and environment for all different software packages. A brief overview of the relevant software packages (some of them will be used in the later chapters of this document) is given in following.

- **GAUSS:** The GAUSS software [67] is designed for generating simulated data samples. It integrates two independent phases, the Generator phase, which consists of generating the p-p collisions, using PYTHIA software [56], and the decay of the particles produced, simulated either with EVTGEN or PYTHIA. The second phase is the simulation phase, which consists in the simulation of the tracking of the particles in the detectors and simulating the physics processes occurring in the experimental setup, using GEANT4 software [68, 69].

- **BOOLE:** BOOLE software [70] is the LHCb digitization program. It reads in the output of the detector simulation, adds hits from Spillover events and LHCb background, and applies the detector response. The output of BOOLE has the same format as that of real LHCb data.

- **MOORE:** The MOORE software [71] is used to run the HLT selection on reconstruction events. This software is especially useful to emulate the HLT response on the simulated data.

- **BRUNEL:** The BRUNEL software is the LHCb reconstruction application, analysing events from both real or simulated data based on the information from the sub-detectors.

- **DaVinci:** The DaVinci software [72] is an analysis framework to perform analysis and manipulation of the reconstructed events output from Brunel.
- **PIDCalib:** The PIDCalib [73] software is used to determine PID performance results from both collision real and simulated data. Also used to correct the PID probability variables of the simulated samples using the PID performance from the real data.

Besides the LHCb software, much of the analysis studies in this thesis is performed using external software, specially Root and CRAFT. Root [74] is an object-oriented program, for large scale data analysis, developed at CERN. CRAFT (Clermont Roofit-based Amplitude Fitter Tool) is a Dalitz-plot fitter developed by Stéphane Monteil and myself, used to make Dalitz-plot analysis. For more details, see Appendix E.

Chapter 4

Study of $B^0_{(s)} \to K^0_S h^+ h'^-$ decays

The analyses of the three-body charmless decays of neutral B mesons, including a neutral K meson in the final state, represent a good environment for the search for CP violation effects. The neutral K^0-$\bar{K}^0$ system has two eigenstates, K^0_S and K^0_L, where the second state is long-lived CP-odd component, which can't be easily detected with the LHCb detector. It requires indeed the identification of an isolated neutral calorimetric cluster. Thus, the analysis in this thesis concerns six charmless three-body decay modes, $B^0_{d,s} \to K^0_S \pi^+ \pi^-$, $B^0_{d,s} \to K^0_S K^\pm \pi^\mp$ and $B^0_{d,s} \to K^0_S K^+ K^-$, where more attention will be given to the first decay mode.

This chapter discusses the studies performed on the dataset collected by the LHCb detector in Run I, commencing by the selection made on the data set to establish the signal and closing by the results of the invariant mass fit to the $K^0_S h^+ h^-$ data. The studies performed in this part are done by the collaboration of three groups within LHCb: LPC Clermont-Ferrand, LPNHE Paris and Warwick university. My main contribution is related to the selection tools designed to establish the signals in the different data samples.

4.1 Dataset, trigger and stripping

The analysis of the $K^0_S h^\pm h'^\mp$ modes is performed using the full LHC Run I data sample, recorded in 2011 and 2012 by the LHCb experiment [47]. This corresponds to an integrated luminosity of $\int \mathcal{L} = 3$ fb^{-1}.

The analysis makes use of both signal and background Monte Carlo (MC) samples generated using `Sim08` [1]. The simulation conditions have a pile-up factor of $\nu = 2.0$ for 2011 and $\nu = 2.5$ for 2012 in order to match the data taking conditions.

A significant change was made to the HLT2 topological lines during the technical stop in June 2012, in order to include K^0_S candidates reconstructed from two Downstream tracks in addition to those, already included, reconstructed from two Long tracks (these two types of K^0_S, and hence B, candidate are referred to as Down-Down and Long-Long candidates). As a consequence, the trigger efficiency for the Down-Down candidates was significantly higher following the June technical stop. It is therefore necessary for the 2012 data and

[1] Monte Carlo events based on PYTHIA 8 [56]

MC samples to be divided into two running periods, which we will refer to as the pre-June and post-June or more simply 2012a and 2012b periods. In order to simulate the various trigger conditions correctly, samples have been produced using TCKs (*cf.* Section 3.2.5.3) that are representative of the three periods (2011, 2012a and 2012b), which are `0x40760037`, `0x4097003d` and `0x409f0045`, respectively.

The number of MC events that have been generated for each of the signal modes under consideration are given in Table 4.1. The MC signal is generated uniform in the square Dalitz plot ("sqDalitz"). This permits a more straightforward calculation of the various efficiencies as a function of the Dalitz-plot position (see Section 5.3 for more details).

The ntuples for both data and MC have been produced with a dedicated software written in the framework `Bender v24r1` by the Warwick group.

Table 4.1: *Number of generated signal Monte Carlo events for each decay mode.*

Mode	Sample size		
	2011 Conditions	2012a Conditions	2012b Conditions
$B^0 \to K^0_S\pi^+\pi^-$ (sqDalitz)	2020495	-	4058986
$B^0 \to K^0_S K^\pm\pi^\mp$ (sqDalitz)	2021494	-	4034487
$B^0 \to K^0_S K^+K^-$ (sqDalitz)	2015746	-	4062988
$B^0_s \to K^0_S\pi^+\pi^-$ (sqDalitz)	2023743	-	4069987
$B^0_s \to K^0_S K^\pm\pi^\mp$ (sqDalitz)	2023746	-	4046483
$B^0_s \to K^0_S K^+K^-$ (sqDalitz)	2020494	-	4068489

4.1.1 Trigger

The same trigger requirements as used in the analysis [75] are applied in this thesis. They are listed in Table 4.2.

Comments are in order to define the LHCb jargon used in the following of this chapter:

- `TOS`: events classified as Trigger on Signal (*cf.* Section 3.2.5.3).
- `TIS`: events classified as Trigger independent of Signal (*cf.* Section 3.2.5.3).
- `L0Hadron`: the hadron trigger line that selects events in which a significant amount of transverse energy is deposited in a cluster of the hadron calorimeter.
- `Hlt1TrackAllL0`: The inclusive beauty and charm trigger line selects good quality track candidate based on their transverse momentum p_T ($p_T > 1.6$ GeV) and displacement from the primary vertex.
- `Hlt2TopoN(Simple)`: is the topological trigger lines based on the properties of combinations of 2,3, or 4 Topo-Tracks [2]. For a 2-body candidate two Topo-Tracks are combined into 2-body object by requiring their distance of closest approach (DOCA)

[2]Topo-Tracks are a subset of HLT2 tracks selected with additional requirements on their track fit quality (χ^2/ndf).

less than 0.2 mm. For 3(4)-body object is made by combining a 2(3)-body object and another Topo-Track with the same DOCA cut (DOCA $< 0.2\,\text{mm}$), where the DOCA is calculated between the 2(3)-body object and the additional Topo-Track.

- `Hlt2TopoNBBDT`: In this trigger line, the combination of the Topo-Tracks is made by a Bonsai boosted decision tree [76] (BBDT).

Table 4.2: *L0 and HLT trigger requirements for the $K^0_S h^\pm h'^\mp$ analysis. The HLT2 requirement should be understood as an 'OR' of the lines mentioned.*

Trigger level	Trigger requirements
L0	`L0Hadron TOS` OR `L0Global TIS`
HLT1	`Hlt1TrackAllL0 TOS`
HLT2 (2011)	`Hlt2Topo2(3,4)BBDT(Simple) TOS`
HLT2 (2012)	`Hlt2Topo2(3,4)BBDT TOS`

4.1.2 Stripping

The stripping lines created by the `StrippingB2KShh` line builder in the `Stripping20` campaign have been used for this thesis analysis.

The stripping of the $B^0_{d,s} \to K^0_S h^\pm h'^\mp$ modes responds to the double demanding technical requirement of a small minimum bias retention rate ($< 5 \times 10^{-4}$) and a fast processing of the events ($< 1\,\text{ms}$ per event). Additionally, mild cuts on the momenta and impact parameters of individual daughter particles are necessary to obtain an unbiased Dalitz plane of the decay modes. As a consequence, cuts on topological variables such as flight distance of the B candidate or its pointing are used as the main discriminative information.

Within the `B2KShh` stripping, first an event filter is applied that only retains events with fewer than 250 `Long` tracks, see Table 4.3. Then B candidates are formed by combining a K^0_S candidate with two oppositely charged pion tracks.

The pion candidates are drawn from the `StdLoosePions` list. The requirements of this list is detailed in Table 4.4. Two additional requirements are made by the stripping for this analysis, namely that the χ^2 per degree of freedom of the track fit be less than 4 and that the ghost probability be less than 0.5. The K^0_S candidates are reconstructed in their decay to $\pi^+\pi^-$ and are drawn from both the `StdLooseKsLL` and `StdLooseKsDD` lists. The former list takes its pion candidates from the `StdLoosePions`, which are formed only from `Long` tracks. The latter list uses pion candidates from the `StdNoPIDsDownPions`, which are formed from `Downstream` tracks, *i.e.* those which do not have hits in the VELO. Details of the selection requirements placed on the K^0_S candidates, both by the list definitions and by the `B2KShh` stripping algorithms are given in Table 4.5.

Initially the B candidates are formed from simple four-momentum addition and some loose "Combination Cuts" are applied to reduce the number of candidates that undergo a full vertex fit. Following the vertex fit further quality cuts ("Mother Cuts") are made on

Table 4.3: *Stripping – global selection requirements.*

Variable definition	Selection requirement
Number of `Long` tracks per event	$N_{\text{Long}} < 250$
Number of primary vertices per event	$N_{\text{PV}} \geq 1$

Table 4.4: *Stripping – selection requirements for the pion/kaon candidates.*

Variable definition	Selection requirement
`StdLoosePions` plus additional requirements	
Track fit χ^2 per degree of freedom	$\chi^2_{\text{trk}}/\text{ndof} < 4$
"Clone distance"	CloneDist > 5000
Track ghost probability	GhostProb < 0.5
Transverse momentum	$p_{\text{T}} > 250\,\text{MeV}/c$
Minimum impact parameter χ^2 w.r.t. PVs	$\chi^2(\text{IP})_{\text{min}} > 4$

the B candidate. Details of both sets of stripping cuts, which differ for Long-Long and Down-Down candidates, are given in Tables 4.6 and 4.7.

Table 4.5: *Stripping – selection requirements for the K^0_S candidates.*

Variable definition	Selection requirement
`StdLooseKsLL` plus additional requirements	
K^0_S daughter track fit χ^2/ndof	$\chi^2_{\pi\text{trk}}/\text{ndof} < 4$
K^0_S daughter track ghost probability	$\text{GhostProb}_\pi < 0.5$
K^0_S daughter track momentum	$p_{K^0_S\text{daug}} > 2\,\text{GeV}/c$
K^0_S daughter minimum impact parameter χ^2 wrt PVs	$\chi^2(\text{IP})_{\min} > 9$
Mass difference wrt nominal K^0_S mass	$\left\lvert m_{\pi^+\pi^-} - m_{K^0_S}\right\rvert < 20\,\text{MeV}/c^2$
χ^2 of K^0_S vertex fit	$\chi^2_{K^0_S\,\text{vtx}} < 12$
χ^2 separation of K^0_S vertex and associated PV	$\chi^2_{K^0_S\text{PV VD}} > 80$
`StdLooseKsDD` plus additional requirements	
K^0_S daughter track momentum	$p_{K^0_S\text{daug}} > 2\,\text{GeV}/c$
K^0_S daughter minimum impact parameter χ^2 wrt PVs	$\chi^2(\text{IP})_{\min} > 4$
Mass difference wrt nominal K^0_S mass	$\left\lvert m_{\pi^+\pi^-} - m_{K^0_S}\right\rvert < 30\,\text{MeV}/c^2$
χ^2 of K^0_S vertex fit	$\chi^2_{K^0_S\text{vtx}} < 12$
χ^2 separation of K^0_S vertex and associated PV	$\chi^2_{K^0_S\text{PV VD}} > 50$
K^0_S momentum	$p_{K^0_S} > 6\,\text{GeV}/c$

Table 4.6: *Stripping – selection requirements for the Long-Long B candidates.*

Variable definition	Selection requirement
Combination cuts	
Transverse momentum of the B candidate	$p_\text{T} > 1000\,\text{MeV}/c$
Sum of the daughters' transverse momenta	$\sum_\text{daug} p_\text{T} > 3000\,\text{MeV}/c$
p_T of at least 2 B daughters	$p_\text{T} > 800\,\text{MeV}/c$
Mass of the B candidate	$4000 < m_{K^0_S h^+h^-} < 6200\,\text{MeV}/c^2$
IP wrt PV of highest p_T B daughter	$\text{IP} > 0.05\,\text{mm}$
Maximum DOCA χ^2 of any 2 daughters	$\chi^2(\text{DOCA})_{\max} < 5$
Mother Cuts	
Transverse momentum of the B candidate	$p_\text{T} > 1500\,\text{MeV}/c$
χ^2 of B vertex fit	$\chi^2_{B\,\text{vtx}} < 12$
Cosine of B pointing angle	$\cos(\text{DIRA}_B) > 0.9999$
Minimum B IP χ^2 wrt PVs	$\chi^2(\text{IP})_{\min} < 8$
Minimum vertex distance wrt PVs	$\lvert B_\text{vtx} - PV\rvert_{\min} > 1\,\text{mm}$
χ^2 separation of B vertex and associated PV	$\chi^2_{B\text{PV VD}} > 50$

Table 4.7: *Stripping – selection requirements for the Down-Down B candidates.*

Variable definition	Selection requirement
Combination cuts	
Transverse momentum of the B candidate	$p_{\mathrm{T}} > 1000\,\mathrm{MeV}/c$
Sum of the daughters' transverse momenta	$\sum_{\mathrm{daug}} p_{\mathrm{T}} > 4200\,\mathrm{MeV}/c$
p_{T} of at least 2 B daughters	$p_{\mathrm{T}} > 800\,\mathrm{MeV}/c$
Mass of the B candidate	$4000 < m_{K^0_{\mathrm{S}}h^+h^-} < 6200\,\mathrm{MeV}/c^2$
IP wrt PV of highest p_{T} B daughter	$\mathrm{IP} > 0.05\,\mathrm{mm}$
Maximum DOCA χ^2 of any 2 daughters	$\chi^2(\mathrm{DOCA})_{\mathrm{max}} < 5$
Mother Cuts	
Transverse momentum of the B candidate	$p_{\mathrm{T}} > 1500\,\mathrm{MeV}/c$
χ^2 of B vertex fit	$\chi^2_{B\,\mathrm{vtx}} < 12$
Cosine of B pointing angle	$\cos(\mathrm{DIRA}_B) > 0.999$
Minimum B IP χ^2 wrt PVs	$\chi^2(\mathrm{IP})_{\mathrm{min}} < 6$
Minimum vertex distance wrt PVs	$\lvert B_{\mathrm{vtx}} - PV\rvert_{\mathrm{min}} > 1.7\,\mathrm{mm}$
χ^2 separation of B vertex and associated PV	$\chi^2_{B\mathrm{PV\,VD}} > 50$
Sum of the daughters' impact parameter χ^2 wrt PVs	$\sum_{\mathrm{daug}} \min(\chi^2_{\mathrm{IP}}) > 50$

4.2 Selection

Multivariate discriminants (MVA) have been designed in order to further reduce the background events in the stripped sample. The aim of the multivariate selection is to reject the combinatorial background, which is expected to be the largest contribution under the signal peaks. Prior to the multivariate selection, a preselection based on sanity cuts is applied to both the data and the optimization samples in order to remove more than half of the combinatorial background. In addition, the training of the multivariate selection is performed after the trigger and some very loose PID cuts, in order to ensure the background sample to train against to be the most realistic as possible.

The final objective of this ensemble of analyses is to perform an amplitude measurement by studying the Dalitz plane of these three-body decays. Therefore, the multivariate selection relies mostly on topological variables in view of keeping as uniform as possible the selection efficiency over the Dalitz plane. In particular, no preselection cuts on the kinematics of the daughter particles were applied and neither was such information included in the MVA training. For each of the three datasets (2011, 2012a and 2012b) the selection is optimized for K^0_S reconstructed in Down-Down and Long-Long modes independently.

In order to avoid swamping the reader with too many plots, only those for 2011 are shown in this section. Those for the two 2012 running periods are placed in Appendix C. In each case the references (with hyperlinks) are given to all plots.

Eventually, a selection of the signal decay by means of particle identification (PID) cuts is performed. This allows to separate the similar final states according to the presence of a pion or kaon. In particular, the signal cross-feed of the decay $B^0_s \to K^0_S K^\pm \pi^\mp$ can be greatly reduced. The PID cuts are also useful to remove further the combinatorial background.

4.2.1 Preselection

Simple high signal efficiency cuts are applied on top of the stripping to reduce the amount of combinatorial background. First, events with a clearly isolated B vertex are retained by requiring that the addition of the most consistent charged track to the vertex does not improve the quality of the vertex fit. A variable denoted $\Delta\chi^2$ is formed from the difference of the vertex χ^2 with and without the additional track and required to be $\Delta\chi^2 > 4$. Partially reconstructed B decays where a charged track is missed, together with a fraction of the combinatorial background, are hence removed by this cut. A further requirement that the separation of the B and K^0_S vertices in the `z` direction be larger than 30 mm is also applied, removing the events where the K^0_S is reconstructed upstream the B vertex. Finally, candidate events having one or more tracks that are consistent with being a muon (*i.e* having information in the muon stations) are removed.

The efficiencies of the above cuts on the combinatorial background are detailed in Table 4.8. The invariant mass distributions after the preselection cuts for 2011 data are shown in Fig. 4.1 for illustration.

Figure 4.1: *Distribution of the B candidate invariant mass after preselection for (top) $K^0_S K^+ K^-$, (middle) $K^0_S K^\pm \pi^\mp$, (bottom) $K^0_S \pi^+ \pi^-$ candidates reconstructed in the (left) Down-Down and (right) Long-Long K^0_S categories.*

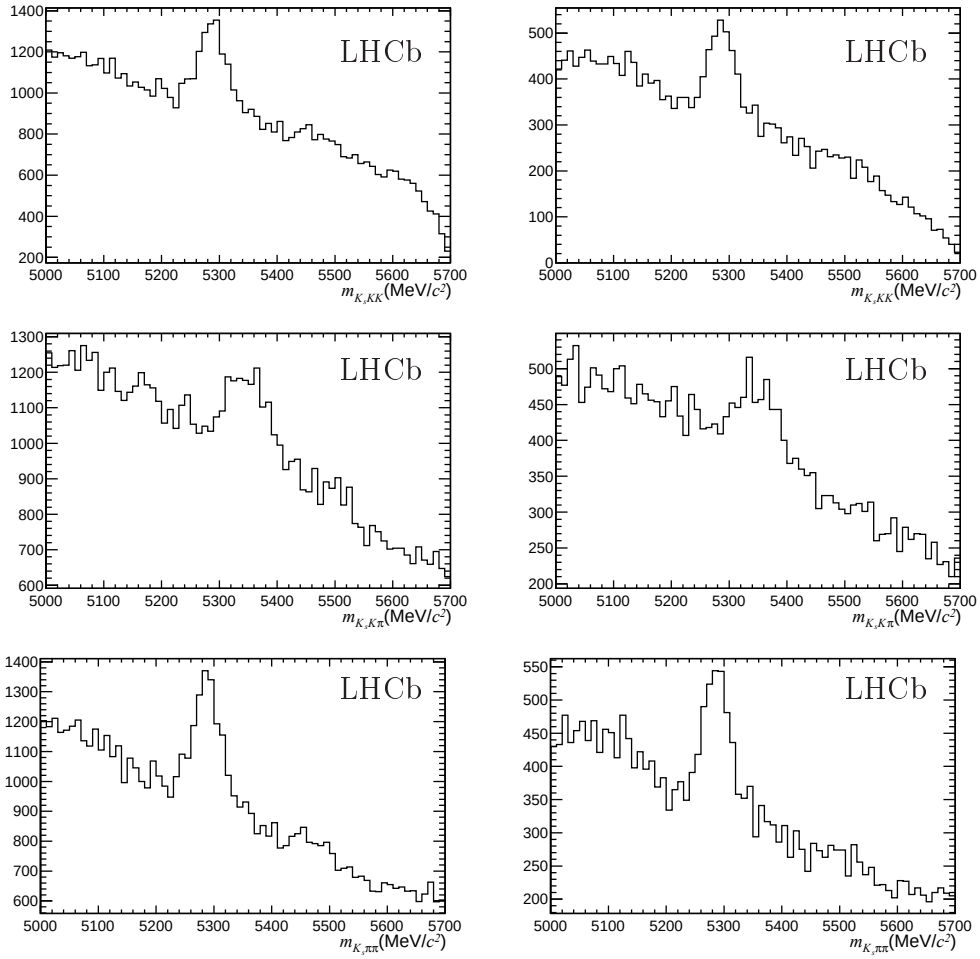

Table 4.8: *Preselection cuts applied and their acceptance rates for events in the right-hand side-band of the stripped data.*

Cuts	Bkg efficiency DD			Bkg efficiency LL		
	2011	2012a	2012b	2011	2012a	2012b
`B_SMALLESTDELTACHI2` > 4	0.707	0.709	0.696	0.608	0.605	0.615
`KS_ENDVERTEX_Z - B_ENDVERTEX_Z` > 30	1.000	1.000	1.000	0.507	0.608	0.464
Σ_i `h`$_i$`_isMuon` $== 0$	0.761	0.775	0.787	0.772	0.782	0.779
`Total Preselection`	0.534	0.547	0.545	0.227	0.292	0.230

4.2.2 Datasets for the MVA training

The boosted decision tree (BDT) discriminant is independently trained for each K^0_S reconstruction category. In addition, the training samples are further subdivided into the three trigger operation conditions, denoted 2011, 2012a, 2012b. It has been chosen to use MC truth matched $B^0 \to K^0_S\pi^+\pi^-$ simulated events as signal training sample and $B^0 \to K^0_S\pi^+\pi^-$ data events in the right-hand side-band ($m_{K^0_S\pi^+\pi^-} > 5425\,\mathrm{MeV}/c^2$) as the background sample. The same Stripping and preselection is applied to all the MC events and the data used in the training. Additionally, the potential contributions from b-baryon decays are removed from the data by explicitly vetoing the mass combinations of $pK^0_S\pi$ and pK^0_S consistent with a Λ_b and a Λ_c, respectively. Since the topological properties of the $K^0_S\pi^+\pi^-$ and the other signal modes are observed to be essentially the same, this training will serve for all decay modes in the analysis. However, the optimal point at which to place a cut has to be determined separately for each spectrum (*i.e.* $B^0_{(s)} \to K^0_S h^\pm h'^\mp$ mode, trigger operation condition and K^0_S category), since the level of combinatorial background varies.

In order to increase the useful background sample statistics for the training of the MVA, without biasing our analysis, a set of two BDTs is constructed. The full training samples are arbitrarily split in two by using a reproducible pseudo-random number, lying in the range $[0, 1]$, issued from the linear congruential generator. This pseudo-random number is given to each event according to the run and event number according to the following algorithmic sequence:

$$\mathrm{rndm} = ((134 \times \mathrm{eventNumber} + \mathrm{runNumber})\%531241)/531241$$

The sample of events with rndm > 0.5 is used to train the first BDT (denoted in the following `BDT_1`) and the response is validated on the other half of the sample. The reciprocal procedure is used to train the second BDT (denoted `BDT_2`), yielding the very same statistics in the test and training samples. The use of two independent BDTs ensures that no bias is induced in the analysis. The data events used to train `BDT_1` will be selected (or not) by means of a cut on `BDT_2`, and vice versa. The size of the samples used for training the MVA discriminants according to the different operation conditions are given in Table 4.9.

Table 4.9: *Number of events in the samples used for training and validating the BDT discriminants for the signal (MC) and background (data).*

Event type	Down-Down K_S	Long-Long K_S
Signal 2011	7162	3729
Bkg 2011	21579	12964
Signal 2012 pre-June	10696	5296
Bkg 2012 pre-June	8074	7662
Signal 2012 post-June	15803	6108
Bkg 2012 post-June	31615	15438

4.2.3 Discriminating variables

Following the necessary requirement of minimally biasing the Dalitz plane, already at work in the previous analysis [77], the discriminating variables are chosen to be of topological nature only, as far as the final state particles are concerned. B candidate vertex reconstruction properties, B pointing estimators and lifetime-related observables are hence considered at first. The impact parameter of a b-hadron daughter is known to bias the Dalitz plane of the decay through its correlation with the kinematic properties. It has therefore been chosen to consider the sum of the individual impact parameters of all the daughters of the b-hadron. The p_{T} and η of the B meson complete the set of B-related discriminating variables.

Two discriminating variables are further added related the isolation of the B candidate vertex. First, the so-called p_{T} asymmetry is constructed according to

$$p_{\mathrm{T}}^{\mathrm{asym}} = \frac{p_{\mathrm{T}}(B) - p_{\mathrm{T}}(\mathrm{cone})}{p_{\mathrm{T}}(B) + p_{\mathrm{T}}(\mathrm{cone})},$$

where $p_{\mathrm{T}}(B)$ is the transverse momentum of the B candidate and $p_{\mathrm{T}}(\mathrm{cone})$ is the transverse component of the sum of all particle momenta inside a 1.5 mrad cone around B-candidate direction. Second, the estimator of the difference of the quality of the vertex $\Delta\chi^2$, already used as a sanity cut in the preselection described above, is included.

The full set of variables, as well as their definitions, used in the optimization is given in Table 4.10.

Table 4.10: *List of variables used as inputs of the $K^0_{\mathrm{S}}h^+h^-$ BDT discriminant, split by K^0_{S} reconstruction categories.*

Variable	Description	Down-Down	Long-Long
`B_PT`	B transverse momentum	✓	✓
`B_ETA`	B pseudorapidity	✓	✓
`B_IPCHI2_OWNPV`	B IP significance w.r.t PV	✓	✓
`B_VDCHI2_OWNPV`	B flight distance significance w.r.t PV	✓	✓
`B_DIRA_OWNPV`	B pointing angle	✓	✓
`B_ENDVERTEX_CHI2`	B vertex fit χ^2	✓	✓
`B_SMALLESTDELTACHI2`	Isolation of the B vertex	✓	✓
`B_PTASYM_1_5`	B transverse momentum asymmetry	✓	✓
Σ_i `h`$_i$`_IPCHI2_OWNPV`	Sum of the hadron IP significances w.r.t PV	✓	✓
`KSLL_VDCHI2_OWNPV`	K^0_{S} flight distance significance w.r.t PV	-	✓

4.2.3.1 Data / MC compatibility

In order to check the data/MC compatibility of the signal, the $s\mathcal{P}$lot technique [78] is used on the data with the B candidate invariant mass as the discriminating variable. The distributions of each of the discriminating variables are shown superimposed for both data and MC (2011 conditions) in Figs. 4.2 and 4.3. The plots for the two 2012 running periods can be found in Figs. C.1 to C.4 in Appendix C. A Kolmogorov-Smirnov test is computed for each comparison plot. A satisfactory agreement is observed for all variables in each sample except

for the B-candidate vertex χ^2 for the Down-Down K^0_S category [3]. Although this discrepancy will result in a slightly sub-optimal performance of the BDT, we checked that the inclusion of this variable improves the response.

Figure 4.2: *Compatibility of signal MC/data using 2011 events provided for Long-Long K^0_S, for the signal MC (red) and sWeighted signal events (black).*

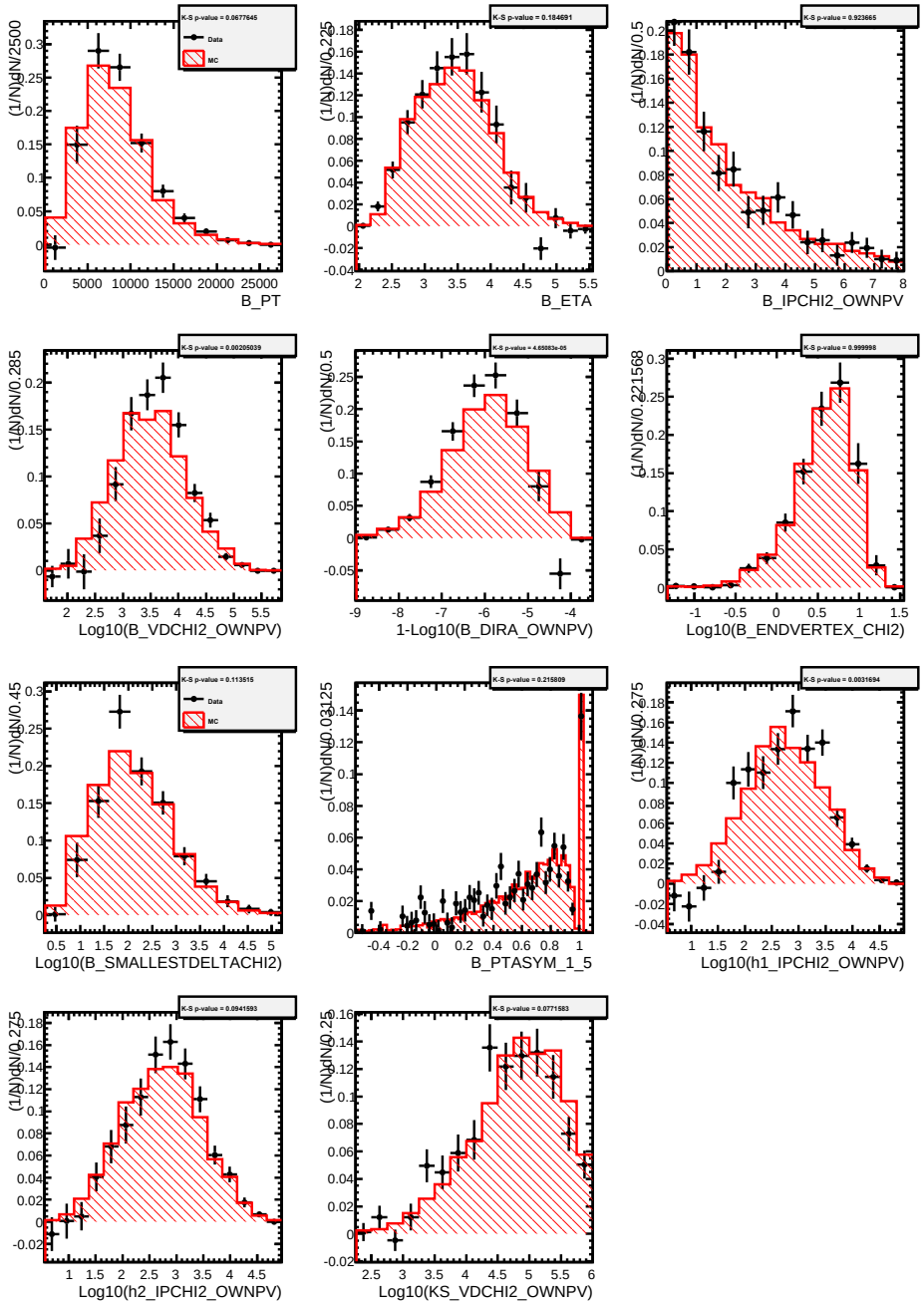

[3] This observation has been shared with the tracking performance group

Figure 4.3: *Compatibility of signal MC/data using 2011 events provided for Down-Down K^0_S for the signal MC (red) and sWeighted signal events (black).*

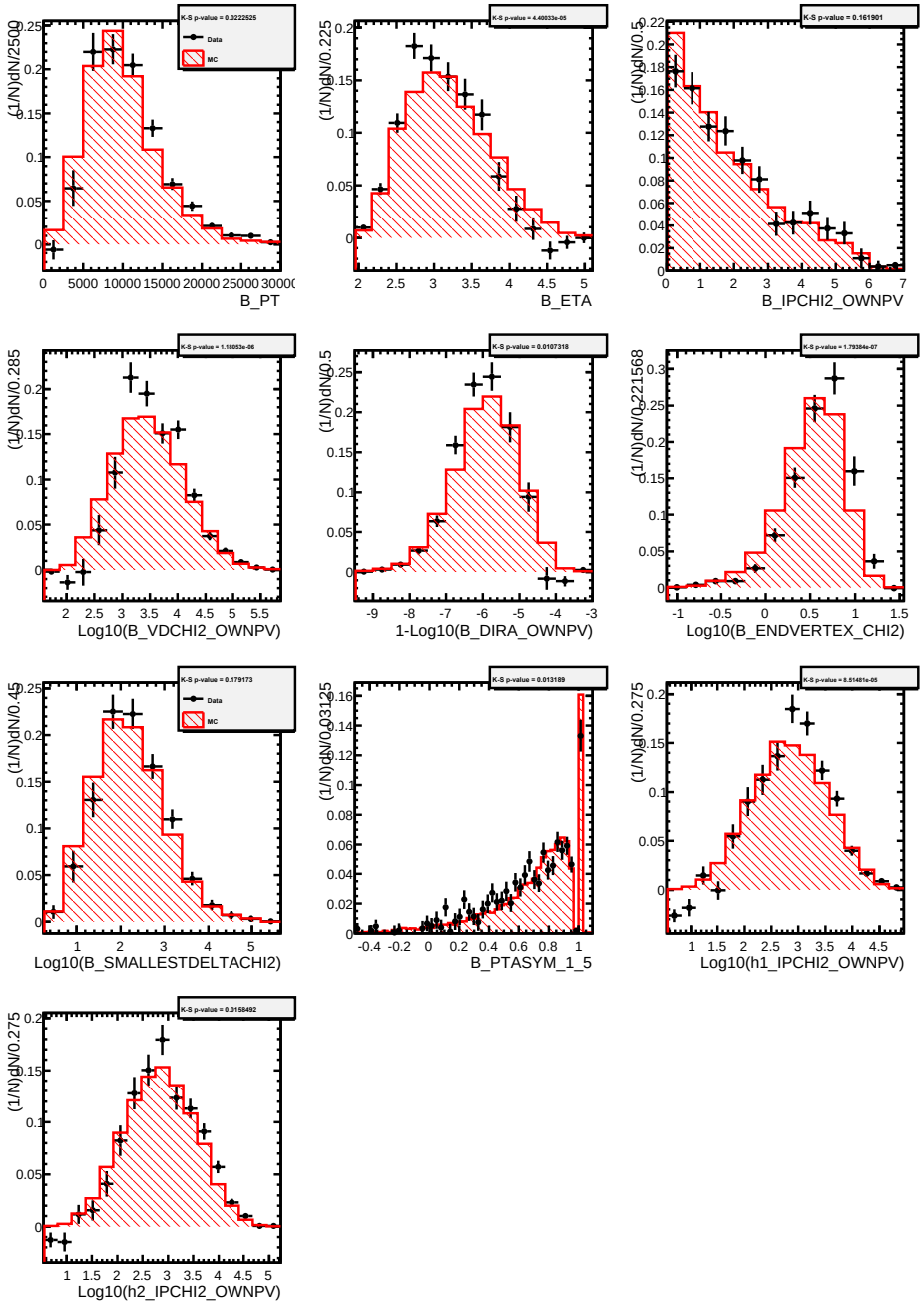

4.2.3.2 Correlations

The histograms of the variable distributions as well as the linear correlation plots are provided for 2011 conditions and the Long-Long K^0_S category in Figs. 4.4 and 4.6. Similar plots obtained for Down-Down candidates are displayed in Figs. 4.5 and 4.7. The very same information for 2012a and 2012b conditions are displayed in Figs. C.5 to C.12 in Appendix C. It is

worth to mention that the linear correlations for a given variable do not represent all possible correlations that might exist. For instance, the non-linear correlations between topological variables (and to a less extent kinematic ones) justifies to employ the BDT discriminative technique. Likewise, the different observed correlations which exist for background and signal events again act to favour a selection based on a multivariate approach. The importance of the variables in the BDT decision process for 2011 conditions can be found in Table 4.11, while those for 2012a and 2012b can be found in Tables C.1 and C.2 in Appendix C.

A few comments are in order:

- The transverse momentum asymmetry measured in a 1.5 mrad cone around the B meson candidate is among the most discriminative variables, irrespective of the K^0_S reconstruction. Despite the fact that this variable is not completely accurately simulated, it has been checked that the global performance of the MVA improves and makes it worth to be considered in the set of discriminative variables. We note as well that the choice of the cone angle provides the best agreement between real and simulated data.

- The combinatorial background candidates appear to be kinematically softer than the signal, making both the transverse momentum and pseudorapidity of the B candidate powerful discriminators.

- The range of some of the topological variables covers a few orders of magnitude; hence the logarithm of their value is used both in the optimisation and in the plotting of the variables.

Table 4.11: *BDT variable importance ranking [0,1] with 2011 data. Variables are presented in the hierarchical order as obtained for Down-Down.*

Variable	Importance DD		Importance LL	
	BDT1	BDT2	BDT1	BDT2
B_PTASYM_1_5	0.160	0.162	0.097	0.137
Σ_i h$_i$_IPCHI2_OWNPV	0.159	0.160	0.175	0.190
B_VDCHI2_OWNPV	0.151	0.156	0.096	0.106
B_ENDVERTEX_CHI2	0.143	0.144	0.073	0.061
B_ETA	0.140	0.138	0.120	0.116
B_SMALLESTDELTACHI2	0.074	0.070	0.082	0.074
B_DIRA_OWNPV	0.069	0.070	0.113	0.097
B_IPCHI2_OWNPV	0.051	0.055	0.051	0.054
B_PT	0.051	0.049	0.075	0.049
KSLL_VDCHI2_OWNPV	-	-	0.117	0.117

Figure 4.4: *Distribution of variables used in the optimisation of the BDT discriminant for Long-Long* K^0_S *using 2011 events.*

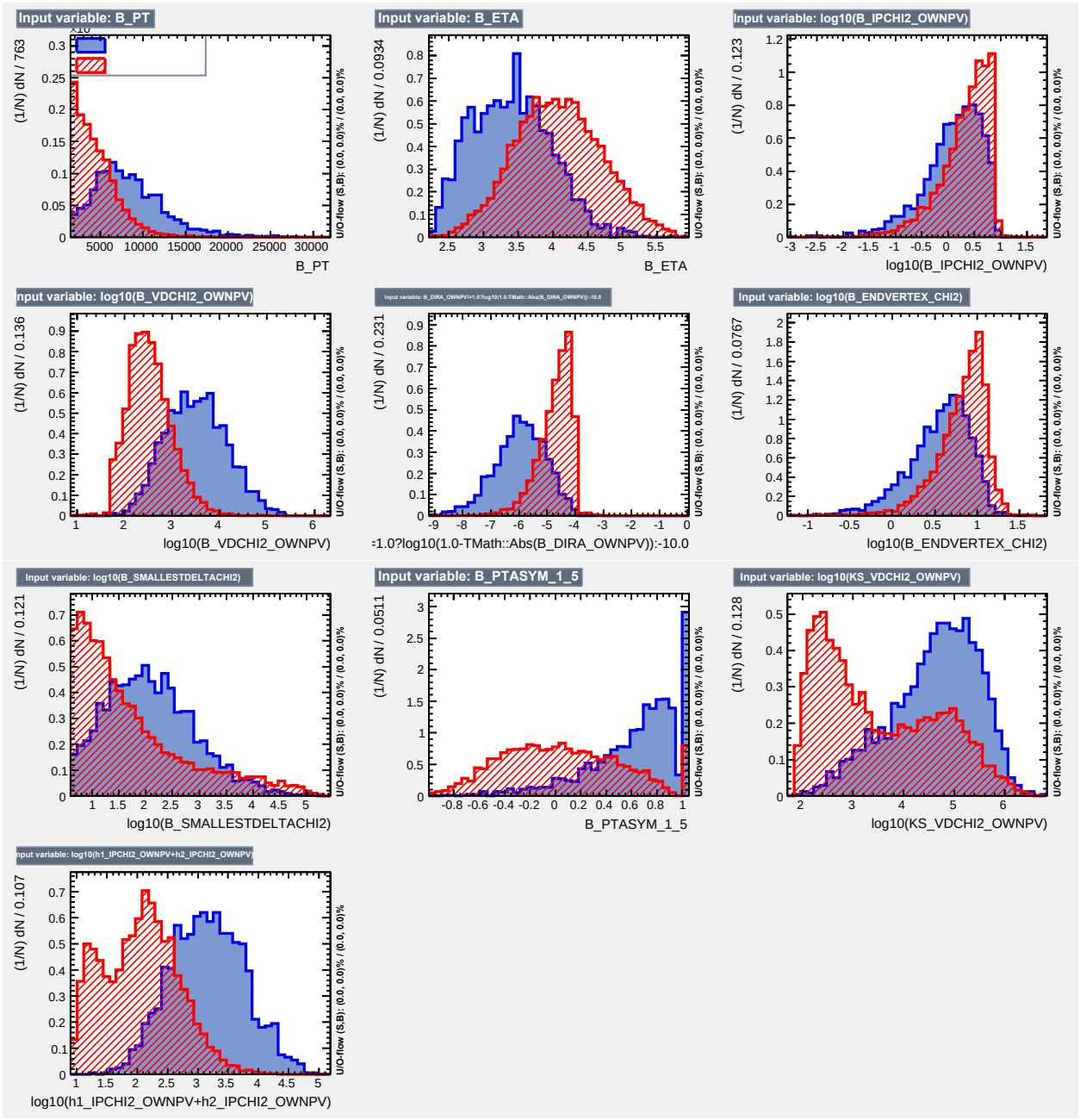

Figure 4.5: *Distribution of Variables used in the optimisation of the BDT discriminant for Down-Down* K^0_S *using 2011 events.*

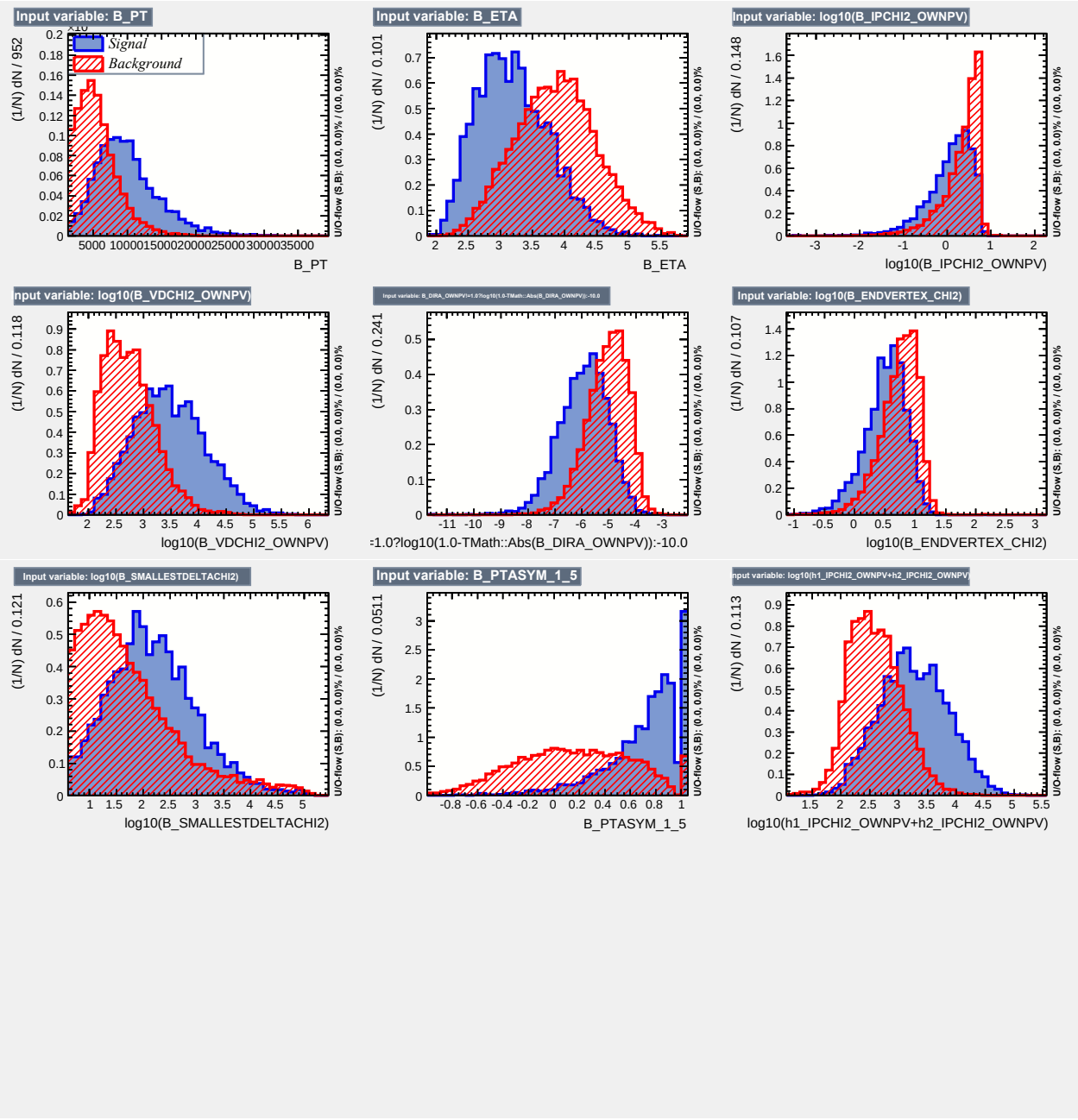

Figure 4.6: *Linear correlations between the variables used in the optimisation of the BDT for Long-Long (top) and Down-Down (bottom) K^0_S using 2011 events.*

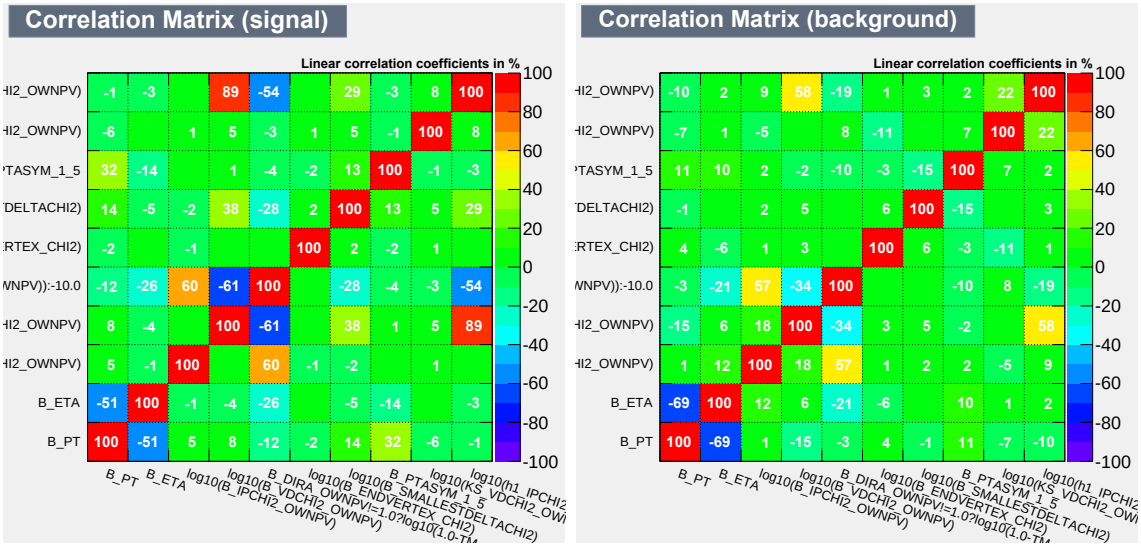

Figure 4.7: *Linear correlations between the variables used in the optimisation of the BDT for Down-Down K^0_S using 2011 events.*

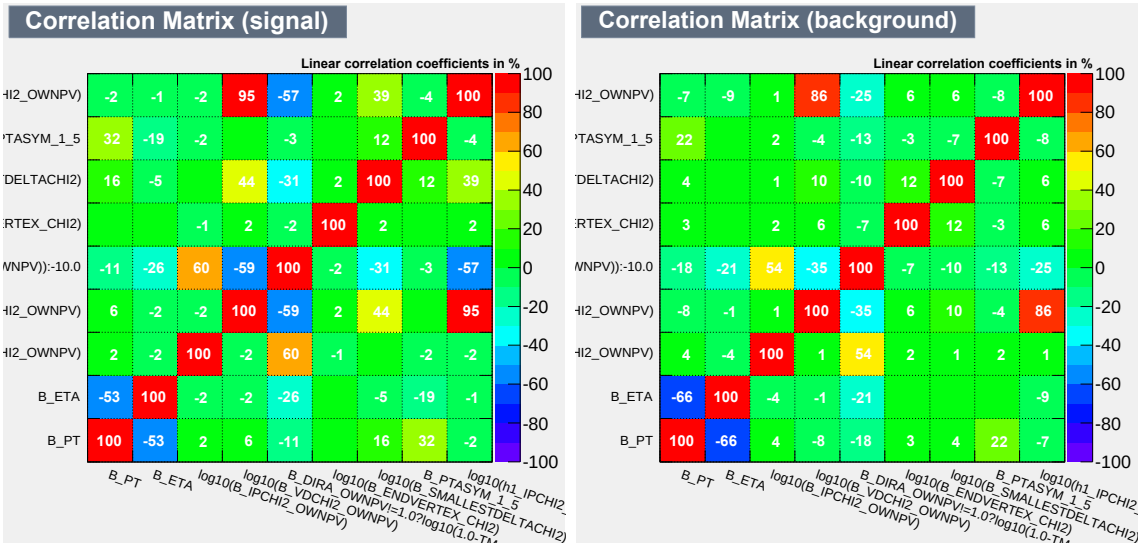

4.2.4 Training and validation of the BDT

The discriminant response histograms for 2011 conditions are displayed in Fig. 4.8 for Down-Down (Top) and Long-Long (Bottom), and for `BDT_1` (left) and `BDT_2` (right). Those for 2012a, 2012b can be found in Figs. C.13 and C.14 in Appendix C. Although the details of the training of each BDT according to the years are different (and even for a given year), there is an overall similarity of the shapes. Kolmogorov-Smirnov statistics tests have been computed in each case and did not indicate the presence of any overtraining. This test should be taken with care since it does not address all the possible sources of overtraining. It was elsewhere for instance explicitly checked that no correlation with the B candidate invariant mass was induced by the variable choices nor the training of the MVA. `BDT_1` and `BDT_2` distributions for training and testing are also compatible. In order not to bias the analysis towards one given training, the final selection variable, denoted `BDT` in the following, is arbitrarily taken as `BDT_1` or `BDT_2` for the events which were not used in the training procedure.

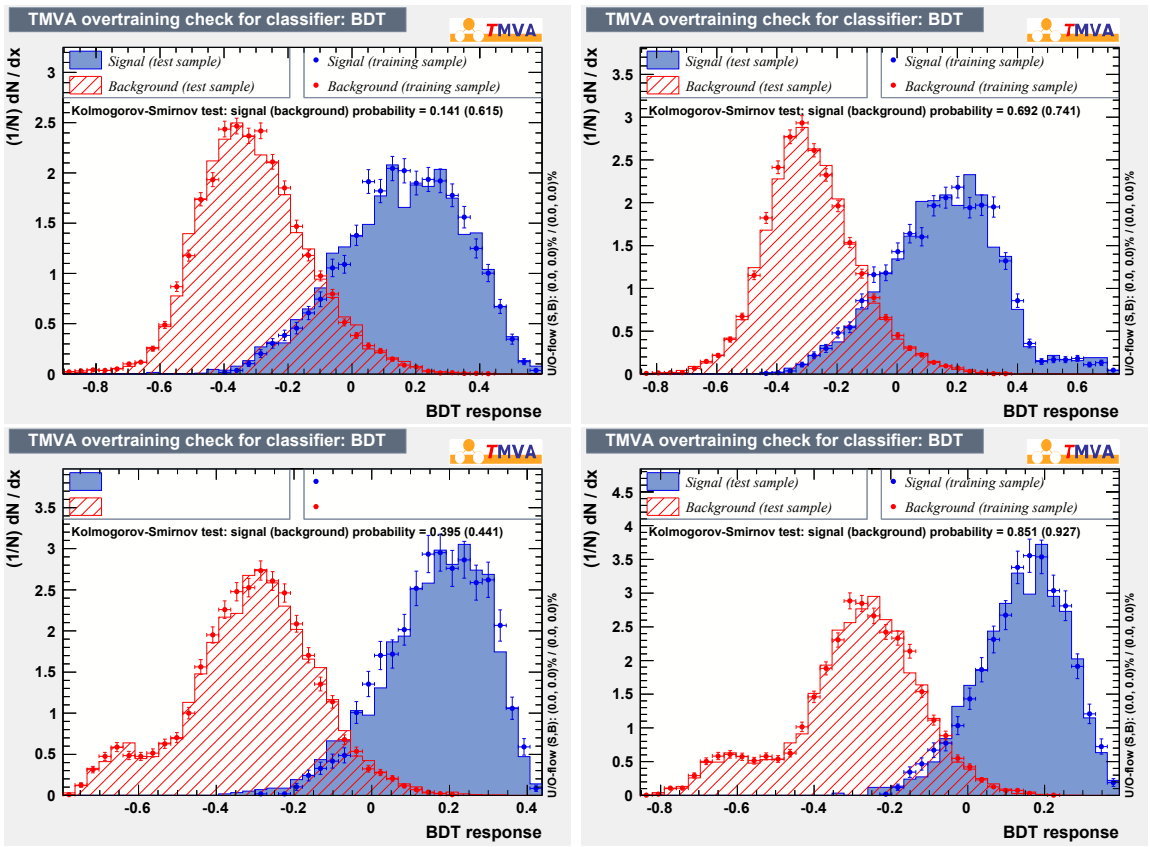

Figure 4.8: *Training and Validation samples response for the `BDT_1` (left) and `BDT_2` (right) discriminants for Down-Down (top) and Long-Long (bottom). MC2011 is used for signal events and background events are selected from the right-handed side-bands of the 2011 data. The histograms are normalized to the same number of entries.*

4.2.5 Optimisation of the BDT cuts

The choice of the optimal cut on the BDT response can be defined using several figures of merit (FoM), each appropriate for a certain situation. For example, the choice of the maximal significance of the signal (S) with respect to background (B)

$$\mathrm{FoM}_1 = \frac{S}{\sqrt{(S+B)}}, \tag{4.1}$$

is suitable for a branching fraction measurement when there is already a measurement or a very reliable prediction, such that the value of S can be calculated given the efficiency of the BDT cut. This is therefore an appropriate FoM for the selection of $B^0 \to K^0_S\pi^+\pi^-$, $B^0 \to K^0_S K^\pm\pi^\mp$, $B^0_s \to K^0_S K^\pm\pi^\mp$, and $B^0 \to K^0_S K^+K^-$ for the branching fraction analysis.

Since the branching fraction of the mode $B^0_s \to K^0_S K^+K^-$ is unknown, it is more suitable to use as the FoM a frequentist ansatz [79]

$$\mathrm{FoM}_{\mathrm{Punzi}} = \frac{\epsilon_{sig}}{\frac{a}{2} + \sqrt{B}}, \tag{4.2}$$

where the signal efficiency (ϵ_{sig}), which can be obtained by counting the MC events that pass the multivariate selection, is used instead of the expected signal yield. The expected number of background events (B) is estimated from an exponential fit of the right-hand side-band of the data [4] by extrapolating from the measured slope the number of combinatorial background in the mass peak region. The parameter a corresponds to the significance of the limit (in units of Gaussian standard deviations σ) that one wants to place on the branching fraction. We have chosen $a = 2$ (*i.e.*90% CL).

For the Dalitz analyses of these various modes, the measurements of interest are those of the amplitude magnitudes and phases and it is likely that the optimisation of the yields does not correspond to an optimum. Detailed toy studies have shown [80] that the "significance $\times$ purity" figure of merit

$$\mathrm{FoM}_2 = \frac{S^2}{(S+B)^{\frac{3}{2}}}, \tag{4.3}$$

provides a response to minimise the uncertainties on these measurements. In simpler physical terms, a purer sample is preferred for the determination of the isobar parameters. Consequently, this figure has been used to optimise the selection for the Dalitz-plot analyses of $B^0 \to K^0_S K^\pm\pi^\mp$ and $B^0_s \to K^0_S K^\pm\pi^\mp$. Note that the understanding of the optimisations owns a necessary arbitrariness level in the sense that they are model-dependent. The prejudice for the Dalitz Plot analysis of the decay $B^0 \to K^0_S\pi^+\pi^-$ is that the competition between the non-resonant phase space, the 2-body S-wave and the combinatorial background contributions is a key point of the understanding of the Dalitz Plot. Among the optimisations considered here, the so-called tight optimisation provides the purest sample of signal for a still satisfactory signal efficiency and has been retained as a conservative choice for the working point of this analysis.

[4] Only events satisfying $m_{K^0_S h_i h_i} > 5550\ (5530)\,\mathrm{MeV}/c^2$ are considered in order to avoid the Λ_b veto region in Down-Down (Long-Long).

The optimisation made for the favoured modes, $B^0 \to K^0_S\pi^+\pi^-$, $B^0_s \to K^0_S K^\pm\pi^\mp$ and $B^0 \to K^0_S K^+K^-$, gives loose BDT cuts, whereas the optimisation made for the non-favoured modes, $B^0_s \to K^0_S\pi^+\pi^-$, $B^0 \to K^0_S K^\pm\pi^\mp$ and $B^0_s \to K^0_S K^+K^-$, gives tight BDT cuts. As mentioned above, the optimal tight BDT cut found for the mode $B^0_s \to K^0_S\pi^+\pi^-$ will be used for the DP analysis, since it gives the greater $B^0 \to K^0_S\pi^+\pi^-$ signal purity. Therefore, we have chosen to report in this manuscript only the tight optimisation, as illustrated in Fig. 4.9. For the sake of comparison, Tables 4.12 to 4.14 gather all the optimal cuts for 2011, 2012a and 2012b samples. The results for all the optimisations of the BDT cut performed in this work can be found in [81]. Table 4.16 shows the MC signal and background efficiencies of the tight BDT cuts (with loose cuts for comparison) of the mode $B^0 \to K^0_S\pi^+\pi^-$, which are used for the DP analysis.

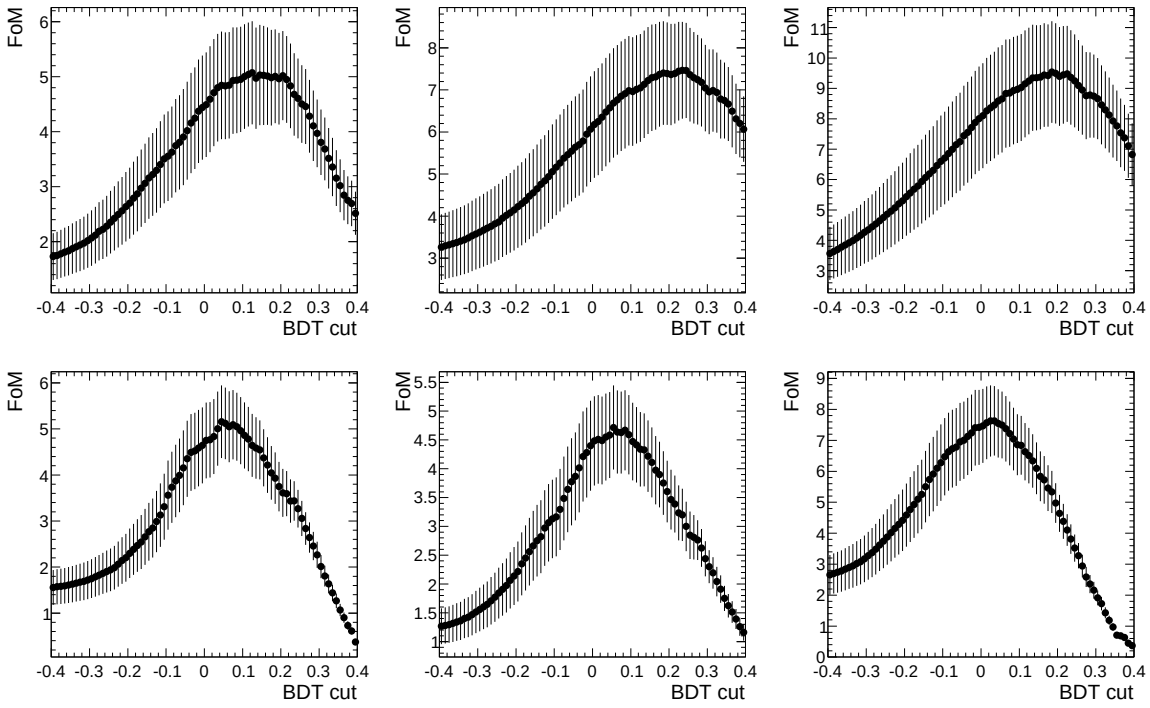

Figure 4.9: *Figures of merit computed as $S/\sqrt{(S+B)}$ for the observed mode $B^0_s \to K^0_S\pi^+\pi^-$ using 2011 events (left), 2012a events (middle) and 2012b events (right) for Down-Down (top) and Long-Long (bottom) reconstruction categories.*

4.2.6 Particle Identification

When the neutral B^0 or B^0_s mesons decay to the final states $K_S hh'$, there are six competing decay modes states only different by the nature of the h and h' particles. This results in signal cross-feeds. The level of misidentification can be controlled by PID cuts. The variables used for the charged hadron identification in this analysis are the `PROBNNh`, where h can either denotes a pion or a kaon.

Table 4.12: *BDT discriminant optimal cuts and efficiencies as determined from the training validation sample 2011 in the different $K^0_S h^+ h^-$ modes. The hierarchy in the cuts reflects the relative impact of the combinatorial background in each spectra.*

		FoM$_1$ Optimisation			FoM$_2$ Optimisation		
K^0_S category	Decay mode	BDT Cut	ϵ Signal	ϵ Bkg	BDT Cut	ϵ Signal	ϵ Bkg
Down-Down	$B^0 \to K^0_S \pi^+ \pi^-$	−0.06	0.834	0.082	0.03	0.706	0.033
	$B^0_s \to K^0_S \pi^+ \pi^-$	0.12	0.567	0.011	0.21	0.389	0.004
	$B^0 \to K^0_S K^\pm \pi^\mp$	0.03	0.708	0.037	0.19	0.412	0.007
	$B^0_s \to K^0_S K^\pm \pi^\mp$	−0.02	0.788	0.057	0.08	0.640	0.024
	$B^0 \to K^0_S K^+ K^-$	−0.10	0.875	0.106	−0.04	0.815	0.061
Long-Long	$B^0 \to K^0_S \pi^+ \pi^-$	−0.05	0.925	0.053	−0.04	0.914	0.069
	$B^0_s \to K^0_S \pi^+ \pi^-$	0.04	0.816	0.012	0.08	0.732	0.008
	$B^0 \to K^0_S K^\pm \pi^\mp$	0.04	0.814	0.041	0.06	0.776	0.032
	$B^0_s \to K^0_S K^\pm \pi^\mp$	0.04	0.821	0.041	0.06	0.790	0.032
	$B^0 \to K^0_S K^+ K^-$	−0.17	0.983	0.316	−0.06	0.934	0.114

Table 4.13: *BDT discriminant optimal cuts and efficiencies as determined from the training validation 2012a sample in the different $K^0_S h^+ h^-$ modes. The hierarchy in the cuts does reflect the relative impact of the combinatorial background in each spectra.*

		FoM$_1$ Optimisation			FoM$_2$ Optimisation		
K^0_S category	Decay mode	BDT Cut	ϵ Signal	ϵ Bkg	BDT Cut	ϵ Signal	ϵ Bkg
Down-Down	$B^0 \to K^0_S \pi^+ \pi^-$	0.03	0.836	0.104	0.15	0.700	0.038
	$B^0_s \to K^0_S \pi^+ \pi^-$	0.23	0.606	0.015	0.31	0.462	0.006
	$B^0 \to K^0_S K^\pm \pi^\mp$	0.21	0.614	0.024	0.30	0.454	0.009
	$B^0_s \to K^0_S K^\pm \pi^\mp$	0.11	0.773	0.064	0.23	0.595	0.019
	$B^0 \to K^0_S K^+ K^-$	0.03	0.846	0.144	0.11	0.764	0.008
Long-Long	$B^0 \to K^0_S \pi^+ \pi^-$	−0.03	0.837	0.025	0.00	0.796	0.016
	$B^0_s \to K^0_S \pi^+ \pi^-$	0.05	0.714	0.007	0.08	0.659	0.005
	$B^0 \to K^0_S K^\pm \pi^\mp$	0.00	0.793	0.043	0.07	0.680	0.026
	$B^0_s \to K^0_S K^\pm \pi^\mp$	−0.03	0.838	0.053	0.04	0.726	0.032
	$B^0 \to K^0_S K^+ K^-$	−0.06	0.874	0.079	0.02	0.773	0.028

4.2.6.1 Calibration of PID efficiency

The simulation does not satisfactorily describe the PID variables. Hence, a data-driven calibration must be undertaken. It basically follows the methods and prescriptions provided in the `PIDCalib` tool developed in the collaboration. First, the calibration samples of charged kaons and pions provided by the `PIDCalib` tool and formed from $D^{*+} \to D^0(\to K^-\pi^+)\pi^+$ reconstructed candidates are used to build efficiency maps of the PID cuts designed for this analysis, which will be detailed in the next Section 4.2.6.2, as a function of both the track momentum and pseudo-rapidity. It has been checked that the additional granularity brought by the multiplicity of the tracks in the events was not required for this analysis.

Table 4.14: *BDT discriminant optimal cuts and efficiencies as determined from the training validation 2012b sample in the different $K^0_S h^+ h^-$ modes. The hierarchy in the cuts does reflect the relative impact of the combinatorial background in each spectra.*

		FoM_1 Optimisation			FoM_2 Optimisation		
K^0_S category	Decay mode	BDT Cut	ϵ Signal	ϵ Bkg	BDT Cut	ϵ Signal	ϵ Bkg
Down-Down	$B^0 \to K^0_S \pi^+ \pi^-$	0.01	0.748	0.050	0.13	0.592	0.017
	$B^0_s \to K^0_S \pi^+ \pi^-$	0.18	0.531	0.011	0.30	0.341	0.003
	$B^0 \to K^0_S K^\pm \pi^\mp$	0.10	0.636	0.030	0.22	0.452	0.012
	$B^0_s \to K^0_S K^\pm \pi^\mp$	0.07	0.696	0.036	0.22	0.472	0.012
	$B^0 \to K^0_S K^+ K^-$	−0.08	0.844	0.117	0.04	0.716	0.056
Long-Long	$B^0 \to K^0_S \pi^+ \pi^-$	−0.10	0.913	0.063	−0.02	0.808	0.022
	$B^0_s \to K^0_S \pi^+ \pi^-$	0.03	0.716	0.009	0.05	0.669	0.007
	$B^0 \to K^0_S K^\pm \pi^\mp$	0.02	0.727	0.023	0.07	0.597	0.015
	$B^0_s \to K^0_S K^\pm \pi^\mp$	−0.05	0.872	0.047	0.02	0.742	0.023
	$B^0 \to K^0_S K^+ K^-$	−0.13	0.940	0.094	−0.10	0.912	0.060

Table 4.15: *Optimal cut values for the as yet undiscovered mode $B^0_s \to K^0_S K^+ K^-$ for each data sample. Also given are the efficiencies of the cut for both signal and background samples.*

Data sample	BDT Cut	ϵ Signal	ϵ Bkg
2011, Down-Down	0.15	0.490	0.008
2012a, Down-Down	0.20	0.641	0.036
2012b, Down-Down	0.22	0.473	0.013
2011, Long-Long	0.05	0.790	0.038
2012a, Long-Long	0.05	0.740	0.019
2012b, Long-Long	0.12	0.493	0.003

Table 4.16: *MC signal and background efficiencies of the BDT cut, loose and tight, for the mode $B^0 \to K^0_S \pi^+ \pi^-$.*

		Tight Optimisation			Loose Optimisation		
K^0_S category	Running period	BDT Cut	ϵ Signal	ϵ Bkg	BDT Cut	ϵ Signal	ϵ Bkg
Down-Down	2011	0.12	0.552	0.011	−0.06	0.834	0.082
	2012a	0.23	0.587	0.015	0.03	0.836	0.104
	2012b	0.18	0.525	0.011	0.01	0.748	0.050
Long-Long	2011	0.04	0.797	0.012	−0.05	0.925	0.053
	2012a	0.05	0.703	0.007	−0.03	0.837	0.025
	2012b	0.03	0.693	0.009	−0.10	0.913	0.063

The PID efficiency and misidentification (misID) efficiency from MC signal samples are then reweighted on an event-by-event basis according to these maps. The calibration samples can

not be valuably defined for all momenta. It has been chosen to restrict the signal selection to the kinematical range for any track h $3\,\mathrm{GeV}/c < p_h < 100\,\mathrm{GeV}/c$. The binning has been chosen in order to have a similar number of events in each bin keeping a resolved enough granularity of the kinematic variable distributions. It is detailed in Table 4.17.

Table 4.17: *The binning scheme used to produce the* $\mathrm{PID}_{k\pi}$ *(mis)identification efficiency maps.*

Particle type (year)	p binning boundaries (in GeV/c^2)	η binning boundaries
K's (2011)	{3000; 9300; 15600; 18515; 28325; 40097; 59717; 100000}	{1.5; 2.4975; 2.7075; 3.0575; 3.3725; 3.7225; 4.0025; 5.0}
K's (2012)	{3000; 9300; 15600; 16553; 26363; 38135; 57755; 100000}	{1.5; 2.4625; 2.6725; 2.9875; 3.3025; 3.6525; 3.8975; 5.0}
π's (2011)	{3000; 9300; 15600; 16553; 24401; 36173; 55793; 100000}	{1.5; 2.4625; 2.7075; 3.0225; 3.3375; 3.6875; 3.9675; 5.0}
π's (2012)	{3000; 9300; 14591; 15600; 24401; 34211; 53831; 100000}	{1.5; 2.4275; 2.6375; 2.9525; 3.2675; 3.6175; 3.8975; 5.0}

As an illustration of the calibration procedure, Fig. 4.10 provides the PID and misID efficiency of the MC and the Calibration sample as a function of track momentum for a given arbitrary PID cut.

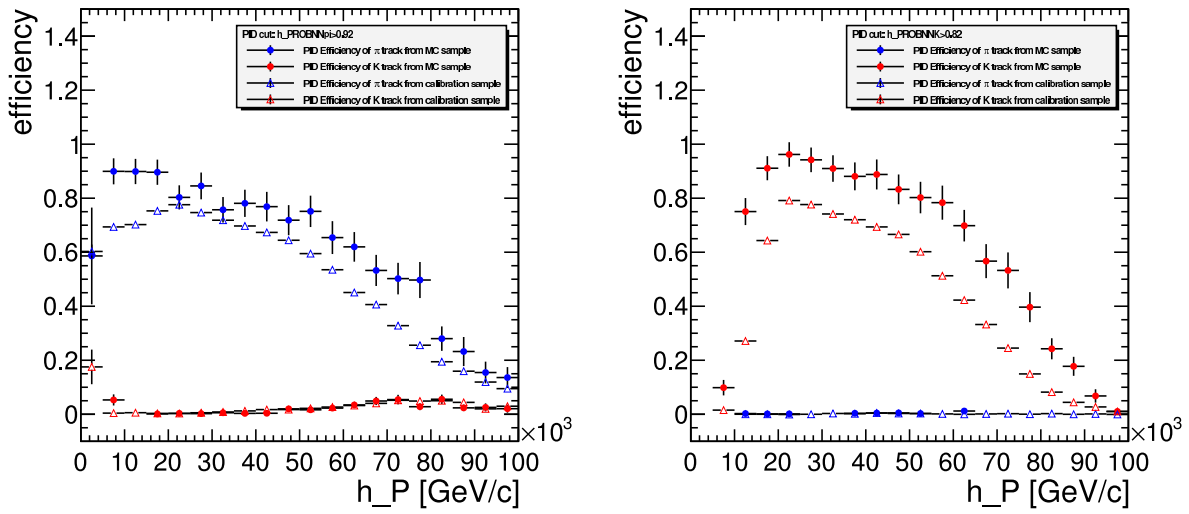

Figure 4.10: *The PID and MisID efficiency of MC and calibration events is given for pion tracks (left) and kaon tracks (right), as a function of track momentum, for two arbitrary cuts set at* `PROBNNpi` > 0.92 *and* `PROBNNK` > 0.82*, respectively for pions and kaons.*

Continuing this illustration of the calibration procedure with arbitrary cuts on `PROBNNh`, the overall PID cut efficiencies for the modes $B^0 \to K^0_S\pi^+\pi^-$ and $B^0 \to K^0_S K^+ K^-$ (Down-

Down, 2011) have been corrected, as shown in Fig. 4.11. This figure displays as well the unweighted PID efficiency.

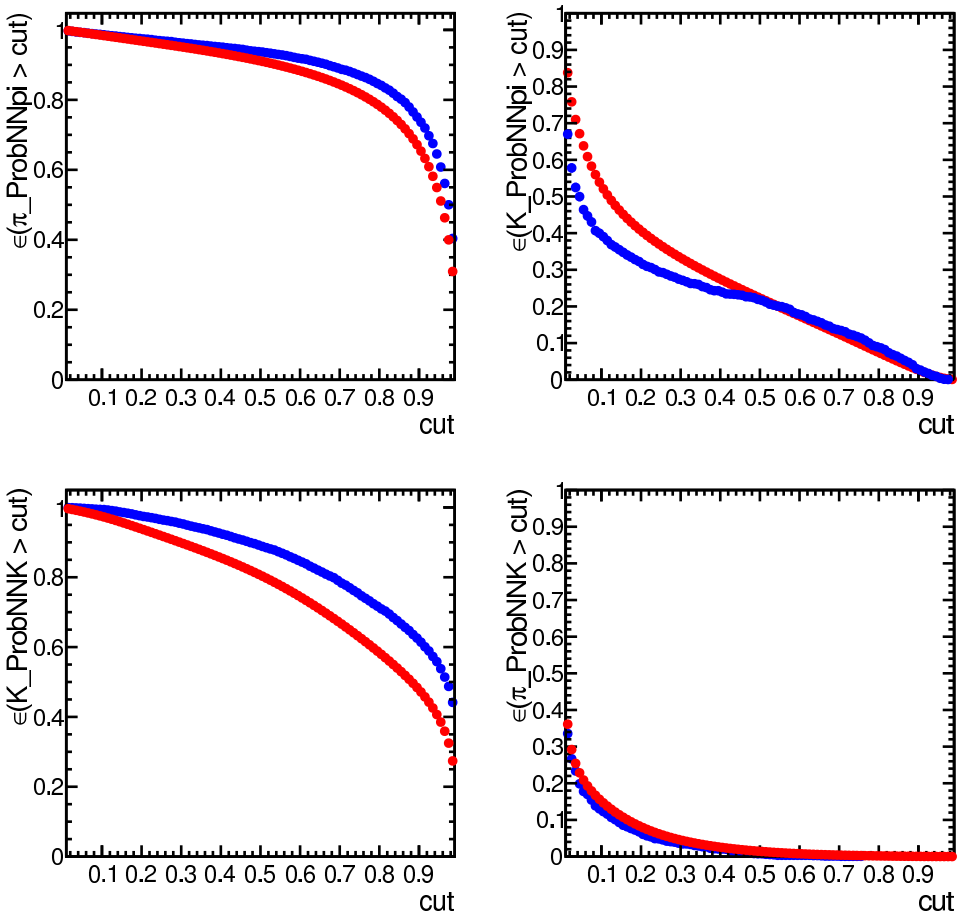

Figure 4.11: *The PID (left) and MisID (right) efficiency, weighted (red) and unweighted (blue), of pion tracks (up) taken from the MC sample* $B \to K_S\pi\pi$ *and kaon (bottom) taken from the MC sample* $B \to K_S KK$*. The cut on* `PROBNNh` *is lying in the range* $0.01 < \text{cut} < 0.99$.

4.2.6.2 Particle Identification Selection

As mentioned in Section 4.2.1, the first PID selection is requiring the charged hadrons to have `isMuon` $== 0$ cut, in order to reject possible charmonia transitions. This cut as well as the whole selection is applied prior to build the calibration tables.

The cuts on charged hadrons ID `PROBNNh` are defined to be the same in the decay modes with a pair of identical charged hadrons. The shape of the cut in the plane {`PROBNNpi`, `PROBNNK`}, is chosen to be triangular as illustrated in Fig. 4.12. This type of cut can be made by requiring the following conditions:

- The final state $K^0_S\pi^+\pi^-$ is selected with:

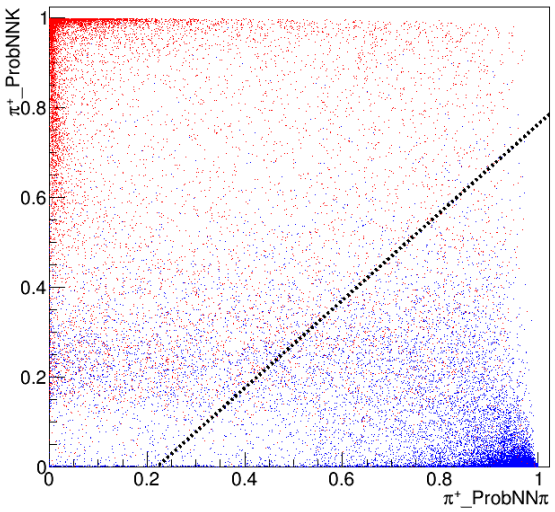

Figure 4.12: *Signal MC events $B^0 \to K^0_S\pi^+\pi^-$ (blue) and Crossfeed MC events $B^0 \to K^0_S K^\pm\pi^\mp$ reconstructed as $B^0 \to K^0_S\pi^+\pi^-$ (red) distributed in the plane {PROBNNpi, PROBNNK}. The dashed black line illustrates the type of PID cut used in this thesis analysis with an offset equal to 0.21.*

$$\texttt{h\_PROBNNpi} > \texttt{h\_PROBNNK} + a_\pi \ .$$

- The final state $K^0_S K^\pm\pi^\mp$ is selected with:

$$\texttt{h1\_PROBNNK} > \texttt{h1\_PROBNNpi} - a_K \ ,$$

and

$$\texttt{h2\_PROBNNpi} > \texttt{h2\_PROBNNK} + a_\pi \ ,$$

where h_1 and h_2 are the kaon and pion candidates, respectively.

- The final state $K^0_S K^+K^-$ is selected with :

$$\texttt{h\_PROBNNK} > \texttt{h\_PROBNNpi} - a_K \ .$$

a_π and a_K represent the offsets to be optimized for each sample.

The choice of the cut shape is derived by the distribution of cross-feed and signal events, that are usually distributed in opposite corners of the two-dimensional (PROBNNpi, PROBNNK) plane. It is worth to mention that a definition of the PID cuts with $a_\pi = a_K$ ensures that the $B^0_{d,s} \to K^0_S h^\pm h'^\mp$ spectra are mutually exclusive. The calibration maps have been produced using the former equations, hence depending on the value of a_h, with a granularity of 200 (a_h varies in between -1. and 1. by steps of 0.01).

In order to optimize the cuts, it has been chosen to focus on the $K^0_S\pi^+\pi^-$ and $K^0_S K^+K^-$ spectra. The values of the offsets obtained for π and K will be subsequently used to select the $K^0_S K^\pm\pi^\mp$ sample. As in the BDT cut optimisation, the figure of merit used to obtain the

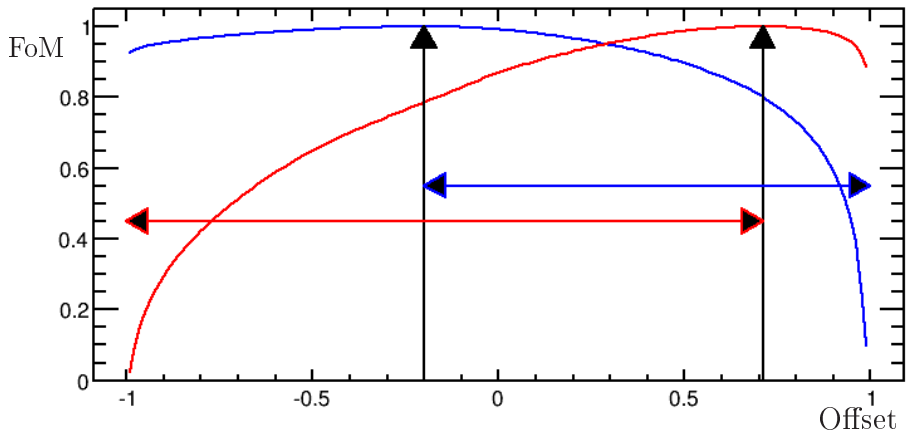

Figure 4.13: *Figure of merit for the favoured modes* $B^0 \to K^0_S\pi^+\pi^-$ *(blue) and* $B^0 \to K^0_S K^+K^-$ *(red), the red (blue) arrow shows the region where the pion (kaon) candidates are.*

optimal cut of the offset(s) is in most cases the standard significance $S/\sqrt{(S+B)}$, except for $B_s \to K_S KK$, where we used the frequentist ansatz [79]. In the case of the PID cut optimisation, the background comprises the combinatorial background as well as the signal cross-feeds. The combinatorial number expectation is estimated from an exponential fit to the invariant mass right side-band and the number of events is extrapolated in the signal region. The signal cross-feed background (as well as the signal S) is estimated from the product of the luminosity, cross-section, fragmentation fraction, acceptance efficiency and visible branching ratio.

For the favoured modes, the condition $a_\pi \geq a_K$ is not realized in any condition if the optimization is realized on each sample independently. Indeed, Fig. 4.13 shows one realization in which $a_K \geq a_\pi$. To preserve the mutually-exclusive definition of the spectra, the figure of merits of the $B^0 \to K_S\pi^+\pi^-$ and $B^0 \to K_S K^+K^-$ are multiplied and used to determine the optimal offsets for those two modes. The non-favoured modes optimal offsets are already meeting the requirement of exclusive spectra and do not require any corrective action. Following the notation of the multivariate selection, the optimization of the favoured (non-favoured) modes is said Loose (Tight). The complete set of optimal offsets are gathered in Tables 4.18 and 4.19. The distributions of FoM are displayed in Figs. 4.14 and 4.15. We take note that the PID cuts not only act on the signal cross-feeds but also on the level of combinatoric. Following the strategy of minimizing the combinatorial background exposed in the subsection 4.2.4, the tight optimisation is used in the DP analysis of the decay $B^0 \to K^0_S\pi^+\pi^-$.

Table 4.18: *Optimal cuts for $K^0_S\pi^+\pi^-$ and $K^0_S K^+K^-$ spectra and table of Signal (Sig) and crossfeed (CF) efficiencies, corrected by the PIDCalib tool, as well the combinatorial efficiency, for all years and K^0_S reconstruction categories.*

Year	K^0_S reco.	mode	a_{h_i}	Sig. eff.	CF. eff.	Comb. eff.
2011	Down-Down	$B^0 \to K^0_S\pi\pi$	0.20	86.1 ± 0.2	10.4 ± 0.1	47.1 ± 1.3
		$B^0_s \to K^0_S\pi\pi$	0.25	82.6 ± 0.3	8.9 ± 0.1	41.2 ± 3.2
		$B^0 \to K^0_S KK$	0.20	79.0 ± 0.2	6.7 ± 0.1	7.9 ± 0.4
		$B^0_s \to K^0_S KK$	-0.03	65.4 ± 0.4	2.9 ± 0.1	1.8 ± 0.4
	Long-Long	$B^0 \to K^0_S\pi\pi$	0.25	86.5 ± 0.4	10.5 ± 0.2	42.4 ± 2.2
		$B^0_s \to K^0_S\pi\pi$	0.35	82.9 ± 0.3	7.7 ± 0.2	40.3 ± 4.0
		$B^0 \to K^0_S KK$	0.25	79.2 ± 0.2	6.1 ± 0.2	8.9 ± 0.5
		$B^0_s \to K^0_S KK$	0.00	65.8 ± 0.5	2.3 ± 0.1	1.2 ± 0.4
2012	Down-Down	$B^0 \to K^0_S\pi\pi$	0.20	84.8 ± 0.1	10.1 ± 0.1	44.9 ± 0.6
		$B^0_s \to K^0_S\pi\pi$	0.22	82.5 ± 0.1	9.5 ± 0.1	40.4 ± 1.2
		$B^0 \to K^0_S KK$	0.20	80.0 ± 0.1	7.0 ± 0.1	9.7 ± 0.2
		$B^0_s \to K^0_S KK$	-0.02	66.1 ± 0.2	3.2 ± 0.0	3.3 ± 0.3
	Long-Long	$B^0 \to K^0_S\pi\pi$	0.25	86.3 ± 0.2	10.3 ± 0.1	39.9 ± 1.5
		$B^0_s \to K^0_S\pi\pi$	0.36	80.2 ± 0.2	7.2 ± 0.1	29.8 ± 3.3
		$B^0 \to K^0_S KK$	0.25	80.1 ± 0.2	6.7 ± 0.1	7.4 ± 0.4
		$B^0_s \to K^0_S KK$	0.00	65.1 ± 0.3	2.7 ± 0.1	1.4 ± 0.4

Table 4.19: *Cuts and table of the PID cut efficiencies for $K_S K^\pm\pi^\pm$ spectra, corrected by the PIDCalib, CF1 and CF2 represent the signal crossfeed $B^0 \to K^0_S\pi^+\pi^-$ and $B^0 \to K^0_S K^+K^-$, respectively.*

Year	K^0_S reco.	mode	a_{h1}	a_{h2}	Sig. eff.	CF1. eff.	CF2. eff.	Comb. eff.
2011	Down-Down	B^0	-0.03	0.25	79.0 ± 0.4	2.7 ± 0.1	7.9 ± 0.1	9.3 ± 0.7
		B^0_s	0.20	0.20	81.9 ± 0.3	6.8 ± 0.1	9.9 ± 0.1	24.6 ± 0.9
	Long-Long	B^0	0.00	0.35	72.8 ± 0.5	2.6 ± 0.1	6.7 ± 0.1	9.8 ± 1.1
		B^0_s	0.25	0.25	83.0 ± 0.3	6.8 ± 0.2	9.7 ± 0.1	26.1 ± 1.6
2012	Down-Down	B^0	-0.02	0.22	73.3 ± 0.2	3.5 ± 0.0	8.3 ± 0.1	11.5 ± 0.4
		B^0_s	0.20	0.20	82.0 ± 0.1	7.8 ± 0.1	9.6 ± 0.1	23.7 ± 0.5
	Long-Long	B^0	0.00	0.36	71.6 ± 0.3	2.7 ± 0.1	6.3 ± 0.1	9.1 ± 0.8
		B^0_s	0.25	0.25	81.9 ± 0.2	7.0 ± 0.1	9.6 ± 0.1	23.2 ± 0.9

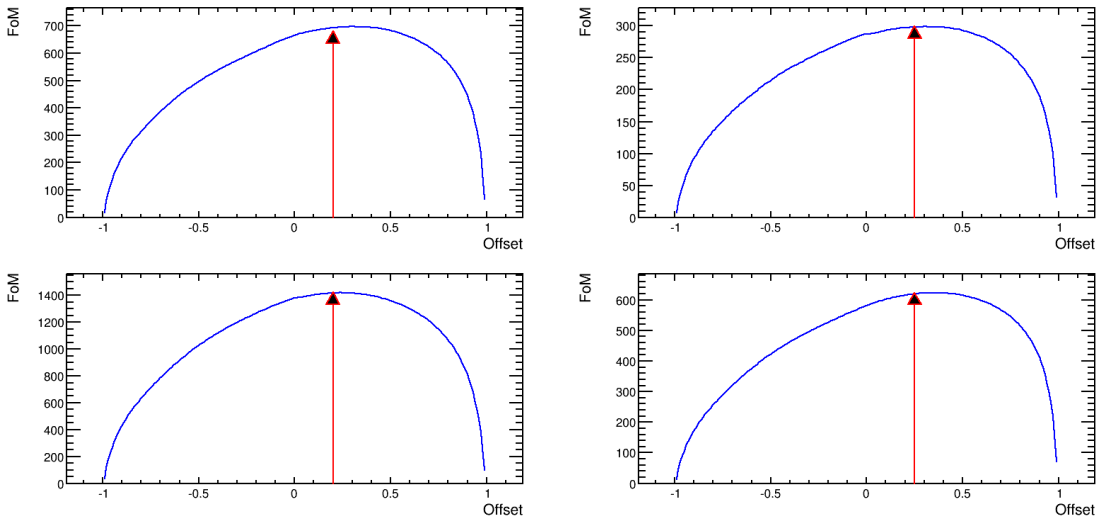

Figure 4.14: *The product of the figure of merits for* $B^0 \to K^0_S \pi^+ \pi^-$ *and* $B^0 \to K^0_S K^+ K^-$. *The red arrow points to the optimal value* $a_\pi = a_K$.

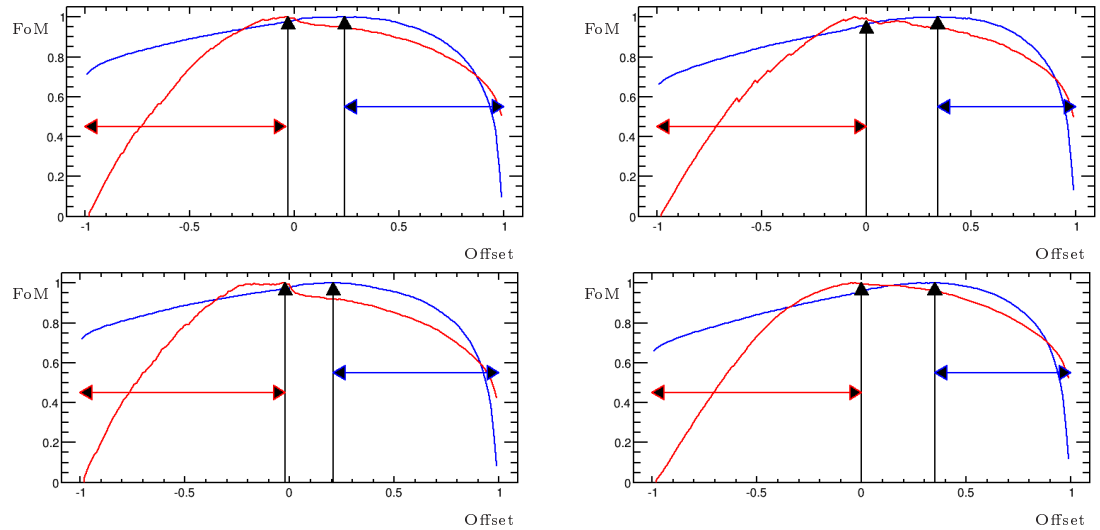

Figure 4.15: *Figures of merit for the non-favoured modes* $B^0_s \to K^0_S \pi^+ \pi^-$ *(blue) and* $B^0_s \to K^0_S K^+ K^-$ *(red). The red (blue) arrow shows the region where the pion (kaon) candidates are.*

4.3 Background studies

The structure of the backgrounds in the charmless decays $B^0_{d,s} \to K^0_S h^\pm h'^\mp$ is rich. Four main categories were identified. They are described in details in [82]. The purpose of this Section is to review them rapidly and to emphasize those which play a significant role for the Dalitz Plot analysis.

- The first category corresponds to the **fully reconstructed and peaking background**, where the final state is identical to the signal but proceeds through a charmed or charmonia resonance. In some events, the reflections of misidentified resonances (under the exchange of a kaon to a pion) are as well considered. This type of background can be vetoed by reconstructing the final state under the proper daughter particle hypotheses for the given intermediate state and cut on the newly formed invariant mass of the hypothesized resonance. The possible J/ψ and χ_{c0} charmonia transitions and the D and Λ_c intermediate states are hence vetoed by requiring their reconstructed to be $|m_{\rm rec} - m_{\rm PDG}| < 48\,{\rm MeV}/c^2$ for charmonia and $|m_{\rm rec} - m_{\rm PDG}| < 30$ MeV/c^2 for D mesons and Λ_c baryon (*cf.* Fig. 4.16). The ensemble of vetoes are:
  - $D^0 \to K^-\pi^+$, $D^0 \to \pi^+\pi^-$, $D^0 \to K^+K^-$, $D^+ \to K^0_S K^+$, $D^+ \to K^0_S \pi^+$, $D^+_s \to K^0_S K^+$, $D^+_s \to K^0_S \pi^+$ and $\Lambda_c \to p K^0_S$
  - $J/\psi \to \pi^+\pi^-$,
  - $\chi_c \to \pi^+\pi^-$ is removed in the measurements of the $B^0_{d,s} \to K^0_S h^\pm h'^\mp$ branching fractions series. As a strongly interacting state, the χ_c is taking part of the interference figure of the $B^0 \to K^0_S \pi\pi$ and is kept in this DP analysis.

- The **partially reconstructed background** are four-body decays in which one particle is not reconstructed. The multivariate selection tool contains an isolation variable which identifies any additional charged track consistent with the analysis candidate vertex. Hence, most of the partially reconstructed background correspond to a missing π^0 or γ in the reconstruction. As an example, on can cite the charmless decay $B^0 \to \eta' K^0_S$ followed by $\eta' \to \rho\gamma$, the γ being not reconstructed. A cocktail of charmed and charmless transitions have been studied using to MC simulated events, out of which a model to describe the shape of the partially reconstructed $K^0_S h^\pm h'^\mp$ mass distribution is derived. Let us notice that this background is innocuous for the DP analysis, in reason of the tight selection and its non-peaking nature.

- The **reflections or cross-feeds** from other signal modes: the six modes $B^0_{d,s} \to K^0_S h^\pm h'^\mp$ are competing up to the PID identification cuts. By definition of the particle identification criteria, none of the selected candidates can enter simultaneously in two distributions. Despite this mutually exclusive definition of the samples, PID misidentifications can occur and require these contributions to be accurately modelled. The choice of hard PID cuts is however making the dominant signal cross-feeds in the $B^0 \to K^0_S \pi^+\pi^-$ spectrum negligible.

- On top of these physical backgrounds, there is a **combinatorial background** where at least one particle is not coming from the signal decay. The Long-Long and Down-Down categories are very different in this respect, the latter receiving a higher level of

fake combinations. They are expected to be the largest background under the signal peaks for the DP analysis. The multivariate selection described in Section 4.2 aims at removing them maximally. Combinatorics are modelled with a linear or an exponential shape in the invariant mass fit.

Figure 4.16: *Figures show the 2-body invariant masses with 2011 Down-Down K^0_S candidate where the $K^0_S\pi\pi$ selection is applied with tight BDT and PID: the top plots show the reconstructed mass of $K^0_S\pi^+$, $K^0_S\pi^-$ and $\pi^+\pi^-$ without any vetoes, the two bottom left plots show the reconstructed mass of $K^0_SK^\pm$ and $K^\pm\pi^\mp$ (with dominant charm meson vetoes), the two bottom right plots show the reconstructed mass of K^0_Sp and $p\pi$ with dominant charm meson and MisId (K/π) charm meson vetoes.*

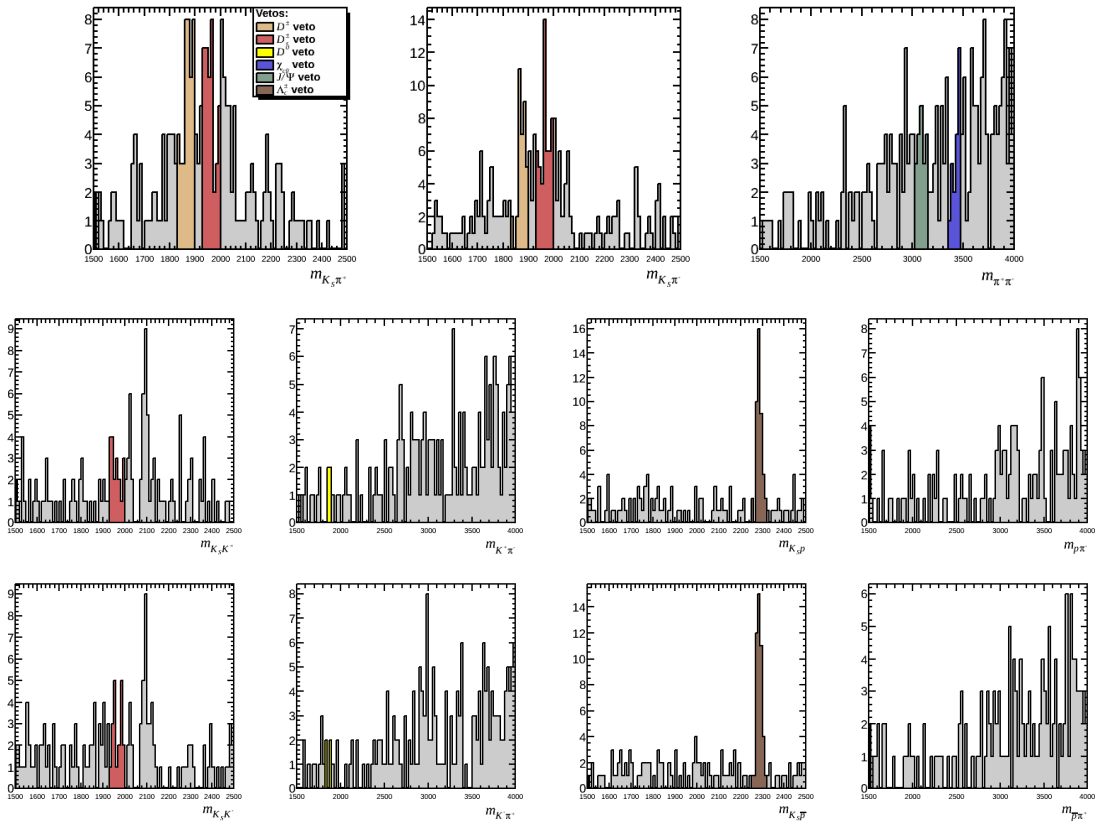

4.4 Mass fit model

This Section is meant to provide useful information for the reader to understand the mass fit results presented in the next Section 4.5. The detailed presentation of this model can be found in Ref. [83]. A simultaneous unbinned extended maximum likelihood fit to the invariant mass distributions, $K^0_{\rm S}K^+K^-$, $K^0_{\rm S}K^\pm\pi^\mp$ and $K^0_{\rm S}\pi^+\pi^-$, is performed to determine the yields of the different modes. The models used in this fit are described in this section.

As the $B_s^0 \to K_S^0 K^+ K^-$ decay has not yet been observed, a blinding procedure is applied to this mode.

4.4.1 General strategy

The underlying strategy employed for the mass fit is the following:

- most of signal model parameters are taken from the simulation except the reconstructed mean masses of B^0 and B_s^0, and the resolution of the signal;
- generic shapes for partially-reconstructed backgrounds are parametrised using samples generated with the fast MC method documented in [84], and their yields are constrained using signal yields, relative branching fractions and adequate efficiencies;
- when not negligible, cross-feed contributions are modelled using fully-simulated samples, and their yields are constrained using signal yields, relative branching fractions and adequate efficiencies;
- combinatorial background in each spectrum is modelled with a first-degree polynomial.

4.4.2 Signal model

As in the same previous analysis given by the Ref. [85], each signal shape is modelled with a sum of two Crystal Ball (2CB) functions sharing a common mean and width. The corresponding tail parameters are extracted after the whole selection, and fixed to the values obtained on the simulation. No truth-matching requirement is added at this level in order to account for mis-matched and misreconstructed signals in the signal shape. For consistency, the matching will not be required either when calculating the efficiencies. Unmatched events are at the sub-percent level after the whole selection is applied and would contribute to systematic uncertainties at a negligible level (and are thus neglected). The turnover point (α_0) and the tail parameter (n_0) that are modelling the radiative tail are allowed to be different for each reconstruction mode and periods, but universal for B^0 and B_s^0's, and Down-Down and Long-Long. The right-hand side parameters (α_1 and (n_1)), allowing for a parametrisation of pathological signal candidates that typically lie at higher masses than the signal, are taken to be universal for all the modes, periods, and meson types. They are indeed thought to be linked to tracking effects, all the modes under study having similar kinematics at first order. The fraction of the second CB (f_1) is left free on the fit to the simulation but fixed in the fit to data. It is assumed to be universal for B^0 and B_s^0's, and Down-Down and Long-Long, but is allowed to vary between reconstruction modes. Both the mean and the width of each of the two CB function are assumed to be identical. The mean value of the B^0 and B_s^0 masses are let free in the fit and universal for all reconstruction modes. The width of the $K_S^0\pi^+\pi^-$ decays is left free in the fit and two (multiplicative) scale factors for the width of the $K_S^0 K^\pm \pi^\mp$ and $K_S^0 K^+ K^-$ decays are also left free in the fit to data. The ratio of the widths for Down-Down and Long-Long candidates is assumed to be universal, in order to reduce the number of free parameters. At last, the ratio of the widths for B^0 and B_s^0 is also assumed to be universal. In both cases, this assumption has been successfully tested on the fit on MC samples.

A fit of all the simulated samples is performed simultaneously to extract the various parameters in a consistent way after the whole selection using the loose and tight BDT optimisations. The parameters fit results for the different optimisation can be found in [83]. Fit results for the decay mode $B^0 \to K^0_S\pi^+\pi^-$ in the tight optimisation are shown in Fig. 4.17. Fit results for other periods and other decay modes are shown in Appendix D.

Figure 4.17: *Result of the simultaneous fit of the reconstructed invariant mass on simulated samples of the signal decay $B^0 \to K^0_S\pi^+\pi^-$, using the tight optimisation of the BDT. The running periods 2011, 2012a and 2012b are shown from top to bottom, while Down-Down decays are shown on the left and Long-Long decays on the right.*

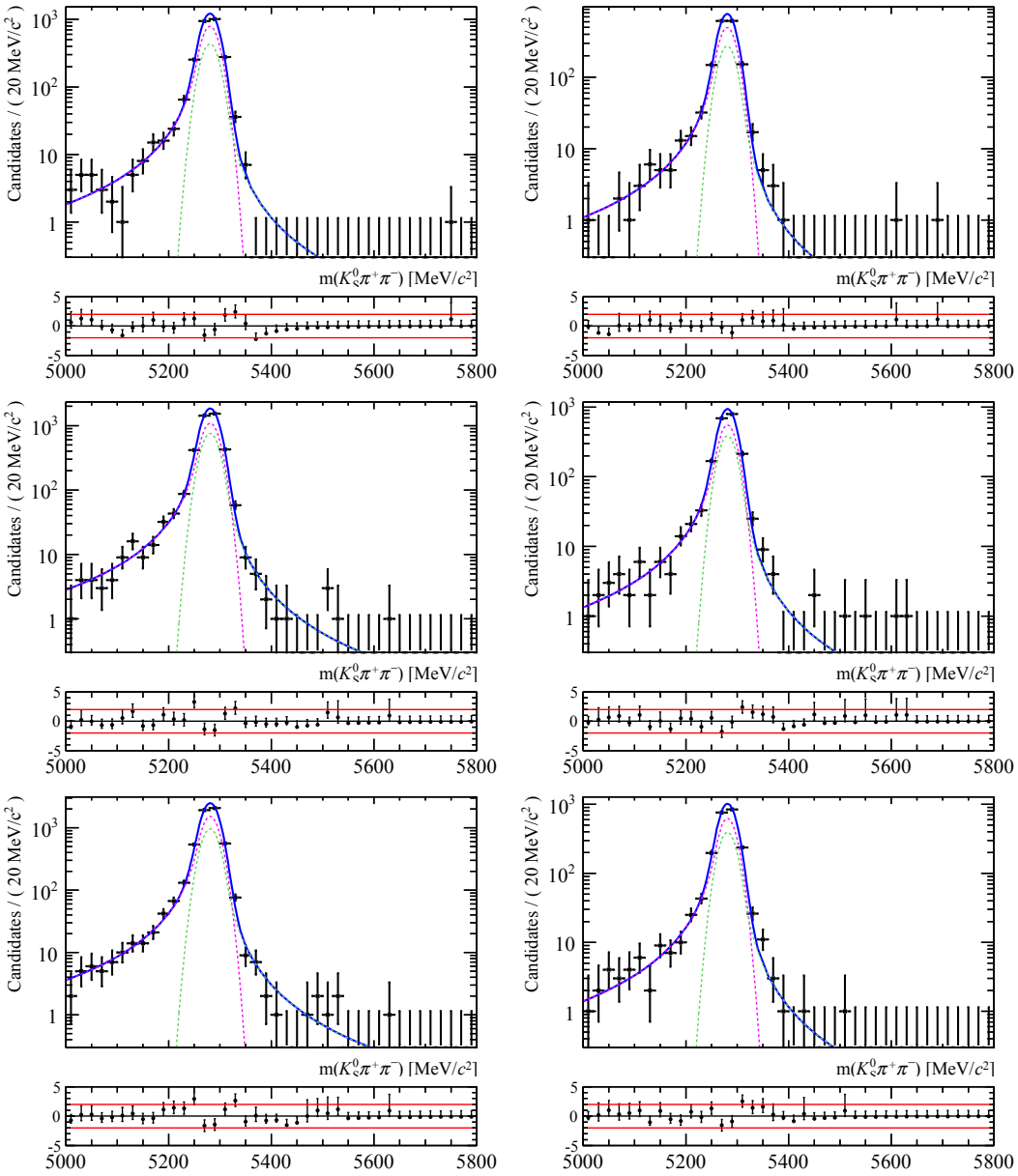

4.4.3 Models for crossfeed background

We model the misidentified signals using a double Crystal-Ball distribution, and we fix the mean and the width of the Gaussian core to be the same in the two components.
We assume all parameters to be the same between the Down-Down and Long-Long reconstruction modes and the periods of data taking. We also share all parameters except for means between same kind of mis-ID. For instance, this means that all non-mean parameters are shared between the $B^0 \to K^0_S\pi^+\pi^-$ as $K^0_S K^\pm\pi^\mp$ and $B^0_s \to K^0_S K^\pm\pi^\mp$ as $K^0_S K^+K^-$ contributions. This hypothesis is supported by the values obtained for these parameters in a fit where they are left independent. It allows to greatly reduce the number of parameters and thus improves the stability of the fit .

The fit on the simulated data samples, after the whole selection except for the BDT [5], is performed simultaneously on B^0, B^0_s, Down-Down, Long-Long, 2011, 2012a, and 2012b for each channel. The fit results for the different optimisation can be found in [83]. The results for the tight optimisation considered for the DP study of the decay $B^0 \to K^0_S\pi^+\pi^-$ are displayed in Fig. 4.18. Results for other modes are shown in Appendix D.

The yields of the cross-feed contributions cannot be free in the fit to the data, because they correspond to small contributions, close to signal peaks. Thus the rates of the misidentified signal contributions relative to their well-identified counterparts are constrained with Gaussians using central values and widths extracted from Monte-Carlo efficiencies for the BDT (since the cut is different for each reconstruction mode) and from calibrated PID efficiencies described in Section 4.2.6.2. The uncertainties are from systematic uncertainties of the PID calibration procedure and the statistical uncertainty on the relative BDT efficiencies. Both simulated samples generated flat on the square Dalitz and the phase-space are used. The relative difference of the values obtained for these two Monte-Carlo samples is added in quadrature to the other uncertainties. These constraints are summarised in Table 4.20.

4.4.4 Partially-reconstructed backgrounds

The former strategy to model the partially-reconstructed backgrounds is also kept in this update of the analysis included in this thesis, with some adaptations. Four categories of partially-reconstructed backgrounds are identified. Each shape is modelled with Argus functions convoluted with a Gaussian, parametrised by the equation:

$$f_{\text{Argus}} = m \cdot (1 - (\frac{m}{m_t})^2)^p \exp\left(s \cdot (1 - (\frac{m}{m_t})^2)\right) \tag{4.4}$$

Two categories of charmless radiative partially-reconstructed backgrounds are parametrised in the $K^0_S\pi^+\pi^-$ reconstruction mode. They consist of $B^0 \to \eta'(\rho^0\gamma)K^0_S$ and $B^0 \to K^0_S\pi^+\pi^-\gamma$. These have been considered in the $K^0_S K^+K^-$ and $K^0_S K^\pm\pi^\mp$ reconstruction modes, but their contributions have been estimated to account for a negligible amount of events.
The other categories are the charmless and open-charm decays with a missing $\pi^{\pm,0}$. These are modelled using a canonical mode, and are allowed to come from both B^0 and B^0_s. Contributions from B^+ decays are generically taken into account in the B^0 contribution. Any

[5] The BDT cuts are not applied to increase the statistics of the crossfeed samples

Figure 4.18: *Results of the fit of the reconstructed invariant mass of the misidentified signal decay* $B_s^0 \to K_S^0 K^\pm \pi^\mp$ *as* $K_S^0 \pi^+ \pi^-$*, using the tight optimisation of the BDT. Running periods 2011, 2012a and 2012b are shown from top to bottom, while Down-Down decays are shown on the left and Long-Long decays on the right.*

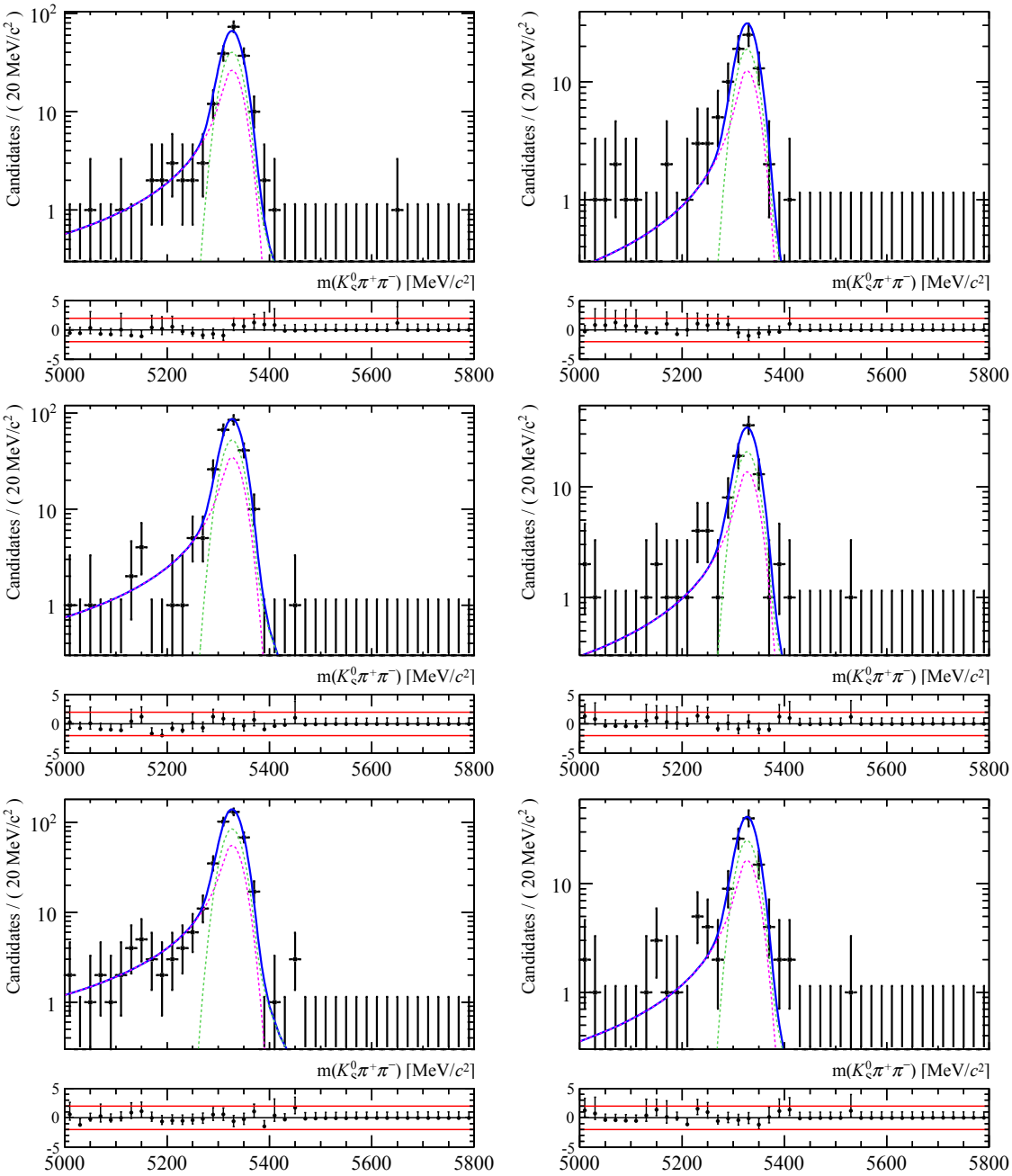

decay where a K or an η is missing do not fall into the invariant mass window of the final fit, and thus are not parametrised. The same comment is also valid for B to excited open-charm mesons.

The threshold parameter (m_t, see Eq. (4.4)) of each contribution is taken to be equal

Table 4.20: *Constraints on the relative yields of the cross-feed contributions, from BDT MC efficiencies and calibrated PID efficiencies. Contributions not present in this table are neglected because they are expected to contribute less than one event in the final fit. The constraints given in this table are under Tight BDT optimisations.*

relative yield	mean [%]
$\frac{N(B^0\to K^0_S K^+K^-\text{ as }K^0_S K^\pm\pi^\mp)}{N(B^0\to K^0_S K^+K^-)}$	7.1 ± 12.3
$\frac{N(B^0\to K^0_S K^\pm\pi^\mp\text{ as }K^0_S K^+K^-)}{N(B^0\to K^0_S K^\pm\pi^\mp)}$	2.31 ± 2.3
$\frac{N(B^0\to K^0_S K^\pm\pi^\mp\text{ as }K^0_S \pi^+\pi^-)}{N(B^0\to K^0_S K^\pm\pi^\mp)}$	7.72 ± 3.5
$\frac{N(B^0\to K^0_S \pi^+\pi^-\text{ as }K^0_S K^\pm\pi^\mp)}{N(B^0\to K^0_S K^+K^-)}$	1.61 ± 1.8
$\frac{N(B^0_s\to K^0_S K^\pm\pi^\mp\text{ as }K^0_S K^+K^-)}{N(B^0_s\to K^0_S K^\pm\pi^\mp)}$	2.28 ± 2.8
$\frac{N(B^0_s\to K^0_S K^\pm\pi^\mp\text{ as }K^0_S \pi^+\pi^-)}{N(B^0_s\to K^0_S K^\pm\pi^\mp)}$	8.85 ± 3.5
$\frac{N(XasY)}{N(Y)}(2012a/2011)$	88.2 ± 4.1
$\frac{N(XasY)}{N(Y)}(2012b/2011)$	94.5 ± 3.7
$\frac{N(XasY)}{N(Y)}(LL/DD)$	106 ± 5

to the physical threshold of the partially-reconstructed decay under consideration: the B mass minus the π mass for a decay with a missing pion, or the B mass in case of a radiative charmless decay. The other parameters are extracted from samples generated with the fast MC method. The parameters p and s of the $K^0_S K^\pm\pi^\mp$ and $K^0_S K^+K^-$ modes are assumed to be identical to the $K^0_S\pi^+\pi^-$ parameters for all categories of partially-reconstructed background. This assumption was checked to be correct on independent simulated samples, given the limited statistics of the simulated samples at hand. B^0, B^0_s, Down-Down and Long-Long parameters are kept identical, expect for the threshold mass in the case of the B^0_s decays. In any case the width of the Gaussian resolution model is kept fixed to the well identified signal decays.

The result of the fit on simulated samples and the corresponding parameters can be found in [83] and shown in Figs. 4.19 and 4.20.

The yields of these partially-reconstructed contributions are constrained with Gaussian functions in the final fit using the known efficiencies from reference fully-simulated samples, and a parameter representing the inclusive branching fraction of these modes when it is not well-known. This factorisation is presented in the following equation, where X is a given mode of partially-reconstructed background contributing to the Y decay mode:

$$\frac{\mathrm{N(X)}}{\mathrm{N(Y)}} = \mathrm{BR(X)} \times \mathrm{h(X,Y)}\ , \tag{4.5}$$

where

$$\mathrm{h(X,Y)} = \frac{\epsilon(Y)}{\mathrm{BR(Y)} \times \epsilon(X)}\ , \tag{4.6}$$

Figure 4.19: *Results of the fit of the reconstructed invariant mass of the partially-reconstructed decays (Down-Down). On the top the two radiative charmless decays (resonant on the left, non-resonant on the right), On the bottom the two decays where a pion is not reconstructed, charmless on the left, from B to open charm decays on the right.*

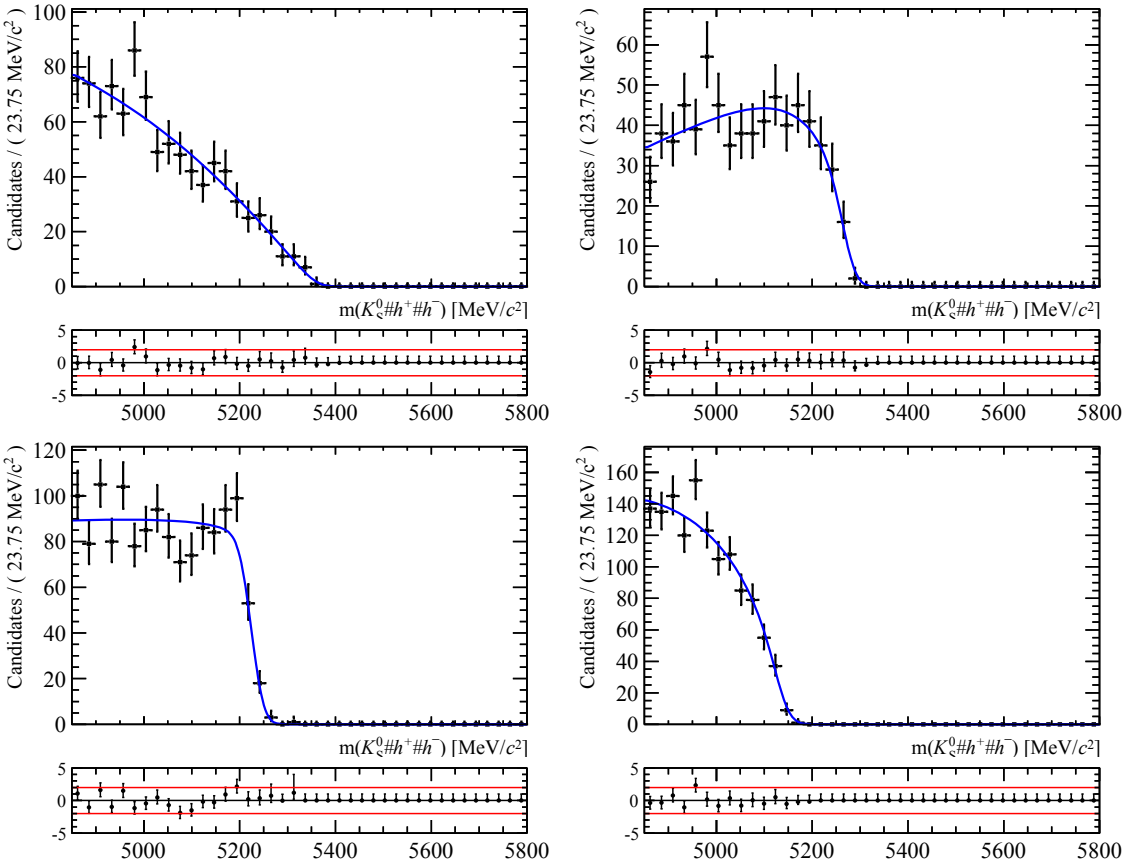

ϵ here is the efficiency of the corresponding decay mode.

The constraints used in the fit are summarised in Table 4.21. We multiply the width of the Gaussian constraints by a factor 5, since the efficiencies are modelled using a single decay mode. The minimum of the parameter representing the branching fraction is fixed using the sum of known branching fractions reported in the PDG, and the maximum is set to an arbitrarily large value (several 10^{-3}).

4.4.5 Combinatorial background

The polynomial coefficient of the combinatorial background is left free in the fit. A scale factor is added to generically allow for a difference between Long-Long and Down-Down slopes, and two others are added to account for a difference between data-taking periods. Systematic uncertainties are assigned to these assumptions.

Figure 4.20: *Results of the fit of the reconstructed invariant mass of the partially-reconstructed decays (Long-Long). On the top the two radiative charmless decays (resonant on the left, non resonant on the right), On the bottom the two decays where a pion is not reconstructed, charmless on the left, from B to open charm decays on the right.*

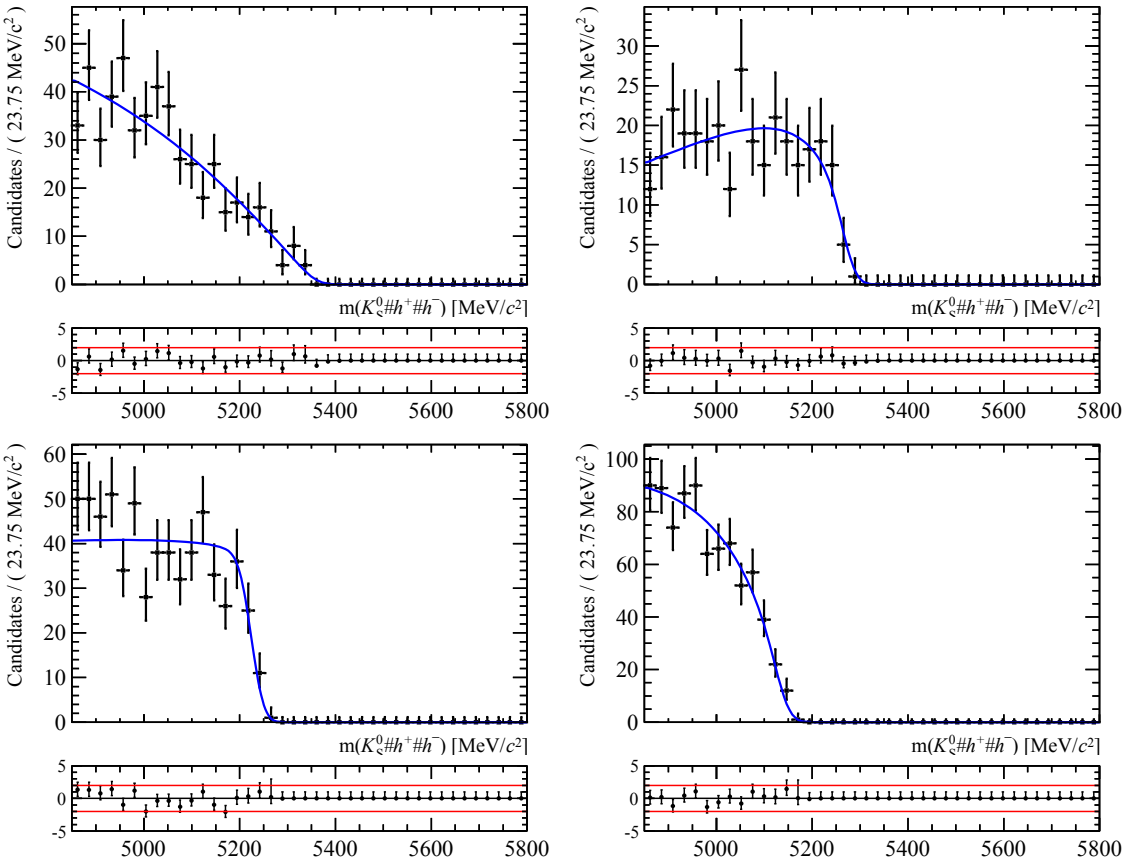

Table 4.21: *Constraints on the relative yields of the partially-reconstructed contributions, from relative MC efficiencies. Contributions not present in this table are neglected.*

h parameter $\left(\propto \frac{\mathrm{N(Bkg.)}}{\mathrm{N(Sig.)}}\right)$	mean	uncertainty
$h(B^0 \to DX \to K^0_S K^+ K^- + \pi)$	10202.7	16471.8
$h(B^0 \to K^0_S K^+ K^- + \pi)$	5911.86	6358.4
$h(B^0 \to DX \to K^0_S K^\pm \pi^\mp + \pi)$	3002.23	6974.3
$h(B^0_s \to DX \to K^0_S K^\pm \pi^\mp + \pi)$	3002.23	6974.3
$h(B^0_s \to K^0_S K^\pm \pi^\mp + \pi)$	1739.62	3456.1
$h(B^0 \to DX \to K^0_S \pi^+ \pi^- + \pi)$	2446.74	4772.5
$h(B^0_s \to DX \to K^0_S \pi^+ \pi^- + \pi)$	2446.74	4772.5
$h(B^0 \to K^0_S \pi^+ \pi^- + \pi)$	1417.74	2175.7
$h(B^0_s \to K^0_S \pi^+ \pi^- + \pi)$	1417.74	2175.7
relative yield	mean [%]	uncertainty [%]
$\frac{N(B^0 \to K^0_S \pi^+ \pi^- + \gamma)}{N(B^0 \to K^0_S \pi^+ \pi^-)}$	1.6	0.33
$\frac{N(B^0 \to K^0_S \eta'(\to \pi^+ \pi^- \gamma))}{N(B^0 \to K^0_S \pi^+ \pi^-)}$	2.7	0.5
$h(X)(2012a/2011)$	75	10
$h(X)(2012b/2011)$	90	12
$h(X)(LL/DD)$	100	10

4.5 Mass fit results

The fit results with both the loose and tight BDT optimisations are discussed. As mentioned earlier in this document, the tight selection has been retained as the baseline selection for the DP analysis of $B^0 \to K^0_S\pi^+\pi^-$ in order to suppress both the combinatorial background and the cross-feed from $B^0_s \to K^0_S K^\pm\pi^\mp$. However, we choose to reproduce here the mass fit results for both optimisations in view of judging the relative level of contamination. The number of signal and combinatorial events are used in order to determine the fraction of signal which is an input of the total p.d.f. of the DP model (see Section 5.1.2).

4.5.1 Fit results for the loose BDT optimisation

The result of the fit is shown in Fig. 4.21 for $K^0_S\pi^+\pi^-$ spectra and in Figs. D.3 to D.5 for $K^0_S K^\pm\pi^\mp$ and $K^0_S K^+K^-$ spectra. The measured fit parameters are summarised in Table 4.22, the signal yields being given separately in Table 4.23 for clarity. The residuals of the fit are as well provided and show a reasonably good behaviour in the whole mass range.

4.5.2 Fit results for the tight BDT optimisation

The result of the fit is shown in Fig. 4.22 for $K^0_S\pi^+\pi^-$ spectra and in Figs. D.6 to D.8 for $K^0_S K^\pm\pi^\mp$ and $K^0_S K^+K^-$ spectra. The measured fit parameters are summarised in Table 4.24,

Table 4.22: *Fit results for the loose optimisation of the BDT.*

$(\mu(B^0_s) - \mu(B^0))(2011)$	88.1 ± 1.3
$(\mu(B^0_s) - \mu(B^0))(2012a)$	88.16 ± 1.7
$(\mu(B^0_s) - \mu(B^0))(2012b)$	85.92 ± 1
$\sigma(B^0 \to K^0_S\pi^+\pi^-)(2011)$	19.17 ± 0.64
$\sigma(B^0 \to K^0_S\pi^+\pi^-)(2012a)$	18.49 ± 0.73
$\sigma(B^0 \to K^0_S\pi^+\pi^-)(2012b)$	19.03 ± 0.49
$Slope(Comb)(2012a/2011)$	1.08 ± 0.14
$Slope(Comb)(2012b/2011)$	0.753 ± 0.097
$Slope(Comb)(K^0_S K^+K^-)(2011)$	-0.000794 ± 0.00024
$Slope(Comb)(K^0_S K^\pm\pi^\mp)(2011)$	-0.00162 ± 0.00028
$Slope(Comb)(Long - Long/Down - Down)$	1.61 ± 0.18
$Slope(Comb)(K^0_S\pi^+\pi^-)(2011)$	-0.00133 ± 0.00018
$\sigma(B^0_s)/\sigma(B^0)(2011)$	1 ± 0.0097
$\sigma(B^0 \to K^0_S K^+K^-)/\sigma(B^0 \to K^0_S\pi^+\pi^-)(2011)$	0.903 ± 0.0096
$\sigma(B^0 \to K^0_S K^\pm\pi^\mp)/\sigma(B^0 \to K^0_S\pi^+\pi^-)(2011)$	0.903 ± 0.0097
$\sigma(Long - Long)/\sigma(Down - Down)(2011)$	0.989 ± 0.031
$\mu(B^0)(2011)$	5284.78 ± 0.64
$\mu(B^0)(2012a)$	5285.68 ± 0.74
$\mu(B^0)(2012b)$	5285.12 ± 0.47

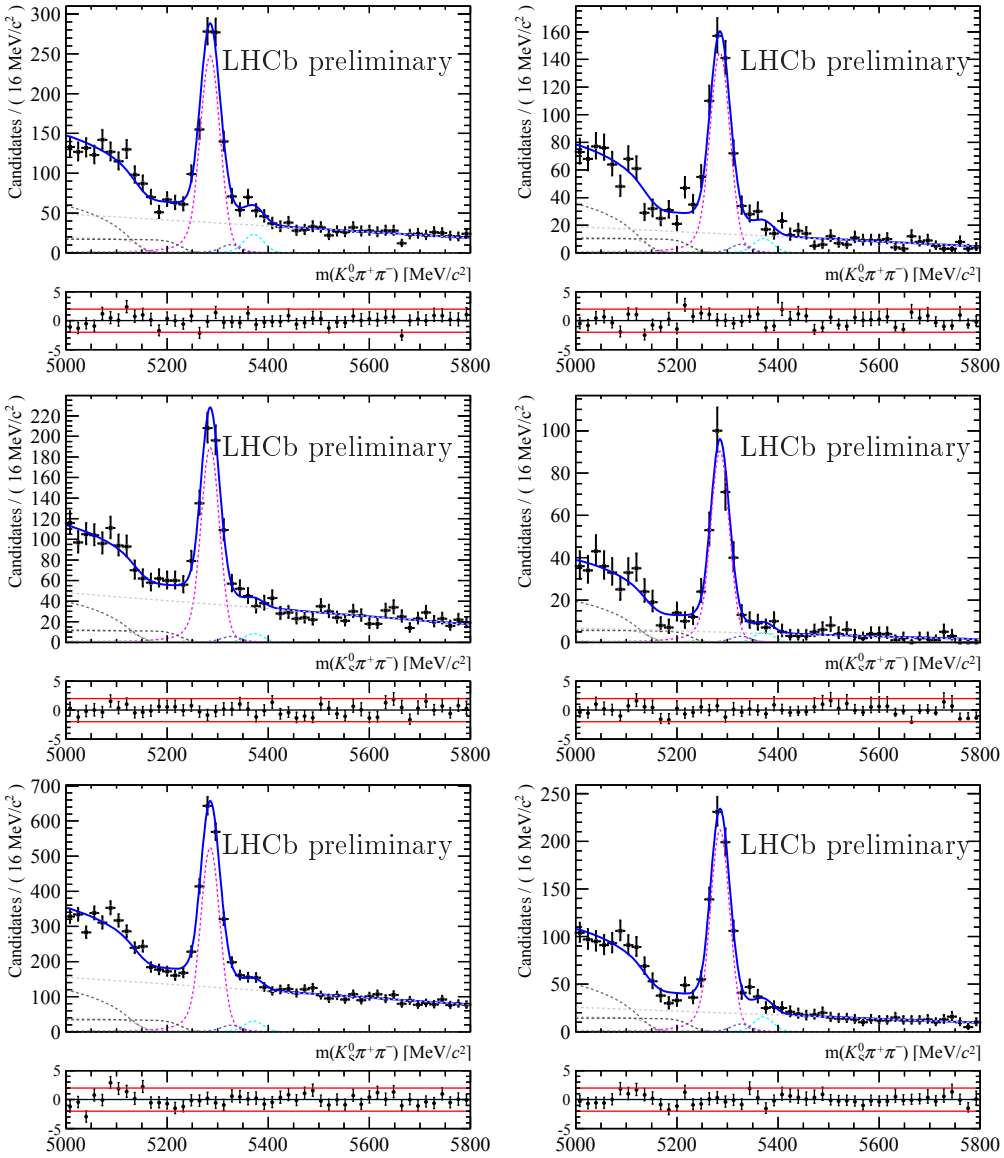

Figure 4.21: *Result of the simultaneous fit of the $K^0_S\pi^+\pi^-$ data with the loose BDT optimisation. Running period 2011, 2012a and 2012b are shown from top to bottom, while the left and right plots show the result of Down-Down and Long-Long K^0_S reconstruction, respectively. Each component of the fit model is displayed as following: the B^0 (B^0_s) components are the pink (cyan) dashed line; misidentified decay $B^0_s \to K^0_S K^\pm\pi^\mp$ is the magenta dashed line; partially reconstructed contributions from B to open charm decay is the gray dashed line, charmless hadronic decays is the brown dashed line, $B^0 \to \eta' K^0_S$ is the dark-gray dashed line and charmless radiative decays is the plum dashed line; and the combinatorial background is the light-gray dashed line.*

the signal yields being given separately in Table 4.25 for clarity.

Table 4.23: *Fit results for the signal yields using the loose optimisation of the BDT.*

Yield	2011	2012a	2012b
$N(B^0 \to K^0_S\pi^+\pi^-)(DD)$	823 ± 33	593 ± 30	1688 ± 55
$N(B^0 \to K^0_S\pi^+\pi^-)(LL)$	482 ± 23	286 ± 16	685 ± 28
$N(B^0_s \to K^0_S\pi^+\pi^-)(DD)$	78 ± 19	27 ± 16	100 ± 31
$N(B^0_s \to K^0_S\pi^+\pi^-)(LL)$	35 ± 12	15 ± 7	50 ± 14
$N(Combinatorial)(DD)$	1690 ± 50	1641 ± 48	5815 ± 85
$N(Combinatorial)(LL)$	589 ± 29	205 ± 19	882 ± 41

Table 4.24: *Fit results for the tight optimisation of the BDT.*

$(\mu(B^0_s) - \mu(B^0))(2011)$	87.38 ± 1.3
$(\mu(B^0_s) - \mu(B^0))(2012a)$	87.7 ± 1.8
$(\mu(B^0_s) - \mu(B^0))(2012b)$	85.77 ± 1.1
$\sigma(B^0 \to K^0_S\pi^+\pi^-)(2011)$	19.08 ± 0.67
$\sigma(B^0 \to K^0_S\pi^+\pi^-)(2012a)$	19.24 ± 0.77
$\sigma(B^0 \to K^0_S\pi^+\pi^-)(2012b)$	19.39 ± 0.5
$Slope(Comb)(2012a/2011)$	0.989 ± 0.16
$Slope(Comb)(2012b/2011)$	0.663 ± 0.11
$Slope(Comb)(K^0_S K^+K^-)(2011)$	-0.00194 ± 0.00075
$Slope(Comb)(K^0_S K^\pm\pi^\mp)(2011)$	-0.00203 ± 0.00032
$Slope(Comb)(Long - Long/Down - Down)$	1.5 ± 0.22
$Slope(Comb)(K^0_S\pi^+\pi^-)(2011)$	-0.00202 ± 0.00037
$\sigma(B^0_s)/\sigma(B^0)(2011)$	1 ± 0.0097
$\sigma(B^0 \to K^0_S K^+K^-)/\sigma(B^0 \to K^0_S\pi^+\pi^-)(2011)$	0.898 ± 0.0097
$\sigma(B^0 \to K^0_S K^\pm\pi^\mp)/\sigma(B^0 \to K^0_S\pi^+\pi^-)(2011)$	0.905 ± 0.0097
$\sigma(Long - Long)/\sigma(Down - Down)(2011)$	0.986 ± 0.032
$\mu(B^0)(2011)$	5284.36 ± 0.69
$\mu(B^0)(2012a)$	5285.42 ± 0.81
$\mu(B^0)(2012b)$	5284.91 ± 0.52

Table 4.25: *Fit results for the signal yields using the tight optimisation of the BDT.*

Yield	2011	2012a	2012b
$N(B^0 \to K^0_S\pi^+\pi^-)(DD)$	512 ± 23	418 ± 21	1224 ± 40
$N(B^0 \to K^0_S\pi^+\pi^-)(LL)$	388 ± 20	208 ± 13	452 ± 20
$N(B^0_s \to K^0_S\pi^+\pi^-)(DD)$	46 ± 10	24 ± 8	111 ± 19
$N(B^0_s \to K^0_S\pi^+\pi^-)(LL)$	24 ± 8	21 ± 5	39 ± 8
$N(Combinatorial)(DD)$	258 ± 17	238 ± 16	1236 ± 38
$N(Combinatorial)(LL)$	184 ± 15	36 ± 7	114 ± 11

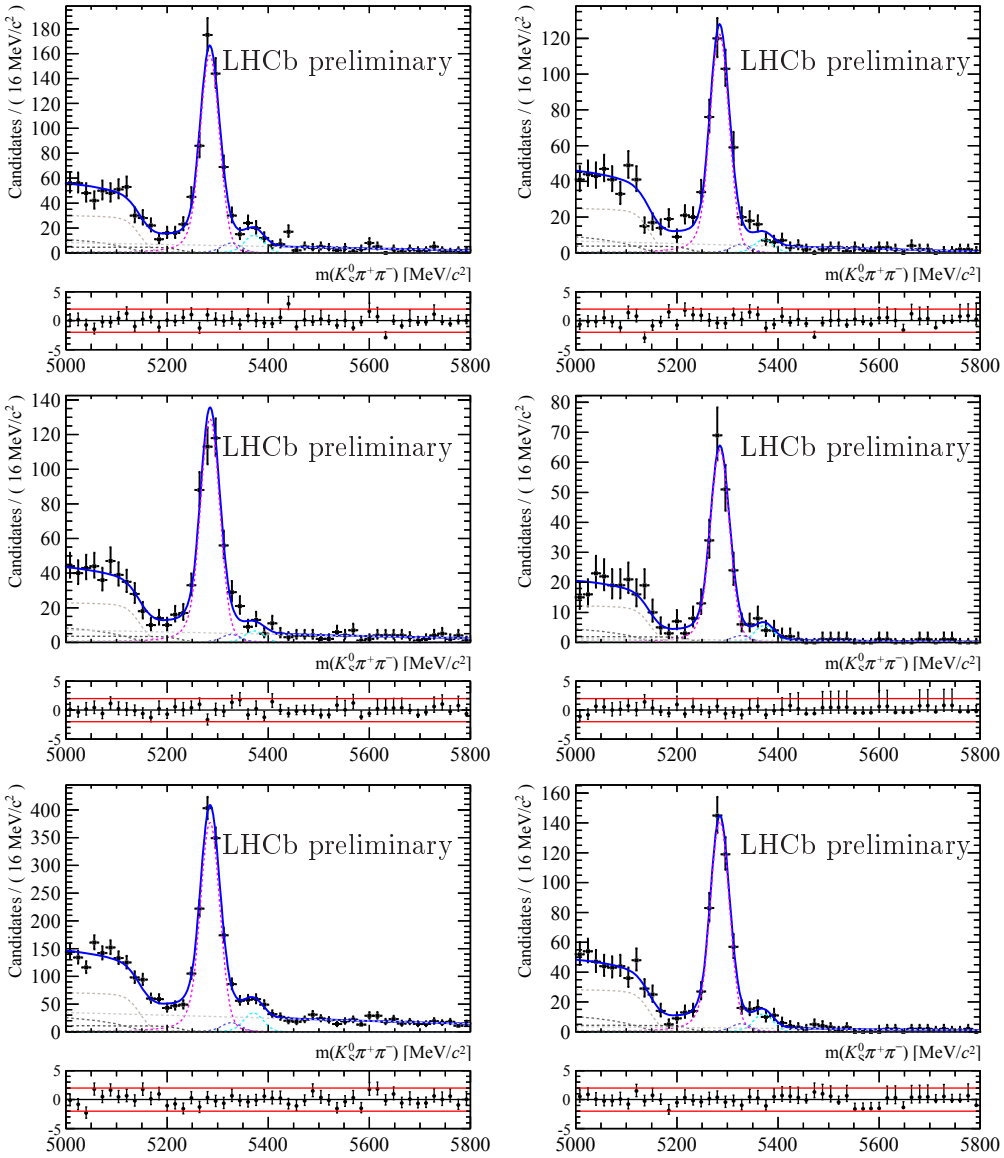

Figure 4.22: *Result of the simultaneous fit of the $K^0_S\pi^+\pi^-$ data with the tight BDT optimisation. Running period 2011, 2012a and 2012b are shown from top to bottom, while the left and right plots show the result of Down-Down and Long-Long K^0_S reconstruction, respectively. Each component of the fit model is displayed as following: the B^0 (B^0_s) components are the pink (cyan) dashed line; misidentified decay $B^0_s \to K^0_S K^\pm\pi^\mp$ is the magenta dashed line; partially reconstructed contributions from B to open charm decay is the gray dashed line, charmless hadronic decays is the brown dashed line, $B^0 \to \eta' K^0_S$ is the dark-gray dashed line and charmless radiative decays is the plum dashed line; and the combinatorial background is the light-gray dashed line.*

Table 4.26: *Fit results, for tight selection, of the $B^0 \to K^0_S\pi^+\pi^-$ signal, combinatorial and crossfeed fraction in the $B^0 \to K^0_S\pi^+\pi^-$ DP region.*

Fraction	K^0_S reco. category	2011	2012a	2012b
Signal	Long-Long	$(91.60 \pm 1.16)\%$	$(95.17 \pm 0.87)\%$	$(94.42 \pm 0.68)\%$
	Down-Down	$(90.37 \pm 0.97)\%$	$(89.87 \pm 1.15)\%$	$(84.79 \pm 0.90)\%$
Combinatorial	Long-Long	$(6.50 \pm 1.13)\%$	$(2.45 \pm 0.82)\%$	$(3.59 \pm 0.65)\%$
	Down-Down	$(6.88 \pm 0.92)\%$	$(7.79 \pm 1.11)\%$	$(12.99 \pm 0.88)\%$
Crossfeed	Long-Long	$(1.90 \pm 0.76)\%$	$(2.38 \pm 0.95)\%$	$(1.99 \pm 0.79)\%$
	Down-Down	$(2.75 \pm 1.09)\%$	$(2.34 \pm 0.93)\%$	$(2.23 \pm 0.88)\%$

4.5.3 Fraction of signal in the B^0 mass window for the tight BDT.

The fraction of $B^0 \to K^0_S\pi^+\pi^-$ signal and backgrounds found in the signal DP region [6] is determined from the measured yields of signal and background in the full spectrum given in Table 4.25 multiplied by the area of their respective p.d.f. in the mass window around the nominal B^0 mass defined by $\pm$ three times the resolution obtained for each spectrum. The Table 4.26 reports the values of the signal fraction obtained for each spectrum and K^0_S reconstruction category. Expectedly, high purity signal samples are obtained.

[6]The signal DP region is represented by $-3\sigma < m_{K^0_S\pi^+\pi^-} - \mu(B^0) < +3\sigma$, where σ is the resolution of $B^0 \to K^0_S\pi^+\pi^-$ signal and $\mu(B^0)$ is the reconstructed mean mass of B^0.

Chapter 5

Dalitz-plot analysis of $B^0 \to K^0_S \pi^+ \pi^-$

This chapter details the Dalitz plot analysis of the decay $B^0 \to K^0_S \pi^+ \pi^-$ using the full Run I data. It includes the description of the likelihood, as well as the efficiency and background modelling in DP. A detailed discussion is given also for the Dalitz fit techniques and the underlying strategy employed for the determination of the nominal signal model. Then the simultaneous maximum likelihood fit to the dataset with its validation are presented. Finally, the systematic study is described.

5.1 Amplitude analysis formalism

The Dalitz plot technique [38] allows to construct a realistic signal p.d.f., where both the kinematical and dynamical properties of the decay can be accurately modelled. The kinematics and the dynamics of the process of interest is given in Chapter 2, where the general formalism of the time-dependent p.d.f. is spelled out and the untagged time-integrated form is eventually derived.

5.1.1 Dalitz Signal p.d.f.

The general time-dependent p.d.f. for the process $B^0 \to K^0_S \pi^+ \pi^-$ was described in Section 2.5. By integrating over time and disregarding tagging information, the Dalitz p.d.f. becomes simply an incoherent sum of the inclusive decay amplitudes $\mathcal{A}(s_+, s_-)$ and $\bar{\mathcal{A}}(s_+, s_-)$ along

$$\mathcal{P}(s_+, s_-) = \frac{|\mathcal{A}(s_+, s_-)|^2 + |\bar{\mathcal{A}}(s_+, s_-)|^2}{\iint_{\rm DP} \left(|\mathcal{A}(s_+, s_-)|^2 + |\bar{\mathcal{A}}(s_+, s_-)|^2\right) {\rm d}s_+ {\rm d}s_-} \,. \tag{5.1}$$

Some comments are in order as far as the *CP* eigenstates final states are concerned. The tagging information is obviously required in order to get a sensitivity on the time-dependent parameter S which carries the information of the interference between the mixing and decay amplitudes. On another hand, the time-dependent $\mathcal{C}$ parameter has a specific status. It is in principle possible to measure it in a time-integrated untagged analysis through the interference patterns of the *CP* eigenstates amplitudes with the flavour specific ones. We

have proven this possibility with pseudo-experiment studies and the details of the proof is given in Section 5.7.

5.1.2 Likelihood function

The selected data sample of this analysis consists mostly of charmless $B^0 \to K^0_S\pi^+\pi^-$ signal and combinatorial background. The data are split in categories depending on the data taking periods and the trigger conditions (2011, 2012a, 2012b) and K^0_S reconstruction type (Down-Down or Long-Long), where the difference between the categories is the reconstruction efficiency and the background distribution. The fit machinery hence takes as input the model for the signal, the model of the backgrounds and selection efficiencies for each category, and maximizes, simultaneously for the different sample categories, a likelihood function by floating the isobar parameters (and resonance parameters if required) of the signal p.d.f. in a fit. The negative logarithm likelihood is actually used instead of the standard likelihood. Maximizing the likelihood means minimizing the negative logarithm likelihood. The negative log likelihood function to be minimized reads

$$-\ln\mathcal{L}_{tot} = -\sum_{n=1}^{N_{tot}} \ln\mathcal{P}_{tot}\ , \tag{5.2}$$

where $\mathcal{L}_{tot}$ is the total likelihood, N_{tot} is the total number of events and $\mathcal{P}_{tot}$ is the general p.d.f. which has the following form

$$\begin{aligned}\mathcal{P}_{tot} &= f_{\rm sig}\frac{\epsilon(s_+,s_-)\mathcal{S}(s_+,s_-)}{\iint_{\rm DP}(\epsilon(s_+,s_-)\mathcal{S}(s_+,s_-))\mathrm{d}s_+\mathrm{d}s_-} + f_{\rm cf}\frac{\mathcal{C}(s_+,s_-)}{\iint_{\rm DP}\mathcal{C}(s_+,s_-)\mathrm{d}s_+\mathrm{d}s_-} \\ &+ (1-f_{\rm cf}-f_{\rm sig})\frac{\mathcal{B}(s_+,s_-)}{\iint_{\rm DP}\mathcal{B}(s_+,s_-)\mathrm{d}s_+\mathrm{d}s_-}\,,\end{aligned} \tag{5.3}$$

where,

- s_+ and s_- are the invariant mass squared,
- $\epsilon(s_+,s_-)$ is the reconstruction efficiency across the Dalitz plot, detailed in Section 5.3.
- $\mathcal{S}(s_+,s_-)$ is the signal p.d.f. given by

$$\mathcal{S}(s_+,s_-) = \sum_{j=1}^{N}\left(|\frac{a_j}{a_r}e^{i(\delta_j-\delta_r)}F_j|^2 + |\frac{\bar{a}_j}{a_r}e^{i(\bar{\delta}_j-\bar{\delta}_r)}\bar{F}_j|^2\right)\ , \tag{5.4}$$

  - N is the number of resonant and non-resonant signal components in the DP,
  - F_j is the spin-dependent dynamical part of the amplitude of the component j,
  - a_j and δ_j ($\bar{a}_j$ and $\bar{\delta}_j$) are the magnitude and phase of the component j,
  - a_r, δ_r and $\bar{\delta_r}$ are the isobar parameters of the reference resonance and its conjugate which are fixed in the fit.

- $\mathcal{B}(s_+, s_-)$ and $\mathcal{C}(s_+, s_-)$ are the distribution of the combinatorial and cross-feed background, respectively, mapped in the square Dalitz-plot and transformed across the Dalitz-plot, detailed in Section 5.2,
- $f_{\rm sig}$ is the signal fraction produced by the invariant mass fit, given in Table 4.26,
- $f_{\rm cf}$ is the fraction of the cross-feed taken from the invariant mass fit. This fraction within the current selection is found to be negligible in the DP. Therefore, in this thesis work the cross-feed fraction is fixed to zero in the DP fit. However, the effect of the cross-feed will be taken as a source of systematic uncertainties.

5.1.3 Physical observables from DP fit

5.1.3.1 Isobar parameters

As mentioned in Section 2.3 the dynamical amplitudes, either resonant or non-resonant, are multiplied by complex coefficients (isobar parameters) that describe the relative strengths of the components. A fit to data allows us to measure directly the relative magnitudes of the isobar amplitudes, for all components in the signal DP model. The isobar parameters can be written either as polar coordinates or Cartesian coordinates. Both parameterisations can yield biases in the measurements and there is no indisputable argument for one or the other. On the contrary, when coming to the combination of several measurements, the Cartesian parameterisation proves to be far more convenient. Anticipating further combinations or averages with other experimental results, the latter has been preferred.

$$\begin{aligned} c_j &= x_j + iy_j \ , \\ \bar{c}_j &= \bar{x}_j + i\bar{y}_j \ . \end{aligned} \tag{5.5}$$

5.1.3.2 CP asymmetry observables

From the measured isobar parameters of an amplitude j, c_j and $\bar{c}_j$, the direct CP asymmetry can be derived

$$\begin{aligned} \mathcal{A}_{CP} &= \frac{|\bar{c}_j|^2 - |c_j|^2}{|\bar{c}_j|^2 + |c_j|^2} \\ &= \frac{(\bar{x}_j^2 - x_j^2) + (\bar{y}_j^2 - y_j^2)}{(\bar{x}_j^2 + x_j^2) + (\bar{y}_j^2 + y_j^2)} \ . \end{aligned} \tag{5.6}$$

We will provide results for the main flavour specific decay amplitudes but also for the quasi 2-body CP eigenstates involving the $f_0(980)$ resonance.

5.1.3.3 Fit fractions

The definition of the rate of a single process j, given a set of isobar amplitudes c_j, is the square of the relevant matrix element (see 5.1.1), and hence involves the ensemble of its interferences with other components. In this context, it is convenient to define the fit fraction

of the process, expressed as the integral over the Dalitz plane of a single amplitude squared divided by the integral over the Dalitz plane of the squared of the coherent sum of all amplitudes,

$$FF_j = \frac{\iint_{\mathrm{DP}} |c_j F_j(s_+, s_-)|^2 \, \mathrm{d}s_+ \mathrm{d}s_-}{\iint_{\mathrm{DP}} \left|\sum_j c_j F_j(s_+, s_-)\right|^2 \mathrm{d}s_+ \mathrm{d}s_-} \tag{5.7}$$

The sum of the fit fractions of all components will in general not be unity due to interference between resonances.

5.1.3.4 Resonance parameters

The DP fit is very CPU-consuming when the parameters of a resonance lineshape (usually mass and width) are allowed to float in the fit. This amounts to recalculate at each step of the fit scan the normalization associated to the component. Therefore, the mass and width in most cases are fixed and the uncertainties associated to their knowledge is addressed as systematic uncertainties.

5.1.4 Analysis method

The strategy for the $B^0 \to K^0_S \pi^+ \pi^-$ DP analysis, and singularly the choice of the nominal models and resonances therein has been defined prior to the study of the data. The strategy steps are gathered in the following items:

- Fit the invariant mass spectrum $K^0_S \pi^+ \pi^-$, and define a signal window around B^0 signal peak.
- Determine the fraction and distribution of combinatorial backgrounds in the Dalitz plot of $B^0 \to K^0_S \pi^+ \pi^-$.
- Obtain the histogram of the efficiency variation across the DP, evaluated from signal MC.
- Fit simultaneously the different samples and educate the final model by adding relevant new contributions to the baseline and decide on the basis of an algorithm involving a statistical dissimilarity test (detailed in Appendix F), the change in the negative log-likelihood (nll) values obtained with and without that contribution and eventually the statistical significance of the measured decay amplitude.

The analysis strategy is planned for a simultaneous DP fit of the six possible categories: two K^0_S reconstructions categories (Down-Down and Long-Long) and three running periods (2011, 2012a and 2012b). In this approach, all isobar parameters are shared for the K^0_S and year categories. The measurements are performed from an unbinned maximum likelihood fit, embedded in a homemade amplitude fitter package, CRAFT. Details about the CRAFT package are provided in Appendix E.

5.2 DP background

The knowledge of the background sources in $B^0 \to K^0_S\pi^+\pi^-$ Dalitz plane is a crucial input required in the amplitude fit. As shown in Section 4.5, combinatorial background and cross-feed from $B^0_s \to K^0_S K^\pm\pi^\mp$ saturates the background contributions under the $B^0 \to K^0_S\pi^+\pi^-$ signal region.

5.2.1 Combinatorial background

The combinatorial background DP distribution is obtained from the upper mass side-band, $5450 < m_{K^0_S\pi^+\pi^-} < 5800$ MeV, supposedly free from other background contributions. Figs. 5.1 to 5.3 show the combinatorial events invariant mass distribution in the above-mentioned mass window after the full tight selection, the $K^0_S\pi^+\pi^-$ Dalitz and Square Dalitz planes distributions, respectively.

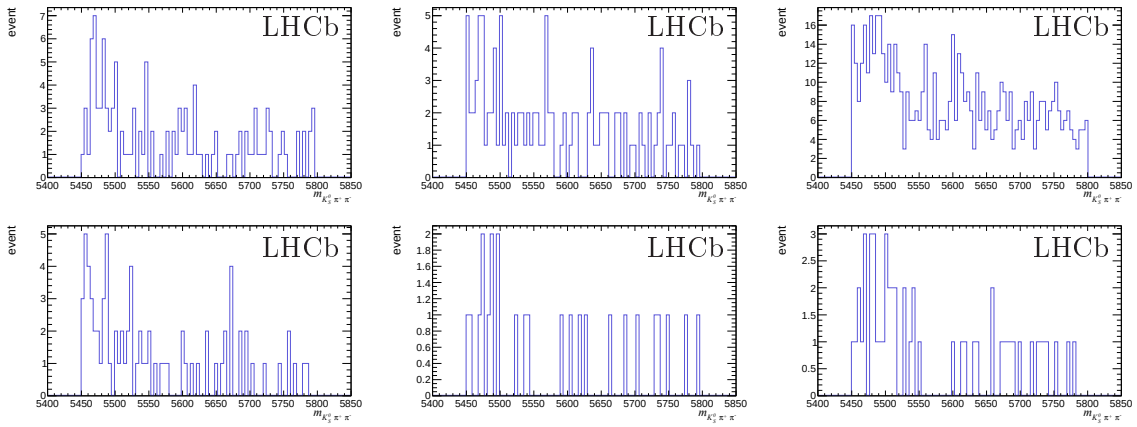

Figure 5.1: *$K^0_S\pi^+\pi^-$ invariant mass distribution in the right-handed side-band data ($5450 < m_{K^0_S\pi^+\pi^-} < 5800$ MeV) for 2011 data (left), 2012a data (middle) and 2012b data (right), classified in Down-Down K^0_S (top) and Long-Long (bottom) categories.*

As in the efficiency section (*cf.* Section 5.3), the combinatorial background histograms with 10×10 bins in SDP, are smoothed out using 2D cubic spline [86] across the SDP. The method used to propagate the uncertainties through the spline fit, is the same method used for the efficiency. The smoothed combinatorial histograms are gathered respectively in Fig. 5.4 for Down-Down and Fig. 5.5 for Long-Long K^0_S category.

5.2.2 $B^0_s \to K^0_S K^\pm\pi^\mp$ cross-feed background

In addition to the combinatorial background, the other source of background events in the signal region is the cross-feed signal from $B^0_s \to K^0_S K^\pm\pi^\mp$ where a kaon is misidentified as pion, as discussed in Section 4.2.6.2.

The cross-feed distribution is obtained from $B^0_s \to K^0_S K^\pm\pi^\mp$ data by making use of the *sPlot* technique [78]. The $K^0_S K^\pm\pi^\mp$ invariant mass is used as the discriminating variable to

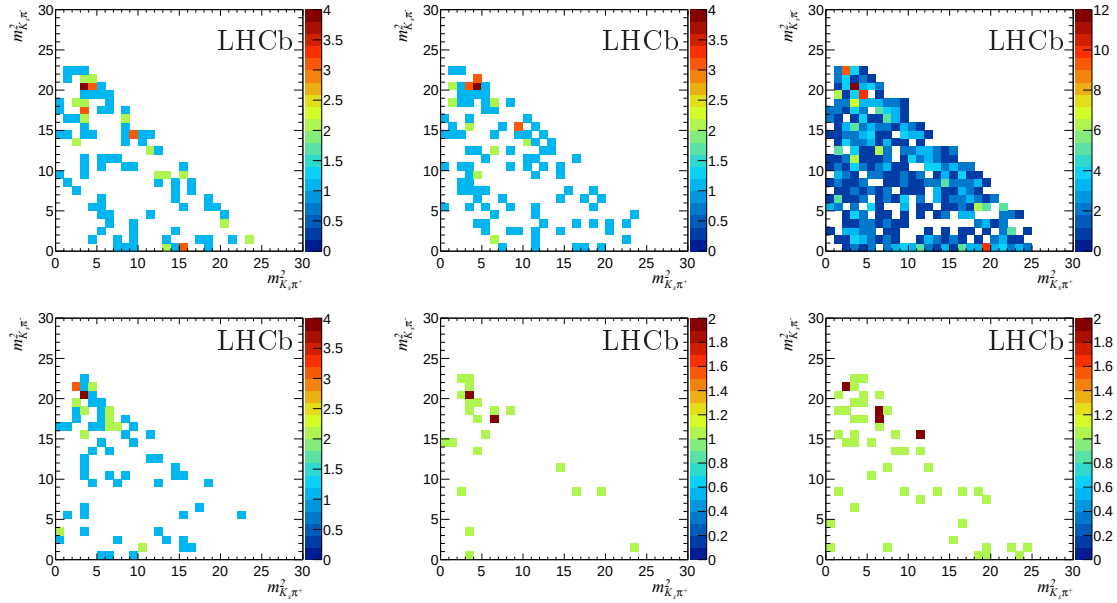

Figure 5.2: *Right-handed side-band data* ($5450 < m_{K^0_S\pi^+\pi^-} < 5800$ MeV) *projected on* $B^0 \to K^0_S\pi^+\pi^-$ *standard-Dalitz plane for 2011 events (left), 2012a (middle) and 2012b (right), classified in Down-Down* K^0_S *(top) and Long-Long (bottom) categories.*

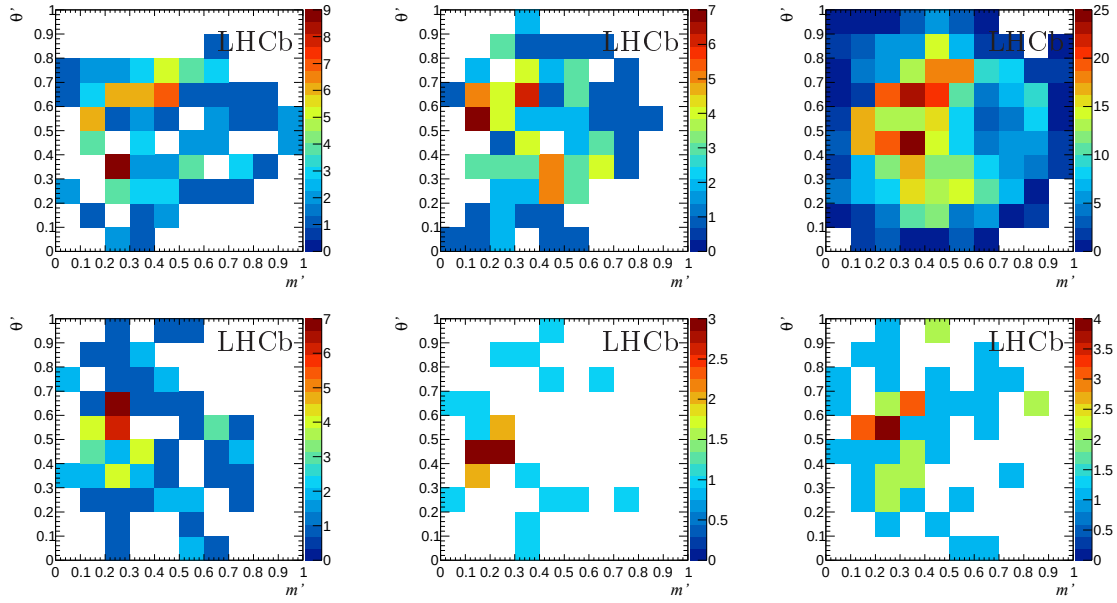

Figure 5.3: *Right-handed side-band data* ($5450 < m_{K^0_S\pi^+\pi^-} < 5800$ MeV) *projected on* $B^0 \to K^0_S\pi^+\pi^-$ *Square-Dalitz plane for 2011 events (left), 2012a (middle) and 2012b (right), classified in Down-Down* K^0_S *(top) and Long-Long (bottom) category.*

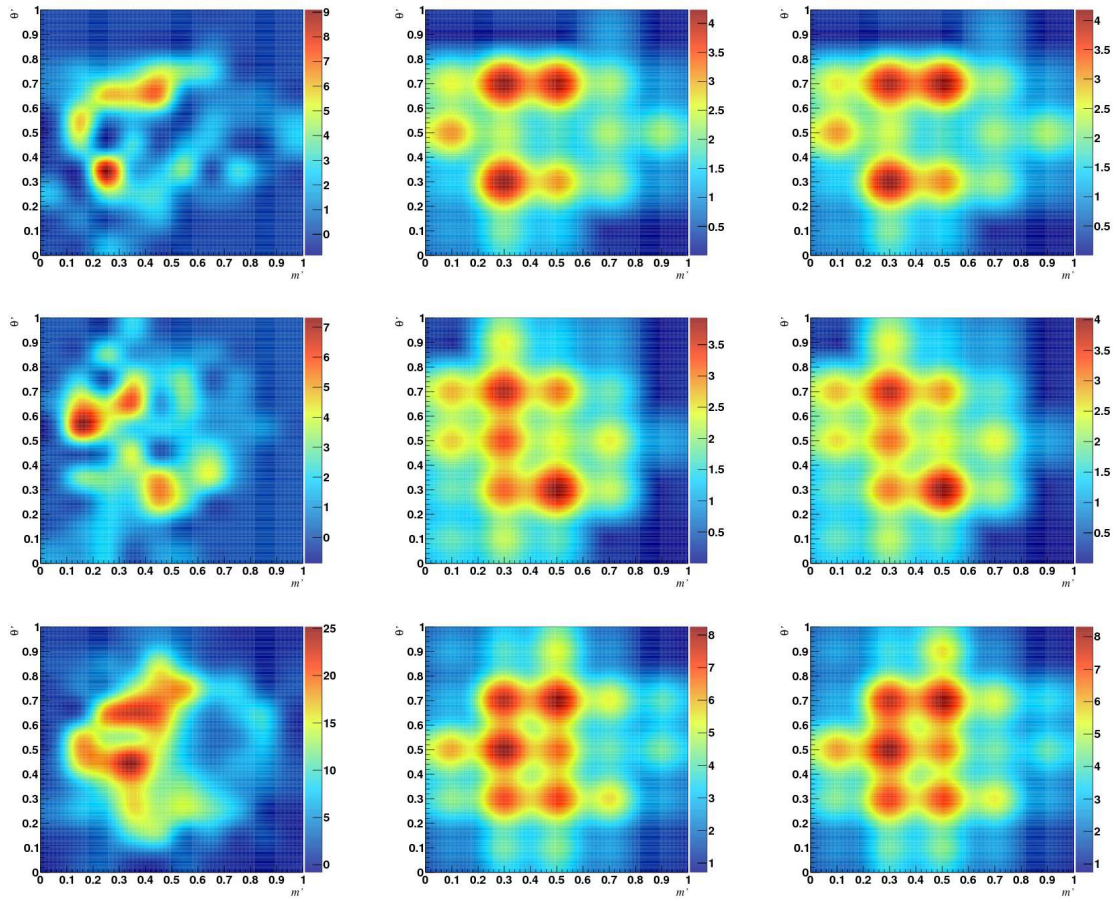

Figure 5.4: *The plots on the left represents combinatorial background histograms from Down-Down samples, smoothed by the 2D cubic spline techniques separated in 2011 (top), 2012a (centre) and 2012b (bottom) samples, the plots on the middle (right) represents the high (low) uncertainties on each combinatorial spline bin, organized in the same year order as the combinatorial maps.*

separate statistically $B_s^0 \to K_S^0 K^{\pm}\pi^{\mp}$ decays from background. The signal and background weights returned by this method are applied to the events, which are in turn used to model the cross-feed under the hypothesis of $B^0 \to K_S^0\pi^+\pi^-$ reconstruction.

As we did with the combinatorial background to avoid the edge limitation, the cross-feed is modelled in the SDP plane, where the two SDP variables m' and θ' are constrained to have the B^0 mass and depend on $m_{\pi^+\pi^-}$ variable. After applying the full selection on $B_s^0 \to K_S^0 K^{\pm}\pi^{\mp}$ samples, the number of events for each sample category is small to smooth properly the crossfeed maps with the spline techniques. Therefore, we multiplied the histogram events by two, by adding the conjugate of the initial histogram, assuming no *CP* violation in $B_s^0 \to K_S^0 K^+\pi^-$. The weighted events of each sample category are shown in Fig. 5.7. The same technique used for the reconstruction efficiency maps in Section 5.3, is applied on cross-feed distribution, where the cubic spline functions are used to smooth the cross-feed histograms across the SDP plane. The procedure used to estimate and propagate the uncertainties in the cross-feed maps follows the same procedure used for reconstruction efficiency maps

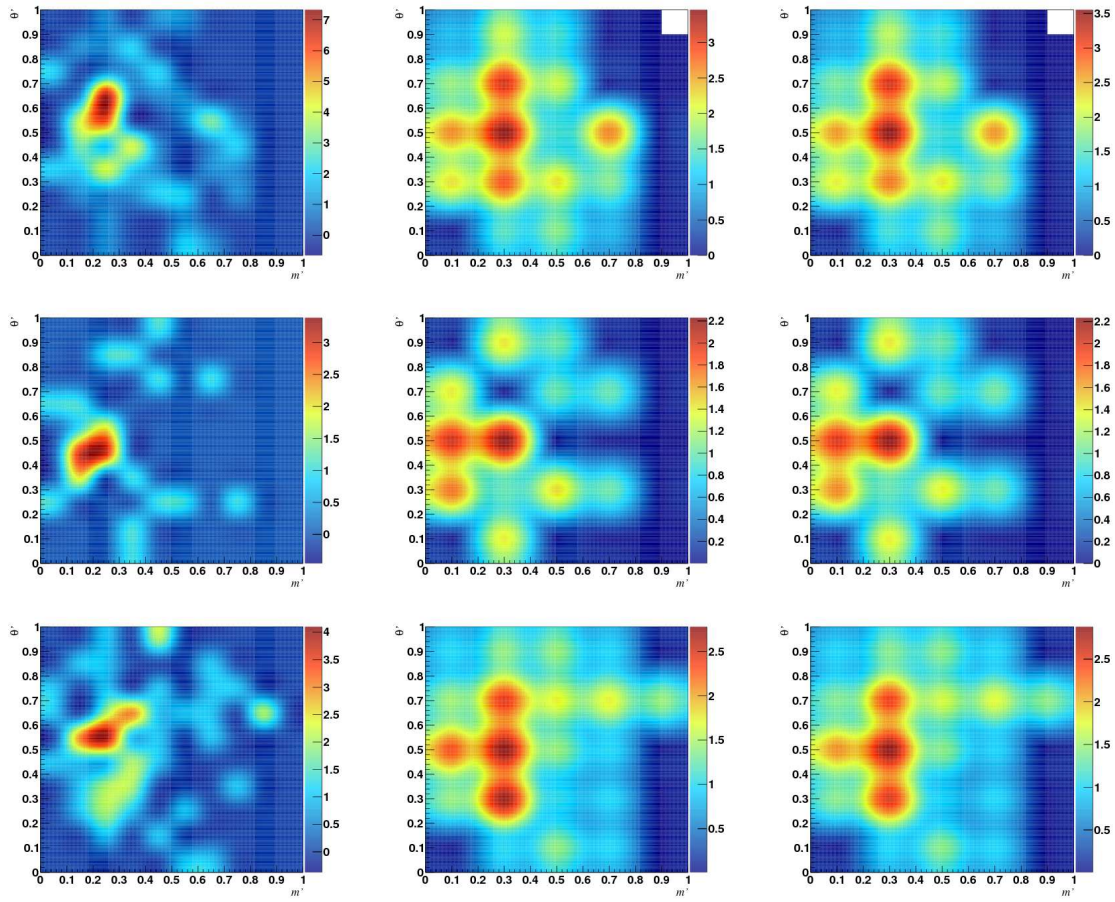

Figure 5.5: *The plots on the left represents combinatorial background histograms from Long-Long samples, smoothed by the 2D cubic spline techniques separated in 2011 (top), 2012a (centre) and 2012b (bottom) samples, the plots on the middle (right) represents the high (low) uncertainties on each combinatorial spline bin, organized in the same year order as the combinatorial maps.*

in Section 5.3. The resulting histograms are shown in Fig. 5.8 for Down-Down and Fig. 5.9 for Long-Long K^0_S category.

As mentioned in the previous section, with the tight selection currently used in this thesis analysis, the fraction of the cross-feed events is small. Therefore, in a first approach, the smoothed histograms of the cross-feed will not be included in the nominal DP fit. A systematic uncertainty related to the assumption that we can neglect that contribution will be assigned. The inclusion of the cross-feed as a DP fit component will be considered for the publication.

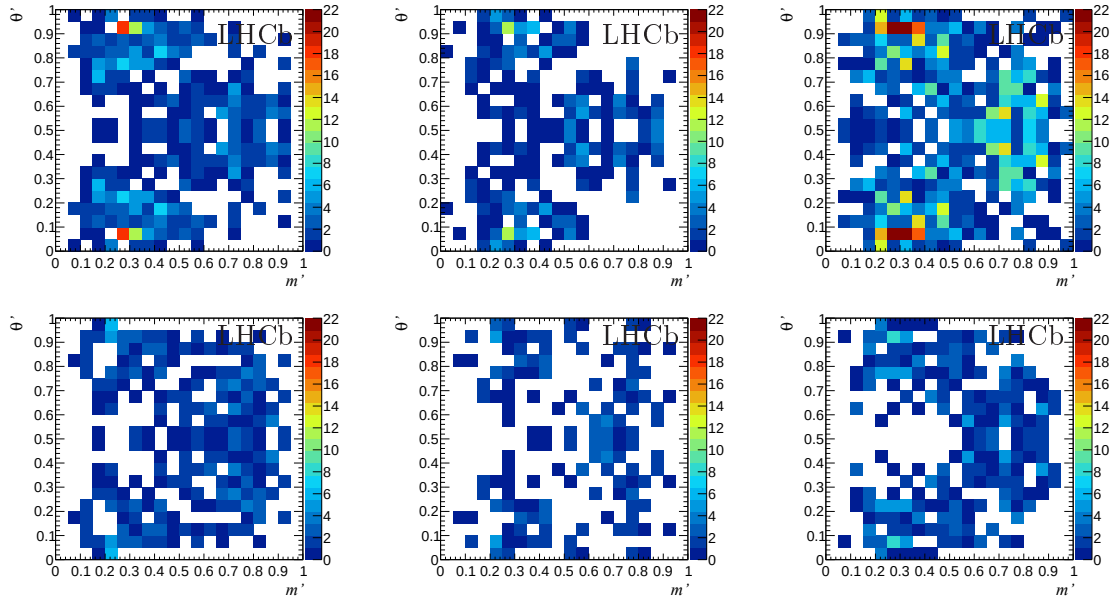

Figure 5.6: *sWeighted $B_s^0 \to K_S^0 K^\pm \pi^\mp$ cross-feed projected onto $B^0 \to K_S^0 \pi^+ \pi^-$ Square-Dalitz plane for 2011 events (left), 2012a (middle) and 2012b (right), classified in Down-Down K_S^0 category (top) and Long-Long (bottom).*

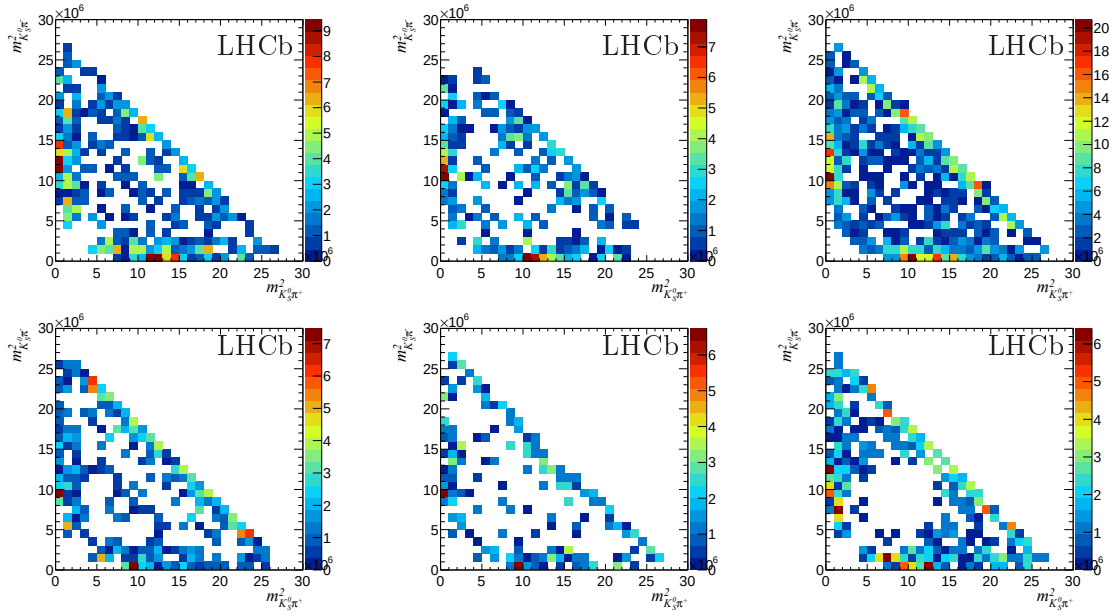

Figure 5.7: *sWeighted $B_s^0 \to K_S^0 K^\pm \pi^\mp$ cross-feed projected onto $B^0 \to K_S^0 \pi^+ \pi^-$ standard Dalitz plane for 2011 events (left), 2012a (middle) and 2012b (right), classified in Down-Down K_S^0 category (top) and Long-Long (bottom).*

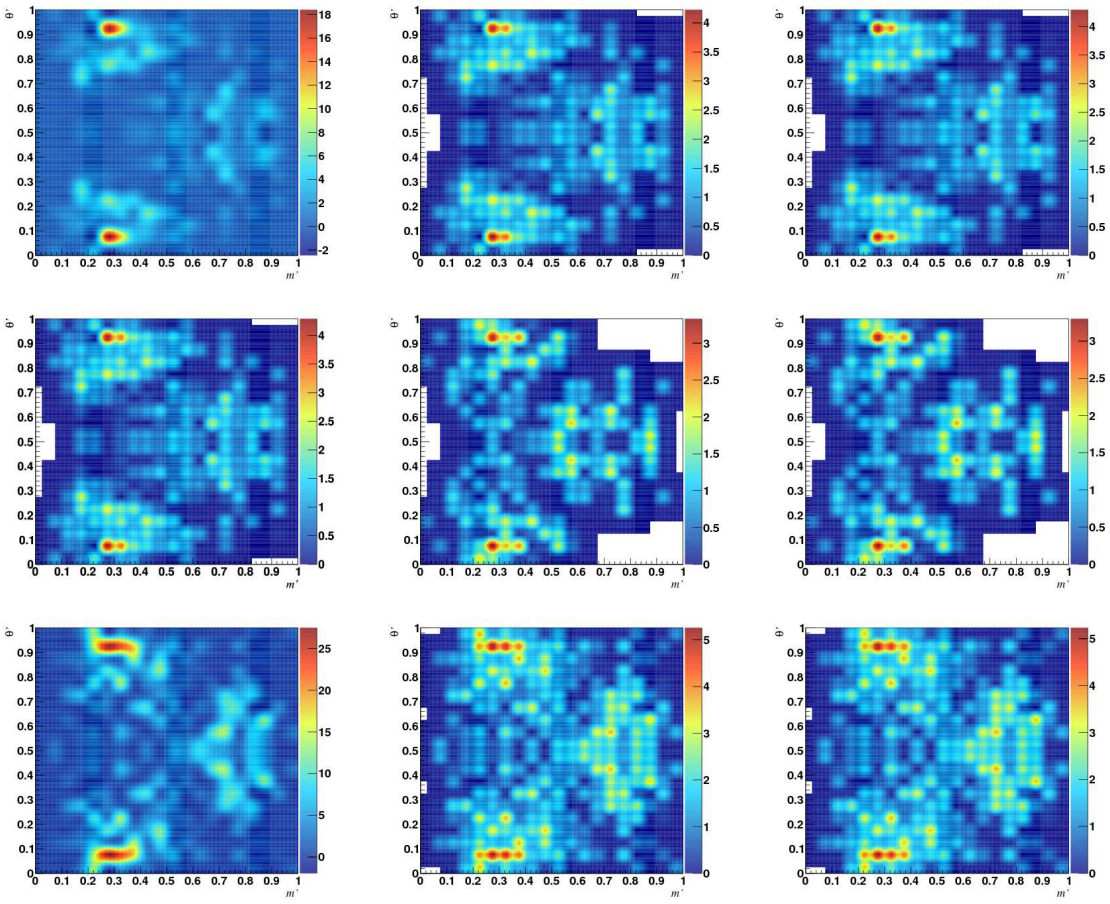

Figure 5.8: *The plots on the left represents* $B_s^0 \to K_S^0 K^{\pm}\pi^{\mp}$ *crossfeed sweighted histograms from Down-Down samples, smoothed by the 2D cubic spline techniques separated in 2011 (top), 2012a (centre) and 2012b (bottom) samples, the plots on the middle (right) represents the high (low) uncertainties on each combinatorial spline bin, organized in the same year order as the combinatorial maps.*

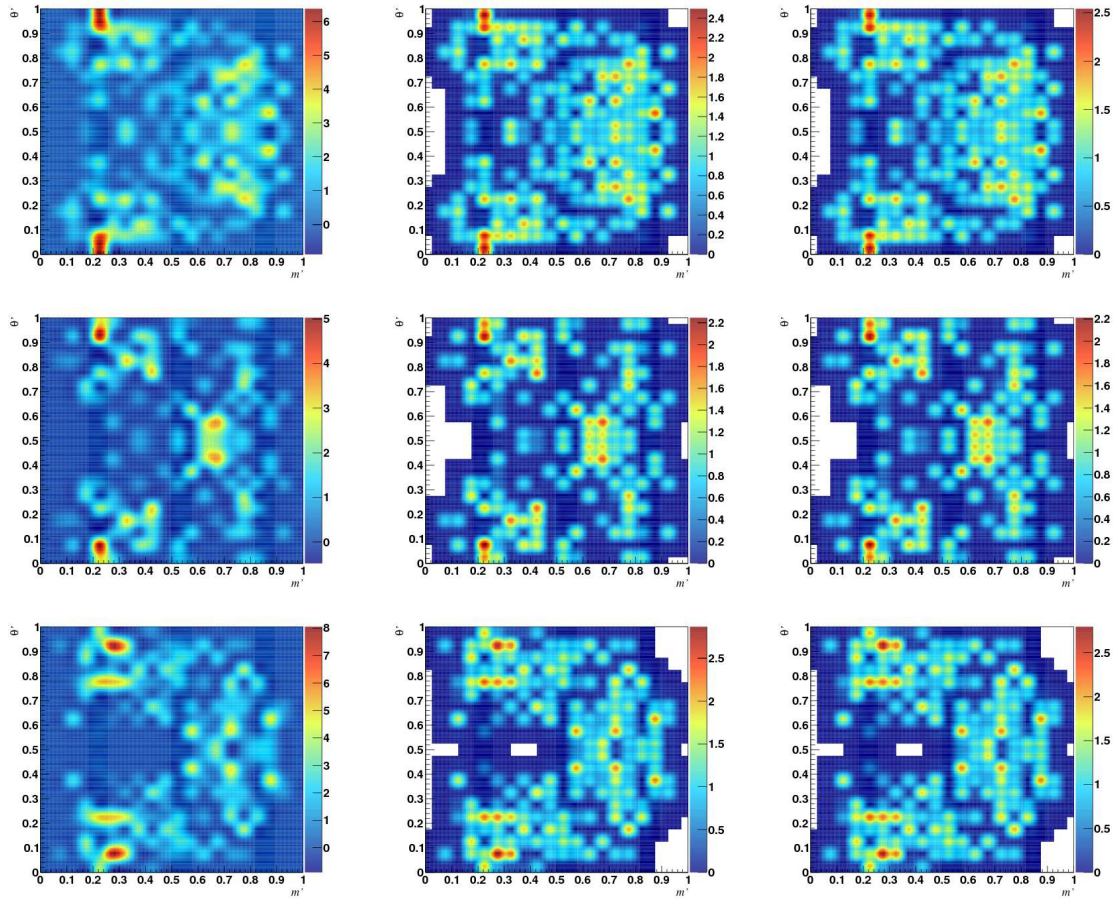

Figure 5.9: *The plots on the left represents $B_s^0 \to K_S^0 K^{\pm}\pi^{\mp}$ crossfeed sweighted histograms from Long-Long samples, smoothed by the 2D cubic spline techniques separated in 2011 (top), 2012a (centre) and 2012b (bottom) samples, the plots on the middle (right) represents the high (low) uncertainties on each combinatorial spline bin, organized in the same year order as the combinatorial maps.*

5.3 Signal efficiency variation across the Dalitz plot

An ideal analysis would select events equally from any region of the phase space, but the selection cuts, the geometrical acceptance, the trigger efficiency all favour or deplete some regions of the DP over others. The DP fit to the data hence requires to know the variation of efficiency across the DP.

In order to have a better understanding of the efficiency and its variation across the phase space of the decay, the contributions from individual sources are studied separately, as

$$\epsilon^{\text{tot}} = \epsilon^{\text{geom}} \times \epsilon^{\text{sel|geom}} \times \epsilon^{\text{PID|sel\&geom}}, \tag{5.8}$$

where

- ϵ^{geom} is the geometrical efficiency, and is determined from MC samples (see Sec. 5.3.1);
- $\epsilon^{\text{sel|geom}}$ is the selection efficiency (trigger, stripping and off-line selection), determined from MC samples corrected for possible data/MC differences in the tracking and trigger efficiencies (see Sec. 5.3.2);
- $\epsilon^{\text{PID|sel\&geom}}$ is the particle identification efficiency and is determined from data using `PIDCalib` tools (see Sec. 5.3.3).

The variation across the (square) Dalitz plot from each of these sources of efficiency is studied separately, in order to help the study of potential systematic biases, discussed in Section 5.8. However, only the total efficiency functions are used in the Dalitz plot fit. Note that the available MC samples correspond to three periods of year (2011/2012a/2012b) and are also separated accordingly to the K^0_S category. Fluctuations due to limited statistics are smoothed out by fitting each efficiency function to a 2D cubic spline across the SDP. The total efficiency is then obtained by multiplying together the values of the spline for each contribution at the given point in the DP.

This Section takes most of the corresponding section in the analysis note dedicated to the DP study of the decay modes $B^0_s \to K^0_S K^\pm \pi^\mp$ [87] but focuses on the results for the decay channel $B^0 \to K^0_S \pi^+ \pi^-$. The interested reader can go to [87] where all details of the procedure are given.

5.3.1 Geometrical efficiency

We determine the geometrical efficiency, ϵ^{geom}, from generator-level MC samples produced without any cuts on the daughter particles (GAUSS configured with `NoCuts` option). This efficiency is defined as the fraction of these MC events with all of the daughter tracks within the LHCb acceptance. Notice that no distinction between 2012a/2012b trigger nor K^0_S Long-Long and Down-Down categories need to be considered here since this efficiency is purely an effect of the detector geometry and the kinematics of the B^0. It is, however, necessary to treat separately 2011 and 2012 data because the B^0 kinematics are different due to the different beam energy.

5.3.2 Selection efficiency

The selection efficiency including contributions from trigger, stripping and off-line selection, $\epsilon^{\text{sel|geom}}$, is determined from full-simulation MC samples generated with the `DecProdCut` option applied. It is worth to mention that both stripping and multivariate selections were designed to minimize the efficiency variation across the DP. As such, the trigger selection is the dominant source of stiff variation of efficiency across the DP. Correction factors are applied to account for data/MC differences in the tracking and `L0` trigger. In particular, trigger corrections are evaluated by separating the samples into `L0Hadron_TOS` and `L0Global_TIS&&!L0Hadron_TOS` candidates.

5.3.2.1 Data/MC tracking efficiency correction

A correction is applied to the selection efficiency to take into account the difference between the tracking efficiency for MC and data. The standard procedure as documented in Ref. [88] is used. The corrective factors are determined in two bins of pseudorapidity η (1.9–3.2, 3.2–4.9) and five bins of momentum p (5–10, 10–20, 20–40, 40–100, 100–200 GeV/c).

Initially, each MC track is weighted to match the data distributions p and η obtained from the sample of $B^0 \to K^0_S\pi^+\pi^-$ candidates selected in the invariant mass region $2.5\,\sigma$ around the B mass. The p and η values of each B^0-daughter tracks (*i.e.*excluding the K^0_S daughters) in the weighted MC samples and the tracking calibration tables are used to determine an average correction factor for each bin in the SDP. The corresponding total tracking efficiency correction, which is obtained from the event-by-event multiplication of the corrections for each track, is shown along with its related uncertainties in Fig. 5.10.

5.3.2.2 Data/MC K^0_S reconstruction correction

No such tables as the ones built for long tracks do exist as far as K^0_S tracking is concerned. An efficiency mapping is desirable and an ongoing work is envisaging its measurement. For the time being, the Long-Long K^0_S are reweighted with the former tracking tables and no action so far is taken for a systematics estimate for Down-Down.

5.3.2.3 Data/MC `L0Hadron_TOS` trigger efficiency correction

A correction is also applied to the selection efficiency due to differences between the `L0Hadron_TOS` trigger efficiency in data and MC. Note that corrections are applied to both those MC candidates passing the `L0Hadron_TOS` trigger and those failing it. Due to the limited available MC statistics, we evaluate a single correction using the combination of the 2011, 2012a and 2012b samples. By doing so, we assume that the data/MC differences are the same for all running periods, which does not imply that the absolute trigger efficiency itself is invariant with time.

The standard method to obtain the `L0Hadron` efficiency [89] returns the absolute efficiency for data, rather than a data/MC correction. Since we need the latter, the trigger efficiency for MC events is determined in order to derive the correction. The data efficiency is obtained from calibration data samples for each track based on the type of particle, the magnet polarity, the part of the calorimeter that the track hits and the transverse energy deposited.

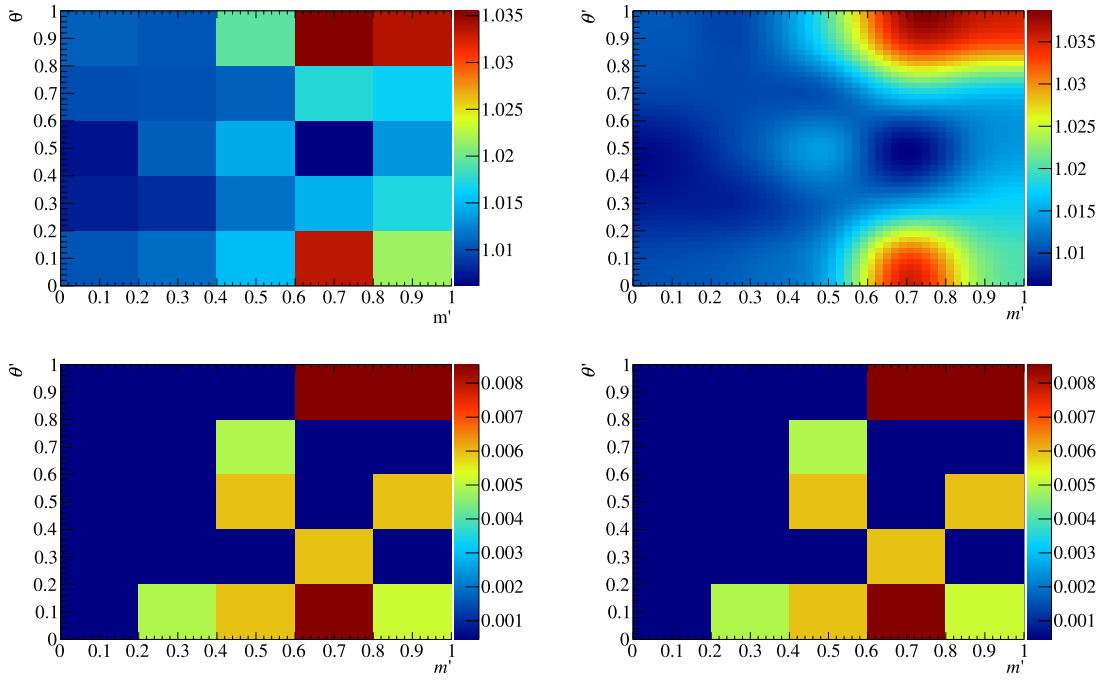

Figure 5.10: *(Top) Combined tracking efficiency corrections in the $K^0_S\pi^+\pi^-$ final state for DD and 2011 configuration: (left) the raw histogram obtained from MC simulation and (right) smoothed using a 2D cubic spline. (Bottom) the (left) upper and (right) lower uncertainties on the histogram bins.*

This is obtained independently for each of the four tracks in each B candidate in the MC `L0Global_TIS` sample.

The efficiency for the B candidate is calculated as the probability that at least one of the four tracks passes the `L0Hadron_TOS` trigger. The average efficiency in each bin of the SDP is then obtained, giving the SDP distribution of the `L0Hadron_TOS` efficiency for data. The corresponding distribution for MC is simply obtained from the ratio of the distribution of events passing `L0Global_TIS&&L0Hadron_TOS` to that for `L0Global_TIS` alone. Finally, the data/MC correction histogram is obtained by dividing the data and MC efficiencies.

In addition, we also correct for the data/MC `L0Hadron_TOS` trigger efficiency difference in the `L0Global_TIS&&!L0Hadron_TOS` category. The data efficiency is calculated as the probability that none of the tracks pass the `L0Hadron_TOS` trigger and the MC distribution is obtained from the ratio of `L0Global_TIS&&!L0Hadron_TOS` to `L0Global_TIS`. The correction histogram is again obtained by dividing the data and MC efficiencies.

The calculated corrections are shown in Figs. 5.11 and 5.12 for the `L0Hadron_TOS` and `L0Global_TIS&&!L0Hadron_TOS` categories for the $K^0_S\pi^+\pi^-$ DD final state. Those for the other final states are gathered in [87]. Significant variations are observed across the phase space, indicating the importance of applying this correction.

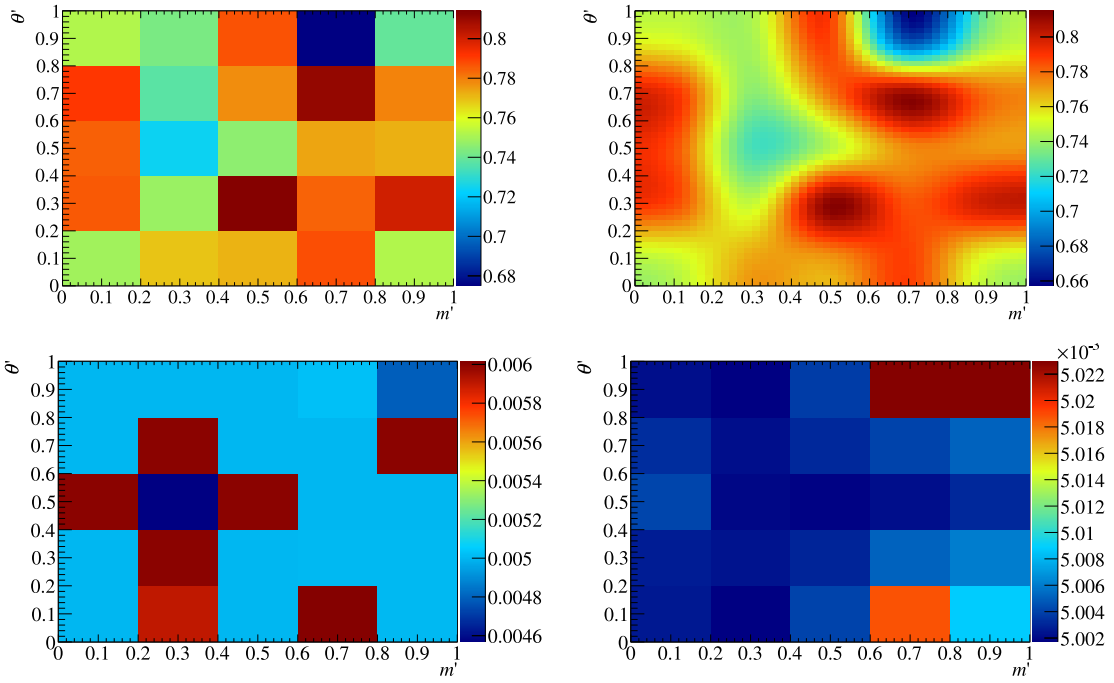

Figure 5.11: *(Top)* $\epsilon^{\text{L0TOS|sel\&geom}}_{\text{data}}/\epsilon^{\text{L0TOS|sel\&geom}}_{\text{MC}}$ *across the* $B^0 \to K^0_S\pi^+\pi^-$ *DD square Dalitz plot (2011+2012 combined): (left) the raw histogram obtained using the procedure described in the text and (right) smoothed using a 2D cubic spline. (Bottom) the (left) upper and (right) lower uncertainties on the histogram bins.*

5.3.2.4 Total selection efficiency

The tracking and `L0Hadron_TOS` corrections, smoothed using 2D cubic splines as described above, are multiplied by the spline-smoothed selection efficiency to give the total efficiency used in the DP fit. Since the two `L0Hadron_TOS` corrections are appropriate only for the part of the signal that is triggered in the corresponding way, we separate MC events into `L0Hadron_TOS` and `L0Global_TIS&&!L0Hadron_TOS`, and obtain efficiency histograms for both. We then apply the appropriate `L0Hadron_TOS` correction to each. The total (selection) efficiency is then defined as $\epsilon_{\texttt{TOS||TIS}} = \epsilon_{\texttt{TOS}} + \epsilon_{\texttt{TIS\&\&!TOS}}$, *i.e.*it is the sum (not the average) of the two efficiencies. Therefore, we combine the efficiencies taking into account the relative amounts of `L0Hadron_TOS` and `L0Global_TIS&&!L0Hadron_TOS` in data, as

$$\epsilon_{\texttt{TOS||TIS}} = \frac{f^{\text{data}}_{\texttt{TOS}}}{f^{\text{MC}}_{\texttt{TOS}}}\epsilon_{\texttt{TOS}} + \frac{f^{\text{data}}_{\texttt{TIS\&\&!TOS}}}{f^{\text{MC}}_{\texttt{TIS\&\&!TOS}}}\epsilon_{\texttt{TIS\&\&!TOS}}\,, \tag{5.9}$$

where the f terms are the fractions of each category in data and MC, as labelled ($f^{\text{data}}_{\texttt{TOS}} + f^{\text{data}}_{\texttt{TIS\&\&!TOS}} = f^{\text{MC}}_{\texttt{TOS}} + f^{\text{MC}}_{\texttt{TIS\&\&!TOS}} = 1$).

The uncorrected selection efficiency histograms for $B^0 \to K^0_S\pi^+\pi^-$ DD 2011 decays and the asymmetric uncertainty on each bin are shown in Figs. 5.13 and 5.14, for `L0Hadron_TOS` and `L0Global_TIS&&!L0Hadron_TOS` candidates, respectively. Uncertainties on the selection efficiency are due to MC statistics and are evaluated using the Clopper-Pearson method as implemented in the `TEfficiency` class. The correction histograms include uncertainties due

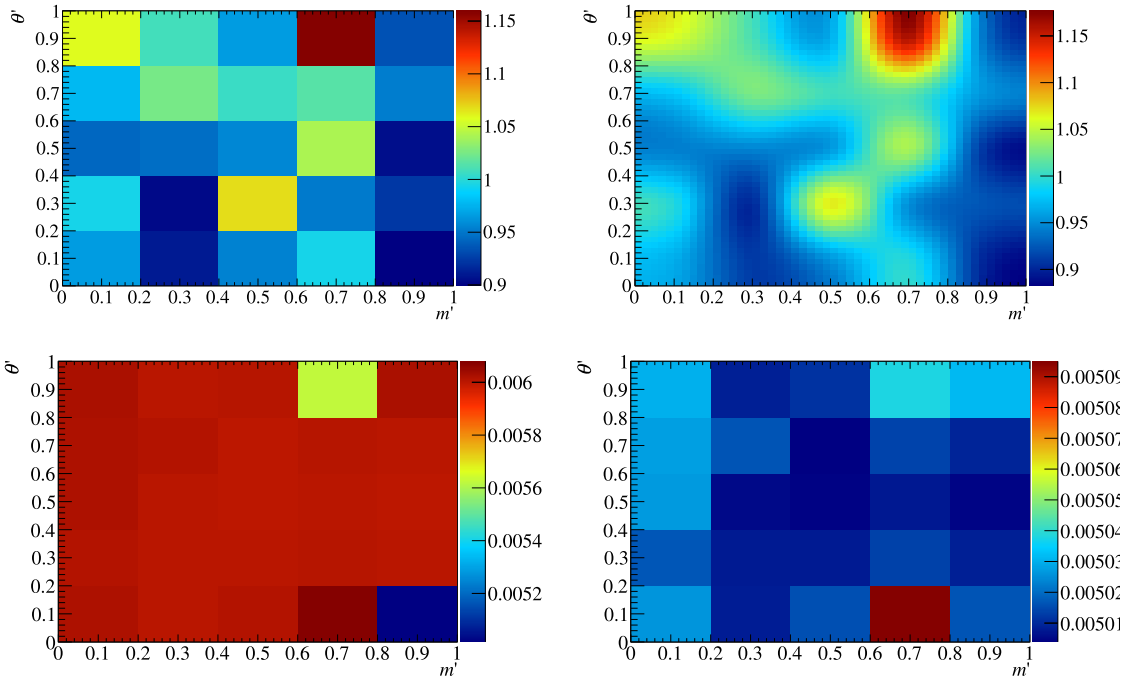

Figure 5.12: *(Top)* $\epsilon^{\text{!L0TOS|sel\&geom}}_{\text{data}}/\epsilon^{\text{!L0TOS|sel\&geom}}_{\text{MC}}$ *across the* $B^0 \to K^0_S\pi^+\pi^-$ *DD square Dalitz plot (2011+2012 combined): (left) the raw histogram obtained using the procedure described in the text and (right) smoothed using a 2D cubic spline. (Bottom) the (left) upper and (right) lower uncertainties on the histogram bins.*

to MC statistics and uncertainties due to the calibration samples and procedures. These contributions are combined in quadrature to produce the total uncertainties in this section. A detailed account of the uncertainty calculations is given in [87].

5.3.3 PID efficiency

The PID efficiency, $\epsilon^{\text{PID|sel\&geom}}$, is determined from calibration data, reweighted to the signal kinematics (from MC), using the `PIDCalib` tool. The evaluation of the calibration sample efficiency was performed separately for positive and negative tracks and was also split by magnet polarity. We then use the `PIDCalib` multibody tools with the signal MC samples as the reference for the kinematics (specifically p and η of the bachelor tracks) sampled from the $B^0 \to K^0_S\pi^+\pi^-$ data. For each signal MC event, the PID efficiency was evaluated by using the appropriate efficiency maps to find the PID efficiency of each bachelor track. The total PID efficiency for a single event is then defined as the product of the two bachelor track efficiencies. This method correctly accounts for the correlation between the kinematics of the two bachelor tracks (expressed in terms of p and η). The results for the $B^0 \to K^0_S\pi^+\pi^-$ DD final state for 2011 conditions are shown in Fig. 5.15, where uncertainties arise due to the statistics of both the calibration and reference samples. These contributions are combined in quadrature to produce the total uncertainties in this section.

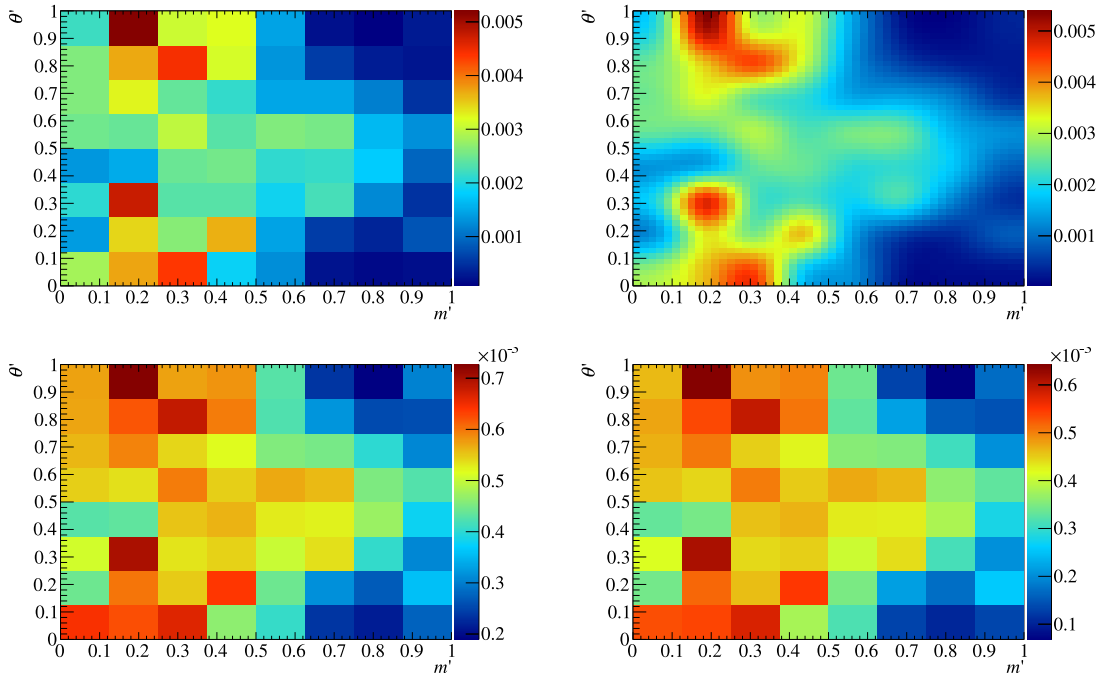

Figure 5.13: *(Top)* $\epsilon^{\text{sel|geom}}$ *across the* $B^0 \to K^0_S\pi^+\pi^-$ *Down-Down 2011 square Dalitz plot for* `L0Hadron_TOS` *candidates: (left) the raw histogram obtained using the procedure described in the text and (right) smoothed using a 2D cubic spline. (Bottom) the (left) upper and (right) lower uncertainties on the histogram bins.*

5.3.4 Total efficiency

The total efficiency is the product of the individual components shown in Eq. (5.8). The relevant spline-smoothed histograms are therefore multiplied together, and the outcome ϵ^{tot} for each running period and K^0_S category is shown in Figs. 5.16 and 5.17.

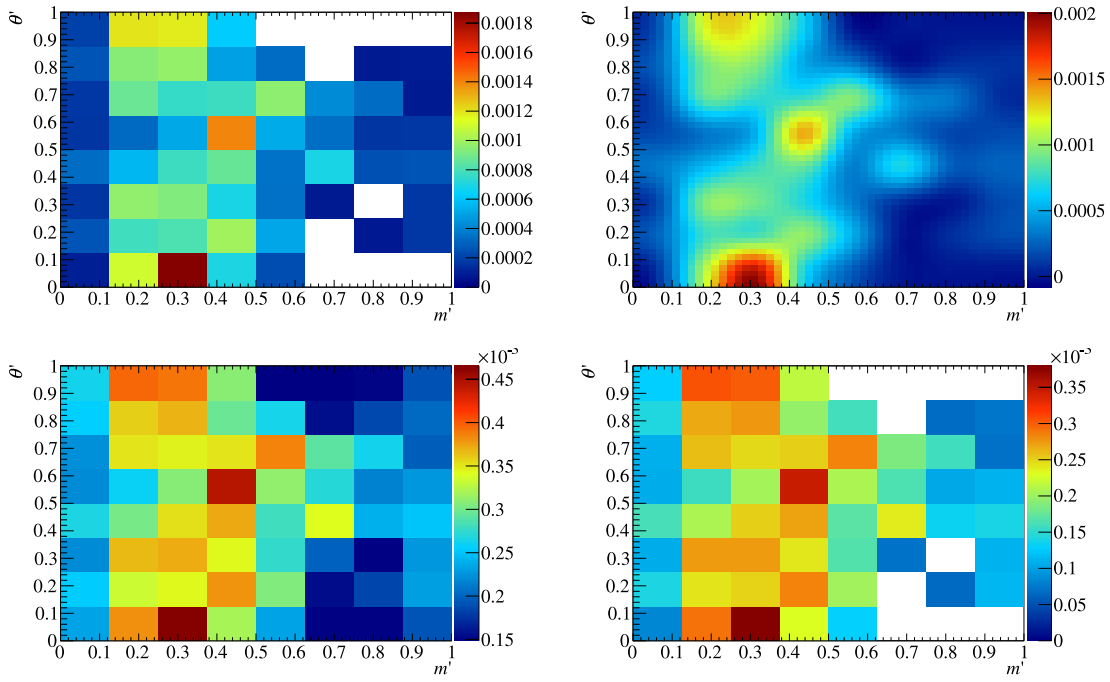

Figure 5.14: *(Top)* $\epsilon^{\text{sel|geom}}$ *across the* $B^0 \to K^0_S\pi^+\pi^-$ *Down-Down 2011 square Dalitz plot for* `LOGlobal_TIS&&!L0Hadron_TOS` *candidates: (left) the raw histogram obtained using the procedure described in the text and (right) smoothed using a 2D cubic spline. (Bottom) the (left) upper and (right) lower uncertainties on the histogram bins.*

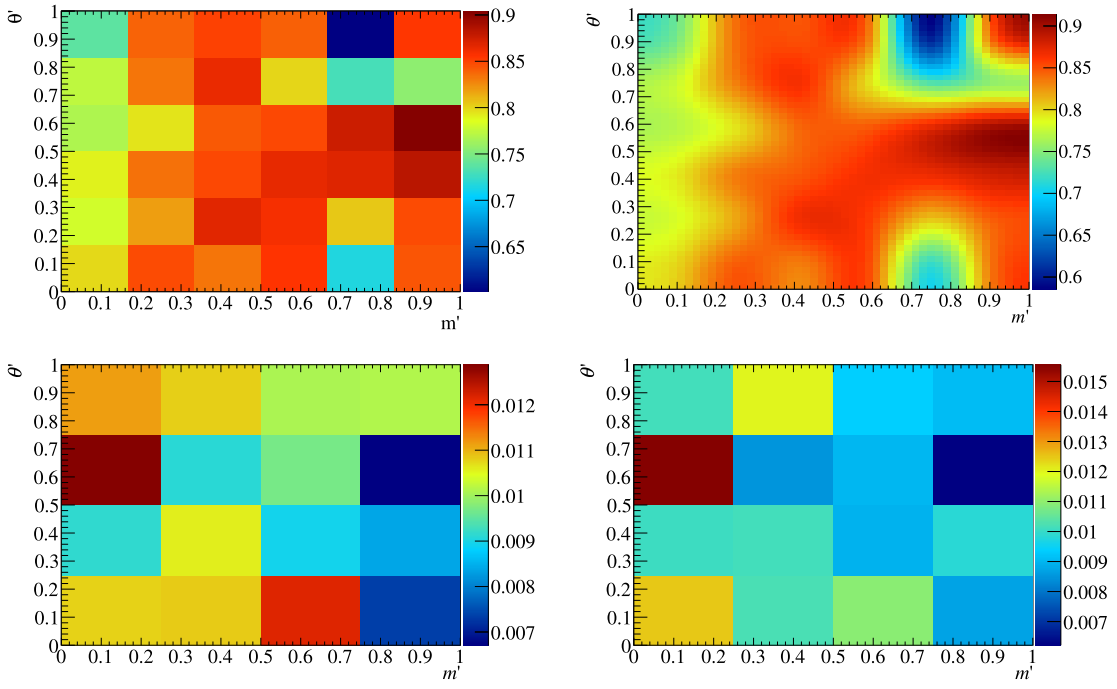

Figure 5.15: *(Top)* $\epsilon^{\text{PID|sel\&geom}}$ *across the* $B^0 \to K^0_S\pi^+\pi^-$ *Down-Down 2011 square Dalitz plot: (left) the raw histogram obtained using the* `PIDCalib` *procedure described in the text and (right) smoothed using a 2D cubic spline. (Bottom) the (left) upper and (right) lower uncertainties on the histogram bins.*

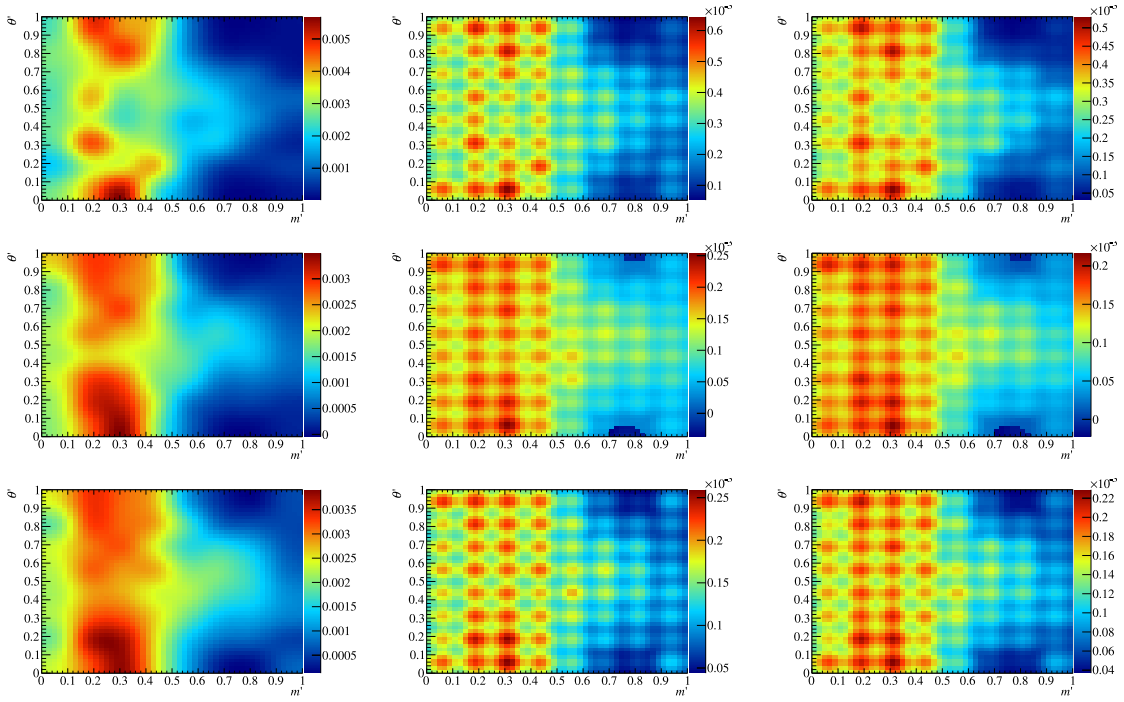

Figure 5.16: The plots on the left represent total efficiency histograms from Down-Down signal MC, smoothed by the 2D cubic spline techniques separated in 2011 (top), 2012a (centre) and 2012b (bottom) samples, the plots on the middle (right) represents the high (low) uncertainties on each efficiency spline bin, organized in the same year order as the efficiency maps.

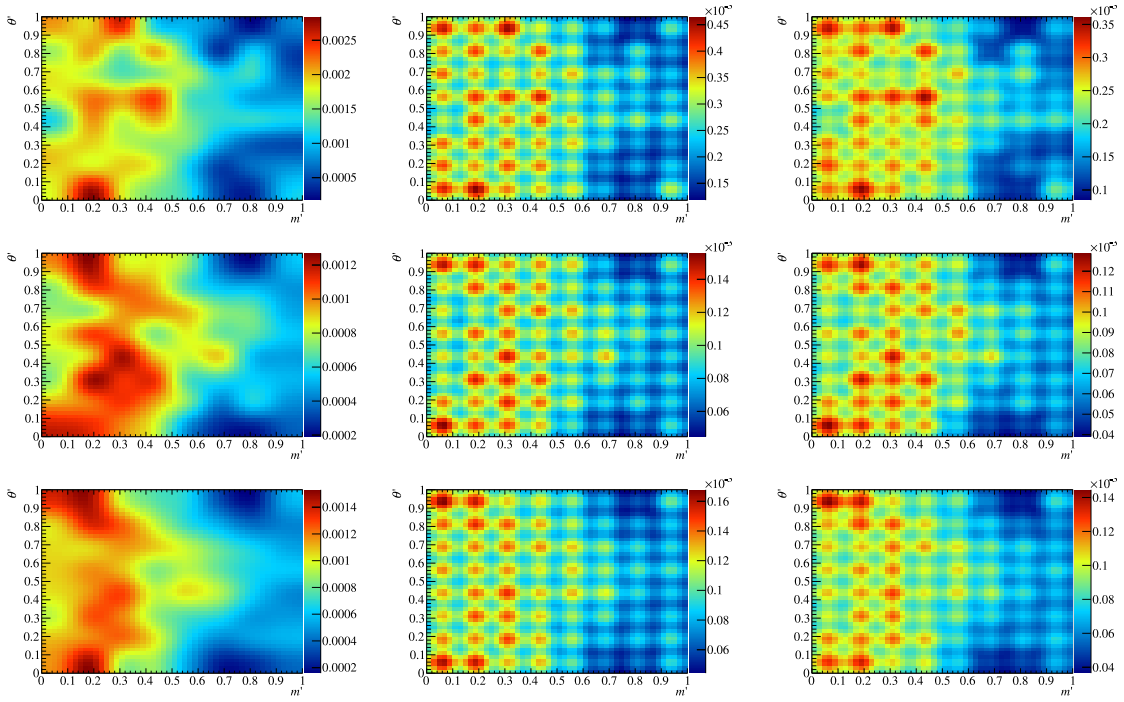

Figure 5.17: The plots on the left represent total efficiency histograms from Long-Long signal MC, smoothed by the 2D cubic spline techniques separated in 2011 (top), 2012a (centre) and 2012b (bottom) samples, the plots on the middle (right) represents the high (low) uncertainties on each efficiency spline bin, organized in the same year order as the efficiency maps.

5.4 Multiple solutions

It is mandatory, given the complexity of the Dalitz Plot fits, to search for the appearance of multiple solutions. They might occur in particular in case of a significant overlapping between two broad resonances with the same spin (it is noticeable for scalar components) in presence of low statistics. The data can be similarly described by close scenarii of interplay between the amplitudes and the interference patterns. An obvious candidate for this analysis is the large overlap between $K_0^*(1430)$ and the flat phase-space non-resonant.

To ensure the discovery of the global minimum, each fit is ran 100 times, starting with a randomized set of initial parameters. The solution with the smallest negative log-likelihood (nll) will be taken as the default result but all the solutions found in a range of 9 units of 2Δnll (3 standard deviation) from the default solution, will be *a priori* also reported. The frequency of the best solution will be an invaluable estimator of the soundness of the fit.

The appearance of multiple solutions is illustrated by a toy MC study performed with the generation of the same number of events as present in the data sample. The study considers at first a simple model which contains only three resonances with modest overlap between them. The 100 fits with randomized initial parameters show a unique solution in the predefined range of three standard deviation from the best solution, as illustrated in Fig. 5.18. The model is then enhanced to an increasing number of resonances in three additional tests, with broad resonances as well as non-resonant contributions. The number of multiple solutions increases accordingly to the complexity of the model. It is worth to notice however that the best solution is still the most frequent for a model equivalent to our nominal DP model.

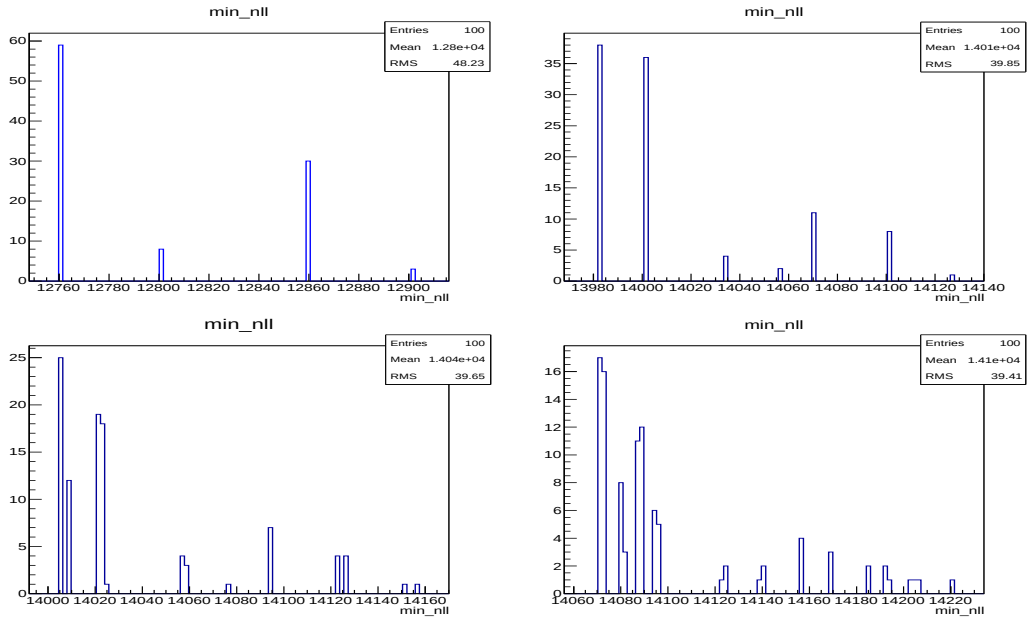

Figure 5.18: Distribution of the minimum nll from a fit to a toy-experiment using the same generator model. The plot on the top left represents minimum nll distribution using a simple model composed by $K^*(892)$, $K^*(1430)$ and $f_0(980)$. The plot on the top right represents minimum nll distribution using the first model plus a non-resonant component flat in phase-space. The plot on the bottom left represents minimum nll distribution using the second model plus $\rho(770)$. The plot on the bottom right represents minimum nll distribution using the third model plus $f_0(500)$ and $f_0(1500)$.

5.5 Dalitz Plot Fit

The Dalitz-plot technique used to perform the amplitude analysis of any three-body decays requires advanced numerical tools to perform the fit of two-dimensional p.d.f. to the data in order to determine the relevant Physics parameter measurements. The Dalitz-plot fitting software that is used for the $B^0 \to K^0_S\pi^+\pi^-$ amplitude analysis is homemade and named CRAFT (Clermont Root-based Amplitude Fitter Tool). CRAFT is a maximum likelihood fitting software, written in C++ and depending on the ROOT package and the minuit software. It contains a large amount of resonance line-shapes modelling (obviously the ones required for the $B^0 \to K^0_S\pi^+\pi^-$ analysis) and allows to perform fits of isobar model parameters in versatile parameterisations of their coefficients. Efficiencies of the data selection can be unfolded either by means of analytical functions or histogram parameterisations. Eventually, the package provides the possibility of performing a DP analysis by making use of a simultaneous fitting to several data spectra.

5.5.1 Baseline model and additional resonances

The first exploration of the data is performed using a preliminary DP model, which will be referred to as baseline model. The fit quality is addressed by a p-value formed from the dissimilarity test defined in Appendix F. The baseline model is educated from the results of BaBar [14] and Belle [90] analyses. The data distribution in the DP from the previous

analysis of BaBar and Belle shows four dominant amplitude contributions:

- $B^0 \to K^{*+}(892)(\to K^0_S\pi^+)\pi^-$,
- $B^0 \to (K\pi)^{*+}_0(\to K^0_S\pi^+)\pi^-$,
- $B^0 \to \rho^0(770)(\to \pi^+\pi^-)K^0_S$,
- $B^0 \to f_0(980)(\to \pi^+\pi^-)K^0_S$.

The lineshapes of the intermediate strongly interacting resonances are modelled with a Relativistic Breit-Wigner (RBW) for the $K^{*+}(892)$, a LASS lineshape corresponding to the $K\pi$ S-wave contribution $(K\pi)^{*+}_0$ which includes the resonant component $K^*_0(1430)$, a Gounaris-Sakurai lineshape for the $\rho^0(770)$ and eventually a Flatté parameterisation for the scalar $f_0(980)$.

In addition to these dominant four components, the B-factories data favour the existence of a non-resonant (NR) contribution filling isotropically the phase space. Fig. 5.19 shows, for the different categories of data in the center of the Dalitz plane, the presence of flat distribution of events, where no resonance is expected in this region of phase-space, which proves the existence of a non-resonant component. In BaBar approach, the NR is modelled by a flat distribution in the Dalitz plot. Instead, the Belle experiment makes use of an empirical parameterisation, built from two independent exponential functions of the DP mass variables s_+ and s_-. In this analysis, the NR flat in the phase space of the decay is chosen as a further but last component of the baseline model.

The flavour specific amplitudes $B^0 \to K^{*+}(892)(\to K^0_S\pi^+)\pi^-$ and $B^0 \to (K\pi)^{*+}_0(\to K^0_S\pi^+)\pi^-$ have an implicit conjugate counterpart. Initial studies conducted with pseudo-experiments showed that the interference pattern of $B^0 \to f_0(980)(\to \pi^+\pi^-)K^0_S$ with the flavour specific decays makes possible to distinguish and measure the $B^0 \to f_0(980)K^0_S$ and $\bar{B}^0 \to f_0(980)K^0_S$ amplitudes. Both are then considered in the baseline model. On the contrary, the same initial study with pseudo-experiments concluded that no sensitivity to separate the $B^0 \to \rho^0(770)(\to \pi^+\pi^-)K^0_S$ amplitude form its conjugate nor the NR and conjugated NR amplitudes. Following the results from the B-factories which are not indicating any CP violation for these amplitudes (*e.g.* $\mathcal{A}_{cp}(\mathrm{NR}) = -0.01 \pm 0.26$), a unique amplitude is shared for each of these decays.

A summary of the baseline model is reported in the Table 5.1.

Additional decay amplitude components must be tested one by one. Few comments are made first in order based on the existing data for the decay $B^0 \to K^0_S\pi^+\pi^-$.

- A specific comment is in order regarding the mass range $m_{\pi\pi} \sim 0.280$ - $0.700\,\mathrm{GeV}$, where the Belle experiment reports a signal excess which is modelled by a third exponential function of s_0. We have chosen to not include this component. Instead, a S-wave is introduced as an additional contribution but will be examined on the same footing as the marginal components of the model. It is modelled by means of a reduced K-matrix, described in Section 2.4.5, where the $f_0(500)$, with mass and width fixed to the values measured by CLEO experiment [92] .

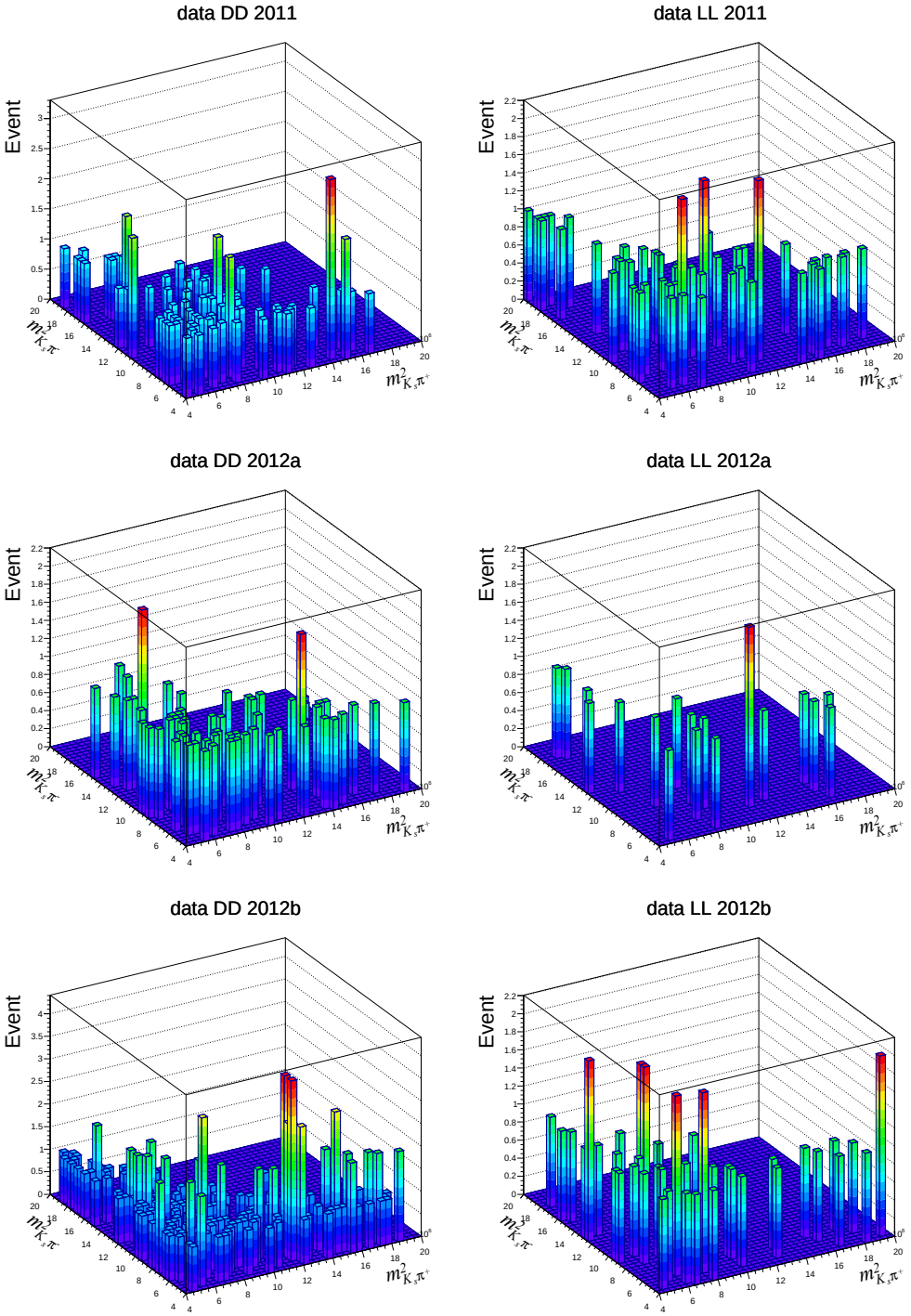

Figure 5.19: *Data in the center of the Dalitz plane* ($m^2_{K^0_S\pi^\pm}, m^2_{\pi^+\pi^-} > 3.5\ \mathrm{GeV}^2/\mathrm{c}^4$). *Plots on the left (right) side show the fit results to samples with* K^0_S *Down-Down (Long-Long) category. Plots in a row display the functions fitted to 2011, 2012a and 2012b running period samples, respectively.*

Table 5.1: *List of the five amplitude contributions used in the baseline model. The line-shape parameter values are given in* MeV*, unless mentioned otherwise.*

Resonance	Parameters	Lineshape	Value references
$K^{*\pm}(892)$	$m_0 = 891.66 \pm 0.26$ $\Gamma_0 = 50.8 \pm 0.9$	RBW	[20]
$(K\pi)_0^{*\pm}$	$m_0 = 1415 \pm 3$ $\Gamma_0 = 300 \pm 6$ $m_{K_S\pi}^{\text{cutoff}} = 1800$ $a = 2.07 \pm 0.10(\text{ GeV}/c)^{-1}$ $r = 3.32 \pm 0.34(\text{ GeV}/c)^{-1}$	LASS	[45]
$f_0(980)$	$m_0 = 965 \pm 10$ $g_\pi = 165 \pm 18$ $g_K = 695 \pm 93$	Flatté	[91]
$\rho^0(770)$	$m_0 = 775.26 \pm 0.25$ $\Gamma_0 = 149.8 \pm 0.8$	GS	[20]
NR		Flat	

- Both BaBar and Belle time-dependent analysis of $B^0 \to K^0_S\pi^+\pi^-$ [14,90] report a signal excess in the $m_{\pi\pi} \sim 1.2$ - $1.5\,\text{GeV}$ range. This signal is taken into account using a two-component model, the tensor resonance $f_2(1270)$, plus the scalar resonance $f_0(1500)$ (denoted $f_X(1300)$). Given the poor knowledge on this object, it is not considered in the baseline model. On the contrary, the better defined $f_2(1270)$ and $f_0(1500)$ will be tested as additional resonances to the baseline model.

- No hint of the decay amplitude $B^0 \to K_2^{*+}(1430)(\to K^0_S\pi^+)\pi^-$ was reported so far. However, we will test this component as additional resonances to the baseline model.

- Finally, there is a decay amplitude involving a strongly interacting charmonium resonance that might interfere with the above-mentioned charmless amplitude, χ_{c0}. It will be tested as well as an additional resonance to the baseline model.

We defined two categories of additional decay amplitudes, which are involving: the well-defined resonances on one hand and the amplitudes involving poorly-defined resonances. These additional resonances are:

- well-defined resonances in [93]: $K_2^*(1430)$, $f_2(1270)$, $f_0(1500)$, χ_{c0}.

- poorly-defined resonances in [93]: $K(800)$, $K^*(1410)$, $K^*(1680)$, $K_3^*(1780)$, $f_0(500)$, $f_0(1370)$, $\rho(1450)$.

The former amplitudes will be tested to be included in the nominal fit model. The latter will be considered solely for the determination of the systematic uncertainties related to the DP model definition.

5.5.2 Towards the nominal DP model

The simultaneous fit to all data categories using the baseline model gave a satisfactory result according to the dissimilarity test. As shown in Fig. 5.20 and ?????????? all main contributions of the baseline model are well identified. However, there are still regions of the data spectra not well described by the baseline model, which require in turn additional contributions to be included. In view of educating the nominal model in an objective way, an algorithm has been defined a priori to determine whether a component must be added or not. A resonance is added if one at least of the following requirements is met:

- The dissimilarity g.o.f. of the DP model including the additional contribution increases.
- The likelihood ratio of the two hypotheses -2Δnll (with or without the additional component) decreases by 11.83(16.25) units (corresponds to three standard deviations), in case of 2(4) degrees-of-freedom more.
- The magnitude of the additional contribution is measured far from zero by $3\sigma_a$ (magnitude precision greater than 33.3%), where σ_a is the statistical uncertainty of the amplitude measurement.

Table 5.2 gathers the values of the above-mentioned estimators for impacts and the decisions taken. All components are accepted by the algorithmic decision except $f_2(1270)$. The low $\pi\pi$ invariant mass S-wave is certainly not a well-defined object but was part of the exploratory studies that we have conducted at the beginning of this work. Despite the positive answer of the algorithm, a model systematic will be assigned by removing it.

Table 5.2: *p-values from the dissimilarity test, likelihood ratio significance and precision of the magnitude measurement of the tested additional contributions to the baseline model. The first part of the table concerns the test made for the inclusion of the well-defined resonance. The lower part deals with the low $\pi\pi$ invariant mass S-wave. Only the resonance $f_2(1270)$ is rejected by the algorithm.*

Additional contribution	p-value	-2Δnll	Mag. precision (%)
baseline	0.09	-	-
(baseline) + $K_2^*(1430)$	0.11	42.6	(15.00, 18.12)
(baseline) + $f_2(1270)$	0.07	4.8	52.27
(baseline) + $f_0(1500)$	0.10	107.6	7.77
(baseline) + χ_{c0}	0.13	87.0	8.01
(baseline + χ_{c0}) + $K_2^*(1430)$	0.12	37.2	(19.92, 38.56)
(baseline + χ_{c0}) + $f_0(1500)$	0.11	95.6	9.33
(baseline + χ_{c0} + $f_0(1500)$) + $K_2^*(1430)$	0.16	43.0	(18.65, 37.90)
(baseline + χ_{c0} + $f_0(1500)$ + $K_2^*(1430)$) + $f_0(500)$	0.16	8.8	31.03

The nominal DP model that will be used for the final DP fit is eventually given in Table 5.3.

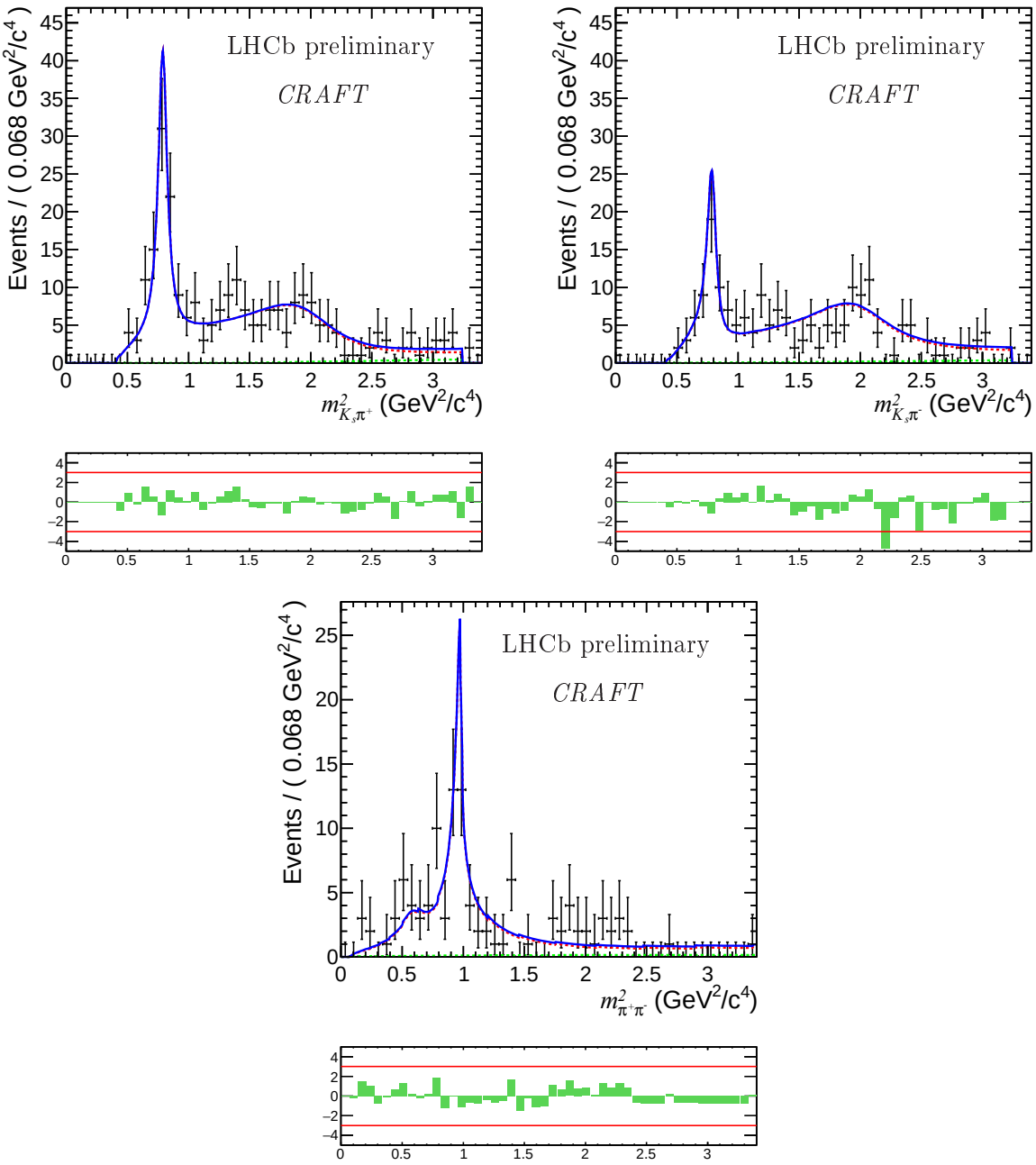

Figure 5.20: *Projections of the 2011 data with Down-Down K^0_S category given in black points, and the baseline fit, with a zoomed view, onto $m^2_{K^0_S\pi^+}$ (left), $m^2_{K^0_S\pi^-}$ (right) and $m^2_{\pi^+\pi^-}$ (bottom). The full fit is shown in blue, combinatorial background in green and signal model in red.*

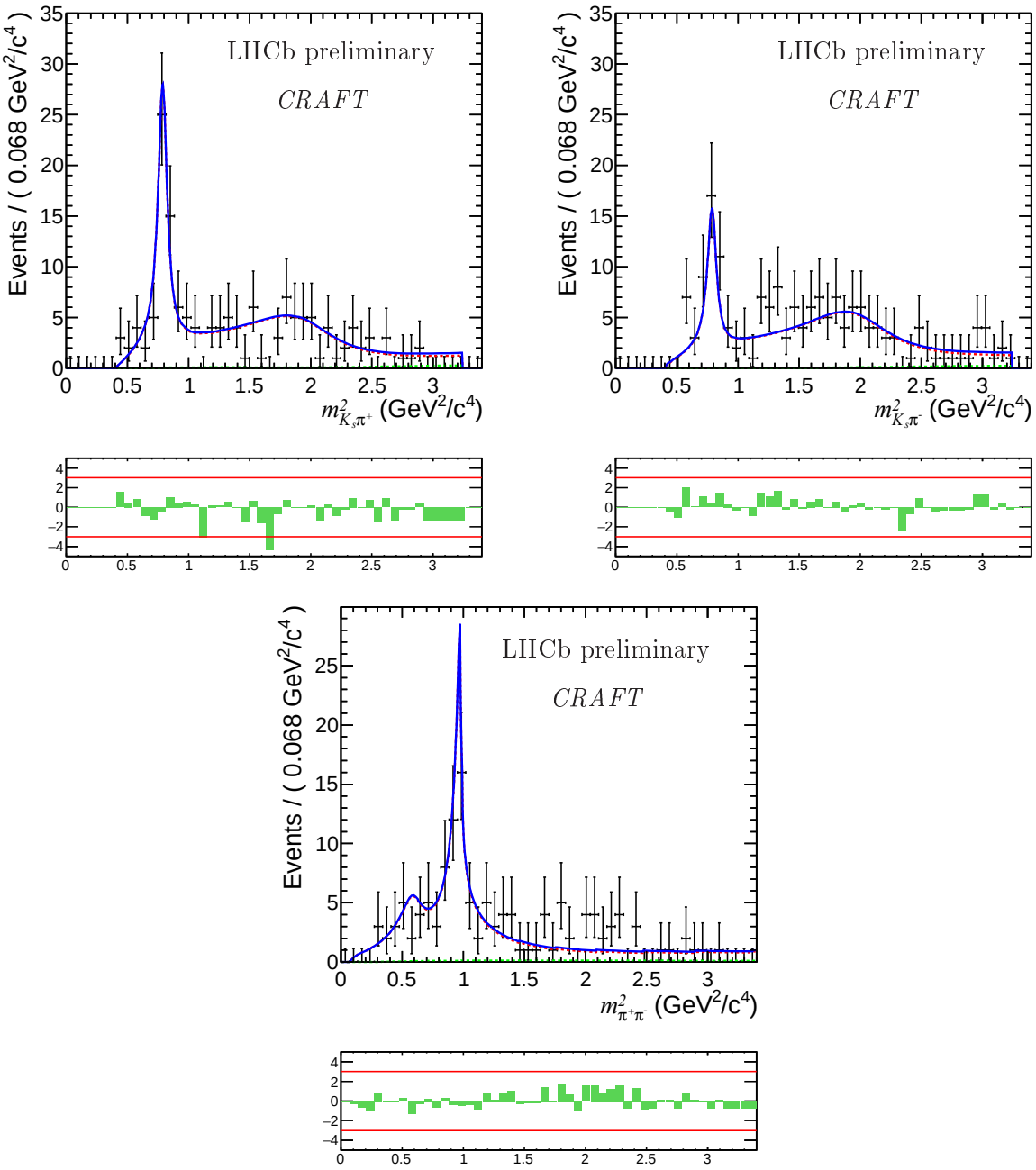

Figure 5.21: *Projections of the 2011 data with Long-Long K^0_S category given in black points, and the baseline fit, with a zoomed view, onto $m^2_{K^0_S\pi^+}$ (left), $m^2_{K^0_S\pi^-}$ (right) and $m^2_{\pi^+\pi^-}$ (bottom). The full fit is shown in blue, combinatorial background in green and signal model in red.*

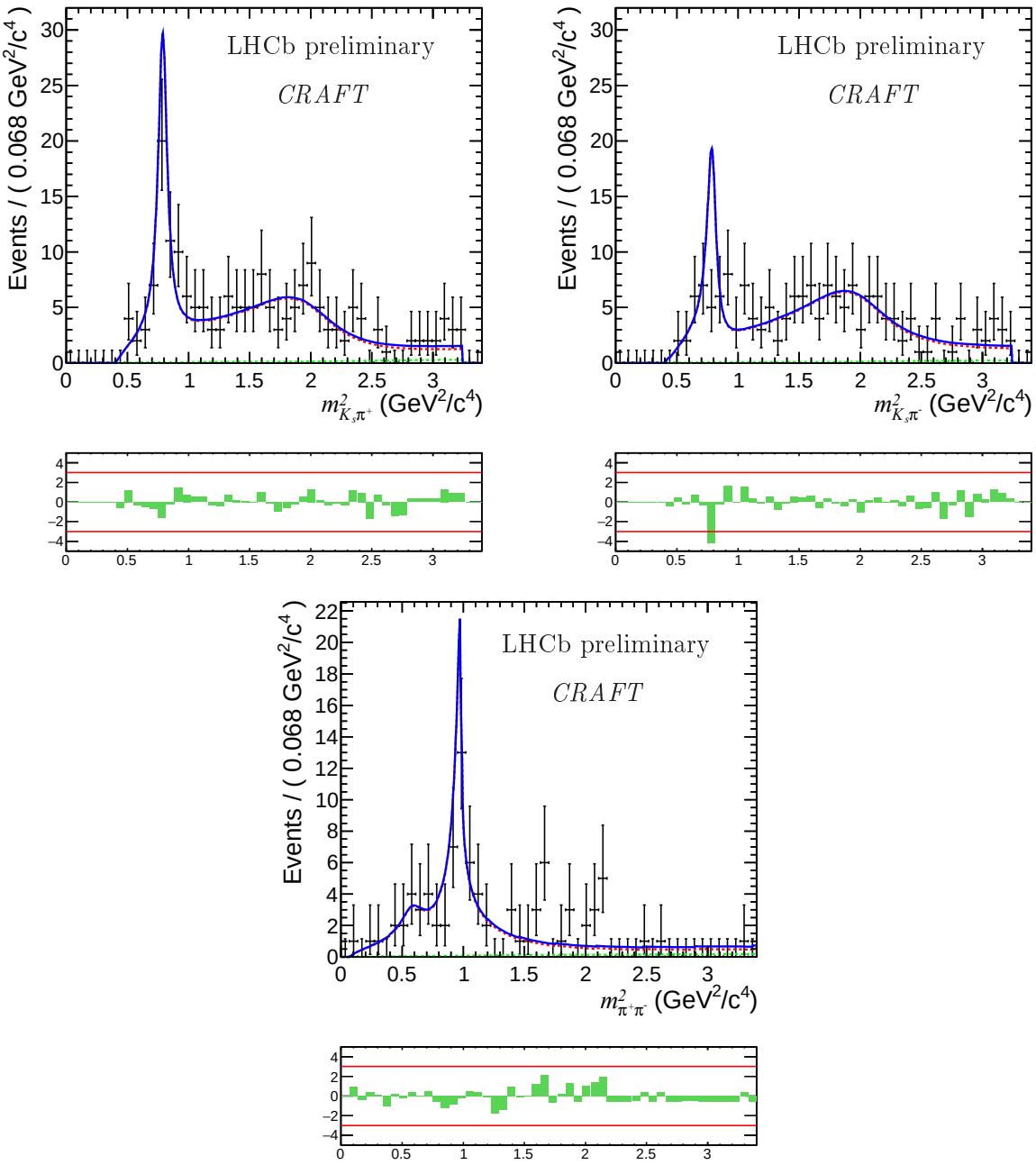

Figure 5.22: *Projections of the 2012a data with Down-Down K^0_S category given in black points, and the baseline fit, with a zoomed view, onto $m^2_{K^0_S\pi^+}$ (left), $m^2_{K^0_S\pi^-}$ (right) and $m^2_{\pi^+\pi^-}$ (bottom). The full fit is shown in blue, combinatorial background in green and signal model in red.*

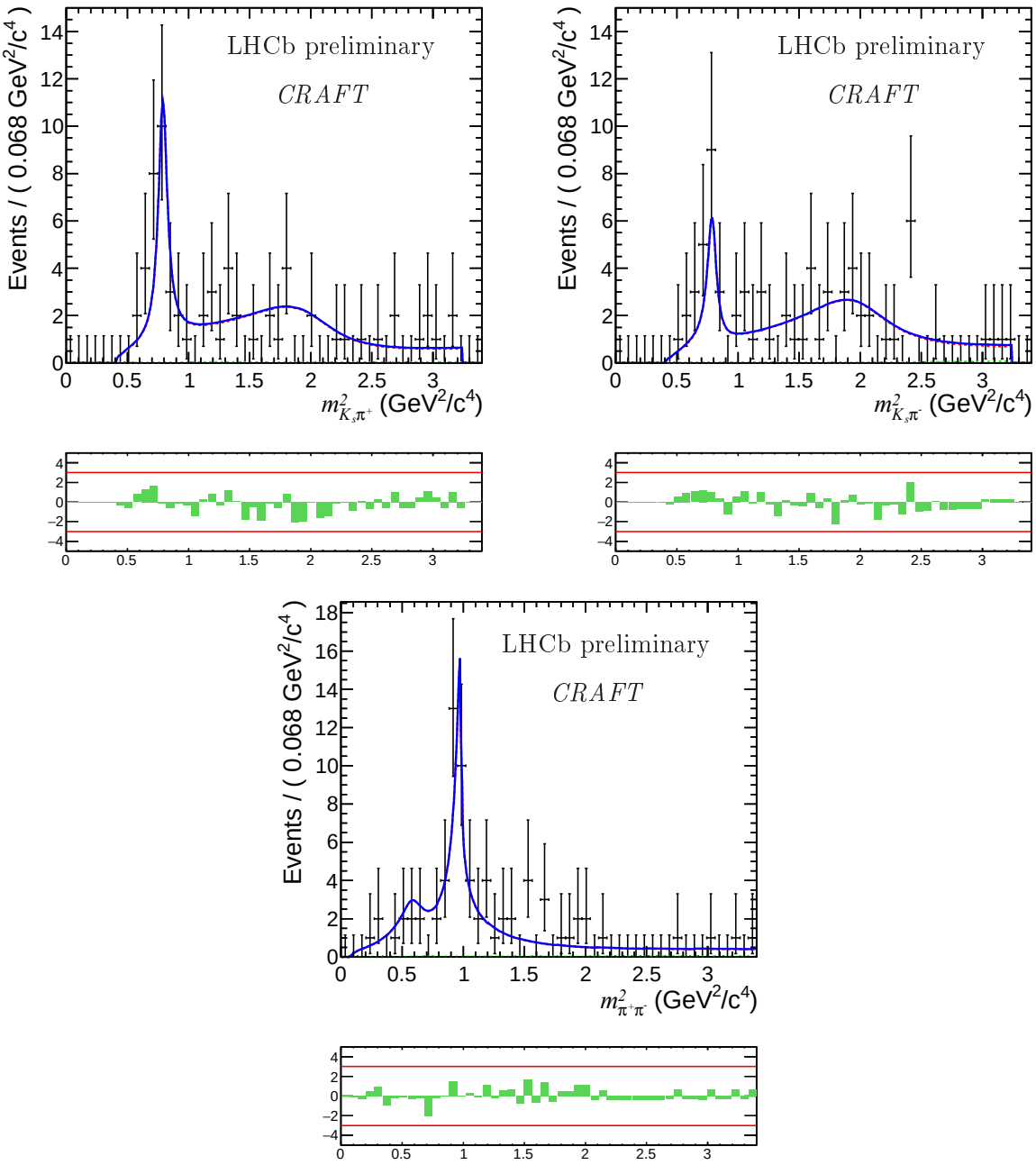

Figure 5.23: *Projections of the 2012a data with Long-Long K^0_S category given in black points, and the baseline fit, with a zoomed view, onto $m^2_{K^0_S\pi^+}$ (left), $m^2_{K^0_S\pi^-}$ (right) and $m^2_{\pi^+\pi^-}$ (bottom). The full fit is shown in blue, combinatorial background in green and signal model in red.*

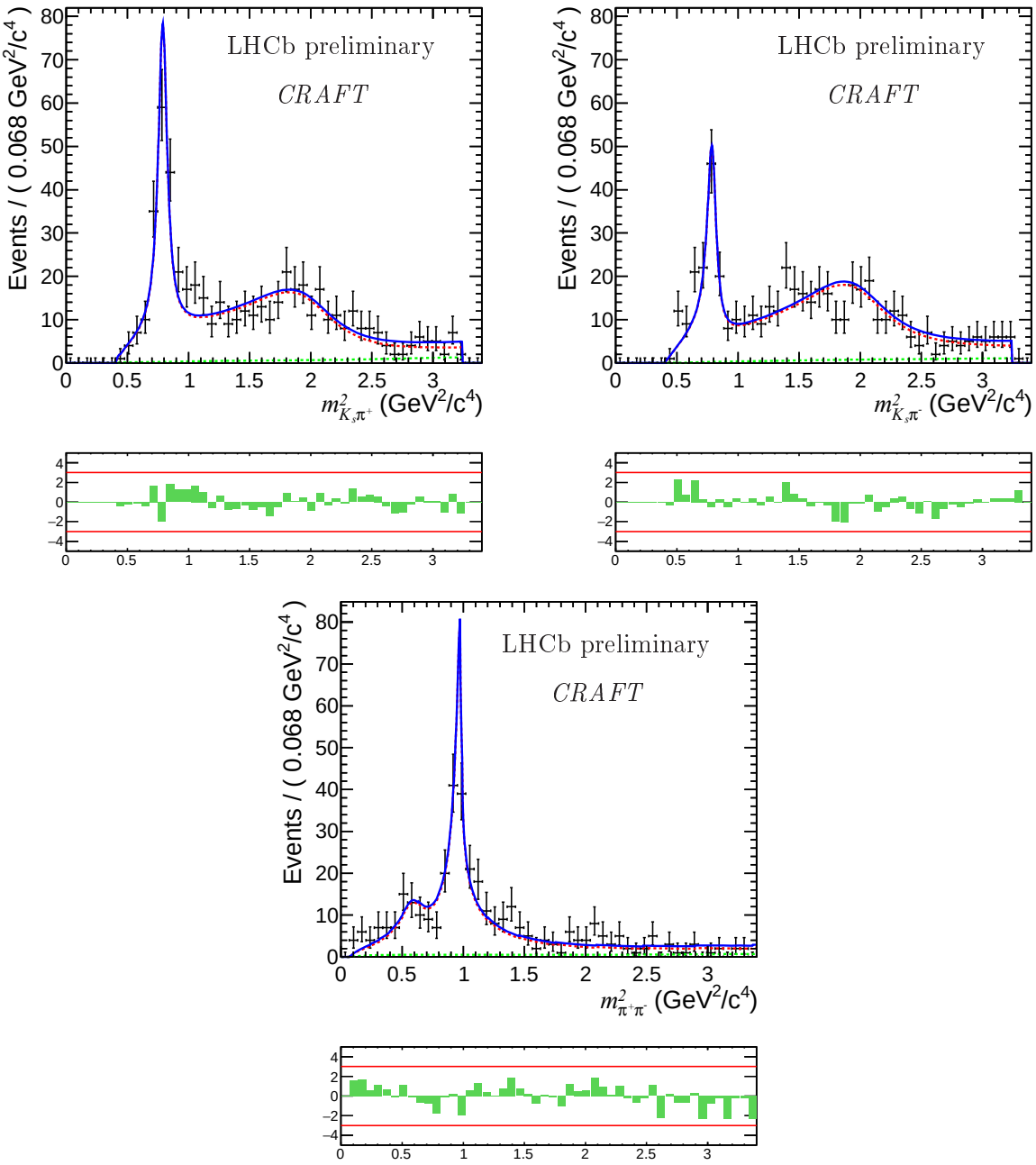

Figure 5.24: *Projections of the 2012b data with Down-Down K^0_S category given in black points, and the baseline fit, with a zoomed view, onto $m^2_{K^0_S\pi^+}$ (left), $m^2_{K^0_S\pi^-}$ (right) and $m^2_{\pi^+\pi^-}$ (bottom). The full fit is shown in blue, combinatorial background in green and signal model in red.*

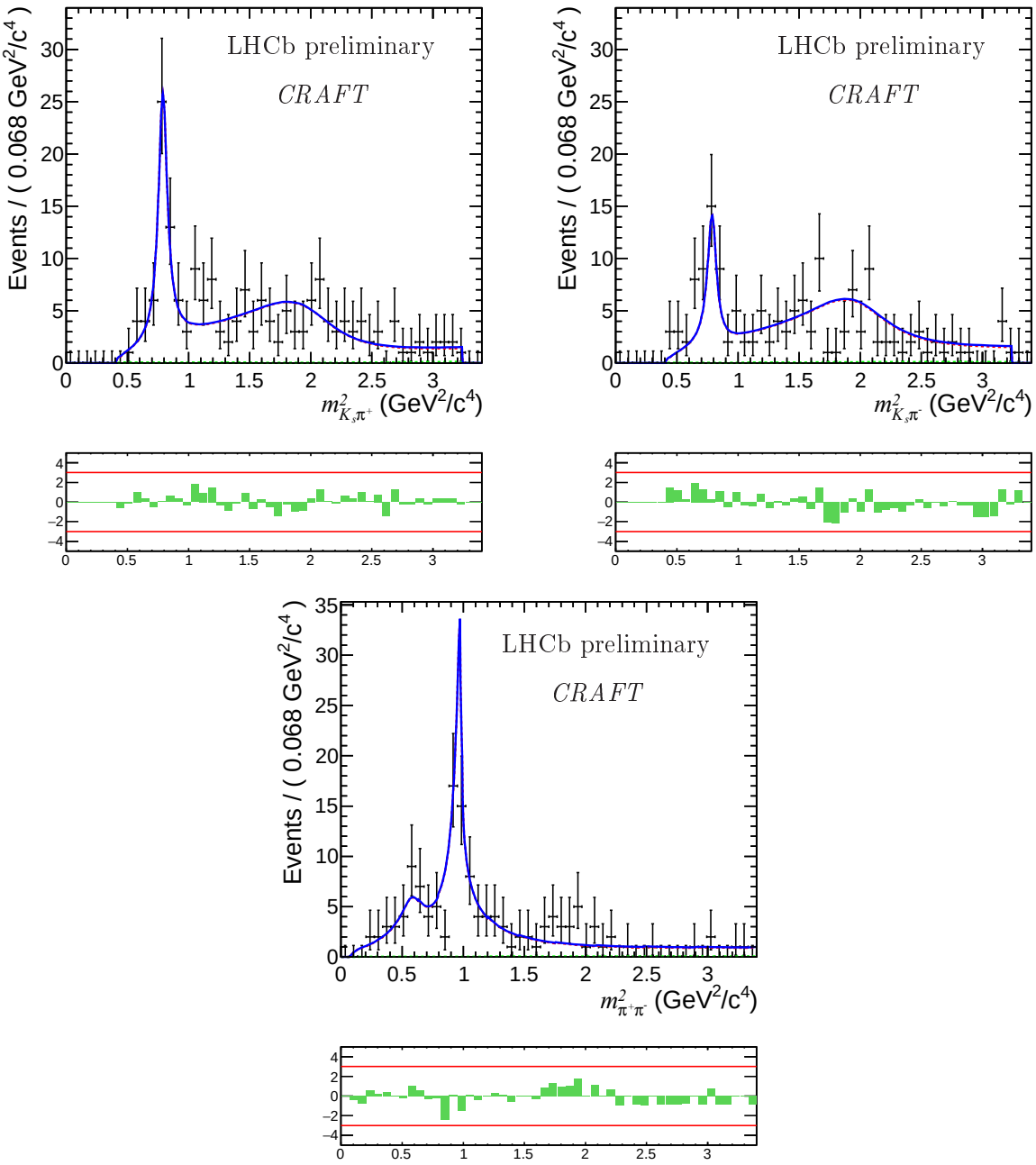

Figure 5.25: *Projections of the 2012b data with Long-Long K^0_S category given in black points, and the baseline fit, with a zoomed view, onto $m^2_{K^0_S\pi^+}$ (left), $m^2_{K^0_S\pi^-}$ (right) and $m^2_{\pi^+\pi^-}$ (bottom). The full fit is shown in blue, combinatorial background in green and signal model in red.*

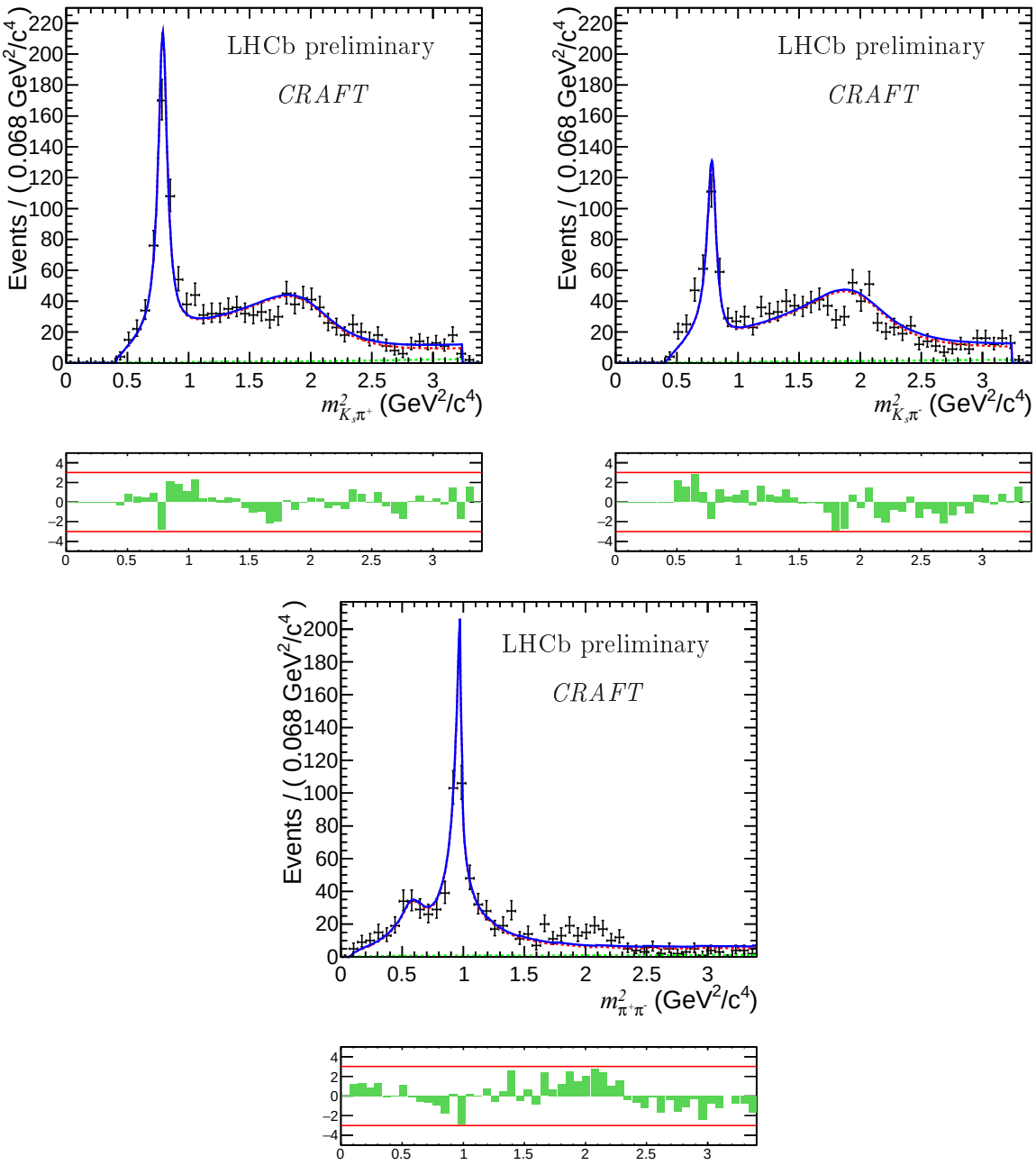

Figure 5.26: *Projections of the sum of all data category (black points), and the baseline fit, with a zoomed view, onto* $m^2_{K^0_S\pi^+}$ *(left),* $m^2_{K^0_S\pi^-}$ *(right) and* $m^2_{\pi^+\pi^-}$ *(bottom). The full fit is shown in blue, combinatorial background in green and signal model in red.*

Table 5.3: *Components of the DP nominal model used in the nominal fit. The line-shape parameter values are given in* MeV*, unless mentioned otherwise.*

Resonance	Parameters	Lineshape	Value references
$K^{*\pm}(892)$	$m_0 = 891.66 \pm 0.26$ $\Gamma_0 = 50.8 \pm 0.9$	RBW	[20]
$(K\pi)_0^{*\pm}$	$m_0 = 1415 \pm 3$ $\Gamma_0 = 300 \pm 6$ $m_{K_S\pi}^{\text{cutoff}} = 1800$ $a = 2.07 \pm 0.10(\text{ GeV}/c)^{-1}$ $r = 3.32 \pm 0.34(\text{ GeV}/c)^{-1}$	LASS	[45]
$K_2^{*\pm}(1430)$	$m_0 = 1425.6 \pm 1.5$ $\Gamma_0 = 98.5 \pm 2.7$	RBW	[20]
$f_0(500)$	$m_0 = 513 \pm 32$ $\Gamma_0 = 335 \pm 67$ $\kappa = 0$	Red. K-Matrix = RBW	[92]
$\rho^0(770)$	$m_0 = 775.26 \pm 0.25$ $\Gamma_0 = 149.8 \pm 0.8$	GS	[20]
$f_0(980)$	$m_0 = 965 \pm 10$ $g_\pi = 165 \pm 18$ $g_K = 695 \pm 93$	Flatté	[91]
$f_0(1500)$	$m_0 = 1505 \pm 6$ $\Gamma_0 = 109 \pm 7$	RBW	[20]
χ_{c0}	$m_0 = 3414.75 \pm 0.31$ $\Gamma_0 = 10.5 \pm 0.6$	RBW	[20]
NR		DP flat	

5.6 Dalitz Plot fit results

The best nll for the simultaneous fit to the data using the nominal model is found to be 28587.95. In the range of $2\Delta\text{nll} < 9$ units, a second solution is found at nll equal to 28590.7. The likelihood ratio hence reads $-2\Delta\text{nll} = 5.4$, which can be interpreted as disfavoured by the data at more than 95 % Confidence Level. We have chosen to report in the main body of this thesis the results for the best solution but provide in Appendix H the complete set of results for this secondary minimum as well as an interpretation of the differences. The p-value of the best fit is estlmated to be 16 %.

The results of the best fit in terms of complex amplitudes are gathered in Table 5.4. The fit fractions and the *CP* asymmetry measurements are given in Table 5.5. The interference fit fraction results are given in Table 5.6. The statistical uncertainties for the Cartesian isobar parameters are obtained directly from the fit output using the likelihood parabolic estimation around the minimum, and propagated to the derived quantities, the magnitudes and *CP* asymmetries, taking into account the covariance matrix of the fit. However, the likelihood profile for the phases and fit fractions do not follow a χ^2 law and hence the statistical uncertainties on these observables must be determined using pseudo-experiments (see Section 5.6.1). The method of uncertainties evaluation is discussed in details in the next section.

Table 5.4: *Fit results for the Cartesian coefficients. Polar coordinates measurements are also provided.*

Resonance	Real part	Imaginary part	Magnitude	phase
$K^{*+}(892)$	2.00	0.00	2.00	0.0
$K^{*-}(892)$	-1.47 ± 0.09	0.00	1.47 ± 0.09	0.0
$(K\pi)_0^{*+}$	1.82 ± 0.16	1.69 ± 0.19	2.48 ± 0.13	$43.0^{+4.2}_{-4.8}$
$(K\pi)_0^{*-}$	2.57 ± 0.12	0.03 ± 0.25	2.57 ± 0.12	-0.2 ± 4.8
$K_2^{*+}(1430)$	0.00 ± 0.11	0.59 ± 0.11	0.59 ± 0.11	$-98.5^{+4.8}_{-6.0}$
$K_2^{*-}(1430)$	0.30 ± 0.09	0.23 ± 0.13	0.38 ± 0.10	$39.3^{+20.4}_{-14.4}$
$f_0(980)$ from B^0	1.25 ± 0.46	1.61 ± 0.45	2.04 ± 0.39	55.6 ± 12.6
$f_0(980)$ from $\overline{B}^0$	1.93 ± 0.36	1.14 ± 0.49	2.25 ± 0.35	26.5 ± 11.2
$\rho^0(770)$	-0.63 ± 0.41	1.14 ± 0.24	1.30 ± 0.13	$-61.2^{+31.0}_{-40.3}$
$f_0(500)$	0.31 ± 0.10	0.10 ± 0.16	0.32 ± 0.11	$16.9^{+31.5}_{-23.1}$
$f_0(1500)$	-0.65 ± 0.32	0.66 ± 0.14	0.92 ± 0.17	$-45.6^{+11.2}_{-9.6}$
χ_{c0}	-0.60 ± 0.09	0.48 ± 0.09	0.77 ± 0.06	-37.9 ± 12.6
NR	1.37 ± 0.33	2.34 ± 0.15	2.72 ± 0.16	59.6 ± 4.8

Projections of the fit results onto the Dalitz variables $m^2_{K^0_S\pi^+}$, $m^2_{K^0_S\pi^-}$ and $m^2_{K^0_S\pi^+}$ for the 2011, 2012a and 2012b data samples are shown in Figs. 5.34 to 5.39, respectively. It is worth to scrutinize the Phase Space regions of the decay where most of the Q2-body processes are occurring. They are displayed in ?????? with linear y-axis and ?????? with a logarithmic y-axis. Fig. 5.42 shows the helicity angle distribution of the $K^0S\pi^\pm$ and $\pi\pi$ systems in several 2-body invariant mass regions containing the main resonances in the nominal model.

Table 5.5: *Fit results interpreted as fit fractions and, when relevant, CP asymmetries.*

Resonance	Fit fraction (%)	Direct *CP* asymm.
$K^*(892)$	$11.7^{+0.5}_{-0.4}$	-0.296 ± 0.053
$(K\pi)^*_0$	$24.4^{+1.0}_{-0.9}$	0.034 ± 0.049
$K^*_2(1430)$	$0.92^{+0.04}_{-0.03}$	-0.41 ± 0.27
$f_0(980)$	$17.6^{+0.8}_{-0.6}$	0.09 ± 0.32
$\rho^0(770)$	$6.4^{+1.6}_{-1.9}$	-
$f_0(500)$	$0.54^{+0.95}_{-0.13}$	-
$f_0(1500)$	$3.2^{+0.4}_{-0.6}$	-
χ_{c0}	2.2 ± 0.3	-
NR	$27.9^{+2.1}_{-2.0}$	-

Table 5.6: *Fit fractions for the interference terms expressed in percent.*

Resonance	K^*	$(K\pi)^*_0$	K^*_2	f_0	ρ^0	σ	$f_0(1500)$	χ_{c0}	NR
K^*	11.65	0.00	-0.31	-0.61	0.11	-0.09	0.03	-0.14	0.00
$(K\pi)^*_0$		24.40	1.05	0.40	-0.91	0.12	-0.61	-0.17	10.12
K^*_2			0.92	-0.02	-0.08	-0.02	0.01	-0.04	1.99
f_0				17.60	0.00	0.89	3.99	0.27	-4.89
ρ^0					6.40	0.00	0.00	0.00	0.00
σ						0.54	0.43	0.04	-0.68
$f_0(1500)$							3.13	-0.03	-3.88
χ_{c0}								2.18	-1.02
NR									27.87

These spin-dependent angular distributions support in any region the additional resonances set in the nominal DP model.

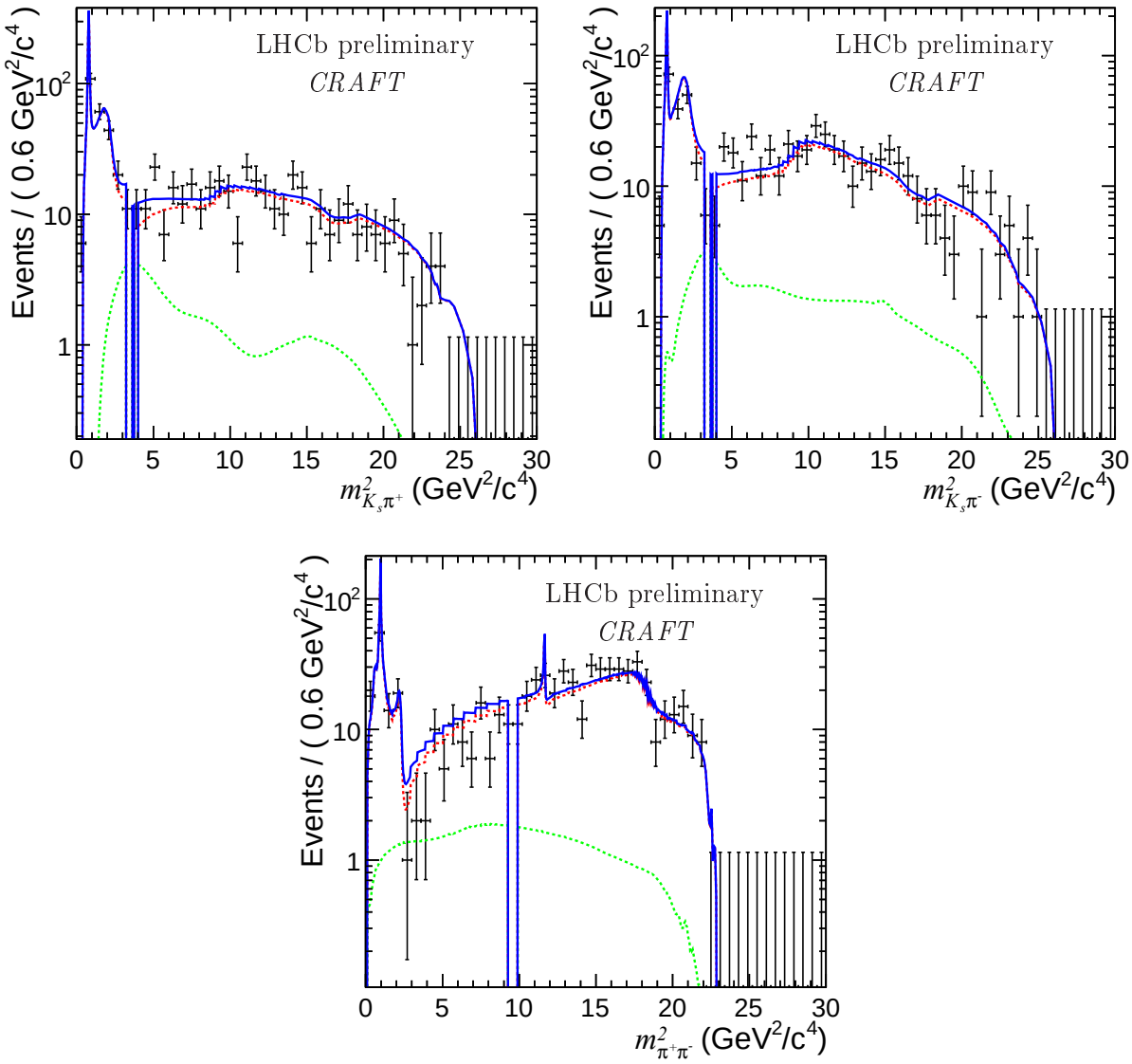

Figure 5.27: *Projections of the 2011 data with Down-Down K^0_S category given in black points, and the nominal fit, onto $m^2_{K^0_S\pi^+}$ (left), $m^2_{K^0_S\pi^-}$ (right) and $m^2_{\pi^+\pi^-}$ (bottom). The full fit is shown in blue, combinatorial background in green and signal model in red.*

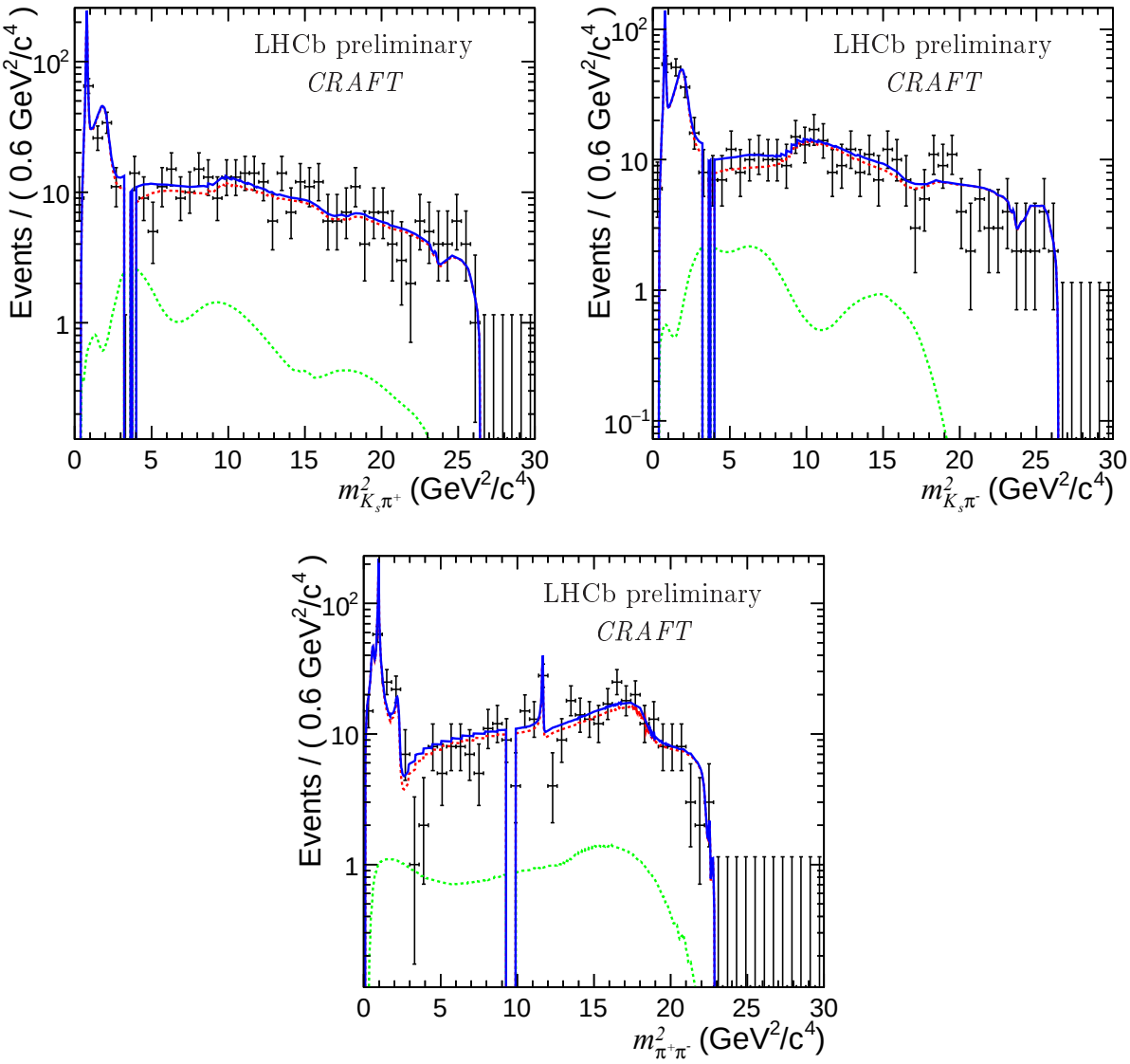

Figure 5.28: *Projections of the 2011 data with Long-Long K^0_S category given in black points, and the nominal fit, onto $m^2_{K^0_S\pi+}$ (left), $m^2_{K^0_S\pi-}$ (right) and $m^2_{\pi+\pi-}$ (bottom). The full fit is shown in blue, combinatorial background in green and signal model in red.*

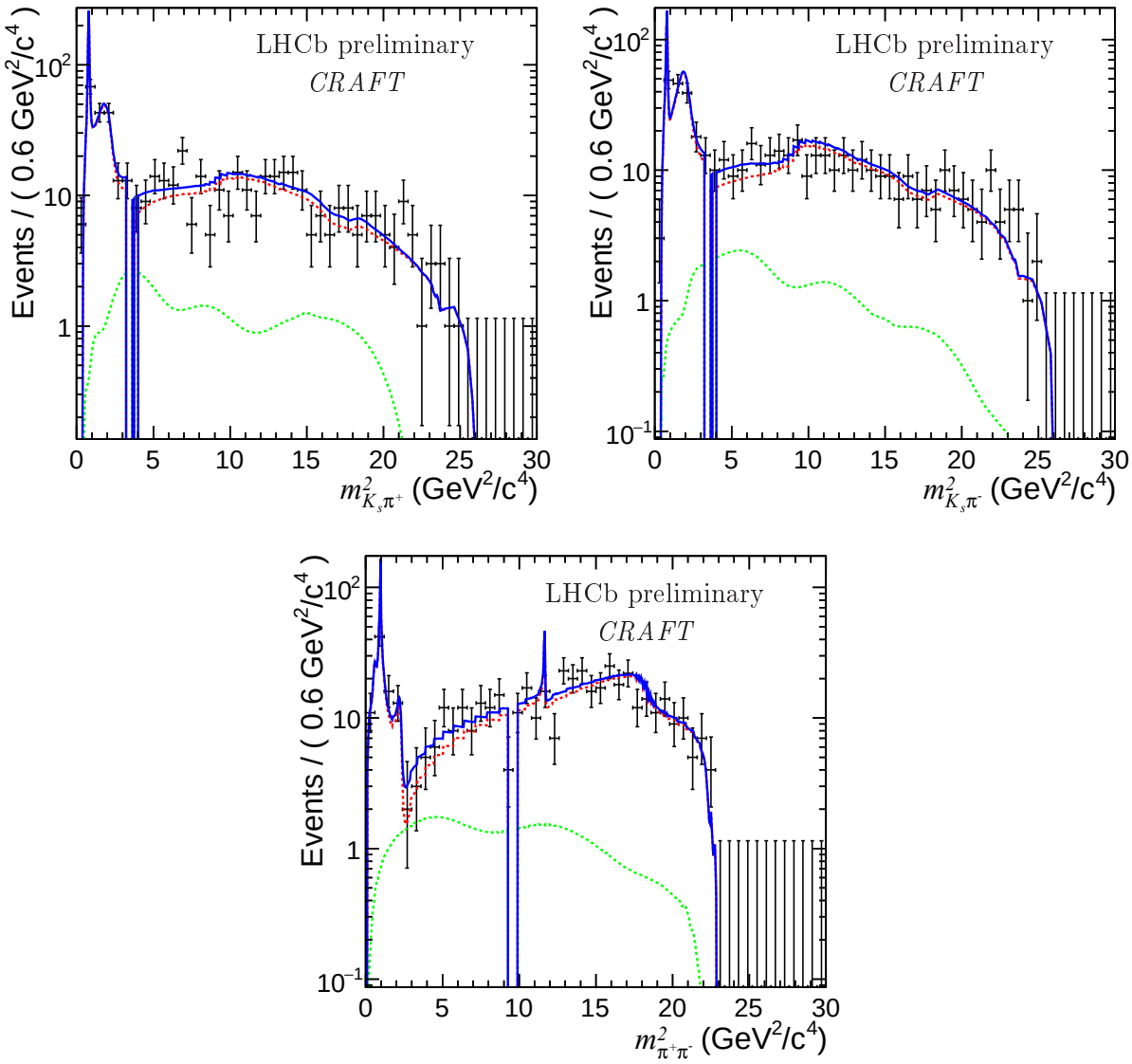

Figure 5.29: *Projections of the 2012a data with Down-Down K^0_S category given in black points, and the nominal fit, onto $m^2_{K^0_S\pi+}$ (left), $m^2_{K^0_S\pi-}$ (right) and $m^2_{\pi+\pi-}$ (bottom). The full fit is shown in blue, combinatorial background in green and signal model in red.*

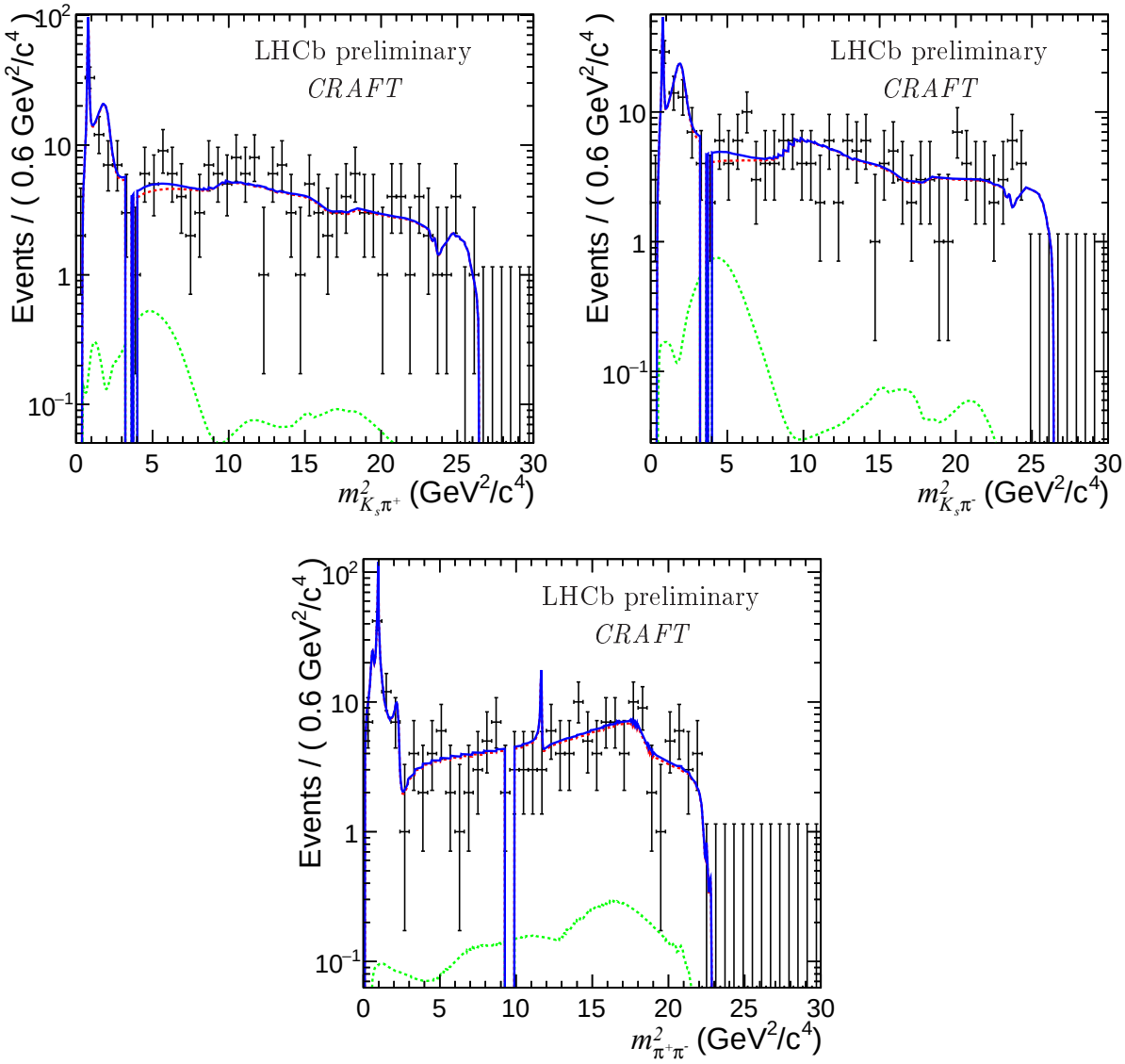

Figure 5.30: *Projections of the 2012a data with Long-Long K^0_S category given in black points, and the nominal fit, onto $m^2_{K^0_S\pi^+}$ (left), $m^2_{K^0_S\pi^-}$ (right) and $m^2_{\pi^+\pi^-}$ (bottom). The full fit is shown in blue, combinatorial background in green and signal model in red.*

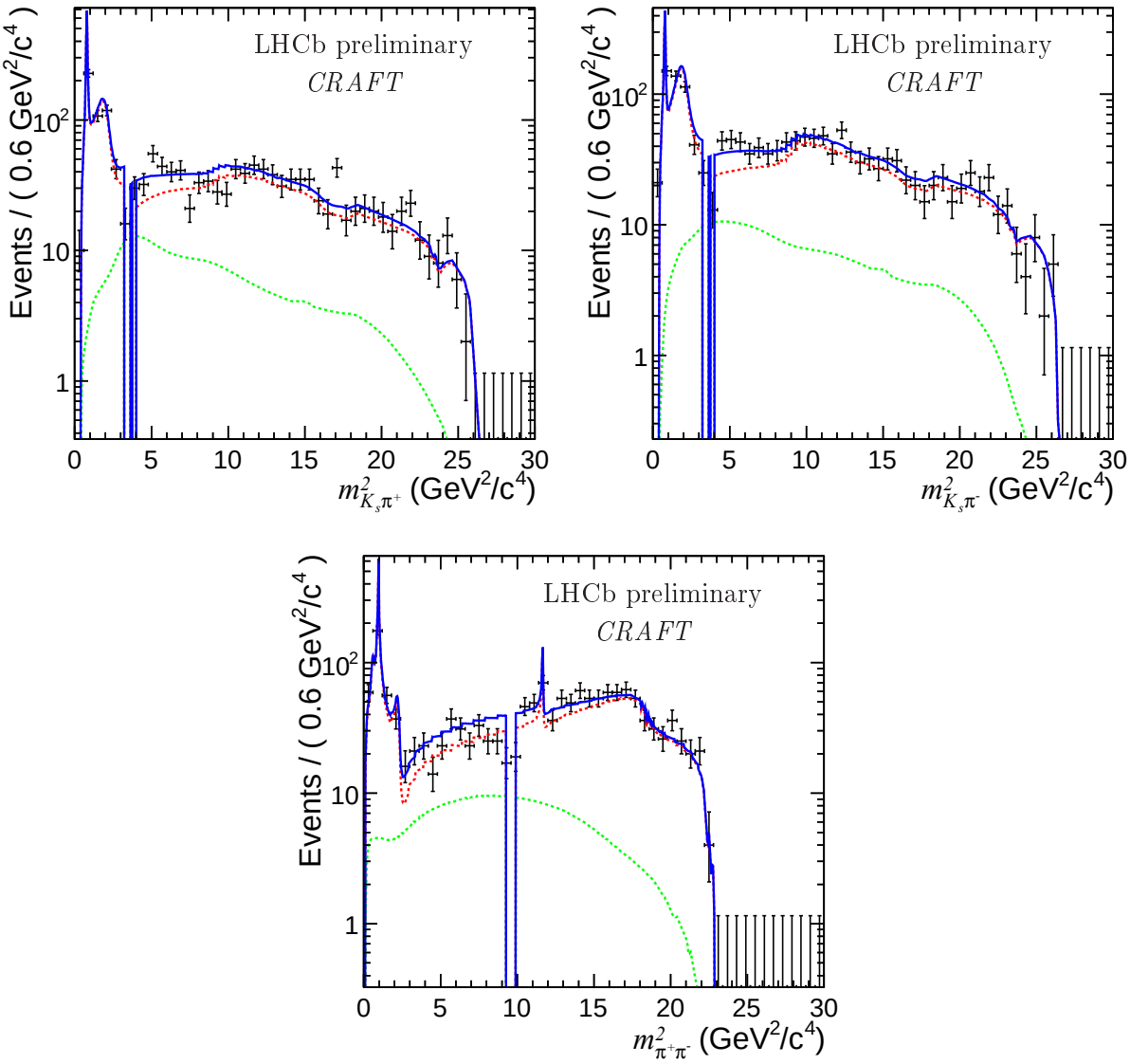

Figure 5.31: *Projections of the 2012b data with Down-Down K^0_S category given in black points, and the nominal fit, onto $m^2_{K^0_S\pi+}$ (left), $m^2_{K^0_S\pi-}$ (right) and $m^2_{\pi+\pi-}$ (bottom). The full fit is shown in blue, combinatorial background in green and signal model in red.*

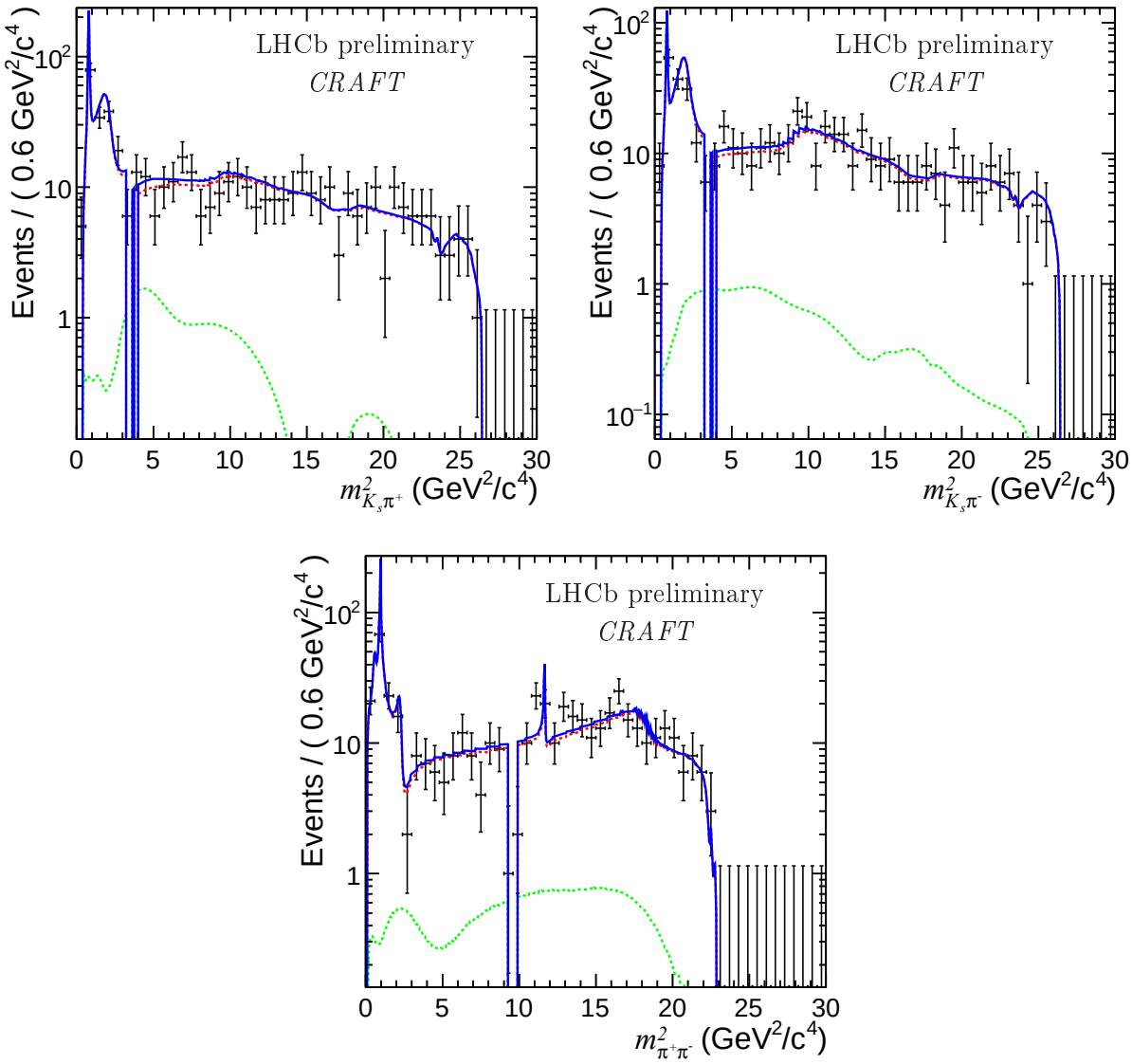

Figure 5.32: *Projections of the 2012b data with Long-Long K^0_S category given in black points, and the nominal fit, onto $m^2_{K^0_S\pi^+}$ (left), $m^2_{K^0_S\pi^-}$ (right) and $m^2_{\pi^+\pi^-}$ (bottom). The full fit is shown in blue, combinatorial background in green and signal model in red.*

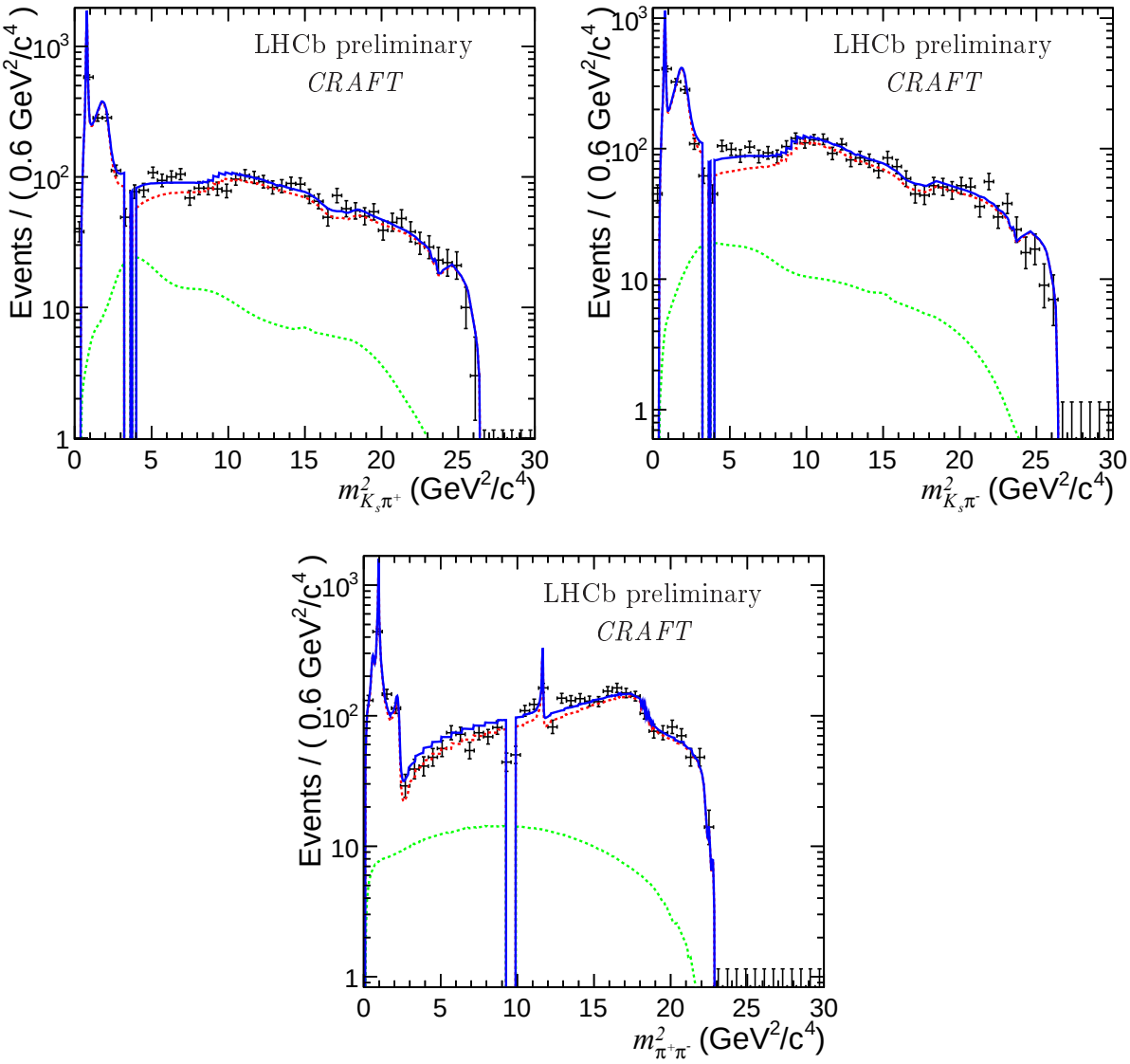

Figure 5.33: *Projections of the sum of all data category (black points) and the nominal fit, onto* $m^2_{K^0_S\pi^+}$ *(left),* $m^2_{K^0_S\pi^-}$ *(right) and* $m^2_{\pi^+\pi^-}$ *(bottom). The full fit is shown in blue, combinatorial background in green and signal model in red.*

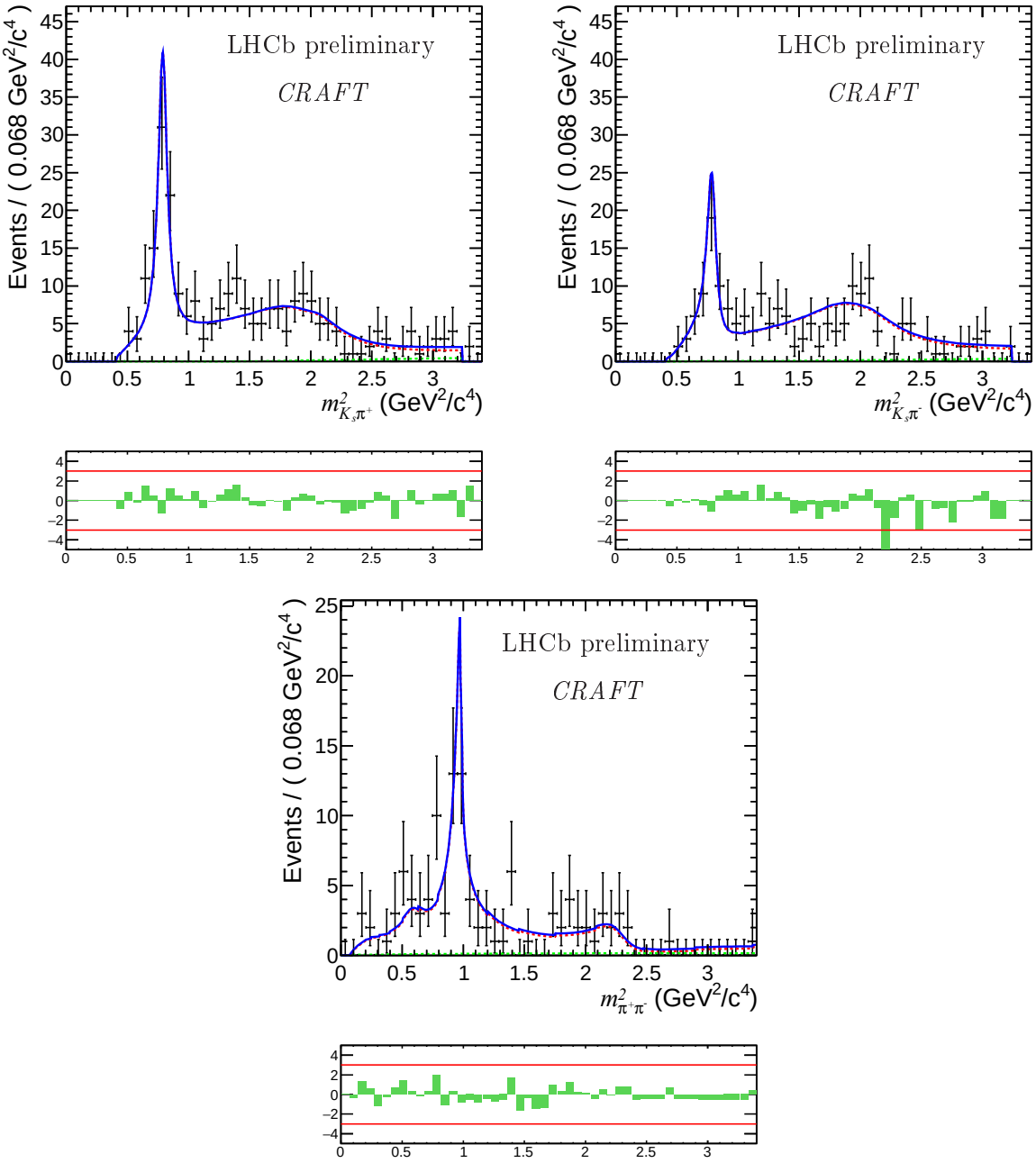

Figure 5.34: *Projections of the 2011 data with Down-Down K^0_S category given in black points, and the nominal fit, with a zoomed view, onto $m^2_{K^0_S\pi^+}$ (left), $m^2_{K^0_S\pi^-}$ (right) and $m^2_{\pi^+\pi^-}$ (bottom). The full fit is shown in blue, combinatorial background in green and signal model in red.*

5.6.1 Phase and fit fraction statistical uncertainties

The statistical uncertainties on the phases and fit fractions cannot be determined reliably from the output of the fit uncertainty. The rationale is that the angles can reach the boundary

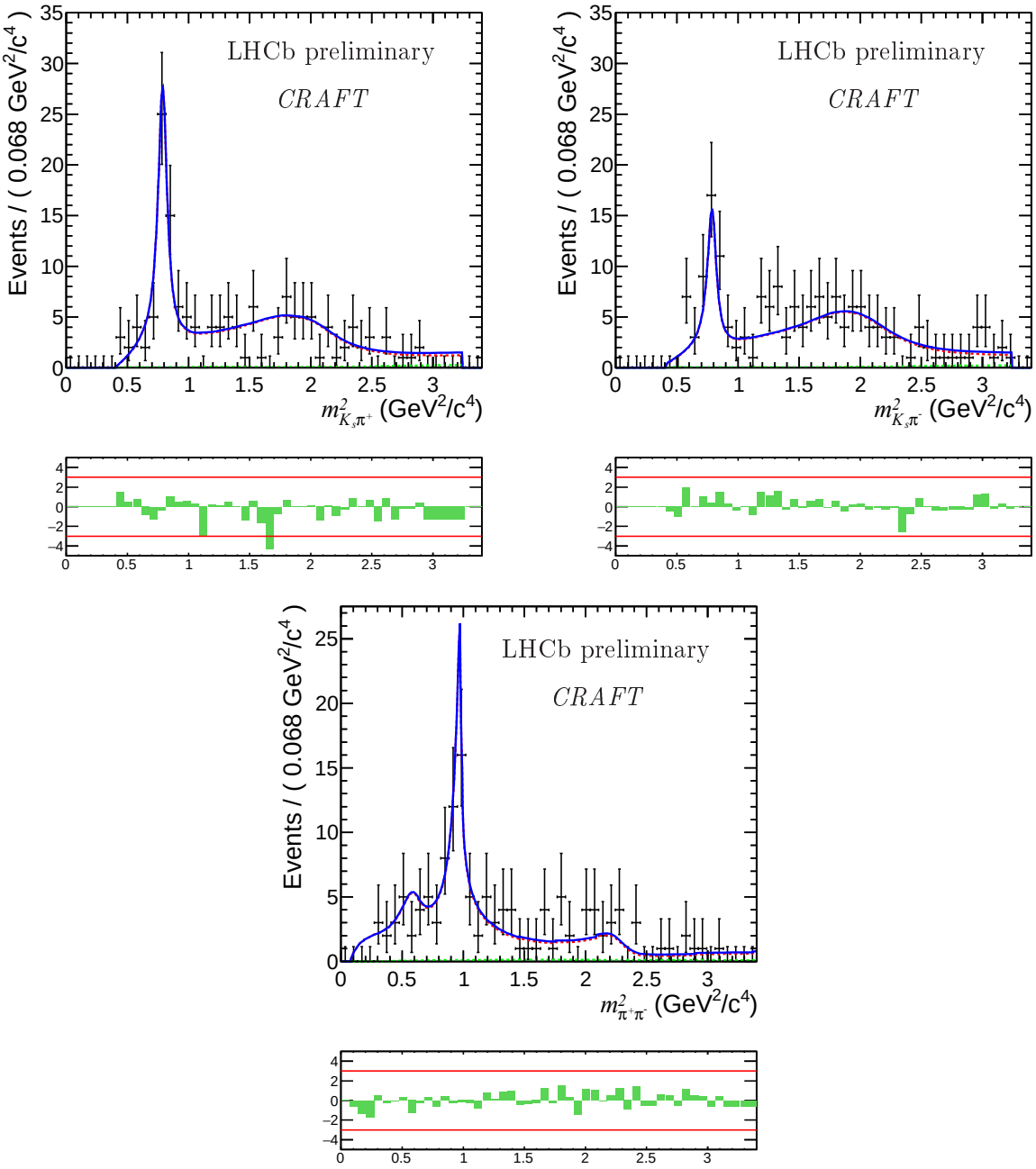

Figure 5.35: *Projections of the 2011 data with Long-Long K^0_S category given in black points, and the nominal fit, with a zoomed view, onto $m^2_{K^0_S\pi^+}$ (left), $m^2_{K^0_S\pi^-}$ (right) and $m^2_{\pi^+\pi^-}$ (bottom). The full fit is shown in blue, combinatorial background in green and signal model in red.*

limit of their cyclic definition range when their likelihoods are scanned. This effect reflects as well on the fit fractions. The statistical uncertainties are then instead evaluated using MC toy-experiments. 500 toy experiments from the nominal fit results are generated and fit to these samples back with the very same model. The distribution of the residuals (the difference

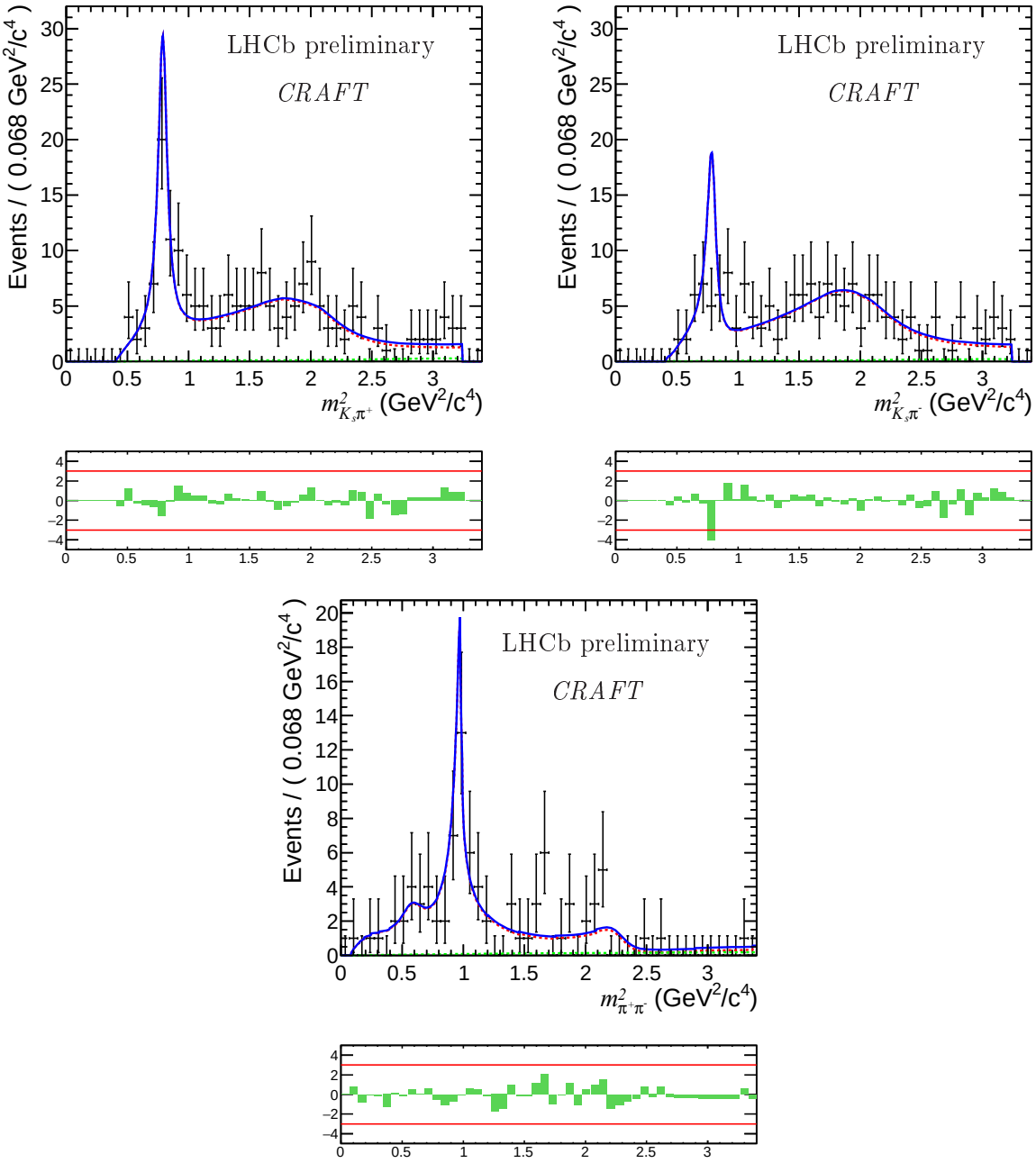

Figure 5.36: *Projections of the 2012a data with Down-Down K^0_S category given in black points, and the nominal fit, with a zoomed view, onto $m^2_{K^0_S\pi^+}$ (left), $m^2_{K^0_S\pi^-}$ (right) and $m^2_{\pi^+\pi^-}$ (bottom). The full fit is shown in blue, combinatorial background in green and signal model in red.*

between generated and fitted value) is built. The mean value of the histogram is used as a correction to the nominal fitted value while the integration of $\pm 34\,\%$ of the distribution around the central value is taken as the statistical uncertainties. Figs. 5.43 and 5.44 show the distributions of residuals of the phases and fit fractions, respectively, highlighting the

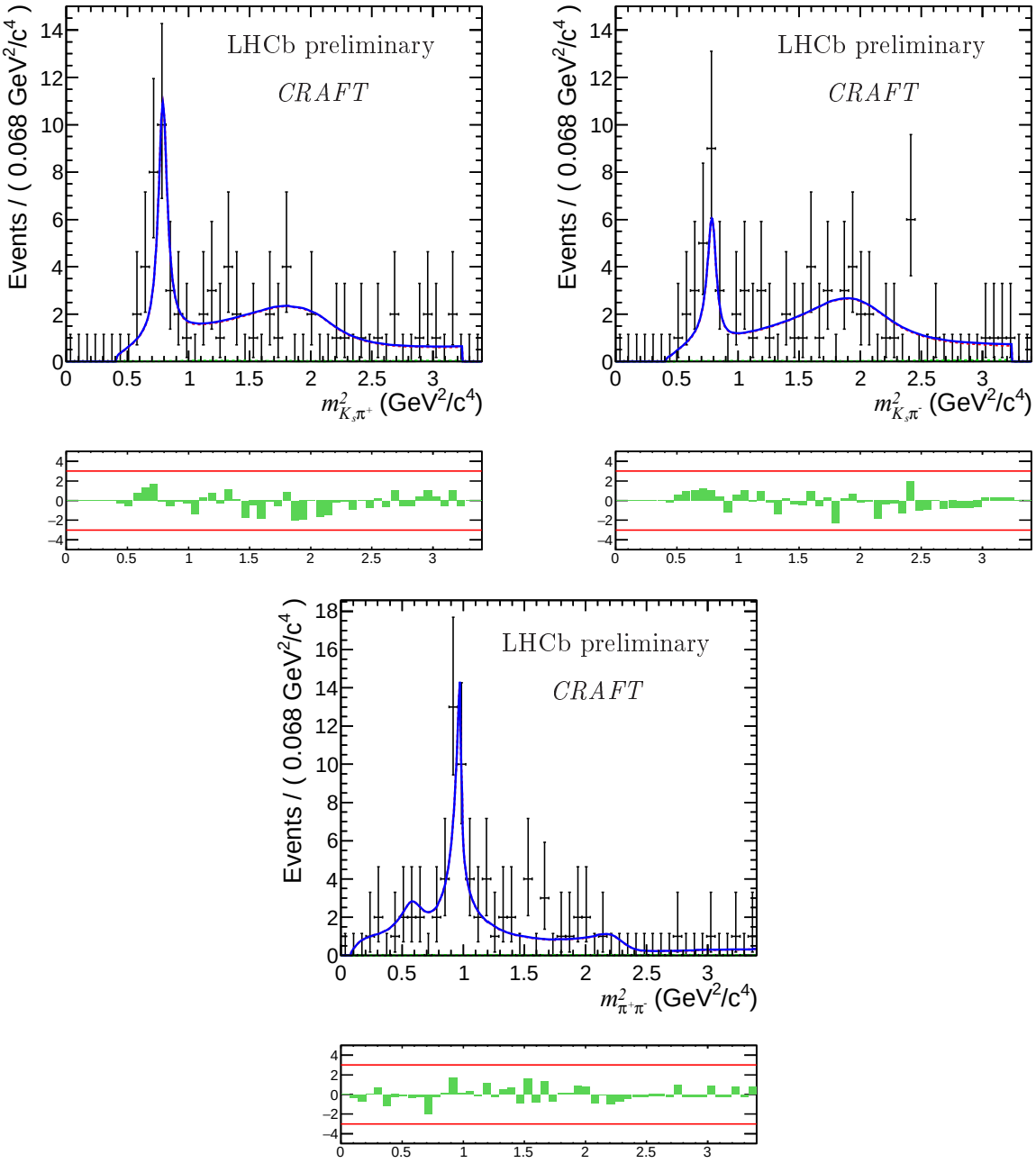

Figure 5.37: *Projections of the 2012a data with Long-Long K^0_S category given in black points, and the nominal fit, with a zoomed view, onto $m^2_{K^0_S\pi^+}$ (left), $m^2_{K^0_S\pi^-}$ (right) and $m^2_{\pi^+\pi^-}$ (bottom). The full fit is shown in blue, combinatorial background in green and signal model in red.*

estimates of the nominal values corrections and statistical uncertainties.

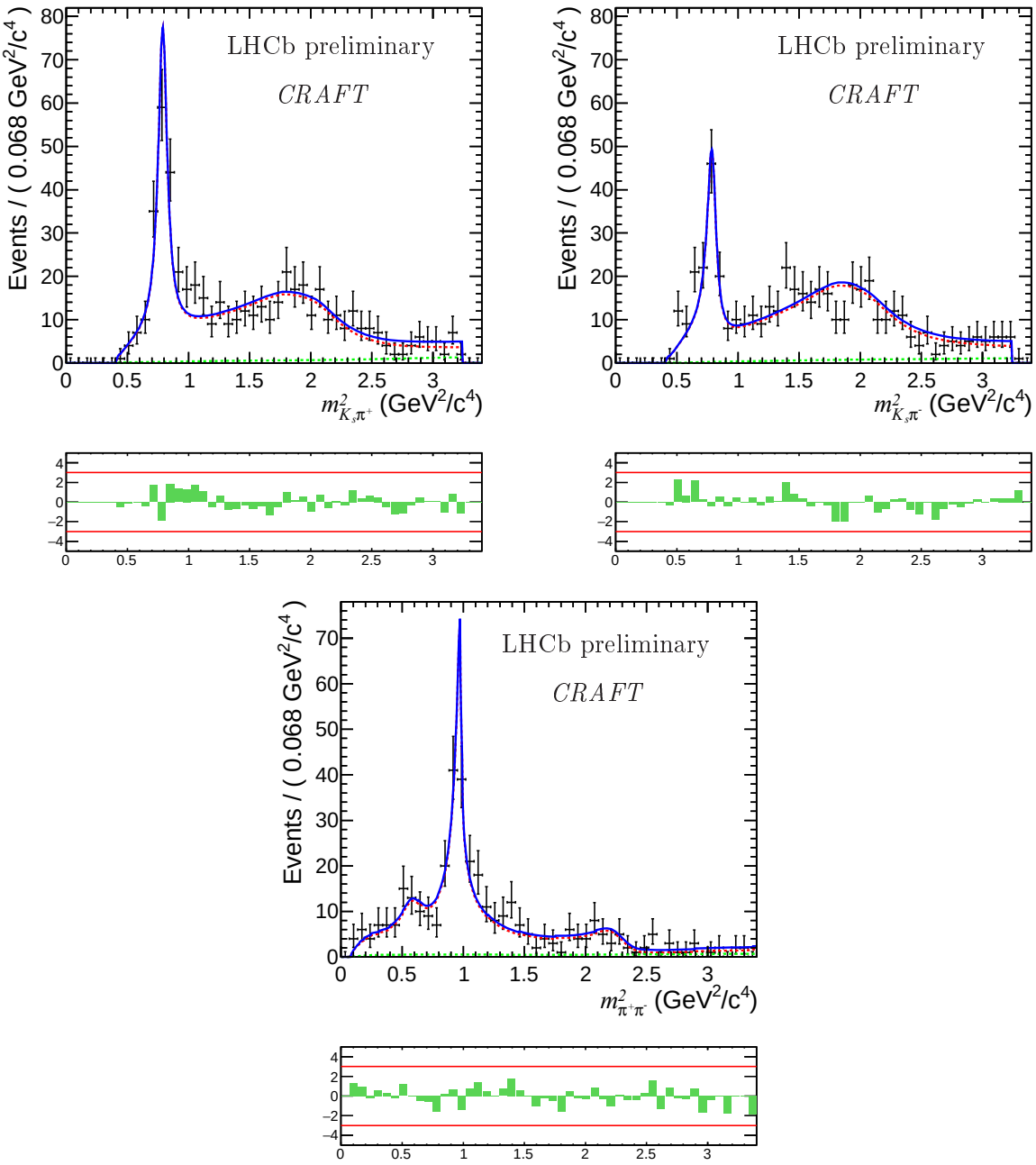

Figure 5.38: *Projections of the 2012b data with Down-Down K^0_S category given in black points, and the nominal fit, with a zoomed view, onto $m^2_{K^0_S\pi^+}$ (left), $m^2_{K^0_S\pi^-}$ (right) and $m^2_{\pi^+\pi^-}$ (bottom). The full fit is shown in blue, combinatorial background in green and signal model in red.*

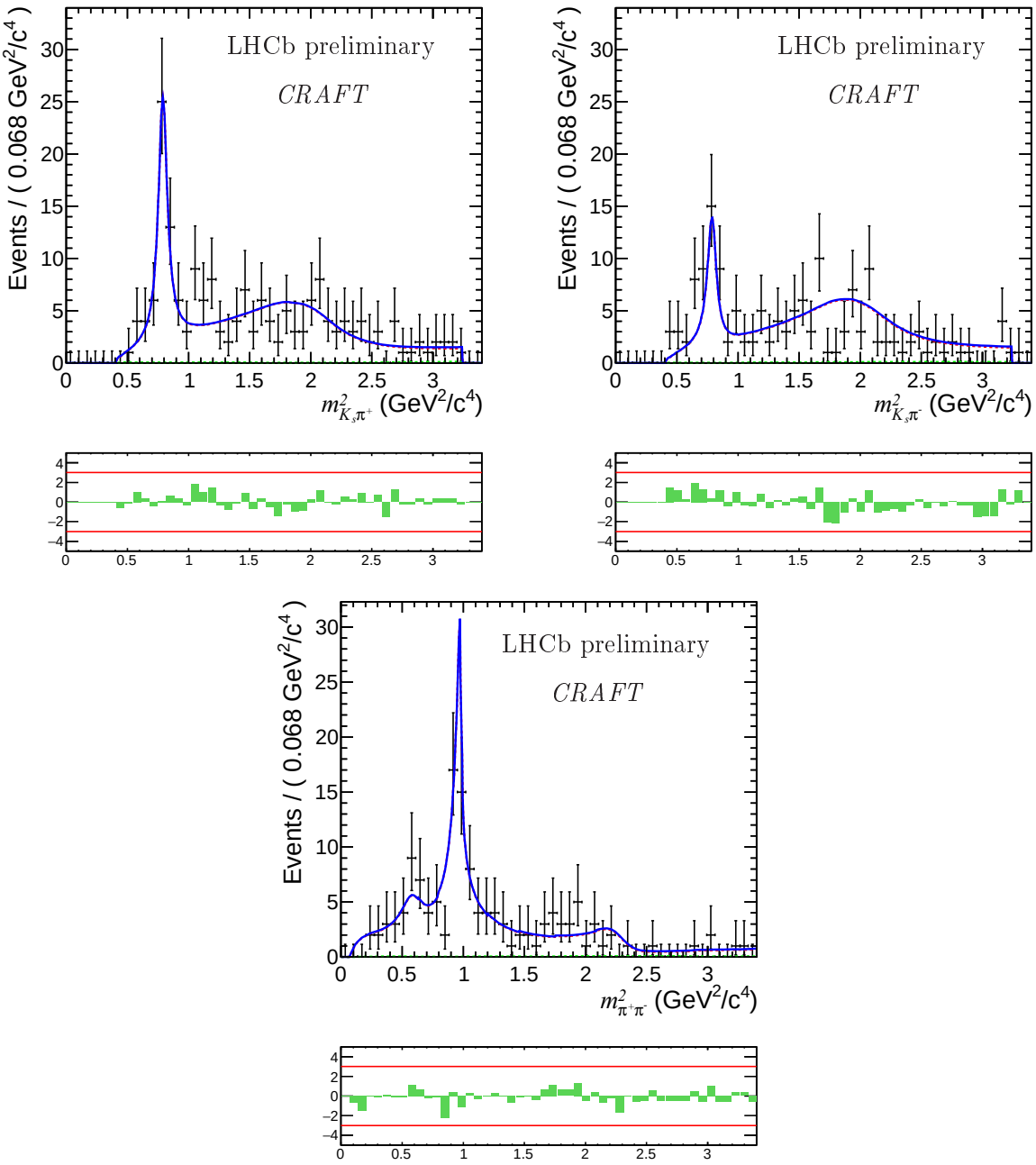

Figure 5.39: *Projections of the 2012b data with Long-Long K^0_S category given in black points, and the nominal fit, with a zoomed view, onto $m^2_{K^0_S\pi^+}$ (left), $m^2_{K^0_S\pi^-}$ (right) and $m^2_{\pi^+\pi^-}$ (bottom). The full fit is shown in blue, combinatorial background in green and signal model in red.*

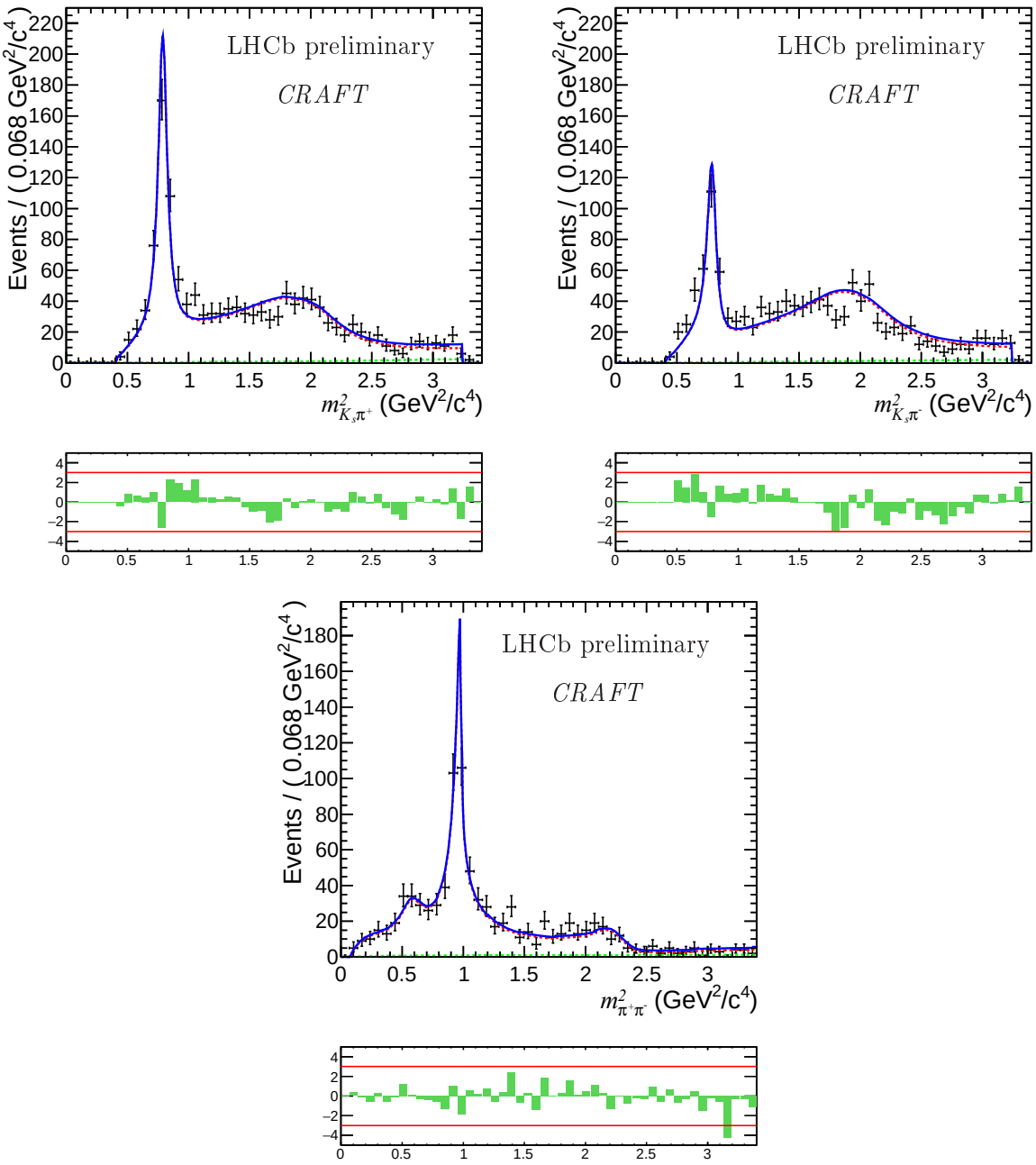

Figure 5.40: *Projections of the sum of all data category (black points) and the nominal fit, with a zoomed view, onto* $m^2_{K^0_S\pi^+}$ *(left),* $m^2_{K^0_S\pi^-}$ *(right) and* $m^2_{\pi^+\pi^-}$ *(bottom). The full fit is shown in blue, combinatorial background in green and signal model in red.*

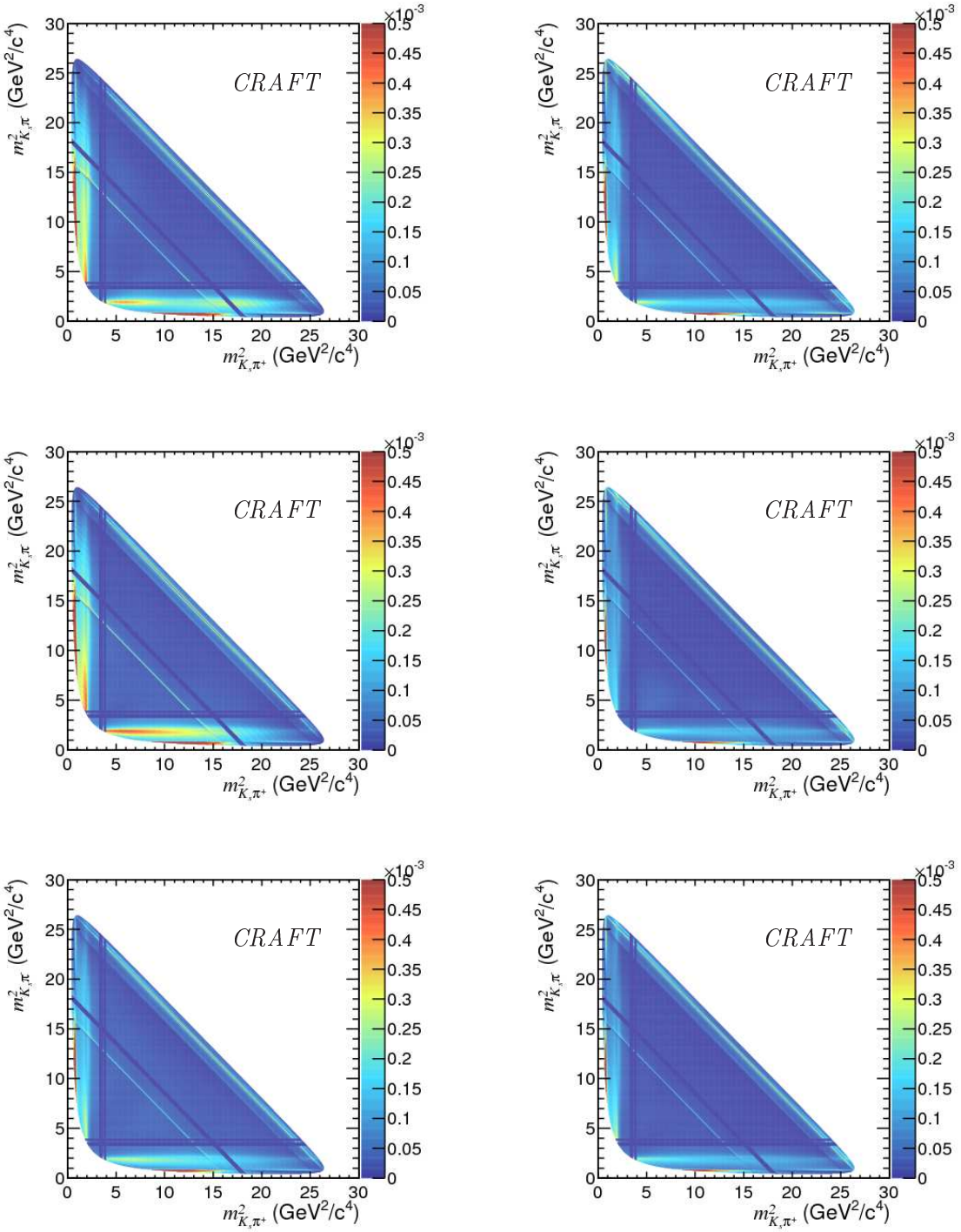

Figure 5.41: *The fitted nominal model functions in 2D Dalitz-plane. Plots on the left (right) side show the fit results to samples with K^0_S Down-Down (Long-Long) category. Plots in a row display the functions fitted to 2011, 2012a and 2012b running period samples, respectively.*

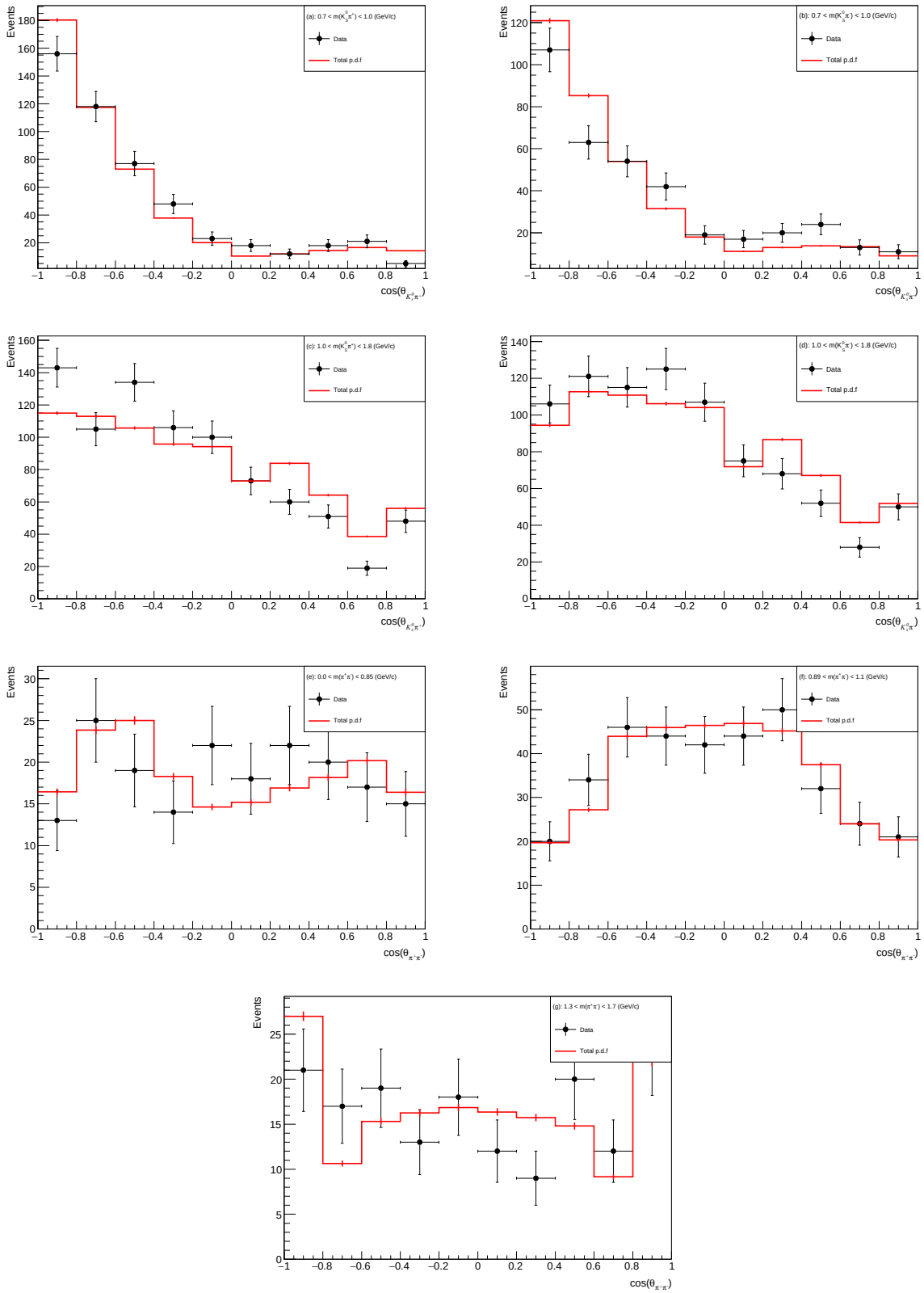

Figure 5.42: *Helicity angle projections of the* $K^0_S\pi^\pm$ *and* $\pi^+\pi^-$ *pairs in the mass region around:* $K^{*\pm}(892)$ *(a and b),* $K^{*\pm}_0(1430)$ *(c and d),* $f_0(500) + \rho(770)$ *(f),* $f_0(980)$ *(e) and* $f_0(1500)$ *(g).*

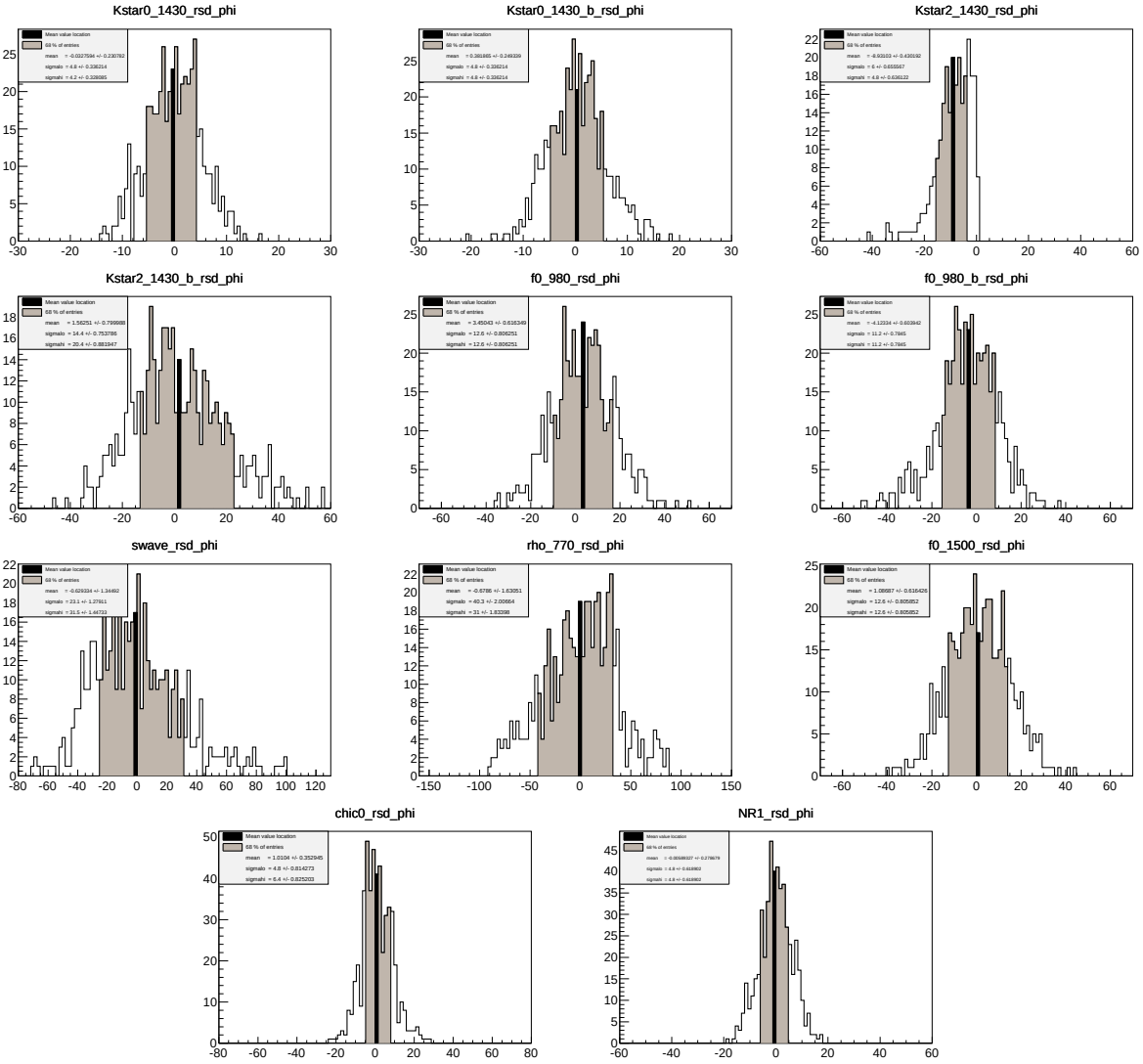

Figure 5.43: *The distribution of the residuals of the phases returned by the toy study. The corresponding amplitude contribution is labelled on each plot. The wide black line indicates the central value of the histogram. The shaded regions are the* $\pm 34\,\%$ *integrands of the distribution on each side of the central value.*

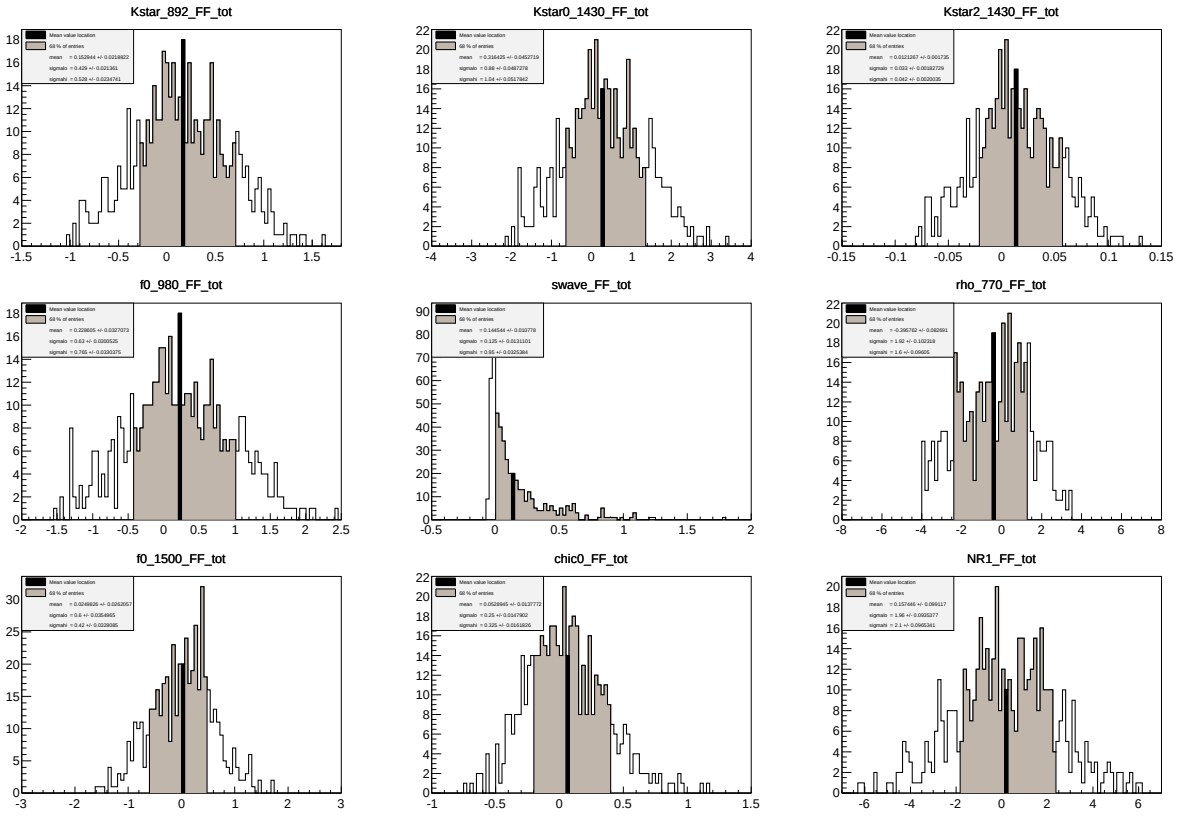

Figure 5.44: *The distribution of the residuals of the fit fractions returned by the toy study. The corresponding amplitude contribution is labelled on each plot. The wide black line indicates the central value of the histogram. The shaded regions are the* $\pm 34\,\%$ *integrands of the distribution on each side of the central value.*

5.7 Fit validation

The fit procedure and the fit results relevance are addressed in two steps. First, the likelihood function for each parameter is scanned in order to ensure that no local minimum is present in the solution of the fit. Second an ensemble of pseudo-experiments are performed in order to search for biases in the fit results.

5.7.1 Likelihood scans

The negative logarithm of the likelihood distributions for all the Cartesian parameters measured from the nominal fit are shown in Fig. 5.45.

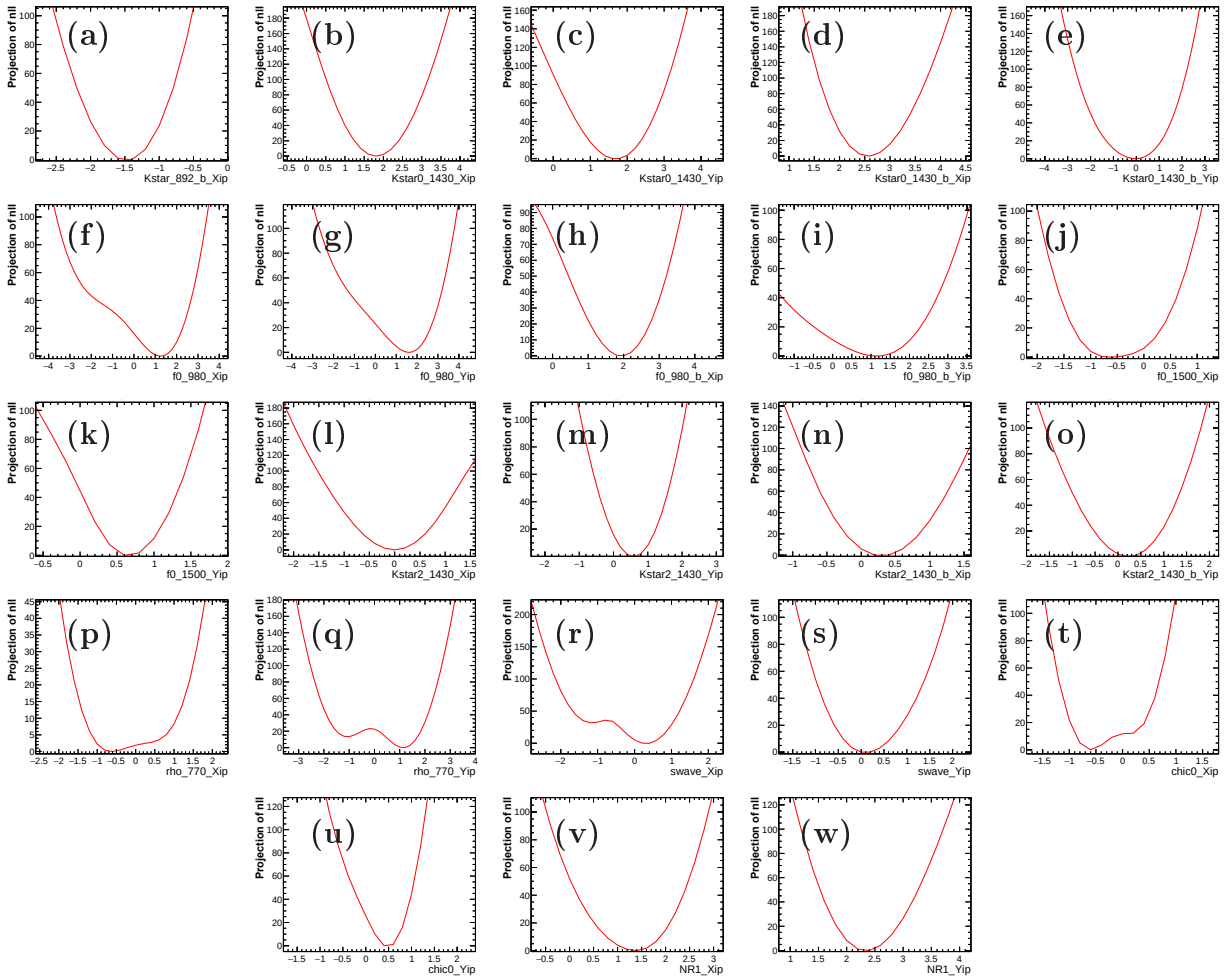

Figure 5.45: *Likelihood function scanned as a function of the Cartesian parameter values in the nominal fit. The likelihood profile is built by taking the minimum of the log likelihood to be 0.*

No additional local minimum occurs for most of the likelihood projection in the range of $\Delta\text{nll} = (\text{nll} - \text{nll}_{\text{min}}) \in [0, 100]$, except for the parameters $y_{\rho(770)}$ (Fig. 5.45.q), $x_{f_0(500)}$

(Fig. 5.45.r) and $x_{\chi_{c0}}$ (Fig. 5.45.t), where the difference between the two minima is $-2\Delta\text{nll} = 20$, 60 and 25 units, respectively. Furthermore, most of the likelihood functions have a parabolic behaviour around the minimum, although an asymmetric estimate of the uncertainties must be performed in some cases.

5.7.2 Pseudo-experiments study from the fit results

Pseudo-experiments are generated according to the fit results of the nominal DP model, including the background p.d.f.. In a first approach, a high statistics sample has been generated and fitted back with the very same model. This allows to ensure that no intrinsic bias related to the fit package or the fit model is present. Figs. 5.46 to 5.48 show the fit result and Table 5.7 gathers the residuals of the fit. This asymptotic test shows that no significant fit bias occurs within a sample equivalent to 300 times the actual size of the data sample.

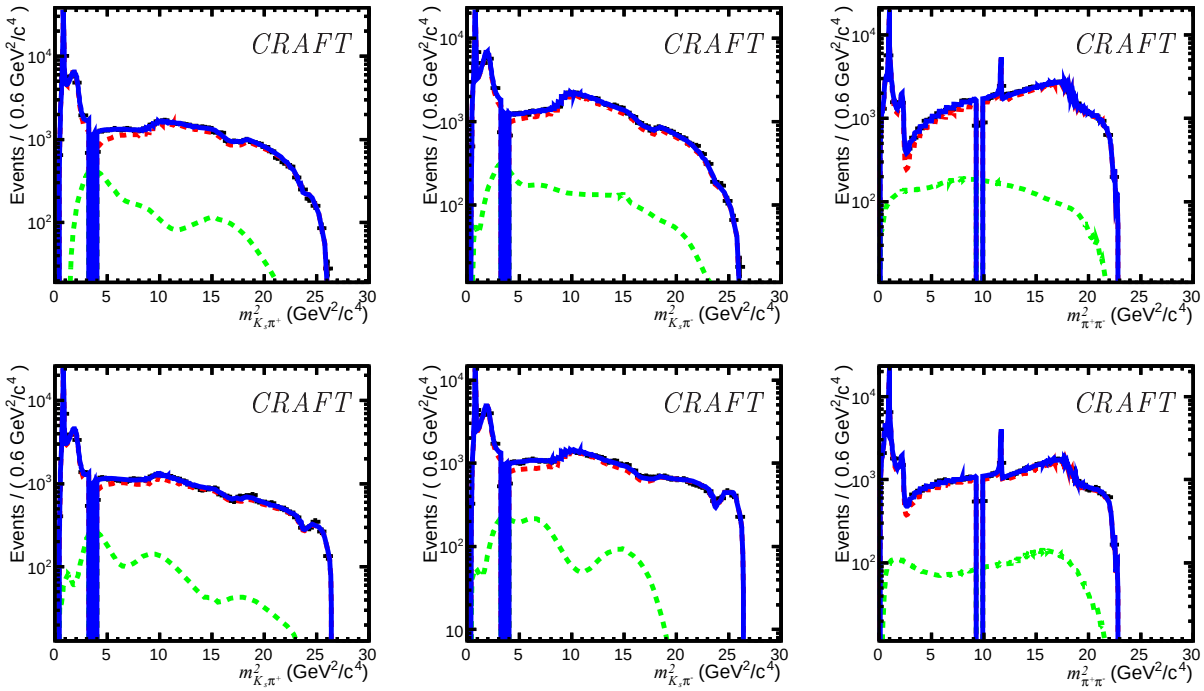

Figure 5.46: *Projections of the 2011 asymptotic pseudo-experiment* ($100 \times N^{\text{data}}_{2011}$) *and the asymptotic fit, with a logarithmic y-axis scale, onto* $m^2_{K^0_S\pi^+}$ *(left),* $m^2_{K^0_S\pi^-}$ *(middle) and* $m^2_{K^0_S\pi^+}$. *Plot on the top (bottom) presents the Down-Down (Long-Long)* K^0_S *category sample.*

The second toy study is a pull study with realistic number of events equal to the real data events. This test enables us to evaluate any bias due to actual statistics of the data sample and, when applicable, to correct for them. The pull study consists of several MC generations following the nominal Dalitz model including the combinatorial background histograms, and

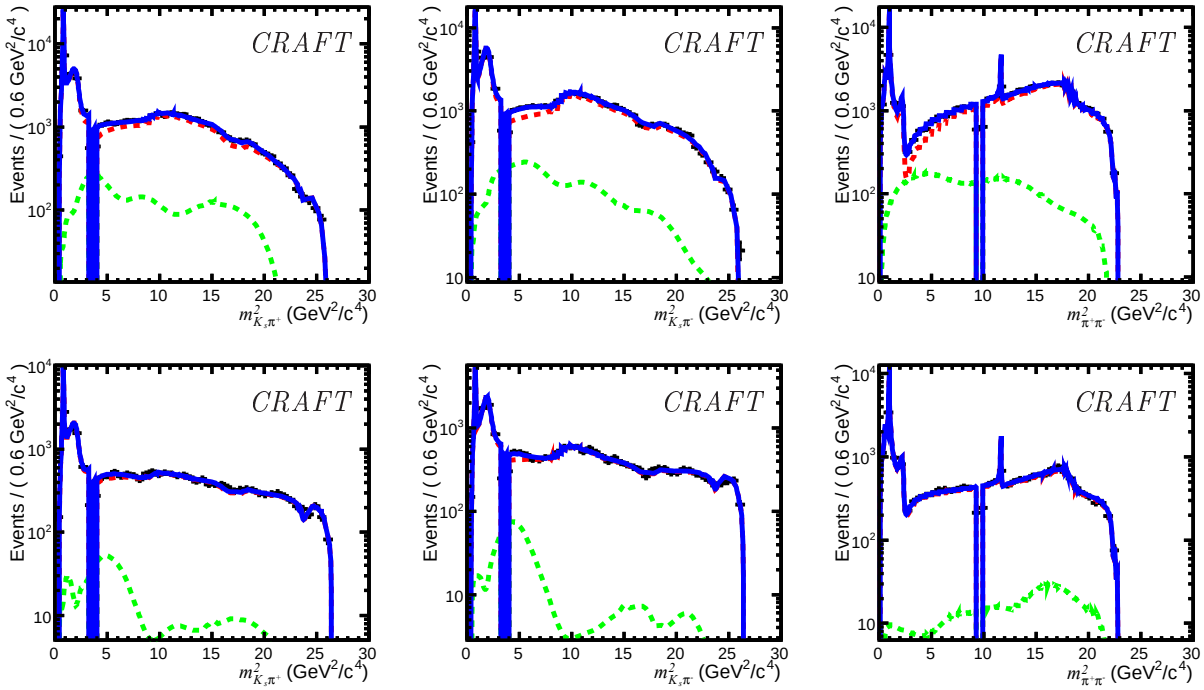

Figure 5.47: *Projections of the 2012a asymptotic pseudo-experiment* ($100 \times N^{\text{data}}_{2012a}$) *and the asymptotic fit, with a logarithmic y-axis scale, onto* $m^2_{K^0_S\pi^+}$ *(left),* $m^2_{K^0_S\pi^-}$ *(middle) and* $m^2_{K^0_S\pi^+}$*. Plot on the top (bottom) presents the Down-Down (Long-Long)* K^0_S *category sample.*

Table 5.7: *The residual results of the asymptotic toy MC test.*

Resonance	Real part residual	Imag. part residual
$K^{*+}(892)$	-	-
$K^{*-}(892)$	0.006 ± 0.008	-
$(K\pi)^{*+}_0$	0.003 ± 0.016	0.008 ± 0.020
$(K\pi)^{*-}_0$	0.000 ± 0.012	0.032 ± 0.024
$K^{*+}_2(1430)$	0.007 ± 0.011	0.007 ± 0.011
$K^{*-}_2(1430)$	0.011 ± 0.009	0.013 ± 0.013
$f_0(980)$ from B^0	0.043 ± 0.046	0.036 ± 0.046
$f_0(980)$ from $\overline{B}^0$	0.009 ± 0.035	0.081 ± 0.051
$f_0(500)$	0.005 ± 0.010	0.006 ± 0.017
$\rho^0(770)$	0.085 ± 0.061	0.049 ± 0.038
$f_0(1500)$	0.013 ± 0.028	0.019 ± 0.042
NR	0.029 ± 0.029	0.007 ± 0.016
χ_{c0}	0.009 ± 0.008	0.005 ± 0.008

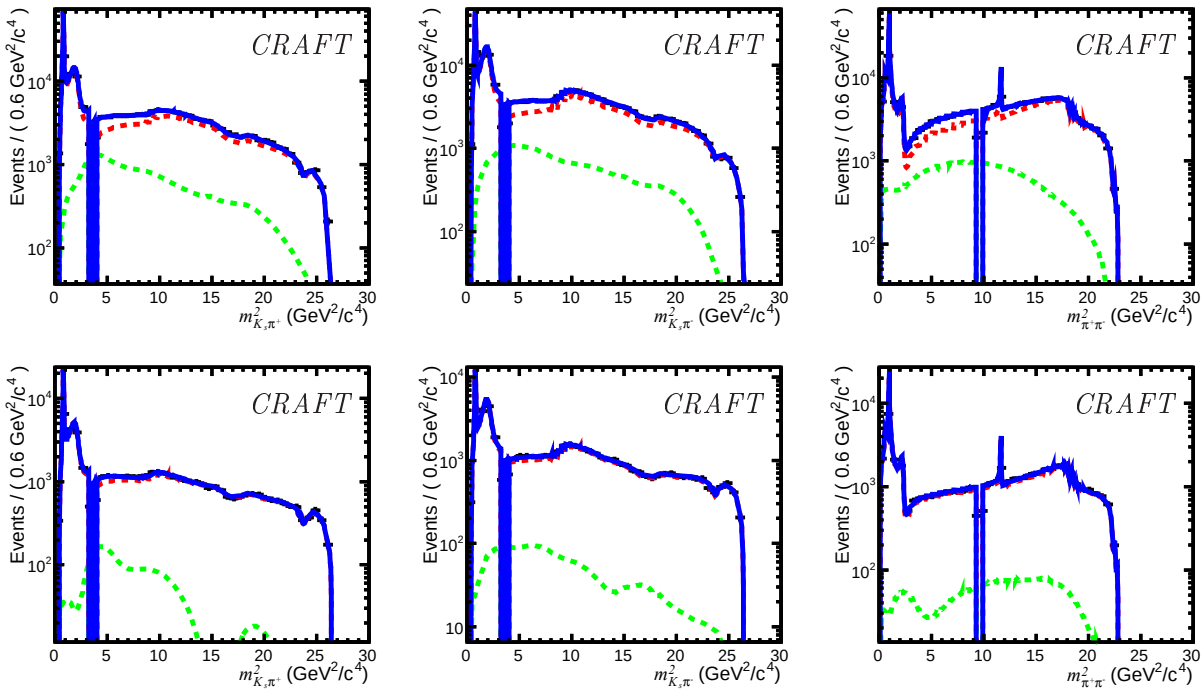

Figure 5.48: *Projections of the 2012b asymptotic pseudo-experiment* ($100 \times N^{\text{data}}_{2012b}$) *and the asymptotic fit, with a logarithmic y-axis scale, onto* $m^2_{K^0_S\pi^+}$ *(left),* $m^2_{K^0_S\pi^-}$ *(middle) and* $m^2_{K^0_S\pi^+}$. *Plot on the top (bottom) presents the Down-Down (Long-Long)* K^0_S *category sample.*

fitted back by the very same model. Mathematically, the pull is expressed as:

$$\text{Pull} = \frac{x_{\text{gen}} - x_{\text{fit}}}{\sigma_{\text{fit}}} \,, \tag{5.10}$$

where x_{fit} and σ_{fit} are the parameter values returned by the fit and its uncertainty, respectively, and x_{gen} is the parameter value used in generation. An unbiased fit for a set of toy experiments implies that the pull distribution is a standard Gaussian ($\mu_{\text{pull}} = 0$, $\sigma_{\text{pull}} = 1$) distribution. If the mean of pull distribution is significantly different from zero, it characterizes a bias in the measurement. A width less than 1 indicates that the statistical uncertainty is overestimated, and conversely a width larger than 1 shows that the uncertainty is underestimated. Pull studies are performed only for Cartesian, amplitude and direct *CP* asymmetry parameters, since their uncertainties can be directly evaluated from the fit results. The final pull study results on Cartesian coordinates are displayed in Figs. 5.49 to 5.51 and gathered in Table 5.8. As well, the final pull study results on magnitudes and *CP* asymmetries are displayed in Figs. 5.52 to 5.54 and gathered in Table 5.9. The pull study on cartesian parameters shows negligible biases, except for the resonances $f_0(500)$, $\rho(770)$ and $f_0(980)$, where small but significant biases are found. These biases can be corrected for and the error on the correction will be considered as a systematic uncertainty. The method is discussed with more details in Section 5.8.1.2.

Table 5.8: *Results of the fit of the pull distributions of the Cartesian parameters by a gaussian function.*

Resonance	Real part		Imaginary part	
	Pull mean	Pull width	Pull mean	Pull width
$K^{*+}(892)$	-	-	-	-
$K^{*-}(892)$	0.017 ± 0.045	0.999 ± 0.032	-	-
$(K\pi)_0^{*+}$	-0.042 ± 0.045	0.998 ± 0.032	-0.032 ± 0.046	1.016 ± 0.032
$(K\pi)_0^{*-}$	-0.101 ± 0.042	0.947 ± 0.030	-0.070 ± 0.046	1.022 ± 0.032
$K_2^{*+}(1430)$	-0.041 ± 0.045	0.998 ± 0.032	-0.109 ± 0.044	0.983 ± 0.031
$K_2^{*-}(1430)$	-0.075 ± 0.043	0.955 ± 0.030	-0.038 ± 0.045	1.000 ± 0.032
$f_0(980)$ from B^0	0.212 ± 0.046	1.022 ± 0.032	-0.201 ± 0.044	0.989 ± 0.031
$f_0(980)$ from $\overline{B}^0$	-0.202 ± 0.043	0.966 ± 0.031	0.267 ± 0.050	1.112 ± 0.035
$f_0(500)$	-0.109 ± 0.043	0.957 ± 0.030	0.148 ± 0.046	1.025 ± 0.032
$\rho^0(770)$	0.071 ± 0.120	1.091 ± 0.077	-0.199 ± 0.099	0.965 ± 0.058
$f_0(1500)$	0.018 ± 0.052	1.158 ± 0.037	0.048 ± 0.042	0.946 ± 0.030
NR	0.035 ± 0.045	1.008 ± 0.032	-0.054 ± 0.047	1.047 ± 0.033
χ_{c0}	0.137 ± 0.043	0.969 ± 0.031	0.061 ± 0.044	0.990 ± 0.031

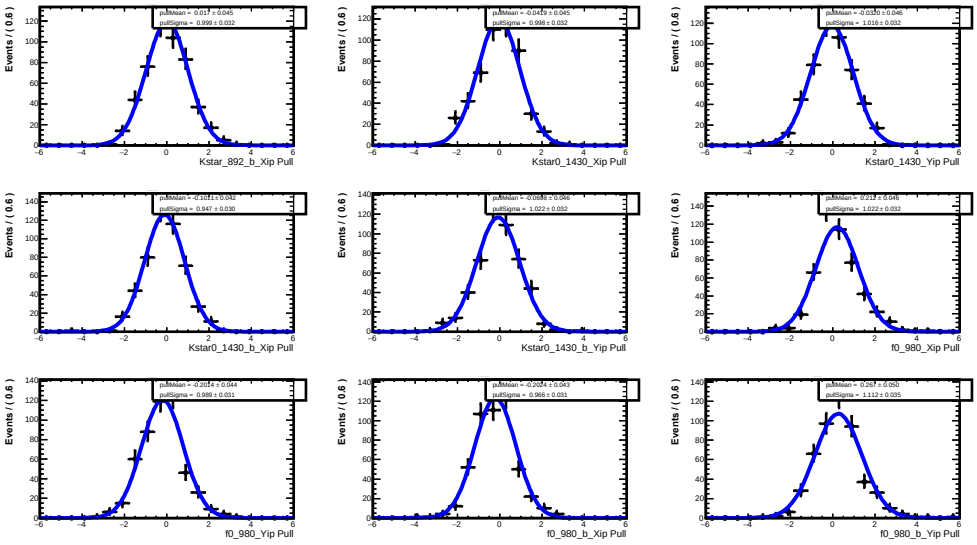

Figure 5.49: *Real and imaginary coordinates pull distributions from 500 pseudo-experiments. Each pull distribution is fitted by a Gaussian (blue line).*

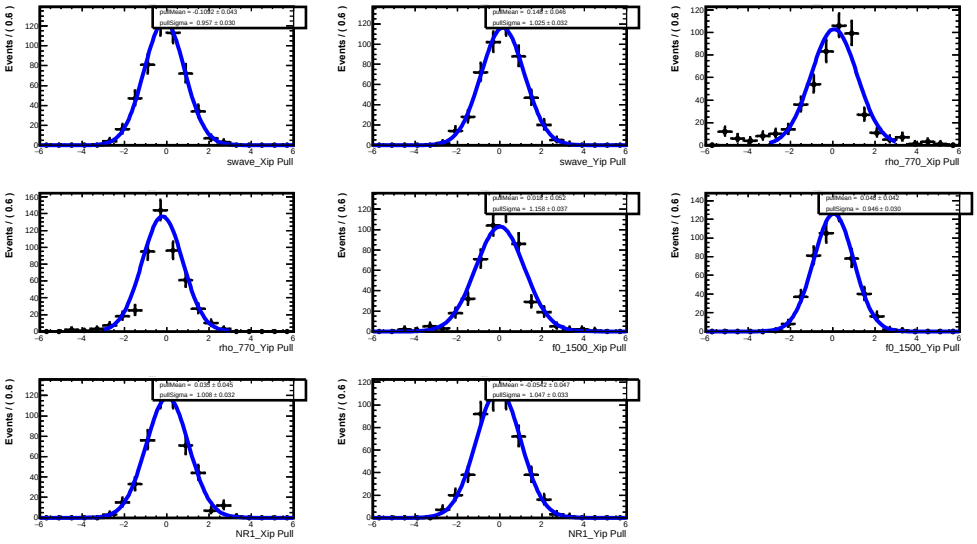

Figure 5.50: *Real and imaginary coordinates pull distributions from 500 pseudo-experiments. Each pull distribution is fitted by a Gaussian (blue line). The pull distribution of* $\rho^0(770)$ *parameters are fitted in the specific range* $[-3, 3]$ *because of non-gaussian tails.*

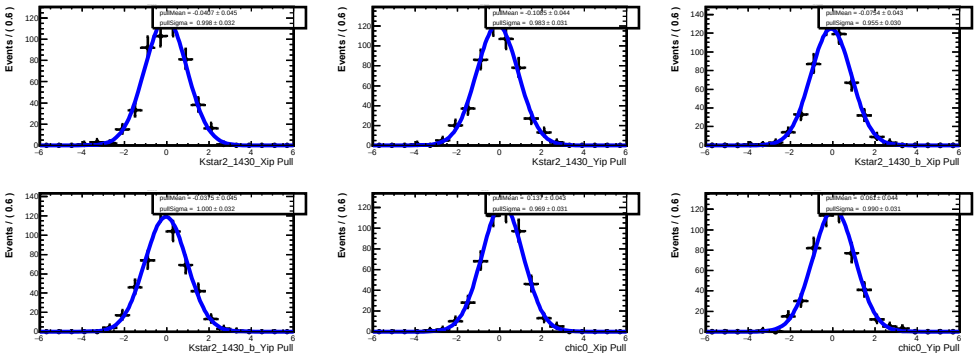

Figure 5.51: *Real and imaginary coordinates pull distributions from 500 pseudo-experiments. Each pull distribution is fitted by a Gaussian (blue line).*

Table 5.9: *Results of the fit of the pull distribution of the magnitudes and CP asymmetries by a gaussian function.*

Resonance	Amplitude		Direct *CP* asymm.	
	Pull mean	Pull width	Pull mean	Pull width
$K^{*+}(892)$	-	-	0.027 ± 0.046	0.997 ± 0.030
$K^{*-}(892)$	0.040 ± 0.047	1.000 ± 0.030		
$(K\pi)_0^{*+}$	-0.024 ± 0.042	0.909 ± 0.031	-0.084 ± 0.043	0.954 ± 0.031
$(K\pi)_0^{*-}$	-0.019 ± 0.043	0.940 ± 0.030		
$K_2^{*+}(1430)$	0.003 ± 0.046	1.010 ± 0.040	-0.055 ± 0.048	1.029 ± 0.043
$K_2^{*-}(1430)$	-0.087 ± 0.044	0.964 ± 0.032		
$f_0(980)$ from B^0	-0.079 ± 0.045	1.010 ± 0.030	-0.010 ± 0.053	1.100 ± 0.100
$f_0(980)$ from $\overline{B}^0$	-0.100 ± 0.053	1.075 ± 0.049		
$f_0(500)$	-0.295 ± 0.046	0.986 ± 0.037	-	-
$\rho^0(770)$	0.024 ± 0.045	0.988 ± 0.036	-	-
$f_0(1500)$	-0.057 ± 0.047	1.036 ± 0.038	-	-
NR	-0.033 ± 0.049	1.061 ± 0.042	-	-
χ_{c0}	0.137 ± 0.046	0.999 ± 0.035	-	-

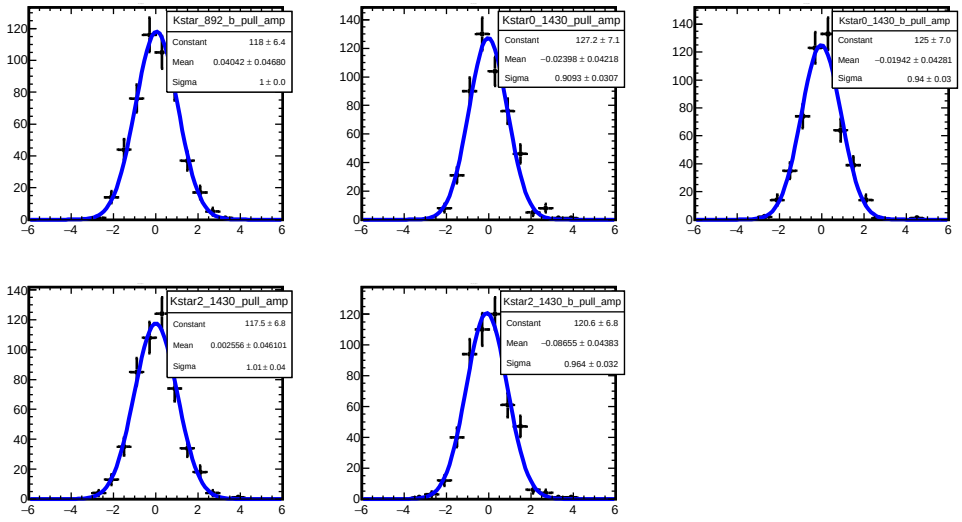

Figure 5.52: *Amplitudes pull distributions from 500 pseudo-experiments. Each pull distribution is fitted by a Gaussian (blue line).*

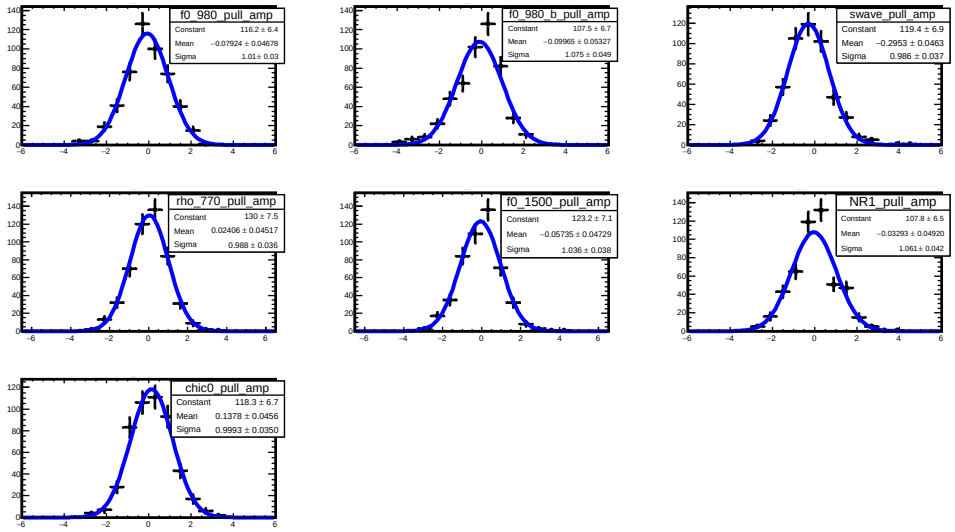

Figure 5.53: *Amplitudes pull distributions from 500 pseudo-experiments. Each pull distribution is fitted by a Gaussian (blue line).*

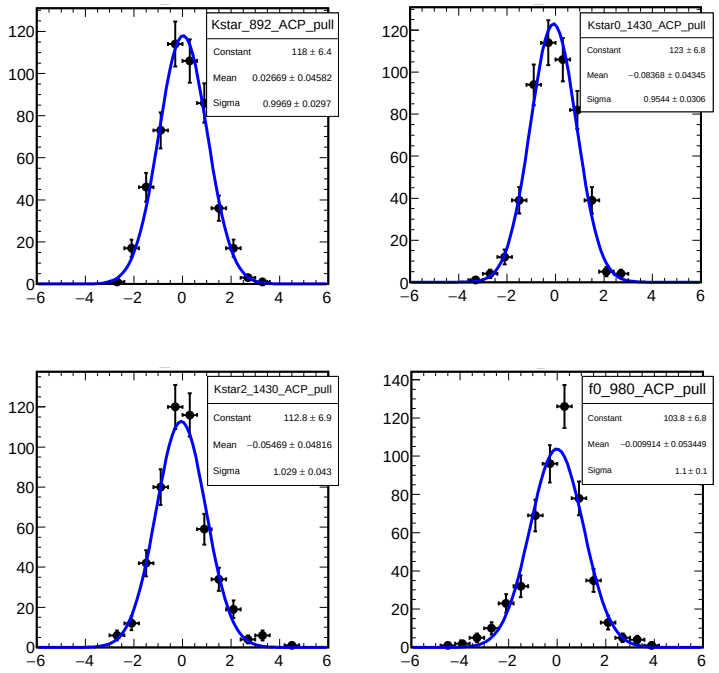

Figure 5.54: *Direct CP asymmetries pull distributions from 500 pseudo-experiments. Each pull distribution is fitted by a Gaussian (blue line).*

5.8 Systematics studies

In this section we address the determination of the systematic uncertainties related to the Dalitz fit of $B^0 \to K^0_S\pi^+\pi^-$. The sources of systematic uncertainties considered in this analysis are divided in two categories. The first is called experimental systematics and gathers the following sources:

- the fraction of signal/background extracted from the invariant mass fit of the candidates,
- the biases related to the Dalitz fit to the data,
- the signal efficiency across the SDP,
- the binning choice for the signal efficiency histograms,
- the combinatorial background model across the SDP.

The second category is Dalitz model uncertainty, and includes:

- the fixed parameters of the resonance line-shapes models;
- the addition or removal of marginal components to the nominal amplitude fit model,
- alternative models for the K^0_S π and $\pi\pi$ S-waves.

5.8.1 Experimental systematic uncertainties

The systematic uncertainties discussed in this Section relies on studies based on pseudo-experiments, in which we build data-equivalent samples for each spectrum which can be fit simultaneously as it is done for the data sample. On a general ground, the method we followed consists in changing (solely) the parameter governing a systematic uncertainty effect according to its uncertainty distribution for each pseudo-experiment and fit back the ensemble of pseudo-experiments with the nominal model. The observed dispersion is taken as the corresponding systematic error estimate.

5.8.1.1 Systematic uncertainty related to the knowledge of the fraction of signal

The $B^0 \to K^0_S\pi^+\pi^-$ signal fraction in the analysed sample is derived from the measured yields of the signal and background components as given by the invariant mass fit. This signal fraction is fixed in the Dalitz plot p.d.f. to its measured central value. In order to evaluate the effect of its uncertainty in the Dalitz plot analysis, an ensemble of 500 pseudo-experiments is built: for each single pseudo-experiment, a new signal fraction is generated such that the ensemble of pseudo-experiments covers its measured uncertainty. The nominal Dalitz plot p.d.f. is then fitted to each pseudo-experiment of the ensemble and the distribution of the difference between the nominal and fitted values (residual) of the parameters of interest is formed. The root mean square (RMS) of the residuals distribution is taken as the systematic uncertainty estimate. The systematic uncertainties on the complex amplitude, fit fraction and CP asymmetry (when applicable) for each component are given in Table 5.10. The corresponding distributions of the residuals are shown in Fig. 5.56, Fig. 5.57 and Fig. 5.58.

Table 5.10: *Systematic uncertainties related to the signal fraction.*

Resonance	Real part	Imag. part	Mag.	Phase	FF (%)	Direct $\mathcal{A}_{CP}$
$K^{*+}(892)$	-	-	-	-	0.063	0.000
$K^{*-}(892)$	0.001	-	0.001	-		
$(K\pi)_0^{*+}$	0.004	0.008	0.007	0.111	0.130	0.000
$(K\pi)_0^{*-}$	0.008	0.004	0.007	0.103		
$K_2^{*+}(1430)$	0.002	0.002	0.002	0.182	0.005	0.002
$K_2^{*-}(1430)$	0.001	0.001	0.001	0.159		
$f_0(980)$ from B^0	0.009	0.012	0.005	0.418	0.094	0.005
$f_0(980)$ from $\overline{B}^0$	0.005	0.005	0.005	0.339		
$f_0(500)$	0.003	0.004	0.002	0.770	0.002	-
$\rho^0(770)$	0.005	0.003	0.001	0.246	0.028	-
$f_0(1500)$	0.007	0.007	0.007	0.371	0.018	-
NR	0.014	0.023	0.025	0.113	0.247	-
χ_{c0}	0.002	0.003	0.003	0.150	0.008	-

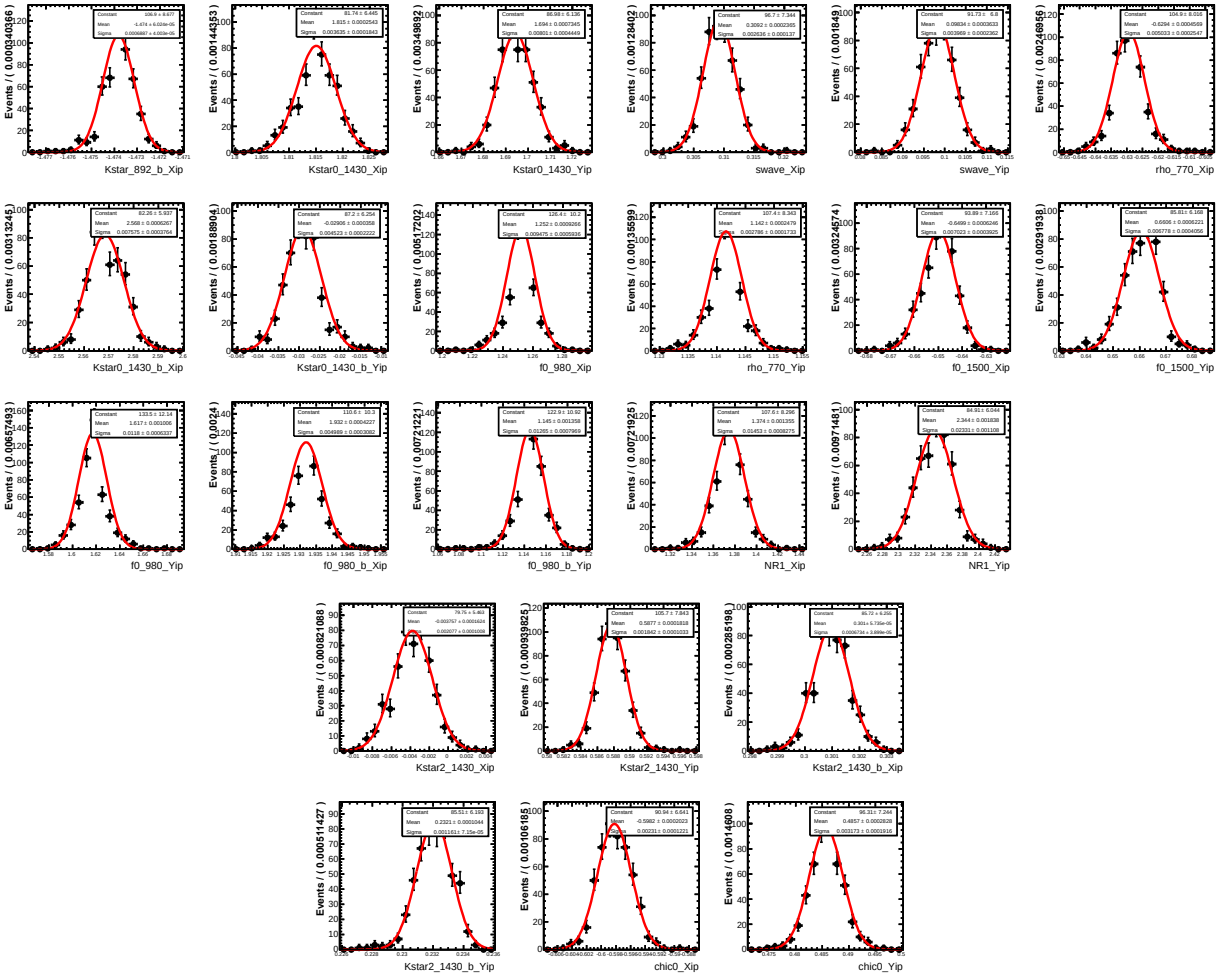

Figure 5.55: *Distribution of the Cartesian parameters from 500 toy-experiments generated by varying the signal fractions within uncertainties, fitted by a Gaussian (red function).*

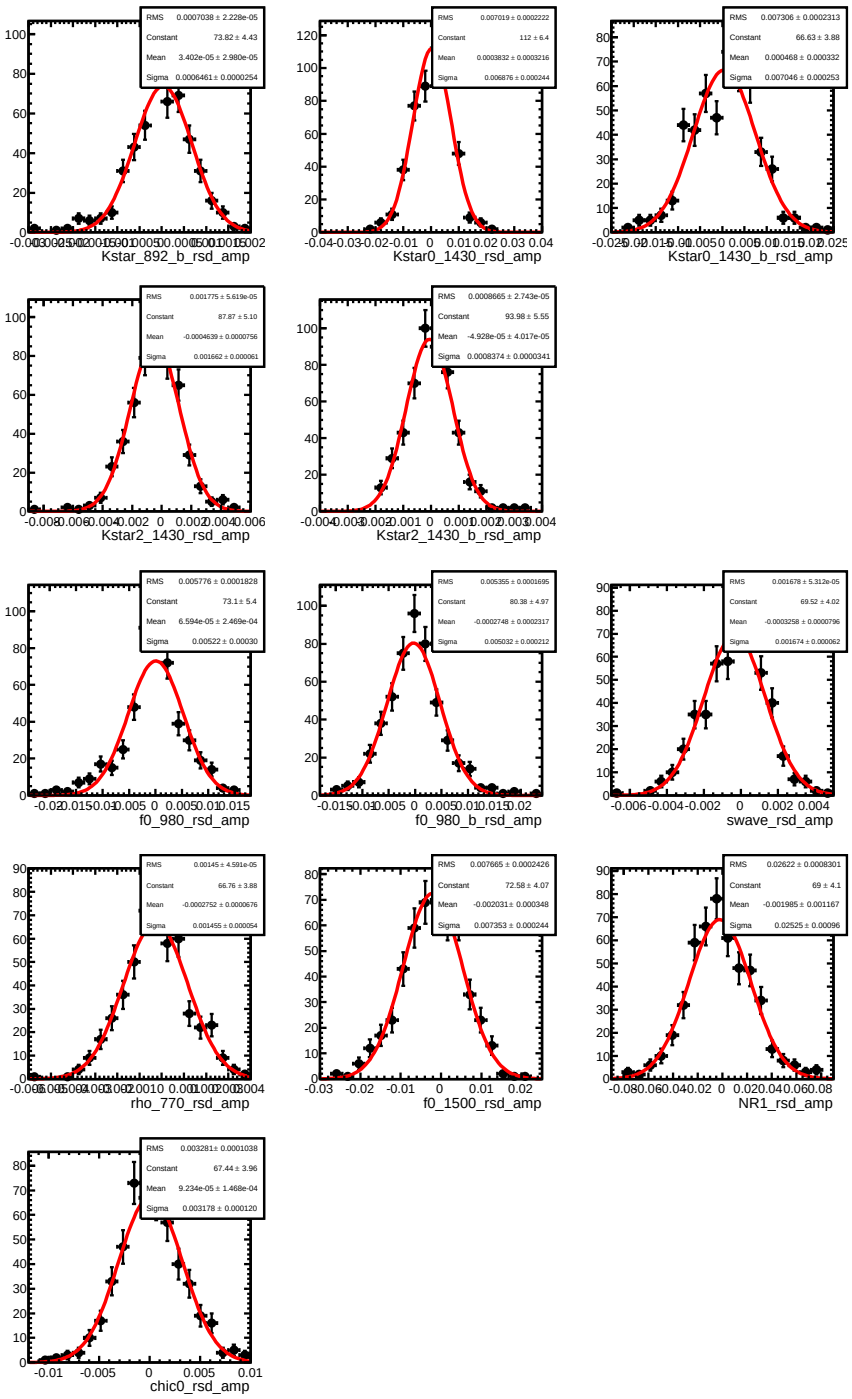

Figure 5.56: *Distribution of the residuals of amplitudes from 500 toy-experiments generated by varying the signal fractions within uncertainties, fitted by a Gaussian (red function).*

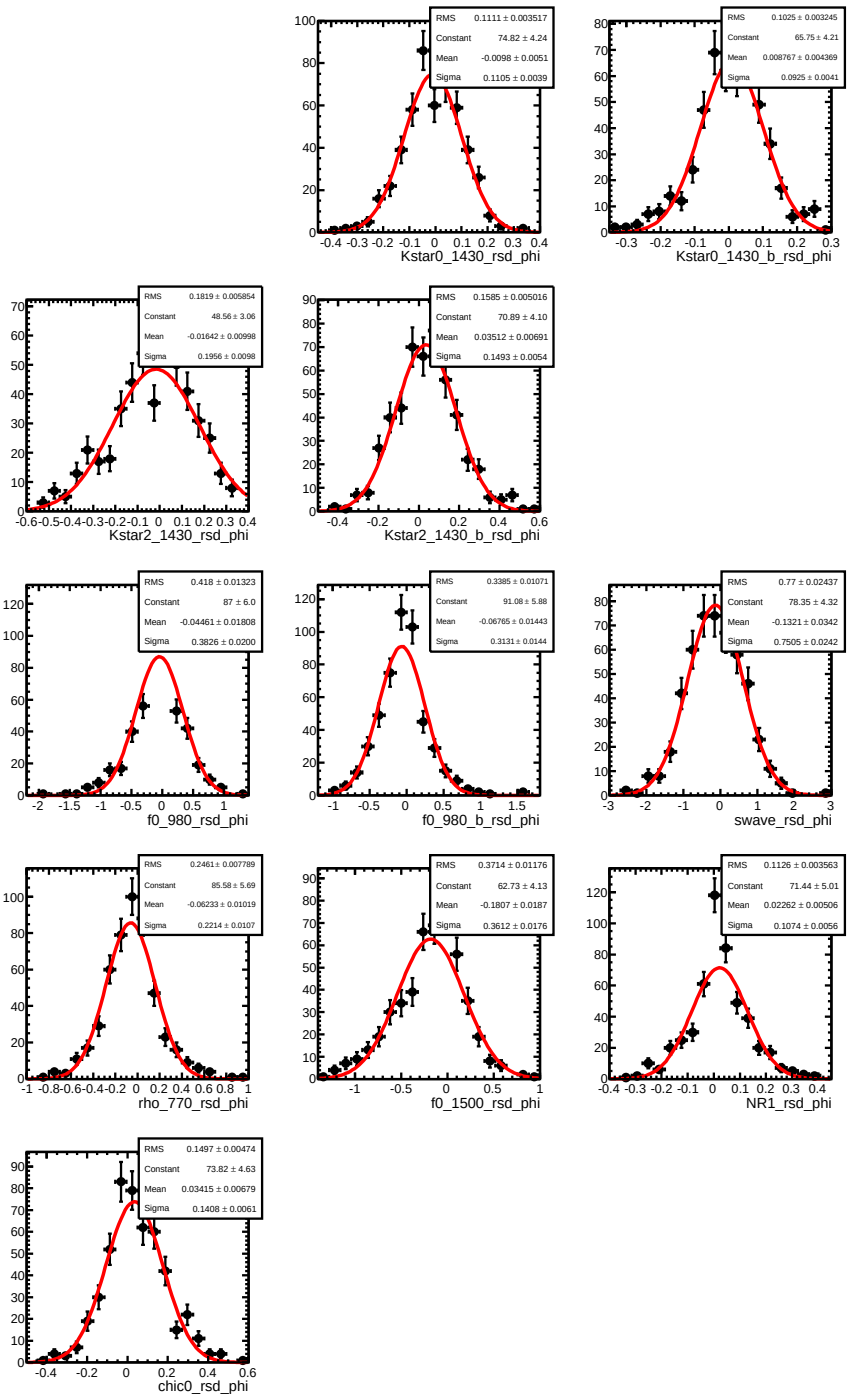

Figure 5.57: *Distribution of the residuals on the phases from 500 toy-experiments generated by varying the signal fractions within uncertainties, fitted by a Gaussian (red function).*

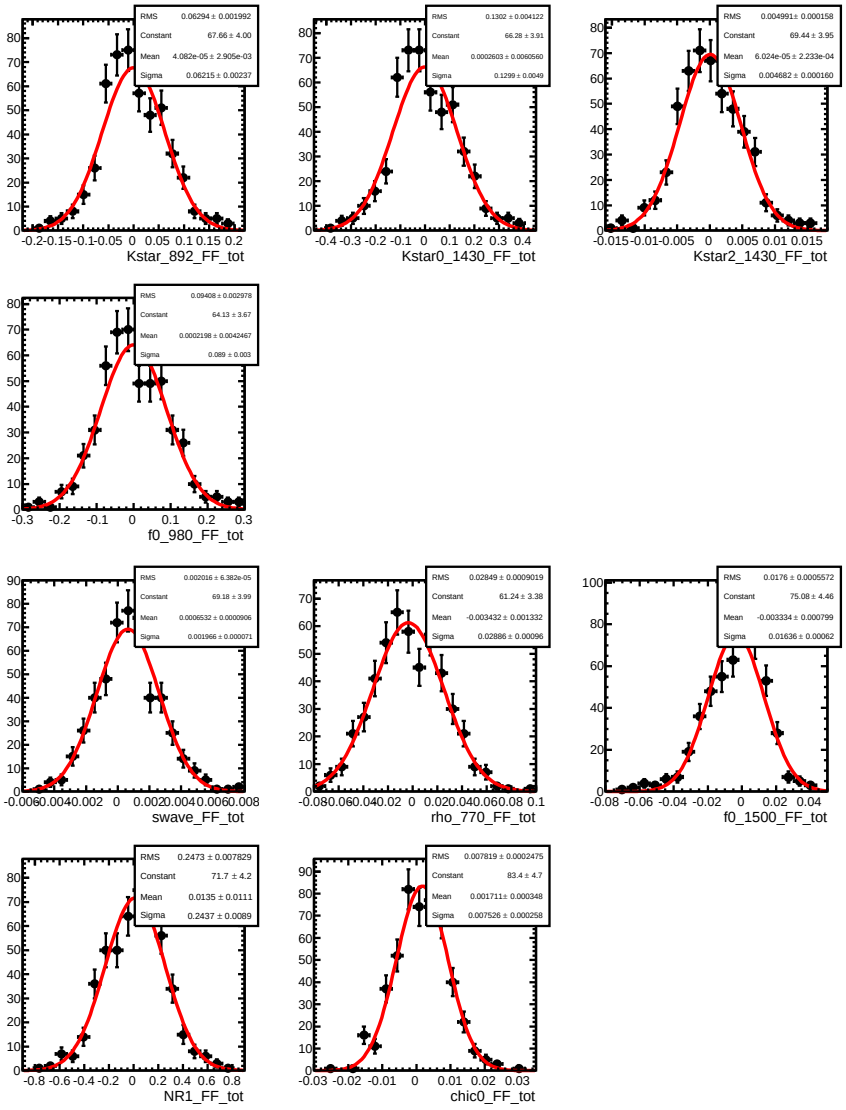

Figure 5.58: *Distribution of the residuals of the fit fractions from 500 toy-experiment generated by varying the signal fractions within uncertainties, fitted by a Gaussian (red function).*

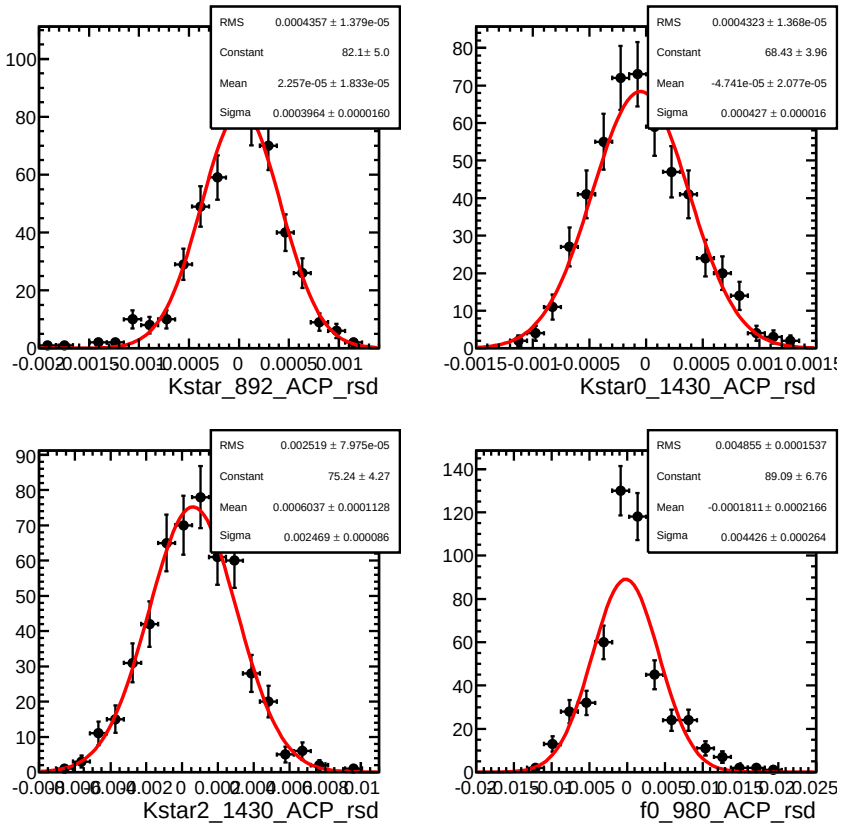

Figure 5.59: *Distribution of the residuals of the direct CP asymmetries from 500 toy-experiment generated by varying the signal fractions within uncertainties, fitted by a Gaussian (red function).*

5.8.1.2 Systematic uncertainties due to DP fit biases

The fit stability was tested by means of a large set of pseudo-experiments generated from the nominal model and varying the yields from one experiment to the other according to their uncertainties. The distributions of the difference between the values of the parameters of interest in the nominal fit and the values obtained from each pseudo-experiment fit have been exploited to evaluate a systematic uncertainty attached to the potential fit biases. The mean value of the residual distribution is used to correct the mean value measured in the data fit (if the difference is significant). The uncertainty on the mean of the residual distribution is assigned as the systematic uncertainty due to the fit bias. The correction of the amplitudes and direct *CP* asymmetry as well as the systematic uncertainties estimates are given in Table 5.11. The distribution of the residuals for all parameters are shown in the figures Fig. 5.60 and Fig. 5.61.

Table 5.11: *Corrective factors applied to the amplitudes and the direct CP asymmetries and associated systematic uncertainty.*

Resonance	Amplitude		Direct *CP* asymmetry	
	Correction	Systematic	Correction	Systematic
$K^{*+}(892)$	-	-	-0.001	0.002
$K^{*-}(892)$	0.000	0.004		
$(K\pi)_0^{*+}$	0.000	0.005	-0.004	0.002
$(K\pi)_0^{*-}$	-0.004	0.005		
$K_2^{*+}(1430)$	0.003	0.005	-0.028	0.012
$K_2^{*-}(1430)$	-0.008	0.004		
$f_0(980)$ from B^0	-0.028	0.019	0.020	0.015
$f_0(980)$ from $\overline{B}^0$	-0.007	0.017		
$f_0(500)$	-0.035	0.005	-	-
$\rho^0(770)$	0.000	0.006	-	-
$f_0(1500)$	-0.007	0.005	-	-
NR	-0.009	0.007	-	-
χ_{c0}	0.007	0.003	-	-

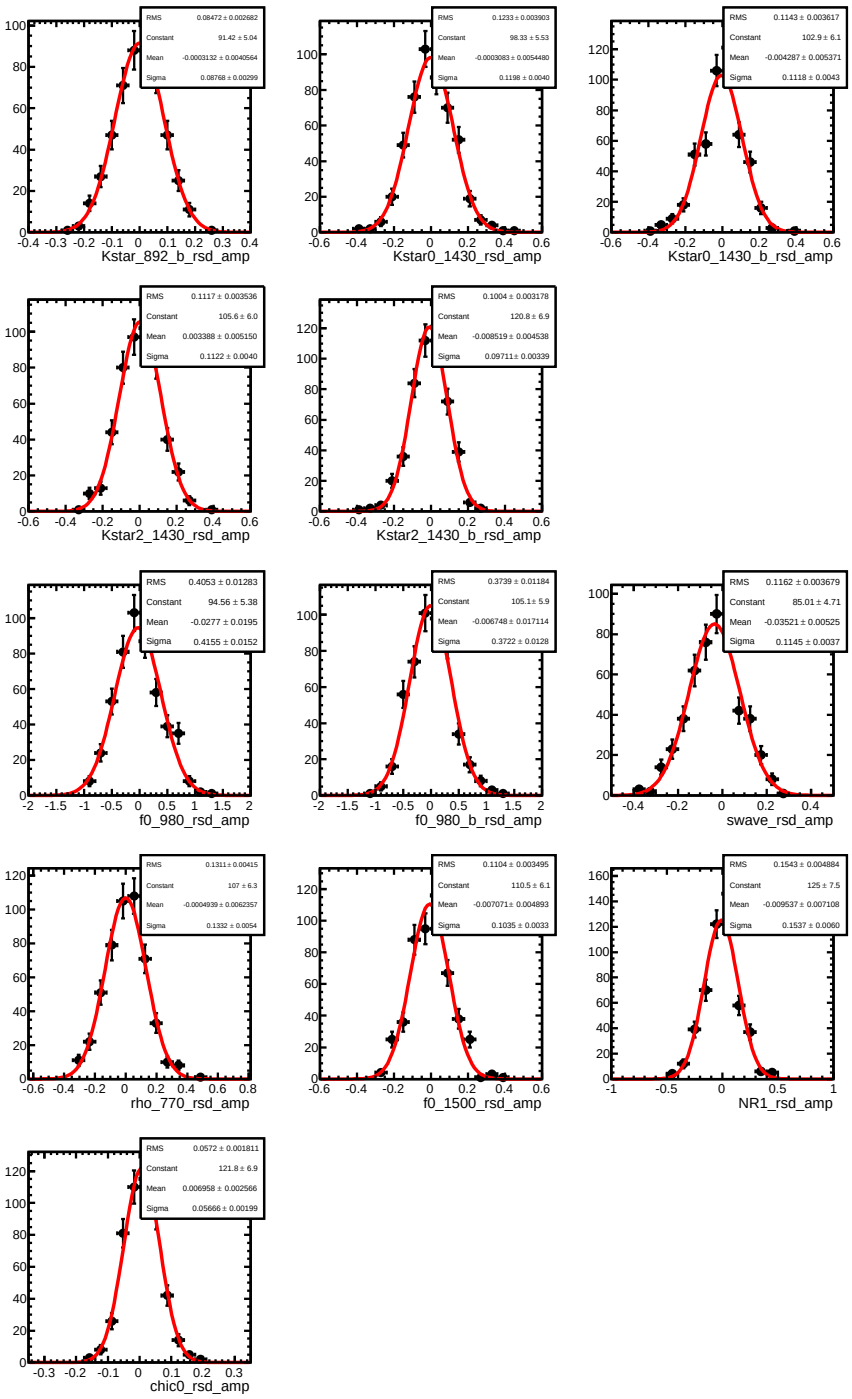

Figure 5.60: *Distribution of the residuals of the amplitudes from 500 pseudo-experiments, measured from the fit bias study. The distribution is fit by a Gaussian (red function).*

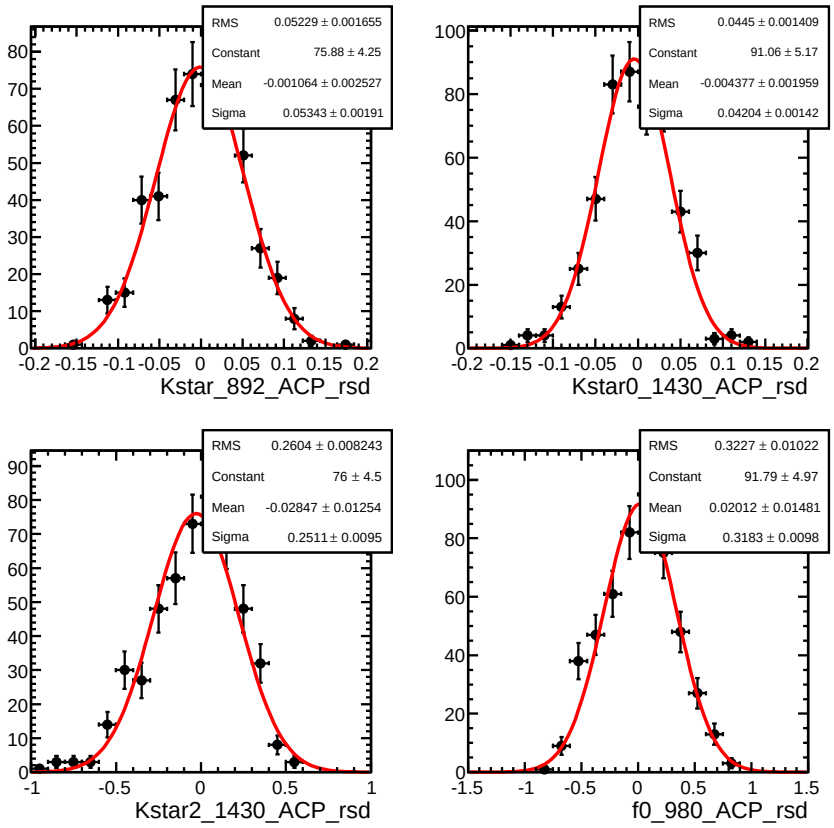

Figure 5.61: *Distribution of the residuals of the direct CP asymmetries from 500 pseudo-experiments, measured from the fit bias study. The distribution is fit by a Gaussian (red function).*

5.8.1.3 Systematic uncertainties from total signal selection, tracking and L0 trigger efficiency

The efficiency maps discussed in Section 5.3 come with an uncertainty due to the statistics of the MC samples. The procedure to evaluate the systematic uncertainties due to the signal efficiency variation across SDP, consists in repeating the nominal fit 500 times, where for each single fit the default efficiency histogram is replaced by another histogram obtained by varying each bin in SDP within its uncertainties. The RMS of the residuals distribution in each fitted parameter is taken as the systematic uncertainty. The very same procedure is applied for the evaluation of the systematic uncertainty due to the tracking and L0 trigger efficiency. The systematic uncertainties on the complex amplitudes, fit fractions and direct *CP* asymmetries are given in Table 5.12 and Table 5.14 for the systematics due to selection efficiency and tracking efficiency knowledge, respectively. The distributions of the residuals are shown in Fig. 5.63, Fig. 5.64 and Fig. 5.65.

Table 5.12: *Systematic uncertainty related to the knowledge of the SDP efficiency due to MC statistics.*

Resonance	Real part	Imag. part	Mag.	Phase	FF (%)	Direct $\mathcal{A}_{CP}$.
$K^{*+}(892)$	-	-	-	-	0.087	0.014
$K^{*-}(892)$	0.022	-	0.022	-		
$(K\pi)_0^{*+}$	0.029	0.032	0.032	0.700	0.182	0.009
$(K\pi)_0^{*-}$	0.030	0.039	0.029	0.844		
$K_2^{*+}(1430)$	0.017	0.017	0.017	1.269	0.007	0.043
$K_2^{*-}(1430)$	0.014	0.020	0.017	2.801		
$f_0(980)$ from B^0	0.072	0.075	0.075	2.024	0.131	0.057
$f_0(980)$ from $\overline{B}^0$	0.063	0.075	0.065	1.790		
$f_0(500)$	0.010	0.017	0.010	2.850	0.013	-
$\rho^0(770)$	0.039	0.030	0.023	1.916	0.227	-
$f_0(1500)$	0.041	0.022	0.024	2.464	0.096	-
NR	0.053	0.029	0.034	1.011	0.339	-
χ_{c0}	0.012	0.012	0.011	0.995	0.042	-

Table 5.13: *Systematic uncertainty related to the knowledge of the tracking efficiency.*

Resonance	Real part	Imag. part	Mag.	Phase	FF (%)	Direct $\mathcal{A}_{CP}$.
$K^{*+}(892)$	-	-	-	-	0.002	0.000
$K^{*-}(892)$	0.001	-	0.001	-		
$(K\pi)_0^{*+}$	0.001	0.001	0.001	0.015	0.004	0.000
$(K\pi)_0^{*-}$	0.001	0.001	0.001	0.026		
$K_2^{*+}(1430)$	0.001	0.001	0.001	0.056	0.000	0.002
$K_2^{*-}(1430)$	0.000	0.001	0.001	0.103		
$f_0(980)$ from B^0	0.001	0.001	0.001	0.030	0.003	0.001
$f_0(980)$ from $\overline{B}^0$	0.001	0.001	0.001	0.033		
$f_0(500)$	0.000	0.000	0.000	0.087	0.000	-
$\rho^0(770)$	0.001	0.001	0.001	0.051	0.005	-
$f_0(1500)$	0.001	0.000	0.001	0.059	0.002	-
NR	0.001	0.001	0.001	0.017	0.007	-
χ_{c0}	0.000	0.000	0.000	0.020	0.001	-

Table 5.14: *Systematic uncertainty related to the knowledge of the L0 trigger efficiency.*

Resonance	Real part	Imag. part	Mag.	Phase (°)	FF (%)	Direct $\mathcal{A}_{CP}$.
$K^{*+}(892)$	-	-	-	-	0.003	0.001
$K^{*-}(892)$	0.001	-	0.001	-		
$(K\pi)_0^{*+}$	0.002	0.001	0.001	0.026	0.007	0.000
$(K\pi)_0^{*-}$	0.001	0.002	0.001	0.045		
$K_2^{*+}(1430)$	0.001	0.001	0.001	0.077	0.000	0.002
$K_2^{*-}(1430)$	0.001	0.001	0.001	0.144		
$f_0(980)$ from B^0	0.001	0.002	0.001	0.035	0.005	0.001
$f_0(980)$ from $\overline{B}^0$	0.001	0.002	0.001	0.036		
$f_0(500)$	0.000	0.001	0.000	0.101	0.000	-
$\rho^0(770)$	0.001	0.001	0.001	0.060	0.006	-
$f_0(1500)$	0.001	0.000	0.001	0.056	0.002	-
NR	0.001	0.001	0.001	0.026	0.011	-
χ_{c0}	0.000	0.000	0.000	0.031	0.001	-

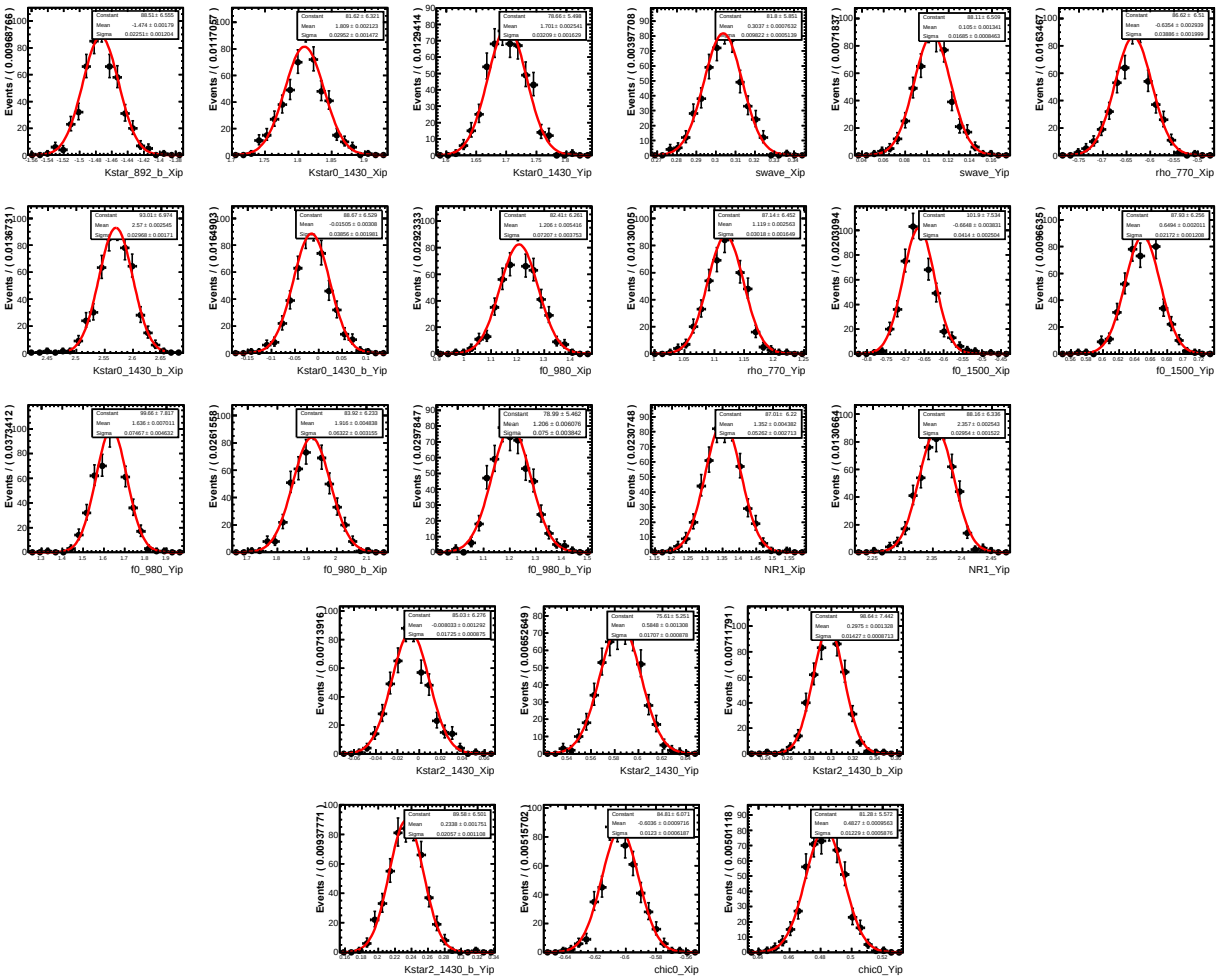

Figure 5.62: *Distributions of the Cartesian parameters for the three data from 500 toy-experiments generated by varying the signal efficiency bins within uncertainties, fitted by a Gaussian (red function).*

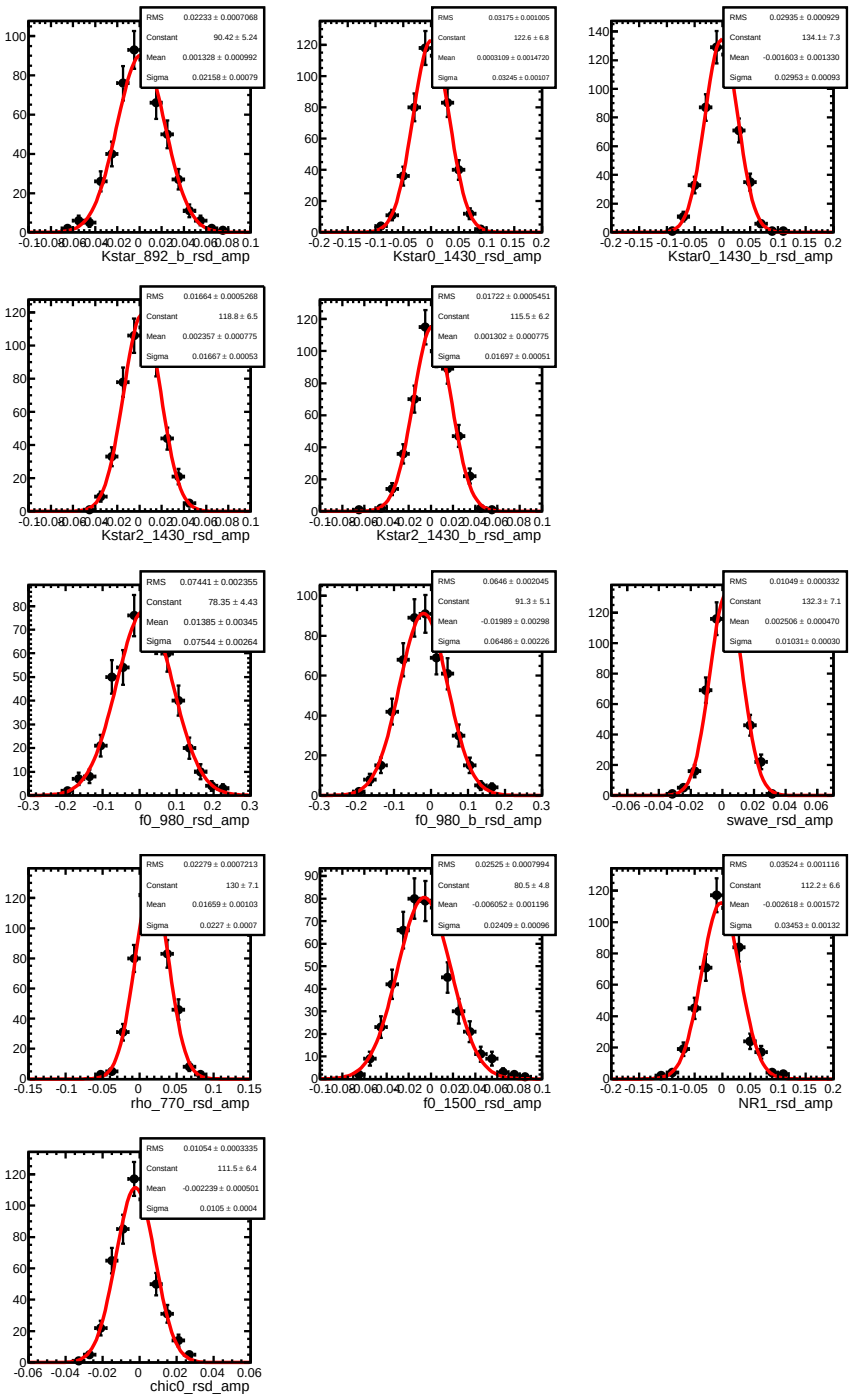

Figure 5.63: *Distributions of the residuals of the isobar amplitudes from 500 toy-experiments generated by varying the signal efficiency within uncertainties, fitted by a Gaussian (red function).*

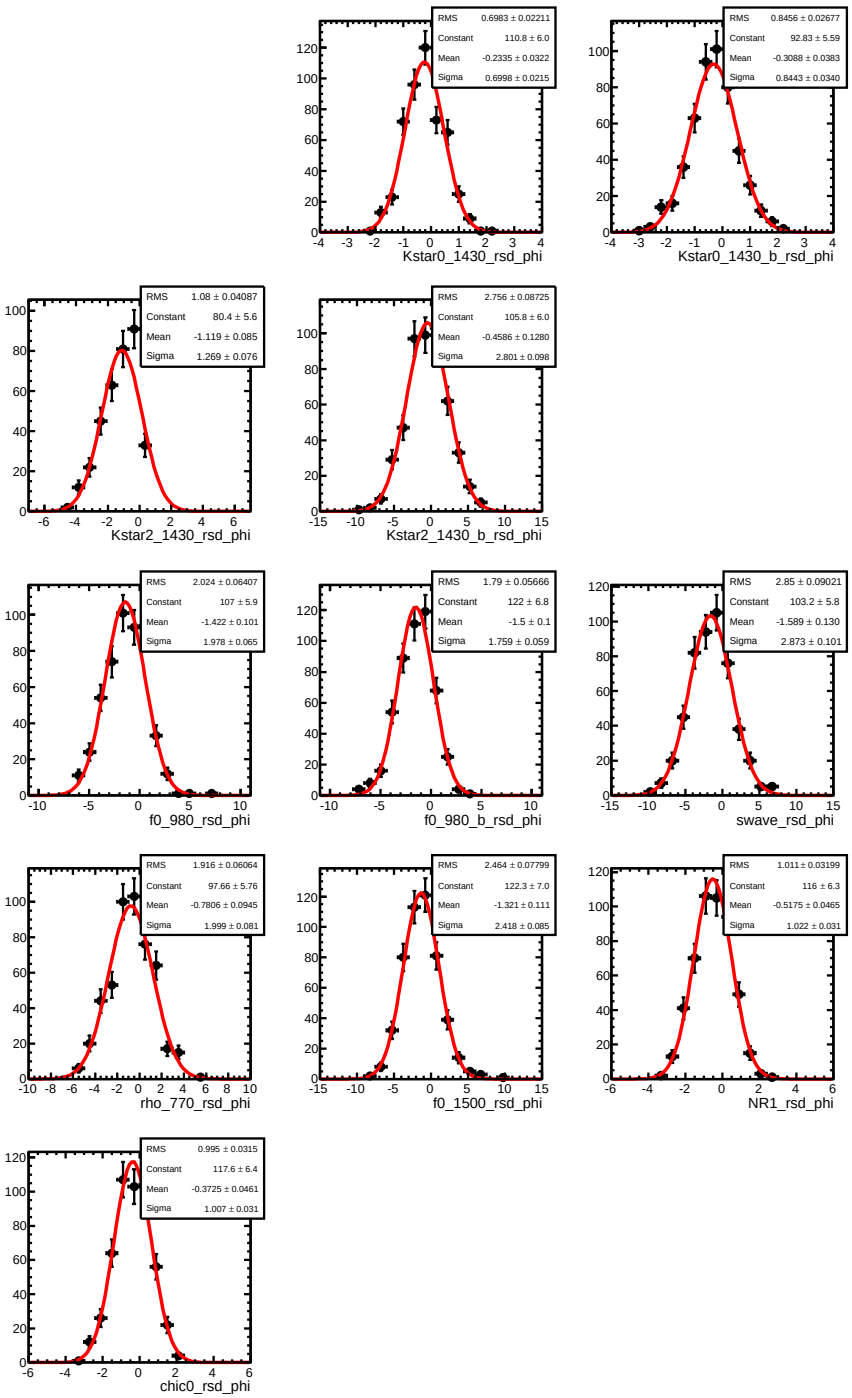

Figure 5.64: *Distributions of the residuals of the isobar phases from 500 toy-experiments generated by varying the signal efficiency bins within uncertainties, fitted by a Gaussian (red function).*

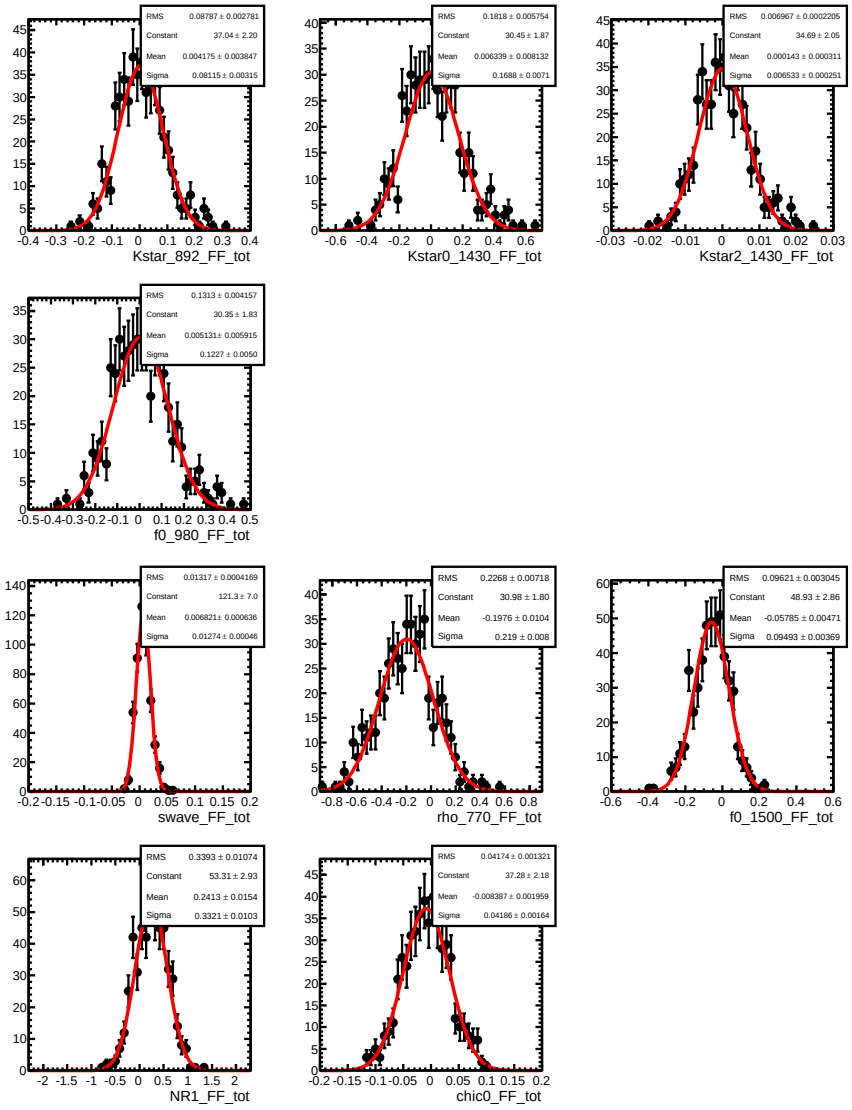

Figure 5.65: *Distributions of the residuals of the fit fractions from 500 toy-experiment generated by varying the signal efficiency bins within uncertainties, fitted by a Gaussian (red function).*

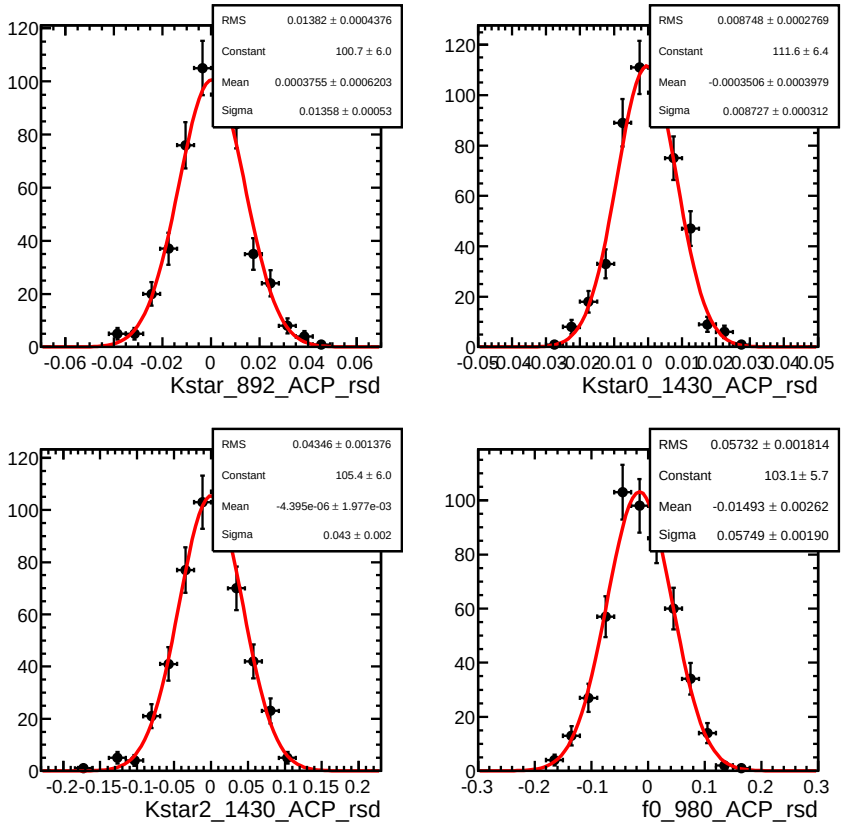

Figure 5.66: *Distributions of the residuals of the direct CP asymmetries from 500 toy-experiment generated by varying the signal efficiency bins within uncertainties, fitted by a Gaussian (red function).*

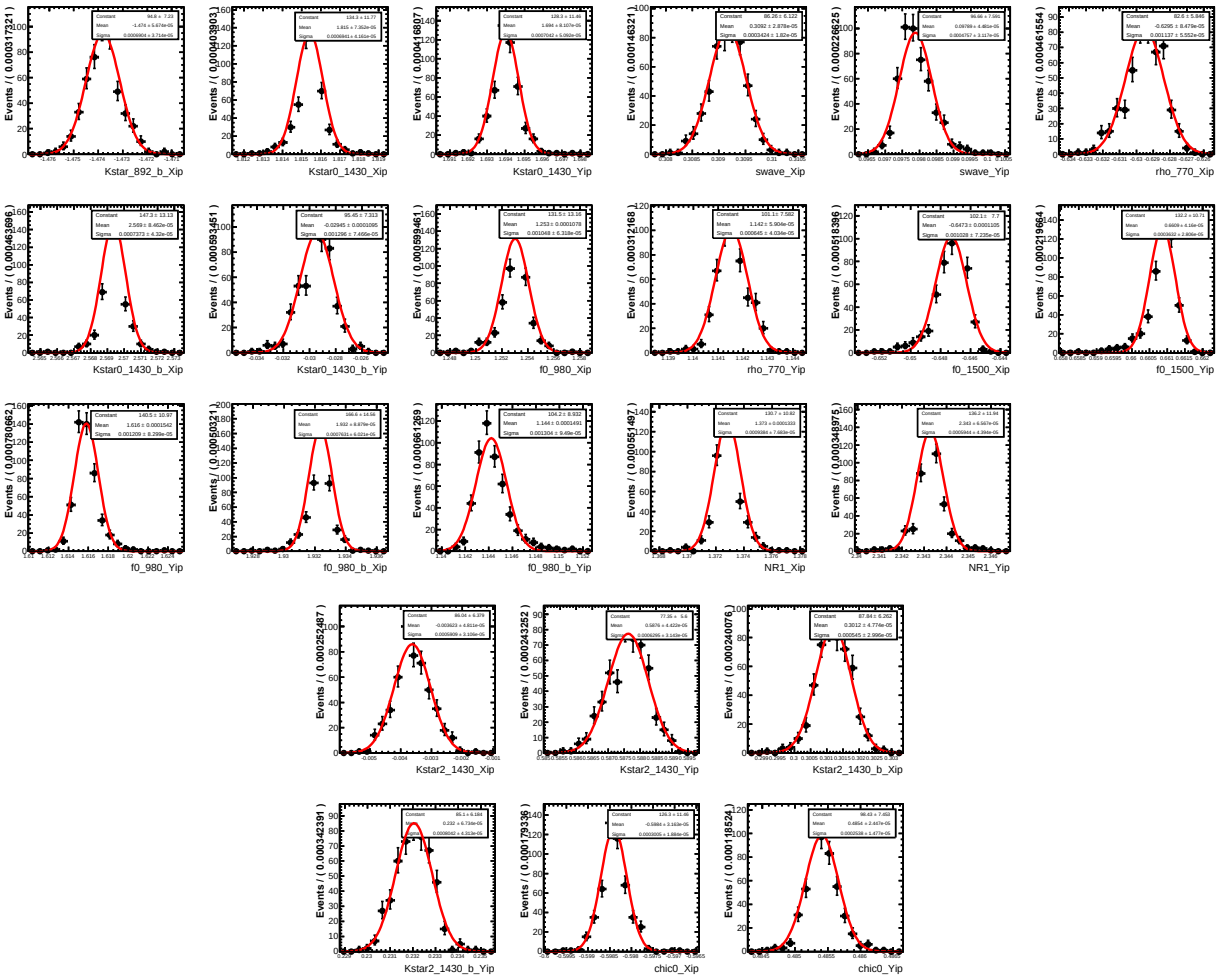

Figure 5.67: *Distribution of the Cartesian parameters from 500 toy-experiments generated by varying the tracking efficiency bins within uncertainties, fitted by a Gaussian (red function).*

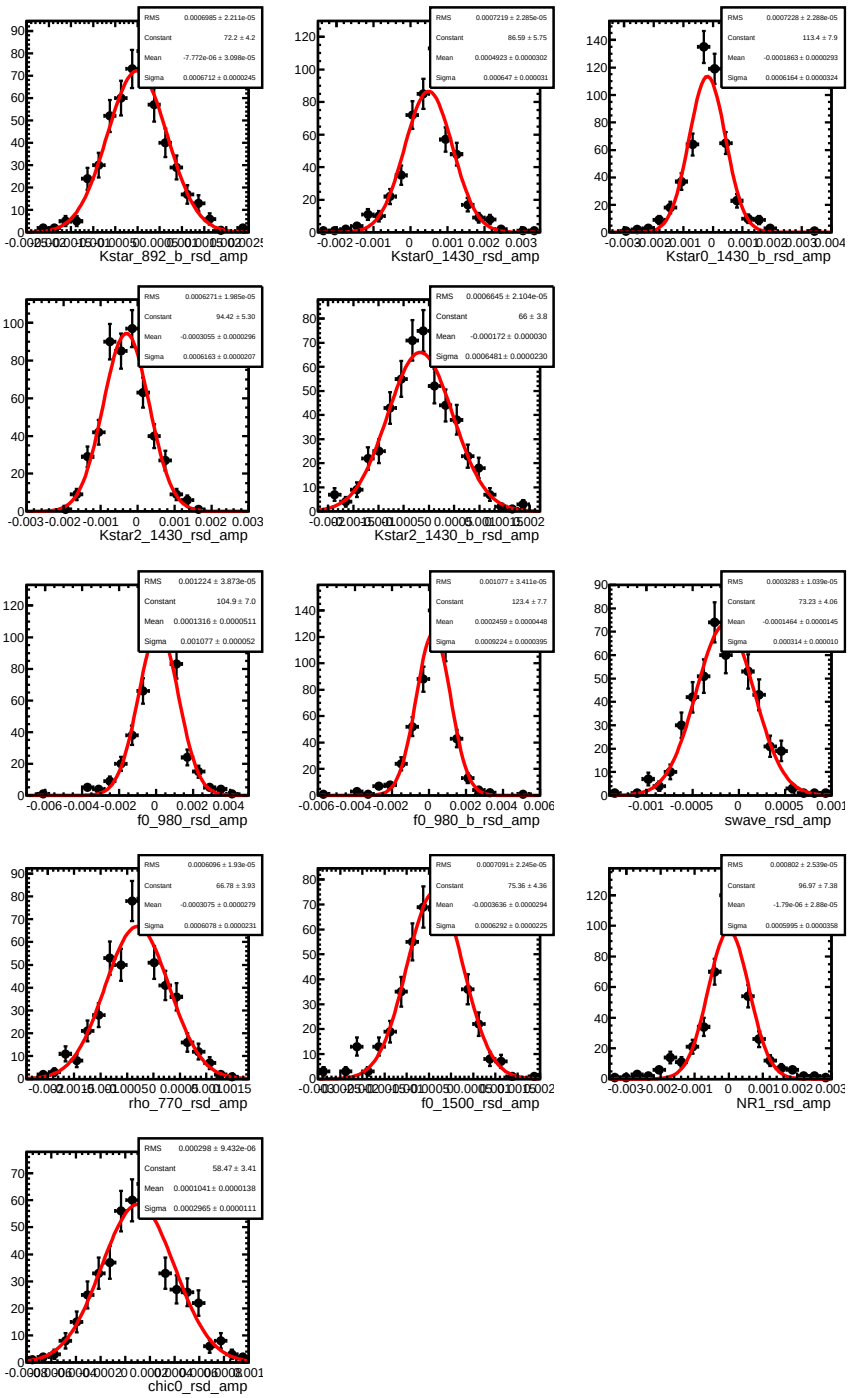

Figure 5.68: *Distributions of the residuals of the isobar amplitudes from 500 toy-experiments generated by varying the tracking efficiency bins within uncertainties, fitted by a Gaussian (red function).*

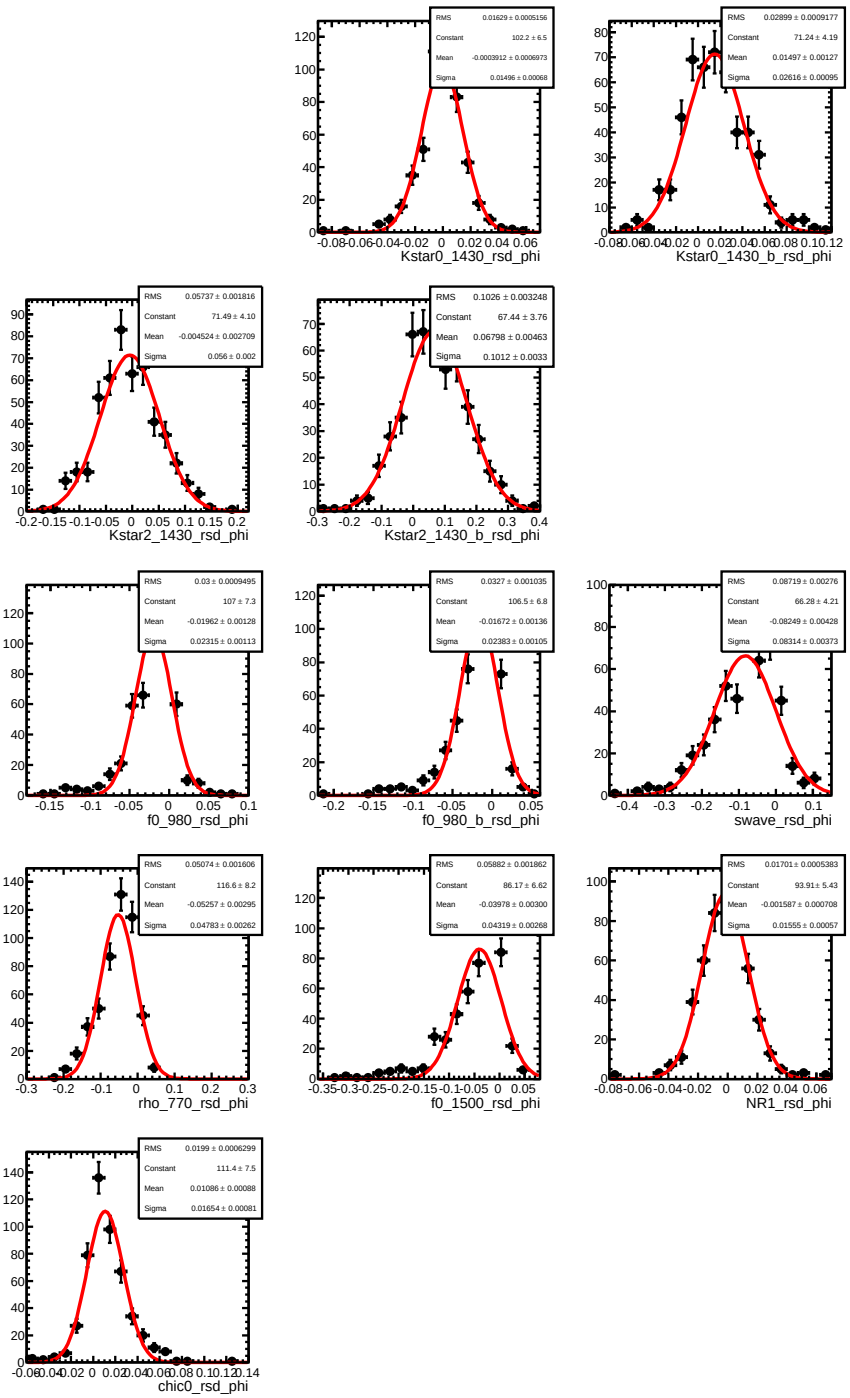

Figure 5.69: *Distributions of the residuals of the isobar phases from 500 toy-experiments generated by varying the tracking efficiency bins within uncertainties, fitted by a Gaussian (red function).*

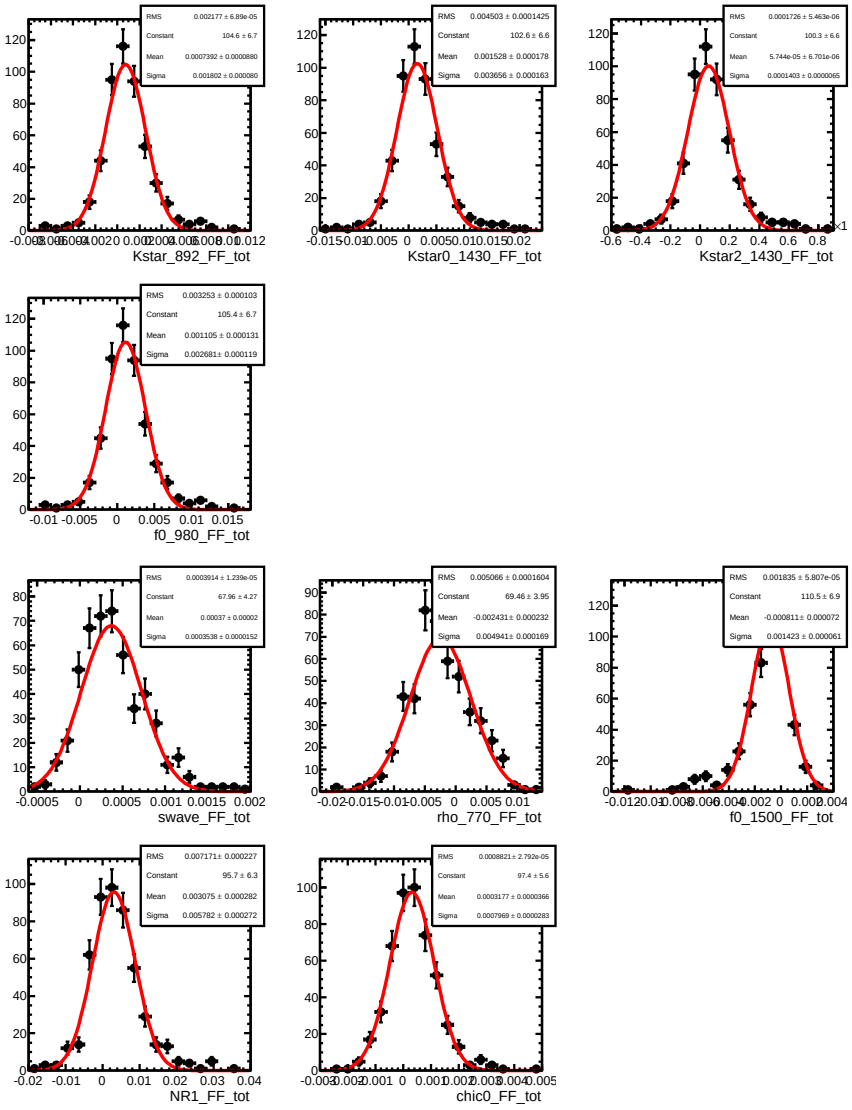

Figure 5.70: *Distributions of the residuals of the fit fractions from 500 toy-experiment generated by varying the tracking efficiency bins within uncertainties, fitted by a Gaussian (red function).*

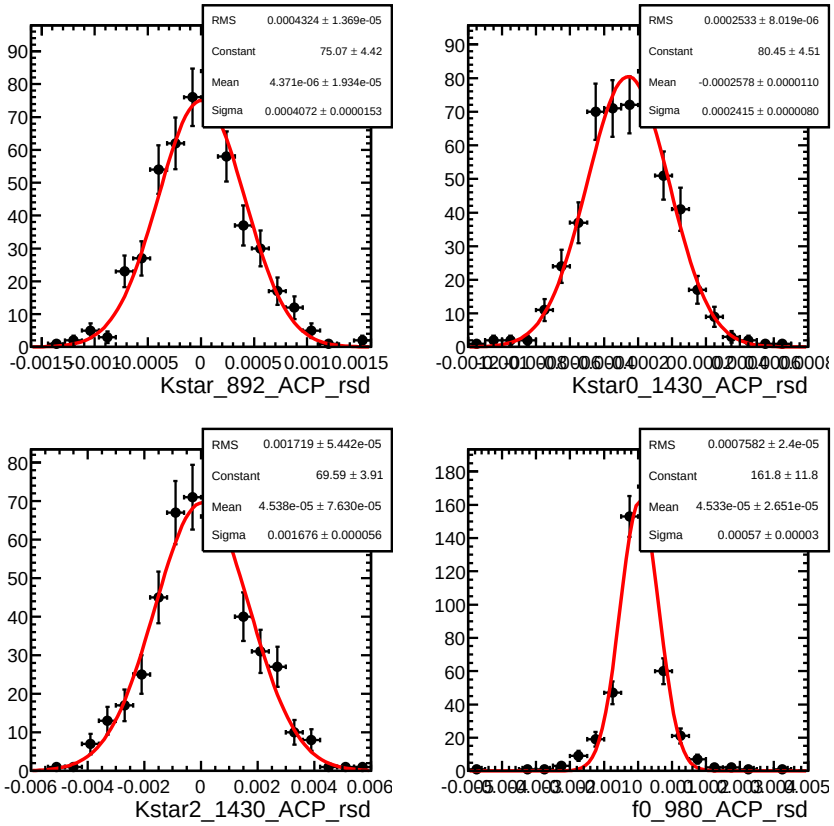

Figure 5.71: *Distributions of the residuals of the direct CP asymmetries from 500 toy-experiment generated by varying the tracking efficiency bins within uncertainties, fitted by a Gaussian (red function).*

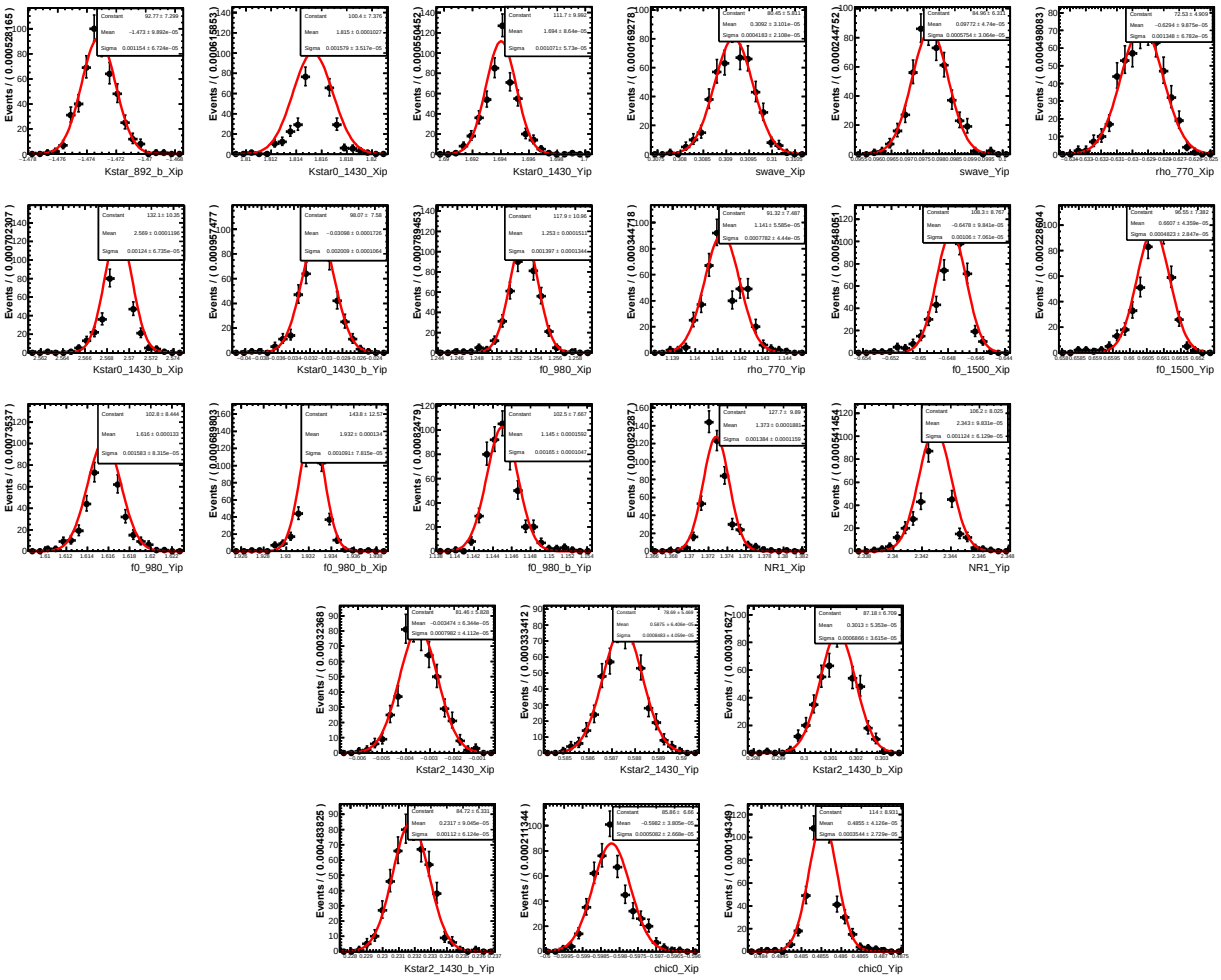

Figure 5.72: *Distribution of the Cartesian parameters from 500 toy-experiments generated by varying the L0 trigger efficiency bins within uncertainties, fitted by a Gaussian (red function).*

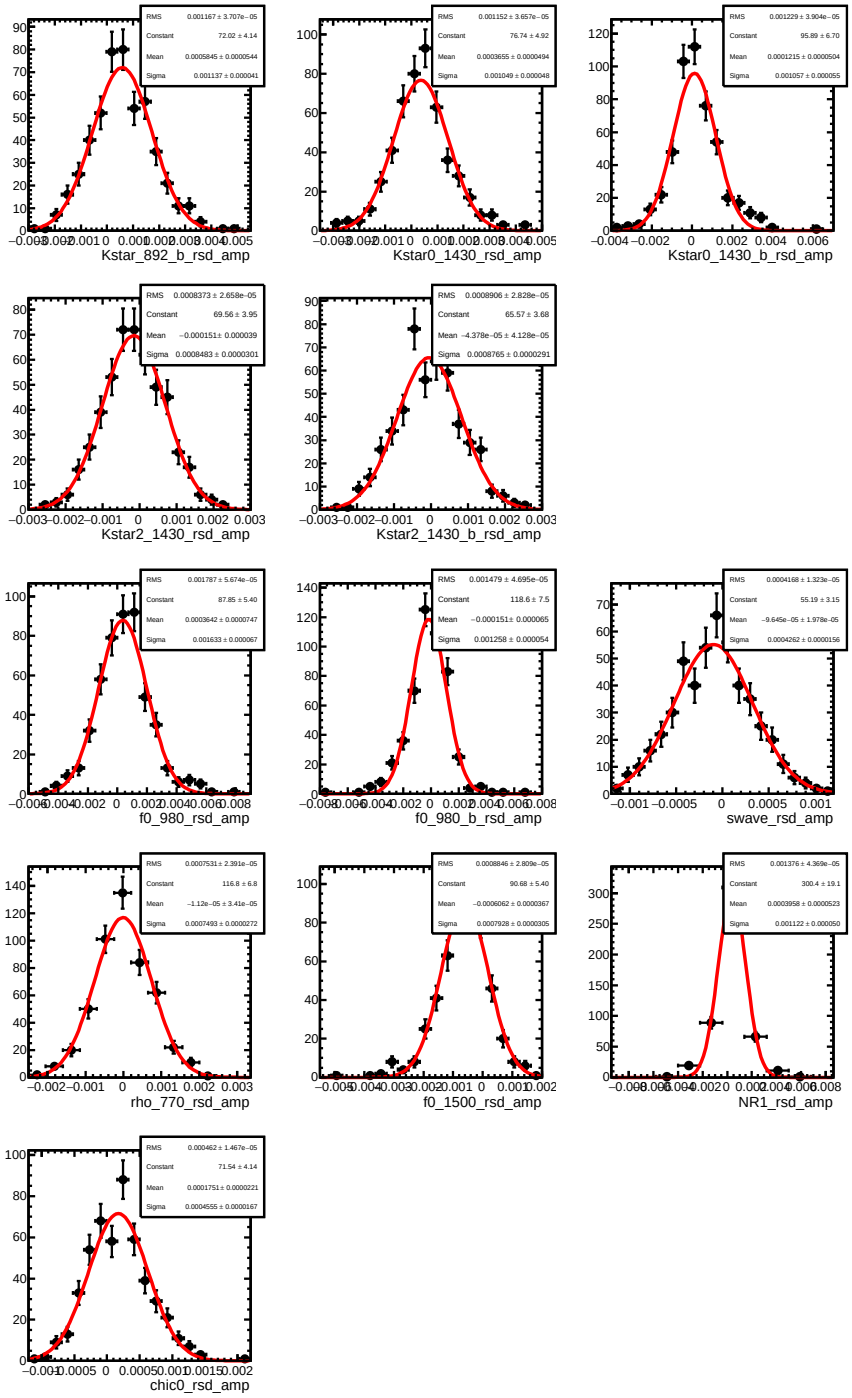

Figure 5.73: *Distributions of the residuals of the isobar amplitudes from 500 toy-experiments generated by varying the L0 trigger efficiency bins within uncertainties, fitted by a Gaussian (red function).*

On top of the MC statistics and tracking uncertainties, there is an additional systematic uncertainty related to the choice of the SDP binning to produce the efficiency maps. The table 5.15 gathers estimates of the systematic uncertainties obtained by varying the binning

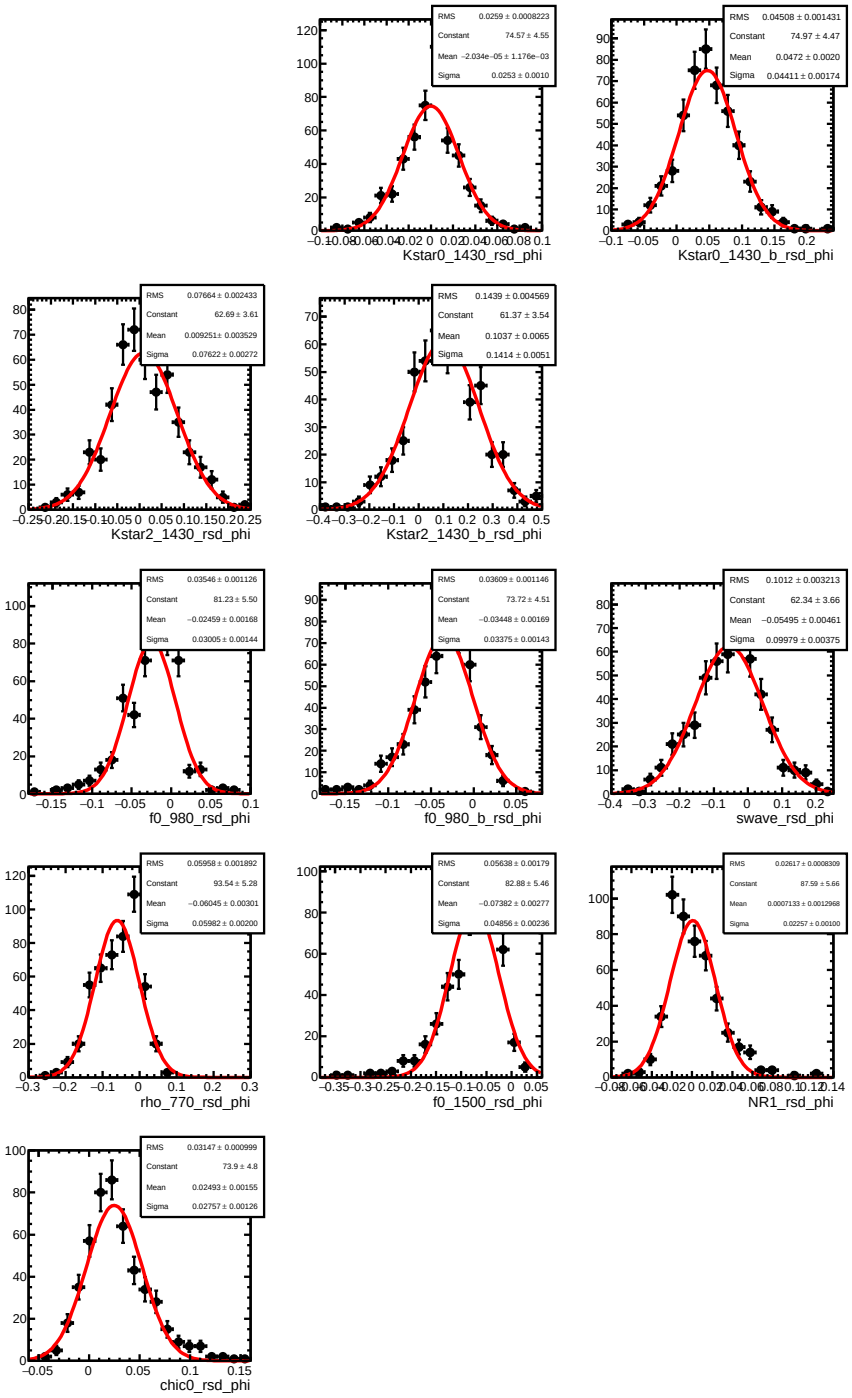

Figure 5.74: *Distributions of the residuals of the isobar phases from 500 toy-experiments generated by varying the L0 trigger efficiency bins within uncertainties, fitted by a Gaussian (red function).*

from 64 bins to 100 bins in the SDP. This estimate is believed to be very conservative. The current estimate of this efficiency binning systematic is dominating some of the experimental magnitude and fit fractions uncertainties.

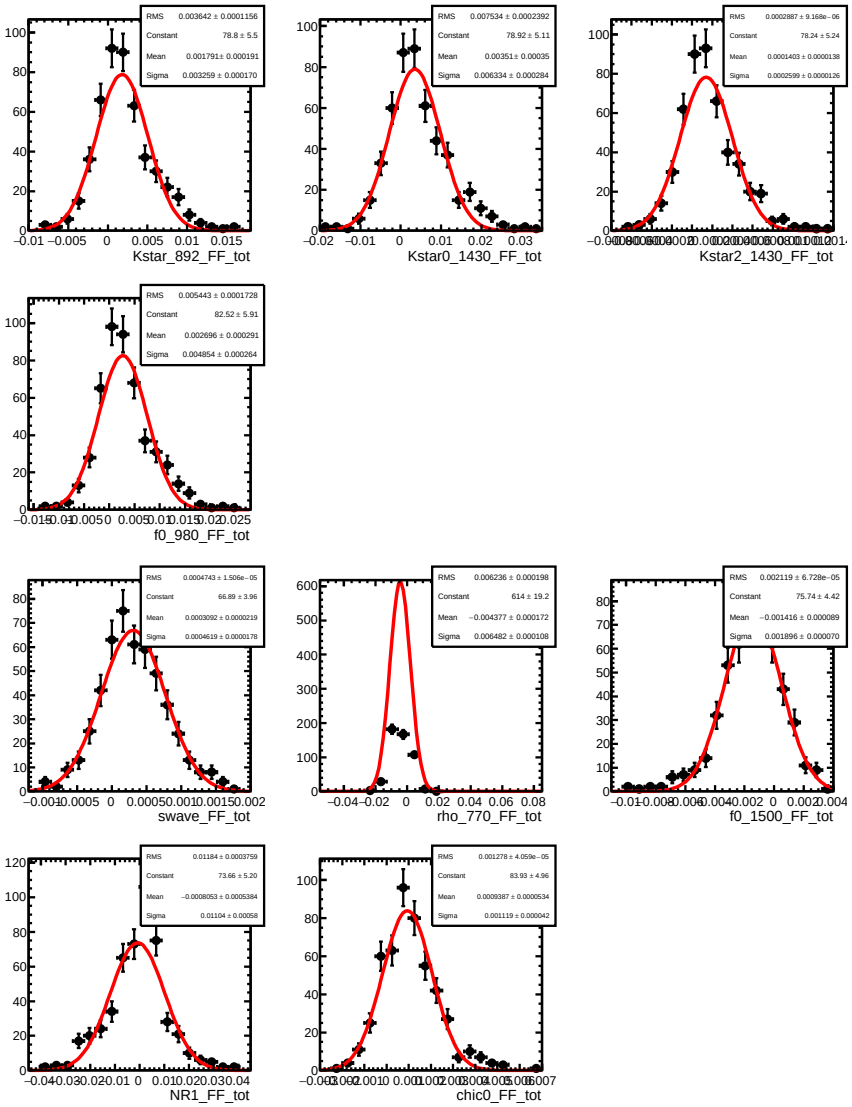

Figure 5.75: *Distributions of the residuals of the fit fractions from 500 toy-experiment generated by varying the L0 trigger efficiency bins within uncertainties, fitted by a Gaussian (red function).*

5.8.1.4 Systematic uncertainty from combinatorial background

The background distribution in this Dalitz analysis is intentionally small in reason of the choice of the so-called tight optimisation. As a consequence, its modelling from the right-hand side-band of the invariant mass distribution on the amplitude measurements has expectedly a limited impact. The very same procedure employed for the estimate of the systematics due to the knowledge of the efficiencies is at work. The histograms describing the combinatorial background distributions are each varied within statistical uncertainties to generate 500 pseudo-experiments. Each of them is fit back with the nominal model and the RMS of the subsequent distribution of residuals is used to assign the systematic uncertainty. The systematic uncertainties on the parameters of interest are given in Table 5.16. The distributions of

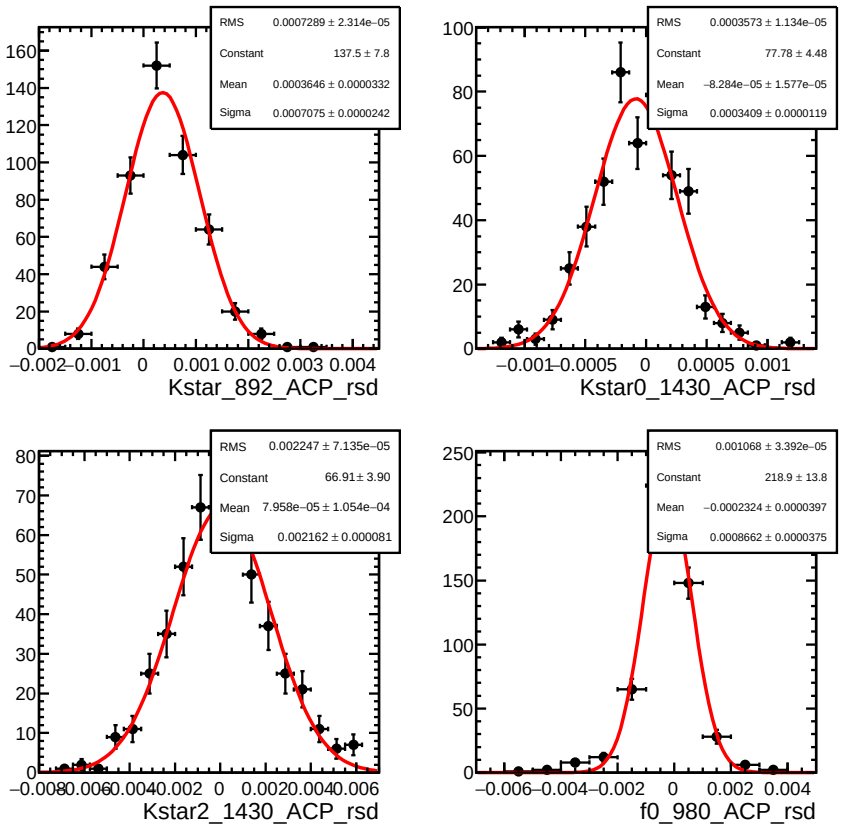

Figure 5.76: *Distributions of the residuals of the direct CP asymmetries from 500 toy-experiment generated by varying the L0 trigger efficiency bins within uncertainties, fitted by a Gaussian (red function).*

the residuals are shown in Fig. 5.77, Fig. 5.78 and Fig. 5.79.

5.8.1.5 Systematic uncertainty from cross-feed background

The fractions of the cross-feed background for each sample category are given in Table 4.26. They are found to be small and were not included in the nominal fit for this thesis work. However, the assumption that they can be neglected has been considered as a systematic uncertainty source. A fit has been done including this time the cross-feed components and the difference observed in the final results was assigned as a systematic uncertainty. The projections on the invariant mass square variables of the nominal fit including the cross-feed components are given in Fig. 5.81 and the related systematic uncertainties on the parameters of interest are gathered in Table 5.17. It can be noted that these systematic uncertainties are among the largest experimental systematics uncertainties. It is therefore foreseen that the publication includes the cross-feed components in the nominal DP model. The remaining uncertainty will hence be given by the knowledge of the cross-feed shape and is expected to be greatly reduced.

Table 5.15: *Systematic uncertainty related to the choice of a binning to produce the efficiency maps.*

Resonance	Real part	Imag. part	Mag.	Phase	FF (%)	Direct $\mathcal{A}_{CP}$.
$K^{*+}(892)$	-	-	-	-	0.200	0.003
$K^{*-}(892)$	0.005	-	0.005	-		
$(K\pi)_0^{*+}$	0.010	0.108	0.065	2.033	0.260	0.054
$(K\pi)_0^{*-}$	0.071	0.071	0.072	1.524		
$K_2^{*+}(1430)$	0.008	0.065	0.066	0.679	0.174	0.034
$K_2^{*-}(1430)$	0.025	0.008	0.025	1.251		
$f_0(980)$ from B^0	0.093	0.054	0.012	3.006	1.190	0.081
$f_0(980)$ from $\overline{B}^0$	0.150	0.097	0.179	0.174		
$f_0(500)$	0.052	0.010	0.045	5.201	0.108	-
$\rho^0(770)$	0.039	0.034	0.049	0.754	0.387	-
$f_0(1500)$	0.115	0.025	0.096	4.485	0.672	-
NR	0.142	0.020	0.051	2.848	1.440	-
χ_{c0}	0.027	0.019	0.010	2.326	0.022	-

Table 5.16: *Estimates of the systematic uncertainty due to the modelling of the combinatorial background.*

Resonance	Magnitude	Phase	Fit fraction (%)	Direct *CP* asymm.
$K^{*+}(892)$	-	-	0.055	0.002
$K^{*-}(892)$	0.003	-		
$(K\pi)_0^{*+}$	0.010	0.703	0.114	0.005
$(K\pi)_0^{*-}$	0.011	0.548		
$K_2^{*+}(1430)$	0.009	0.352	0.004	0.013
$K_2^{*-}(1430)$	0.005	0.818		
$f_0(980)$ from B^0	0.042	2.318	0.082	0.037
$f_0(980)$ from $\overline{B}^0$	0.043	2.622		
$f_0(500)$	0.008	2.652	0.013	-
$\rho^0(770)$	0.004	1.563	0.126	-
$f_0(1500)$	0.065	6.689	0.164	-
NR	0.021	0.902	0.174	-
χ_{c0}	0.004	0.960	0.041	-

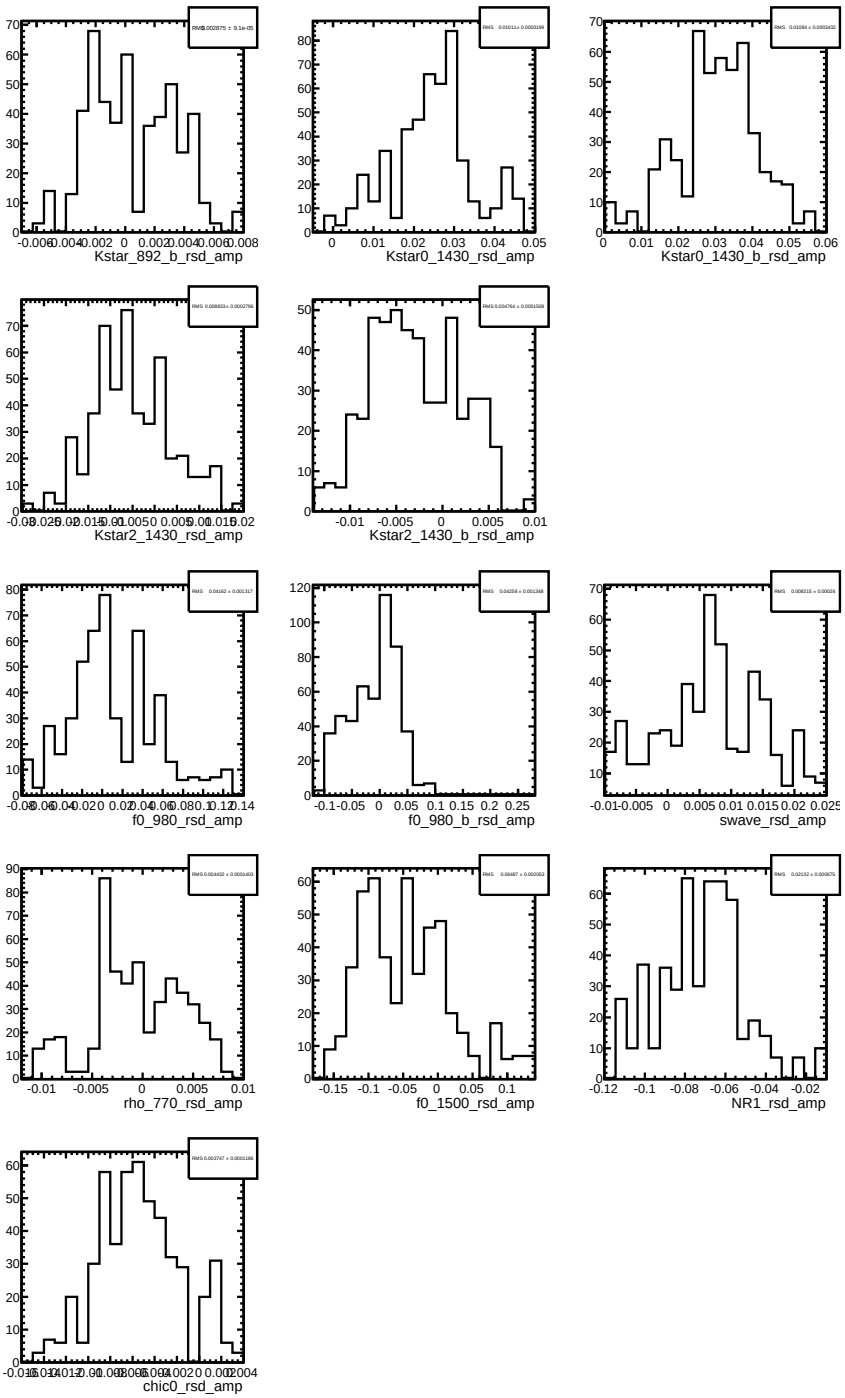

Figure 5.77: *Distributions of the residuals of the isobar amplitudes from 500 toy-experiments generated by varying the combinatorial histogram bins within uncertainties.*

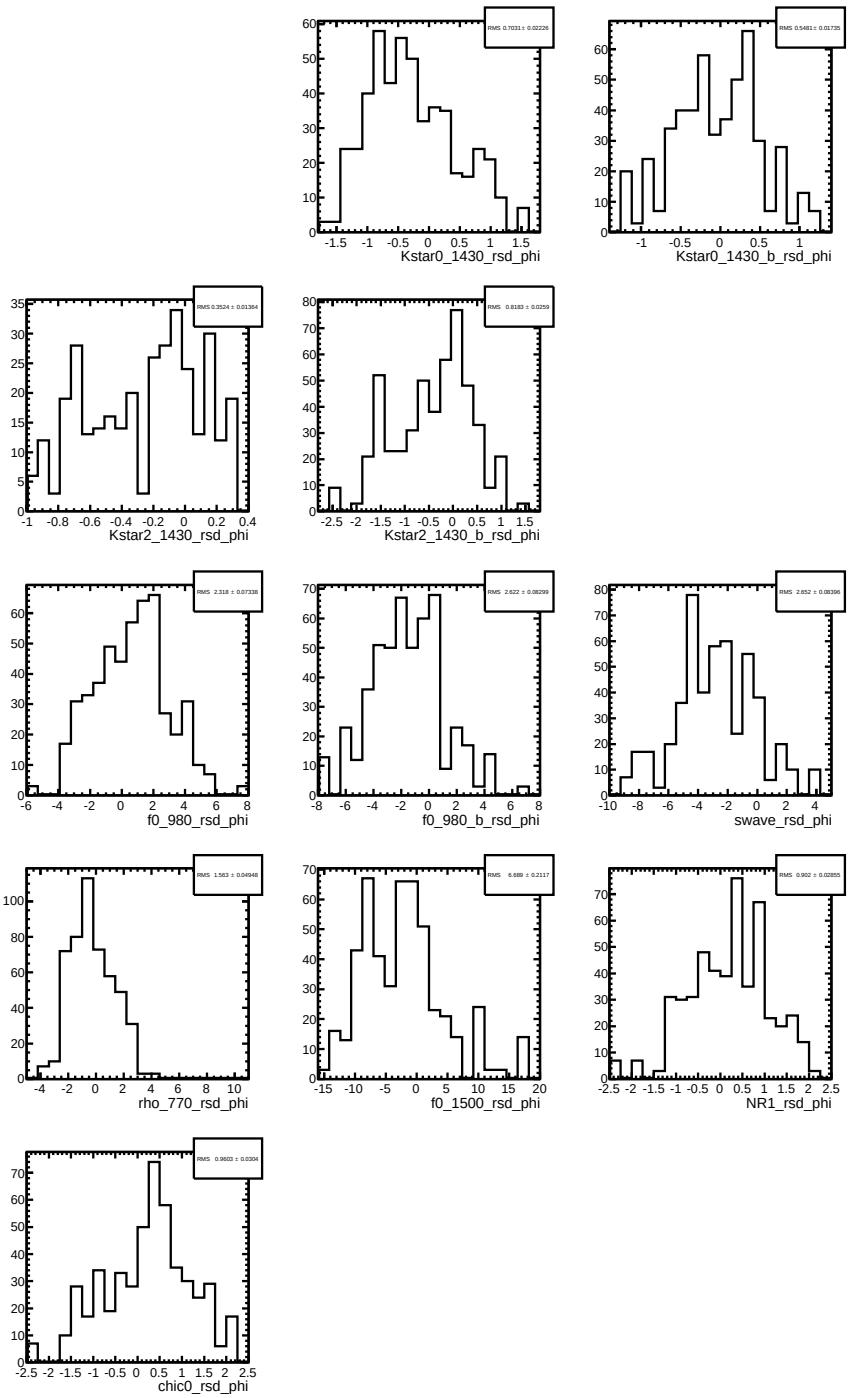

Figure 5.78: *Distributions of the residuals of the isobar phases from 500 toy-experiments generated by varying the combinatorial histogram bins within uncertainties.*

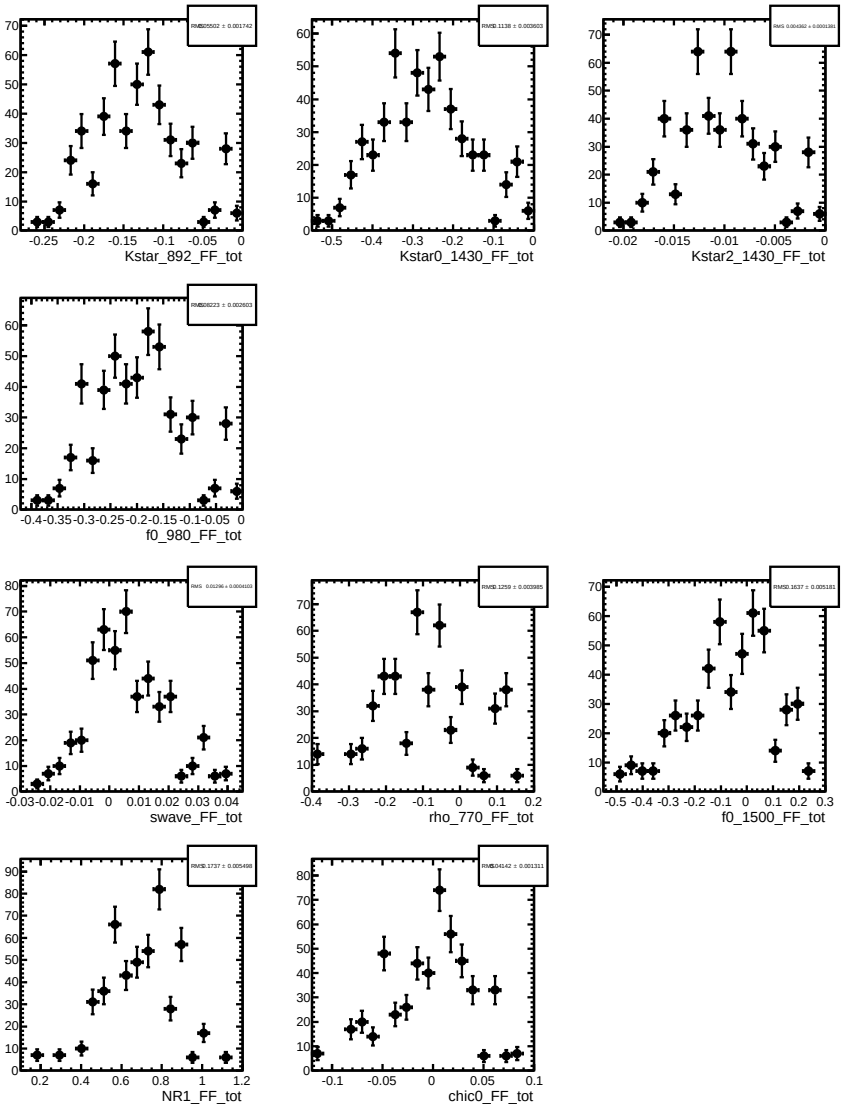

Figure 5.79: *Distributions of the residuals of the fit fractions from 500 toy-experiment generated by varying the combinatorial histogram bins within uncertainties.*

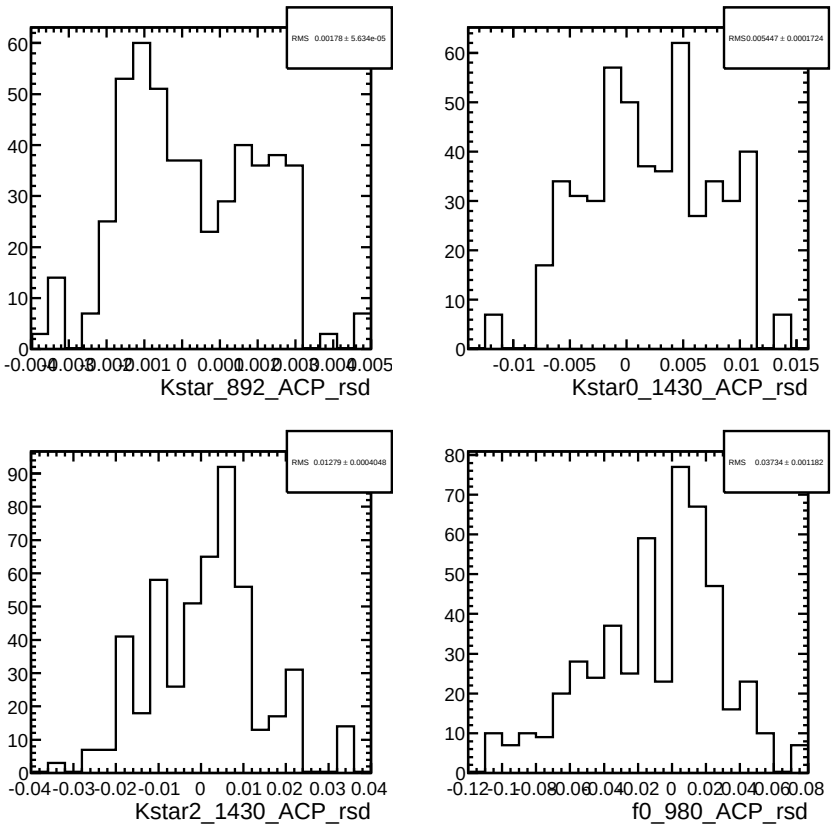

Figure 5.80: *Distributions of the residuals of the direct CP asymmetries from 500 toy-experiment generated by varying the combinatorial histogram bins within uncertainties.*

Table 5.17: *Estimates of the systematic uncertainty due to the addition of the cross-feed components.*

Resonance	Magnitude	Phase	Fit fraction (%)	Direct *CP* asymm.
$K^{*+}(892)$	-	-	0.230	0.004
$K^{*-}(892)$	0.006	-		
$(K\pi)_0^{*+}$	0.016	1.044	0.630	0.015
$(K\pi)_0^{*-}$	0.024	0.392		
$K_2^{*+}(1430)$	0.003	0.840	0.029	0.027
$K_2^{*-}(1430)$	0.010	0.318		
$f_0(980)$ from B^0	0.037	0.170	0.560	0.023
$f_0(980)$ from $\overline{B}^0$	0.014	7.855		
$f_0(500)$	0.013	10.463	0.043	-
$\rho^0(770)$	0.003	0.379	0.110	-
$f_0(1500)$	0.056	2.777	0.313	-
NR	0.090	2.757	1.220	-
χ_{c0}	0.004	1.811	0.027	-

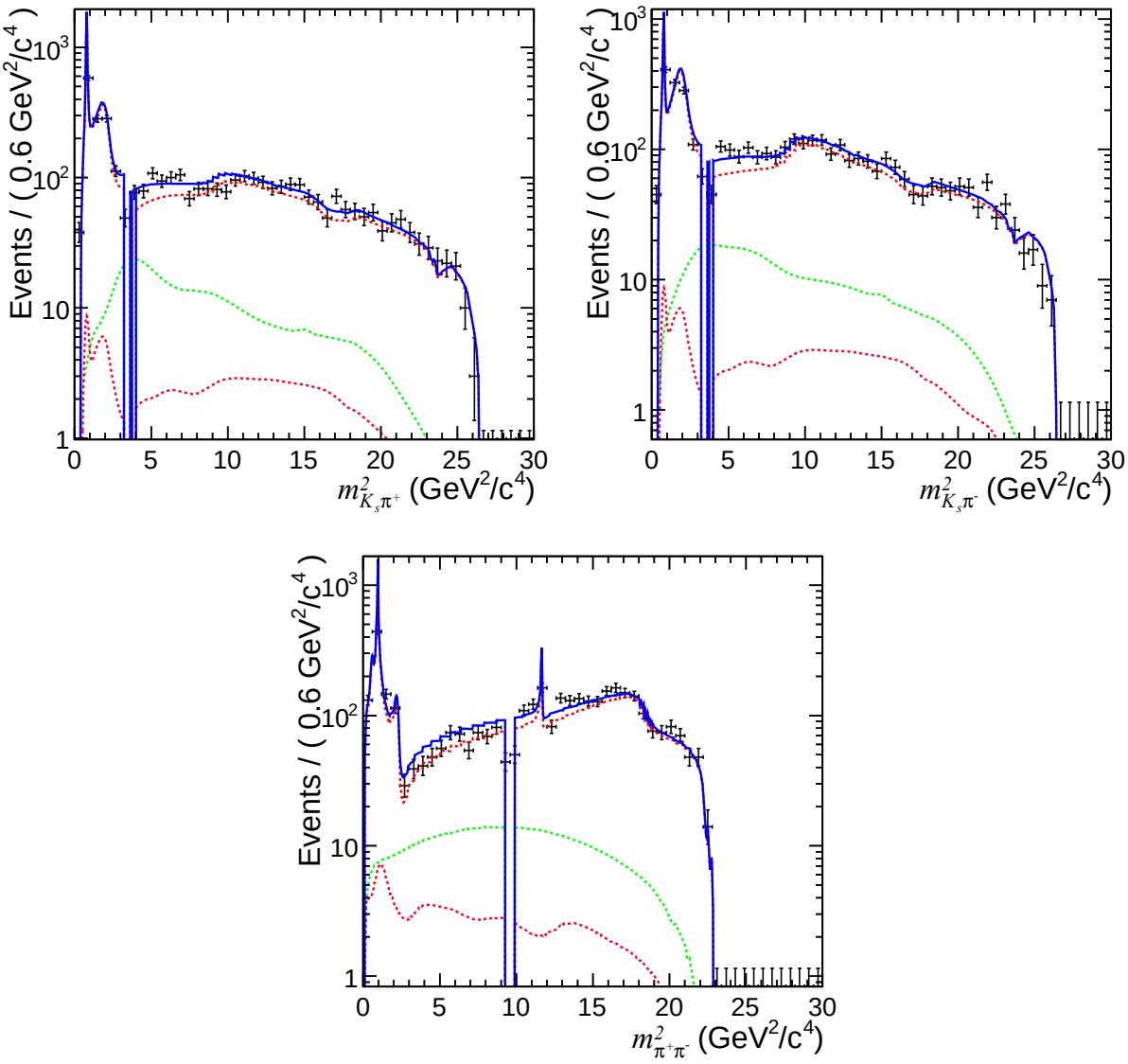

Figure 5.81: *Projections of the sum of all data category (black points) and the nominal fit, with a zoomed view, onto $m^2_{K^0_S\pi^+}$ (left), $m^2_{K^0_S\pi^-}$ (right) and $m^2_{\pi^+\pi^-}$ (bottom). The full fit is shown in blue, combinatorial background in green, cross-feed background in pink and signal model in red.*

5.8.1.6 Summary of experimental systematic uncertainties

The experimental systematic uncertainties due to the above-mentioned error sources described in Section 5.8.1 are combined in quadrature to form the total experimental systematic uncertainty. The dominant sources of error are the MC statistics to determine the efficiency, the choice of the binning and the absence of the cross-feed components in the nominal DP model. The table Table 5.18 gathers them for the isobar amplitudes, fit fractions and direct *CP* violation asymmetries.

Table 5.18: *Summary of experimental systematic uncertainties.*

Resonance	Mag.	Phase	FF (%)	Direct $\mathcal{A}_{CP}$.
$K^{*+}(892)$	-	-	0.328	0.015
$K^{*-}(892)$	0.024	-		
$(K\pi)_0^{*+}$	0.076	2.494	0.726	0.057
$(K\pi)_0^{*-}$	0.082	1.870		
$K_2^{*+}(1430)$	0.069	1.714	0.176	0.064
$K_2^{*-}(1430)$	0.033	3.197		
$f_0(980)$ from B^0	0.096	4.325	1.624	0.109
$f_0(980)$ from $\overline{B}^0$	0.196	8.481		
$f_0(500)$	0.050	12.340	0.117	-
$\rho^0(770)$	0.055	2.624	0.480	-
$f_0(1500)$	0.131	8.876	0.766	-
NR	0.114	4.191	1.941	-
χ_{c0}	0.016	3.260	0.068	-

5.8.2 Model systematic uncertainties

The systematic uncertainties related to the isobar model definition comprise:

- The impact of fixed line-shape parameters in the Dalitz plot model. For instance, the masses and widths of the resonances entering in the DP model are fixed to values determined in previous experiments and the uncertainties attached to their measurements must be addressed as a systematic uncertainty.

- The effect of the addition or removal of marginal amplitudes: several components of the isobar model have been hypothesized and we defined a tentatively objective algorithm to select or reject them from the nominal fit model. If a component is close to the limit but accepted, a model systematic uncertainty is assigned by removing it from the fit. Conversely, if a component was rejected, a model systematic uncertainty is assigned by adding it to the nominal fit model.

- The choices of the models for the controversial $K\pi$ and $\pi\pi$ S-wave components have been questioned and systematic uncertainties have been estimated. For illustration,

the $(K\pi)_0^*$ component, modelled in the nominal fit by a LASS parameterisation has been changed to a simple RBW dedicated for $K_0^*(1430)$ resonance. As far as $(\pi\pi)_0^0$ S-wave component is concerned, the reduced K-matrix parameterisation is used and a fraction of non-resonant component in it is varied to estimate the related model systematic uncertainty.

The uncertainties due to all of these sources are combined in quadrature to form the total model systematic uncertainties. Each source of uncertainty will be examined in more details in the following subsections.

5.8.2.1 Systematic uncertainties related to fixed parameters in the isobar line-shape models

To evaluate the impact of the fixed parameters of the isobar resonances line-shapes, we vary individually and symmetrically by one standard deviation the mass and the width of each resonance as they are given in the Table 5.1. The observed deviation in the measurements is reported as a systematic uncertainty. The Blatt-Weisskopf radius parameter is varied by ± 1 GeV^{-1} and the observed differences between this fit and the nominal fit is assigned as a systematic uncertainty. The individual systematic uncertainties are then added in quadrature to form the total uncertainty related to the fixed parameters in the isobar model. The total systematic uncertainties are gathered in the Tab Table 5.19.

Table 5.19: *Systematic uncertainties due to the fixed line-shape parameters.*

Resonance	Real part	Imag. part	Mag.	Phase	FF (%)	Direct $\mathcal{A}_{CP}$.
$K^{*+}(892)$	-	-	-	-	0.201	0.004
$K^{*-}(892)$	0.007	-	0.006	-		
$(K\pi)_0^{*+}$	0.047	0.053	0.025	1.528	0.291	0.016
$(K\pi)_0^{*-}$	0.035	0.058	0.036	1.275		
$K_2^{*+}(1430)$	0.036	0.015	0.014	3.494	0.032	0.026
$K_2^{*-}(1430)$	0.013	0.021	0.008	3.469		
$f_0(980)$ from B^0	0.168	0.222	0.114	7.009	1.013	0.057
$f_0(980)$ from $\overline{B}^0$	0.085	0.161	0.059	4.390		
$f_0(500)$	0.048	0.098	0.063	16.031	0.164	-
$\rho^0(770)$	0.042	0.031	0.017	2.096	0.179	-
$f_0(1500)$	0.092	0.056	0.071	5.088	0.511	-
NR	0.152	0.085	0.084	3.180	1.472	-
χ_{c0}	0.035	0.029	0.023	3.312	0.129	-

5.8.2.2 Systematic uncertainties related to the marginal components of the DP model.

To evaluate the systematic uncertainties related to the marginal components of the DP model, the addition of resonances $K^*(1680)$ and $f_2(1270)$ on one hand and the removal of

the $f_0(500)$ component have been examined. This set of resonances are actually the least significant in the nominal model. The first step of the estimation consists in fitting the data using the nominal model with or without the marginal component. A high statistics pseudo-experiment based upon this new model is then generated and fit back with the nominal model. The related systematic uncertainty estimate is taken as the difference between the generated and fit values. Some details about the modelling of each resonance are provided below.

$K^*(1680)$ **resonance** : the mass and width of this resonance are poorly known. It is an a priori broad P-wave resonance which can interfere with the $K^*(892)$ and $K^*(1430)$ series. However, the $K^*(1680)$ resonance is inelastic and hence should be modelled with a Flatté parameterisation. The coupling constants of the Flatté are taken from the up-to-date knowledge of this resonance given in Ref. [20]. The fit to the data with the nominal model including the $K^*(1680)$ gives a likelihood ratio -2Δnll equal to 7.4, which is rather similar to the nominal one. The systematic uncertainties on the fit parameters due to the addition of $K^*(1680)$ are given in Table 5.20.

Table 5.20: *Systematic uncertainty from the addition of* $K^*(1680)\pi$ *amplitude.*

Resonance	Real part	Imag. part	Mag.	Phase	FF (%)	Direct $\mathcal{A}_{CP}$.
$K^{*+}(892)$	-	-	-	-	0.150	0.002
$K^{*-}(892)$	0.003	-	0.003	-		
$(K\pi)_0^{*+}$	0.026	0.035	0.007	1.003	0.310	0.003
$(K\pi)_0^{*-}$	0.002	0.017	0.002	0.387		
$K_2^{*+}(1430)$	0.029	0.028	0.031	2.381	0.089	0.009
$K_2^{*-}(1430)$	0.007	0.036	0.017	4.378		
$f_0(980)$ from B^0	0.152	0.435	0.156	13.715	0.130	0.104
$f_0(980)$ from $\overline{B}^0$	0.014	0.508	0.071	9.035		
$f_0(500)$	0.017	0.054	0.012	6.077	0.024	-
$\rho^0(770)$	0.177	0.160	0.041	4.332	0.329	-
$f_0(1500)$	0.128	0.002	0.004	9.451	0.016	-
NR	0.083	0.005	0.051	7.988	0.750	-
χ_{c0}	0.012	0.000	0.007	7.692	0.014	-

$f_2(1270)$ **resonance** : this D-wave resonance has not passed the selection algorithm. It should be noted that the amplitude $f_2(1270)K^0_{\rm S}$ is part of the model defined in the BaBar and Belle analyses [14, 90]. It can be modelled by a relativistic Breit-Wigner and its mass and width are pretty fairly known [20]. The addition of the $f_2(1270)$ provides systematic uncertainties estimates gathered in Table 5.21.

$f_0(500)$ **resonance** : this is the least significant component accepted in the nominal model. We therefore consider the removal of the corresponding amplitude to assign a model systematic uncertainty. The fit with the nominal model excluding $f_0(500)$ gives a likelihood ratio

Table 5.21: *Systematic uncertainty from the addition of $f_2(1270)K^0_S$ amplitude.*

Resonance	Real part	Imag. part	Mag.	Phase	FF (%)	Direct $\mathcal{A}_{CP}$.
$K^{*+}(892)$	-	-	-	-	0.230	0.006
$K^{*-}(892)$	0.010	-	0.010	-		
$(K\pi)^{*+}_0$	0.063	0.032	0.023	1.552	0.020	0.004
$(K\pi)^{*-}_0$	0.016	0.058	0.014	1.290		
$K^{*+}_2(1430)$	0.051	0.001	0.004	4.990	0.033	0.010
$K^{*-}_2(1430)$	0.014	0.008	0.007	2.186		
$f_0(980)$ from B^0	0.099	0.075	0.119	0.985	0.210	0.079
$f_0(980)$ from $\overline{B}^0$	0.026	0.047	0.049	0.500		
$f_0(500)$	0.002	0.041	0.010	7.001	0.018	-
$\rho^0(770)$	0.146	0.087	0.004	7.634	0.136	-
$f_0(1500)$	0.006	0.012	0.002	0.767	0.046	-
NR	0.051	0.012	0.036	0.836	1.140	-
χ_{c0}	0.001	0.006	0.005	0.287	0.008	-

w.r.t. the nominal model -2Δnll worse by 8.8 units. The systematic uncertainties on the fit parameters due to the removal of $f_0(500)$ are reported in Table 5.22.

Table 5.22: *Systematic uncertainty related to the removal of the $f_0(500)K^0_S$ amplitude from the nominal model.*

Resonance	Real part	Imag. part	Mag.	Phase	FF (%)	Direct $\mathcal{A}_{CP}$.
$K^{*+}(892)$	-	-	-	-	0.140	0.006
$K^{*-}(892)$	0.009	-	0.009	-		
$(K\pi)^{*+}_0$	0.060	0.036	0.018	1.578	0.010	0.007
$(K\pi)^{*-}_0$	0.001	0.047	0.001	1.053		
$K^{*+}_2(1430)$	0.051	0.001	0.004	5.012	0.028	0.012
$K^{*-}_2(1430)$	0.012	0.002	0.008	1.372		
$f_0(980)$ from B^0	0.148	0.062	0.143	2.136	0.020	0.113
$f_0(980)$ from $\overline{B}^0$	0.019	0.170	0.102	3.359		
$f_0(500)$	0.000	0.000	0.000	0.000	0.000	-
$\rho^0(770)$	0.020	0.012	0.020	0.518	0.149	-
$f_0(1500)$	0.050	0.012	0.022	2.811	0.184	-
NR	0.021	0.007	0.005	0.439	0.320	-
χ_{c0}	0.008	0.014	0.003	1.207	0.000	-

5.8.2.3 Systematic uncertainties from $K\pi$ S-wave modelling

The LASS parameterisation is found to give the best fit to the data. Several alternative models for the $K\pi$ S-wave have been tried. None of them has been found to compete satisfactorily with the data-driven LASS parameterisation. The best alternative model that we found is however reported for completeness in the following lines.

κ + $\mathbf{K_0^*(1430)}$: this line-shape is modelled with a Flatté function which describes the inelastic $K_0^*(1430)$ resonance plus a broad κ resonance at low $m_{K^0_S\pi}$. Since the κ could be extremely broad, it is necessary to use a modified description of the mass-dependent width, as discussed in Ref. [94]. The line-shape to describe the κ component is:

$$\mathcal{R}_j = \frac{m_0\Gamma_0}{m_0^2 - m^2 - im_0\Gamma(m)}\,, \tag{5.11}$$

where the different terms have their usual self-explanatory meanings. The mass dependent width $\Gamma(m)$ is defined by

$$\Gamma(m) = \rho\left(\frac{m^2 - s_A}{m_0^2 - s_A}\right) f(m) \exp\left(\frac{-(m^2 - m_0^2)}{A}\right)\,. \tag{5.12}$$

Here $\rho = 2q/m$ stands for a phase-space factor, $f(m) = b_2m^2 + b_1$, where b_1 and b_2 are constants. The term A is also a constant and s_A is the Adler zero. The values of the constants used in this model are taken from the Ref. [94]:

$$\begin{aligned} b_1 &= 24.49 \text{ GeV}/c\,, \\ b_2 &= 0.0 \text{ GeV}/c\,, \\ A &= 2.5 \text{ GeV}^2/\text{c}^4 \\ s_A &= 0.234 \text{ GeV}^2/\text{c}^4 \\ m_0 &= 3.3 \text{ GeV}/\text{c}^2\,. \end{aligned} \tag{5.13}$$

The Flatté line-shape used to describe the $K^*(1430)$ has the same form as in Eq. (5.11), but the mass dependent width is taken to be

$$\Gamma(m) = \begin{cases} \left(\frac{m^2-s_A}{m_0^2-s_A}\right)(g_1\rho_{K\pi}(m) + g_2\rho_{K\eta'}(m)), & \text{if } m \geq (m_K + m_{\eta'}) \\ \left(\frac{m^2-s_A}{m_0^2-s_A}\right)(g_1\rho_{K\pi}(m) - ig_2\rho_{K\eta'}(m)), & \text{if otherwise .} \end{cases}$$

where $\rho_{K\pi}$ and $\rho_{K\eta'}$ are the phase-space factors for the $K\pi$ and $K\eta\prime$ channels respectively and $g_{1,2}$ parameterise the couplings to these two channels. This line-shape accounts for the $\rho_{K\eta'}$ channel opening close to the $K_0^*(1430)$ pole mass. The values of the constants used in this shape, taken from BES data [94], are

$$\begin{aligned} m_0 &= 1.513 \text{ GeV}/\text{c}^2\,, \\ g_1 &= 0.304 \text{ GeV}/\text{c}^2\,, \\ g_2 &= 0.380 \text{ GeV}/\text{c}^2\,, \\ s_A &= 0.234 \text{ GeV}^2/\text{c}^4\,. \end{aligned} \tag{5.14}$$

The likelihood ratio with this model w.r.t. the nominal model reads $-2\Delta\text{nll} = 315$ units. Since this description is strongly disfavoured by the data, it seems not adequate to assign a valuable systematic uncertainty.

5.8.2.4 Systematic uncertainties due to the $\pi\pi$ S-wave modelling

In order to determine a systematic uncertainty related to the modelling of the $\pi\pi$ S-wave component, the value of the κ constant in the reduced K-matrix parameterisation is varied to create a non-resonant $\pi\pi$ component which can interfere with the $f_0(500)$ component. One takes note that this parameterisation has the same concept as LASS line-shape. The likelihood ratios for values of $\kappa > 0.25$ are large and suggest that this limit defines the maximal affordable non-resonant contribution. Therefore, a pseudo-experiment with high statistics is generated according to a DP model with $\kappa = 0.25$ and fit back with the nominal model. The difference observed between the generated and fit values is taken as the related systematic uncertainty. The systematic estimates are gathered in the table Table 5.23.

Table 5.23: *Systematic uncertainties due to the modelling of the $\pi\pi$ S-wave component.*

Resonance	Real part	Imag. part	Mag.	Phase	FF (%)	Direct $\mathcal{A}_{CP}$.
$K^{*+}(892)$	-	-	-	-	0.170	0.007
$K^{*-}(892)$	0.011	-	0.011	-		
$(K\pi)_0^{*+}$	0.067	0.051	0.013	1.925	0.250	0.012
$(K\pi)_0^{*-}$	0.016	0.047	0.016	1.032		
$K_2^{*+}(1430)$	0.042	0.002	0.006	4.097	0.037	0.016
$K_2^{*-}(1430)$	0.021	0.009	0.011	3.086		
$f_0(980)$ from B^0	0.269	0.011	0.160	6.852	0.250	0.119
$f_0(980)$ from $\overline{B}^0$	0.047	0.253	0.083	6.131		
$f_0(500)$	0.024	0.085	0.061	10.071	0.165	-
$\rho^0(770)$	0.010	0.035	0.027	1.167	0.198	-
$f_0(1500)$	0.040	0.030	0.006	3.004	0.074	-
NR	0.125	0.229	0.146	4.572	2.760	-
χ_{c0}	0.019	0.034	0.006	2.874	0.014	-

5.8.2.5 Summary of model systematic uncertainties

The systematic uncertainties due to all sources of model errors described in Section 5.8.2.2 are combined in quadrature to form the total model systematic uncertainties. Their values are reported in the table Table 5.24 for the isobar amplitudes, fit fractions and direct CP violation asymmetries.

Table 5.24: *Total model systematic uncertainties.*

Resonance	Mag.	Phase	FF (%)	Direct $\mathcal{A}_{CP}$.
$K^{*+}(892)$	-	-	0.406	0.012
$K^{*-}(892)$	0.019	-		
$(K\pi)_0^{*+}$	0.041	3.456	0.494	0.021
$(K\pi)_0^{*-}$	0.042	2.369		
$K_2^{*+}(1430)$	0.035	9.203	0.110	0.035
$K_2^{*-}(1430)$	0.024	6.884		
$f_0(980)$ from B^0	0.313	17.010	1.072	0.217
$f_0(980)$ from $\overline{B}^0$	0.169	12.249		
$f_0(500)$	0.090	9.114	0.234	-
$\rho^0(770)$	0.056	21.080	0.469	-
$f_0(1500)$	0.075	11.521	0.550	-
NR	0.180	9.783	3.428	-
χ_{c0}	0.025	8.940	0.131	-

Chapter 6

Result interpretation

This chapter presents the final results of the simultaneous Dalitz fit of the decay $B^0 \to K^0_S\pi^+\pi^-$ along with the first observation of the direct CP asymmetry in the Q2B decay $B^0 \to K^{*+}(892)\pi^-$.

6.1 Interpretation of the DP fit results

The Dalitz fit presented in the previous chapter is a simultaneous fit to the different running periods and K^0_S reconstruction categories data. For illustration, the same nominal fit given in Section 5.6 is sketched in Fig. 6.1, where this time the individual p.d.f. per spectrum are combined and displayed together with the full data spectrum. The results of this work are compared to former measurements performed by the BaBar and Belle experiments.

6.1.1 Isobar parameter and fit fractions measurements

The results for the isobar parameter measurements with statistical and systematics uncertainties are gathered in Table 6.1.

These results can be interpreted in terms of fit fractions related to the quasi-two-body amplitudes:

$$\begin{aligned}
&\mathcal{FF}(K^{*\pm}(892)\pi^{\mp}) = 11.7^{+0.5}_{-0.4}\,(\text{stat}) \pm 0.3\,(\text{syst}) \pm 0.4\,(\text{model})\,,\\
&\mathcal{FF}((K\pi)^{*\pm}_0\pi^{\mp}) = 24.4^{+1.0}_{-0.9}\,(\text{stat}) \pm 0.7\,(\text{syst}) \pm 0.5\,(\text{model})\,,\\
&\mathcal{FF}(K^{*\pm}_2(1430)\pi^{\mp}) = 0.92^{+0.04}_{-0.03}\,(\text{stat}) \pm 0.18\,(\text{syst}) \pm 0.11\,(\text{model})\,,\\
&\mathcal{FF}(f_0(980)K^0_S) = 17.6^{+0.8}_{-0.6}\,(\text{stat}) \pm 1.6\,(\text{syst}) \pm 1.1\,(\text{model})\,,\\
&\mathcal{FF}(f_0(500)K^0_S) = 0.54^{+0.95}_{-0.13}\,(\text{stat}) \pm 0.12\,(\text{syst}) \pm 0.23\,(\text{model})\,,\\
&\mathcal{FF}(\rho^0(770)K^0_S) = 6.4^{+1.6}_{-1.9}\,(\text{stat}) \pm 0.5\,(\text{syst}) \pm 0.5\,(\text{model})\,,\\
&\mathcal{FF}(f_0(1500)K^0_S) = 3.2^{+0.4}_{-0.6}\,(\text{stat}) \pm 0.8\,(\text{syst}) \pm 0.5\,(\text{model})\,,\\
&\mathcal{FF}(\chi_{c0}K^0_S) = 2.2 \pm 0.3\,(\text{stat}) \pm 0.1\,(\text{syst}) \pm 0.1\,(\text{model})\,,\\
&\mathcal{FF}(K^0_S\pi^+\pi^-)^{\text{NR}} = 27.9^{+2.1}_{-2.0}\,(\text{stat}) \pm 1.9\,(\text{syst}) \pm 3.4\,(\text{model})
\end{aligned}$$

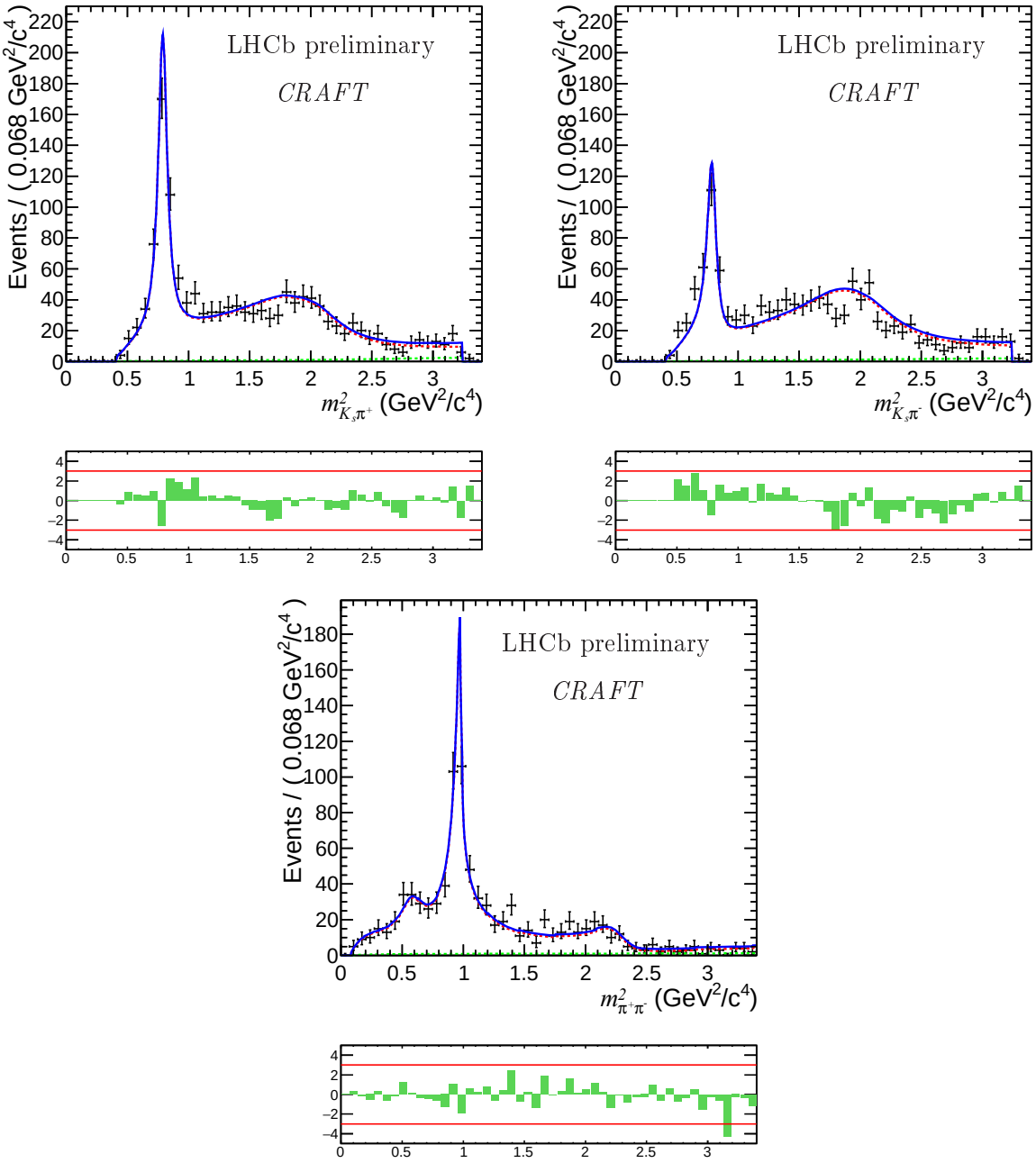

Figure 6.1: *Projections of the sum of all data category (black points) and the nominal fit, with a zoomed view, onto* $m^2_{K^0_S\pi^+}$ *(left),* $m^2_{K^0_S\pi^-}$ *(right) and* $m^2_{\pi^+\pi^-}$ *(bottom). The full fit is shown in blue, combinatorial background in green and signal model in red.*

where the statistical, experimental and model uncertainties are split accordingly. Some comments are in order about the comparison of these measurements with previous results obtained at B-factories. A fair comparison is not straightforward in reason of the differences in the definition of the nominal DP model. By the way, a fair comparison of the two above-

Table 6.1: *Final results for the magnitudes and phases, the first uncertainty is statistical, the second is experimental systematic, and the third represents the DP model systematic.*

Resonance	Magnitude	phase
$K^{*+}(892)$	2.00	0.0
$K^{*-}(892)$	$1.47 \pm 0.09 \pm 0.02 \pm 0.02$	0.0
$(K\pi)_0^{*+}$	$2.48 \pm 0.13 \pm 0.08 \pm 0.04$	$43.0^{+4.2}_{-4.8} \pm 2.5 \pm 3.5$
$(K\pi)_0^{*-}$	$2.57 \pm 0.12 \pm 0.08 \pm 0.04$	$-0.2 \pm 4.8 \pm 1.9 \pm 2.4$
$K_2^{*+}(1430)$	$0.59 \pm 0.11 \pm 0.07 \pm 0.03$	$-98.5^{+4.8}_{-6.0} \pm 1.7 \pm 9.2$
$K_2^{*-}(1430)$	$0.37 \pm 0.10 \pm 0.03 \pm 0.02$	$39.3^{+20.4}_{-14.4} \pm 3.2 \pm 6.9$
$f_0(980)$ from B^0	$2.02 \pm 0.39 \pm 0.10 \pm 0.31$	$55.6 \pm 12.6 \pm 4.3 \pm 17.0$
$f_0(980)$ from $\overline{B}^0$	$2.22 \pm 0.35 \pm 0.20 \pm 0.17$	$26.5 \pm 11.2 \pm 8.5 \pm 12.2$
$f_0(500)$	$0.29 \pm 0.11 \pm 0.05 \pm 0.09$	$16.9^{+31.5}_{-23.1} \pm 12.3 \pm 9.1$
$\rho^0(770)$	$1.30 \pm 0.13 \pm 0.06 \pm 0.06$	$-61.2^{+31.0}_{-40.3} \pm 2.6 \pm 21.1$
$f_0(1500)$	$0.92 \pm 0.17 \pm 0.13 \pm 0.07$	$-45.6^{+11.2}_{-9.6} \pm 8.9 \pm 11.5$
NR	$2.71 \pm 0.16 \pm 0.11 \pm 0.18$	$59.6 \pm 4.8 \pm 4.2 \pm 9.8$
χ_{c0}	$0.78 \pm 0.06 \pm 0.02 \pm 0.03$	$-37.9 \pm 12.6 \pm 3.3 \pm 8.9$

mentioned results cannot be easily made neither. We are hence choosing here to focus on the comparison with the results obtained by the BaBar experiment with a time-dependent tagged analysis [14]. The following observations about the differences in the DP models, data samples and results can be made:

- The fit fractions of the non resonant component, modelled in the very same way for the two analyses, is found significantly larger in the LHCb data. In turn, the scalar S-wave $(K\pi)_0^{*\pm}\pi^{\mp}$, also similarly modelled, is found accordingly smaller.

- The other magnitudes, for the ones which can be compared, seem to lie in the same ballpark. In particular, the fit fractions of the very well defined amplitude $K^{*\pm}(892)\pi^{\mp}$ are similar.

- A single solution is distinguished by the LHCb data at more than two standard deviations while two almost degenerated solutions are found in [14].

- As a tagged analysis, the results in [14] could distinguish the *CP* eigenstates amplitudes and their conjugates. As untagged, the analysis described here must assume *CP* conservation in most of these decays.

- The exact model defined in [14] has been tested against the LHCb data. The agreement with the LHCb data is mediocre.

- Among the experimental differences, it is worth to notice that the level of background passing the selection in LHCb data is much smaller than in [14].

Trying to conclude this ill-defined comparison exercise, we'd like to emphasize what we think is the main physics difference between the two results. The NR component and the $(K\pi)_0^{*\pm}\pi^{\mp}$ S-wave are found in both cases to provide the main contributions to the decay $B^0 \to K^0_{\rm S}\pi^+\pi^-$. Their interplay (and interference patterns) is the main difference and [14] finds $(K\pi)_0^{*\pm}\pi^{\mp}$ dominant while we find the magnitudes of these two amplitudes very similar.

6.1.2 Direct CP asymmetries measurements

The asymmetries computed directly from the isobar magnitudes are actually raw asymmetries. In order to derive the direct CP asymmetry $\mathcal{A}_{CP}$ from the raw asymmetry, effects induced by the production asymmetry of $B^0/\overline{B}^0$, as well as the asymmetry due to the interactions of the final state pions with detector material, must be accounted for. The direct CP asymmetry is related to the raw asymmetry by $\mathcal{A}_{CP} = \mathcal{A}_{\rm raw} - \mathcal{A}_{\Delta}$, where the correction $\mathcal{A}_{\Delta}$ is defined at the first order as

$$\mathcal{A}_{\Delta} = A_P(B^0) + A_D(\pi)\,, \tag{6.1}$$

where $A_P(B^0)$ is the B^0-$\overline{B}^0$ production asymmetry and $A_D(\pi)$ is the pion detection asymmetry. The production asymmetry $A_P(B^0)$ is determined to be $A_P(B^0) = (-0.35 \pm 0.81)\%$ [95]. The pion detection asymmetry was measured to be consistent with zero in the average of magnet polarity with a 0.0025 uncertainty using D_s^+ decay modes [96]. The uncertainties on the correction to asymmetries are added in quadrature to the experimental systematic uncertainties. The measurements of the direct CP asymmetries, after applying these corrective factors, read

$$\begin{aligned}
&\mathcal{A}_{CP}(B^0 \to K^{*+}(892)\pi^-) = -0.293 \pm 0.053\,(\text{stat}) \pm 0.017\,(\text{syst}) \pm 0.012\,(\text{model})\\
&\mathcal{A}_{CP}(B^0 \to (K\pi)_0^{*+}\pi^-) = 0.038 \pm 0.049\,(\text{stat}) \pm 0.057\,(\text{syst}) \pm 0.025\,(\text{model})\\
&\mathcal{A}_{CP}(B^0 \to K_2^{*+}(1430)\pi^-) = -0.43 \pm 0.27\,(\text{stat}) \pm 0.06\,(\text{syst}) \pm 0.04\,(\text{model})\\
&\mathcal{A}_{CP}(B^0 \to f_0(980)K^0_{\rm S}) = 0.12 \pm 0.32\,(\text{stat}) \pm 0.11\,(\text{syst}) \pm 0.22\,(\text{model})
\end{aligned}$$

6.1.3 First observation of direct CP asymmetry in $B^0 \to K^*(892)^+\pi^-$

The direct CP asymmetry $\mathcal{A}_{CP}(K^{*\pm}(892)\pi^{\mp})$ can be expressed as a function of the Cartesian isobar parameters ($\mathcal{A}_{\rm raw} = \frac{\bar{x}^2-4}{\bar{x}^2+4}$). Since x is fixed, the significance of a non vanishing $\mathcal{A}_{CP}$ can be derived from the significance of the $\bar{x}$ parameter departing from the value $x = 2$. The figure Fig. 6.2 shows the negative likelihood projection on the parameter $\bar{x}(K^*(892)^-)$. The statistical significance of having observed a non-vanishing CP asymmetry in the decay $B^0 \to K^*(892)^+\pi^-$, built from the likelihood ratio (see Fig. 6.2), is found to be 7.3 standard deviations. A naive (gaussian) scaling of the significance including the systematics uncertainties brings it down to 6 standard deviations.

The current world average for this asymmetry together with this measurement for the sake of the comparison read:

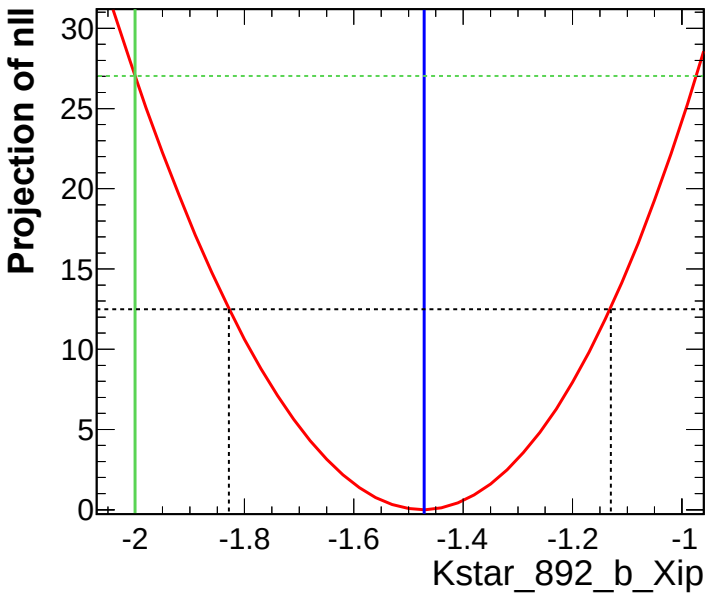

Figure 6.2: Projections of the nominal likelihood (red line) on the real part parameter of $K^{*-}(892)$. The blue solid line points on the fitted value, the black dashed lines represents the region of five statistical standard deviations, and the green line points on the value of the real part which corresponds to no *CP* asymmetry.

$$\begin{aligned} \mathcal{A}_{CP}(B^0 \to K^{*+}(892)\pi^-) &= -0.23 \pm 0.06 \text{ (WA)}, \\ \mathcal{A}_{CP}(B^0 \to K^{*+}(892)\pi^-) &= -0.293 \pm 0.057 \text{ (This result)}. \end{aligned}$$

The measurement presented in this document is in good agreement with the world average with an improved precision. It is accordingly by itself the first observation of a *CP*-violating asymmetry in the decay $B^0 \to K^*(892)^+\pi^-$.

Conclusion

The data recorded in 2011 and 2012 by the LHCb experiment corresponding to an integrated luminosity of $3\,\text{fb}^{-1}$ have been analysed to select the signal of the charmless three-body decays $B^0_{d,s} \to K^0_S h^\pm h'^\mp$ and to perform an amplitude analysis of the decay $B^0 \to K^0_S \pi^+\pi^-$ using the Dalitz Plot technique.

In the first part of this thesis analysis, an update of the selection designed for any $B^0_{d,s} \to K^0_S h^+ h^-$ decays has been presented. This selection was made as part of the inclusive branching fraction measurement, a collaborative study shared between three groups within LHCb: LPC Clermont-Ferrand, LPNHE Paris and Warwick university. In the same context, a simultaneous maximum likelihood fit to the invariant mass spectra $K^0_S K^+ K^-$, $K^0_S K^\pm \pi^\mp$ and $K^0_S \pi^+\pi^-$ was performed in order to establish the signals. This programme was extended to the amplitude analysis, where this thesis is concerned by the decay mode $B^0 \to K^0_S \pi^+\pi^-$.

The untagged Dalitz Plot analysis of the decay $B^0 \to K^0_S \pi^+\pi^-$ represents the main part of this thesis work. A dedicated fitting software, named CRAFT, has been designed using mainly ROOT classes. The fitter was tested with thoroughly pseudo-experiment studies to check the performance of the fits and the credibility of the measurements.

The isobar approximation was used to describe the signal distribution in the Dalitz plot. The amplitude model that was used for the nominal fit derives from a decision algorithm designed on three statistical criteria, the model likelihood significance, the quality of fit formed from the dissimilarity test and the significance of the amplitude. The resulting model contains twelve components, six flavour-specific resonances, five *CP*-eigenstate resonances and one non-resonant component modelled flat in phase-space. When the nominal simultaneous fit is repeated starting from input parameters values randomly chosen, the process of minimization converges toward two solutions in the range of difference log likelihood $2\Delta\text{nll} < 9$ units, with a gap of 5.4 units. The main difference between these two solutions occurs in the interpretation of the low mass $\pi\pi$ S-wave. The magnitude of $f_0(500)$ is found five times larger in the second solution with respect to the best solution. The best nominal fit to data gave a satisfactory result according to the goodness-of-fit test (p-value $= 16\,\%$). In the final step of this Dalitz Plot analysis, the determination of the systematic uncertainties was presented.

The results of the final fit were presented in Chapter 6. The result of the isobar parameter in Cartesian coordinates were obtained directly from the fit, and they were propagated to

the derived quantities, the fit fractions and *CP* asymmetries. A fair comparison of the fit fractions measurements with *B*-factories results is not straightforward due to the differences in the definition of the Dalitz Plot nominal model. However, from a preliminary comparison between the time-dependent tagged analysis of BaBar [14] and the analysis presented in this thesis, we can draw the following comments: the fit fractions of the non resonant component, modelled in the very same way for the two analyses, is found significantly larger in the LHCb data. In turn, the scalar *S*-wave $(K\pi)^{*\pm}_0\pi^{\mp}$, also similarly modelled, is found accordingly smaller. However, the fit fractions of the very well defined amplitude $K^{*\pm}(892)\pi^{\mp}$ are similar, where our result reads

$$\mathcal{FF}(B^0 \to K^{*+}(892)\pi^-) = 11.7^{+0.5}_{-0.4}\,(\text{stat}) \pm 0.2\,(\text{syst}) \pm 0.4\,(\text{model})\ .$$

Regarding the direct *CP* asymmetry results, the largest sensitivity is obtained for the decay $B^0 \to K^{*+}(892)\pi^-$ we find

$$\mathcal{A}_{CP}(B^0 \to K^{*+}(892)\pi^-) = -0.293 \pm 0.053\,(\text{stat}) \pm 0.017\,(\text{syst}) \pm 0.012\,(\text{model})\ .$$

The measurement presented in this thesis analysis is in good agreement with the world average $\mathcal{A}_{CP}(B^0 \to K^{*+}(892)\pi^-) = -0.23 \pm 0.06$ (WA), with an improved precision. It is accordingly by itself the first observation of a *CP*-violating asymmetry in the decay $B^0 \to K^*(892)^+\pi^-$.

The future analysis of $B^0 \to K^0_S\pi^+\pi^-$ will clearly benefit from the increase in the size of dataset provided by the LHCb Run II. A dedicated exploration is however required to devise whether a time-dependent tagged analysis is making sense.

Appendices

Appendix A

Dalitz plot kinematics

This section describes the formalism used to reduce the problem of three-body decays to the minimal number of independent variables describing the kinematic of the process. Let's consider a particle with mass M and a 4-vector energy momentum P decaying in three particles with masses m_1, m_2 and m_3. We define the squared invariant mass by $m_{ij}^2 = (p_i + p_j)^2$, the indices i and j running from 0 to 3.

One can write In the rest frame of the initial particle:

$$M = p_1 + p_2 + p_3 \implies M^2 = m_1^2 + m_2^2 + m_3^2 + 2p_1p_2 + 2p_2p_3 + 2p_1p_3. \tag{A.1}$$

One can then build the expression of the sum of the three squared invariant masses:

$$m_{12}^2 + m_{13}^2 + m_{23}^2 = 2m_1^2 + 2m_2^2 + 2m_3^2 + 2p_1p_2 + 2p_2p_3 + 2p_1p_3, \tag{A.2}$$

which simplifies as:

$$m_{12}^2 + m_{13}^2 + m_{23}^2 = M^2 + m_1^2 + m_2^2 + m_3^2. \tag{A.3}$$

In the same move, one obtains:

$$m_{12}^2 = (P - p_3)^2 = M^2 + m_3^2 - 2ME_3, \tag{A.4}$$

where E_3 is the energy of the particle 3 in the rest frame of the mother particle. In this frame, the momenta of the three particles are in the same plane. The relative orientation of these three momenta is fixed if the energies are known. The momenta can be taken up in the phase space by giving three Euler angles (α, β, γ) which specify the orientation of the final system w.r.t. the initial particle.

The partial decay rate of this three-body process is given by:

$$\mathrm{d}\Gamma = \frac{(2\pi)^4}{2M}|\mathcal{M}|^2 \mathrm{d}\phi_3(p_1, p_2, p_3), \tag{A.5}$$

with $\mathrm{d}\phi_3$ being the phase space element:

$$\mathrm{d}\phi_3(p_1, p_2, p_3) = \delta^{(4)}(P - p_1 - p_2 - p_3)\frac{\mathrm{d}^3p_1}{(2\pi)^3 2E_1}\frac{\mathrm{d}^3p_2}{(2\pi)^3 2E_2}\frac{\mathrm{d}^3p_3}{(2\pi)^3 2E_3}. \tag{A.6}$$

One has defined in the former equation $\mathcal{M}$ as the Lorentz invariant matrix element of transition.

The four-momentum conservation of this decay process implies:

$$\begin{aligned} \vec{0} &= \vec{p}_1 + \vec{p}_2 + \vec{p}_3, \\ M &= E_1 + E_2 + E_3. \end{aligned} \tag{A.7}$$

Integrating on d^3p_3 and taking into account the relation of the four-momentum conservation, one gets:

$$\mathrm{d}\phi_3 = \delta(M - E_1 - E_2 - E_3)\frac{\mathrm{d}^3p_1}{(2\pi)^3 2E_1}\frac{\mathrm{d}^3p_2}{(2\pi)^3 2E_2 (2\pi)^3 2E_3}. \tag{A.8}$$

Changing the volume element d^3p_i in spherical coordinates, the transformation reads:

$$\mathrm{d}^3p_1 = |\vec{p}_1|^2 \mathrm{d}p_1 \mathrm{d}\Omega_1, \qquad \mathrm{d}^3p_2 = |\vec{p}_2|^2 \mathrm{d}p_1 \mathrm{d}\Omega_{12}, \tag{A.9}$$

where Ω_1 is the solid angle for $\vec{p}_1$ direction and Ω_{12} is the solid angle for $\vec{p}_2$ w.r.t. $\vec{p}_1$ direction.

$$\mathrm{d}\Omega_1 = \mathrm{d}\phi_1 \mathrm{d}(\cos\theta_1), \qquad \mathrm{d}\Omega_{12} = \mathrm{d}\phi_2 \mathrm{d}(\cos\theta_{12}), \tag{A.10}$$

where θ_{12} is the angle between $\vec{p}_1$ and $\vec{p}_2$. If the mother particle is a pseudo-scalar, such as the B^0 in the process $B^0 \to K^0_{\mathrm{S}}\pi^+\pi^-$, one must integrate on all possible values of θ_1, ϕ_1 and ϕ_2 angles.

After integration, the element of volume becomes:

$$\mathrm{d}^3p_1 = 4\pi|\vec{p}_1|^2 \mathrm{d}p_1, \qquad \mathrm{d}^3p_2 = 2\pi|\vec{p}_2|^2 \mathrm{d}p_1 \mathrm{d}(\cos\theta_{12}), \tag{A.11}$$

and Eq. (A.8) reads as:

$$\mathrm{d}\phi_3 = \delta(M - E_1 - E_2 - E_3)\frac{8\pi^2|p_1|^2\mathrm{d}p_1|p_2|^2\mathrm{d}p_2\mathrm{d}(\cos\theta_{12})}{8(2\pi)^9 E_1 E_2 E_3}. \tag{A.12}$$

Introducing the change of variable $|p_1|\mathrm{d}p_1 = E_1\mathrm{d}E_1$, one obtains:

$$\mathrm{d}\phi_3 = \delta(M - E_1 - E_2 - E_3)\frac{8\pi^2|p_1|\mathrm{d}E_1|p_2|\mathrm{d}E_2\mathrm{d}(\cos\theta_{12})}{8(2\pi)^9 E_3}. \tag{A.13}$$

The momentum conservation law implies that:

$$\begin{aligned} \vec{p}_3 &= -\vec{p}_1 - \vec{p}_2\,, \\ \vec{p}_3^{\,2} &= \vec{p}_1^{\,2} + \vec{p}_2^{\,2} + 2|p_1||p_2|\cos\theta_{12}\,, \\ E_3^2 &= \vec{p}_1^{\,2} + \vec{p}_2^{\,2} + 2|p_1||p_2|\cos\theta_{12} + m_3^2\,, \\ \Longrightarrow\ E_3\mathrm{d}E_3 &= |p_1||p_2|\mathrm{d}(\cos\theta_{12})\,, \end{aligned} \tag{A.14}$$

which imposes the following form for the phase-space element:

$$\mathrm{d}\phi_3 = \delta(M - E_1 - E_2 - E_3)\frac{\pi^2}{(2\pi)^9}\mathrm{d}E_1\mathrm{d}E_2\mathrm{d}E_3. \tag{A.15}$$

The integration on E_3 gives:

$$\mathrm{d}\phi_3 = \frac{\pi^2}{(2\pi)^9}\mathrm{d}E_1\mathrm{d}E_2. \tag{A.16}$$

Introducing explicitly this phase space element, the partial decay rate becomes

$$\mathrm{d}\Gamma = \frac{|\mathcal{M}|}{(2\pi)^3 8M}\mathrm{d}E_1\mathrm{d}E_2, \tag{A.17}$$

One can advantageously write Eq. (A.17) as a function of the variables m_{ij}^2:

$$\begin{aligned} m_{23}^2 &= M^2 + m_1^2 - 2E_1M\,, \\ \mathrm{d}m_{23}^2 &= -2M\mathrm{d}E_1\,, \qquad (A.18) \\ \mathrm{d}m_{13}^2 &= -2M\mathrm{d}E_2\,. \qquad (A.19) \end{aligned}$$

such that the integration elements read:

$$\mathrm{d}E_1\mathrm{d}E_2 = \frac{\mathrm{d}m_{23}^2\mathrm{d}m_{13}^2}{4M^2}\,. \tag{A.20}$$

Finally, the decay rate as a function of m_{23}^2 and m_{13}^2 can be expressed as

$$\mathrm{d}\Gamma = \frac{1}{(2\pi)^3 32M^3}|\mathcal{M}|^2\mathrm{d}m_{13}^2\mathrm{d}m_{23}^2\,, \tag{A.21}$$

for which we have explicitly proven the dependence as a function of only two kinematics variables.

Appendix B

Angular distribution in Dalitz plot

The spin of resonances plays a major role in the events distribution of the three-body decay in the Dalitz plane. This section discusses this formalism starting by the helicity constraints.

Let's take as example here the decay $B^0 \to X(\to \pi^+\pi^-)K^0_S$ where X is an intermediate resonance. We take as work frame the rest frame of the resonance X, suppose that we measure the angles θ and ϕ which characterize the direction of the momentum and the helicity of $\pi^\pm$.

Let's consider the decay in the direction ($\theta = 0$, $\phi = 0$), the pion is issued in the direction Oz. Due to the helicity properties, the projection of the total angular momentum on the direction of the pion is equal to λ (the helicity eigenvalue). with null angles we must have $\lambda = m$, where m represents the eigenvalue of the projection of the angular momentum on Oz axis. Accordingly, we can know the direction of the momentum if the state of the spin is known, Or, knowing the angular distribution of the particles daughters we can know the spin of the mother particle.

The helicity is an invariant observable under rotation, we can define the state $|\theta, \phi, \lambda\rangle$ by constructing two successive rotations: one rotation with $-\theta$ around Oy followed by a second rotation with $-\phi$ around Oz. This transformation can be expressed mathematically as following

$$|\theta, \phi, \lambda\rangle = D_y(\theta) D_z(\phi) |0, 0, \lambda\rangle \,. \tag{B.1}$$

This analysis is clear geometrically but complicated to describe mathematically. It's more convenient to study from the angular momentum state $|j, m\rangle$. Instead projecting the spin of the pion on the axis of the particle X, we project it on his flight direction, which is the helicity definition and the transformation from one state to another given by Wigner rotations

$$\mathcal{R}_w |j, m\rangle = \sum \mathcal{D}^j_{m,m'} |j, m'\rangle \,, \tag{B.2}$$

with

$$\mathcal{D}^j_{m,m'} = d^j_{m,m'}(\theta) e^{i|m-m'|\phi} \,, \tag{B.3}$$

where $d^j_{m,m'}$ is an element of the Wigner matrix corresponding to the angle rotation θ. m' is obtained from the helicities λ_{π^+} and λ_{π^-} of π^+ and π^-, respectively, as following: We start from the expression of the total angular momentum

$$\vec{j}_0 = \vec{l}_{+,-} + \vec{s}_{\pi^+} + \vec{s}_{\pi^-} \,, \tag{B.4}$$

where

$$\vec{l}_{+,-} = \vec{r}_+ \wedge \vec{p}_+ + \vec{r}_- \wedge \vec{p}_- \,, \tag{B.5}$$

where $\vec{r}_i$ is the from the origin of particle i, and $\vec{p}_i$ is its momentum.

Since we are in the particle mother rest frame, therefore $\vec{p}_+ = -\vec{p}_- = -\vec{p}$, so $\vec{l}_{+,-} = (\vec{r}_+ - \vec{r}_-) \wedge \vec{p}$.

By projecting $\vec{j}$ according to the flight line of π^+ ($\vec{u}_p = \frac{\vec{p}}{\|\vec{p}\|}$), we get

$$\vec{j} \cdot \vec{u}_p = \vec{l} \cdot \vec{u}_p + \vec{s}_{\pi^+} \cdot \vec{u}_p + \vec{s}_{\pi^-} \cdot \vec{u}_p \,, \tag{B.6}$$

we have, $\lambda_\pm = \vec{s}_{\pi^\pm} \cdot \vec{u}_p$ and $\vec{l} \cdot \vec{u}_p = 0$, thus

$$m' = \vec{j} \cdot \vec{u}_p = \lambda_+ - \lambda_- \,. \tag{B.7}$$

The angular distributions are determined by

$$\begin{aligned}
\tau_m &= \langle j, m | \sum \mathcal{D}^j_{m,m'} | j, m' \rangle \,, \\
\tau_m &= \langle j, m | \sum d^j_{m,m'}(\theta) e^{i|m-m'|\phi} | j, m' \rangle \,, \\
\tau_m &= \sum d^j_{m,m'}(\theta) e^{i|m-m'|\phi} \langle j, m | j, m' \rangle \,. \qquad \text{(B.8)} \\
N &= \iint |\tau_m|^2 \mathrm{d}\Omega = \int |d^j_{m,m'}|^2 c_{m,m'} \mathrm{d}(\cos\theta) \,, \qquad \text{(B.9)}
\end{aligned}$$

where $c_{m,m'} = |\langle j, m | j, m' \rangle|^2$. Finally, the angular distribution reads

$$\frac{\mathrm{d}N}{\mathrm{d}\cos\theta} = \sum_{m,m'} c_{m,m'} |d^j_{m,m'}|^2 \,. \tag{B.10}$$

In the specific case of a vector meson ($J = 1$), three spin projections are accessible, each state described by the correspondent coefficients and Wigner matrix elements

$$\frac{\mathrm{d}N}{\mathrm{d}\cos\theta} = c^1_{0,0} |d^1_{0,0}|^2 + c^1_{1,0} |d^1_{1,0}|^2 + c^1_{-1,0} |d^1_{-1,0}|^2 \,. \tag{B.11}$$

In the case of the decay $B^0 \to X K^0_S \to K^0_S \pi^+ \pi^-$, we are dealing with final pseudo-scalar mesons.Therefore, the helicity of X is constrained only to the value 0, and the angular distribution of its decay products depends only on the first term in Eq. (B.11), $c^1_{0,0} |d^1_{0,0}|^2$. According to the values of $d^s_{m,m'}$ in the PDG [20] we have:

- for $s = 0$, $d^0_{0,0} = 1$,
- for $s = 1$, $d^1_{0,0} = \cos\theta$,

- for $s = 0$, $d^2_{0,0} = \left(\frac{3}{2}\cos^2\theta - \frac{1}{2}\right)^2$,

The expression of the angular distribution in the case of vector meson is given by

$$\frac{\mathrm{d}N}{\mathrm{d}\cos\theta} = c^1_{0,0}\cos^2\theta\,, \tag{B.12}$$

which explains the presence of two events distribution separated in the Dalitz plane for an intermediate vector meson.

For X with type pseudo-scalar meson the angular distribution expressed as

$$\frac{\mathrm{d}N}{\mathrm{d}\cos\theta} = c^0_{0,0}\,. \tag{B.13}$$

The angular distribution is equal to a constant so the resonance is distributed isotropically in the band that occupies in the DP.

For X with type tensor meson the angular distribution expressed as

$$\frac{\mathrm{d}N}{\mathrm{d}\cos\theta} = c^2_{0,0}\left(\frac{3}{2}\cos^2\theta - \frac{1}{2}\right)^4\,. \tag{B.14}$$

For $\frac{\mathrm{d}N}{\mathrm{d}\cos\theta} = 0$, the angular distribution presents an extremum for $\cos\theta = \pm 1/3$. Therefore in the Dalitz plan, the intermediate tensor resonance is distributed in three regions.

Hence, the spin of the intermediate particles plays a capital role on the way the events are distributed in the Dalitz plane.

Appendix C

Selection - extra plots

This appendix contains plots related to the selection, in particular the training and optimisation of the BDT. In the main text of Section 4.2 plots were often shown only for 2011 conditions. In such cases the equivalent plots for the two 2012 running periods (PreJune and PostJune) can be found here.

Firstly, in Figs. C.1 to C.4, we have the plots of the compatibility between signal MC and data for the variables used as input to the BDT training.

Figure C.1: Compatibility of signal MC/data using 2012 pre-June events provided for Long-Long K^0_S.

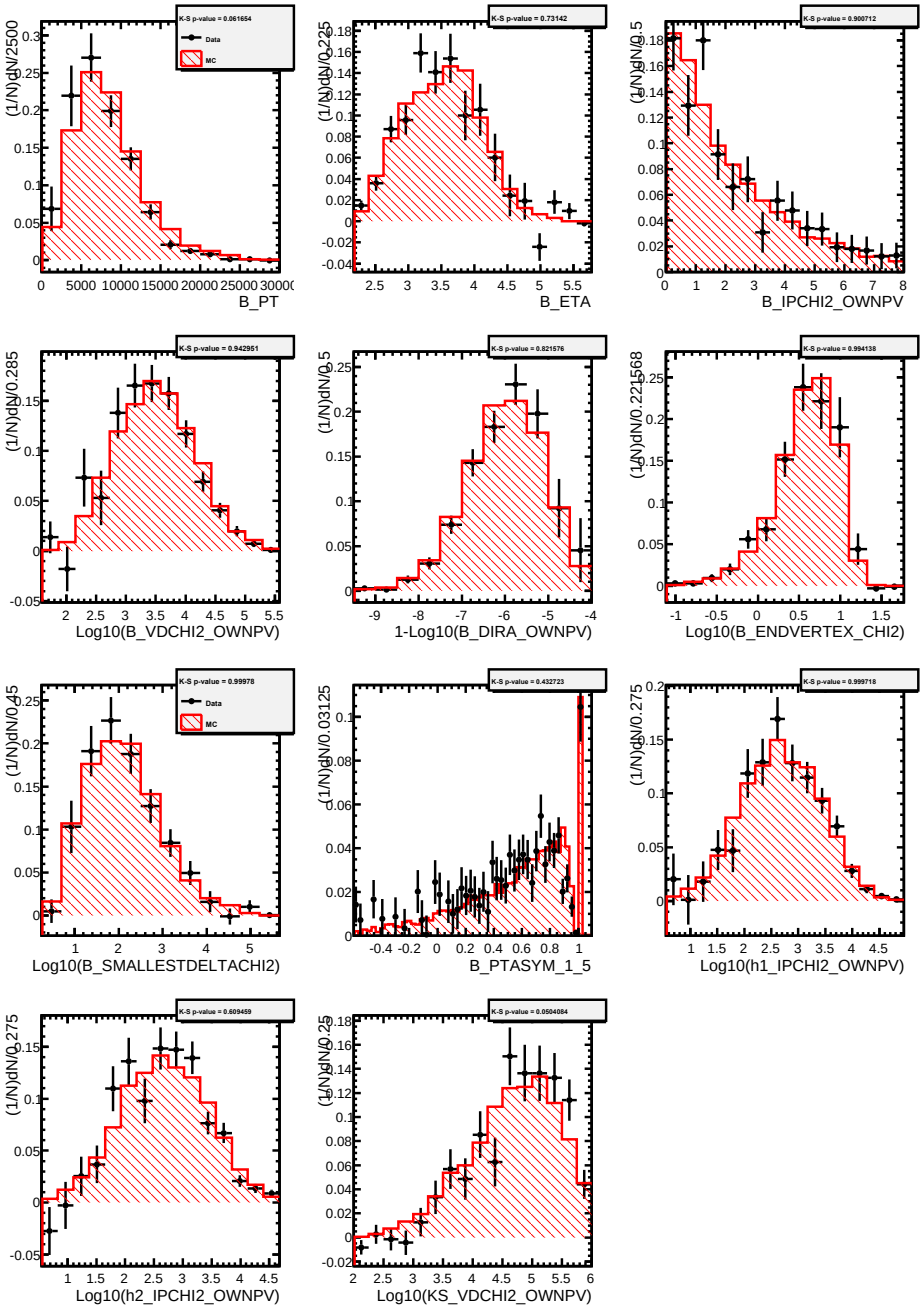

Figure C.2: Compatibility of signal MC/data using 2012 post-June events provided for Long-Long K^0_S.

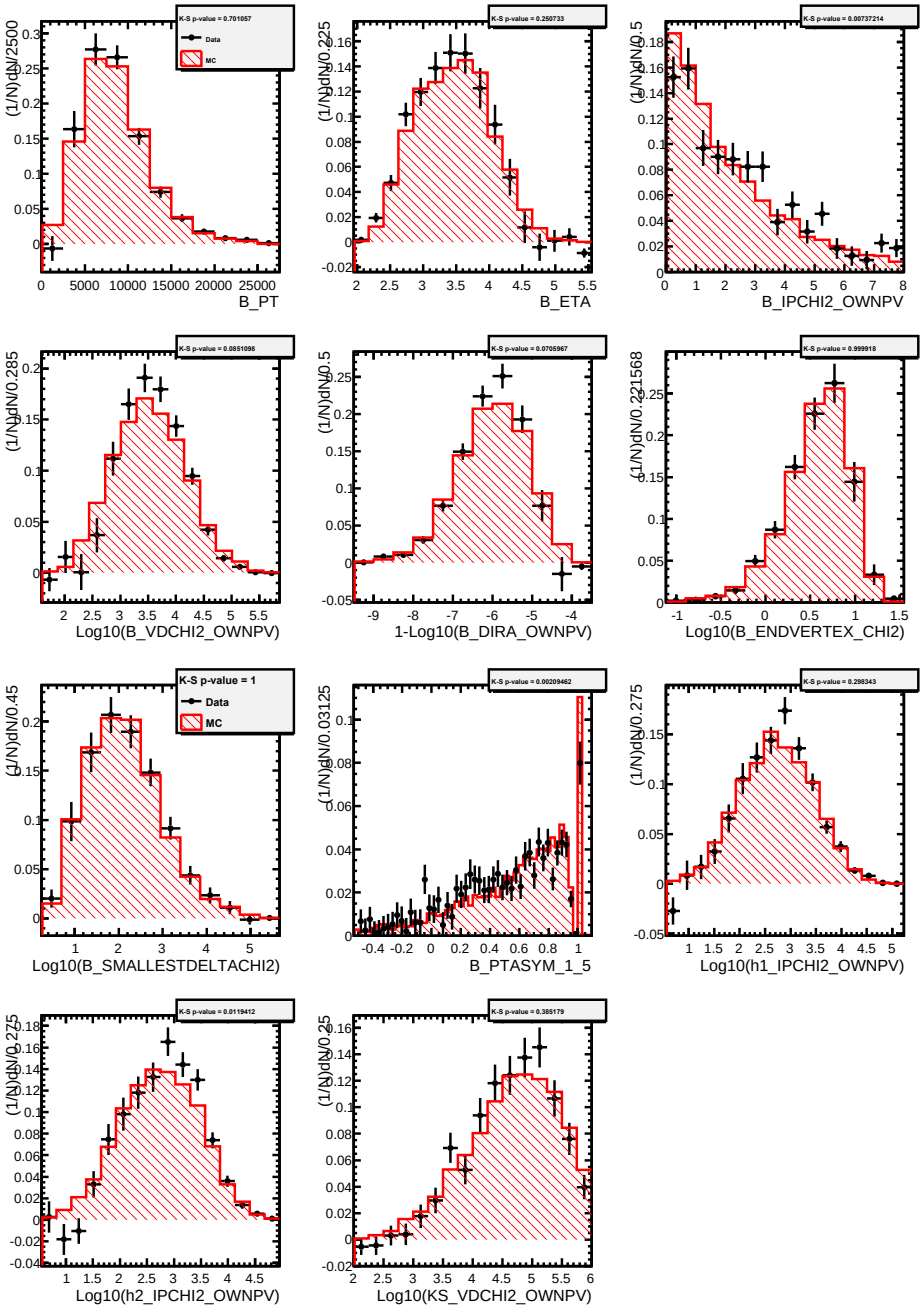

Figure C.3: Compatibility of signal MC/data using 2012 pre-June events provided for Down-Down K^0_S.

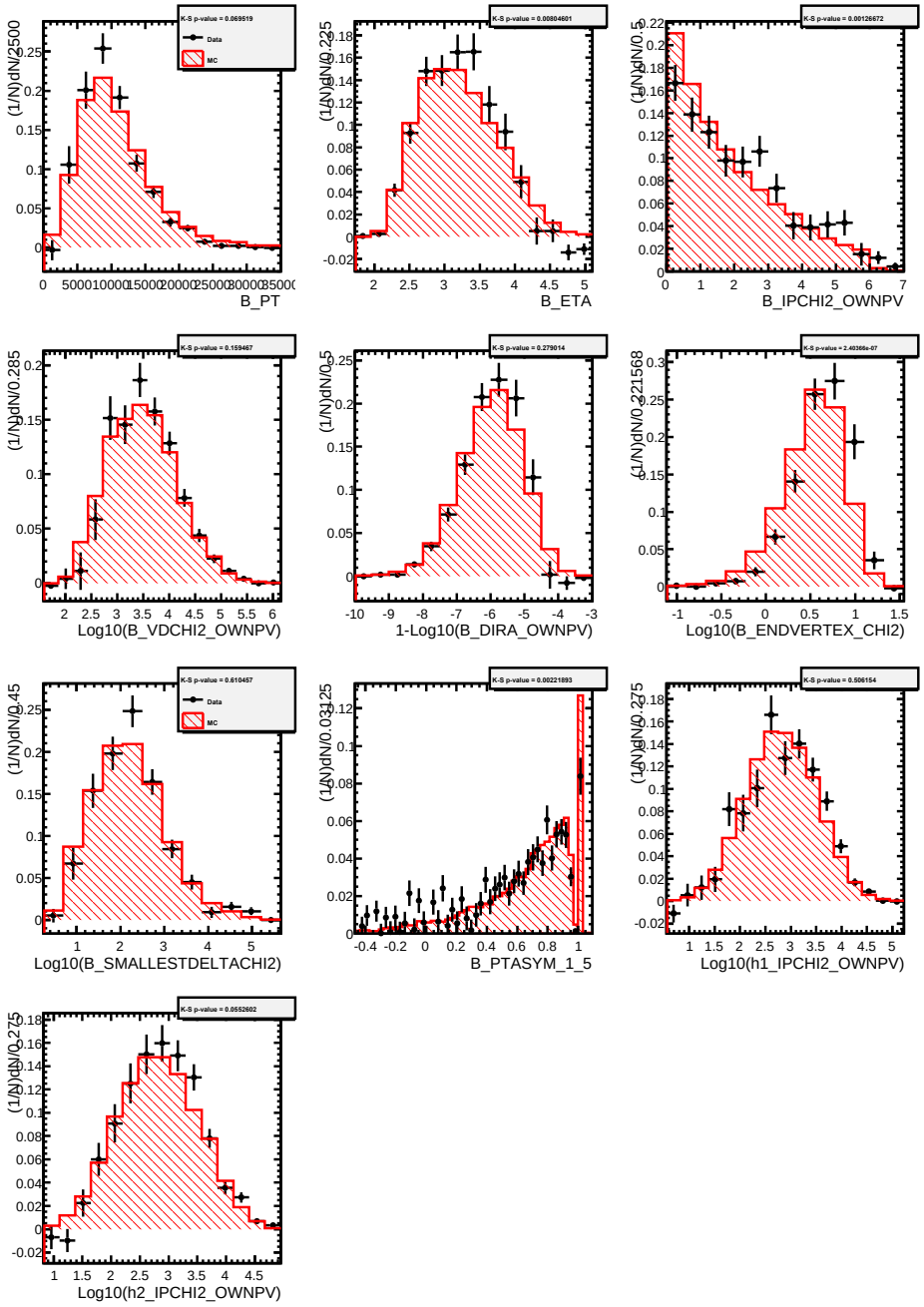

Figure C.4: Compatibility of signal MC/data using 2012 post-June events provided for Down-Down K^0_S.

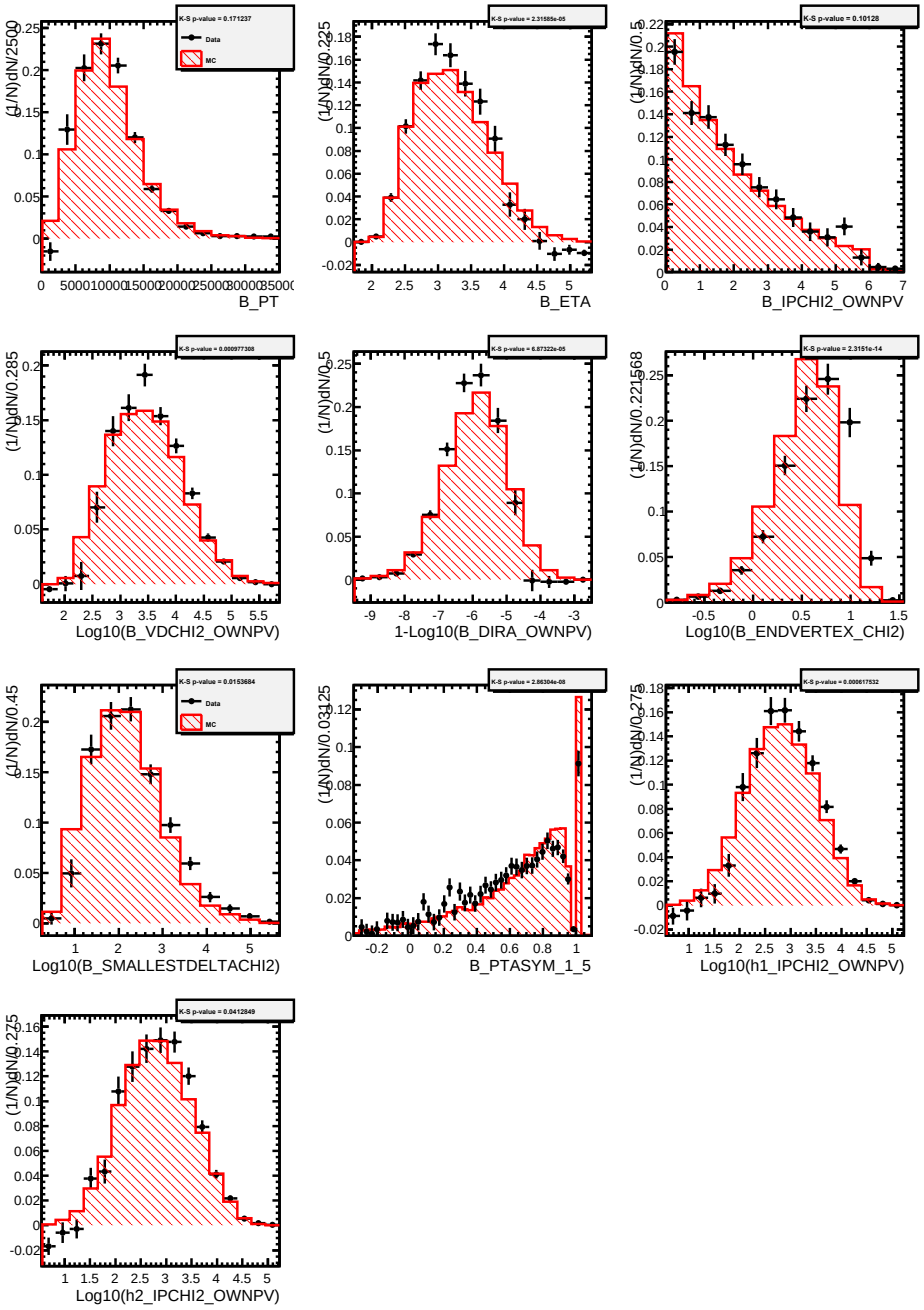

Next we have the distributions (Figs. C.5, C.6, C.9 and C.10) and linear correlations (Figs. C.7, C.8, C.11 and C.12) of the variables used in the training of the BDT discriminant, along with the ranking of their importance in Tables C.1 and C.2.

Figure C.5: Distribution of variables used in the training of the BDT discriminant for Long-Long K^0_S using 2012 pre-June events.

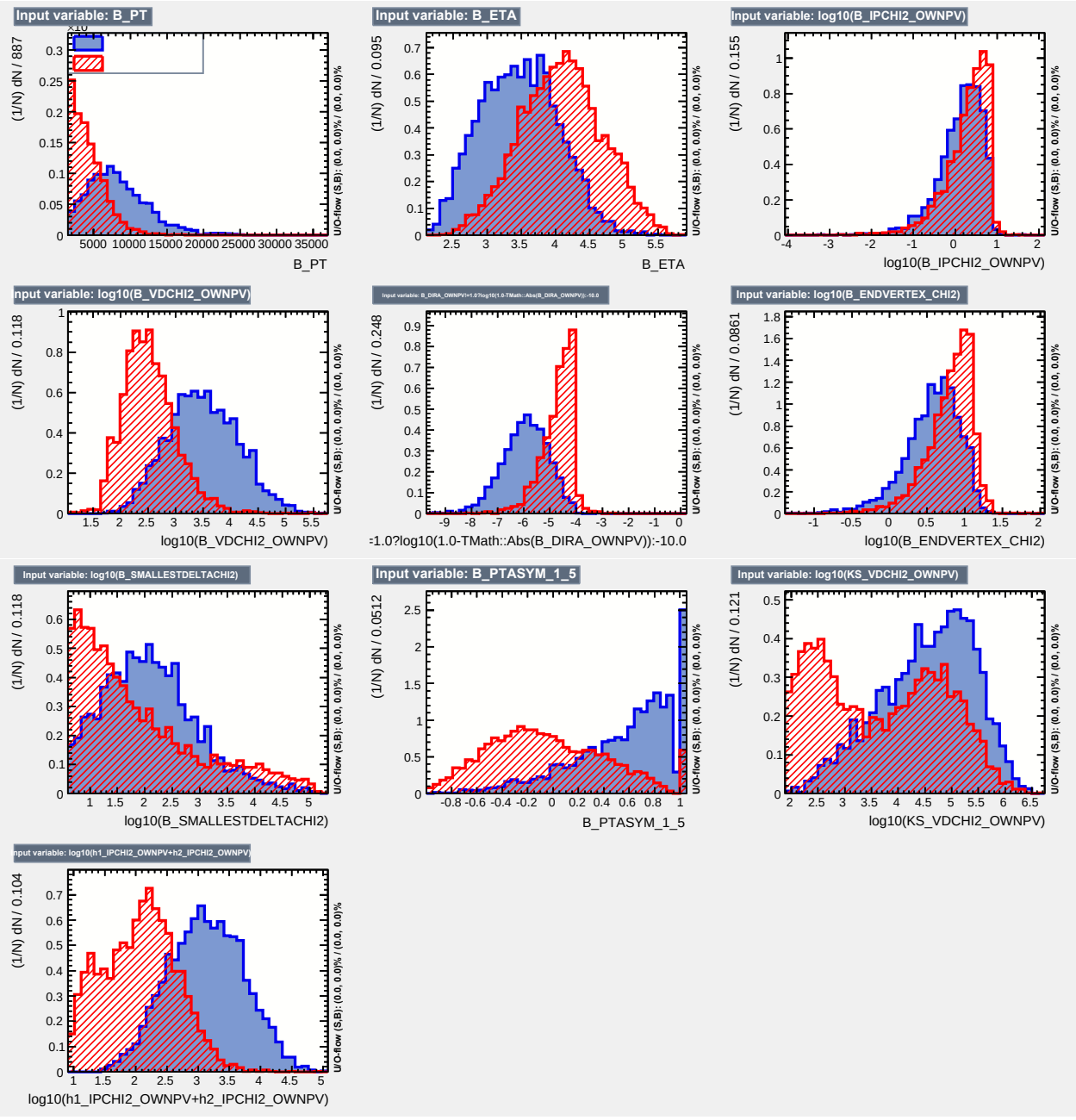

Figure C.6: Distribution of variables used in the training of the BDT discriminant for Long-Long K^0_S using 2012 post-June events.

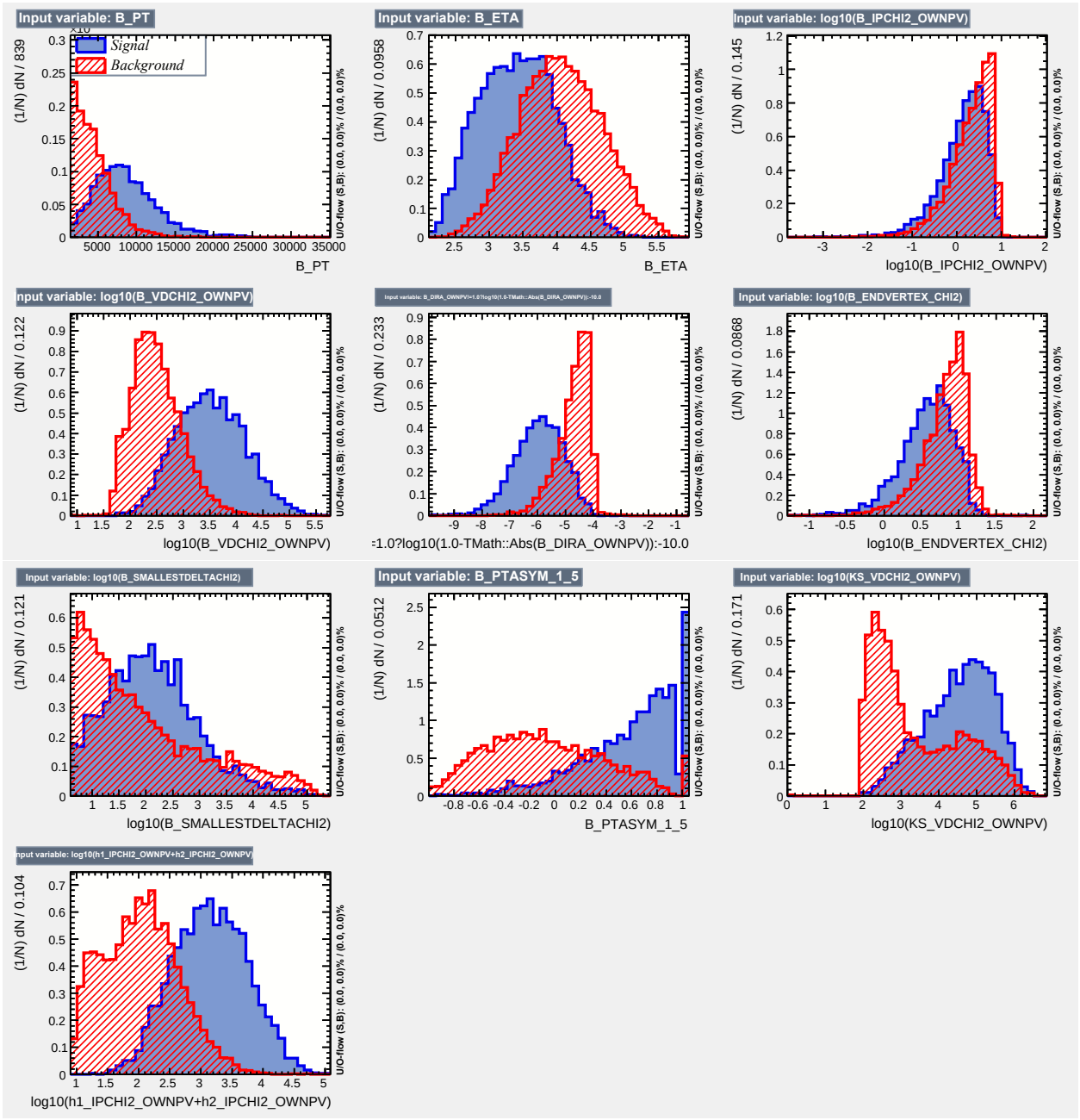

Figure C.7: Linear correlations between the variables used in the optimisation of the BDT for Long-Long K^0_S using 2012 pre-June events.

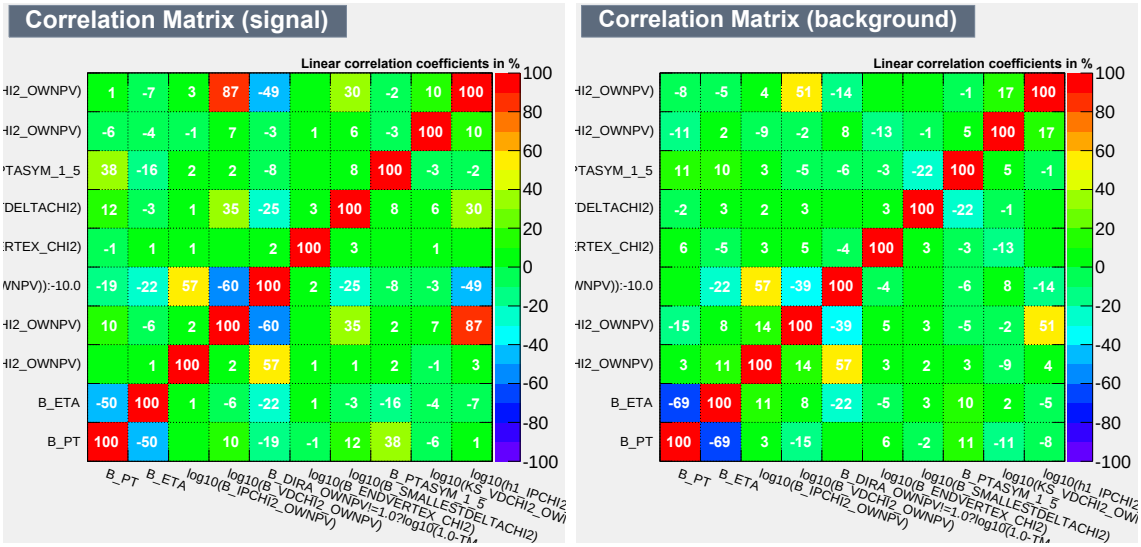

Figure C.8: Linear correlations between the variables used in the optimisation of the BDT for Long-Long K^0_S using 2012 post-June events.

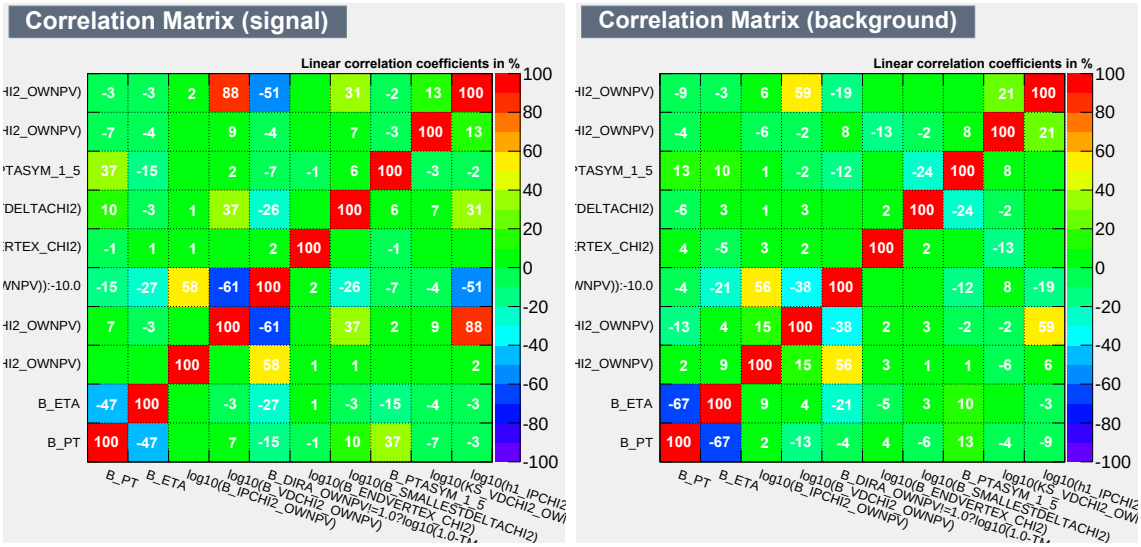

Figure C.9: Distribution of Variables used in the optimisation of the BDT discriminant for Down-Down K^0_S using 2012 pre-June events.

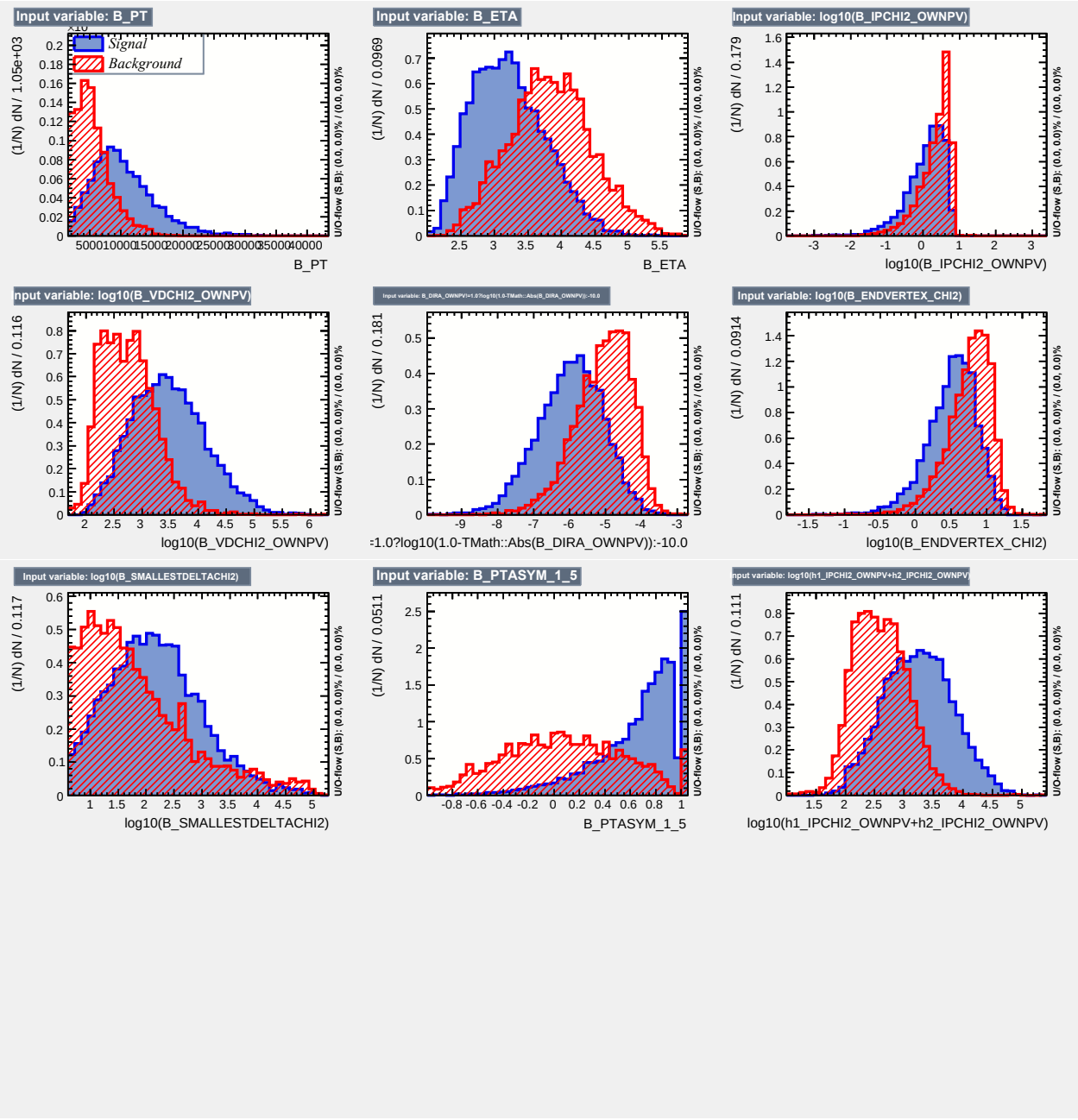

Figure C.10: Distribution of Variables used in the optimisation of the BDT discriminant for Down-Down K^0_S using 2012 post-June events.

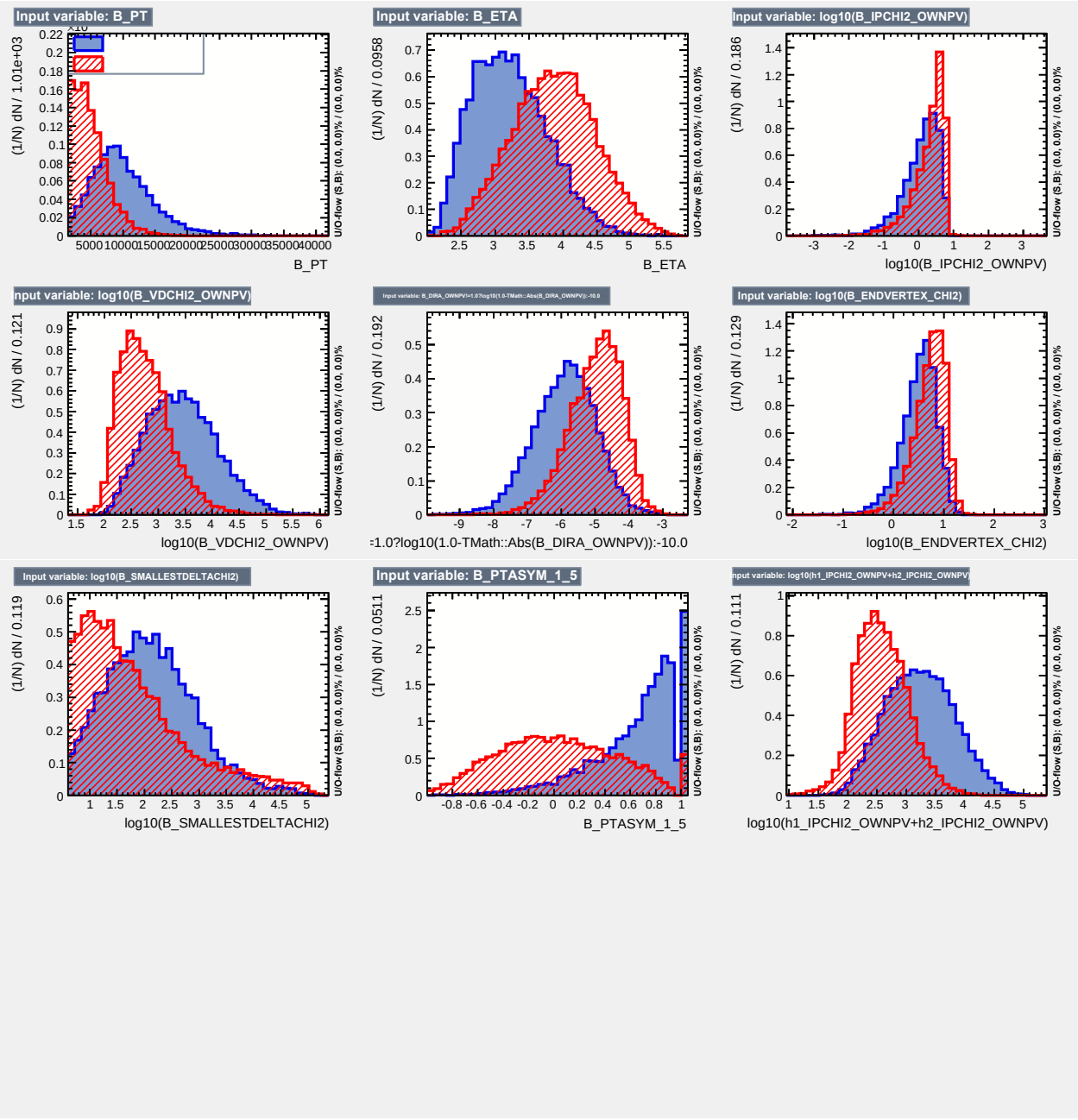

Figure C.11: Linear correlations between the variables used in the optimisation of the BDT for Down-Down K^0_S using 2012 pre-June events.

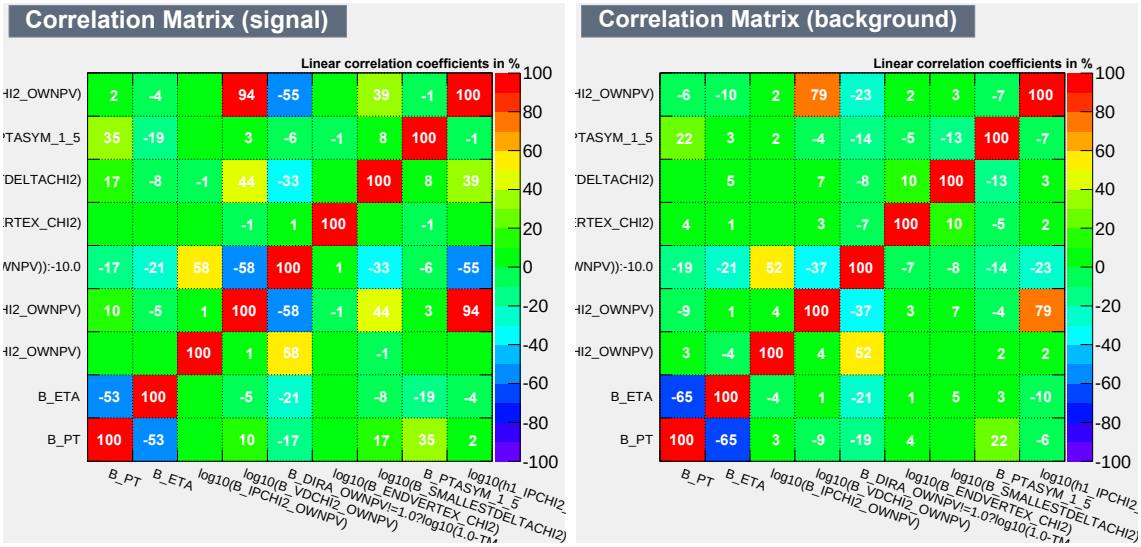

Figure C.12: Linear correlations between the variables used in the optimisation of the BDT for Down-Down K^0_S using 2012 post-June events.

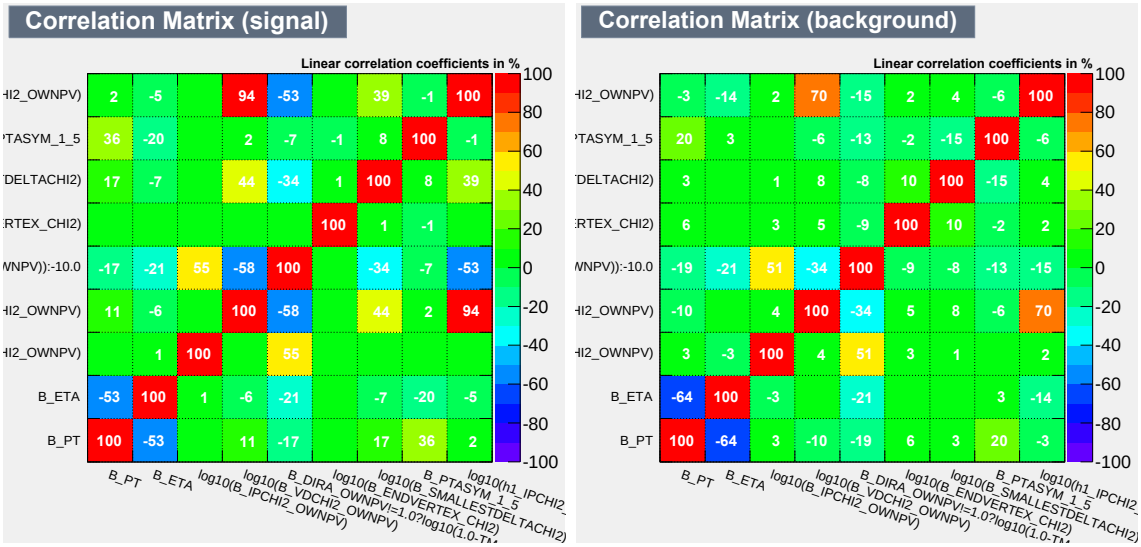

Table C.1: BDT variable importance ranking [0,1] with 2012 pre-June data. Variables are presented in the hierarchical order as obtained for Down-Down.

Variable	Importance DD		Importance LL	
	BDT1	BDT2	BDT1	BDT2
B_PT	0.240	0.164	0.061	0.071
B_PTASYM_1_5	0.183	0.175	0.136	0.095
B_ETA	0.110	0.103	0.122	0.082
Σ_i h$_i$_IPCHI2_OWNPV	0.093	0.133	0.160	0.165
B_ENDVERTEX_CHI2	0.092	0.086	0.076	0.064
B_IPCHI2_OWNPV	0.089	0.106	0.076	0.108
B_VDCHI2_OWNPV	0.084	0.100	0.098	0.143
B_SMALLESTDELTACHI2	0.062	0.047	0.031	0.041
B_DIRA_OWNPV	0.046	0.086	0.127	0.140
KSLL_VDCHI2_OWNPV	-	-	0.112	0.091

Table C.2: BDT variable importance ranking [0,1] with 2012 post-June data. Variables are presented in the hierarchical order as obtained for Down-Down.

Variable	Importance DD		Importance LL	
	BDT1	BDT2	BDT1	BDT2
B_PTASYM_1_5	0.191	0.194	0.111	0.121
Σ_i h$_i$_IPCHI2_OWNPV	0.174	0.186	0.166	0.154
B_ETA	0.110	0.117	0.140	0.096
B_IPCHI2_OWNPV	0.110	0.079	0.059	0.080
B_DIRA_OWNPV	0.107	0.120	0.120	0.114
B_ENDVERTEX_CHI2	0.092	0.092	0.055	0.091
B_PT	0.087	0.164	0.094	0.079
B_VDCHI2_OWNPV	0.084	0.091	0.097	0.121
B_SMALLESTDELTACHI2	0.044	0.042	0.034	0.061
KSLL_VDCHI2_OWNPV	-	-	0.097	0.080

Next come the plots of the BDT response for the training and validation samples, Figs. C.13 and C.14.

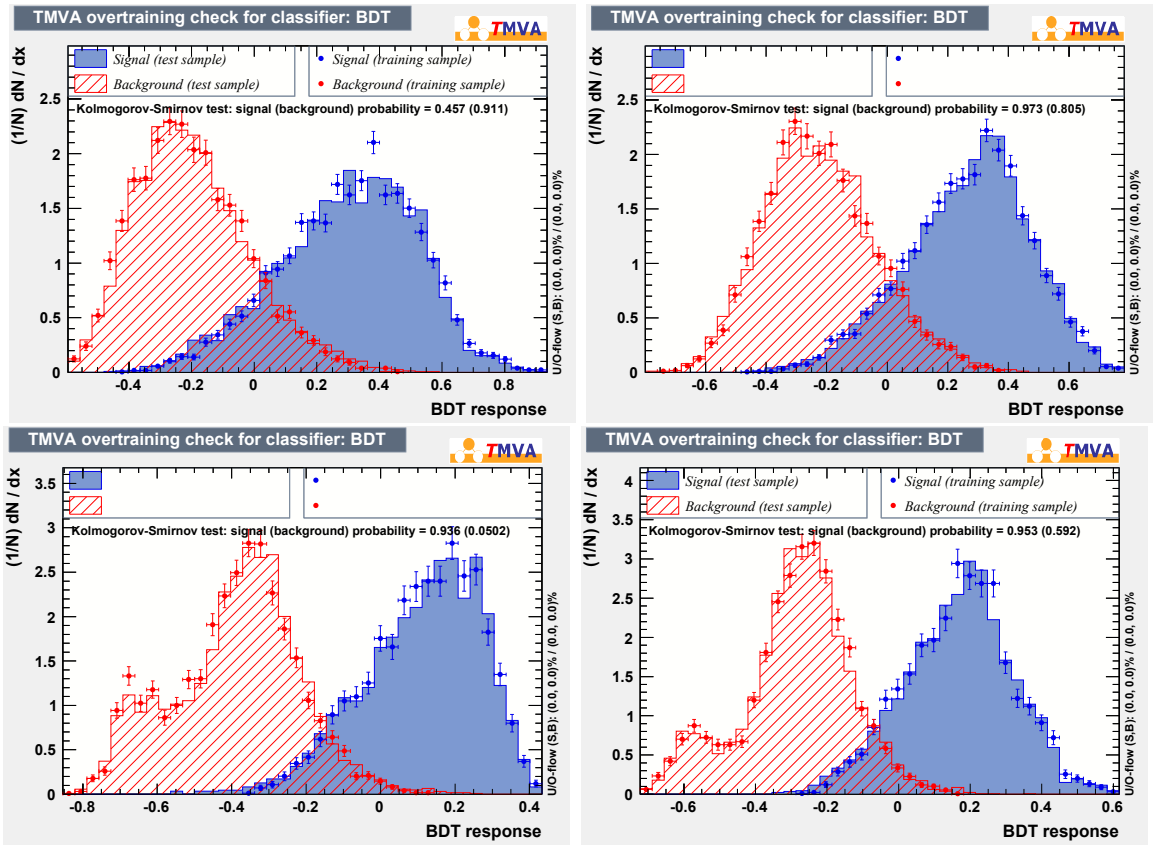

Figure C.13: Training and Validation samples response for the `BDT_1` (left) and `BDT_2` (right) discriminants for Down-Down (top) and Long-Long (bottom). MC2012PreJune is used for signal events and background events are selected from the right-handed side-bands of the 2012PreJune data sample. The histograms are normalized to the same number of entries.

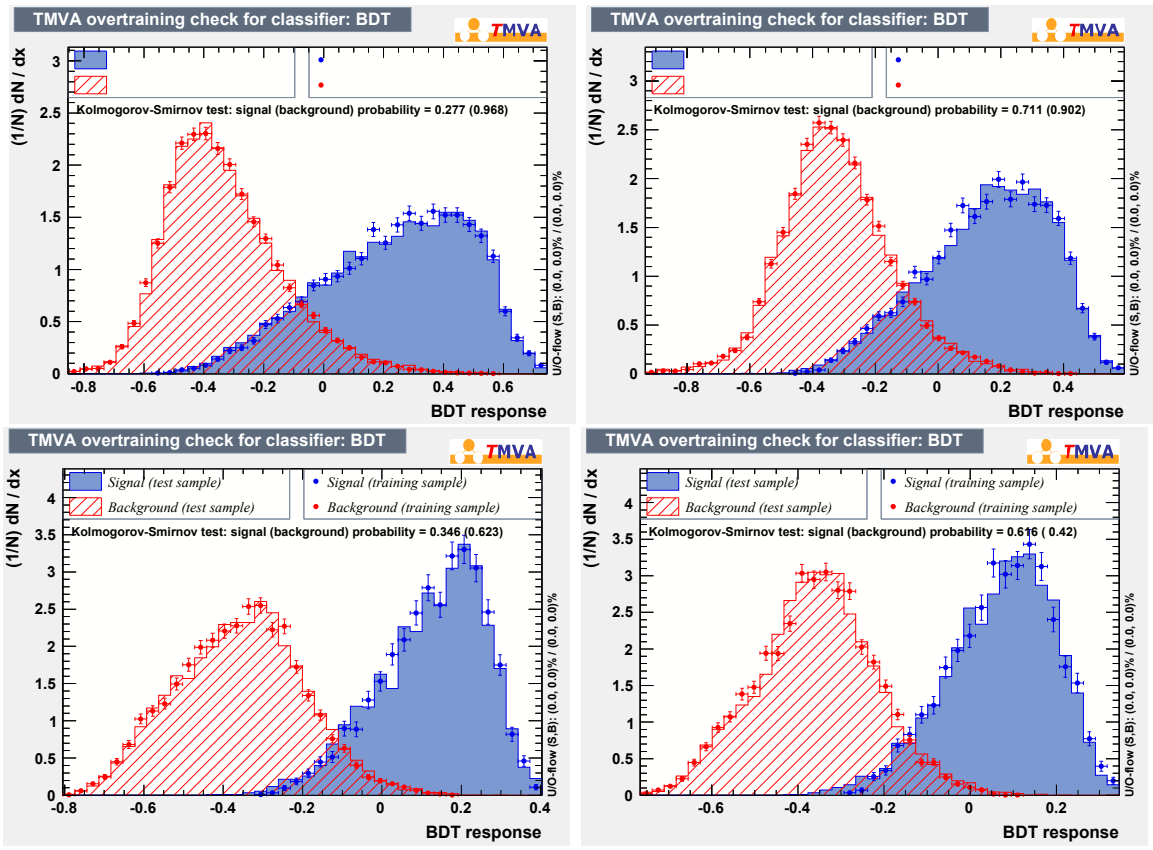

Figure C.14: Training and Validation samples response for the `BDT_1` (left) and `BDT_2` (right) discriminants for Down-Down (top) and Long-Long (bottom). MC2012PostJune is used for signal events and background events are selected from the right-handed side-bands of the 2012 PostJune data. The histograms are normalized to the same number of entries.

Finally, come the plots of the figures of merit as a function of the BDT cut value used to determine the optimal selection for the branching fraction measurements and Dalitz-plot analyses of the already-observed decays modes. Figs. C.15 to C.18 and 4.9 show FoM_1 and Figs. C.20 to C.24 show FoM_2.

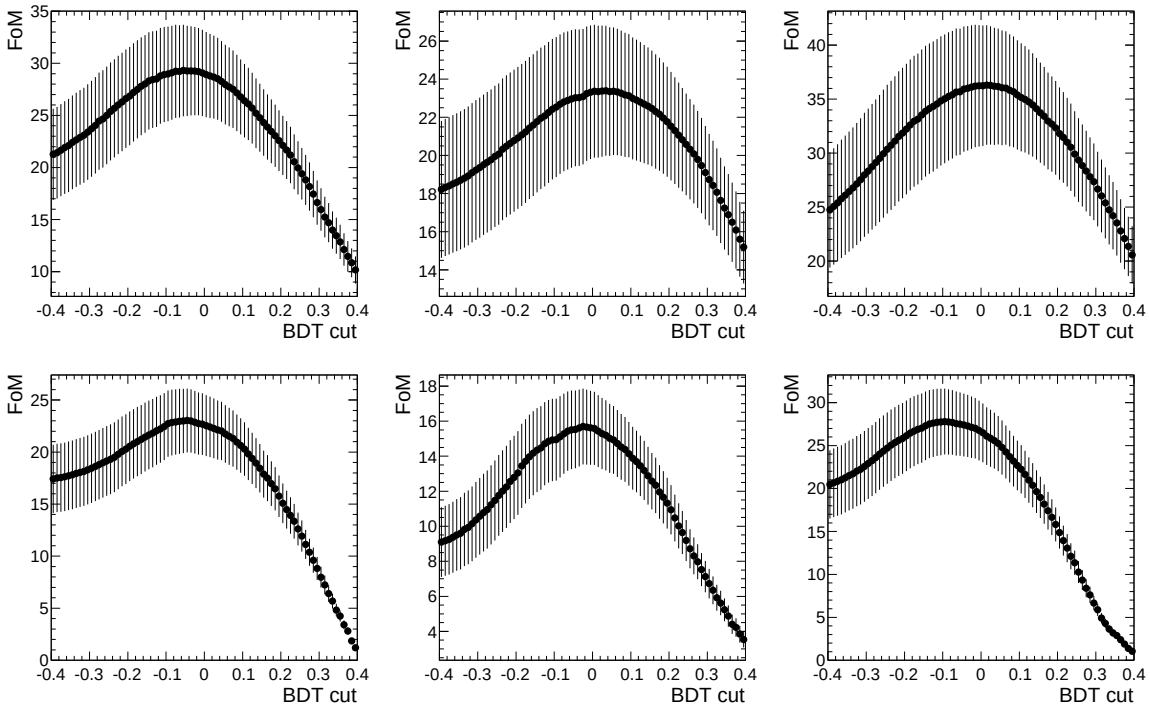

Figure C.15: Figures of merit computed as $S/\sqrt{(S+B)}$ for the observed mode $B^0 \to K^0_S\pi^+\pi^-$ using 2011 events (left), 2012-PreJune events (middle) and 2012-PostJune events (right) for Down-Down (top) and Long-Long (bottom) reconstruction categories.

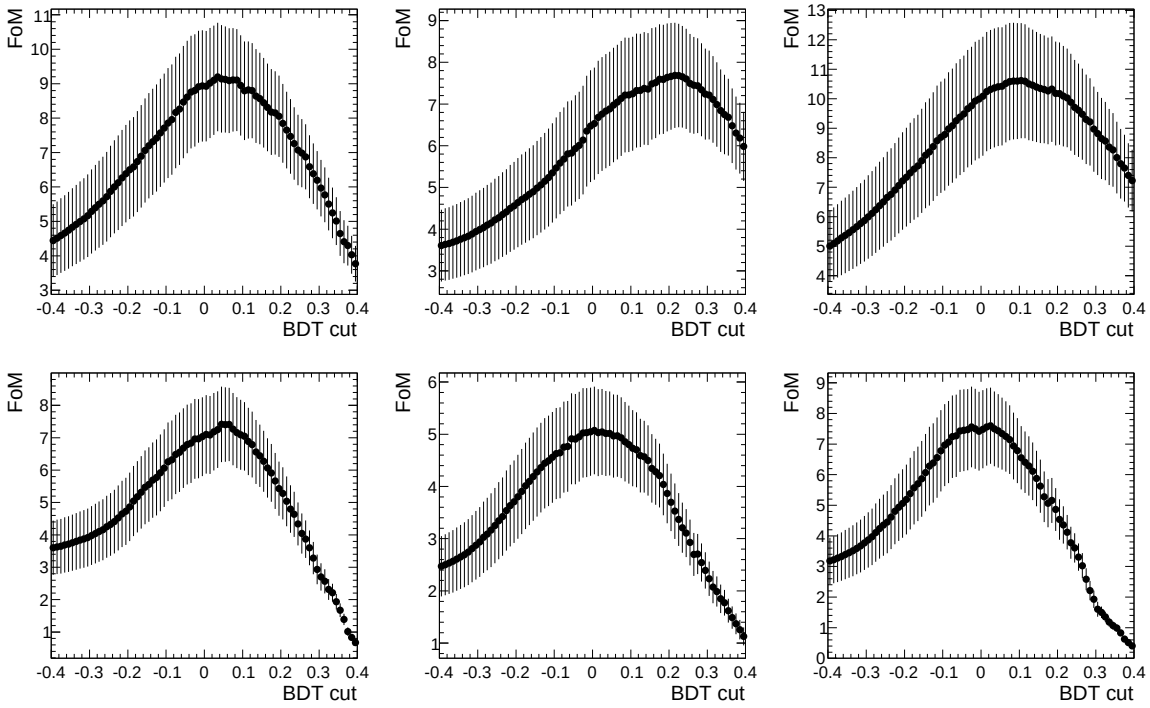

Figure C.16: Figures of merit computed as $S/\sqrt{(S+B)}$ for the observed mode $B^0 \to K^0_S K^{\pm}\pi^{\mp}$ using 2011 events (left), 2012-PreJune events (middle) and 2012-PostJune events (right) for Down-Down (top) and Long-Long (bottom) reconstruction categories.

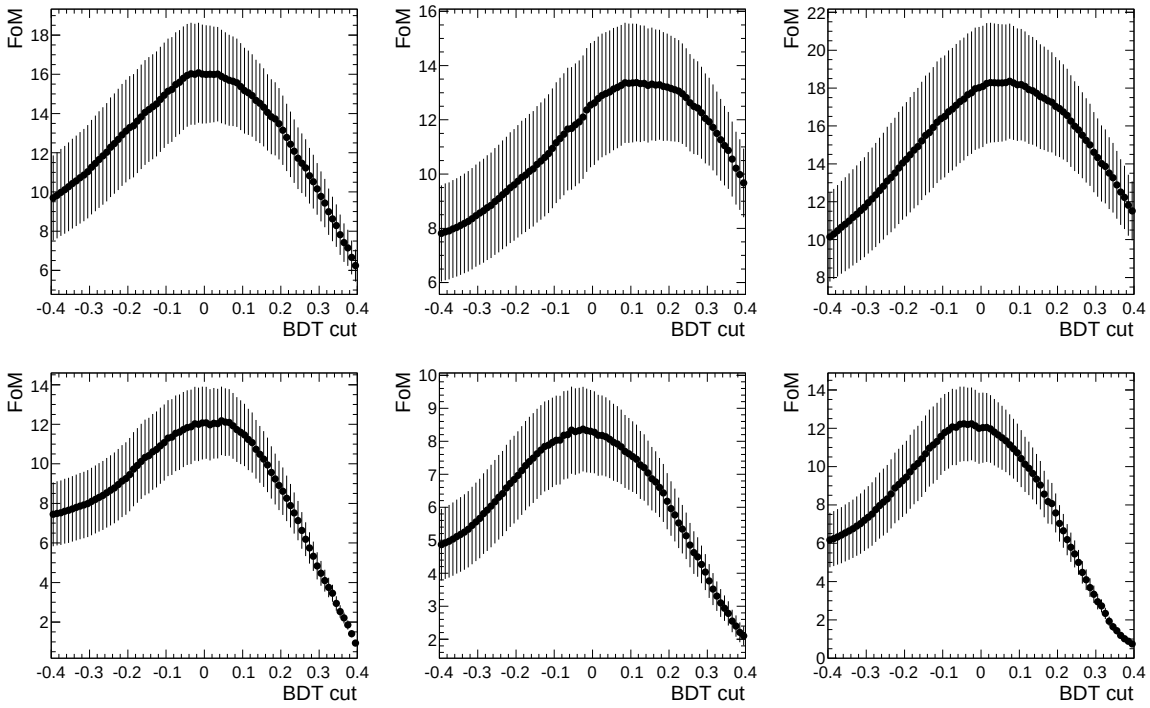

Figure C.17: Figures of merit computed as $S/\sqrt{(S+B)}$ for the observed mode $B_s^0 \to K_S^0 K^{\pm}\pi^{\mp}$ using 2011 events (left), 2012-PreJune events (middle) and 2012-PostJune events (right) for Down-Down (top) and Long-Long (bottom) reconstruction categories.

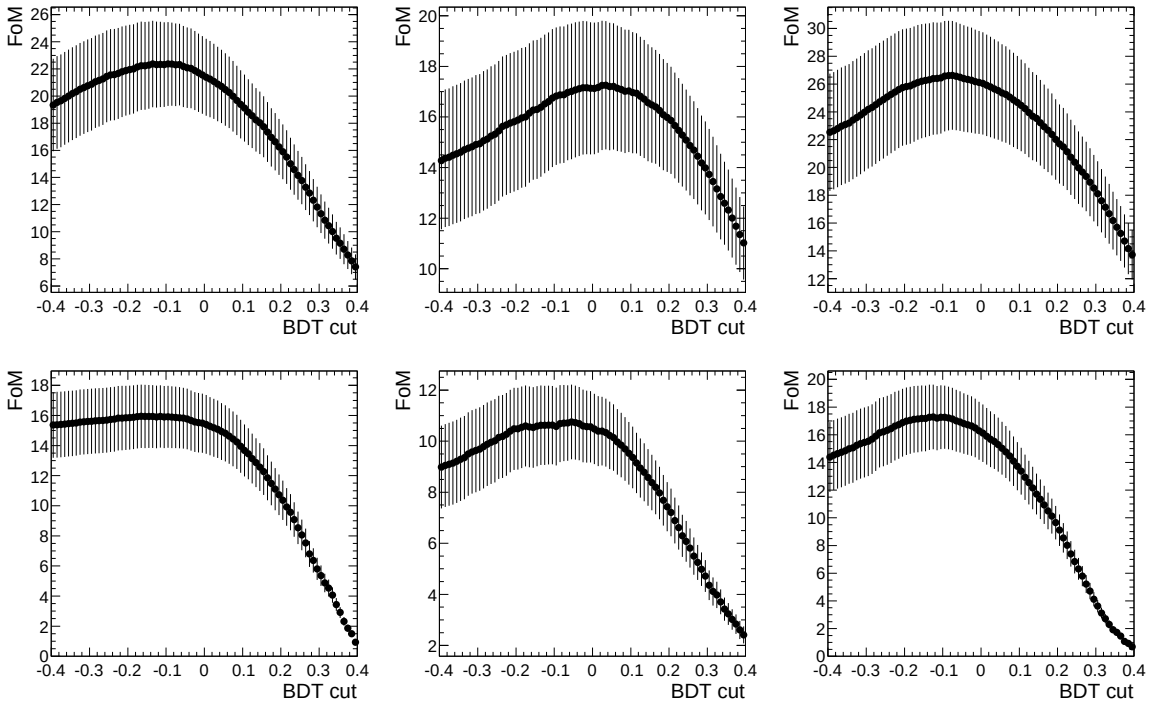

Figure C.18: Figures of merit computed as $S/\sqrt{(S+B)}$ for the observed mode $B^0 \to K^0_S K^+ K^-$ using 2011 events (left), 2012-PreJune events (middle) and 2012-PostJune events (right) for Down-Down (top) and Long-Long (bottom) reconstruction categories.

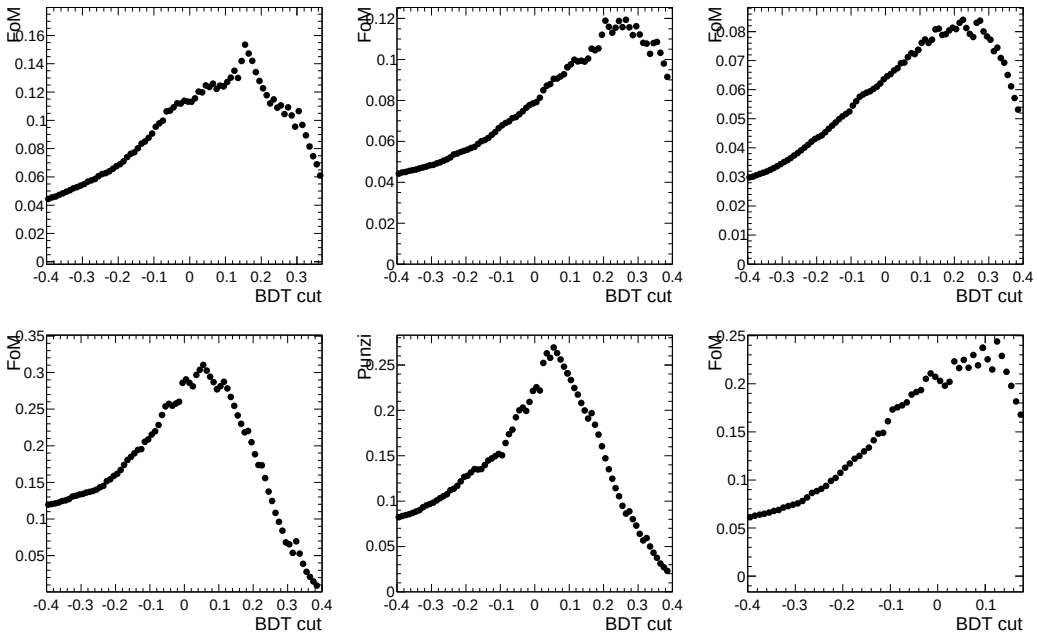

Figure C.19: *Figure of merit defined in Eq.* (4.2) *for the undiscovered mode* $B_s^0 \to K_S^0 K^+ K^-$ *using (left) 2011 events, (middle) 2012-PreJune events and (right) 2012-PostJune events, for (top) Down-Down and (bottom) Long-Long reconstruction categories.*

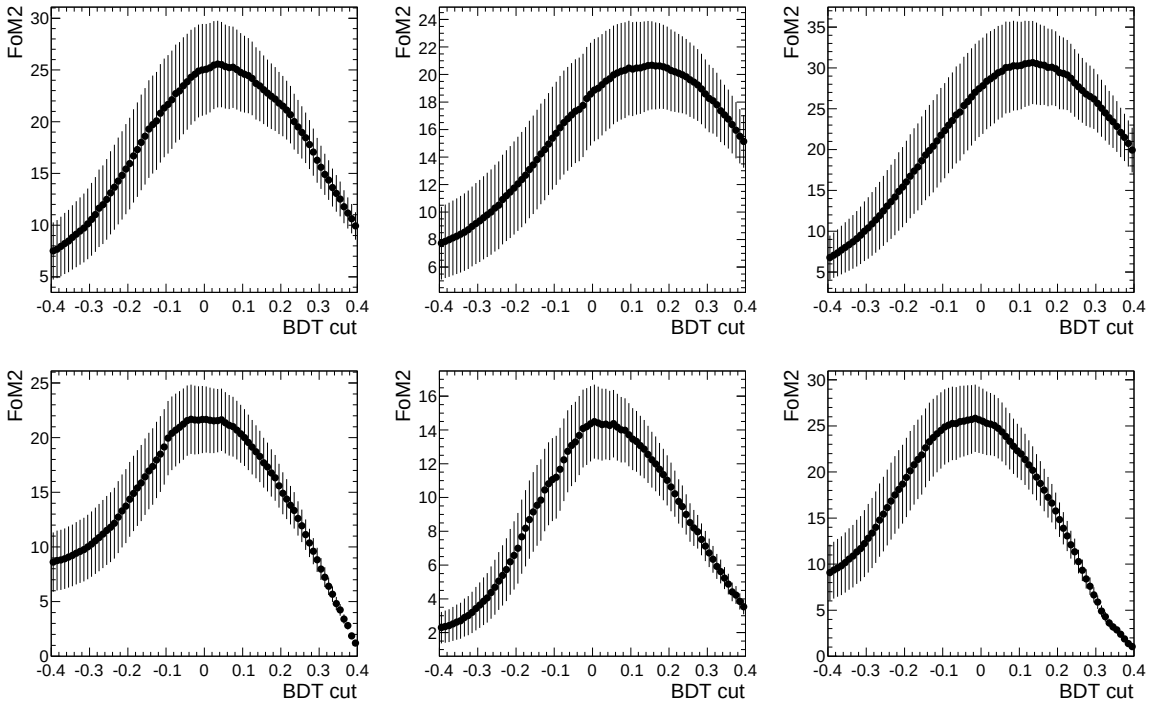

Figure C.20: Figures of merit computed as $S^2/(S+B)^{3/2}$ for the observed mode $B^0 \to K^0_S\pi^+\pi^-$ using 2011 events (left), 2012-PreJune events (middle) and 2012-PostJune events (right) for Down-Down (top) and Long-Long (bottom) reconstruction categories.

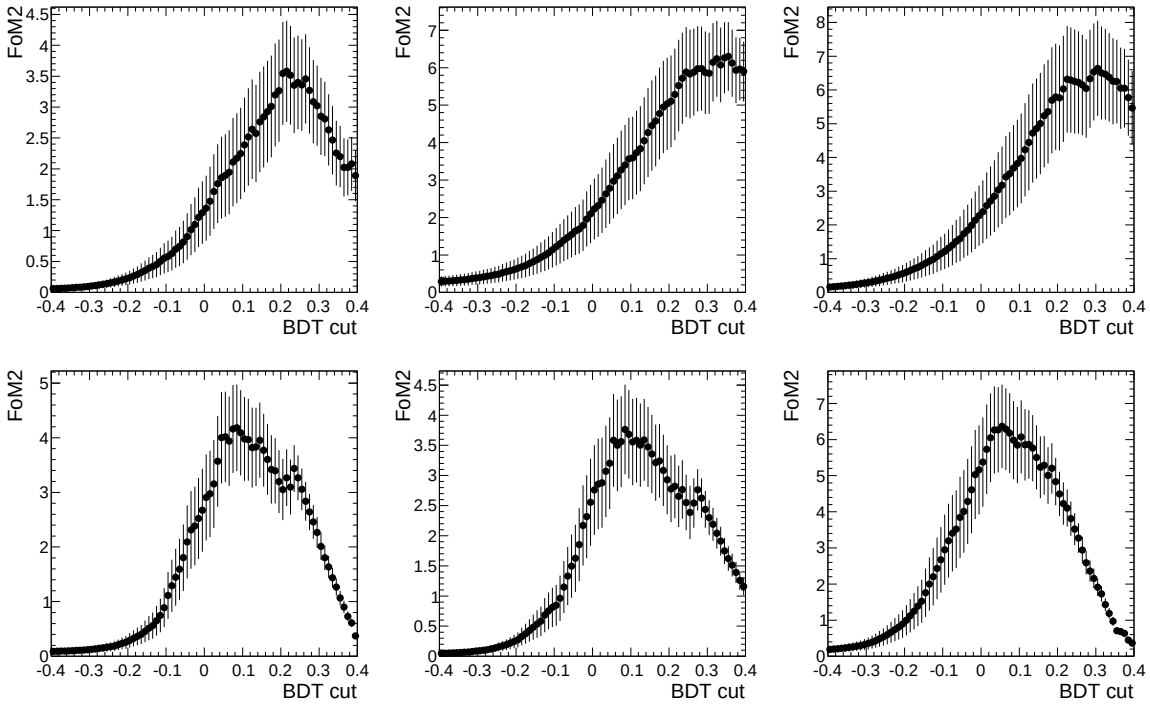

Figure C.21: Figures of merit computed as $S^2/(S+B)^{3/2}$ for the observed mode $B_s^0 \to K_S^0\pi^+\pi^-$ using 2011 events (left), 2012-PreJune events (middle) and 2012-PostJune events (right) for Down-Down (top) and Long-Long (bottom) reconstruction categories.

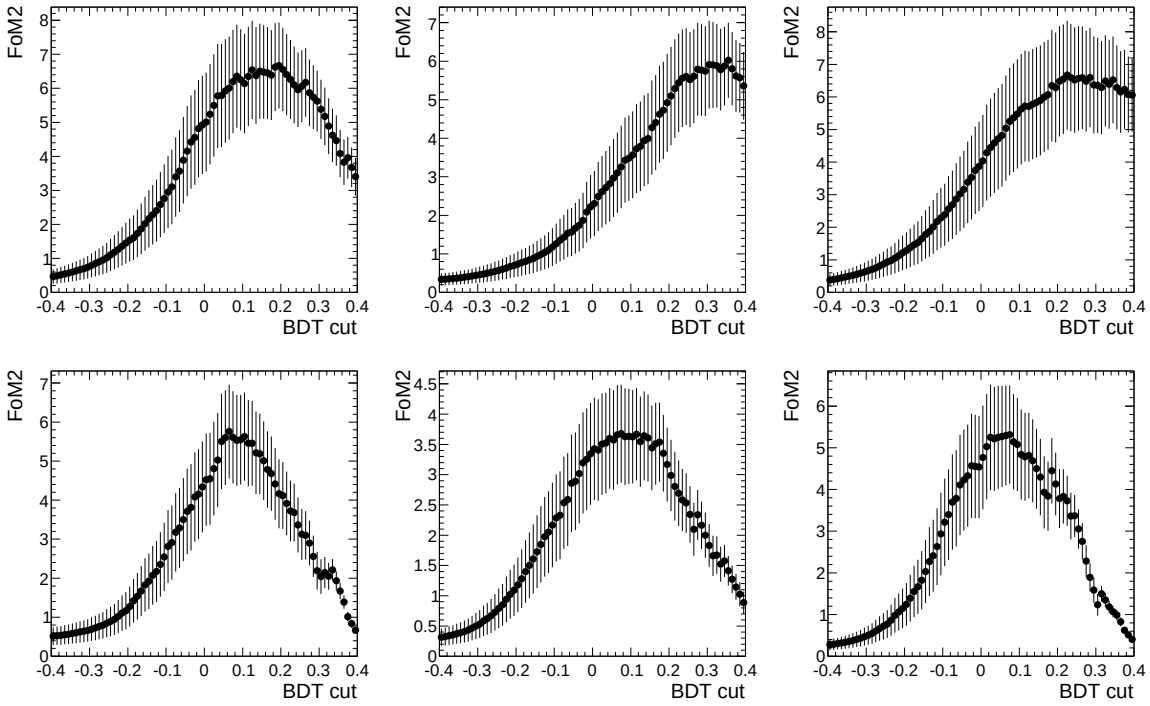

Figure C.22: Figures of merit computed as $S^2/(S+B)^{3/2}$ for the observed mode $B^0 \to K^0_S K^\pm \pi^\mp$ using 2011 events (left), 2012-PreJune events (middle) and 2012-PostJune events (right) for Down-Down (top) and Long-Long (bottom) reconstruction categories.

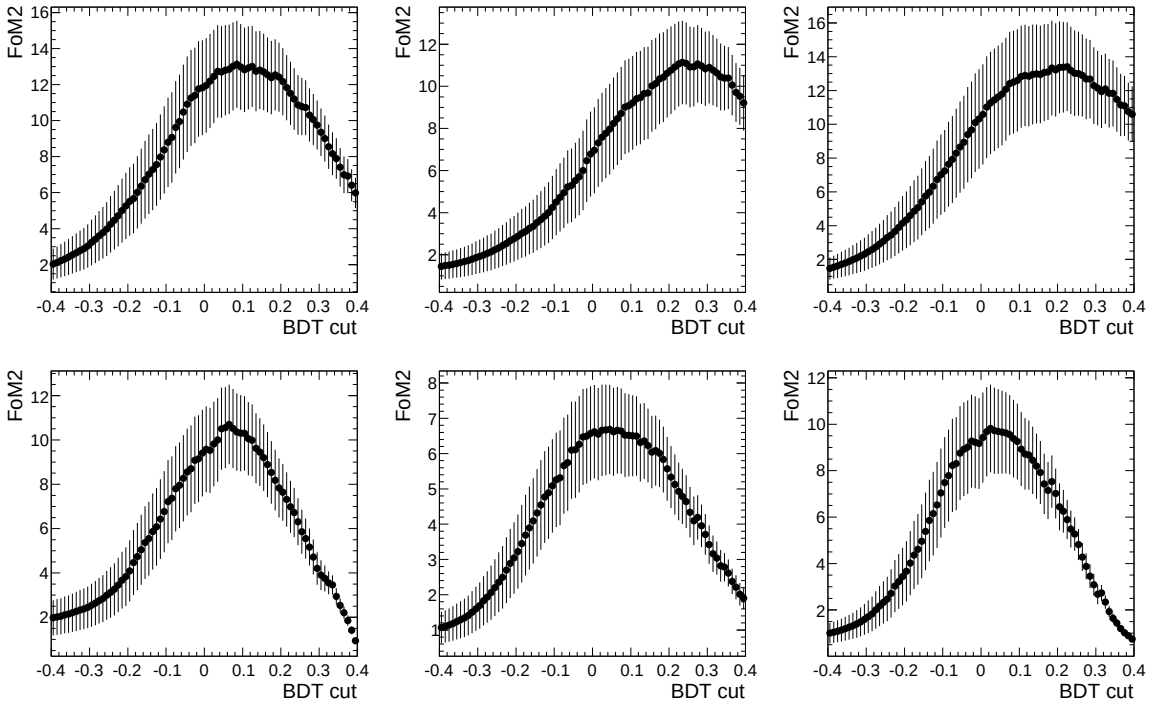

Figure C.23: Figures of merit computed as $S^2/(S+B)^{3/2}$ for the observed mode $B_s^0 \to K_S^0 K^{\pm}\pi^{\mp}$ using 2011 events (left), 2012-PreJune events (middle) and 2012-PostJune events (right) for Down-Down (top) and Long-Long (bottom) reconstruction categories.

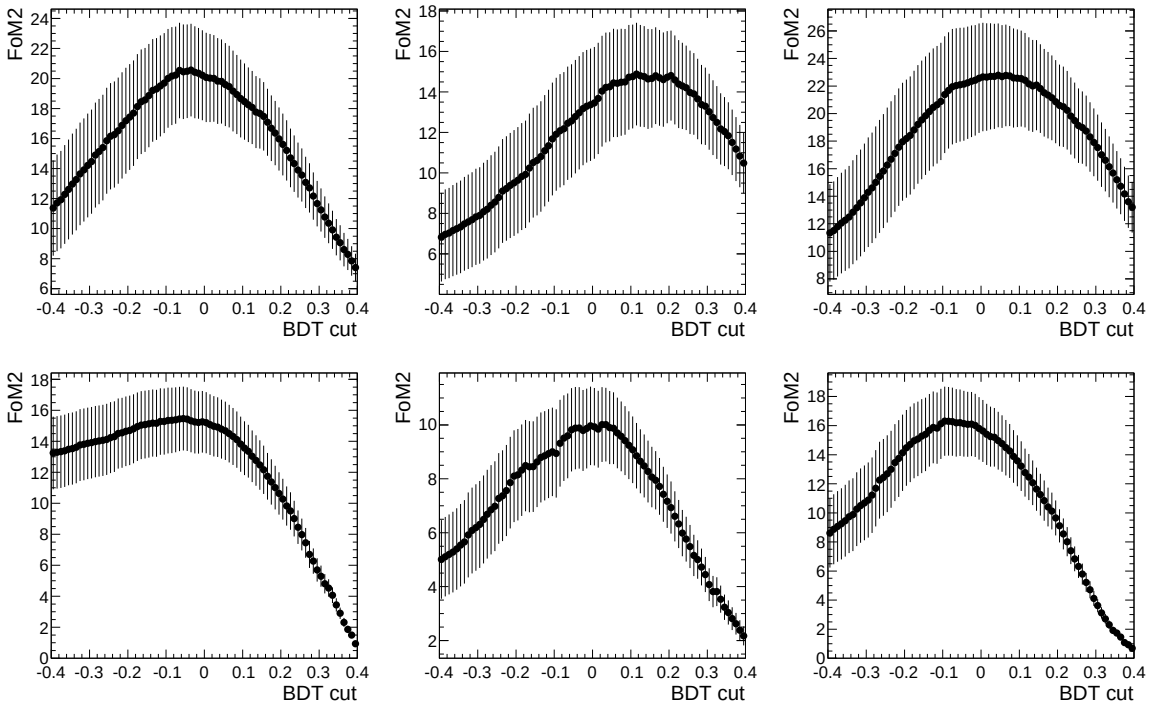

Figure C.24: Figures of merit computed as $S^2/(S+B)^{3/2}$ for the observed mode $B^0 \to K^0_S K^+ K^-$ using 2011 events (left), 2012-PreJune events (middle) and 2012-PostJune events (right) for Down-Down (top) and Long-Long (bottom) reconstruction categories.

Appendix D

Fit model - extra plots

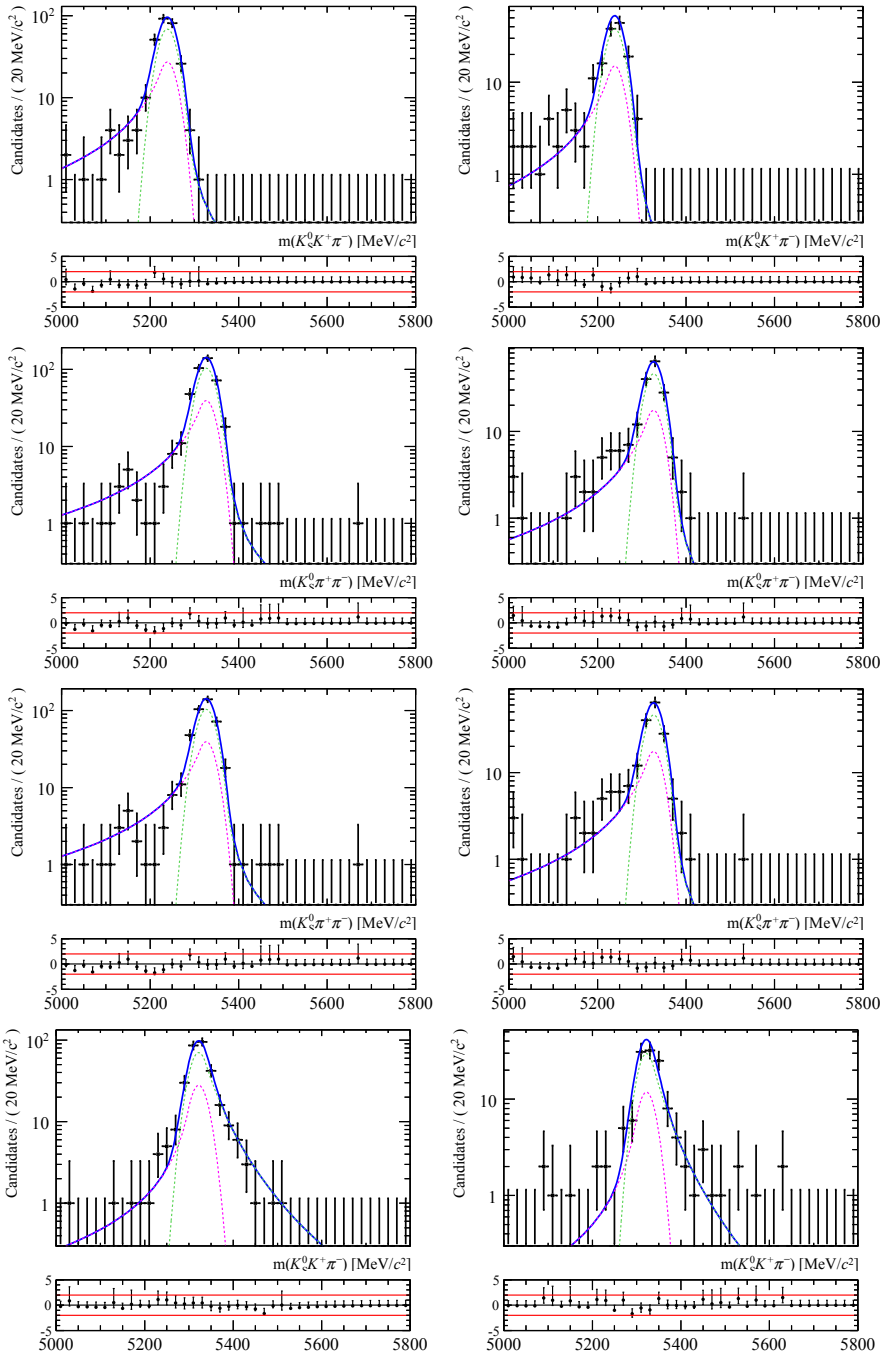

Figure D.1: Results of the fit of the reconstructed invariant mass of the misidentified signal decays, using the loose optimisation of the BDT on 2012a data.$B^0 \to K^0_S K^+ K^-$ as $K^0_S K^\pm \pi^\mp$, $B^0_s \to K^0_S K^\pm \pi^\mp$ as $K^0_S \pi^+ \pi^-$, $B^0_s \to K^0_S K^\pm \pi^\mp$ as $K^0_S K^+ K^-$, and $B^0 \to K^0_S \pi^+ \pi^-$ as $K^0_S K^\pm \pi^\mp$ are shown from top to bottom, while Down-Down decays are shown on the left and Long-Long decays on the right.

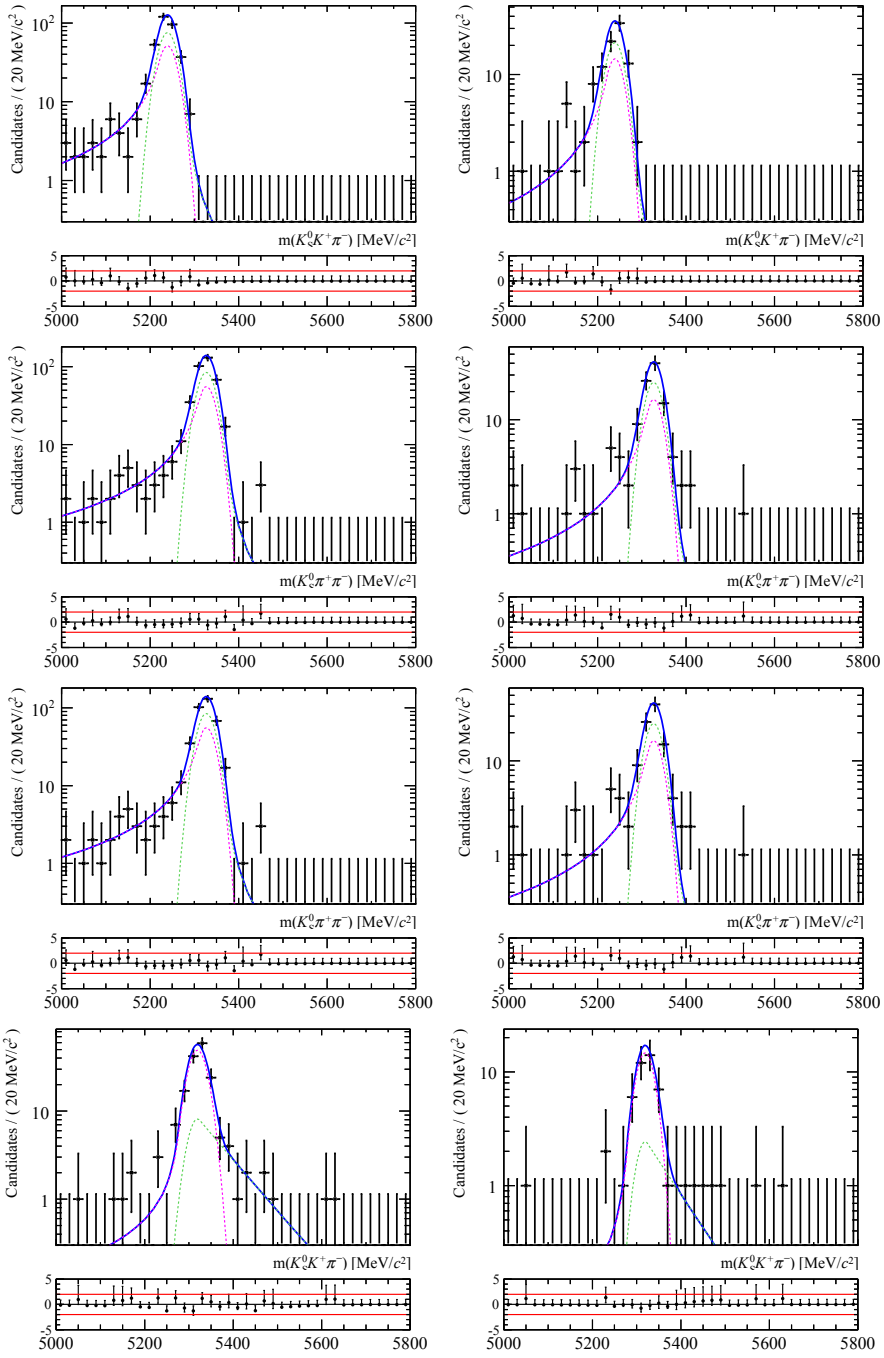

Figure D.2: Results of the fit of the reconstructed invariant mass of the misidentified signal decays, using the tight optimisation of the BDT.$B^0 \to K^0_S K^+ K^-$ as $K^0_S K^\pm \pi^\mp$, $B^0_s \to K^0_S K^\pm \pi^\mp$ as $K^0_S \pi^+ \pi^-$, $B^0_s \to K^0_S K^\pm \pi^\mp$ as $K^0_S K^+ K^-$, and $B^0 \to K^0_S \pi^+ \pi^-$ as $K^0_S K^\pm \pi^\mp$ are shown from top to bottom, while Down-Down decays are shown on the left and Long-Long decays on the right.

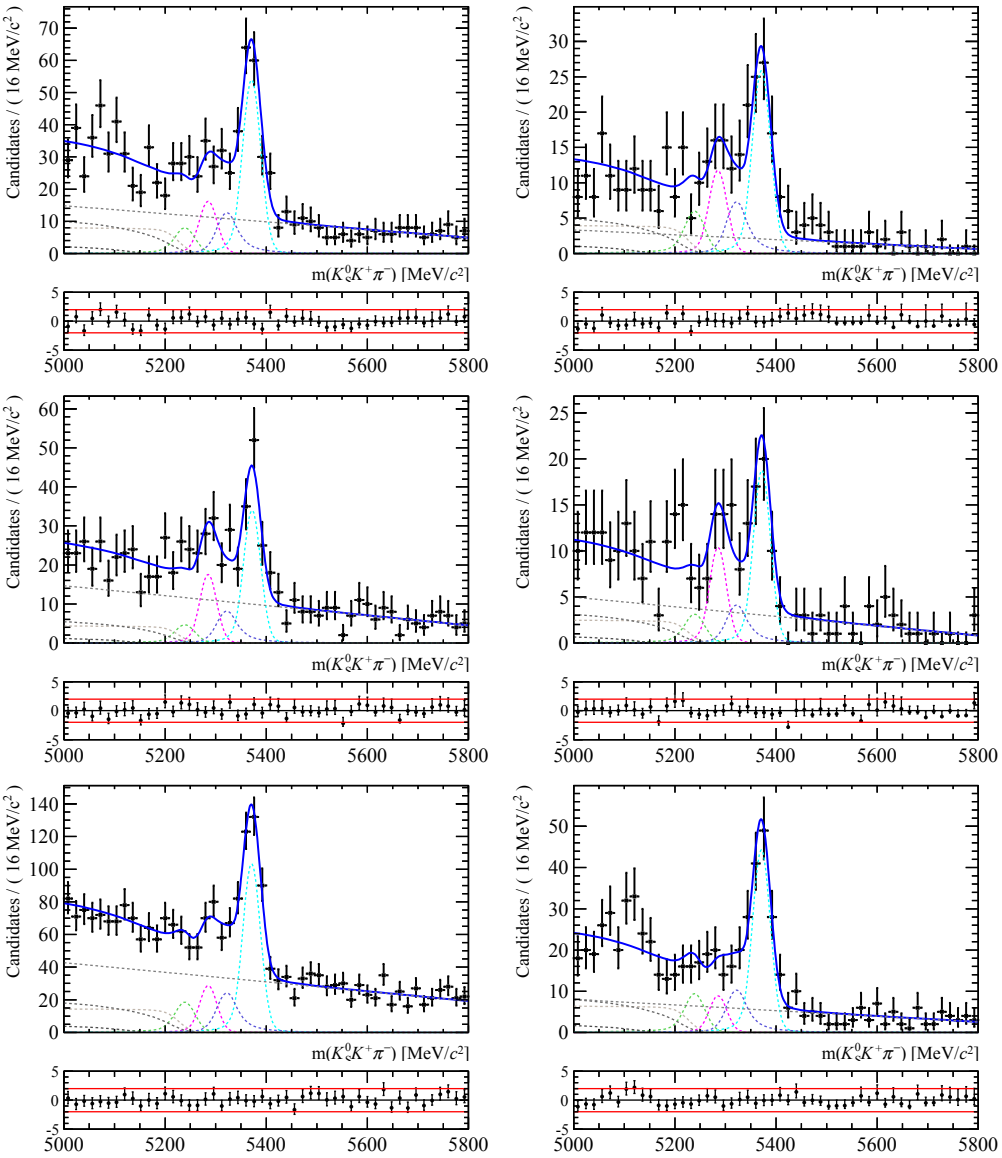

Figure D.3: *Result of the simultaneous fit of the $K^0_S K^+\pi^-$ data with the loose BDT optimisation. Running period 2011, 2012a and 2012b are shown from top to bottom, while the left and right plots show the result of Down-Down and Long-Long K^0_S reconstruction, respectively.*

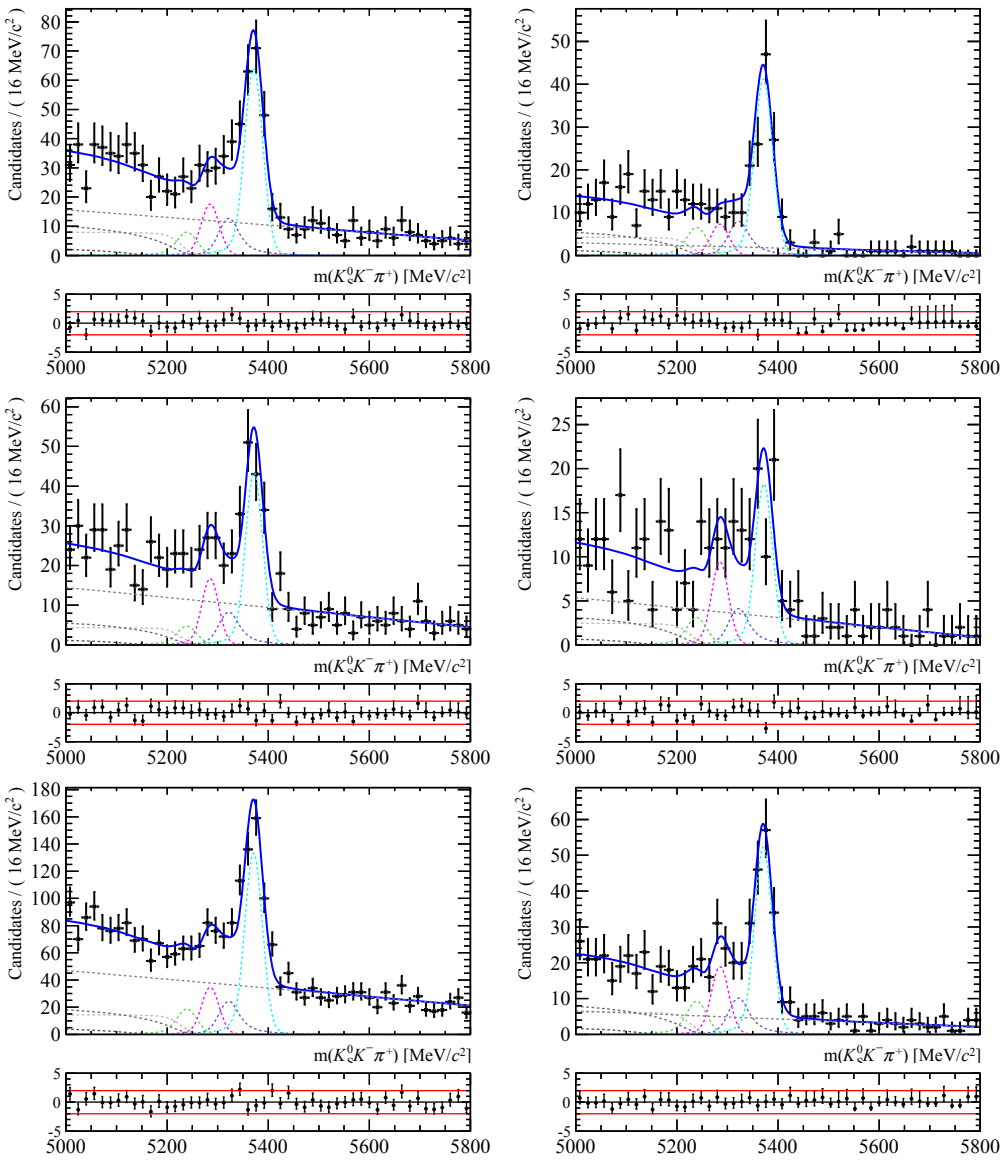

Figure D.4: *Result of the simultaneous fit of the $K^0_S\pi^+K^-$ data with the loose BDT optimisation. Running period 2011, 2012a and 2012b are shown from top to bottom, while the left and right plots show the result of Down-Down and Long-Long K^0_S reconstruction, respectively.*

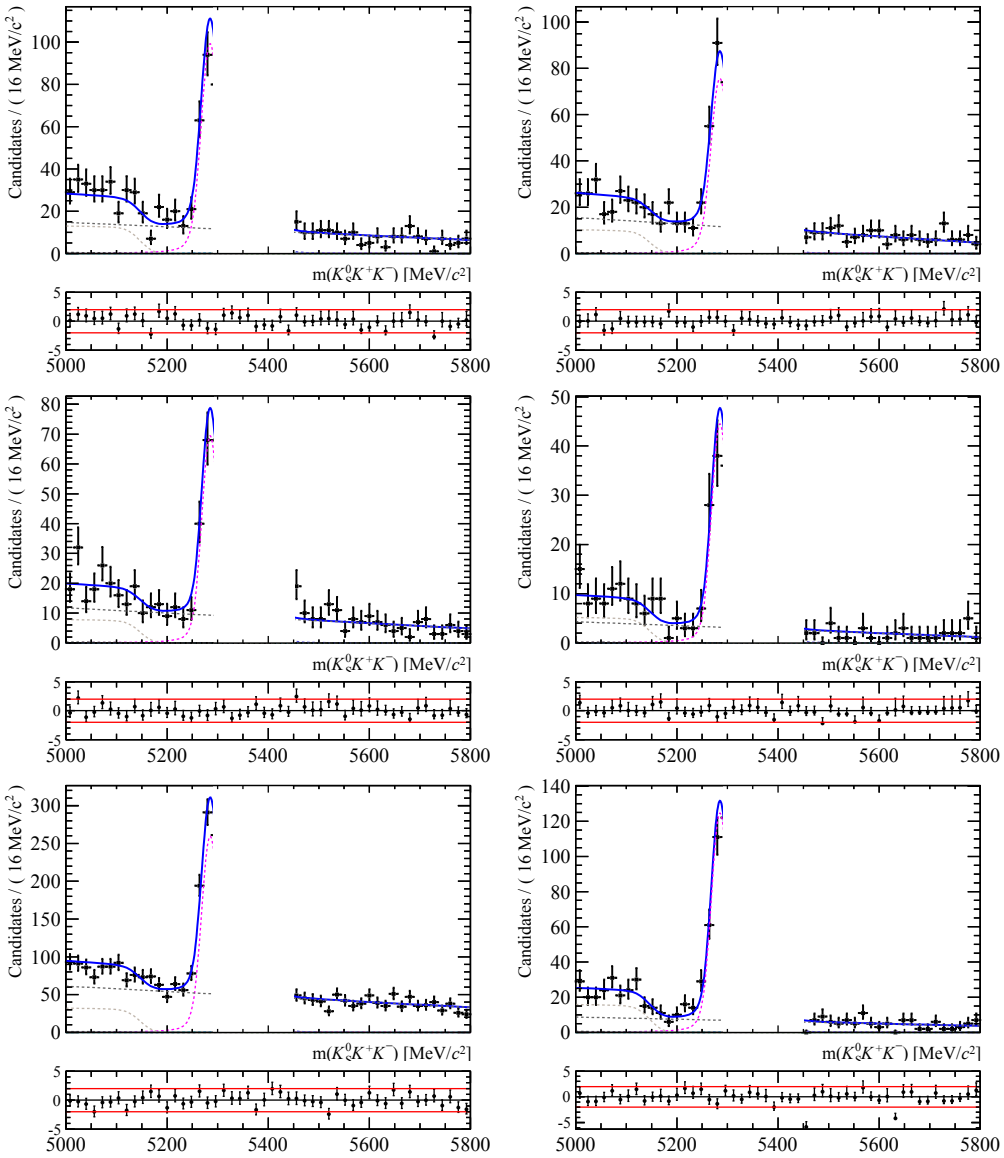

Figure D.5: *Result of the simultaneous fit of the $K^0_S K^+ K^-$ data with the loose BDT optimisation. Running period 2011, 2012a and 2012b are shown from top to bottom, while the left and right plots show the result of Down-Down and Long-Long K^0_S reconstruction, respectively.*

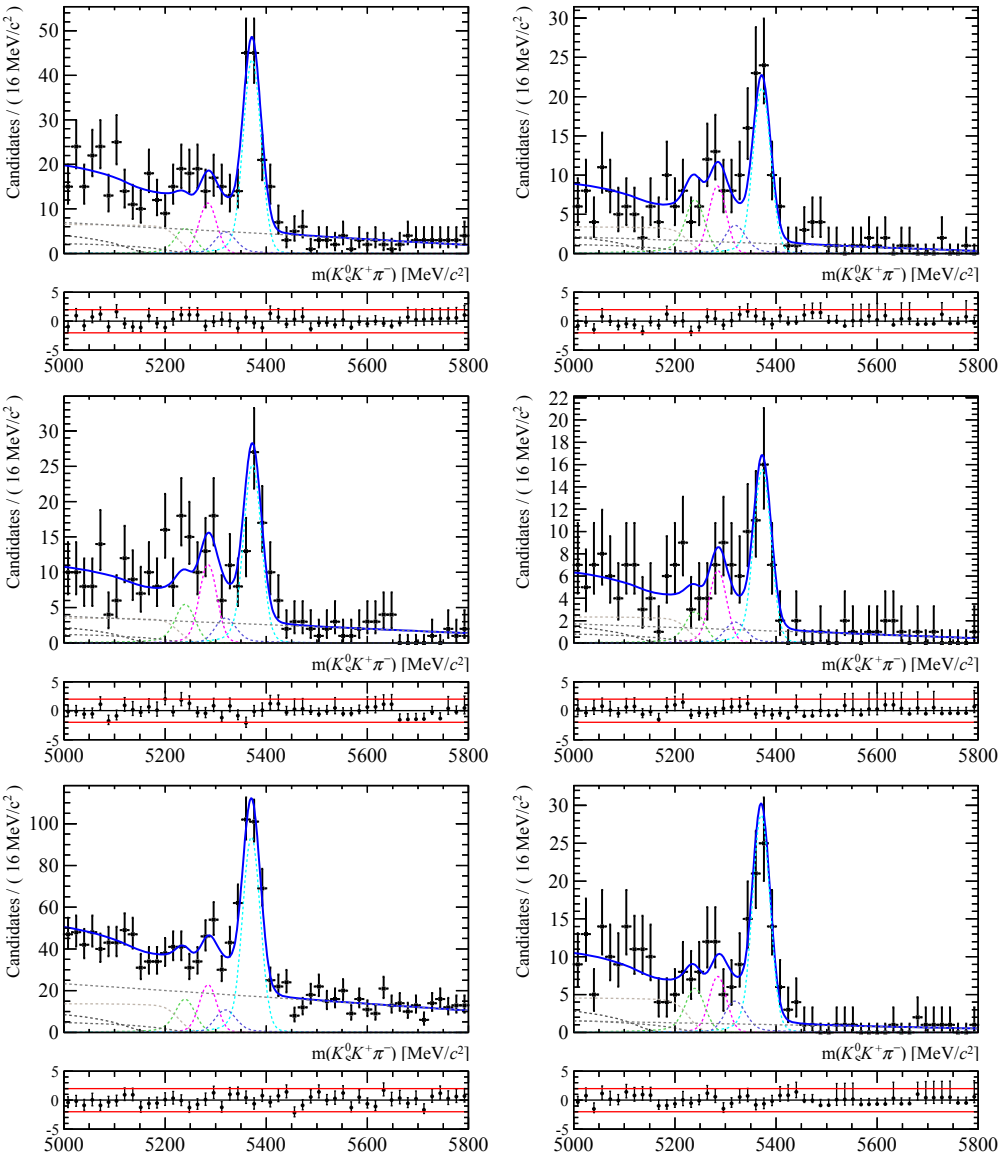

Figure D.6: *Result of the simultaneous fit of the $K^0_S K^+\pi^-$ data with the tight BDT optimisation. Running period 2011, 2012a and 2012b are shown from top to bottom, while the left and right plots show the result of Down-Down and Long-Long K^0_S reconstruction, respectively.*

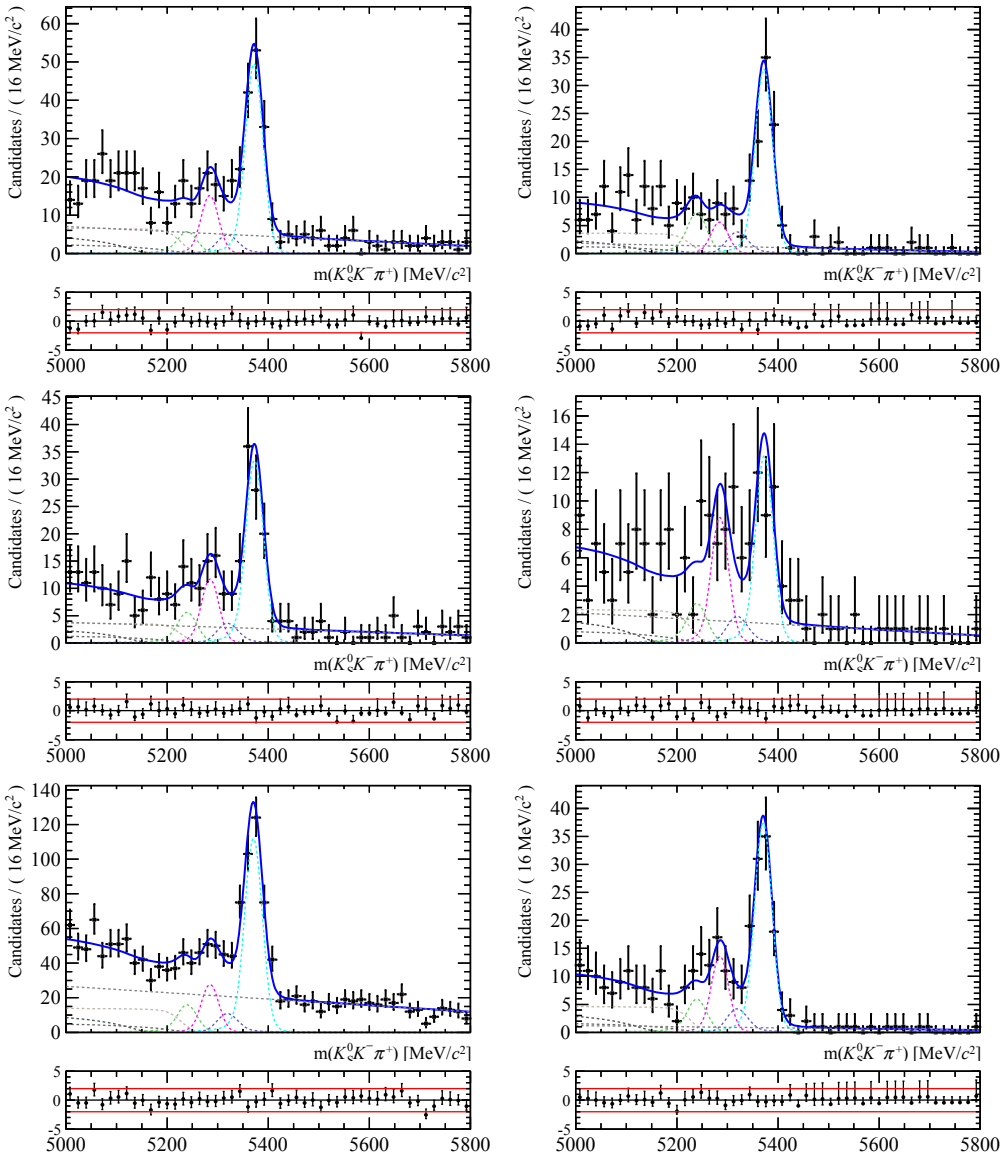

Figure D.7: *Result of the simultaneous fit of the $K^0_S\pi^+K^-$ data with the tight BDT optimisation. Running period 2011, 2012a and 2012b are shown from top to bottom, while the left and right plots show the result of Down-Down and Long-Long K^0_S reconstruction, respectively.*

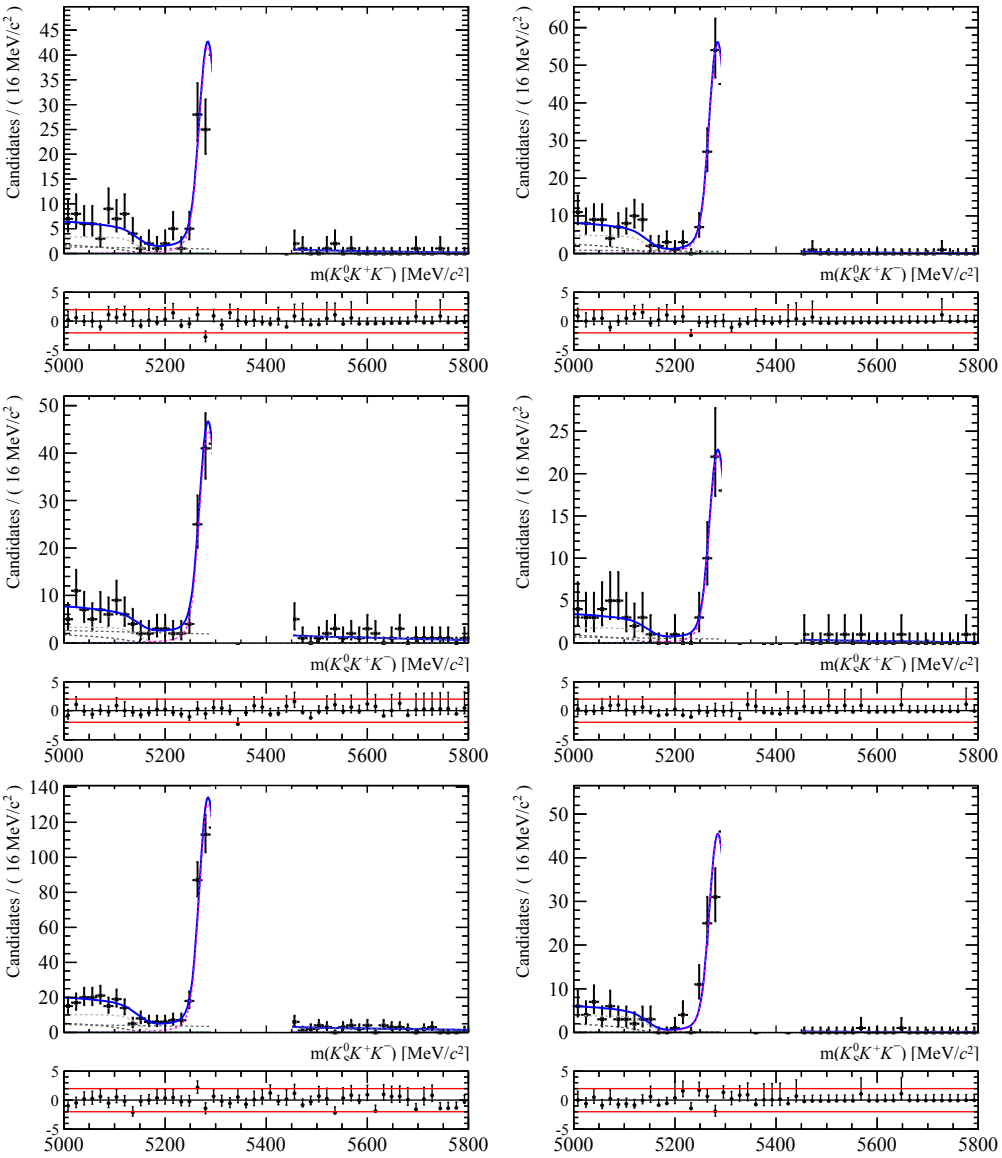

Figure D.8: *Result of the simultaneous fit of the $K^0_S K^+ K^-$ data with the tight BDT optimisation. Running period 2011, 2012a and 2012b are shown from top to bottom, while the left and right plots show the result of Down-Down and Long-Long K^0_S reconstruction, respectively.*

Appendix E

CRAFT fitter

CRAFT (Clermont Root-based Amplitude Fitter Tool) is a ROOT-based package designed for the charmless decays analysis $B^0 \to K^0_S h^+ h^-$, developed by Stéphane Monteil, Stéphane Pruvot and myself. CRAFT contains a set of C++ classes depending on ROOT and its sub-library RooFit. It was built to perform Dalitz Plot fits to determine the parameters of interest using the isobar formalism for the description of the dynamics of the decay, reviewed in Section 2.3. All mass-dependent lineshapes described in Section 2.4 and further models (Gaussian, experiential, polynomial *etc.*) are implemented in CRAFT. CRAFT contains two main parts: the description of the multivariate p.d.f. and the description of the model. CRAFT is based on three pillars: the numerical integration, the pseudo-experiment generation and the fitting machinery.

E.1 Numerical integration technique

The numerical integration is used mainly to compute the likelihood normalization and plots drawing. Three types of numerical integration were tested. Denoting P as a generic p.d.f., they are:

- The Midpoint rule: $I(\mathcal{P}) = (b-a)\mathcal{P}\left(\frac{a+b}{2}\right)$,
- The Trapezoidal rule: $I(\mathcal{P}) = (b-a)\left(\frac{\mathcal{P}(a)+\mathcal{P}(b)}{2}\right)$
- The Simpson's rule: $I(\mathcal{P}) = \frac{b-a}{6}\left[\mathcal{P}(a)\left(\frac{\mathcal{P}(a)+\mathcal{P}(b)}{2}\right)\mathcal{P}(b)\right]$

With a sharp integration binning (~ 15 MeV), there is no significant difference between the three types of numerical integration. Therefore, the faster method (Midpoint rule integration) is chosen to be the standard integration in the software. Another type of numerical integration implemented in CRAFT, referred to in the literature as Monte Carlo integration, is making use of random numbers (uniform sampling). This method is particularly useful for higher-dimensional integrals.

E.2 Generation technique of pseudo-experiments

CRAFT has the versatility to generate Monte Carlo pseudo-experiments. We made an immoderate use of this feature in order to drive our ideas for the analysis design but also for the actual determination of various systematic uncertainties. The generation technique implemented in the Dalitz fitter is the Accept-Reject method. The algorithm of this method consists of two steps: the generation of two dimensional vectors $v_{ij}((s_+)_i,(s_-)_j)$ uniform in the plan (s_+,s_-) and then the generation of a random number u uniformly distributed between 0 and $\mathcal{P}_{\max}$, where $\mathcal{P}_{\max}$ is fixed by the user. Eventually, if u is less then $\mathcal{P}(v_{ij})$ then the event living at coordinates $\{(s_+)_i,(s_-)_j\}$ is accepted, if not, it is rejected and the operation is repeated with a new event.

E.3 Efficiency

The reconstruction efficiency depends on the position of the candidate in DP. Therefore, the DP distribution must be corrected for this efficiency in the fit to the data. The efficiency is calculated as a function of DP position from the Monte Carlo samples where the acceptance effects is included. Two methods are used in CRAFT to model the efficiency: the spline method and the analytical method. For the spline method, the acceptance variations are smoothed out by fitting each efficiency function (polynomial with low degrees) by a 2D cubic spline across the phase-space, as described in Section 5.3.2.4. For the analytical method, a two dimensional polynomial function, fitted to the relevant MC sample, implemented in the signal p.d.f. instead of the smoothed efficiency histogram. An efficiency study has been made with the analytical method in the analysis of $B^0 \to K^0_S\pi^+\pi^-$, driving to a 2D polynomial function as:

$$\epsilon(s_+,s_-) = m'^{a_5}(1-m')^{a_6}(1+a_0(s_++s_-)+a_1(s_+^2+s_-^2)+a_2 s_+s_-+a_3(s_+^3+s_-^3)+a_4(s_+^2s_-+s_+s_-^2)\ , \tag{E.1}$$

where a_i are the floated parameters, s_+ and s_- are the standard Dalitz variables and m' is the Square Dalitz variable.

E.4 Fitting machinery

CRAFT is a maximum likelihood fitting software, using minuit software for the minimization procedure. As shown in Section 4.1, the data present a difference in terms of background and reconstruction efficiency between each sample categories, which requires a simultaneous fit to use the maximum of information. Eventually, the package provides the possibility of performing a DP analysis by making use of a simultaneous fitting to several data spectra. In other words, the fitter can perform a simultaneous fit of independent samples with different efficiency ($\{x_i^{(1)}\}_{i=1}^n$, $\{x_j^{(2)}\}_{j=1}^m$, ..., $\{x_k^{(t)}\}_{k=1}^l$) to determine a common set of parameters (isobar parameters, line-shape parameters ...) $\vec{\theta}$ by maximizing the product of all the likelihoods (minimizing the sum of all negative log likelihoods (nll)).

$$\mathrm{nll} = \sum_{i=1}^{n} -\ln(\mathcal{P}(\{s_+, s_-\}_i^{(1)})) + \sum_{j=1}^{m} -\ln(\mathcal{P}(\{s_+, s_-\}_j^{(2)})) + \cdots + \sum_{k=1}^{l} -\ln(\mathcal{P}(\{s_+, s_-\}_k^{(t)})) \ . \tag{E.2}$$

Appendix F

Definition of a goodness-of-fit estimator

The Dalitz Plane fit to the data presented in this document is a simultaneous unbinned fit of several spectra, where the events distribution in the phase space may vary rapidly due to the decay dynamics. A convenient goodness of fit (g.o.f) test for this type of analysis must take into account the agreement in the full phase space on an event by event basis. The point-to-point dissimilarity test [97] meets this requirement. Being $f(s_+, s_-)$ ($f(\vec{s})$) the true PDF of the data with true Dalitz model M, and ($f_0(\vec{s})$) the PDF to be tested based in the Dalitz model M_0, a test statistic depending on f and f_0 is defined. This test statistic T quantifies the agreement between the data and the test model M_0. The larger is T, the worse is the level of agreement.

The significance of any discrepancy between the data and the test PDF is quantified by a p-value defined as

$$p = \int_T^\infty g(T'|\vec{\theta}, M_0)\mathrm{d}T' = \int_T^\infty g_{f_0}(T)\mathrm{d}T' \,, \tag{F.1}$$

where $g_{f_0}(T)$ is the PDF of test statistic and $\vec{\theta}$ the set of the free parameters in the fit. It is worth to notice that the p-value is not the probability of the compatibility of the tested model M_0 with the data distribution M ($M = M_0$). It is instead the probability of observing data at least as incompatible with the $M = M_0$ hypothesis as the data actually observed, and hence the p-value behaves as the confidence level. The hypothesis $M = M_0$ is rejected at a confidence level α if $p < 1 - \alpha$.

Should the parent PDF of the data be known (which is not), the statistic test T is then formed from the integral of the quadratic difference between f and f_0,

$$T = \frac{1}{2}\int [f(\vec{s}) - f_0(\vec{s})]^2 \mathrm{d}\vec{s} \,, \tag{F.2}$$

Since f is not known, a weighting function $\psi(|\vec{s}' - \vec{s}|)$ is introduced to correlate the differences between the two PDF's at different points in the multivariate space [98]. The statistic test reads:

$$T = \frac{1}{2}\int (f(\vec{s}) - f_0(\vec{s}))(f(\vec{s}') - f_0(\vec{s}'))\psi(|\vec{s} - \vec{s}'|)\mathrm{d}\vec{s}\mathrm{d}\vec{s}' \,, \tag{F.3}$$

where $\psi(|\vec{s}-\vec{s}'|)$ depends on the Euclidean distance $|\vec{s}-\vec{s}'|$.

Several correlating function $\psi(|\vec{s}-\vec{s}'|)$ can be found in the literature. The most relevant for Dalitz plot fits have been discussed in [97]:

$$\psi_{\mathrm{Gau}}(|\vec{s}-\vec{s}'|) = \exp\left(\frac{|\vec{s}-\vec{s}'|}{2\sigma(\vec{s})\sigma(\vec{s}')}\right) , \tag{F.4}$$

$$\psi_{\mathrm{Log}}(|\vec{s}-\vec{s}'|) = \ln(|\vec{s}-\vec{s}'|+\epsilon) , \tag{F.5}$$

The logarithmic correlating function exhibits poles when the euclidean distance ϵ evaluates to zero. Therefore, a cut-off is introduced to avoid the digitization problems and its value is set as $\epsilon_{mc/d} = \frac{1}{2nf^{\max}}$, where $f^{\max}$ is the maximum of the Dalitz PDF and n is the number of events. Regarding the Gaussian correlating function and following [97], the term $\sigma(\vec{s})$ is chosen to be proportional to the inverse of the PDF:

$$\sigma(\vec{s}) = \frac{\bar{\sigma}}{f(\vec{s})} . \tag{F.6}$$

The preferred range for $\bar{\sigma}$ is $[\bar{\Gamma}, 2\bar{\Gamma}]$, where $\bar{\Gamma}$ is defined from the fit fractions (ff_r) and widths (Γ_r) of the resonances $\bar{\Gamma} = \sum ff_r\Gamma_r / \sum ff_r$.

Expanding the Eq. (F.2), we find:

$$T = \frac{1}{2}\int (f(\vec{s})f(\vec{s}') + f_0(\vec{s})f_0(\vec{s}') + 2f(\vec{s})f_0(\vec{s}'))\psi(|\vec{s}-\vec{s}'|)\mathrm{d}\vec{s}\mathrm{d}\vec{s}' , \tag{F.7}$$

which can be calculated using the data and Monte Carlo data sets (with number of events n_d and n_{MC}, respectively) sampled from f_0 as follows:

$$\begin{aligned} T_{d/mc} &= \frac{1}{n_d(n_d-1)}\sum_{i,j>i}^{n_d}\psi(|\vec{s}_i^{\,d}-\vec{s}_j^{\,d}|) + \frac{1}{n_{MC}(n_{MC}-1)}\sum_{i,j>i}^{n_{MC}}\psi(|\vec{s}_i^{\,MC}-\vec{s}_j^{\,MC}|) \\ &- \frac{1}{n_d n_{MC}}\sum_{i,j}^{n_d n_{MC}}\psi(|\vec{s}_i^{\,d}-\vec{s}_j^{\,MC}|) . \end{aligned} \tag{F.8}$$

The distributions of $T_{d/d}$ or $T_{mc/mc}$ must follow a generalized extreme value distribution (EVD):

$$E(x) = \frac{A}{\sigma}(1+\xi z)^{-\frac{1}{\xi}-1}\exp\left[-(1+\xi z)^{-\frac{1}{\xi}}\right] , \tag{F.9}$$

where $z = (x-\mu)/\sigma$, μ is the location parameter, σ is the distribution scale, and ξ and A are the shape and normalization parameter, respectively. In order to check the statistic test distribution that we are using, pseudo-experiments have been generated using a flat distribution between zero to produce $T_{d/d}$ values (10000 toy samples). The resulting distributions using the logarithmic and Gaussian correlating function behaves along expectation, as illustrated by the fits of the EVD function to the pseudo-experiments shown in Fig. F.1.

Since the statistical fluctuations of the MC term in Eq. (F.2) are negligible in comparison with the other two terms ($n_{mc} \gg n_d$), the master formula used for the actual computations of the statistic test simplifies as:

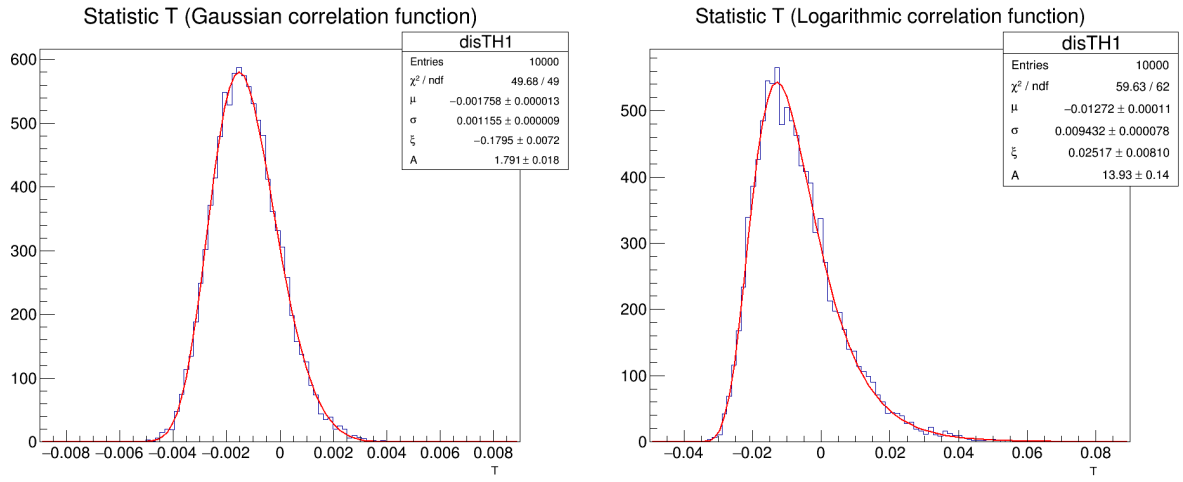

Figure F.1: Distribution of the test statistic $T_{d/d}$ for a uniform PDF with Gaussian and logarithmic correlating function. The curves corresponds to the fit by an extended extreme value distribution.

$$T_{d/mc} = \frac{1}{n_d^2}\sum_{i,j>i}^{n_d}\psi(|\vec{s}_i^{\,d} - \vec{s}_j^{\,d}|) - \frac{1}{n_d n_{mc}}\sum_{i,j>i}^{n_d n_{mc}}\psi(|\vec{s}_i^{\,d} - \vec{s}_j^{\,mc}|)\ . \tag{F.10}$$

The p-value is calculated by means of a re-sampling method often referred to as *permutation test* in the literature. This approach involves combing the data and Monte Carlo into a pooled sample of size $n_d + n_{mc}$. A sample of size n_d is then randomly drawn from the pooled sample and temporarily labelled as "data" while the remaining n_{mc} events are labelled "Monte Carlo". The test statistic T_{perm} is calculated for this configuration and the process is repeated n_{perm} times to obtain $\{T^1_{\text{perm}}, ..., T^{n_{\text{perm}}}_{\text{perm}}\}$. The p-value reads then as the fraction of times where $T < T^i_{\text{perm}}$.

The p-value is a function of the data and Monte Carlo, and is therefore itself a random variable. If the hypothesis $M = M_0$ used to compute the p-value is true, then p will be uniformly distributed between zero and one. Equivalently, the empirical cumulative density function (cdf) of the p-value will be a bisector function. It has been checked by generating several pseudo-experiments with a simplified Dalitz model involving four flavour specific, two CP-eigenstate and one flat non-resonant amplitudes. The logarithmic function is chosen to be the correlating function. The results of this cross-check are gathered in Fig. F.2.

The p-value estimator relevance is eventually tested by fitting two different PDF to a toy Monte Carlo sample. The toy sample is generated w.r.t the baseline model in Section 5.5.1 to which the scalar resonance $f_0(1500)$ is added. The two hypotheses tested are the baseline PDF plus $f_0(1500)$ (true hypothesis) and the baseline PDF. For the first (second) hypothesis test, a p-value equal to 0.83 (0.15) is found, in accordance with the qualitative expectation. Fig. F.3 shows the test statistic distributions for the first and second fit.

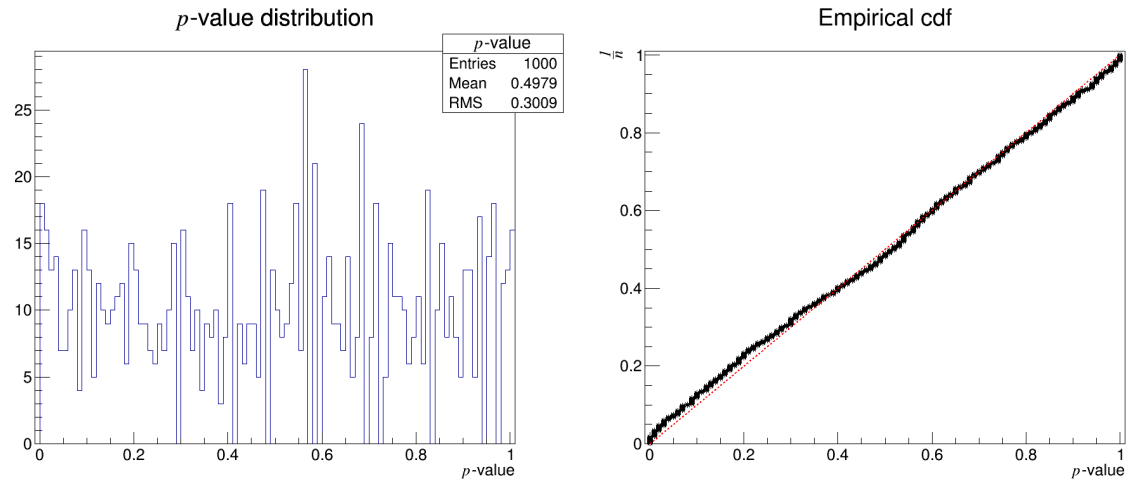

Figure F.2: p-value distribution obtained from data sets generated with Dalitz model containing $K^{*\pm}(892)$, $K_0^{*\pm}(1430)$, $f_0(980)$ and a flat non-resonant, using the point-to-point dissimilarity method, with the logarithmic correlation function, under the true hypothesis. The plot in right shows the empirical cdf of the p-values where the dashed red line represents the bisector function. The black points represent the calculated p-values.

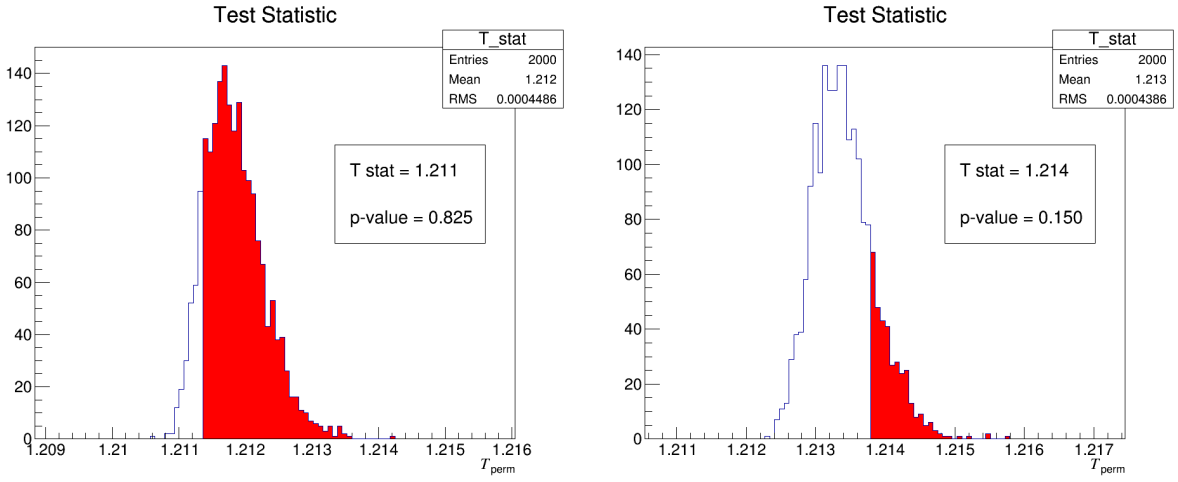

Figure F.3: Distribution of the statistics test T as calculated using the permutation test method. The left and right plots show the values for the first and second hypotheses test as indicated in the text. The red area corresponds to $T_{\text{perm}} > T$, which determines the observed p-value.

Appendix G

Efficiency - extra plots

This appendix contains plots related to the efficiency, in the main text of Section 5.3 plots were often shown only for 2011 conditions. Firstly, Figs. G.1 to G.5 show the corresponding total tracking efficiency correction, which is obtained from the event-by-event multiplication of the corrections for each track. Next, Figs. G.6 to G.15 show the uncorrected selection efficiency histograms for $B^0 \to K^0_S \pi^+ \pi^-$ decays and the asymmetric uncertainty on each bin. For each signal MC event, the PID efficiency was evaluated by using the appropriate efficiency maps to find the PID efficiency of each bachelor track, the results for the $B^0 \to K^0_S \pi^+ \pi^-$ are shown in Figs. G.16 to G.20.

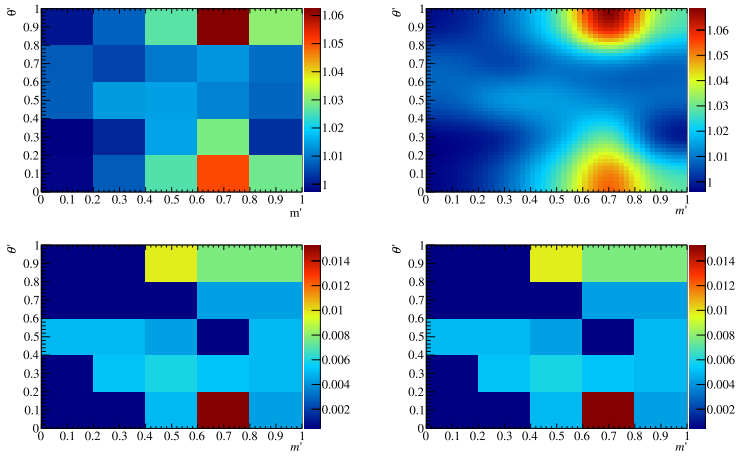

Figure G.1: *(Top) Combined tracking efficiency corrections in the $K^0_S \pi^+ \pi^-$ final state for LL and 2011 configuration: (left) the raw histogram obtained from MC simulation and (right) smoothed using a 2D cubic spline. (Bottom) the (left) upper and (right) lower uncertainties on the histogram bins.*

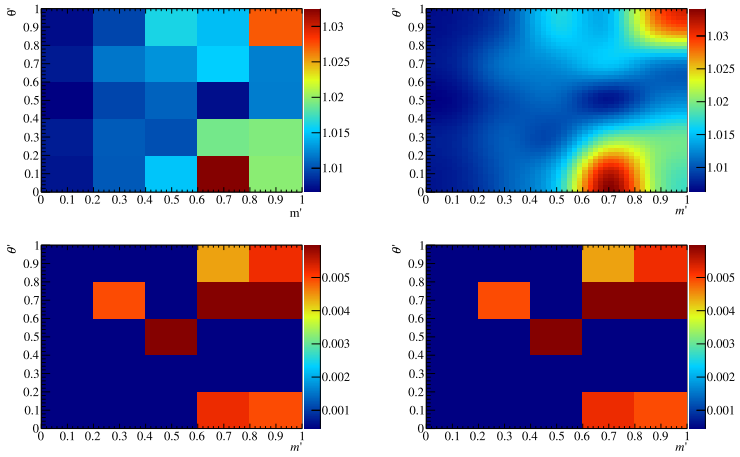

Figure G.2: *(Top) Combined tracking efficiency corrections in the $K^0_S\pi^+\pi^-$ final state for DD and 2012a configuration: (left) the raw histogram obtained from MC simulation and (right) smoothed using a 2D cubic spline. (Bottom) the (left) upper and (right) lower uncertainties on the histogram bins.*

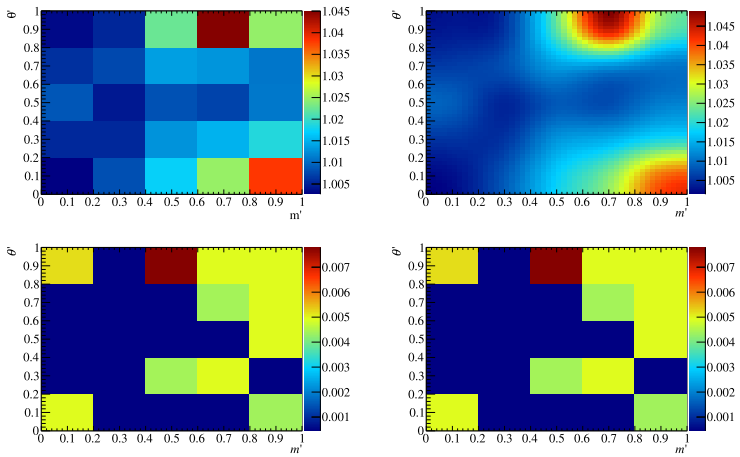

Figure G.3: *(Top) Combined tracking efficiency corrections in the $K^0_S\pi^+\pi^-$ final state for LL and 2012a configuration: (left) the raw histogram obtained from MC simulation and (right) smoothed using a 2D cubic spline. (Bottom) the (left) upper and (right) lower uncertainties on the histogram bins.*

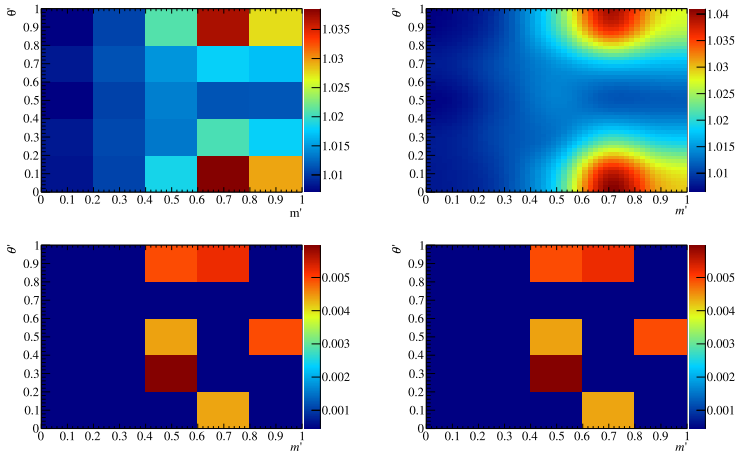

Figure G.4: *(Top) Combined tracking efficiency corrections in the $K^0_S\pi^+\pi^-$ final state for DD and 2012b configuration: (left) the raw histogram obtained from MC simulation and (right) smoothed using a 2D cubic spline. (Bottom) the (left) upper and (right) lower uncertainties on the histogram bins.*

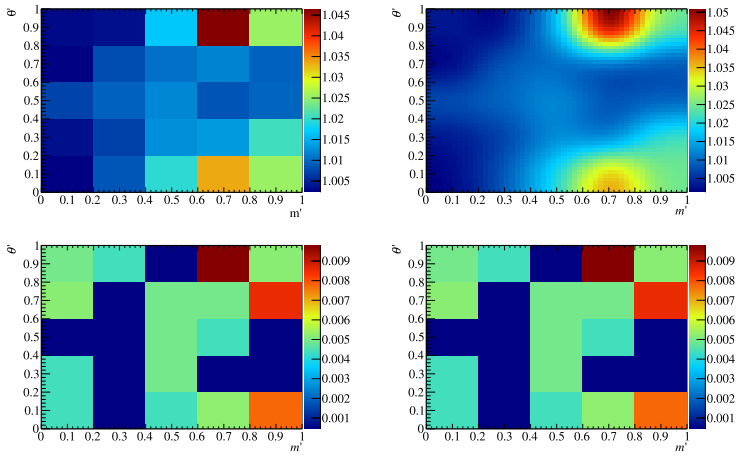

Figure G.5: *(Top) Combined tracking efficiency corrections in the $K^0_S\pi^+\pi^-$ final state for LL and 2012b configuration: (left) the raw histogram obtained from MC simulation and (right) smoothed using a 2D cubic spline. (Bottom) the (left) upper and (right) lower uncertainties on the histogram bins.*

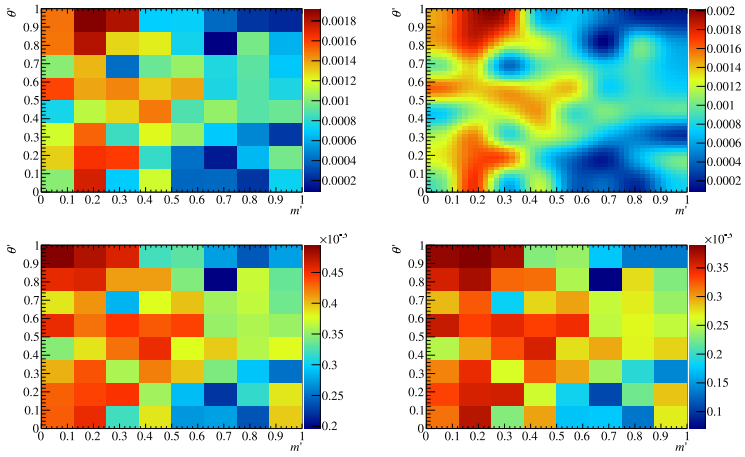

Figure G.6: *(Top)* $\epsilon^{\text{sel|geom}}$ *across the* $B^0 \to K^0_S\pi^+\pi^-$ *Long-Long 2011 square Dalitz plot for* `L0Hadron_TOS` *candidates: (left) the raw histogram obtained using the procedure described in the text and (right) smoothed using a 2D cubic spline. (Bottom) the (left) upper and (right) lower uncertainties on the histogram bins.*

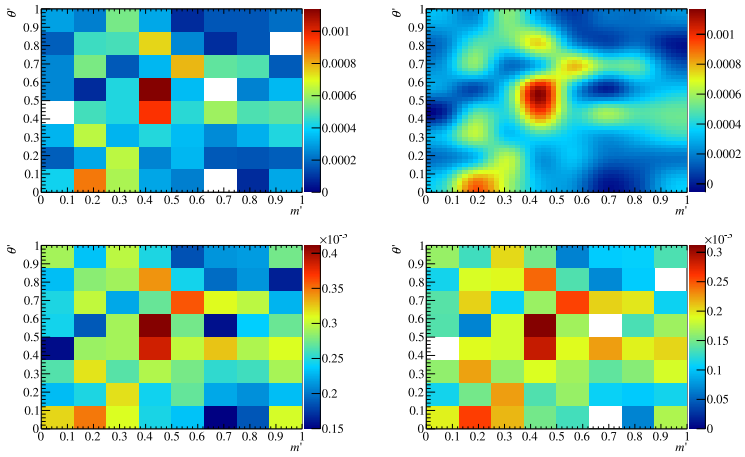

Figure G.7: *(Top)* $\epsilon^{\text{sel|geom}}$ *across the* $B^0 \to K^0_S\pi^+\pi^-$ *Long-Long 2011 square Dalitz plot for* `L0Global_TIS&&!L0Hadron_TOS` *candidates: (left) the raw histogram obtained using the procedure described in the text and (right) smoothed using a 2D cubic spline. (Bottom) the (left) upper and (right) lower uncertainties on the histogram bins.*

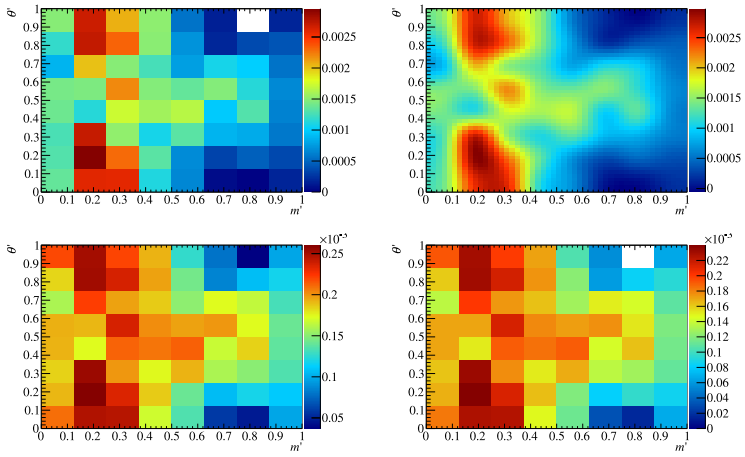

Figure G.8: *(Top)* $\epsilon^{\text{sel|geom}}$ *across the* $B^0 \to K^0_S\pi^+\pi^-$ *Down-Down 2012a square Dalitz plot for* `L0Hadron_TOS` *candidates: (left) the raw histogram obtained using the procedure described in the text and (right) smoothed using a 2D cubic spline. (Bottom) the (left) upper and (right) lower uncertainties on the histogram bins.*

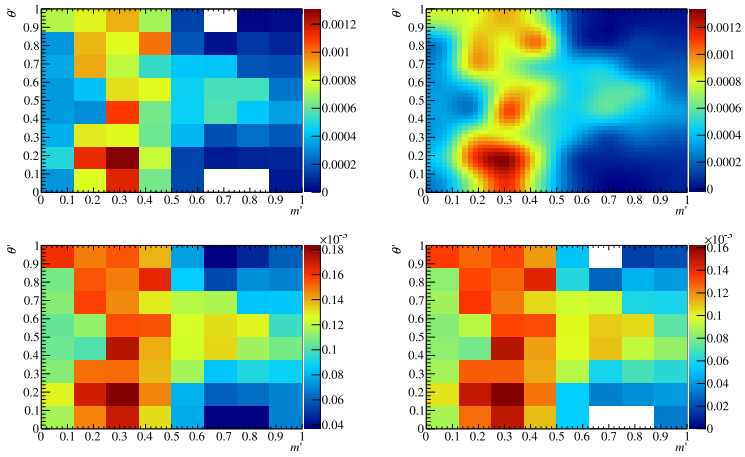

Figure G.9: *(Top)* $\epsilon^{\text{sel|geom}}$ *across the* $B^0 \to K^0_S\pi^+\pi^-$ *Down-Down 2012a square Dalitz plot for* `L0Global_TIS&&!L0Hadron_TOS` *candidates: (left) the raw histogram obtained using the procedure described in the text and (right) smoothed using a 2D cubic spline. (Bottom) the (left) upper and (right) lower uncertainties on the histogram bins.*

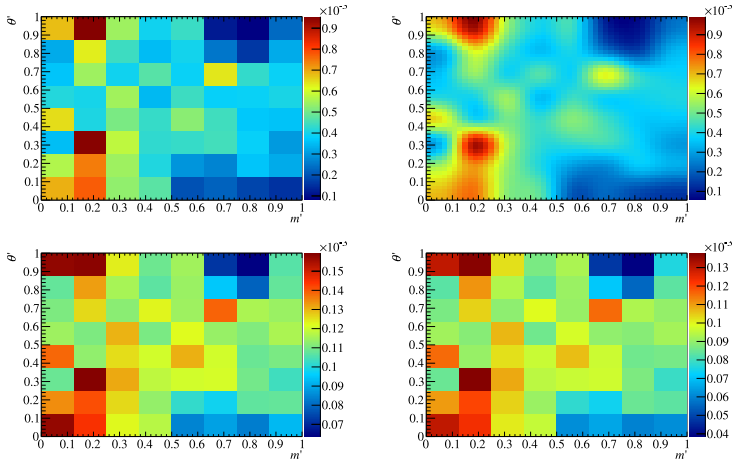

Figure G.10: *(Top)* $\epsilon^{\text{sel|geom}}$ *across the* $B^0 \to K^0_S\pi^+\pi^-$ *Long-Long 2012a square Dalitz plot for* `L0Hadron_TOS` *candidates: (left) the raw histogram obtained using the procedure described in the text and (right) smoothed using a 2D cubic spline. (Bottom) the (left) upper and (right) lower uncertainties on the histogram bins.*

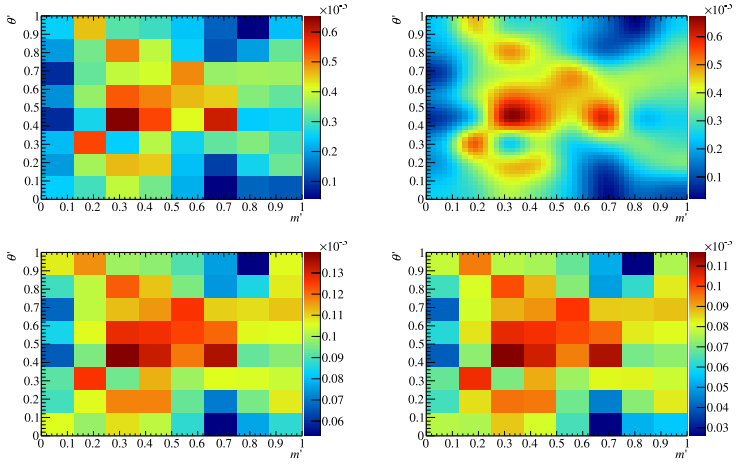

Figure G.11: *(Top)* $\epsilon^{\text{sel|geom}}$ *across the* $B^0 \to K^0_S\pi^+\pi^-$ *Long-Long 2012a square Dalitz plot for* `L0Global_TIS&&!L0Hadron_TOS` *candidates: (left) the raw histogram obtained using the procedure described in the text and (right) smoothed using a 2D cubic spline. (Bottom) the (left) upper and (right) lower uncertainties on the histogram bins.*

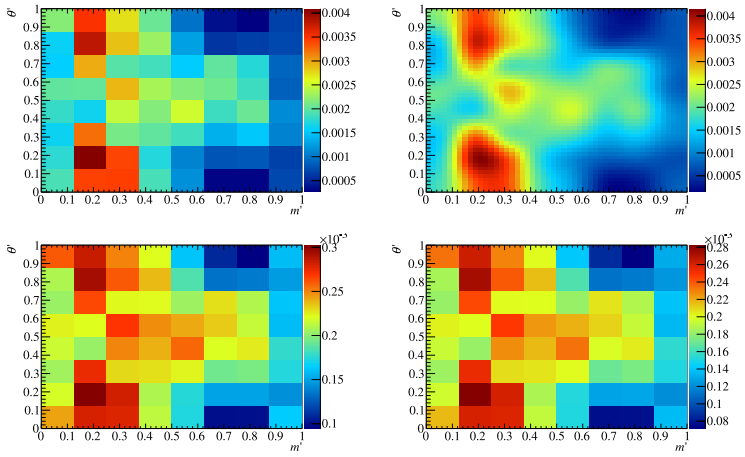

Figure G.12: *(Top)* $\epsilon^{\text{sel|geom}}$ *across the* $B^0 \to K^0_S\pi^+\pi^-$ *Down-Down 2012b square Dalitz plot for* `L0Hadron_TOS` *candidates: (left) the raw histogram obtained using the procedure described in the text and (right) smoothed using a 2D cubic spline. (Bottom) the (left) upper and (right) lower uncertainties on the histogram bins.*

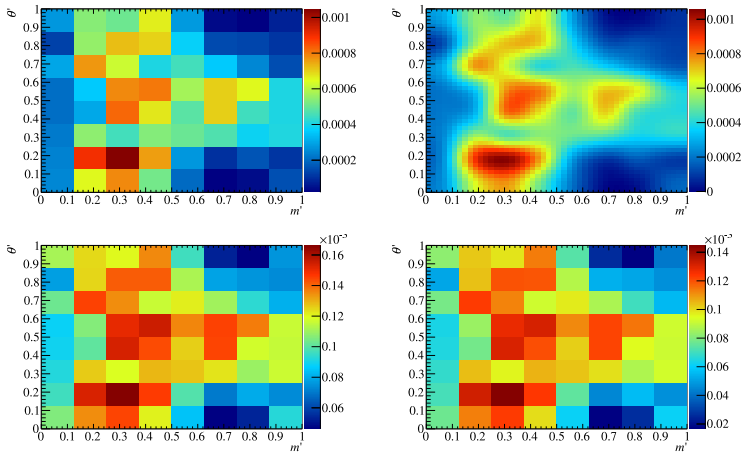

Figure G.13: *(Top)* $\epsilon^{\text{sel|geom}}$ *across the* $B^0 \to K^0_S\pi^+\pi^-$ *Down-Down 2012b square Dalitz plot for* `L0Global_TIS&&!L0Hadron_TOS` *candidates: (left) the raw histogram obtained using the procedure described in the text and (right) smoothed using a 2D cubic spline. (Bottom) the (left) upper and (right) lower uncertainties on the histogram bins.*

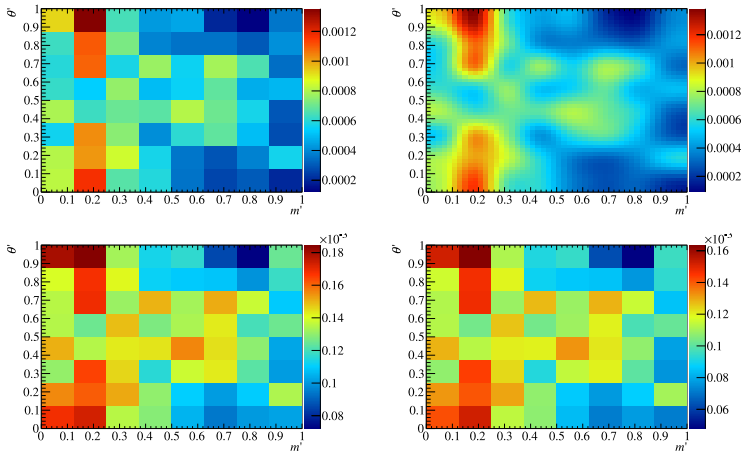

Figure G.14: *(Top)* $\epsilon^{\text{sel|geom}}$ *across the* $B^0 \to K^0_S\pi^+\pi^-$ *Long-Long 2012b square Dalitz plot for* `L0Hadron_TOS` *candidates: (left) the raw histogram obtained using the procedure described in the text and (right) smoothed using a 2D cubic spline. (Bottom) the (left) upper and (right) lower uncertainties on the histogram bins.*

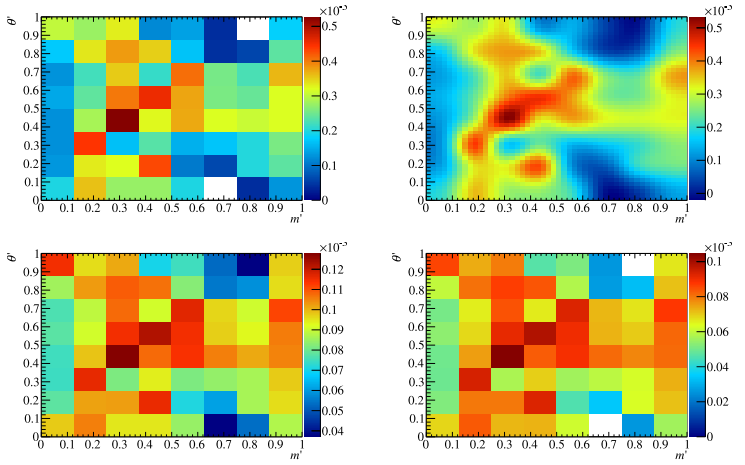

Figure G.15: *(Top)* $\epsilon^{\text{sel|geom}}$ *across the* $B^0 \to K^0_S\pi^+\pi^-$ *Long-Long 2012b square Dalitz plot for* `L0Global_TIS&&!L0Hadron_TOS` *candidates: (left) the raw histogram obtained using the procedure described in the text and (right) smoothed using a 2D cubic spline. (Bottom) the (left) upper and (right) lower uncertainties on the histogram bins.*

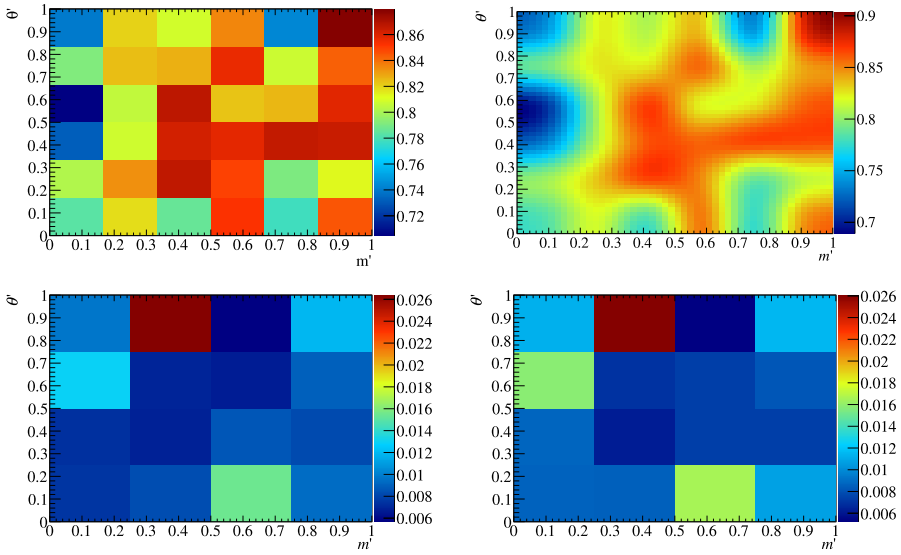

Figure G.16: *(Top)* $\epsilon^{\text{PID|sel\&geom}}$ *across the* $B^0 \to K^0_S\pi^+\pi^-$ *Long-Long 2011 square Dalitz plot: (left) the raw histogram obtained using the* `PIDCalib` *procedure described in the text and (right) smoothed using a 2D cubic spline. (Bottom) the (left) upper and (right) lower uncertainties on the histogram bins.*

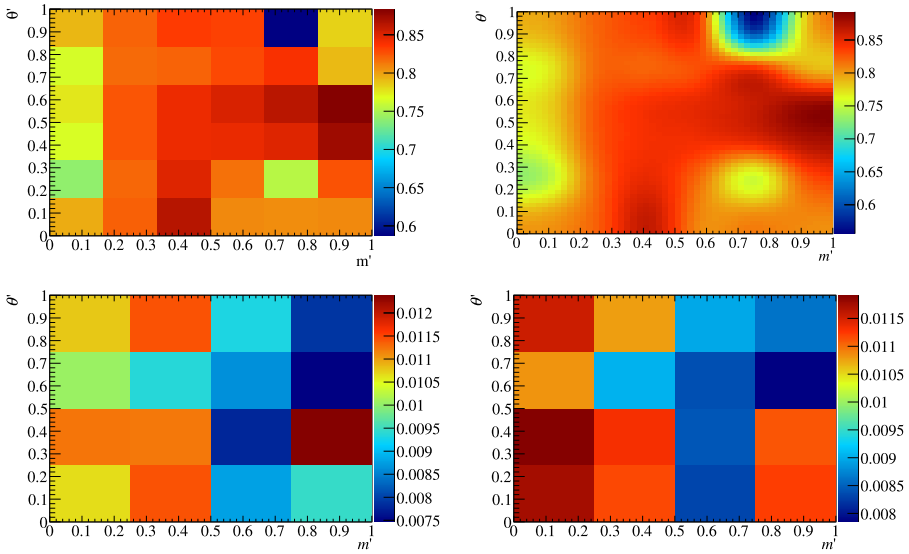

Figure G.17: *(Top)* $\epsilon^{\text{PID|sel\&geom}}$ *across the* $B^0 \to K^0_S\pi^+\pi^-$ *Down-Down 2012a square Dalitz plot: (left) the raw histogram obtained using the* `PIDCalib` *procedure described in the text and (right) smoothed using a 2D cubic spline. (Bottom) the (left) upper and (right) lower uncertainties on the histogram bins.*

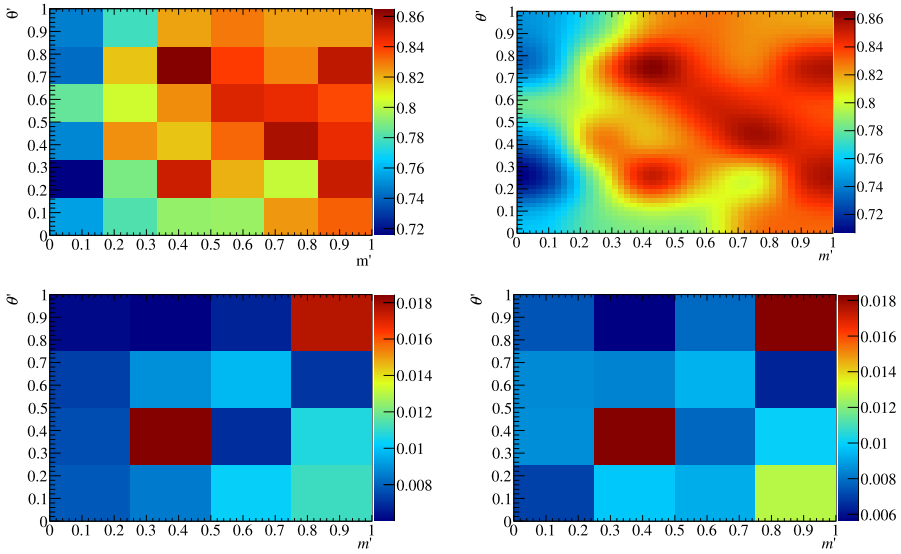

Figure G.18: *(Top)* $\epsilon^{\text{PID|sel\&geom}}$ *across the* $B^0 \to K^0_S\pi^+\pi^-$ *Long-Long 2012a square Dalitz plot: (left) the raw histogram obtained using the* `PIDCalib` *procedure described in the text and (right) smoothed using a 2D cubic spline. (Bottom) the (left) upper and (right) lower uncertainties on the histogram bins.*

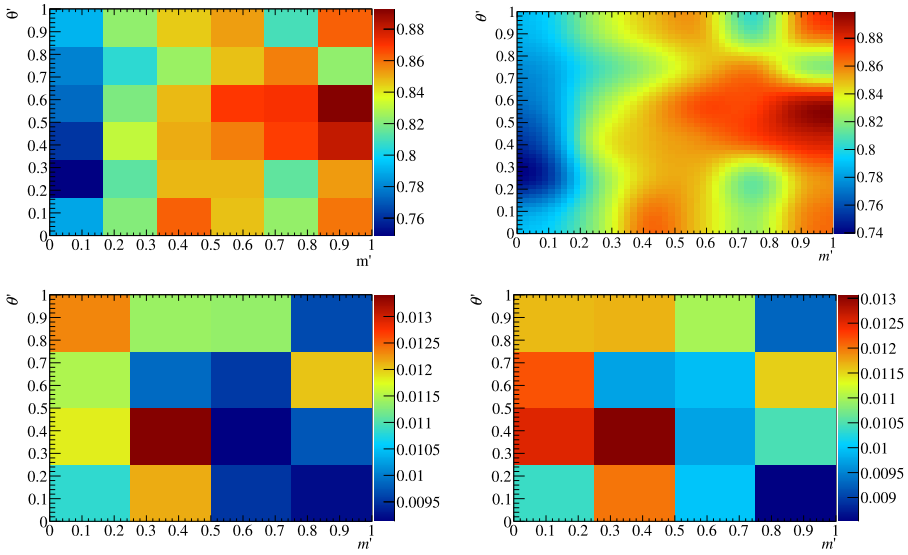

Figure G.19: *(Top)* $\epsilon^{\text{PID|sel\&geom}}$ *across the* $B^0 \to K^0_S\pi^+\pi^-$ *Down-Down 2012b square Dalitz plot: (left) the raw histogram obtained using the* `PIDCalib` *procedure described in the text and (right) smoothed using a 2D cubic spline. (Bottom) the (left) upper and (right) lower uncertainties on the histogram bins.*

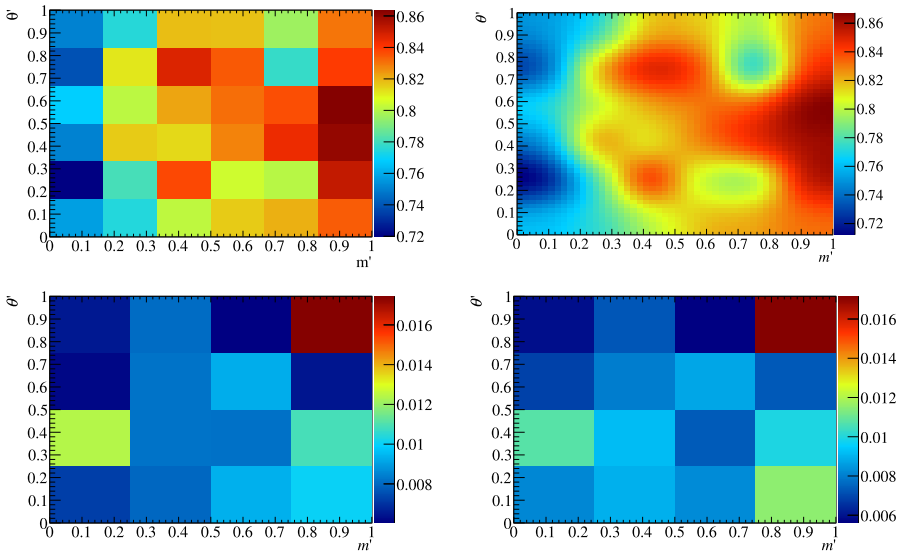

Figure G.20: *(Top)* $\epsilon^{\mathrm{PID|sel\&geom}}$ *across the* $B^0 \to K^0_S\pi^+\pi^-$ *Long-Long 2012b square Dalitz plot: (left) the raw histogram obtained using the* `PIDCalib` *procedure described in the text and (right) smoothed using a 2D cubic spline. (Bottom) the (left) upper and (right) lower uncertainties on the histogram bins.*

Appendix H

Second solution analysis

The best nll for the simultaneous fit to the data using the nominal model is found to be 28587.95. In the range of $2\Delta\text{nll} < 9$ units, a second solution is found at nll equal to 28590.7. The likelihood ratio hence reads $2\Delta\text{nll} = 5.4$, which can be interpreted as disfavoured by the data at more than 95 % Confidence Level. The fitted values of the Cartesian coordinates, magnitudes and *CP* asymmetries from the best and the secondary solution are gathered in Table H.1 and Table H.2, respectively. The main difference between the two solutions occurs in the low-invariant $\pi\pi$ mass region. The magnitude of the $f_0(500)$ is found five times larger in the second solution w.r.t. the best fit. For the rest of the parameters, the values from the two solutions are consistent as far as the magnitudes of the amplitude contributions are concerned.

Table H.1: Fit results of the Cartesian coordinates from the best and the secondary solution.

Resonance	Secondary solution		Best solution	
	Real part	Imag. part	Real part	Imag. part
$K^{*+}(892)$	-	-	-	-
$K^{*-}(892)$	-1.470 ± 0.108	-	-1.474 ± 0.086	-
$(K\pi)_0^{*+}$	1.805 ± 0.193	1.712 ± 0.211	1.816 ± 0.163	1.694 ± 0.190
$(K\pi)_0^{*-}$	2.564 ± 0.150	0.019 ± 0.261	2.569 ± 0.124	-0.029 ± 0.246
$K_2^{*+}(1430)$	-0.015 ± 0.120	0.583 ± 0.122	-0.004 ± 0.112	0.587 ± 0.113
$K_2^{*-}(1430)$	0.289 ± 0.113	0.246 ± 0.149	0.301 ± 0.090	0.232 ± 0.128
$f_0(980)$ from B^0	1.953 ± 0.449	0.745 ± 0.468	1.253 ± 0.456	1.615 ± 0.445
$f_0(980)$ from $\overline{B}^0$	2.547 ± 0.348	0.241 ± 0.508	1.933 ± 0.357	1.143 ± 0.486
$f_0(500)$	-1.231 ± 0.172	0.948 ± 0.227	0.309 ± 0.104	0.097 ± 0.158
$\rho^0(770)$	-0.416 ± 0.406	1.266 ± 0.163	-0.628 ± 0.412	1.142 ± 0.238
$f_0(1500)$	-0.557 ± 0.226	0.818 ± 0.110	-0.647 ± 0.320	0.661 ± 0.144
NR	1.340 ± 0.302	2.289 ± 0.156	1.373 ± 0.335	2.343 ± 0.151
χ_{c0}	-0.602 ± 0.112	0.481 ± 0.095	-0.598 ± 0.094	0.485 ± 0.089

Table H.2: Fit results of the magnitudes and (raw) *CP* asymmetries from the best and the secondary solution.

Resonance	Secondary solution		Best solution	
	Magnitude	*CP* asymm.	Magnitude	*CP* asymm.
$K^{*+}(892)$	-	-0.299 ± 0.067	-	-0.296 ± 0.053
$K^{*-}(892)$	1.470 ± 0.108		1.474 ± 0.086	
$(K\pi)_0^{*+}$	2.488 ± 0.238	0.030 ± 0.116	2.483 ± 0.135	0.034 ± 0.049
$(K\pi)_0^{*-}$	2.564 ± 0.150		2.569 ± 0.125	
$K_2^{*+}(1430)$	0.583 ± 0.122	-0.406 ± 0.357	0.587 ± 0.113	-0.410 ± 0.273
$K_2^{*-}(1430)$	0.379 ± 0.137		0.380 ± 0.105	
$f_0(980)$ from B^0	2.091 ± 0.504	0.199 ± 0.195	2.044 ± 0.386	0.094 ± 0.320
$f_0(980)$ from $\overline{B}^0$	2.558 ± 0.354		2.246 ± 0.350	
$f_0(500)$	1.553 ± 0.115	-	0.324 ± 0.115	-
$\rho^0(770)$	1.332 ± 0.134	-	1.303 ± 0.128	-
$f_0(1500)$	0.990 ± 0.148	-	0.925 ± 0.170	-
NR	2.652 ± 0.161	-	2.716 ± 0.163	-
χ_{c0}	0.770 ± 0.073	-	0.771 ± 0.060	-

Bibliography

[1] N. Cabibbo, *Unitary symmetry and leptonic decays*, Phys. Rev. Lett. **10** (1963) 531.

[2] M. Kobayashi and T. Maskawa, *CP violation in the renormalizable theory of weak interaction*, Prog. Theor. Phys. **49** (1973) 652.

[3] J. Charles *et al.*, *Current status of the Standard Model CKM fit and constraints on $\Delta F = 2$ New Physics*, Phys. Rev. **D91** (2015), no. 7 073007, arXiv:1501.0501.

[4] P. Huet and E. Sather, *Electroweak baryogenesis and standard model CP violation*, Phys. Rev. **D51** (1995) 379, arXiv:hep-ph/9404302.

[5] Heavy Flavor Averaging Group, Y. Amhis *et al.*, *Averages of b-hadron, c-hadron, and τ-lepton properties as of early 2012*, arXiv:1207.1158, updated results and plots available at http://www.slac.stanford.edu/xorg/hfag/.

[6] A. E. Snyder and H. R. Quinn, *Measuring CP asymmetry in $B \to \rho\pi$ decays without ambiguities*, Phys. Rev. **D48** (1993) 2139.

[7] J. Charles *et al.*, *$B^0(t) \to DPP$ time-dependent Dalitz plots, CP- violating angles 2β, $2\beta+\gamma$, and discrete ambiguities*, Phys. Lett. **B425** (1998) 375, arXiv:hep-ph/9801363.

[8] T. Latham and T. Gershon, *A method to measure* $\cos(2\beta)$ *using time-dependent Dalitz plot analysis of $B^0 \to D_{CP}\pi^+\pi^-$*, J. Phys. **G36** (2009) 025006, arXiv:0809.0872.

[9] M. Ciuchini, M. Pierini, and L. Silvestrini, *New bounds on the CKM matrix from $B \to K\pi\pi$ Dalitz plot analyses*, Phys. Rev. **D74** (2006) 051301, arXiv:hep-ph/0601233.

[10] M. Ciuchini, M. Pierini, and L. Silvestrini, *Hunting the CKM weak phase with time-integrated Dalitz analyses of $B_s^0 \to KK\pi$ and $B_s^0 \to K\pi\pi$ decays*, Phys. Lett. **B645** (2007) 201, arXiv:hep-ph/0602207.

[11] M. Gronau, D. Pirjol, A. Soni, and J. Zupan, *Improved method for CKM constraints in charmless three-body B and B_s^0 decays*, Phys. Rev. **D75** (2007) 014002, arXiv:hep-ph/0608243.

[12] M. Gronau, D. Pirjol, A. Soni, and J. Zupan, *Constraint on $\bar{\rho}, \bar{\eta}$ from $B \to K^*\pi$*, Phys. Rev. **D77** (2008) 057504, arXiv:0712.3751.

[13] I. Bediaga, G. Guerrer, and J. M. de Miranda, *Extracting the quark mixing phase γ from $B^\pm \to K^\pm\pi^+\pi^-$, $B^0 \to K_S\pi^+\pi^-$, and $\bar{B}^0 \to K_S\pi^+\pi^-$*, Phys. Rev. **D76** (2007) 073011, arXiv:hep-ph/0608268.

[14] BaBar Collaboration, B. Aubert *et al.*, *Time-dependent amplitude analysis of $B^0 \to K^0_S\pi^+\pi^-$*, Phys. Rev. **D80** (2009) 112001, arXiv:0905.3615.

[15] Belle collaboration, J. Dalseno *et al.*, *Time-dependent Dalitz Plot measurement of CP parameters in $B^0 \to K^0_S\pi^+\pi^-$ decays*, Phys. Rev. **D79** (2009) 072004, arXiv:0811.3665.

[16] P. W. Higgs, *Broken symmetries, massless particles and gauge fields*, Phys. Lett. **12** (1964) 132.

[17] P. W. Higgs, *Broken Symmetries and the Masses of Gauge Bosons*, Phys. Rev. Lett. **13** (1964) 508.

[18] F. Englert and R. Brout, *Broken Symmetry and the Mass of Gauge Vector Mesons*, Phys. Rev. Lett. **13** (1964) 321.

[19] DELPHI, OPAL, LEP Electroweak, ALEPH, L3, S. Schael *et al.*, *Electroweak Measurements in Electron-Positron Collisions at W-Boson-Pair Energies at LEP*, Phys. Rept. **532** (2013) 119, arXiv:1302.3415.

[20] Particle Data Group, K. A. Olive *et al.*, *Review of particle physics*, Chin. Phys. **C38** (2014) 090001.

[21] T. Altomari and L. Wolfenstein, *CALCULATION OF THE RATES FOR SEMILEPTONIC B DECAYS*, .

[22] T. Altomari and L. Wolfenstein, *Constraints on Semileptonic B Decays from the Measurement of the D-prime Polarization in B —> D-prime anti-neutrino*, Phys. Rev. **D37** (1988) 681.

[23] C. S. Wu *et al.*, *Experimental Test of Parity Conservation in Beta Decay*, Phys. Rev. **105** (1957) 1413.

[24] M. Gormley *et al.*, *Experimental test of c invariance in $\eta \to \pi^+\pi^-\pi^0$*, Phys. Rev. Lett. **21** (1968) 402.

[25] J. H. Christenson, J. W. Cronin, V. L. Fitch, and R. Turlay, *Evidence for the 2 pi Decay of the k(2)0 Meson*, Phys. Rev. Lett. **13** (1964) 138.

[26] LHCb collaboration, R. Aaij *et al.*, *First evidence of direct CP violation in charmless two-body decays of B^0_s mesons*, Phys. Rev. Lett. **108** (2012) 201601, arXiv:1202.6251.

[27] LHCb, R. Aaij *et al.*, *Measurement of the $B^0_s - \bar{B}^0_s$ oscillation frequency Δm_s in $B^0_s \to D^-_s(3)\pi$ decays*, Phys. Lett. **B709** (2012) 177, arXiv:1112.4311.

[28] LHCb, R. Aaij *et al.*, *Measurement of the B^0–$\bar{B}^0$ oscillation frequency Δm_d with the decays $B^0 \to D^- \pi^+$ and $B^0 \to J/\psi K^{*0}$*, Phys. Lett. **B719** (2013) 318, arXiv:1210.6750.

[29] LHCb, R. Aaij *et al.*, *Observation of B_s^0-$\bar{B}_s^0$ mixing and measurement of mixing frequencies using semileptonic B decays*, Eur. Phys. J. **C73** (2013), no. 12 2655, arXiv:1308.1302.

[30] J. C. Hardy and I. S. Towner, *Superallowed 0+ —> 0+ nuclear beta decays: A New survey with precision tests of the conserved vector current hypothesis and the standard model*, Phys. Rev. **C79** (2009) 055502, arXiv:0812.1202.

[31] CHARM II, P. Vilain *et al.*, *Leading order QCD analysis of neutrino induced dimuon events*, Eur. Phys. J. **C11** (1999) 19.

[32] DELPHI, P. Abreu *et al.*, *Measurement of |V(cs)| using W decays at LEP-2*, Phys. Lett. **B439** (1998) 209.

[33] CDF, D0, T. E. W. Group, *Combination of CDF and D0 Measurements of the Single Top Production Cross Section*, arXiv:0908.2171.

[34] (CKMfitter Group), J. Charles *et al.*, *Current status of the standard model ckm fit and constraints on $\Delta f = 2$ new physics*, Phys. Rev. D **91** (2015) 073007.

[35] M. Ciuchini *et al.*, *CP violating B decays in the Standard Model and supersymmetry*, Phys. Rev. Lett. **79** (1997) 978, arXiv:hep-ph/9704274.

[36] M. Gronau and J. L. Rosner, *Isospin of new physics in |Delta S| = 1 charmless B decays*, Phys. Rev. **D75** (2007) 094006, arXiv:hep-ph/0702193.

[37] BaBar collaboration, J. P. Lees *et al.*, *Study of CP violation in Dalitz-plot analyses of $B^0 \to K^+K^-K^0_S$, $B^+ \to K^+K^-K^+$, and $B^+ \to K^0_S K^0_S K^+$*, Phys. Rev. **D85** (2012) 112010, arXiv:1201.5897.

[38] R. H. Dalitz, *On the analysis of tau-meson data and the nature of the tau-meson*, Phil. Mag. **44** (1953) 1068.

[39] R. H. Dalitz, *Decay of tau mesons of known charge*, Phys. Rev. **94** (1954) 1046.

[40] G. N. Fleming, *Recoupling effects in the isobar model. 1. General formalism for three-pion scattering*, Phys. Rev. **135** (1964) B551.

[41] C. Zemach, *Determination of the Spins and Parities of Resonances*, Phys. Rev. **140** (1965) B109.

[42] J. Blatt and V. Weisskopf, , Theoretical Nuclear Physics New-York (1952).

[43] G. J. Gounaris and J. J. Sakurai, *Finite width corrections to the vector meson dominance prediction for rho —> e+ e-*, Phys. Rev. Lett. **21** (1968) 244.

[44] S. M. Flatte, *Coupled - Channel Analysis of the pi eta and K anti-K Systems Near K anti-K Threshold*, Phys. Lett. **B63** (1976) 224.

[45] D. Aston *et al.*, *A Study of K- pi+ Scattering in the Reaction K- p —> K- pi+ n at 11-GeV/c*, Nucl. Phys. **B296** (1988) 493.

[46] BaBar, B. Aubert *et al.*, *Dalitz Plot Analysis of B+- —> pi+-pi+-pi-+ Decays*, Phys. Rev. **D79** (2009) 072006, arXiv:0902.2051.

[47] LHCb collaboration, A. A. Alves Jr. *et al.*, *The LHCb detector at the LHC*, JINST **3** (2008) S08005.

[48] T. A. Collaboration, *The atlas experiment at the cern large hadron collider*, Journal of Instrumentation **3** (2008), no. 08 S08003.

[49] T. C. Collaboration, *The cms experiment at the cern lhc*, Journal of Instrumentation **3** (2008), no. 08 S08004.

[50] ATLAS, G. Aad *et al.*, *Observation of a new particle in the search for the Standard Model Higgs boson with the ATLAS detector at the LHC*, Phys. Lett. **B716** (2013) 1, arXiv:1207.7214.

[51] CMS, S. Chatrchyan *et al.*, *Observation of a new boson at a mass of 125 GeV with the CMS experiment at the LHC*, Phys. Lett. **B716** (2013) 30, arXiv:1207.7235.

[52] T. A. Collaboration, *The alice experiment at the cern lhc*, Journal of Instrumentation **3** (2008), no. 08 S08002.

[53] CERN, *The Large Hadron Collider: Conceptual design*, .

[54] M. Lamont, *Status of the lhc*, Journal of Physics: Conference Series **455** (2013), no. 1 012001.

[55] F. Follin and D. Jacquet, *Implementation and experience with luminosity levelling with offset beam*, in *Proceedings, ICFA Mini-Workshop on Beam-Beam Effects in Hadron Colliders (BB2013)*, pp. 183–187, 2014. arXiv:1410.3667. [,183(2014)], doi: 10.5170/CERN-2014-004.183.

[56] T. Sjostrand *et al.*, *High-energy physics event generation with PYTHIA 6.1*, Comput. Phys. Commun. **135** (2001) 238, arXiv:hep-ph/0010017.

[57] LHCb VELO Group, H. L. Snoek, *The LHCb VELO: Performance and radiation damage*, Nucl. Instrum. Meth. **A765** (2014) 35.

[58] LHCb VELO Group, R. Aaij *et al.*, *Performance of the LHCb Vertex Locator*, J. Instrum. **9** (2014) P09007. 61 p, Comments: 61 pages, 33 figures.

[59] LHCb, R. Aaij *et al.*, *Measurement of the track reconstruction efficiency at LHCb*, JINST **10** (2015), no. 02 P02007, arXiv:1408.1251.

[60] LHCb, R. Aaij *et al.*, *Measurement of b-hadron branching fractions for two-body decays into charmless charged hadrons*, JHEP **10** (2012) 037, arXiv:1206.2794.

[61] LHCb, R. Aaij *et al.*, *First Evidence for the Decay $B_s^0 \to \mu^+\mu^-$*, Phys. Rev. Lett. **110** (2013), no. 2 021801, arXiv:1211.2674.

[62] LHCb, R. Aaij *et al.*, *Measurement of the CP-violating phase ϕ_s in the decay $B_s^0 \to J/\psi\phi$*, Phys. Rev. Lett. **108** (2012) 101803, arXiv:1112.3183.

[63] LHCb, R. Aaij *et al.*, *Search for hidden-sector bosons in $B^0 \to K^{*0}\mu^+\mu^-$ decays*, arXiv:1508.0409.

[64] G. Passaleva, *A recurrent neural network for track reconstruction in the lhcb muon system*, in *Nuclear Science Symposium Conference Record, 2008. NSS '08. IEEE*, pp. 867–872, Oct, 2008. doi: 10.1109/NSSMIC.2008.4774532.

[65] Brunel. http://lhcb-release-area.web.cern.ch/LHCb-release-area/DOC/brunel/.

[66] Gaudi. http://lhcb-comp.web.cern.ch/lhcb-comp/Frameworks/Gaudi/.

[67] Gauss. http://lhcb-release-area.web.cern.ch/LHCb-release-area/DOC/gauss/.

[68] Geant4 collaboration, S. Agostinelli *et al.*, *Geant4: a simulation toolkit*, Nucl. Instrum. Meth. **A506** (2003) 250.

[69] Geant4 collaboration, J. Allison *et al.*, *Geant4 developments and applications*, IEEE Trans. Nucl. Sci. **53** (2006) 270.

[70] Boole. http://lhcb-release-area.web.cern.ch/LHCb-release-area/DOC/boole/.

[71] Moore. http://lhcb-release-area.web.cern.ch/LHCb-release-area/DOC/moore/.

[72] Davinci. http://lhcb-release-area.web.cern.ch/LHCb-release-area/DOC/davinci/.

[73] PIDCalib. https://twiki.cern.ch/twiki/bin/view/LHCb/PIDCalibPackage.

[74] I. Antcheva *et al.*, *{ROOT}, a c++ framework for petabyte data storage, statistical analysis and visualization*, Computer Physics Communications **180** (2009), no. 12 2499 , 40 {YEARS} {OF} CPC: A celebratory issue focused on quality software for high performance, grid and novel computing architectures.

[75] M. Baalouch *et al.*, *Update on the $B^0_{(s)} \to K^0_S h^+ h'^-$*, LHCb-ANA-2013-009.

[76] V. V. Gligorov and M. Williams, *Efficient, reliable and fast high-level triggering using a bonsai boosted decision tree*, Journal of Instrumentation **8** (2013) 2013P, arXiv:1210.6861.

[77] LHCb collaboration, R. Aaij *et al.*, *Study of $B^0_{(s)} \to K^0_S h^+ h'^-$ decays with first observation of $B^0_s \to K^0_S K^\pm \pi^\mp$ and $B^0_s \to K^0_S \pi^+ \pi^-$*, JHEP **10** (2013) 143, arXiv:1307.7648.

[78] M. Pivk and F. R. Le Diberder, *sPlot: A statistical tool to unfold data distributions*, Nucl. Instrum. Meth. **A555** (2005) 356, arXiv:physics/0402083.

[79] G. Punzi, *Sensitivity of searches for new signals and its optimization*, in *Statistical Problems in Particle Physics, Astrophysics, and Cosmology* (L. Lyons, R. Mount, and R. Reitmeyer, eds.), p. 79, 2003. arXiv:physics/0308063.

[80] R. Silva Coutinho, T. Gershon, and T. Latham, *Figures of merit for selection optimisation in Dalitz-plot analyses*, LHCb-INT-2015-003.

[81] M. Baalouch *et al.*, *Dalitz-plot analysis of the decay* $B^0 \to K^0_S\pi^+\pi^-$, LHCb-ANA-2014-044.

[82] LHCb collaboration, *Branching fraction measurements of* $B^0_{d,s}$ *decays to* $K^0_S hh'$ *final states, including first observation of* $B^0_s \to K_S K\pi$, LHCb-CONF-2012-023.

[83] M. Baalouch *et al.*, *Search for the decay the decay* $B^0_{(s)} \to K^0_S K^+K^-$, LHCb-ANA-2014-043.

[84] E. Ben Haim, L. Henry, and D. Milanes, *Fast Monte-Carlo method for partially-reconstructed background in* $B_{d,s} \to K^0_S hh'$ *decays*, LHCb-INT-2015-017. CERN-LHCb-INT-2015-017.

[85] LHCb, R. Aaij *et al.*, *Study of* $B^0_{(s)} \to K^0_S h^+h'^-$ *decays with first observation of* $B^0_s \to K^0_S K^\pm\pi^\mp$ *and* $B^0_s \to K^0_S\pi^+\pi^-$, JHEP **10** (2013) 143, arXiv:1307.7648.

[86] G. Walberg, *Cubic spline interpolation: A review*, .

[87] M. Baalouch *et al.*, *Dalitz-plot analysis of the decays* $B^0_s \to K^0_S K^\pm\pi^\mp$, LHCb-ANA-2014-045.

[88] M. De Cian *et al.*, *Measurement of the track finding efficiency*, Tech. Rep. LHCb-PUB-2011-025. CERN-LHCb-PUB-2011-025, CERN, Geneva, Apr, 2012. More details can be found here: https://twiki.cern.ch/twiki/bin/view/LHCb/LHCbTrackingEfficiencies °elax.

[89] A. Martin Sanchez, P. Robbe, and M.-H. Schune, *Performances of the LHCb L0 Calorimeter Trigger*, Tech. Rep. LHCb-PUB-2011-026. CERN-LHCb-PUB-2011-026, CERN, Geneva, Jun, 2012. More details can be found here: https://twiki.cern.ch/twiki/bin/viewauth/LHCbPhysics/CalorimeterObjectsToolsGroupDOC#L0_Hadron_trigger_efficiencies.

[90] Belle Collaboration, J. Dalseno *et al.*, *Time-dependent Dalitz Plot Measurement of CP Parameters in* $B^0 \to K^0_S\pi^+\pi^-$ *Decays*, Phys. Rev. **D79** (2009) 072004, arXiv:0811.3665.

[91] BES, M. Ablikim *et al.*, *Resonances in J / psi —> phi pi+ pi- and phi K+ K-*, Phys. Lett. **B607** (2005) 243, arXiv:hep-ex/0411001.

[92] CLEO, H. Muramatsu *et al.*, *Dalitz analysis of D0 —> K0(S) pi+ pi-*, Phys. Rev. Lett. **89** (2002) 251802, arXiv:hep-ex/0207067.

[93] Particle Data Group, J. Beringer *et al.*, *Review of particle physics*, Phys. Rev. **D86** (2012) 010001, and 2013 partial update for the 2014 edition.

[94] D. V. Bugg, *Comments on the sigma and kappa*, Phys. Lett. **B572** (2003) 1, [Erratum: Phys. Lett.B595,556(2004)].

[95] LHCb collaboration, R. Aaij *et al.*, *First observation of CP violation in the decays of B_s^0 mesons*, Phys. Rev. Lett. **110** (2013) 221601, arXiv:1304.6173.

[96] LHCb collaboration, R. Aaij *et al.*, *Measurement of the D_s^+–D_s^- production asymmetry in 7 TeV pp collisions*, Phys. Lett. **B713** (2012) 186, arXiv:1205.0897.

[97] M. Williams, *How good are your fits? Unbinned multivariate goodness-of-fit tests in high energy physics*, JINST **5** (2010) P09004, arXiv:1006.3019.

[98] L. Baringhaus and C. Franz, *On a new multivariate two-sample test*, Journal of Multivariate Analysis **88** (2004), no. 1 190 .